SOLAR AND SPACE WEATHER RADIO PHYSICS

EDITED BY: Bin Chen, Dale E. Gary and Nicole Vilmer
PUBLISHED IN: Frontiers in Astronomy and Space Sciences

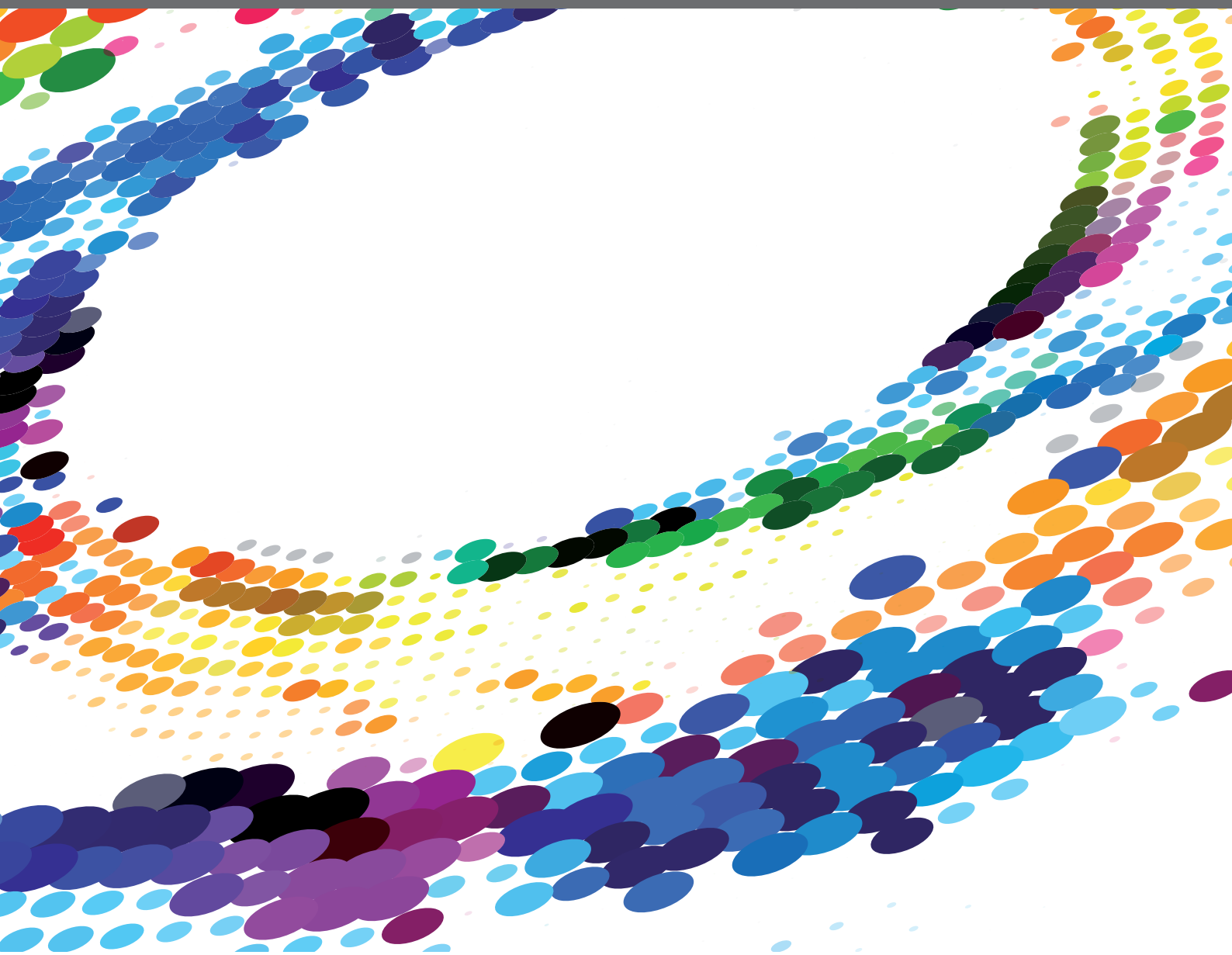

frontiers Research Topics

ISSN 1664-8714
ISBN 978-2-88971-106-2
DOI 10.3389/978-2-88971-106-2

About Frontiers

Frontiers is more than just an open-access publisher of scholarly articles: it is a pioneering approach to the world of academia, radically improving the way scholarly research is managed. The grand vision of Frontiers is a world where all people have an equal opportunity to seek, share and generate knowledge. Frontiers provides immediate and permanent online open access to all its publications, but this alone is not enough to realize our grand goals.

Frontiers Journal Series

The Frontiers Journal Series is a multi-tier and interdisciplinary set of open-access, online journals, promising a paradigm shift from the current review, selection and dissemination processes in academic publishing. All Frontiers journals are driven by researchers for researchers; therefore, they constitute a service to the scholarly community. At the same time, the Frontiers Journal Series operates on a revolutionary invention, the tiered publishing system, initially addressing specific communities of scholars, and gradually climbing up to broader public understanding, thus serving the interests of the lay society, too.

Dedication to Quality

Each Frontiers article is a landmark of the highest quality, thanks to genuinely collaborative interactions between authors and review editors, who include some of the world's best academicians. Research must be certified by peers before entering a stream of knowledge that may eventually reach the public - and shape society; therefore, Frontiers only applies the most rigorous and unbiased reviews.
Frontiers revolutionizes research publishing by freely delivering the most outstanding research, evaluated with no bias from both the academic and social point of view. By applying the most advanced information technologies, Frontiers is catapulting scholarly publishing into a new generation.

What are Frontiers Research Topics?

Frontiers Research Topics are very popular trademarks of the Frontiers Journals Series: they are collections of at least ten articles, all centered on a particular subject. With their unique mix of varied contributions from Original Research to Review Articles, Frontiers Research Topics unify the most influential researchers, the latest key findings and historical advances in a hot research area! Find out more on how to host your own Frontiers Research Topic or contribute to one as an author by contacting the Frontiers Editorial Office: frontiersin.org/about/contact

SOLAR AND SPACE WEATHER RADIO PHYSICS

Topic Editors:
Bin Chen, New Jersey Institute of Technology, United States
Dale E. Gary, New Jersey Institute of Technology, United States
Nicole Vilmer, Centre National de la Recherche Scientifique (CNRS), France

Citation: Chen, B., Gary, D. E., Vilmer, N., eds. (2021). Solar and Space Weather Radio Physics. Lausanne: Frontiers Media SA. doi: 10.3389/978-2-88971-106-2

Table of Contents

frontiers in Astronomy and Space Sciences

ORIGINAL RESEARCH
published: 27 May 2020
doi: 10.3389/fspas.2020.00022

Evolution of Flare-Accelerated Electrons Quantified by Spatially Resolved Analysis

Natsuha Kuroda[1,2]*, *Gregory D. Fleishman*[3], *Dale E. Gary*[3], *Gelu M. Nita*[3], *Bin Chen*[3] and *Sijie Yu*[3]

[1] University Corporation for Atmospheric Research, Boulder, CO, United States, [2] Naval Research Laboratory, Washington, DC, United States, [3] Department of Physics, New Jersey Institute of Technology, Newark, NJ, United States

Non–thermal electrons accelerated in solar flares produce electromagnetic emission in two distinct, highly complementary domains—hard X-rays (HXRs) and microwaves (MWs). This paper reports MW imaging spectroscopy observations from the Expanded Owens Valley Solar Array of an M1.2 flare that occurred on 2017 September 9, from which we deduce evolving coronal parameter maps. We analyze these data jointly with the complementary Reuven Ramaty High-Energy Solar Spectroscopic Imager HXR data to reveal the spatially-resolved evolution of the non-thermal electrons in the flaring volume. We find that the high-energy portion of the non-thermal electron distribution, responsible for the MW emission, displays a much more prominent evolution (in the form of strong spectral hardening) than the low-energy portion, responsible for the HXR emission. We show that the revealed trends are consistent with a single electron population evolving according to a simplified trap-plus-precipitation model with sustained injection/acceleration of non-thermal electrons, which produces a double-powerlaw with steadily increasing break energy.

Keywords: solar flares, microwave, imaging spectroscopy, non-thermal electrons, numerical modeling, X-ray, corona, evolution

OPEN ACCESS

Edited by:
Xueshang Feng, National Space Science Center (CAS), China

Reviewed by:
Yao Chen, Shandong University, China
Siming Liu, Purple Mountain Observatory (CAS), China

***Correspondence:**
Natsuha Kuroda
nkuroda@ucar.edu

Specialty section:
This article was submitted to Stellar and Solar Physics, a section of the journal Frontiers in Astronomy and Space Sciences

Received: *05 January 2020*
Accepted: *27 April 2020*
Published: *27 May 2020*

Citation:
Kuroda N, Fleishman GD, Gary DE, Nita GM, Chen B and Yu S (2020) Evolution of Flare-Accelerated Electrons Quantified by Spatially Resolved Analysis. Front. Astron. Space Sci. 7:22. doi: 10.3389/fspas.2020.00022

1. INTRODUCTION

Solar flares are the manifestations of free magnetic energy conversion to other forms—thermal, non-thermal, and kinetic. Often, a large fraction of this energy goes into acceleration of ambient charged particles (Lin and Hudson, 1971; Emslie et al., 2012; Aschwanden et al., 2016), making the non-thermal particles dynamically and energetically important. Probing the accelerated electrons may be done by exploiting the non-thermal emissions they produce—the hard X-ray (HXR) and microwave (MW) spatial, spectral, and temporal signatures. HXRs are produced by bremsstrahlung from dense regions, as a signature of either the footpoint bombardment by the electron beams (e.g., Hoyng et al., 1981) or dense coronal regions, which might be the particle acceleration region itself (Masuda et al., 1994; Krucker et al., 2010; Krucker and Battaglia, 2014). The MWs are dominated by the gyrosynchrotron (GS) emission due to non-thermal electrons gyrating in the coronal magnetic field with a contribution from free-free emission. As a result of these distinct emission mechanisms, even a single population of non-thermal electrons distributed over a single (but possibly magnetically-asymmetric) flaring loop yields spatially-displaced HXR and MW emissions (e.g., Fleishman et al., 2016b). While most of the HXR spectrum is formed by non-thermal electrons with energies from a few to a (few) hundred keV, the spectrum of the GS-emitting electrons may

extend to much higher energies including the MeV range (Nitta and Kosugi, 1986; Kundu et al., 1994). In the complex magnetic topology of a solar flare, the flare-accelerated electrons tend to fill out any magnetic flux tube to which they have access. The magnetic-field-dominated GS emission can be strong even from those spatial locations that are HXR-faint due to their low ambient density. Indeed, Fleishman et al. (2018a) found that MW low frequency sources, indicative of low magnetic field high in the corona, are typically much larger than the HXR sources. Therefore, the HXR and MW data offer complementary information on both the energy and spatial distributions of the non-thermal electrons. This implies that both spectrally and spatially resolved data are needed to probe the non-thermal electrons most comprehensively.

Compared with the HXRs (White et al., 2011), the spatial distribution of MW-emitting electrons is often much larger (and richer in complexity), so MW emission is well-suited to quantify the accelerated electrons in space. Glesener and Fleishman (2018) studied the non-thermal electrons in a flare-jet configuration and found an equipartition of the non-thermal energies between populations in the closed and open magnetic flux tubes. Closed flaring flux tubes can represent rather large reservoirs of high-energy electrons located either nearby (Kuroda et al., 2018) or far away from Fleishman et al. (Fleishman et al., 2017) the main flare acceleration sites, possibly providing the seed population for solar energetic particles (SEPs). Fleishman et al. (2011, 2013, 2016a) probed the acceleration sites using MW observations and concluded that the acceleration regime was consistent with stochastic acceleration, while Fleishman et al. (2018b) extended in time the studies of Fleishman et al. (2016b) and Kuroda et al. (2018) to quantify the acceleration and transport of the non-thermal electrons in the 3D domain. In all of these studies, broadband MW spectroscopy and imaging have been crucial.

Until recently, a critical element was missing from the observations—the ability to make high-fidelity MW images at many frequencies from which to obtain spatially-resolved spectra. This ability has become available with the Expanded Owens Valley Solar Array (EOVSA; Nita et al., 2016; Gary et al., 2018). This solar-dedicated radio interferometer can image flares anywhere on the solar disk at hundreds of frequencies spread over 1–18 GHz at 1 s cadence. The spatially-resolved spectrum from each pixel in the high-resolution images obtained with EOVSA can be forward-fit with a "cost function" that accounts for GS and free–free radio emission and absorption (Fleishman et al., 2020). As a result, one can now simultaneously obtain all relevant physical parameters over the entire source region at the desired cadence down to 1 s (Fleishman et al., 2009; Fleishman et al., 2020; Gary et al., 2013). This novel and unique methodology allows the quantitative study of the spatial distribution and the temporal evolution of the magnetic field and the plasma in the corona in much greater detail than was previously possible.

Since the start of full operations in April 2017, EOVSA has recorded MW imaging spectroscopic observations of dozens of flares in all sizes, including some of the largest flares in Solar Cycle 24, which occurred during the 2017 September period (Gary et al., 2018). Previous papers using EOVSA imaging data have all focused on the well-observed 2017 Sep 10 flare (the second largest X-class flare of solar cycle # 24) (Gary et al., 2018; Fleishman et al., 2020). This paper reports observations of a second flare observed during the same 2017 September period, a mid-sized M1.2 flare that occurred on 2017 Sep 9. We employ the MW forward-fitting technique, augmented by observations in HXRs and extreme ultra-violet (EUV) available from the *Reuven Ramaty High-Energy Solar Spectroscopic Imager* (*RHESSI*; Lin et al., 2002) and the *Atmospheric Imaging Assembly* (*AIA;* Lemen et al., 2012) on the *Solar Dynamics Observervatory* (*SDO*), respectively. In particular, we focus on the comparison of the electrons emitting MW in the corona and those emitting non-thermal, thick-target HXRs in the lower atmosphere.

2. MULTI-WAVELENGTHS OBSERVATION

The M1.2 flare (SOL2017-09-09T22:04) started at around 22:04 UT and peaked around 23:53 UT in the 1.0–8.0 Å channel of the *Geostationary Operational Environmental Satellite* (*GOES*) soft X-ray monitor on 2017 September 9. The source active region (AR) 12673 was centered at S09W88, very close to the west limb. This active region produced the largest flare in Solar Cycle 24 on September 6 (X9.3) among other large flares in the same period (e.g., M5.5 on September 4, X1.3 on September 7, and X8.2 on September 10).

The EOVSA images were generated by combining multiple frequency channels over the available 134 frequency channels, to yield 30 spectral windows (spws) over the 3.4–17.9 GHz range. The width of each spw was 160 MHz and the center frequencies were $f_{GHz} = 2.92 + n/2$ (Gary et al., 2018). The images were integrated over 4 s to increase the signal-to-noise ratio (SNR), which reduced the temporal cadence to 4 s.

The HXR images were obtained by the image reconstruction software (Schwartz et al., 2002) using the CLEAN algorithm with an integration time of 2 min, collimators 6 and 8, which have the nominal FWHM resolutions of 35.3″ and 105.8″, respectively, and the clean beam width factor of 1.0. The detector choice was made based on the combination of the default detector choice generated by the software at the time of the analysis and the information from the Quicklook per-minute count spectra available from the *RHESSI* Browser[1].

Figure 1 left panel shows the flare development seen in MW by EOVSA (solid colored contours), complemented by EUV 131 and 171 Å (background) images from AIA and the HXR dashed contours from *RHESSI*. The images are plotted for four instances denoted t_1–t_4 during the time range from 22:44:02 to 22:49:26 UT, which are indicated on the right panel with the black vertical lines in the lighcurves from *GOES*, EOVSA, and *The Gamma-ray Burst Monitor* (*GBM*) on board the *Fermi Gamma-Ray Space Telescope* (*FERMI*; Atwood et al., 2009) (**Supplemental Movie 1** available). In the bottom right panel we show the MW total integrated flux density spectra for the selected four times, which are characterized by an overall increase in flux density without significant spectral changes. We chose this time range because the

[1]http://sprg.ssl.berkeley.edu/~tohban/browser/

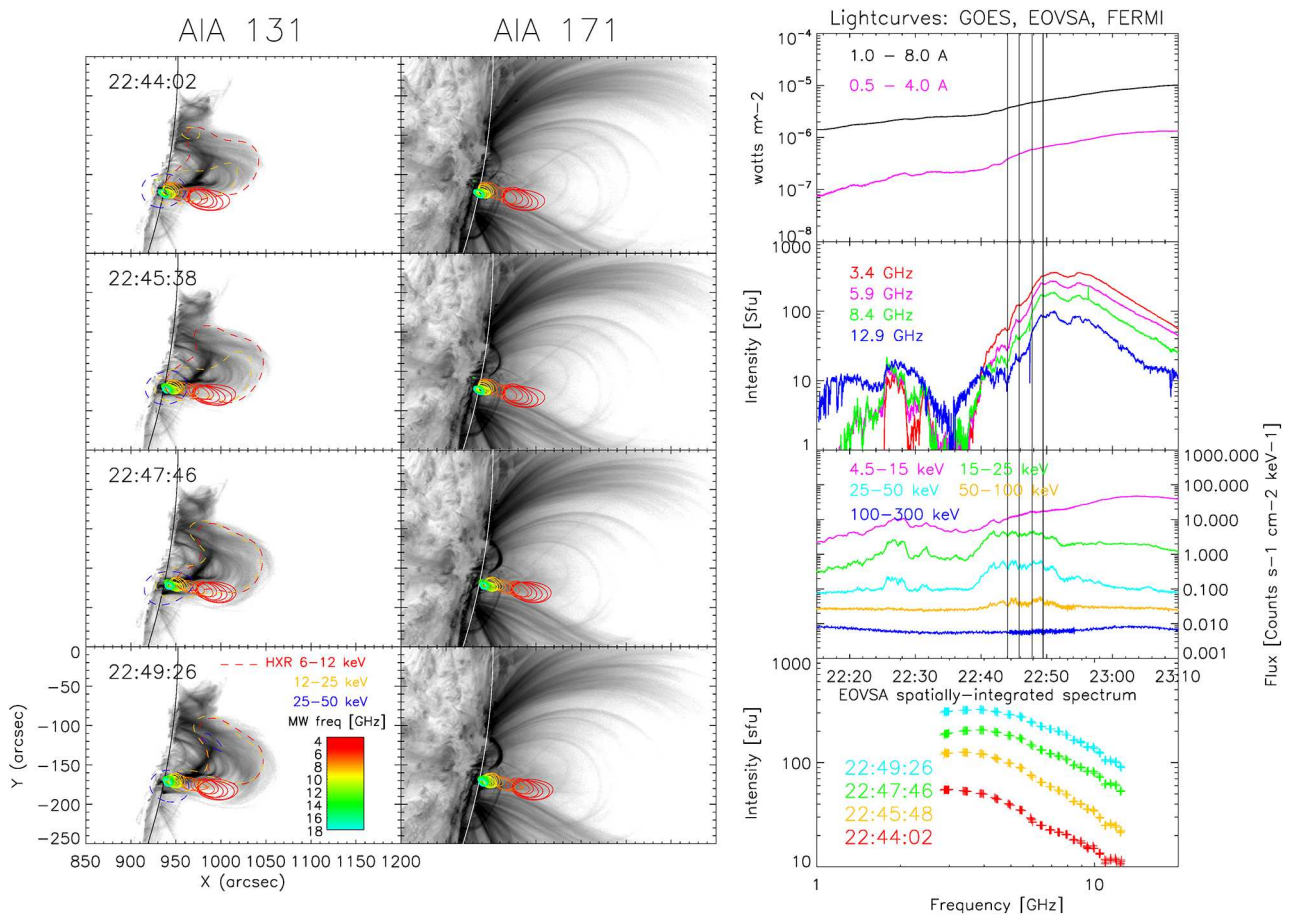

FIGURE 1 | (Left) The flare development seen in MWs by EOVSA (solid contours [The color contours show 50% of the maximum intensity of each of 30 spw images]) and HXR from *RHESSI* (dashed contours), plotted on EUV 131 Å and 171 Å (background inverted grayscale) from *SDO/AIA*, at times t_1–t_4 (22:44:02–22:49:26 UT), indicated by four black vertical lines on the right panel. **(Right)**, from the top: The soft X-ray, MW, and HXR lightcurves from *GOES*, EOVSA, and *FERMI*, respectively, and the total flux density spectra from EOVSA at four times images on the left panel (movie available). All contours are at 50% of the maximum intensity of each image.

evolving source morphology was simpler than that during either earlier or later times.

The flare development throughout the time period shows that the MW high-frequency sources are co-spatial with the HXR non-thermal source (i.e., 25–50 keV) as often observed, indicating the presence of non-thermal electrons in the low solar atmosphere. The centroid of the 25–50 keV HXR source appears to lie very close to the west limb (c.f, **Figure 1**, blue dashed contours), which coincides with the central location of the AR at the photospheric level (S09W88). Although the coarse angular resolution of the detectors we use for imaging does not allow us to derive an accurate height of the HXR source above the limb as in, e.g., Krucker et al. (2015), we assume that it is likely a footpoint source located at chromospheric heights. At progressively lower frequencies, the MW sources extend higher in the corona, indicative of non-thermal electrons extending to higher heights where the magnetic field is relatively low, which is in line with earlier observations (Fleishman et al., 2017, 2018a,b).

Figure 2 overlays the EOVSA source contours with the 17 GHz image (inverted grayscale) obtained with Nobeyama RadioHeliograph (NoRH; Nakajima et al., 1994) near the end of the time period, for the same field of view as in **Figure 1**. A similar observation of an extended non-thermal electron population seen in low-frequency MWs was reported by Gary et al. (2018) in the X8.2 flare, which was produced 1 day later from the same AR. It is interesting to note, however, that the northern footpoint source faintly seen in NoRH image does not appear in the EOVSA images. This is most likely due to the different dynamic ranges of the two instruments. NoRH has 84 antennas, while EOVSA has only 13; thus, NoRH has better UV coverage, which results in a better dynamic range (although at lower spatial resolution). As a check, we confirmed that the northern MW source can be faintly seen when a wider, multi-band frequency-synthesis is used for EOVSA imaging, which increases the UV coverage at the expense of frequency resolution. This suggests that the EOVSA images correspond to the more strongly emitting leg of a large, asymmetric loop.

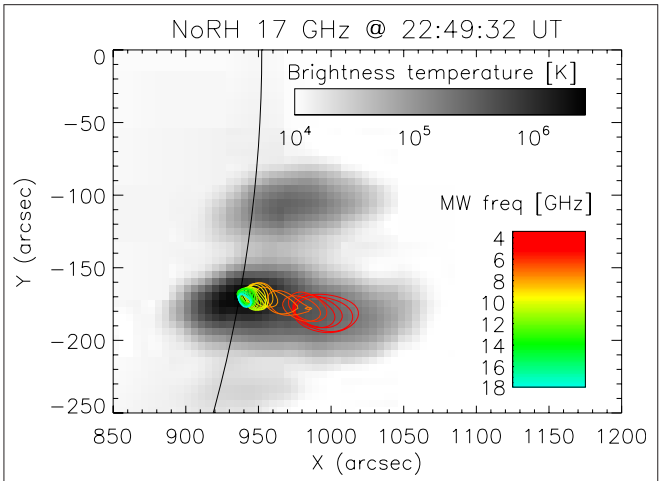

FIGURE 2 | The EOVSA sources overlaid on the NoRH 17 GHz image (inverted grayscale) taken near the end of our time of interest, 22:49:26. The field of view is the same as in **Figure 1**. EOVSA's low frequency coverage reveals the large spatial extent of the non-thermal electron population in the corona with respect to height. At the same time, the higher dynamic range of the NoRH image at a single frequency reveals a possible asymmetry in the magnetic field strength of the loop containing these electrons.

The HXR low-energy sources (i.e., 6–12 and 12–25 keV) grow over time, very closely following the EUV 131 Å loops (**Figure 1**). We are likely observing a super-hot thermal loop of a few tens of MK, caused either by chromospheric evaporation after the initial particle acceleration seen in the HXR lightcurve, or direct heating from reconnection (Ning et al., 2018). The centroids of the EOVSA MW sources are slightly south of the southern leg of this thermal loop, which is a persistent feature (see **Supplemental Movie 1**). Therefore, the loop with the MW-emitting electrons appears to be slightly larger and possibly extends above the super-hot thermal loop. This combination of the HXR and MW source morphology fits the standard flare model: non-thermal electrons are injected from the acceleration region above the super-hot thermal loop, and then travel downward in the magnetic flux tube to emit GS radiation in the corona and bremsstrahlung in the chromosphere.

3. MW AND HXR ANALYSIS OF THE NON-THERMAL ELECTRON DISTRIBUTION

Both HXR and MW emissions are natural outcomes of non-thermal electrons accelerated in flares (White et al., 2011, and references therein). Observables of these emissions depend on both the non-thermal electron population and local properties of the flaring plasma in regions where those emissions are formed. As a result of the topological diversity of flares, the HXR and MW emissions display a variety of appearances and relationships. In some flares, both emissions are produced by a single population of non-thermal electrons in a single flaring loop (e.g., Fleishman et al., 2016b). In other cases, there could be different populations of the non-thermal electrons in distinct flaring loops, thus, different populations can dominate HXR and MW emissions. As a result, the non-thermal electron populations forming the two emissions can appear different in terms of spatial and/or energy distributions (Dennis, 1988; Kundu et al., 1994; Silva et al., 2000), even though they may have originated from the same acceleration site/process.

In this flare, the temporal correlation between HXR and MW lightcurves (seen in **Figure 1** right panel) suggests a common origin of accelerated electrons responsible for the two emissions. Spatial relationships are consistent with the standard flare model, as explained in the previous section. Even so, the HXR- and MW-emitting energy ranges of the population may still exhibit dissimilar energy distributions and evolution thereof. Here, we focus on a comparison of the energy distributions of the non-thermal electrons derived from the spatially resolved MW and HXR data.

3.1. MW Analysis

The MW emission in solar flares depends on many crucial physical parameters including magnetic field strength and orientation, non-thermal electron energy and angular distribution, and ambient plasma density and temperature. To derive those physical parameters, the spatially-resolved spectrum from each pixel in the high-resolution EOVSA images has to be forward-fit with the appropriate cost function. A suitable cost function (Gary et al., 2013; Fleishman et al., 2020) employs a numerical fast GS code that accounts for GS and free–free radio emission and absorption (Fleishman and Kuznetsov, 2010), since analytical approximations (Dulk and Marsh, 1982; Dulk, 1985) are too limited and too approximate for a meaningful forward fit. This fast GS code is an enhancement of a less accurate numerical Petrosian–Klein (PK) approximation of the exact GS equations (Melrose, 1968; Ramaty, 1969), which are highly complicated and computationally slow for our purposes. The fast GS code reduces computation time for GS emission by many orders of magnitude compared to exact calculations, while preserving the needed accuracy. Performing this model fitting, one can obtain the model fitting parameters over the entire source region at the observational cadence (Fleishman et al., 2020) in the form of evolving maps of the physical parameters. These parameter maps reveal the spatial distribution and the temporal evolution of the magnetic field and the plasma in the corona.

For the model spectral fitting, we adopt a homogeneous source along the line-of-sight (LOS) and fix the following parameters: plasma temperature, 30 MK; source depth, 5.8 Mm (equivalent to 8 arcsec); an isotropic pitch-angle distribution, and a single power-law electron energy distribution of the form

$$\frac{dn(E)}{dE} = A_0 E^{-\delta}$$
$$n = \int_{E_{\min}}^{E_{\max}} \frac{dn(E)}{dE} dE \quad (1)$$

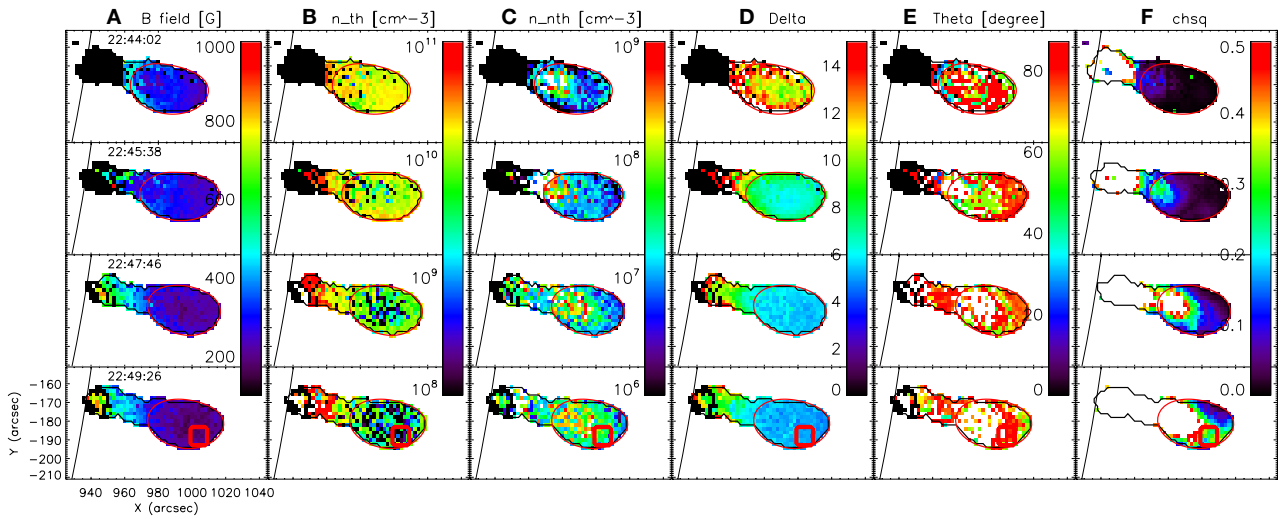

FIGURE 3 | Snapshots of the coronal magnetic field and plasma parameter movie created by forward-fitting the spatially-resolved spectra of EOVSA images at every 4 s (movie available). The four times are the same times as shown in **Figure 1**, and the parameters are: **(A)** magnetic field strength, **(B)** thermal electron density, **(C)** non-thermal electron density, **(D)** electron energy spectral index, **(E)** viewing angle, and **(F)** χ^2 values of the fittings. The black outline marks the union of the 50% contours of the original images at all 30 spws at each time, and the red circles indicate the 50% contours of the lowest frequency images (spw 1, 3.4 GHz) at each time. The time profiles of the parameters in the small red box are shown in **Figure 4**.

where A_0 is the normalization factor, δ is the spectral index, n is the number density of the non-thermal electrons with energies between $E_{\rm min}$ and $E_{\rm max}$, $E_{\rm min}$ is the minimum cutoff energy fixed at 17 keV, and $E_{\rm max}$ is the maximum cutoff energy fixed at 5 MeV. The initial values of the five free parameters are: non-thermal density, 10^7 cm^{-3}; magnetic field strength, 400 G; viewing angle (angle between LOS and the magnetic field line), 60 degrees; thermal density, 10^{10} cm^{-3}; and δ, 4.5. Although the currently available spectral fitting tool, GSFIT, accepts the T and $E_{\rm max}$ as free parameters, we found that they are not constrained for this flare; thus, they were fixed as described above.

The errors of the individual data points, needed to compute the χ^2 metrics, were determined as follows. In each map we selected a region away from the microwave source and computed the rms value of the fluctuations. Then, to take into account the uncertainty introduced by a frequency-dependent spatial resolution of the EOVSA instrument, we added a frequency-dependent systematic uncertainty (Gary et al., 2013; Fleishman et al., 2020). The actual scatter of the adjacent spectral data points is noticeably smaller than the associated error bars (see examples in **Figure A1** and **Figure 5**), which implies that the observational errors have been overestimated. For this reason, in what follows we will use a conservative χ^2 upper threshold smaller than conventional values about one.

Figures 3, **4** show that the derived physical parameters vary smoothly in both space and time. **Figure 3** shows a subset of the parameter maps (**Supplemental Movie 2**) at four selected times indicated in **Figure 1** for: (a) magnetic field strength, (b) thermal electron density, (c) non-thermal electron density, (d) electron energy spectral index, (e) viewing angle, and (f) χ^2 values of the fittings. The black contours are the 50% level of the radio maps at all 30 spws, while the red circles indicate the 50% contours of the 3.4 GHz images (spw 1) at each time. Visual inspection of individual fits suggests that the spectral fits with $\chi^2 \lesssim 0.1$ are acceptable. Others may not be well fit because of: (1) a complex spectrum inconsistent with the uniform source model and contamination of the spectrum due to a sidelobe (see **Figures A1A,B,E**). These ill-fit spectra are excluded from the quantitative analysis. The χ^2 values exceed the threshold in the lower-height part of the sources, which restricts our study to the coronal portion of the flaring loop.

In order to investigate evolution of the parameters, we selected a small area, marked by a red box in the bottom row of **Figure 3**, within the 3.4 GHz source that collectively showed χ^2 values less than 0.1 for the longest time. The χ^2 values in the area northward of the red box are lower, but many spectra have fewer or no optically-thick data points, making the fit formally better there but the parameters less reliable than in the red box.

Figure 4 shows evolution of the fit parameters in the red box. The black lines indicate the median values of the parameters from all 25 individual pixels, while the gray shade shows the associated error range calculated as the standard deviation of the parameters over these 25 pixels. In panel (g), we plot the lightcurves of MW 3.4 GHz and HXR 30–100 keV for the reference. The vertical dashed lines correspond to the times t_1–t_4 shown in **Figures 1**, **3**. During the time range t_1–t_3, when $\chi^2 \lesssim 0.1$, we see the following trends:

(1) magnetic field strength is about ∼250 G; it does not show significant variations;
(2) thermal electron density varies within $\sim (1-2)\times 10^{10}$ cm^{-3},
(3) non-thermal electron density (above 17 keV) stays relatively constant, at $\sim 10^7$ cm^{-3},

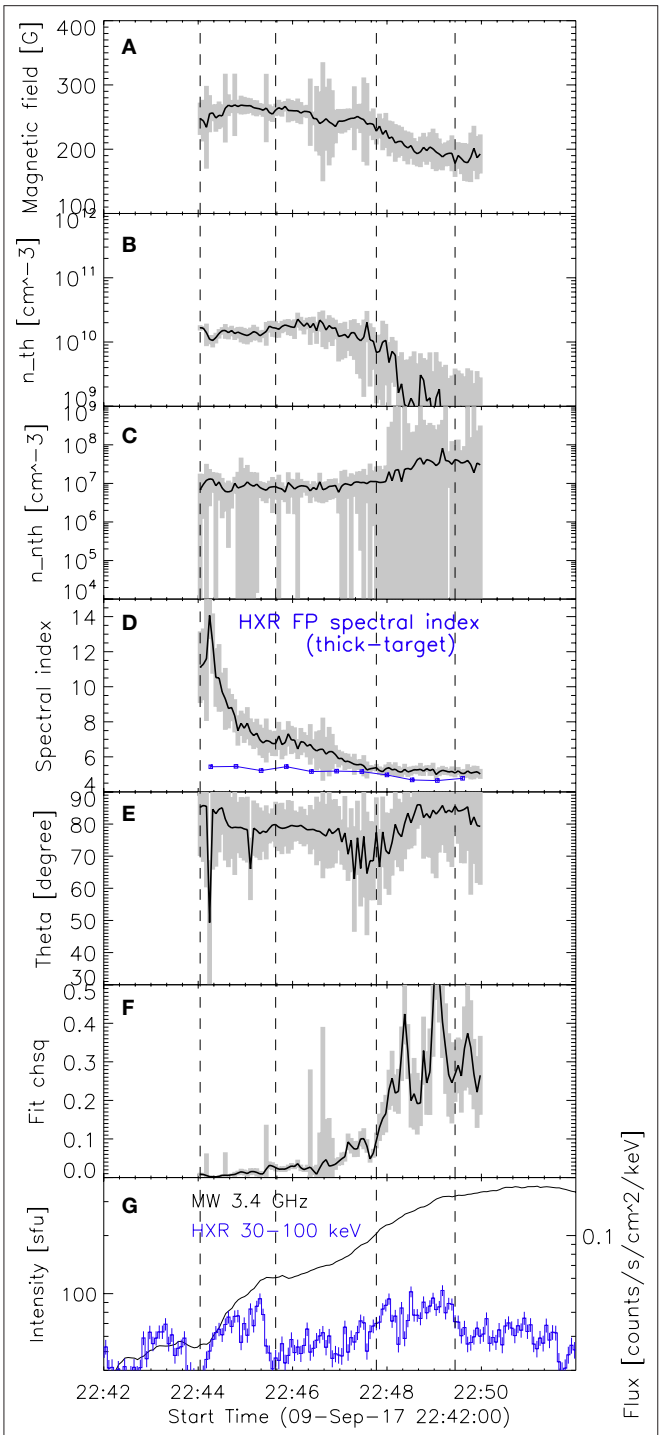

FIGURE 4 | (A–F) Time profiles of the parameters from 25 pixels within the small red square marked in **Figure 4**: gray shade indicates the error bar of each parameter at each instance calculated as the standard deviation of the parameters over 25 pixels, black for their median. The spectral index inferred from the HXR analysis, interpreted as the index of electrons emitting in the lower atmosphere in section 3.2, is plotted in blue in **(D)**. **(G)** The lowest-frequency MW lightcurve and the high-energy HXR lightcurve from *RHESSI* for reference, plotted on the same log scale. The dashed lines indicate time t_1–t_4.

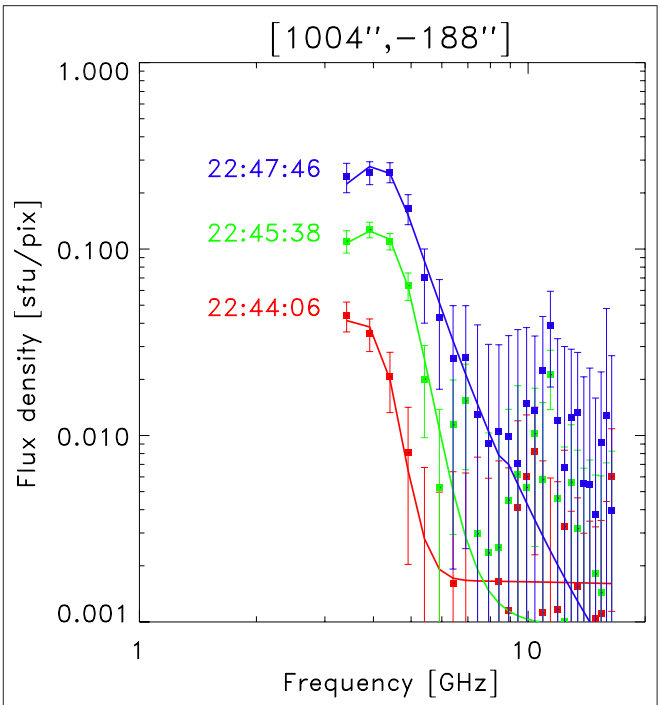

FIGURE 5 | An example of the temporal evolution of the spectra and their fits, taken at one pixel inside the red box in **Figure 3**. The three times correspond to times t_1–t_3.

(4) electron energy spectral index hardens significantly, from 14.1 ± 0.7 to 5.4 ± 0.1,
(5) viewing angle is in the range of 70 to 90 degrees.

To check if these parameter trends are reasonable, we inspect the MW spectral evolution at the center pixel of the red box up to time t_3, as shown in **Figure 5**. The flux density of this spatially-resolved spectrum increases by about a factor of 10 in the peak, and more in optically-thin regions as the spectral slope decreases. This is the expected behavior when the magnetic field strength and non-thermal electron density are both constant, while the spectral index hardens (see **Supplemental Movie 2** in Fleishman et al., 2020).

The trends (1) and (3) found above supports our initial view of the nature of the MW sources observed during this time period, that they are produced by the electrons accelerated at the acceleration cite and are transported inside the magnetic flux tube. This is in contrast with the result found by Fleishman et al. (2020), where they found the correlated decrease in magnetic field strength and increase in non-thermal electron density in the flare particle acceleration region.

In order to evaluate the effect of fixing a subset of parameters on the spectral fitting results, we perform a separate set of model fitting on the time series of spectra from the central pixel of the red square. First, we tested the effect of setting plasma temperature as a free parameter (initial temperature, 5 MK). We found as expected that the fit temperature values

are unstable, varying from $\sim$ 1 to $\sim$ 25 MK, but are smaller than their error values, which means that plasma temperature cannot be well-constrained with these data. Even so, we found that the trends in other parameters in **Figure 4** do not change significantly. We then doubled the source depth to 11.6 Mm (cf. 5.8 Mm) and found the derived magnetic field strength drops slightly to ~225 G without significant temporal variation, which is statistically consistent with 250 G reported above. We then ran the spectral fitting for two alternative values of $E_{\rm min}$, 10 and 30 keV. For the former, we found that the magnetic field strength decreased with time from ~250 to ~210 G, while the non-thermal density remained stable at $\sim 5 \times 10^8$ cm^{-3}. For the latter, the magnetic field remained stable at ~200 G and the non-thermal density did not change from $\sim 10^7$ cm^{-3}. Other fit parameters—thermal electron density, electron energy spectral index, and viewing angle—remained unaffected by changes in those fixed parameters.

One more possible limitation of our model spectral fitting is the assumed isotropic angular distribution of the non-thermal electrons. Although the GS emission certainly depends on the pitch-angle anisotropy (Fleishman and Melnikov, 2003), it is difficult to constrain without imaging spectro-polarimetry data, which is not yet available. Thus, at present we cannot firmly quantify possible bias introduced by the assumption of the isotropic angular distribution.

3.2. HXR Analysis

We conducted the spectral analysis in HXR using the OSPEX package (Schwartz et al., 2002). The spectra were obtained from t_1–t_4 using collimator 3 (which has a good energy resolution and reasonable instrument response matrix), with an integration time of 32 s, an energy range 1–106 keV, and with 1/3-keV-wide energy bins. We then fit the spectrum using the thermal ("vth"), thick-target model ("thick2"), and pile-up correction ("pileup_mod") functions[2]. The equation for the thick-target model is:

$$\mathrm{Flux}(\epsilon) = \frac{n_{th}}{4\pi (AU)^2} \frac{1}{mc^2} \int_{\epsilon}^{E_{\rm max}} \frac{\sigma(\epsilon, E) v}{dE/dt} \int_{\epsilon}^{E_{\rm max}} F(E_0) dE_0 dE \quad (2)$$

where Flux(ϵ) is the photon flux at photon energy ϵ, n_{th} is the number density of the thermal plasma, AU is one astronomical unit, m is the electron mass, c is the speed of light, $\sigma(\epsilon, E)$ is the bremsstrahlung cross section from equation (4) of Haug (1997), v is the non-thermal electron speed, and $F(E_0)$ is the electron flux density distribution function (electrons cm^{-2} s^{-1} keV^{-1}), which is returned in the fitting[3]. In order to make this analysis consistent with the MW analysis, we only considered a single power-law and fixed the low energy cutoff of the electron energy distribution to 17 keV. The fitting energy range was $\sim$ 6 to $\sim$ 70 keV.

In this flare, the instrument had its attenuator state at A0, which made our observation the most affected by the pulse pile-up effect. In order to correct for this effect with some consistency, we have fit each spectrum manually while monitoring that the emission measure from the thermal fit and the first parameter of pile-up correction function ("coefficient to increase or decrease probability of pileup for energies > cutoff") both increase correspondingly as the low-energy count rates increase during this time period. A sample of the spectral fit results is shown in **Figure 6**. The thermal fit returns a plasma temperature of ~32 MK and an emission measure of $\sim 2 \times 10^{46}$cm^{-3}, which translates to a density of high $\sim 10^8$cm^{-3}, if we estimate the thermal source volume from **Figure 1** by assuming a bicone with a diameter of $\sim$ 50" and a height of $\sim$ 50"π. This plasma density is about an order of magnitude lower than that obtained from MW spectral fitting. However, we note that the plasma density from MW spectral fitting may not be well-constrained, since the spectra at higher heights do not have many optically-thick data points in our frequency range. In fact, it is possible to fit those spectra with lower plasma density while all other parameters are nearly the same as before, if we allow the high-frequency plateau from the free-free emission to be lower than the data points (but still within the error bars). Therefore, it is possible that the plasma density from the MW spectral fitting is overestimated and thus, the actual values could be consistent with the lower, HXR-derived values.

We see in **Figure 1** that the 25–50 keV sources obtained during this time period are most likely footpoint sources, and thus conclude that the fit parameters obtained from the thick-target function can be used to evaluate the powerlaw index of electrons producing the 25–50 keV emission. The time profile of this HXR-derived spectral index is plotted in **Figure 4D** as a blue line[4].

3.3. Combining the Results From MW and HXR Analysis

It is apparent from **Figure 4D** that the δ values and their evolutions are very different in the corona and the thick-target source. However, we find that our coronal δ evolution from MW analysis seems to have some correspondence with the light curves of two emissions in **Figure 4G**. The interval up to t_3 is divided into two episodes (guided by vertical dashed lines). In interval t_1–$t2$, the HXR and MW lightcurves show rapid increase and the coronal δ also shows rapid hardening from 14.1 $\pm$ 0.7 to 6.8 $\pm$ 0.3. In interval t_2–t_3, the HXR and MW lightcurves show much slower increase (or perhaps none for HXR) and the coronal δ shows slower hardening as well, from 6.8 $\pm$ 0.3 to 5.4 $\pm$ 0.1. In the first episode, the HXR lightcurve's spiky shape suggests particle acceleration and the precipitation of the non-thermal electrons into the chromosphere. At the same time, the significant hardening of our coronal δ indicates a rapid increase in the number of high-energy non-thermal electrons in the corona, which is reflected by the rapid increase of the coronal MW emission at 3.4 GHz. This correspondence supports our initial view of this flare, where the particle acceleration occurs at or above the 3.4 GHz source, and the accelerated

[2]See documentation at: https://hesperia.gsfc.nasa.gov/ssw/packages/spex/idl/object_spex/fit_model_components.txt.

[3]See documentation at: https://hesperia.gsfc.nasa.gov/ssw/packages/xray/doc/brm_thick_doc.pdf.

[4]Since the spectral index returned by OSPEX fit is that of the electron flux density spectrum, we add 0.5 to the OSPEX values in order to make them comparable to our MW-derived δ, which is that of a number density spectrum. i.e., $n(E) = F(E)/v$, where $n(E) \propto E^{-\delta_{mw}}$, $F(E) \propto E^{-\delta_{HXR}}$, and $v \propto E^{1/2}$.

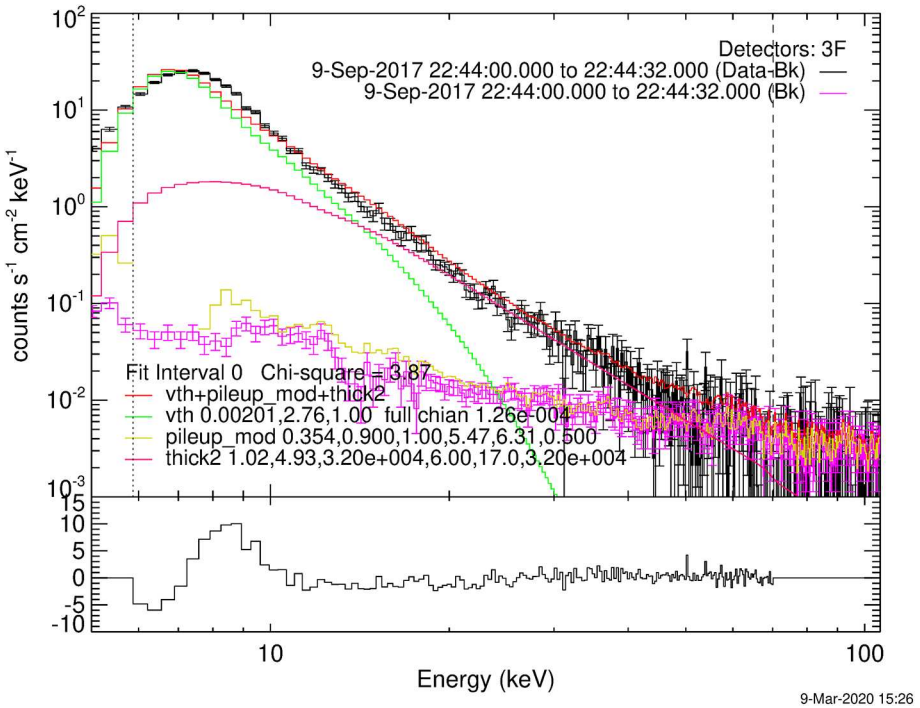

FIGURE 6 | A example of the HXR spectral fit from OSPEX, at 22:44:16 UT.

electrons travel downward along the magnetic field lines to emit GS radiation lower in the corona and thick-target bremsstrahung HXR radiation in the lower atmosphere.

In episode t_2–t_3 the HXR lightcurve suggests no significant increase in precipitation of non-thermal electrons to the chromosphere compared to the first episode. However, the coronal δ continues to harden. In order to comprehend this situation, we compare the observed evolution of the coronal electron energy spectrum with the model evolution provided by previous theoretical studies. We use the so-called trap-plus-precipitation (TPP) model (Melrose and Brown, 1976), which gives the analytical description of the evolution of the energy spectrum of the electrons in the magnetic trap under the influence of electron injection, energy losses due to Coulomb collisions, and precipitation out of the magnetic trap due to the pitch-angle diffusion by Coulomb interactions. This model considers the two extreme cases of (1) initial injection but no continuous injection and (2) no initial injection but continuous injection that is independent of time.

Let $N(E,t)$ be the total number of electrons per unit energy range in the magnetic trap and $Q(E,t)$ be the number of electron per unit energy injected into the trap in unit time. Assuming that the injection function is in the form of a single power-law with power-law index δ, the initial conditions for case (1) is

$$\begin{aligned} N(E,0) &= KE^{-\delta} \\ Q(E,t) &= 0 \text{ for } t > 0, \end{aligned} \tag{3}$$

and for case (2),

$$\begin{aligned} N(E,0) &= 0 \\ Q(E,t) &= AE^{-\delta}\theta(t) \\ \theta(t) &= \begin{cases} 0 \text{ for } t < 0 \\ 1 \text{ for } t > 0. \end{cases} \end{aligned} \tag{4}$$

where A and K are constants. The analytical solution of the transport equation for the temporal evolution of $N(E,t)$ given by Melrose and Brown (1976) for case (1) is

$$\begin{aligned} N(E,t) &= \left(\frac{E_0}{E}\right)^{-5/2} N(E_0,0) \\ E_0 &= E(1+\tfrac{3}{2}\nu_0 E^{-3/2}t)^{2/3}. \end{aligned} \tag{5}$$

For case (2),

$$\begin{aligned} N(E,t) &= \frac{AE^{-\delta}}{(\delta+1)\nu_0 E^{-3/2}} \\ &\{1-(1+\tfrac{3}{2}\nu_0 E^{-3/2}t)^{-2(\delta+1)/3}\} \end{aligned} \tag{6}$$

where $\nu_0 \approx 5\times10^{-9} n_{th}\,\mathrm{s}^{-1}(\mathrm{keV})^{3/2}$.

We take the electron energy spectrum observed in the corona at the end of the first episode as the spectrum of "initial injection" for case (1) and of "continuous injection" for case (2). Therefore, we use $\delta = 6.8$ observed at 22:45:38 UT in Equations (3), (4). We also use $n_{th} \sim 10^{10}$ cm^{-3} from the observation of thermal

electron density shown in **Figure 4**. Lastly, we arbitrarily set A and K to be 1, and plot the normalized $N(E,t)$ for two cases over several times during the time period of the second episode (128 s). **Figure 7B** shows the result for case (1), initial injection without continuous injection, and panel (c) shows the result for case (2), no initial injection but with continuous injection. **Figure 7A** shows the evolution of the total electron number spectrum derived from microwave data, obtained by multiplying the number density spectrum from **Figures 4C,D** by the total volume occupied by the small red square in **Figure 3**.

It is clear from **Figure 7** that the observed spectral evolution cannot be explained by the case with only initial injection, since the number of electrons in higher energies, up to several hundreds of keV, does not increase in the model. On the other hand, the increase in the number of those high-energy electrons is well-captured by the case with continuous injection, although the rate of increase seems to be faster in the model than in the observation. The result of the continuous injection model, as described in Melrose and Brown (1976), is that the spectrum evolves into a double-power law where the spectral index below the break energy E_b is harder than that above E_b by 1.5, and that the break energy increases with time as $E_b = (\frac{3}{2}\nu_0 t)^{2/3}$. If we calculate the evolution of δ in the model by assuming a single power-law with $E_{\rm min} = 17$ keV and $E_{\rm max}$ as the energy up to which the largest change in δ is observed, which is $E_b = (\frac{3}{2}\nu_0 t)^{2/3}$ with $t = 128$ s ($\sim$450 keV) and is marked by the vertical dashed line in **Figure 7C**, then the modeled coronal δ is 6.5 at t=1 s and 5.3 at $t = 128$ s. This is in agreement with our observed values of 6.8 ± 0.3 at time t_2 and 5.4 ± 0.1 at time t_3.

This result shows that the observed coronal δ hardening, which continued into the second episode, is broadly consistent with the TPP model of continuous electron injection into the coronal magnetic trap. However, the fact that there are still some differences, such as the rate of δ hardening and the values of δ above several hundred keV between the model and the observation, suggests that our observation cannot be fully explained by this simple model either. The TPP model's assumption of the time-independent power-law injection function is probably too simplistic, and the real injection function is most likely time-dependent and/or more complex than a single power-law. For example, it can be a double power-law, or a single power-law with the high-energy cut-off increasing in time due to a sustained acceleration process.

Let us discuss further the fact that there is a significant difference between coronal δ evolution from MW analysis and chromospheric δ evolution from HXR analysis. Compared to the coronal δ evolution of 14.1 ± 0.7 to 5.4 ± 0.1, the chromospheric δ changes from 5.4 ± 0.1 to 5.0 ± 0.1. We try to reconcile this observation to our initial picture where the same population of non-thermal electrons, accelerated in the same acceleration episode, is injected into the loop to produce all of the observed MW and HXR emission in this flare. One way to explain the different δ evolution in HXRs and MWs is if by assuming that the injected electrons have a double power-law energy spectrum and that our observed low-frequency coronal MW emission is more sensitive to the spectrum above a certain break energy E_{bk} ($\neq E_b$). This double power-law spectrum could have a low-energy spectral index comparable to the observed HXR-derived δ up to E_{bk} and a much softer high-energy spectral index (or, a cut-off) above E_{bk}. The greater hardening of the MW-derived δ can then be reconciled by a hardening of the spectrum of the injected electrons only above E_{bk}, or by a sustained increase in time of E_{bk} itself. This would be in line with the recent study of Wu et al. (2019), which conducted the detailed simulation of the GS emission from the electrons with double power-law energy distribution and found that the increased high-energy electrons specified by the second spectral index result in a harder spectral index in the MW flux density spectrum, even if the total number of electrons does not change significantly.

4. THE EVOLUTION OF THE TOTAL ENERGY OF THE NON-THERMAL ELECTRONS IN THE CORONA

In the previous section, we introduced the general picture of the evolution of the energy spectrum of the non-thermal electrons injected into the flaring loop in this flare. We did so by interpreting the temporal behavior of the parameters in a small representative volume in the context of the existing theory of electron transport in the corona. We now explore the collective behavior of the non-thermal electrons evolving in the flaring loop. Specifically, we calculate the total energy of non-thermal electrons contained in the corona, defined by the 50% contour of 3.4 GHz image (red contour in **Figure 3**), and plot this energy against time, to obtain the evolution of the total non-thermal electron energy contained in the corona. To do so, for each time frame we proceed with the following steps:

(1) Exclude all ill-fitted pixels within the 50% contour of the 3.4 GHz source,
(2) Calculate the non-thermal electron energy density in all well-fit pixels,
(3) Calculate the weighted mean of (2), then
(4) Multiply this weighted mean of the energy density by the total volume within the 50% contour of the 3.4 GHz source assuming a depth 5.8 Mm.

In step (1), we identify a pixel as ill-fitted if (1) the magnetic field solution is hitting its predefined upper limit of 3,000 G, (2) the number density solution is hitting its predefined lower limit of 10^3 cm^{-3}, (3) the spectral index solution is hitting its predefined lower limit of 4 or upper limit of 15, or (4) $\chi^2 > 0.1$. **Figure 6C** shows the percentage of the well-fit pixels selected for the analysis with respect to the total number of pixels within 50% contour of 3.4 GHz source.

In step (2), we calculate the total energy contained in the coronal MW 3.4 GHz source, which we proposed in the previous section to be sensitive to the electrons that have energies higher than a certain E_{bk}. Therefore, we intentionally "cut" the observed energy distribution at E_{bk}. and obtain the energy density only *above* E_{bk} by using

$$\varepsilon = 1.6 \times 10^{-9}\Big(\frac{\delta-1}{\delta-2}\Big) n_{E>E_{min}} E_{min}$$

$$\boldsymbol{E_{bk} = \alpha E_{min}}$$

$$n_{E>E_{bk}} = \alpha^{1-\delta} n_{E>E_{\rm min}}$$

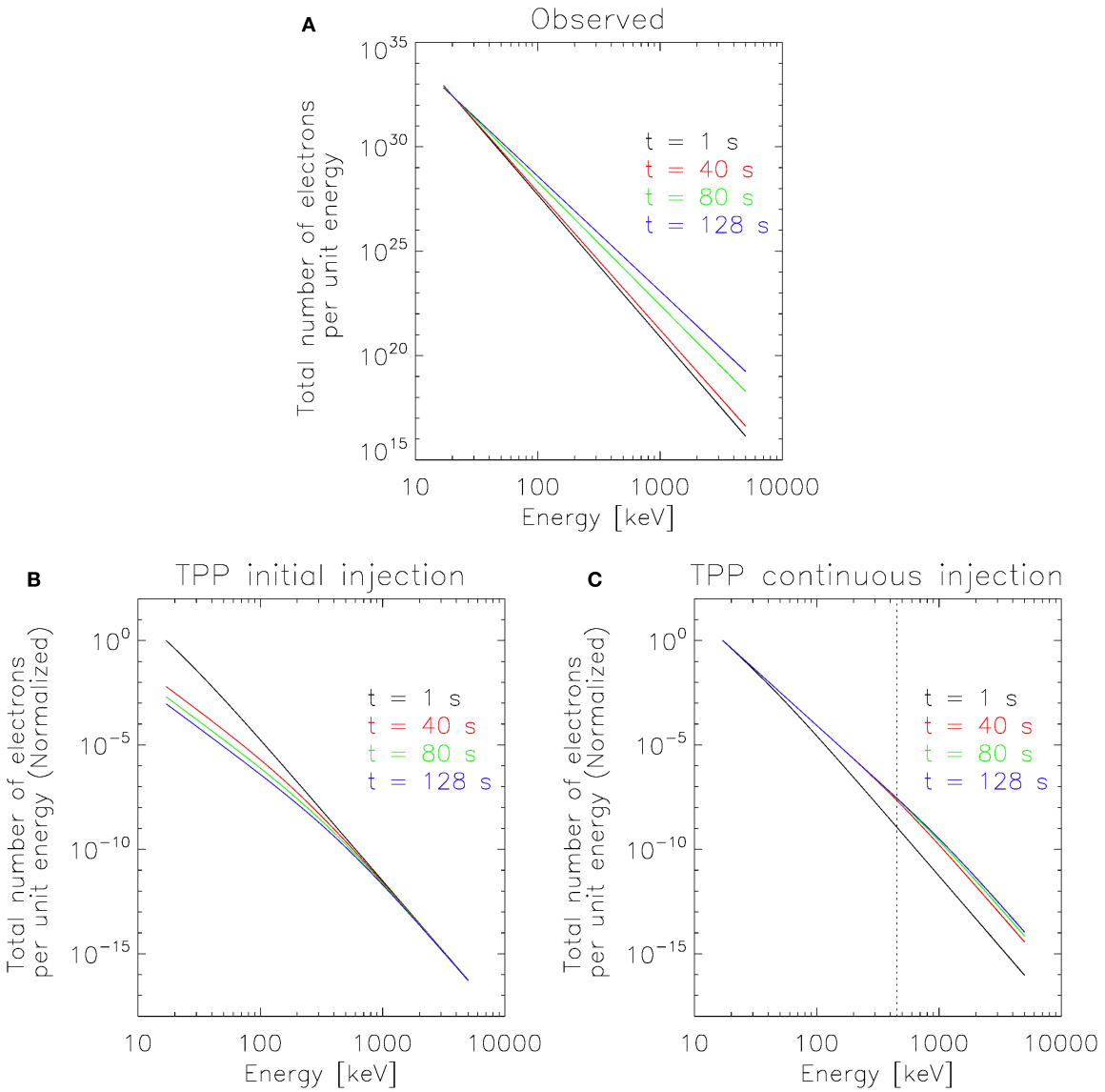

FIGURE 7 | (A) The evolution of total electron number spectrum deduced from the MW fits, obtained by multiplying the number density spectrum from **Figures 4C,D** by the total volume occupied by the red box in **Figure 3**. **(B,C)** The modeled evolution of the total electron number spectrum (normalized) for the trap-plus-precipitation (TPP) model by Melrose and Brown (1976), over several times during the period of 22:45:38 to 22:47:46 UT, when the coronal δ from MW analysis shows a continued hardening despite a lack of apparent change in electron injection deduced from the HXR lightcurve. **(B)** Initial injection without continuous injection. **(C)** No initial injection but with continuous injection. The vertical dotted line marks the analytical value of the energy up to which the largest change in the low-energy spectral index is observed (see section 3.3).

$$\varepsilon_{E>E_{bk}} = 1.6\times10^{-9}\left(\frac{\delta-1}{\delta-2}\right)n_{E>E_{bk}}E_{bk}$$
$$= 1.6\times10^{-9}\left(\frac{\delta-1}{\delta-2}\right)n_{E>E_{min}}E_{min}\alpha^{2-\delta} \quad (7)$$

where $n_{E>E_{min}}$ is n, the number density we obtained in section 3.1 (same as Equation 1), E_{min} is 17 keV, which was used in obtaining n, and α is the factor by which a certain E_{bk} is larger than 17 keV. We do not know the exact value of E_{bk}, but we adopt 70 keV for this analysis, since this is the upper limit of the fitting energy range for HXR spectral analysis that shows generally unchanged spectral indices over time.

In step (3), the weighted mean of the energy density is calculated by

$$<\varepsilon>_{weighted} = \frac{\sum_{i=1}^{n} w_{\varepsilon,i}\varepsilon_i}{\sum_{i=1}^{n} w_{\varepsilon,i}} \quad (8)$$

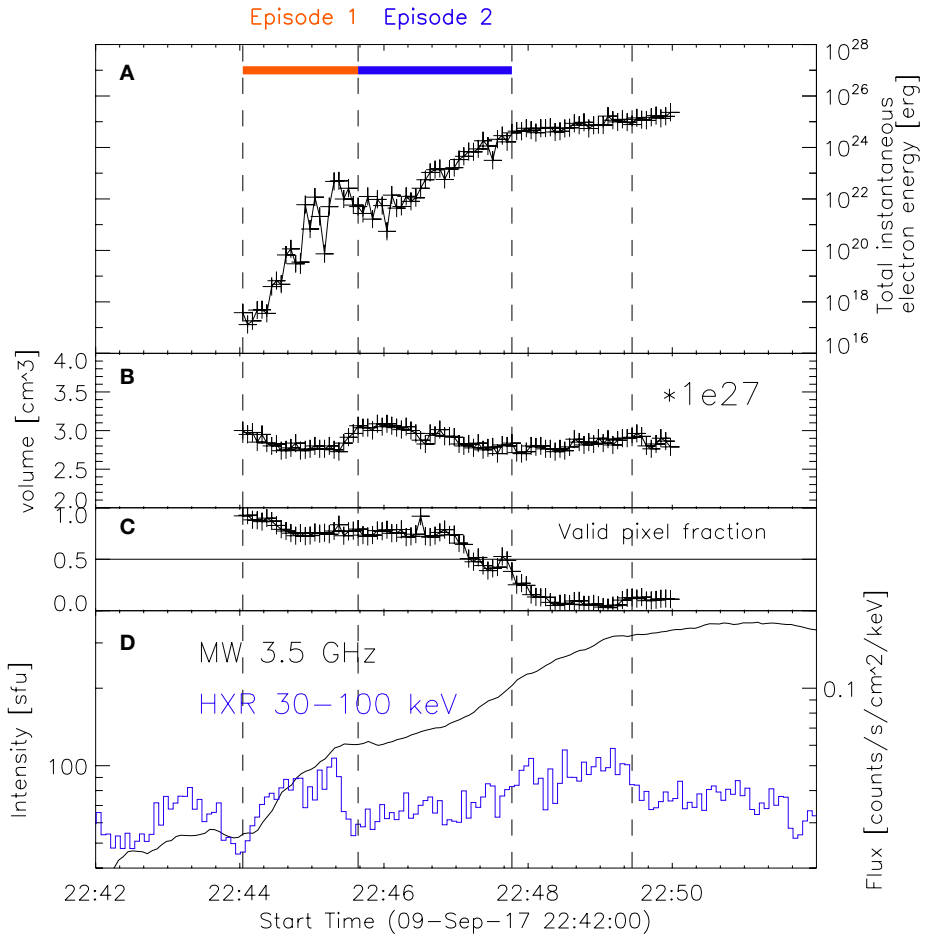

FIGURE 8 | Evolution of parameters within the 50% contour of the observed MW 3.4 GHz source (red contours in **Figure 3**). **(A)** The total instantaneous energy of the non-thermal electrons with energies > 70 keV. **(B)** The total volume. **(C)** The percentage of the total number of pixels in the source that are well-fit and hence selected for analysis. **(D)** The same lightcurves from **Figure 4G** for reference. The dashed lines mark times t_1–t_4.

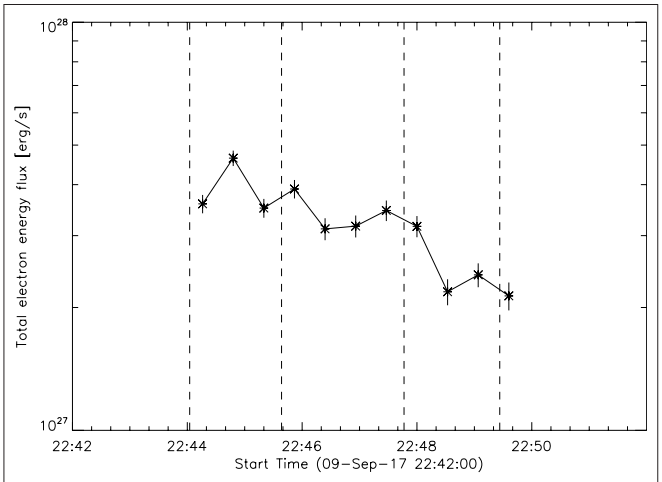

FIGURE 9 | The evolution of the total energy flux of HXR-emitting electrons in the chromosphere, using the result of the analysis from section 3.2.

where $w_{\varepsilon,i}$ is the weight of energy density for i^{th} well-fit pixel, calculated by $1/\varepsilon^2_{err,i}$ where $\varepsilon_{err,i}$ is the error in energy density.

Finally, in step (4) we calculate the total volume within the 50% contour of the 3.4 GHz source by multiplying the total number of pixels within that contour by the 4 arcsec^2 pixel area and the source depth of 5.8 Mm, as adopted in section 3.1. The evolution of this volume is plotted in **Figure 8B**.

Figure 8A shows the evolution of the total instantaneous energy of the non-thermal electrons having energies > 70 keV contained within the 50% contour of the observed MW 3.4 GHz sources. **Figure 8D** shows, for reference, the lightcurves from **Figure 4G**, and the four vertical dashed lines mark the same time boundaries as in **Figures 1**, **3**, **4**. **Figure 8A** shows that, overall, there is a significant increase in the total instantaneous energy of electrons > 70 keV contained in the coronal source. The energies corresponding to each time boundary are $3.8 \pm 0.5 \times 10^{17}$ erg at t_1, $4.9 \pm 0.8 \times 10^{21}$ erg at t_2, $3.9 \pm 0.2 \times 10^{24}$ erg at t_3, and $7.6 \pm 0.5 \times 10^{24}$ erg at t_4. We note that the fraction of well-fit pixels within the source significantly decreases after t_3 (see

Figure 8C), so the results after this time may not be as reliable as in the preceding time intervals. However, up to t_3, at least half of the pixels within the 50% contour of 3.4 GHz sources are considered for the analysis, so our results can be taken with more confidence during this time. From **Figure 8A** it is observed that the total energy reaches about 10^{22} erg by time t_2, and increases by ∼3 orders of magnitude during episode t_2–t_3.

Although this analysis has been done assuming that the observed radio emission during our time of interest is produced by non-thermal electrons, it is possible that, at least during the time when the inferred spectral index is very soft (e.g., during episode 1), the emission is due to thermal electrons. In fact, most of the time during episode 1, we find that the observed spectra within the red box in **Figure 4** could be reproduced without the need for a non-thermal electron distribution. Instead, they could be produced by gyrosynchrotron emission generated by electrons with a ∼20 MK thermal distribution in a source with the same magnetic field, thermal electron density, and viewing angle. Therefore, the result in **Figure 8A** during episode t_1–t_2 should be taken as the extreme case of considering all MW-emitting electrons to be non-thermal. However, purely thermal emission is excluded for t_2–t_3, since many pixels start showing spectra that are too hard in their optically-thin sides to be explained by thermal gyrosynchrotron emission. Therefore, we believe that our results during t_2–t_3 truly reflect the rise in the energy of non-thermal electrons with energies >70 keV in the corona.

5. SUMMARY AND DISCUSSION

In this study, we analyzed the evolution of the non-thermal electrons accelerated during the impulsive phase of the M1.2 flare on 2017 September 9. We focused on a ∼6-min period when a significant increase of MW emission was observed compared to the level of increase in HXR emission. We used multi-wavelength observations to evaluate the overall spatial distribution of electrons in the flare, and combined it with the total energy and energy distribution of electrons derived from the combination of MW and HXR analysis. In particular, our MW analysis was conducted using the new technique of numerical forward-fitting of spatially-resolved MW spectra derived from multi-frequency images from EOVSA. This enabled the quantitative calculation of the spatially-resolved evolution of the non-thermal electrons in the corona. The summary of the main results from this work is the following.

(1) The comparison of EUV-loops, the locations of low- and high-energy HXR emission sources, and the distribution of MW images from 3.4 to 18 GHz suggest that the spatial distribution of the non-thermal electrons in this flare generally fits the traditional standard flare model morphology. We infer that the electrons are accelerated in a region located above the hot loop visible in AIA 131 Å and RHESSI 6-12 keV images and are injected into a somewhat larger "non-thermal" flare loop connecting the low-frequency coronal MW sources with the co-spatial 20-50 keV HXR and 17 GHz MW sources in the lower atmosphere.

(2) The comparison of the spectral index of the non-thermal electrons derived from HXR and MW analysis reveals, however, that their values and evolution are significantly different. More specifically, the spectral index of the non-thermal electrons associated with the coronal 3.4 GHz MW source undergoes much faster hardening than that associated with the footpoint HXR source. The former hardens from 14.1 ± 0.7 to 5.4 ± 0.1 and the latter changes from 5.4 ± 0.1 to 5.0 ± 0.1 over the same period of 128 s. Because the energy range of electrons producing HXR and MW emission differ, we interpret this discrepancy as reflecting a different spectral evolution in different parts of the energy spectrum.

(3) Our findings vividly show that the high-energy tail of the non-thermal electron distribution, which is responsible for the MW emission, underwent more significant evolution compared with the low-energy counterpart of the distribution for this flare. In-depth analysis focusing on the spectral evolution of the coronal electron population suggests that there was a sustained acceleration and continued injection of non-thermal electrons in the corona even when there was no significant signature for that in the HXR lightcurve for a period of time. The difference in the spectral evolution is reconciled by adopting that the energy spectrum of this injected population has a double power-law or a break-down spectrum above an evolving (rising in time) break energy E_{bk} in the form of a cut-off. The population with energies higher than the break energy, to which the MW emission is more sensitive than the HXR emission, have undergone greater spectral hardening, perhaps, due to the sustained acceleration.

(4) Based on this picture of the evolution of the energy spectrum of the non-thermal electrons injected into the flaring loop, we estimated the evolution of the total instantaneous non-thermal (> 70 keV) electron energy contained in a coronal volume enclosed by the coronal 3.4 GHz MW source. We find a significant increase of several orders of magnitude in the total energy of these electrons contained in the coronal source during the ∼4 min period of interest of the flare impulsive phase.

An interesting observation, shown in **Figure 8A**, is that the total instantaneous non-thermal electron energy contained in the coronal source continues to increase during the period we studied. Under the assumption of a single loop, it is interesting to compare this evolution with the development of the total energy flux deposited by HXR-emitting non-thermal electrons into the lower atmosphere. We plot the evolution of the total energy flux of HXR-emitting electrons in **Figure 9**, using the result of the analysis from section 3.2. We use the modification of Equation (7), $1.6 \times 10^{-9}\left(\frac{\delta-1}{\delta-2}\right)\mathcal{F}E_{min}$, where $\mathcal{F}$ is the total electron flux obtained from the thick-target spectral fit. Although this cannot be directly compared with **Figure 8A** because of the different units, this clearly indicates that the evolution of the total energy of non-thermal electrons in the lower atmosphere is different from that in the corona.

A consistency check of the single-population scenario can be performed by assuming a single power-law distribution that extends from tens of keV to hundreds of keV, covering both HXR-emitting and MW-emitting population of energetic electrons, at the time when the spectral indices from two analysis match, around t_3 (see **Figure 4D**). In this analysis we use a simple relation $\mathcal{F}(E) = n(E)\bar{v}A$ where $\mathcal{F}(E)$ is the non-thermal electron

flux distribution from HXR analysis, $n(E)$ is the non-thermal electron density distribution from MW analysis, $\overline{v}$ is the mean speed of non-thermal electrons, and A is the area of the thick-target HXR emission. We obtain from OSPEX analysis that $\mathcal{F} \sim 10^{35}$ electrons/s, estimate A from the 50% contour of 18 GHz MW image in **Figure 1** left panels (circular area with $\sim 10''$ diameter), and $\overline{v} = \frac{\int_{E_{min}}^{E_{max}} vn(E)dE}{\int_{E_{min}}^{E_{max}} n(E)dE} \sim 0.3\,c$ from the energy distribution. This yields $n \sim 3 \times 10^7$ cm^{-3}, which roughly agrees with the value of $n \sim 10^7$ cm^{-3} we obtained from MW analysis at this time.

An alternative explanation for the difference in δ development is that we are observing two electron populations belonging to different loop systems. For instance, our HXR-producing population may be reflecting the evolution of the non-thermal electrons in a small loop unresolved by RHESSI. This will allow the δ evolution in the corona and lower atmosphere to be unrelated, as in our observation. In fact, Kuroda et al. (2018) revealed the presence of an extended "HXR-invisible" non-thermal electron population outside of the traditional flare geometry at one time during another flare by using the *RHESSI* and the EOVSA data, and this snap-shot model required two separate loops to simultaneously reproduce the observed low-frequency MW emission and HXR/high-frequency MW emission. If we adopt a two-loop scenario for this study, however, the two loops must be dynamically connected since time profiles of low-frequency MWs at higher heights are very well-correlated with higher-frequency MWs co-spatial with the 25-50 keV HXR source.

Lastly, we note that electron pitch-angle anisotropy may change our result in **Figure 4** and possibly affect our conclusions. Differences in the inverted non-thermal electron energy distribution for isotropic vs. anisotropic (e.g., beam-like) distributions have been reported in MW both observationally (Lee and Gary, 2000; Melnikov et al., 2002; Altyntsev et al., 2008) and in simulations (Fleishman and Kuznetsov, 2010). For HXR, the bremsstrahlung cross section is also pitch-angle dependent (Equation 2 BN in Koch and Motz 1959). Therefore, an anisotropic electron distribution would produce a HXR photon spectrum that deviates from our results which assume an isotropic electron distribution (see, e.g., discussions in Massone et al., 2004; Chen and Bastian, 2012). However, exploring the effects of different pitch-angle distributions is beyond the scope of this study.

Although the origin of the striking dissimilarities in the evolution of the spectral indices of the non-thermal electrons in the corona and the chromosphere are open to debate, it is important to note that these differences are only revealed through the spatially-resolved analysis of the evolving coronal MW sources below ~10 GHz. The continued electron injection and hardening revealed by the coronal MW analysis seems to affect only the highest electron energies, and therefore lacks the expected counterpart signature in the HXR source. Since the location of the MW peak frequency is most sensitive to the magnetic field strength of the source, this characteristic informs us about non-thermal electrons higher in the corona (weaker magnetic field), where the HXR analysis becomes increasingly difficult due to the scarcity of the target plasma for bremsstrahlung.

DATA AVAILABILITY STATEMENT

EOVSA data are freely available from http://ovsa.njit.edu/data-browsing.html. Fully processed EOVSA spectral imaging data in IDL save format can be downloaded from https://www.dropbox.com/s/6dk40smvea8f66f/eovsa_20170909T223518-231518_r2_XX.sav?dl=0. The package for microwave data fitting, GSFIT, is included in the publicly available library SolarSoftWare under the Packages category at http://www.lmsal.com/solarsoft/ssw_packages_info.html.

AUTHOR CONTRIBUTIONS

NK processed the raw data, performed the fitting, initial analysis of the results, and wrote the initial draft. GF developed the fitting methodology. DG led the construction and commissioning of the EOVSA, developed the strategy for taking and calibrating the data for microwave spectroscopy. GN developed the GSFIT package used in the automated fitting. BC and SY developed the microwave spectral imaging and self-calibration strategy. All authors involved in the discussion and contributed to manuscript preparation.

FUNDING

EOVSA operation is supported by NSF grant AST-1910354. NK was partially supported by the NASA Living With a Star Jack Eddy Postdoctoral Fellowship Program, administered by UCAR's Cooperative Programs for the Advancement of Earth System Science (CPAESS) under award #NNX16AK22G. GF, DG, GN, BC, and SY are supported by NSF grants AGS-1654382, AST-1910354, AGS-1817277, AGS-1743321, and NASA grants 80NSSC18K0667, NNX17AB82G, 80NSSC18K1128, and 80NSSC19K0068 to New Jersey Institute of Technology.

ACKNOWLEDGMENTS

The authors thank the scientists and engineers who helped design and build EOVSA, especially Gordon Hurford, Stephen White, James McTiernan, Wes Grammer, Kjell Nelin, and Tim Bastian.

SUPPLEMENTARY MATERIAL

The Supplementary Material for this article can be found online at: https://www.frontiersin.org/articles/10.3389/fspas.2020.00022/full#supplementary-material

Supplemental Movie 1 | The movie corresponding to **Figure 1** is available as a supplemental material fig1_movie.avi.

Supplemental Movie 2 | The movie corresponding to **Figure 3** is available as a supplemental material fig3_movie.avi.

REFERENCES

Altyntsev, A. T., Fleishman, G. D., Huang, G. L., and Melnikov, V. F. (2008). A broadband microwave burst produced by electron beams. *Astrophys. J.* 677, 1367–1377. doi: 10.1086/528841

Aschwanden, M. J., Holman, G., O'Flannagain, A., Caspi, A., McTiernan, J. M., and Kontar, E. P. (2016). Global energetics of solar flares. III. Nonthermal energies. *Astrophys. J.* 832:27. doi: 10.3847/0004-637X/832/1/27

Atwood, W. B., Abdo, A. A., Ackermann, M., Althouse, W., Anderson, B., Axelsson, M., et al. (2009). The large area telescope on the Fermi gamma-ray space telescope mission. *Astrophys. J.* 697, 1071–1102. doi: 10.1088/0004-637X/697/2/1071

Chen, B., and Bastian, T. S. (2012). The role of inverse compton scattering in solar coronal hard x-ray and γ-ray sources. *Astrophys. J.* 750:35. doi: 10.1088/0004-637X/750/1/35

Dennis, B. R. (1988). Solar flare hard x-ray observations. *Solar Phys.* 118, 49–94. doi: 10.1007/BF00148588

Dulk, G. A. (1985). Radio emission from the sun and stars. *Annu. Rev. Astron. Astrophys.* 23, 169–224. doi: 10.1146/annurev.aa.23.090185.001125

Dulk, G. A., and Marsh, K. A. (1982). Simplified expressions for the gyrosynchrotron radiation from mildly relativistic, nonthermal and thermal electrons. *Astrophys. J.* 259, 350–358. doi: 10.1086/160171

Emslie, A. G., Dennis, B. R., Shih, A. Y., Chamberlin, P. C., Mewaldt, R. A., Moore, C. S., et al. (2012). Global energetics of thirty-eight large solar eruptive events. *Astrophys. J.* 759:71. doi: 10.1088/0004-637X/759/1/71

Fleishman, G. D., Gary, D. E., Chen, B., Kuroda, N., Yu, S., and Nita, G. M. (2020). Decay of the coronal magnetic field can release sufficient energy to power a solar flare. *Science* 367, 278–280. doi: 10.1126/science.aax6874

Fleishman, G. D., Kontar, E. P., Nita, G. M., and Gary, D. E. (2011). A cold, tenuous solar flare: acceleration without heating. *Astrophys. J. Lett.* 731:L19. doi: 10.1088/2041-8205/731/1/L19

Fleishman, G. D., Kontar, E. P., Nita, G. M., and Gary, D. E. (2013). Probing dynamics of electron acceleration with radio and x-ray spectroscopy, imaging, and timing in the 2002 April 11 solar flare. *Astrophys. J.* 768:190. doi: 10.1088/0004-637X/768/2/190

Fleishman, G. D., and Kuznetsov, A. A. (2010). Fast gyrosynchrotron codes. *Astrophys. J.* 721, 1127–1141. doi: 10.1088/0004-637X/721/2/1127

Fleishman, G. D., Loukitcheva, M. A., Kopnina, V. Y., Nita, G. M., and Gary, D. E. (2018a). The coronal volume of energetic particles in solar flares as revealed by microwave imaging. *Astrophys. J.* 867:81. doi: 10.3847/1538-4357/aae0f6

Fleishman, G. D., and Melnikov, V. F. (2003). Gyrosynchrotron emission from anisotropic electron distributions. *Astrophys. J.* 587, 823–835. doi: 10.1086/368252

Fleishman, G. D., Nita, G. M., and Gary, D. E. (2009). Dynamic magnetography of solar flaring loops. *Astrophys. J. Lett.* 698, L183–L187. doi: 10.1088/0004-637X/698/2/L183

Fleishman, G. D., Nita, G. M., and Gary, D. E. (2017). A large-scale Plume in an X-class solar flare. *Astrophys. J.* 845:135. doi: 10.3847/1538-4357/aa81d4

Fleishman, G. D., Nita, G. M., Kontar, E. P., and Gary, D. E. (2016a). Narrowband gyrosynchrotron bursts: probing electron acceleration in solar flares. *Astrophys. J.* 826:38. doi: 10.3847/0004-637X/826/1/38

Fleishman, G. D., Nita, G. M., Kuroda, N., Jia, S., Tong, K., Wen, R. R., et al.. (2018b). Revealing the evolution of non-thermal electrons in solar flares using 3D modeling. *Astrophys. J.* 859:17. doi: 10.3847/1538-4357/aabae9

Fleishman, G. D., Xu, Y., Nita, G. N., and Gary, D. E. (2016b). Validation of the coronal thick target source model. *Astrophys. J.* 816:62. doi: 10.3847/0004-637X/816/2/62

Gary, D. E., Chen, B., Dennis, B. R., Fleishman, G. D., Hurford, G. J., Krucker, S., et al. (2018). Microwave and hard x-ray observations of the 2017 September 10 solar limb flare. *Astrophys. J.* 863:83. doi: 10.3847/1538-4357/aad0ef

Gary, D. E., Fleishman, G. D., and Nita, G. M. (2013). Magnetography of solar flaring loops with microwave imaging spectropolarimetry. *Solar Phys.* 288, 549–565. doi: 10.1007/s11207-013-0299-3

Glesener, L., and Fleishman, G. D. (2018). Electron acceleration and jet-facilitated escape in an M-class solar flare on 2002 August 19. *Astrophys. J.* 867:84. doi: 10.3847/1538-4357/aacefe

Haug, E. (1997). On the use of nonrelativistic bremsstrahlung cross sections in astrophysics. *Astron. Astrophys.* 326, 417–418.

Hoyng, P., Duijveman, A., Machado, M. E., Rust, D. M., Svestka, Z., Boelee, A., et al. (1981). Origin and location of the hard x-ray emission in a two-ribbon flare. *Astrophys. J. Lett.* 246:L155. doi: 10.1086/183574

Koch, H. W., and Motz, J. W. (1959). Bremsstrahlung cross-section formulas and related data. *Rev. Modern Phys.* 31, 920–955. doi: 10.1103/RevModPhys.31.920

Krucker, S., and Battaglia, M. (2014). Particle densities within the acceleration region of a solar flare. *Astrophys. J.* 780:107. doi: 10.1088/0004-637X/780/1/107

Krucker, S., Hudson, H. S., Glesener, L., White, S. M., Masuda, S., Wuelser, J. P., et al. (2010). Measurements of the coronal acceleration region of a solar flare. *Astrophys. J.* 714, 1108–1119. doi: 10.1088/0004-637X/714/2/1108

Krucker, S., Saint-Hilaire, P., Hudson, H. S., Haberreiter, M., Martinez-Oliveros, J. C., Fivian, M. D., et al. (2015). Co-spatial white light and hard x-ray flare footpoints seen above the solar limb. *Astrophys. J.* 802:19. doi: 10.1088/0004-637X/802/1/19

Kundu, M. R., White, S. M., Gopalswamy, N., and Lim, J. (1994). Millimeter, microwave, hard x-ray, and soft x-ray observations of energetic electron populations in solar flares. *Astrophys. J. Suppl.* 90:599. doi: 10.1086/191881

Kuroda, N., Gary, D. E., Wang, H., Fleishman, G. D., Nita, G. M., and Jing, J. (2018). Three-dimensional forward-fit modeling of the hard x-ray and microwave emissions of the 2015 June 22 M6.5 Flare. *Astrophys. J.* 852:32. doi: 10.3847/1538-4357/aa9d98

Lee, J., and Gary, D. E. (2000). Solar microwave bursts and injection pitch-angle distribution of flare electrons. *Astrophys. J.* 543, 457–471. doi: 10.1086/317080

Lemen, J. R., Title, A. M., Akin, D. J., Boerner, P. F., Chou, C., Drake, J. F., et al. (2012). The atmospheric imaging assembly (AIA) on the solar dynamics observatory (SDO). *Solar Phys.* 275, 17–40. doi: 10.1007/s11207-011-9776-8

Lin, R. P., Dennis, B. R., Hurford, G. J., Smith, D. M., Zehnder, A., Harvey, P. R., et al. (2002). The Reuven Ramaty high-energy solar spectroscopic imager (RHESSI). *Solar Phys.* 210, 3–32. doi: 10.1023/A:1022428818870

Lin, R. P., and Hudson, H. S. (1971). 10 100 keV electron acceleration and emission from solar flares. *Solar Phys.* 17, 412–435. doi: 10.1007/BF00150045

Massone, A. M., Emslie, A. G., Kontar, E. P., Piana, M., Prato, M., and Brown, J. C. (2004). Anisotropic bremsstrahlung emission and the form of regularized electron flux spectra in solar flares. *Astrophys. J.* 613, 1233–1240. doi: 10.1086/423127

Masuda, S., Kosugi, T., Hara, H., Tsuneta, S., and Ogawara, Y. (1994). A loop-top hard X-ray source in a compact solar flare as evidence for magnetic reconnection. *Nature* 371, 495–497. doi: 10.1038/371495a0

Melnikov, V. F., Shibasaki, K., and Reznikova, V. E. (2002). Loop-top nonthermal microwave source in extended solar flaring loops. *Astrophys. J. Lett.* 580, L185–L188. doi: 10.1086/345587

Melrose, D. B. (1968). The emission and absorption of waves by charged particles in magnetized plasmas. *Astrophys. Space Sci.* 2, 171–235. doi: 10.1007/BF00651567

Melrose, D. B., and Brown, J. C. (1976). Precipitation in trap models for solar hard X-ray bursts. *Mon. Not. R. Astron. Soc.* 176, 15–30. doi: 10.1093/mnras/176.1.15

Nakajima, H., Nishio, M., Enome, S., Shibasaki, K., Takano, T., Hanaoka, Y., et al. (1994). The Nobeyama radioheliograph. *IEEE Proc.* 82, 705–713. doi: 10.1109/5.284737

Ning, H., Chen, Y., Wu, Z., Su, Y., Tian, H., Li, G., et al. (2018). Two-stage energy release process of a confined flare with double HXR peaks. *Astrophys. J.* 854:178. doi: 10.3847/1538-4357/aaaa69

Nita, G. M., Hickish, J., MacMahon, D., and Gary, D. E. (2016). EOVSA implementation of a spectral kurtosis correlator for transient detection and classification. *J. Astron. Instrum.* 5, 1641009–7366. doi: 10.1142/S2251171716410099

Nitta, N., and Kosugi, T. (1986). Energy of microwave-emitting electrons and hard x-ray / microwave source model in solar flares. *Solar Phys.* 105, 73–85. doi: 10.1007/BF00156378

Ramaty, R. (1969). Gyrosynchrotron emission and absorption in a magnetoactive plasma. *Astrophys. J.* 158:753. doi: 10.1086/150235

Schwartz, R. A., Csillaghy, A., Tolbert, A. K., Hurford, G. J., McTiernan, J., and Zarro, D. (2002). RHESSI data analysis software: rationale and methods. *Solar Phys.* 210, 165–191. doi: 10.1023/A:1022444531435

Silva, A. V. R., Wang, H., and Gary, D. E. (2000). Correlation of microwave and hard x-ray spectral parameters. *Astrophys. J.* 545, 1116–1123. doi: 10.1086/317822

White, S. M., Benz, A. O., Christe, S., Fárník, F., Kundu, M. R., Mann, G., et al. (2011). The relationship between solar radio and hard x-ray emission. *Space Sci. Rev.* 159, 225–261. doi: 10.1007/s11214-010-9708-1

Wu, Z., Chen, Y., Ning, H., Kong, X., and Lee, J. (2019). Gyrosynchrotron emission generated by nonthermal electrons with the energy spectra of a broken power law. *Astrophys. J.* 871:22. doi: 10.3847/1538-4357/aaf474

Conflict of Interest: The authors declare that the research was conducted in the absence of any commercial or financial relationships that could be construed as a potential conflict of interest.

APPENDIX

SAMPLES OF SPATIALLY-RESOLVED SPECTRA AND THEIR FITS

We show in here the sample of spatially-resolved MW spectra (black asterisks) and the fit results (green lines). The examples of successful fits are **(C,D)** and those of unsuccessful fits are **(A,B,E)**. The pixel selected for **(D,E)** is one of the pixels in the small red box shown in **Figure 3**. **(A–D)** show the results from 22:46:14 UT, a time between t_2 and t_3, and Panel **(E)** shows the result from the same pixel as **(D)** but at t_4, at the end of our fitting time period.

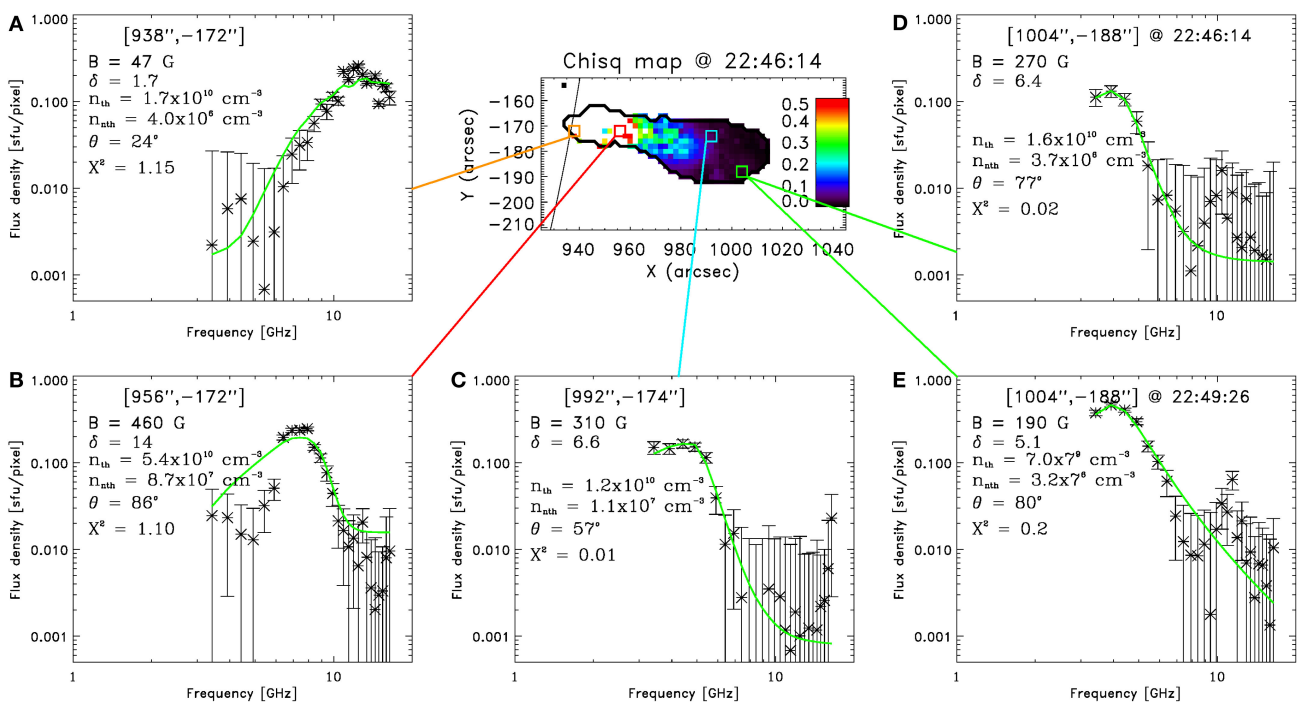

FIGURE A1 | (A) An unsuccessful fit due to the high peak frequency leading to the shortage of good data points in the optically-thin frequency range. Note the unrealistically low magnetic field value of 47 G, far lower than fits of surrounding pixels. **(B)** An unsuccessful fit due to the unusually narrow peak shape of the observed spectrum. **(C,D)** Examples of successful fits. Note that the magnetic field strength reasonably decreases with height. The χ^2 value is < 0:1, which is the criterion used in the quantitative analysis in Section 3. **(E)** An unsuccessful fit due to the contamination of the spectrum by a sidelobe of the highfrequency source at ∼ 11 GHz. The result is shown from the same pixel as **(D)** but at later time, at 22:49:26. This type of unsuccessful fit was more prelavent toward the end of our fitting time period as the flare emission intensity increased. Note that with this fit, the spectral index may be reported harder than the actual value. The χ^2 value is again > 0:1.

frontiers in Astronomy and Space Sciences

REVIEW
published: 11 August 2020
doi: 10.3389/fspas.2020.00045

Measuring Magnetic Field With Atacama Large Millimeter/Submillimeter Array

Maria Loukitcheva [1,2,3]*

[1] Max-Planck-Institut für Sonnensystemforschung, Göttingen, Germany, [2] St. Petersburg Branch of Special Astrophysical Observatory, St. Petersburg, Russia, [3] Mathematics and Mechanics Faculty, St. Petersburg State University, St. Petersburg, Russia

The article discusses the use of magnetic bremsstrahlung at short radio wavelengths for measuring solar magnetic fields. The polarization and brightness spectra observed at millimeter wavelengths can be used to deduce the vertical component of the chromospheric magnetic field both in the quit Sun and in active regions. State-of-the-art three-dimensional (3D) radiative magnetohydrodynamic (R-MHD) simulations of the quiet solar atmosphere were used to synthesize observational deliverables at the wavelengths of the Atacama Large Millimeter/Submillimeter Array (ALMA) and to test the applicability of the method. The article provides selected observational examples of the successful application of the method and presents an overview of the recent developments and potential of the magnetic field measurements with ALMA.

Keywords: radio emission, chromosphere, magnetic field, quiet Sun, active regions

OPEN ACCESS

Edited by:
Dale E. Gary,
New Jersey Institute of Technology, United States

Reviewed by:
Chaowei Jiang,
Harbin Institute of Technology, China
David Kuridze,
Aberystwyth University, United Kingdom

***Correspondence:**
Maria Loukitcheva
lukicheva@mps.mpg.de

Specialty section:
This article was submitted to Stellar and Solar Physics, a section of the journal Frontiers in Astronomy and Space Sciences

Received: *02 March 2020*
Accepted: *18 June 2020*
Published: *11 August 2020*

Citation:
Loukitcheva M (2020) Measuring Magnetic Field With Atacama Large Millimeter/Submillimeter Array. Front. Astron. Space Sci. 7:45. doi: 10.3389/fspas.2020.00045

INTRODUCTION

Magnetic field can affect radio emission in two ways: via the Lorentz force, which causes the emitting electrons to spiral in the magnetic field providing a direct source of opacity for gyroemission, and via modification of the plasma response to electromagnetic fields, leading to different refractive index and polarization for the ordinary (o) and extraordinary (x) magnetoionic wave modes. Their polarization becomes dependent on the properties of the plasma through which they propagate, in particular on the local values of the plasma parameters $u = \left(\frac{\nu_B}{\nu}\right)^2$ (dimensionless magnetic field parameter) and $v = \left(\frac{\nu_p}{\nu}\right)^2$ (dimensionless electron density); where ν is the frequency, ν_B and ν_p are the gyrofrequency and the plasma frequency, respectively (see, e.g., Alissandrakis, 2020). By observing polarized radio emission, we can generally get access to the information it contains on magnetic field (but also on density and temperature).

While gyroresonance emission from non-relativistic plasma at low harmonics of the gyrofrequency, which is an example of the direct effect of magnetic field on opacity, is responsible for the coronal emission of non-flaring solar active regions observed at centimeter (cm) wavelengths, the thermal bremsstrahlung is dominant in the corona of the quiet Sun (QS), as well as in more dense chromospheric layers. Bremsstrahlung emission (also known as free–free emission, as free electrons remain unbound after being deflected by ions), is an example of the plasma response to the presence of magnetic field. Bremsstrahlung becomes weakly polarized in a magnetized plasma like the solar outer atmosphere.

The radio regime has the advantage over the other wavelengths as radio emission gets optically thick in the solar atmosphere. Measuring radio emission at different frequencies,

we in fact get access to different layers of the solar atmosphere. Free–free emission provides sufficient opacity at long radio wavelengths for the solar corona to become optically thick, while at short wavelengths (millimeter and submillimeter) it gets optically thick in the chromospheric layers. Submillimeter (submm) emission gets optically thick already at the heights near the temperature minimum and in the lower chromosphere, while the emission at longest millimeter (mm) wavelengths originates from the upper chromosphere and the transition region. This makes observations of free–free emission at mm and submm wavelengths a vital source of information about the enigmatic layers of the solar atmosphere, which play a significant role in defining the dynamics and energy budget of not only the solar corona, but also of the solar wind.

The Solar Chromosphere

Without any exaggeration, understanding the physics of chromosphere is the key to understanding the whole solar atmosphere, as the major transitions, e.g., from fully ionized to partially ionized plasma, from local thermodynamic equilibrium (LTE) to non-local thermodynamic equilibrium (non-LTE) radiative transfer, from strong to weak collisional coupling, and from plasma-dominated to magnetic field–dominated media, take place at chromospheric heights (Carlsson et al., 2019).

In the solar atmosphere, plasma motions dominate the magnetic field in the photosphere and low chromosphere, but as the density decreases exponentially with height, the magnetic field starts to govern the dynamics of the plasma in the upper chromosphere. Due to exponentially decreasing gas pressure, the magnetic field also starts to spread rapidly horizontally, and already in the lower chromosphere, essentially all the space, including regions of weak photospheric field, is filled with the magnetic field. Thus, the chromospheric structure is largely set by the magnetic field. Images in traditional optical and UV lines clearly show that the chromospheric plasma is organized along the magnetic field lines and concentrations (e.g., De Pontieu et al., 2007; Rutten, 2007). At the same time, numerous chromospheric simulations confirm that the magnetic field plays a critical role in chromospheric heating and dynamics (e.g., see Wiegelmann et al., 2014, for a review).

However, due to its highly structured, dynamic, and physically complex nature, the chromosphere is difficult to observe and those observations are not easy to interpret quantitatively. The traditional chromospheric diagnostic using the UV and IR lines suffers from the fact that it can only sample the hotter component of the gas, as at these wavelengths the Planck function depends on the temperature exponentially, implying that any average is weighted toward the maximum temperature (Carlsson and Stein, 1995). Additionally, as the source function is decoupled from the Planck function, a careful treatment of non-LTE effects is required for these lines.

Mainly due to the shortcomings of the traditional diagnostics, our knowledge about the chromospheric field and its role in creating and maintaining the chromosphere outside active regions remains quite poor. While measuring of Zeeman splitting of the spectral lines has been successfully employed in the optical polarimeters for diagnosing the photospheric field, in the chromosphere, the situation is less prosperous. Spectral lines that are sensitive to the chromospheric heights are usually very broad and only their cores reflect chromospheric features. The few chromospheric lines in the optical and near infrared that are sensitive to the Zeeman and Hanle effects, like the lines of singly ionized calcium, neutral hydrogen, and neutral helium, might be useful for chromospheric magnetometry, but are, in fact, extremely difficult to exploit in the regions of weak field because their polarization signal from the latter is commonly weak and requires high signal-to-noise ratio (SNR). In addition, the use of these lines in the quiet Sun is restricted due to a wide range of formation heights and the necessity for non-LTE treatment in the inversions. Successful examples of measuring chromospheric magnetic field outside of sunspots with these spectral lines typically refer to the observational structures with a relatively strong magnetic field [e.g., fibrils observed in the CaII 854.2 nm line by de la Cruz Rodríguez et al. (2010) and de la Cruz Rodríguez and Socas-Navarro (2011), or erupting filament prior to and during the eruption observed in the He I 1,083 nm line by Wang et al. (2020)] or to observations off-disk [e.g., He D3 line observations of prominences by Casini et al. (2003) and of spicules by López Ariste and Casini (2005)]. Recent unique observations of the active region flaring loops at the limb in the CaII 854.2 nm line with unprecedented spatial and temporal resolution by Kuridze et al. (2019) allowed the use of the chromospheric diagnostics at the coronal heights and to obtain measurements of the coronal magnetic field up to 25 Mm height. Commonly in the corona, measurements of magnetic fields in the spectral lines are obtained by means of the coronal emission line spectropolarimetry [e.g., observation in the Fe XIII 1,075 nm coronal emission line in active regions above the solar limb reported in Lin et al. (2004)]. The most recent reviews on the current and future instrumentation for solar spectropolarimetry and on the results of the solar polarimetric measurements can be found in Iglesias and Feller (2019) and Suárez (2019).

Chromospheric observations at long wavelengths like the mm wavelengths have the advantage that in the Rayleigh-Jeans regime, the Planck function varies linearly with temperature and LTE is a good approximation for the free–free processes dominant in the formation of the radiation at these wavelengths. As a result, at a given wavelength, the temperature of the emitting material is linearly proportional to the observed intensity. This unique capability makes mm wavelengths a primary candidate for diagnostics of the thermal structure of the chromospheric plasma. Furthermore, mm wavelength observations of the free–free polarization contain information on the magnetic field and provide a method of measuring the longitudinal component of magnetic fields in the solar chromosphere.

While previous available radio data were used to address general properties of large-scale solar chromospheric structures, the spatial resolution of those observations was insufficient to diagnose the small-scale processes that define the solar outer atmosphere. The situation has changed drastically after commissioning of the Atacama Large Millimeter/Submillimeter Array (ALMA) for the solar observations.

ALMA

The ALMA is located in Chile at an altitude of 5,000 m and is operated in cooperation between the National Radio Astronomy Observatory, the European Organization for Astronomical Research in the Southern Hemisphere, and the National Astronomical Observatory of Japan. ALMA interferometer is composed of 66 high-precision antennas, including the 12 m Array of 50 antennas for high-resolution imaging, and the Atacama Compact Array of twelve 7 m antennas together with four total power (TP) antennas 12 m in diameter, to enhance wide-field imaging (Wootten and Thompson, 2009; Hills et al., 2010). Currently, ALMA antennas are equipped with eight receivers, covering the range of wavelengths from 0.3 mm (Band 10, 950 GHz) to 3.6 mm (Band 3, 84 GHz). Two receivers for longer wavelengths are planned to be added, with one receiver up to 8.6 mm (Band 1, 35 GHz, Huang et al., 2016, 2018) being in construction, and the second one, for the wavelengths up to 4.6 mm (Band 2, 67–116 GHz, Yagoubov et al., 2020), being under development. The array is reconfigurable in multiple patterns (configurations) ranging in size from 150 m (compact) up to 16 km (extended), depending on the required sensitivity and spatial resolution. At the shortest ALMA wavelengths and in the most extended configurations, the array can achieve the spatial resolution of a few milliarcseconds. The instantaneous field of view (FOV) of the interferometer is a function of wavelength and the primary beam size of the array antennas: when observing at Bands 3 and 6, the 12 m antenna FOV size is $\sim 60''$ and $\sim 25''$, respectively. When observational targets require larger size of FOV, as in the case of mapping of the structures in the solar chromosphere, regime of mosaicing is offered.

Regular ALMA solar observing started in 2016, preceded by commissioning and science verification activities (Shimojo et al., 2017; White et al., 2017). Current solar ALMA capabilities include interferometric observations in the three frequency bands: Band 3 (3 mm), Band 6 (1 mm), and Band 7 (0.85 mm) in compact array configurations, with a maximum spatial resolution of $0.9''$, $0.6''$, and $0.6''$, respectively, with 1 s time integration (Remijan et al., 2019). In principle, ALMA is able to provide about two orders of magnitude improvement in resolution, sensitivity, and frequency coverage, over the previously existing instruments operated at short radio wavelengths. As the emission at ALMA wavelengths is optically thick at different heights in the solar chromosphere and the sampled intensity linearly translates into the local gas temperature, ALMA provides a nearly perfect thermometer for the chromospheric heights. For instance, its ability to probe a wide range of chromospheric temperatures from cool to hot gas and to detect chromospheric features missed by the SDO and IRIS has been recently demonstrated by Loukitcheva et al. (2019). At present ALMA is able to acquire height and time-dependent diagnostics of thermal plasma properties at high spatial, spectral, and temporal resolution. Future ALMA observations of circular polarization (see section ALMA Polarization Measurements) will offer a diagnostic tool for the chromospheric magnetic fields. The use of ALMA observations for solar studies is not limited to diagnostics of the thermal and magnetic structures of the chromosphere and is thoroughly discussed by Wedemeyer et al. (2016).

MEASURING MAGNETIC FIELD FROM FREE–FREE EMISSION

Magnetic Bremsstrahlung

The physics of bremsstrahlung emission in the solar context has been reviewed by many authors (e.g., Zlotnik, 1968; Dulk, 1985; Zheleznyakov, 1996; Gelfreikh, 2004) and can also be found in the previous chapters of this volume. Among the two oppositely polarized natural (or normal) modes of electromagnetic wave that propagate in a magnetized plasma, the extraordinary mode interacts stronger with the magnetic field than the ordinary mode. Consequently, in the presence of magnetic fields, the absorption coefficients for the two modes are different.

The generalized formulas for the free–free absorption coefficients for x- and o-modes include the full anisotropic term, and can be written as follows (e.g., Zlotnik, 1968; Fleishman and Toptygin, 2013; Loukitcheva et al., 2017):

$$k_\sigma \simeq k_\sigma^0 \frac{F_\sigma}{n_\sigma} \tag{1}$$

where subscript σ denotes one of the modes ($\sigma = -1, 1$ for the x- and the o-modes, respectively), k_σ^0 is the absorption coefficient for the isotropic plasma, and n_σ is the refraction index, as defined by, e.g., Alissandrakis (2020).

The magnetic field factor F_σ has the following form:

$$F_\sigma = 2\frac{\sigma\sqrt{D}\left(usin^2\theta + 2\left(1-\nu\right)^2\right) - u^2 sin^4\theta}{\sigma\sqrt{D}\left(2\left(1-\nu\right) - usin^2\theta + \sigma\sqrt{D}\right)^2} \tag{2}$$

where $u = \left(\frac{\nu_B}{\nu}\right)^2$, $\nu = \left(\frac{\nu_p}{\nu}\right)^2$, ν_p is the plasma frequency, and θ is the angle between magnetic field and the line of sight.

Commonly, the absorption coefficients for x- and o-modes are calculated using the quasilongitudinal approximation (QL), which remains valid for most of the angles of the magnetic field to the line of sight except transverse propagation (Zlotnik, 1968; Zheleznyakov, 1996):

$$k_\sigma \doteq \frac{k_\sigma^0}{\left(1 + \sigma\frac{\nu_B}{\nu}\left|cos\theta\right|\right)^2} \tag{3}$$

where ν_B is the gyrofrequency.

As can be seen from Equation (3), the absorption coefficient and thus the opacity for the x-mode are higher, leading to separation of the optically thick layers of the two modes. In isothermal plasma, both modes will have the same brightness temperature that is equal to the temperature of the medium. However, in plasma with a vertical temperature gradient, like in the solar atmosphere with temperature increasing outwards, at a given frequency, the corresponding brightness temperature of the modes will be different, as the x-mode will be observed from higher and thus hotter layers than the o-mode. In other words, the presence of magnetic field shifts the optically thick layers (and consequently the formation heights) of the two

modes in opposite directions along the temperature gradient. The observed temperature difference between two layers is interpreted as net circular polarization. The difference between the formation heights of the two modes is proportional to the magnetic field strength, resulting in a proportionally stronger net polarization. Thus, polarization measurements contain information about the magnetic field strength, but indirectly, via the temperature gradient.

Method for Magnetic Field Estimate

The basic concepts of the method of estimation of magnetic field from thermal free–free were introduced by Bogod and Gelfreikh (1980), while the diagnostic potential as well as the examples of the application of the free–free polarization observations for coronal/chromospheric magnetic field measurements were thoroughly discussed by Gelfreikh (2004). As was noted above, measured polarized signal carries information on the magnetic field indirectly via the temperature gradient. This implies that to isolate the effect of magnetic field in the measured polarization, it is required to deduce the temperature gradient independently. Bogod and Gelfreikh (1980) demonstrated a method to derive the temperature gradient from the variation of brightness temperature with frequency, using the scaling law, which relates the brightness temperatures of the natural modes in a magnetic field T_b^{σ} to the total unpolarized brightness temperature T_b,

$$T_b^{\sigma}(\nu) = T_b(\nu + \sigma \nu_B |cos\theta|) \tag{4}$$

Bogod and Gelfreikh (1980) introduced the logarithmic spectral index n, which corresponds to the slope of the brightness spectrum, as:

$$n = \frac{\partial (lnT_b)}{\partial (ln\nu)} \tag{5}$$

where the frequency serves as a proxy for height, and derived circular polarization degree P using the scaling law from Equation (4) as:

$$P = \frac{T_b^x - T_b^o}{T_b^x + T_b^o} = n\frac{\nu_B}{\nu} cos\theta \tag{6}$$

Taking into account that the longitudinal component of the magnetic field is $B_l = B\ cos\theta$, and the electron gyrofrequency is $\nu_B = 2.8 \cdot 10^6 B$, an estimate for the longitudinal component of the magnetic field can be written as follows:

$$B_l = \frac{P\nu}{2.8 \cdot 10^6 n} \tag{7}$$

Thereby, this technique requires measurements of polarization at a given frequency as well as of the brightness spectrum around the frequency to measure the slope. The method uses the assumption of a homogeneous magnetic field within the layer where the normal modes are formed. According to the simulations (e.g., section Magnetic Fields in the Quiet Sun) in the quiescent regions, the width of this layer does not exceed a few kilometers. The obtained estimation of the magnetic field refers to the height where the emission at a given frequency is generated (further discussed in section Simulating Magnetic Field Measurements With ALMA), implying that, tuning the frequency, we can measure the magnetic field at different heights in the chromosphere. Finally, multi-frequency measurements of polarization degrees and of spectral indexes make chromospheric magnetography (of longitudinal component) possible.

Equation (7) provides a general form for estimation of the longitudinal component of the magnetic field that is applicable for the optically thick at mm wavelengths chromosphere as well as for the optically thin free–free emission from the corona. As bremsstrahlung is sensitive to the regions of the enhanced density, solar images at mm and short cm can reflect not only the optically thick chromospheric part but also plasma structures from the transition region and solar corona. These coronal condensations, characterized by the local density enhancements, are commonly seen in the radio maps at short cm wavelengths as brightness sources and are typically optically thin. Using the fact that for the optically thin isothermal emission we expect the spectral index $n = 2$ and thus spectral observations are not required, we can obtain the following simplified version of Equation (7) in case of optically thin coronal contribution:

$$B_l = \frac{P\nu}{5.6 \cdot 10^6} \tag{8}$$

The magnetic field in coronal condensations both on the limb and on the disk can be studied using thermal bremsstrahlung. However, when observing a bright polarized source on the disk, which implies the presence of inhomogeneous magnetic field over the line of sight, it needs to be found out which of the layers (chromosphere or corona) are responsible for its polarization at a given wavelength and further it is typically required to separate the contributions from the two layers into the recorded polarized emission. In a more general case of inhomogeneous thermal structures (composed of multi-thermal components, such as filaments, chromospheric and coronal jets, flare loops) present on the disk, employment of additional observations from other spectral domains and advanced modeling will be required to separate the contributions from the different structures.

The method to study the magnetic field from the thermal bremsstrahlung was modified by Grebinskij et al. (1998, 2000) to be used for single-frequency observations [at the Nobeyama Radioheliograph (NoRH) at 17 GHz] and for multiple frequencies (for RATAN at 1–18 GHz). A comprehensive review of the applicability of the technique for different combinations of optical thickness in homogeneous and inhomogeneous sources, as well as discussion on how to discriminate between contributions from the chromosphere and corona in the measured polarization, and how to account for the combined effect

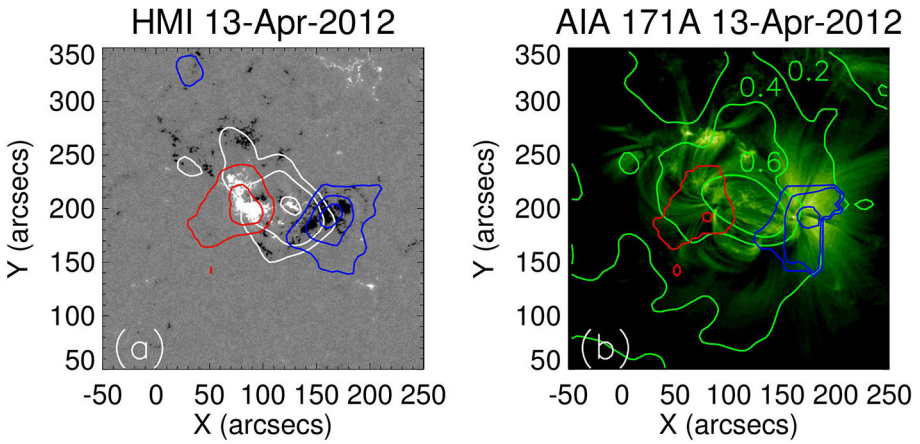

FIGURE 1 | (a) The photospheric magnetogram observed by SDO/HMI on April 13, 2012, with the overlaid contours of radio intensity at 17 GHz plotted in white and circular polarization at 17 GHz with positive components at 0.5 and 1.0% plotted in red, and negative components at 0.5, 1.0, and 1.5% plotted in blue. **(b)** The corresponding EUV image at 171A observed by SDO/AIA with the overlaid contours of the magnetic field (with positive components at 50 and 150 G shown in red, negative components at 50, 150, and 250 G plotted in blue) derived from the measured polarization at 17 GHz and the spectral index, and with the contours of the local spectral index at the levels of 0.2, 0.4, and 0.6 depicted in green.

of bremsstrahlung and gyroresonance emission at cm wavelength, is beyond the scope of the present paper and can be found in Gelfreikh (2004); see also the previous chapter by Kostas Allissandrakis.

At mm wavelengths, the method can be applied effectively in the regions with weak fields, like quiescent and plage areas, coronal holes, prominences, as well as in sunspots where the magnetic field is strong, provided that the measured polarization is of the free–free nature. Thus, using Equation (7), we can get an estimate of the longitudinal component of the magnetic field in the plasma structures of the chromosphere and transition region up to the solar corona, both on the disk and above the solar limb.

Measurements of free–free polarization require high precision and low noise level, as free–free polarization effects are known to be quite weak at these frequencies, with the circular polarization degree not exceeding 10% for the strongest magnetic fields (Grebinskij et al., 2000). This makes observational noise level one of the major concerns for the application of this method. One of the approaches that help to reduce the noise level of the data consists of averaging of the data over time. Thus, as was shown by Gelfreikh (2004), the sensitivity of the NoRH data at 17 GHz can be substantially improved by averaging the images over 10 min intervals. It was demonstrated by Bogod and Gelfreikh (1980) that for the NoRH data, the restored longitudinal magnetic field component can be approximated by the value of the measured polarization signal ($B_l \approx T_b^x - T_b^o = T_b^V$). This implies that for the default image integration of 10 s, the sensitivity of the NoRH maps of about 1% (of the quiet-Sun brightness level of 10,000 K) translates into the accuracy of the restored field of about 100 G, while averaging over 10 min instead of 10 s brings the statistical polarization noise in the synthesized images down to a few Kelvin and thus the sensitivity of the method to a few Gauss.

Selected Observational Examples

The polarization of free–free emissions from the active regions, including sunspots, plages, prominences, coronal holes, loops, and arches has been previously observed with the RATAN-600 (Bogod and Gelfreikh, 1980; Grebinskij et al., 1998, 2000), the VLA (e.g., Shevgaonkar and Kundu, 1984; Schmelz et al., 1994), and the NoRH (e.g., Gelfreikh and Shibasaki, 1999). Longitudinal magnetic fields measured from the circular polarization at short cm were found to be in the range from 60 to 150 G in the chromosphere and corona of active regions. Recently, Kallunki et al. (2020) reported the first successful solar polarization observations at 3 and 13 mm carried out with the Aalto University Metsähovi Radio Telescope. **Figures 1–3** provide the examples of the most recent observations, obtained with the NoRH (Iwai and Shibasaki, 2013; Miyawaki et al., 2016) and with the RATAN-600 (Kaltman, 2019). Iwai and Shibasaki (2013) derived the coronal and chromospheric magnetic fields in the active region NOAA 11455 from the circular polarization observations at 17 GHz and spectral observations at 17 and 34 GHz obtained by NoRH on April 13, 2012 (**Figure 1**). Time averaging of the images over 20 min allowed to reach the minimum detectable polarization level of 0.5%. The observed circular polarization degrees were 0.5 and 1.7% for the two polarities, and the restored magnetic fields were found to be about 20–50% of the their photospheric value. However, for the central part of the active region, the authors were not able to discriminate between the coronal and chromospheric components of the derived magnetic field, and the reported values were considered to be emission-measure-weighted.

An example of the successful separation of the two components is presented in Miyawaki et al. (2016). For analysis of the active region NOAO 11150, the authors selected a part of the active region consisting of coronal loops and only weak chromospheric magnetic field, and combined the circular

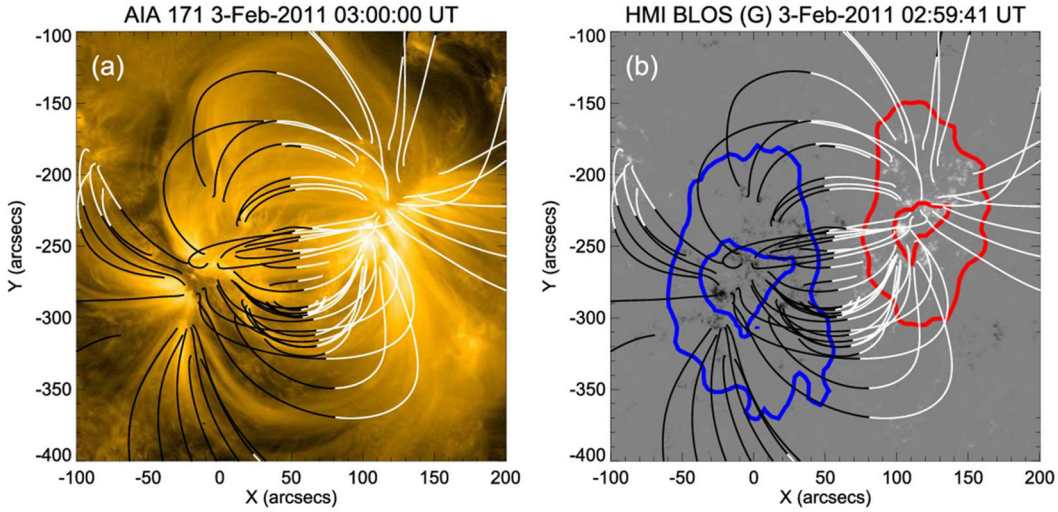

FIGURE 2 | (a) 171A image of AR NOAO 11150 observed with SDO/AIA on February 2, 2011 with the overlaid outward (white) and inward (black) magnetic field lines from the potential field extrapolation. **(b)** The same for the photospheric longitudinal magnetic field observed with SDO/HMI with the contours of the degree of positive circular polarization at 0.4 and 0.8% at 17 GHz, shown in red, and the contours of the degree of negative circular polarization at −0.4 and −0.8% at 17 GHz, shown in blue. From Miyawaki et al. (2016). Reproduced by permission of the AAS.

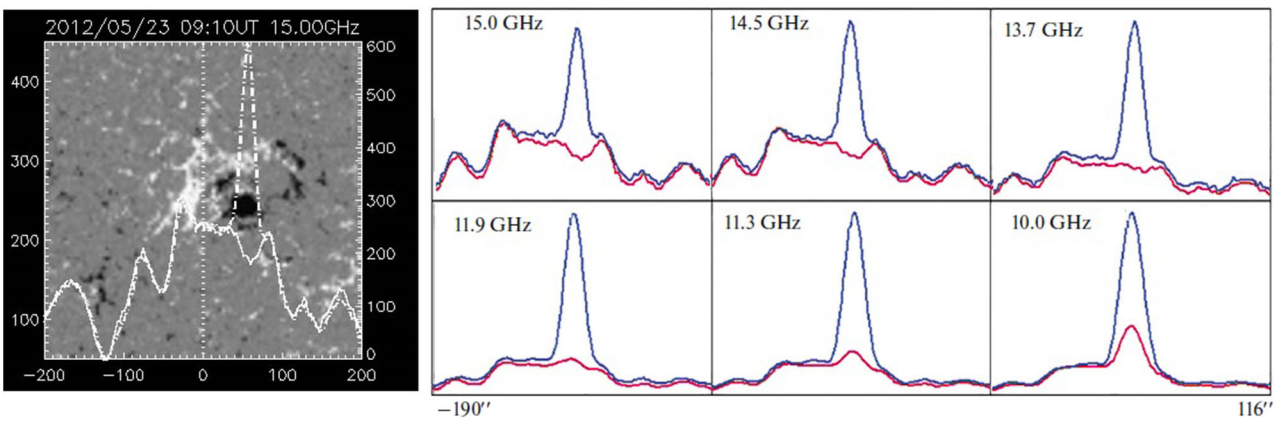

FIGURE 3 | (Left) One-dimensional scans of the active region NOAO 11486 in the ordinary (solid line) and extraordinary (dotted) wave modes observed at 15 GHz with the RATAN-600 on May 23, 2012, superimposed on the SDO/HMI magnetogram. **(Right)** The evolution of the sunspot-associated sources in the range of 10–15 GHz, with the ordinary mode shown in red and the extraordinary mode depicted in blue.

polarization measurements at 17 GHz with the coronal emission measure estimations from the EUV observations. The derived coronal magnetic fields in the range of 100–210 G were compared with the results of the potential field extrapolation using the photospheric magnetograms from the SDO/HMI (**Figure 2**) and were interpreted as the upper limits of the coronal longitudinal magnetic fields.

A recent study of the free–free sources above sunspots observed with the RATAN-600 is presented in Kaltman (2019), with the accurate analysis of the contributions from thermal bremsstrahlung and gyroresonance radiation into the observed polarized emission in the high-frequency part of the RATAN-600 spectrum of 12–20 GHz (1.5–2.5 cm). The observations and the simulations confirmed that at high frequencies (15 and 14.5 GHz), for which the magnetic field is not enough to generate significant gyroresonance emission in both modes, magnetic bremsstrahlung is strong enough to clearly separate the intensities of the two modes (**Figure 3**). At these frequencies, a bright sunspot cyclotron source is observed in the extraordinary mode, while the ordinary mode is due to bremsstrahlung and shows a pronounced dip in the intensity. The wide frequency coverage and fine frequency resolution of the RATAN-600 made it possible to follow the transition from the pure bremsstrahlung to a growing cyclotron source in the ordinary mode, when moving to lower frequencies.

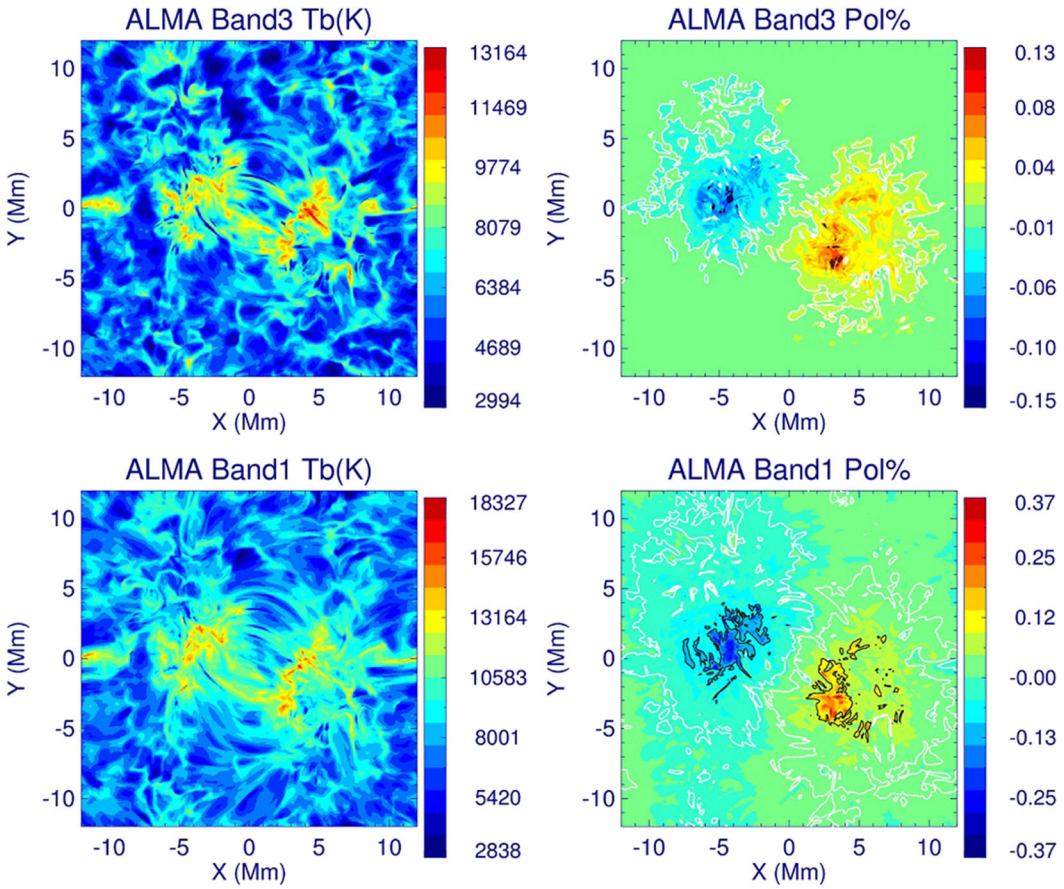

FIGURE 4 | Maps of simulated total brightness **(left)** and circular polarization degree **(right)** at the resolution of the ENW dynamic model (0.06″) for ALMA Bands 3 (3 mm) and 1 (8.6 mm). White and black contours indicate the polarization degrees |P| = 0.01% and |P| = 0.1%, respectively.

SIMULATING MAGNETIC FIELD MEASUREMENTS WITH ALMA

As was reviewed in the previous section, the technique to estimate magnetic fields from the observed free–free emission was employed solely to the measurements at cm wavelengths, primarily because of the absence of the instruments in the mm range, capable to measure the relatively low degree of free–free polarization and brightness temperature spectra with sufficient accuracy. The advent of the ALMA interferometer operating at these wavelengths has changed the scene as the instrument's potential capabilities fully satisfy the requirements for the successful application of the method.

Magnetic Fields in the Quiet Sun

As was noted above, the described method is in general suitable for determination of the chromospheric magnetic fields in the QS regions. Loukitcheva et al. (2017) used advanced three-dimensional (3D) radiative magnetohydrodynamic (R-MHD) simulations of the enhanced network (ENW) made with the Bifrost code (Gudiksen et al., 2011) to predict the polarization that can be observed in the QS with ALMA. The authors calculated the free–free emission in the ALMA frequency bands (including Bands 1 and 2, which have not yet been delivered) from the 3D model and analyzed the simulated brightness temperatures as if they were observational data to derive the longitudinal magnetic field. The latter were then compared with the magnetic field in the model to study the precision of the method.

The Model Atmosphere

The model snapshot that was used by Loukitcheva et al. (2017) is described in detail by Carlsson et al. (2016). The simulation box includes the upper convection zone, photosphere, chromosphere, and the lower corona with the horizontal grid spacing of 48 km (0.06″), and with the non-uniform vertical grid spacing of 19–98 km. The model includes the non-equilibrium ionization of hydrogen. The average unsigned magnetic field strength is 48 G at the photospheric level. It is concentrated in the two clusters of opposite polarity, which represent the QS enhanced network (ENW) with the maximum field strength of 2,000 G, lying about 8 Mm apart. The magnetic field expands with height and fills all space above heights of around 1 Mm with higher temperatures seen in the regions of strong field than in neighboring regions

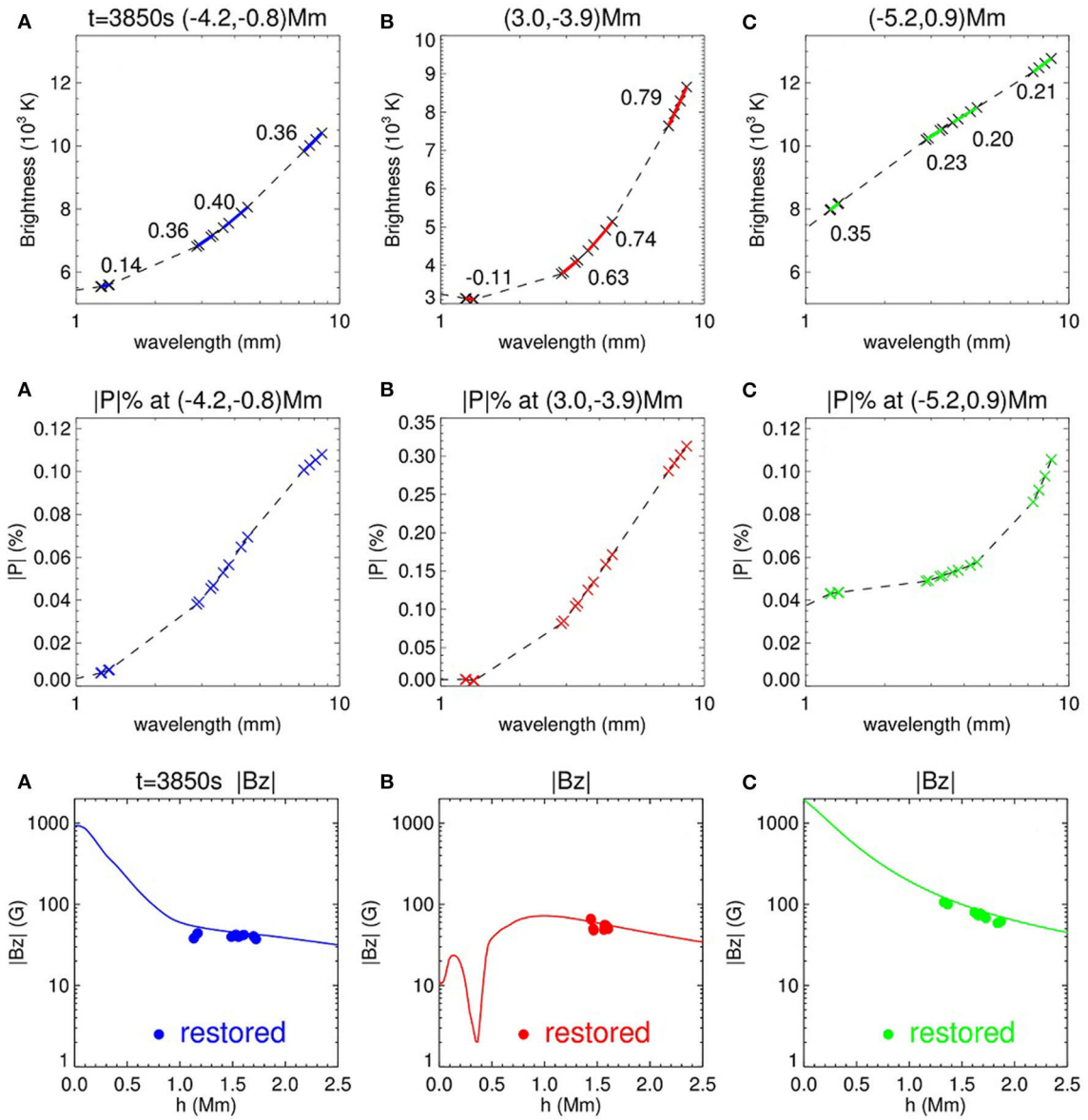

FIGURE 5 | The demonstration of the method for three individual spatial locations within the ENW snapshot. (Top) Simulated total brightness spectrum at mm wavelengths for spatial locations **(A)** (−4.2, 0.8) Mm, **(B)** (3.0, −3.9) Mm, and **(C)** (−5.2, 0.9) Mm, with colored crosses showing the wavelengths of the four ALMA Bands analyzed in detail. The values of the local slope n are given for each band. (Middle) Absolute value of simulated circular polarization degree as a function of wavelength for the same spatial locations and bands. (Bottom) Absolute value of the model longitudinal magnetic field as a function of height plotted together with the values of the magnetic field (circles) derived from the mm brightness spectrum and polarization degree plotted at the effective formation heights of the mm radiation.

and with pronounced loop-like structures connecting the two ENW patches.

Simulated Polarization and Magnetic Field

The time-dependent simulations show evolving chromospheric patterns with a time scale of a few 10 s due to the waves passing through the simulation box in three dimensions. The brightness structure seen in the synthesized mm images is found to be similar: it shows a complex pattern of intermittent bright (hot) and dark (cool) regions, with prominent bright fibrils aligned along the chromospheric magnetic field lines, seen at wavelengths around 3 mm (Band 3) and longer (**Figure 4**).

In Band 3, the simulated brightness temperatures are found in the range from 3,000 to 13,000 K with an average of 6,200 K and a standard deviation of 1,400 K. The values for Band 6 are, respectively, from 2,600 to 12,000 K with an average of 5,000 K and a standard deviation of 1,000 K. In Band 1, the brightness varies from 2,800 to 18,300 K with an average of around 8,200 K. The heights corresponding to the ALMA frequency bands range from about 750 km (Band 9) to 2,000 km (Band 1, see below

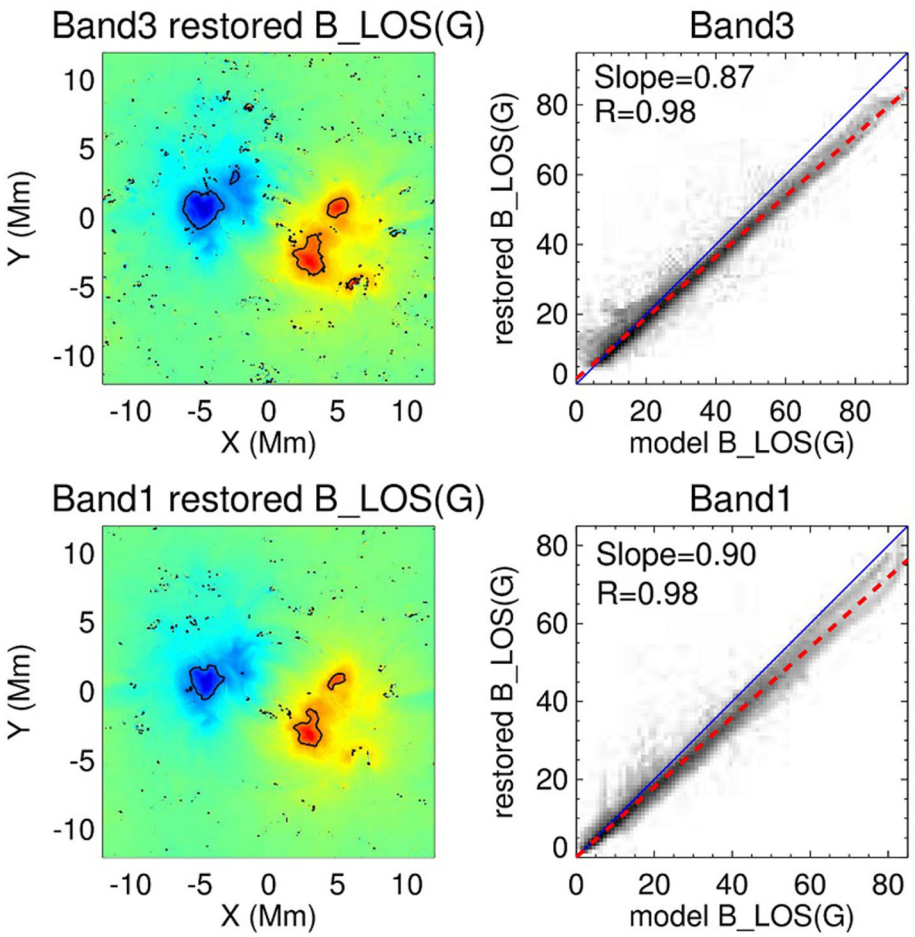

FIGURE 6 | (Left) Maps of the restored longitudinal component of the magnetic field at ALMA Bands 3 and 1, plotted in the range from −100 to 100 G. Black contours depict $|B_{||}| = 50$ G. **(Right)** Restored longitudinal magnetic field vs. model field taken at the effective formation heights plotted in the form of the density plots (2D histograms). Darker shading indicates a higher density of pixels in the bin. Solid lines denote the expectation value, when restored field is equal to the model field. Dashed lines depict the linear regressions with the slopes and the Pearson correlation coefficients given in the upper left corner of each frame.

for the details). Interestingly, in the ALMA commissioning data, the average temperatures at ALMA Bands 3 and 6 were found to be at 7,300 and 5,900 K, respectively (White et al., 2017), which is significantly higher than the values obtained from the ENW simulations.

As can be seen from the maps of simulated circular polarization degree for ALMA Bands 3 and 1, shown in **Figure 4**, the simulated polarization on an absolute scale is quite low, not reaching 0.5% for the longest Band 1, and being only 0.15% in Band 3. Higher polarization degree is found in the regions of enhanced brightness due to steeper temperature gradients at these locations, as well as at the locations of strong magnetic field, which causes stronger separation of the formation heights of the two modes. However, these degrees of polarization are obtained on the absolute temperature scale, while the interferometer measures only brightness temperature contrast (the absolute brightness difference between the two polarizations in K) across the solar atmosphere, which means that measured interferometer polarization will be actually about 10 times larger than the degrees of polarization on the absolute temperature scale, leading to about 1.5% at Band 3 and 5% at Band 1. More details of the measuring the solar polarization with ALMA are given in the next section, but for a detailed discussion, please refer to Loukitcheva et al. (2017). The authors stated that although the estimated polarization is quite low, it is higher than the technical requirement for ALMA circular polarization measurements, which is defined as 0.1%, implying that the ALMA interferometer can be employed to measure solar polarization.

Examples of the reconstruction of the magnetic field from the estimated circular polarization degree and the local brightness spectrum are shown in **Figure 5** for individual spatial locations, and the results of the reconstruction for Band 3 and Band 1 in the form of the 2D maps together with the comparison with the model field are given in **Figure 6**. The restored chromospheric magnetic field lies in the range from −100 to 100 G, and there is a good general correlation between the restored values of the magnetic field and the model field taken at the heights where emission at corresponding frequency is formed. Thus, within

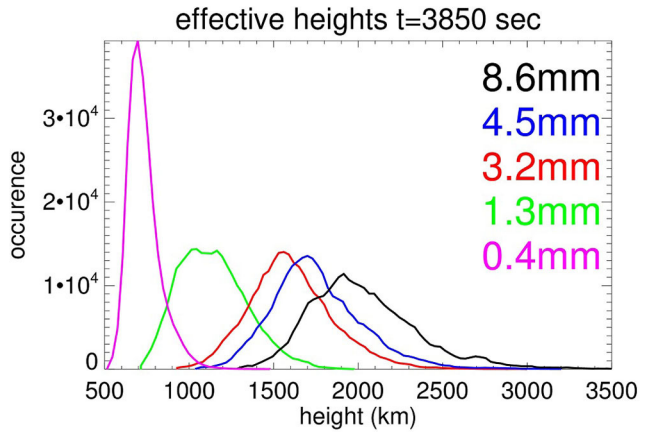

FIGURE 7 | Histograms of the effective heights of formation of the radiation in the ALMA Bands 1 (8.6 mm, plotted in black), 2 (4.5 mm, blue), 3 (3.2 mm, red), 6 (1.3 mm, green), and 9 (0.4 mm, magenta) for all spatial locations within the ENW model snapshot.

the regions where unsigned polarization degree exceeds 0.01%, the relative error does not exceed 10%, and the model and restored fields agree reasonably well, although the restored field is on average systematically underestimated (**Figure 6**). The latter might be due to the fact that the restored field corresponds to the average over the heights contributing to the radiation.

Loukitcheva et al. (2017) concluded that the method is applicable to measurements of weak chromospheric magnetic field in the QS (and stronger fields in active regions), providing the estimate of the longitudinal component of the field at the effective height of formation. From the simulations, it follows that robust application of this technique might require sensitivity in circular polarization better than 0.1%. The simulated degrees of polarization are further reduced, when the effect of instrumental smearing is taken into account, yielding for Band 3 interferometer observations at a resolution of $1''$ polarization smaller than 1% and even lower values at higher frequency bands, implying the importance of the observations in the lower frequency Bands 1 and 2 for reliable polarization measurements in the QS. All in all, the method was found to reproduce the longitudinal magnetic field quite well with the model data. However, realistic ALMA polarization measurements are required for practical estimations of the potential measurements of the magnetic field with ALMA.

Heights of Formation of mm Emission in the Quiet Chromosphere

The individual heights of formation of the ALMA Bands can vary significantly as the local values of electron density and temperature, as well as the steepness of their gradients, which mainly define the location of the optically thick layer, vary in space and time. But in general, the effective formation heights of the mm continuum increase with height and are located around the height of the temperature minimum at the highest frequencies and in the upper chromosphere and transition region at the lowest ALMA frequencies. For instance, average (effective) formation heights for both natural modes, derived from the forms of the contribution functions, which describe how much of the emergent radiation is contributed over height, for Bands 3 and 1 are around 1,600 and 2,000 km above the photosphere, respectively. An overview of the heights of the radiation at different ALMA Bands can be seen in **Figure 7** in the form of the histograms of the effective formation heights for the extraordinary mode at Bands 9, 6, 3, 2, and 1, taken for all spatial locations within the ENW model snapshot. The formation heights of the ordinary mode are similar, with the maximum difference between the effective formation heights of the two individual modes not exceeding 4 km for the longest Band 1 (Loukitcheva et al., 2017). Note that this height difference refers to the width of the layer where the magnetic field is measured. The distributions are seen to be quite wide, with a significant overlap between the frequency bands. There also seems to be a tendency for the effective height range to get wider with wavelength, which implies that the diversity of individual height distributions of electron temperature and density gets more pronounced with height. All in all, the increase of the effective heights with wavelength allows ALMA to observe different chromospheric layers and get access to the magnetic fields at different heights by tuning the wavelength. As was discussed in section Method for Magnetic Field Estimate, ALMA can extend its coverage to coronal heights, when observing bremsstrahlung emission from the coronal condensations.

Polarization and Magnetic Field in AR

In active regions, the observed values of circular polarization are typically higher than the values reported in the previous section for the QS. Thus, degrees of circular polarization in the range from about 1 to 4% were detected in an active region by Kundu and McCullough (1971) at a wavelength of 9 mm. Similar polarization degrees in active regions, ranging from 1–3% at Band 3 to 5–6% at Band 1 were obtained in Loukitcheva et al. (2017), where the authors studied simulated circular polarization at ALMA frequencies using two sets of umbral models with the magnetic field simulated by a vertical dipole located under the photosphere (e.g., Zlotnik, 1968). Fleishman et al. (2015) simulated the radio emission from AR 12158 at the ALMA frequencies using the 3D modeling tool GX Simulator (Nita et al., 2018), which take into account not only free–free emission but also gyroresonance emission. Their findings are also in line with the results reported in Loukitcheva et al. (2017). Higher values of polarization degree in AR can be explained by stronger magnetic field in sunspots than in the QS and also by steeper gradients of temperature in umbral atmosphere, resulting in higher values of brightness spectrum slopes. For active regions, the magnetic fields restored using the discussed above method are found to be in a general agreement with the model fields (Loukitcheva et al., 2017). Another example of successful restoration of magnetic fields in active regions from polarized radio emission using the model atmosphere by Mok et al. (2005) is given in Gary and Hurford (2004) in the context of the future FASR polarization measurements.

ALMA POLARIZATION MEASUREMENTS

The ALMA receivers are sensitive to linear polarization. Consequently, observations are carried in two orthogonal linear polarizations (X and Y) by using a wave-splitting device and then the data are correlated using the 64-input correlator to obtain the four cross-correlation visibilities XX, YY, XY, and YX. The relation between these cross-correlations and the Stokes parameters are given by Remijan et al. (2019):

$$I = \frac{XX + YY}{2}, Q = \frac{XX - YY}{2}, U = \frac{XY + YX}{2}, V = \frac{XY - YX}{2i},$$

and circular polarization $P = \frac{V}{I}$.

The wave-splitting operation produces a residual projection from one polarization into the other, which is called the instrumental polarization or D-terms. Additionally, there exist a relative delay between the X and Y polarizations (the cross-polarization delay), and a phase bandpass between the XY and YX cross-correlations (the XY-phase). The latter is especially crucial for circular polarization measurements, as XY-phase error can cause spurious Stokes V. To account for all these effects, ALMA needs to observe an unresolved strongly polarized source for a certain time (for about 3 h) to cover a sufficient set of parallactic angles (Cortes et al., 2016).

The use of linearly polarized feeds in ALMA receivers is, in fact, an advantage for the precise measurement of circular polarization. As can be seen from above, amplitude gain differences between linear polarizations X and Y do not affect circular polarization, as the latter is determined only from the cross-correlations XY and YX. For the Sun, there is also an additional advantage that Faraday rotation sweeps out linear polarization, resulting in XX = YY. For high-precision circular polarimetry, it is required to measure the instrumental polarization leakage (of linear into circular) terms, which are typically stable in time. In practice, degrees of circular polarization as low as 0.01% can be measured with linearly polarized feeds (Rayner et al., 2000).

The first full-polarization ALMA observations within Science Verification campaign were performed in July 2014 of a bright compact radio quasar 3C 286 (Nagai et al., 2016). Since the last ALMA cycle (Cycle 6), full-polarization mode is available at ALMA (Warmels et al., 2018). Commissioning and science verification of measuring circular polarization with ALMA was based on the observations of the two objects, the SiO maser emission at 86 GHz toward VY-CMA and Band 3 mapping of the highly circularly polarized star HR5907 (V1040 Sco) (Cortes et al., 2019). It was demonstrated that ALMA can detect circular polarization with an estimated error of 0.6% for on-axis observations within 1/10 of the primary beam FWHM, for both narrow-band spectroscopy and wide-band continuum modes. The minimum detectable degree of circular polarization was 1.8% of the peak flux. As the reported level of accuracy is for on-axis measurements, the circular polarization imaging is currently restricted to within 1/10 of the FWHM to avoid beam squint effects (Remijan et al., 2019). However, improving accuracy for circular polarization is one of the capabilities prioritized for Cycle 9. The reported restrictions complicate the use of ALMA for solar polarization measurements, as for the observational targets like the solar chromosphere, we need to measure polarization across the entire FOV. In this case, careful measurement of the beam patterns of the two polarizations independently is required to account for the variations in the circular polarization measurement fidelity within the primary beam. While the absence of the solar disk component from the interferometer data provides larger degrees of polarization and therefore better measurements of circular polarization, The interpretation of polarization measurements, including their conversion into degrees of polarization on the absolute scale, will not be trivial and will additionally require measurements of the disk component, as for obtaining accurate brightness temperature spectrum, the brightness temperatures at each frequency need to be on the same relative scale. First ALMA solar polarization tests were run at the end of 2019 and the obtained data are currently being analyzed. This will be followed by commissioning and science verification phases. In case the solar cycle will grant a suitable observational target during 2020 for completing the commissioning efforts, ALMA might offer a new truly exciting capability of solar polarization measurements already for ALMA Cycle 9 starting in 2021.

CONCLUDING REMARKS

This chapter presented a particular case of measuring the magnetic field at the chromospheric heights from the thermal free–free observed at the mm wavelengths in the light of the future circular polarization measurements with ALMA. Radio observations offer a powerful and diversified diagnostic of chromospheric and coronal magnetic fields. In particular, being applied to multi-wavelength mm data, or being combined with magnetic field measurements from atomic lines, high-precision observations of the polarized emission with ALMA should be able to provide a 3D picture of the longitudinal component of the chromospheric magnetic field. Based on the results presented here, magnetic field measurements in active regions will clearly be feasible. Regarding such measurements for the quiet Sun regions, given ALMA's high sensitivity, they will be possible once ALMA achieves the planned 0.1% polarization accuracy for extended sources.

AUTHOR CONTRIBUTIONS

The author confirms being the sole contributor of this work and has approved it for publication.

FUNDING

Part of the work was supported by Russian RFBR Grant No. 18-29-21016.

ACKNOWLEDGMENTS

The research on the potential use of ALMA for the solar polarization measurements was done in collaboration with Stephen White and Sami K. Solanki. The author acknowledges Dr. Tatyana Kaltman and Dr. Kazumasa Iwai for sharing the results of their work. The work was performed within the SAO RAS state assignment in the part Conducting Fundamental Science Research.

REFERENCES

Alissandrakis, C. (2020). Structure of the solar atmosphere: a radio perspective. *Front. Astron. Space Sci.* 7.

Bogod, V. M., and Gelfreikh, G. B. (1980). Measurements of the magnetic field and the gradient of temperature in the solar atmosphere above a flocculus using radio observations. *Sol. Phys.* 67, 29–46. doi: 10.1007/BF00146680

Carlsson, M., De Pontieu, B., and Hansteen, V. (2019). New view of the solar chromosphere. *Annu. Rev. Astron. Astrophys.* 57, 189–226. doi: 10.1146/annurev-astro-081817-052044

Carlsson, M., Hansteen, V., Gudiksen, B. V., Leenaarts, J., and De Pontieu, B. (2016). A publicly available simulation of an enhanced network region of the sun. *Astron. Astrophys.* 585:A4. doi: 10.1051/0004-6361/201527226

Carlsson, M., and Stein, R. F. (1995). Does a nonmagnetic solar chromosphere exist? *Astrophys. J.* 440:L29. doi: 10.1086/187753

Casini, R., López Ariste, A., Tomczyk, S., and Lites, B. W. (2003). Magnetic maps of prominences from full stokes analysis of the He I D3 line. *Astrophys. J.* 598:L67. doi: 10.1086/380496

Cortes, P., Hull, C. L. H., Kameno, S., Fomalont, E. B., Le Gouellec, V., Etoh, Yu., et al. (2019). "Current status of ALMA EOC polarization commissioning, past, present, and future," in *ALMA2019: Science Results and Cross-Facility Synergies* (Cagliari). doi: 10.5281/zenodo.3585356

Cortes, P. C., Girart, J. M., Hull, Ch. L. H., Sridharan, T. K., Louvet, F., Plambeck, R., et al. (2016). Interferometric mapping of magnetic fields: the alma view of the massive star-forming clump W43-MM1. *Astrophys. J. Lett.* 825:L15.

de la Cruz Rodríguez, J., and Socas-Navarro, H. (2011). Are solar chromospheric fibrils tracing the magnetic field? *Astron. Astrophys.* 527:L8. doi: 10.1051/0004-6361/201016018

de la Cruz Rodríguez, J., Socas-Navarro, H., van Noort, M., and Rouppe van der Voort, L. (2010). Observation and analysis of chromospheric magnetic fields. *Memorie della Societa Astronomica Italiana* 81:716.

De Pontieu, B., Hansteen, V. H., Rouppe van der Voort, L., van Noort, M., and Carlsson, M. (2007). High-resolution observations and modeling of dynamic fibrils. *Astrophys. J.* 655, 624–641. doi: 10.1086/509070

Dulk, G. A. (1985). Radio emission from the sun and stars. *Annual Rev. Astron. Astrophys.* 23, 169–224. doi: 10.1146/annurev.aa.23.090185.001125

Fleishman, G., Loukitcheva, M., and Nita, G. (2015). "Solar ALMA: observation-based simulations of the mm and sub-mm emissions from active regions," in *Revolution in Astronomy with ALMA: The Third Year, Vol. 499, ASP Conference Series*, eds D. Iono, K. Tatematsu, A. Wootten, and L. Testi (San Francisco, CA: Astronomical Soc Pacific), 351–352.

Fleishman, G. D., and Toptygin, I. N. (2013). *Cosmic Electrodynamics*. New York, NY: Springer. doi: 10.1007/978-1-4614-5782-4

Gary, D. E., and Hurford, G. J. (2004). "Radio spectral diagnostics," in *Solar and Space Weather Radio Physics. Current Status and Future Development, Vol. 314*, eds D. E. Gary, and C. U. Keller (Dordrecht: Kluwer), 71–87. doi: 10.1007/1-4020-2814-8

Gelfreikh, G. B. (2004). "Coronal magnetic field measurements through bremsstrahlung emission," in *Solar and Space Weather Radio Physics. Current Status and Future Development, Vol. 314*, eds D. E. Gary, and C. U. Keller (Dordrecht: Kluwer), 115–133.

Gelfreikh, G. B., and Shibasaki, K. (1999). "Radio magnetography of solar active regions using radio observations," in *Magnetic Fields and Solar Processes. The 9th European Meeting on Solar Physics*, ed A. Wilson (Noordwijk: European Space Agency, ESA SP-448), 1339–1343.

Grebinskij, A., Bogod, V., Gelfreikh, G., Urpo, S., Pohjolainen, S., and Shibasaki, K. (2000). Microwave tomography of solar magnetic fields. *Astron. Astrophy. Suppl.* 144, 169–180. doi: 10.1051/aas:2000202

Grebinskij, A., Bogod, V., Gelfrejkh, G., Shibasaki, K., Fu, Q., and Zhang, H. (1998). Microwave measurements of solar magnetic fields at chromosphere – corona. *Astroph. Rep.* 4, 101–106.

Gudiksen, B. V., Carlsson, M., Hansteen, V. H., Hayek, W., Leenaarts, J., and Martínez-Sykora, J. (2011). The stellar atmosphere simulation code Bifrost. Code description and validation. *Astron. Astrophys.* 531:A154. doi: 10.1051/0004-6361/201116520

Hills, R. E., Kurz, R. J., and Peck, A. B. (2010). "ALMA: status report on construction and early results from commissioning, Ground-based and Airborne Telescopes III," in: *Proceedings of the SPIE*, Vol. 7733, eds L. M. Stepp, R. Gilmozzi, H. J. Hall, 773317. doi: 10.1117/12.857017

Huang, Y. D., Morata, O., Koch, P. M., Kemper, C., Hwang, Y.-J., and Chiong, Ch.-Ch. (2016). "The Atacama Large Millimeter/sub-millimeter Array band-1 receiver," in *Modeling, Systems Engineering, and Project Management for Astronomy VII [99111V] (Proceedings of SPIE - The International Society for Optical Engineering), Vol. 9911*, eds P. Dierickx, and G. Z. Angeli (Edinburgh: SPIE).

Huang, Y. D., Morata, O., Koch, P. M., Kemper, C., Hwang, Y.-J., and Chiong, Ch.-Ch. (2018). "Performance of pre-production band 1 receiver for the Atacama Large Millimeter/submillimeter Array (ALMA)," in *SPIE Conf. Ser., Proc. SPIE 10708, Millimeter, Submillimeter, and Far-Infrared Detectors and Instrumentation for Astronomy IX* (Austin, TX), 1070833.

Iglesias, F. A., and Feller, A. (2019). Instrumentation for solar spectropolarimetry: state of the art and prospects. *Opt. Eng.* 58:082417. doi: 10.1117/1.OE.58.8.082417

Iwai, K., and Shibasaki, K. (2013). Measurements of coronal and chromospheric magnetic fields using polarization observations by the Nobeyama radioheliograph. *Publ. Astron. Society Jpn.* 65:S14. doi: 10.1093/pasj/65.sp1.S14

Kallunki, J., Tornikoski, M., Kirves, P., Oinaskallio, E., Aatrokoski, J., Mujunen, A., et al. (2020). Solar polarization observations at 3 and 13 mm. *Astronomische Nachrichten* 341, 118–124. doi: 10.1002/asna.202013684

Kaltman, T. I. (2019). Thermal bremsstrahlung of local sources over solar spots based on microwave observations. *Geomagn. Aeronomy* 59, 1088–1095. doi: 10.1134/S0016793219080097

Kundu, M. R., and McCullough, T. P. (1971). Polarization of solar active regions at 9 millimeter wavelength. *Bull. American Astron. Soc. Conf. Proc.* 3:449.

Kuridze, D., Mathioudakis, M., Morgan, H., Oliver, R., Kleint, L., Zaqarashvili, T. V., et al. (2019). Mapping the magnetic field of flare coronal loops. *Astroph. J.* 874:126. doi: 10.3847/1538-4357/ab08e9

Lin, H., Kuhn, J. R., and Coulter, R. (2004). Coronal magnetic field measurements. *Astrophys. J.* 613, L177–L180. doi: 10.1086/425217

López Ariste, A., and Casini, R. (2005). Inference of the magnetic field in spicules from spectropolarimetry of He I D3. *Astron. Astrophys.* 436, 325–331. doi: 10.1051/0004-6361:20042214

Loukitcheva, M., White, S. M., Solanki, S. K., Fleishman, G. D., and Carlsson, M. (2017). Millimeter radiation from a 3D model of the solar atmosphere. II. Chromospheric magnetic field. *Astron. Astrophys.* 601:A43. doi: 10.1051/0004-6361/201629099

Loukitcheva, M. A., White, S. M., and Solanki, S. K. (2019). ALMA detection of dark chromospheric holes in the quiet Sun. Astrophys. J. *Lett.* 877:L26. doi: 10.3847/2041-8213/ab2191

Miyawaki, S.h., Iwai, K., Shibasaki, K., Shiota, D., and Nozawa, S. (2016). Coronal magnetic fields derived from simultaneous microwave and EUV observations and comparison with the potential field model. *Astrophys. J.* 818:8. doi: 10.3847/0004-637X/818/1/8

Mok, Y., Mikić, Z., Lionello, R., and Linker, J. A. (2005). Calculating the thermal structure of solar active regions in three dimensions. *Astrophys. J.* 621, 1098–1108. doi: 10.1086/427739

Nagai, H., Nakanishi, K., Paladino, R., Hull, C. L. H., Cortes, P., Moellenbrock, G., et al. (2016). ALMA science verification data: millimeter continuum polarimetry of the bright radio quasar 3C 286. *Astrophys. J.* 824:132. doi: 10.3847/0004-637X/824/2/132

Nita, G. M., Viall, N. M., Klimchuk, J. A., Loukitcheva, M. A., Gary, D. E., Kuznetsov, A. A., et al. (2018). Dressing the coronal magnetic extrapolations of active regions with a parameterized thermal structure. *Astrophys. J.* 853:66. doi: 10.3847/1538-4357/aaa4bf

Rayner, D. P., Norris, R. P., and Sault, R. J. (2000). Radio circular polarization of active galaxies. *MNRAS* 319, 484–496. doi: 10.1046/j.1365-8711.2000.03854.x

Remijan, A., Biggs, A., Cortes, P. A., Dent, B., Di Francesco, J., Fomalont, E., et al. (2019). *ALMA Technical Handbook. ALMA Doc. 7.3, ver. 1.1*.

Rutten, R. J. (2007). "Observing the solar chromosphere," in *The Physics of Chromospheric Plasmas: Proc. of the Coimbra conference, Vol. 368*, *ASP Conference Series*, eds. P. Heinzel, I. Dorotovic, and R. J. Rutten (San Francisco, CA: Astronomical Society of the Pacific), 27–48.

Schmelz, J. T., Holman, G. D., Brosius, J. W., and Willson, R. F. (1994). Coronal magnetic structures observing campaign. III. Coronal plasma and magnetic field diagnostics derived from multiwaveband active region observations. *Astrophys. J.* 434:786. doi: 10.1086/174781

Shevgaonkar, R. K., and Kundu, M. R. (1984). Three-dimensional structures of two solar active regions from VLA observations at 2, 6, and 20 centimeter wavelengths. *Astrophys. J.* 283, 413–420. doi: 10.1086/162320

Shimojo, M., Bastian, T. S., Hales, A., White, S. M., Iwai, K., Hills, R. E., et al. (2017). Observing the Sun with ALMA: high resolution interferometric imaging. *Solar Phys*. 292, 87–115. doi: 10.1007/s11207-017-1095-2

Suárez, D. O. (2019). "Polarimetric observations of the Sun," in *Astronomical Polarisation from the Infrared to Gamma Rays, Vol. 460, Astrophysics and Space Science Library*, eds R. Mignani, A. Shearer, A. Słowikowska, and S. Zane (Cham: Springer Nature Switzerland AG), 147–172. doi: 10.1007/978-3-030-19715-5_6

Wang, S., Jenkins, J. M., Martinez Pillet, V., Beck, C., Long, D. M., Prasad Choudhary, D., et al. (2020). Magnetic structure of an erupting filament. *Astrophys. J.* 892:75. doi: 10.3847/1538-4357/ab7380

Warmels, R., Biggs, A., Cortes, P. A., Dent, B., Di Francesco, J., Fomalont, E., et al. (2018). *ALMA Technical Handbook, ALMA Doc. 6.3, ver. 1.0*.

Wedemeyer, S., Bastian, T., Brajša, R., Hudson, H., Fleishman, G., Loukitcheva, M., et al. (2016). Solar science with the Atacama Large Millimeter/Submillimeter Array - a new view of our Sun. *Space Sci. Rev.* 200, 1–73. doi: 10.1007/s11214-015-0229-9

White, S. M., Iwai, K., Phillps, N. M., Hills, R. E., Hirota, A., Yagoubov, P., et al. (2017). Observing the Sun with ALMA: fast-scan single-dish mapping. *Solar Phys*. 292, 88–115. doi: 10.1007/s11207-017-1123-2

Wiegelmann, T., Thalmann, J., and Solanki, S. K. (2014). The magnetic field in the solar atmosphere. *Astron. Astroph. Rev.* 22:78. doi: 10.1007/s00159-014-0078-7

Wootten, A., and Thompson, A. R. (2009). The atacama large millimeter/submillimeter array. Proc. IEEE 97, 1463–1471. doi: 10.1109/JPROC.2009.2020572

Yagoubov, P., Mroczkowski, T., Belitsky, V., Cuadrado-Calle, D., Cuttaia, F., Fuller, G., et al. (2020). Wideband 67-116 GHz receiver development for ALMA band 2. *Astron. Astroph.* 634:A46. doi: 10.1051/0004-6361/201936777

Zheleznyakov, V. V. (1996). *Radiation in Astrophysical Plasmas*. Dordrecht: Kluwer Academic Publisher. doi: 10.1007/978-94-009-0201-5

Zlotnik, E. Y. (1968). Theory of the slowly changing component of solar radio emission. I. *Soviet Astron*. 12:245.

Conflict of Interest: The author declares that the research was conducted in the absence of any commercial or financial relationships that could be construed as a potential conflict of interest.

frontiers in Astronomy and Space Sciences

REVIEW
published: 14 August 2020
doi: 10.3389/fspas.2020.00043

Radio Observations of Coronal Mass Ejections: Space Weather Aspects

Angelos Vourlidas[1]*, *Eoin P. Carley*[2] *and Nicole Vilmer*[3,4]

[1] *Applied Physics Laboratory, Johns Hopkins University, Laurel, MD, United States,* [2] *School of Cosmic Physics, Dublin Institute for Advanced Studies, Dublin, Ireland,* [3] *LESIA, Observatoire de Paris, Université PSL, CNRS, Sorbonne Université, Université de Paris, Meudon, France,* [4] *Station de Radioastronomie de Nançay, Observatoire de Paris, PSL Research University, CNRS, Univ. Orléans, Nançay, France*

We review the current state-of-affairs in radio observations of Coronal Mass Ejections (CMEs) from a Space Weather perspective. In particular, we examine the role of radio observations in predicting or presaging an eruption, in capturing the formation stages of the CME, and in following the CME evolution in the corona and heliosphere. We then look to the future and identify capabilities and research areas where radio observations—particularly, spectropolarimetric imaging—offer unique advantages for Space Weather research on CMEs. We close with a discussion of open issues and possible strategies for enhancing the relevance and importance of radio astronomy for Space Weather science.

Keywords: sun, radio astronomy, coronal mass ejections, space weather, spectropolarimetry

OPEN ACCESS

Edited by:
Luis Eduardo Antunes Vieira, National Institute of Space Research (INPE), Brazil

Reviewed by:
Juan Carlos Martínez Oliveros, University of California, Berkeley, United States
Grzegorz Michalek, Jagiellonian University, Poland

***Correspondence:**
Angelos Vourlidas
angelos.vourlidas@jhuapl.edu

Specialty section:
This article was submitted to Stellar and Solar Physics, a section of the journal Frontiers in Astronomy and Space Sciences

Received: *20 April 2020*
Accepted: *16 June 2020*
Published: *14 August 2020*

Citation:
Vourlidas A, Carley EP and Vilmer N (2020) Radio Observations of Coronal Mass Ejections: Space Weather Aspects. Front. Astron. Space Sci. 7:43. doi: 10.3389/fspas.2020.00043

1. INTRODUCTION

The modulation of the near-Earth space environment by solar activity, over short time scales (days or less), is known as Space Weather (SpWx). The modulation, particularly when it is impulsive and sustained, can have severe effects on space-borne civil and military systems (e.g., satellite operations, communication disruptions) and even on the lower atmosphere and ground (e.g., aviation and electric grids). As our society increasingly depends on those systems, concern on SpWx impacts rises, spurring research and strategy planning worldwide (Schrijver et al., 2015; Opgenoorth et al., 2019). The latest demonstration of the societal importance of SpWx is the publication of the Space Weather Strategy and Action Plan (SWAP) by the Office of Science and Technology Policy (OSTP).

The strongest SpWx effects are caused by the impact of Coronal Mass Ejections (CMEs) and their shocks onto the magnetosphere. The CME momentum, size, and magnetic field strength and configuration, are the most relevant physical parameters for energy input to geospace. Irradiance variations from flares cause perturbations in deeper atmospheric layers while solar energetic particles (SEPs) are a major concern for any human exploration to the Moon and beyond. Mitigation of SpWx impacts relies, at the moment on forecasting primarily CME impacts (and their associated phenomena; shocks and SEPs). Flare short-wavelength, soft X-rays (SXR) to ultraviolet (UV), emissions and intense radio bursts (IRBs) that disrupt radio communications including GPS systems, are currently impossible to forecast because they arrive at Earth nearly instantaneously (i.e., within 8 min of their occurrence on the Sun). In addition, the causes of IRBs are currently unknown, they may or may not occur with other eruptive activity, and their terrestrial impacts can be severe. They are discussed in more detail in Gary (2020).

Their extreme nature aside, IRBs show that radio observations have an important role in both SpWx research and operations. Radio emission arises from a broad range of physical phenomena

with SpWx implications (e.g., flares, SEPs, CMEs and shocks). The observations, and theoretical background, are reviewed in other chapters of the collection. Here, we revisit the phenomena associated with CMEs from a SpWx viewpoint and with emphasis on the CME propagation from the middle corona to 1 AU. We consider 3 R_s as the inner boundary of the middle corona, because it is the approximate height of the cusps of white light streamers and where the magnetic field becomes largely open to the heliosphere. The CME-related radio emissions for lower heights are discussed in Carley et al. (2020b). As the first paper within the Space Weather section, we take a more broad view of radio CMEs and the role of radio observations in the SpWx enterprise. The remaining chapters focus on radio effects that are not strictly related to CMEs, such as SEPs (Klein et al., 2020), IRBs (Gary, 2020) and interplanetary scintillation (IPS) techniques (Jackson et al., 2020).

The paper is organized in three sections. First, we summarize the status of the field around the three SpWx-relevant phases of eruptions (prediction, formation and propagation) with an emphasis on the propagation phase. Then, we give an outlook of the radio observing capabilities (with emphasis on imaging spectroscopy) and the SpWx-areas where radio can play an important or supporting roles. We close with a discussion of considerations and strategies for maximizing the SpWx potential of radio observations in the coming decade.

2. RADIO AND CMES: CURRENT STATUS

Several of the chapters in this book review or discuss the observations and emission processes related to CMEs and associated phenomena, mostly from a research perspective. In this section, we bring them together but organized around a SpWx framework. Specifically, we break down radio CME observations into three SpWx areas (in parentheses): (i) observations before the eruption (event prediction), (ii) observations during the eruption (event geoeffectiveness assessment), and (iii) observations after the eruption (event forecasting). To minimize repetition, we direct the reader to the appropriate references for the details, except where necessary for clarity.

2.1. Before the Eruption

Robust prediction of eruptive activity is considered by many the *"holy grail"* of SpWx research and unsurprisingly is a very active field, focused mostly on flare prediction based on metrics derived from observations of the photospheric magnetic fields (e.g., Leka et al., 2019). Predicting CME eruptions, however, is a very complex issue. While we understand that CMEs are driven by the explosive release of magnetic energy through generally identified physical mechanisms that result in the release of a magnetic flux rope (MFR) (Chen, 2011), the details of how magnetic systems destabilize and erupt escape us. A rather major problem is that CMEs are coronal phenomena but we do not have direct measurements of the coronal magnetic field. We are obligated to resort to proxies, such as photospheric magnetic field measurements or changes in the EUV or SXR emission from coronal structures. Consequently. there is yet no agreement on whether the pre-eruptive morphology is that of sheared magnetic arcades or of an MFR (see Georgoulis et al., 2019, and references therein). Thus, our physical understanding is not yet mature enough to lead to reliable predictions schemes for solar eruptions. Here is where radio observations may help bridge our knowledge gap, either as indications of an impending eruption (precursors) or as gauges of energy accumulation and imbalance in active regions (predictors). We discuss examples of both.

2.1.1. Precursors: Type-I Noise Storms and Other Emissions

Radio emission occurs throughout the solar atmosphere, from the chromosphere to interplanetary space (IP), via a variety of processes (Fleishman et al., 2020; Nindos et al., 2020) all arising from electrons, either in equilibrium or not (**Figure 1**). Non-thermal processes are of particular interest in our discussion because they arise from accelerated electrons and therefore indicate locations of energy release in the corona. Even mildly accelerated electrons of a few keV can emit detectable radio emission, making such observations a sensitive indicator of weakly energetic processes. Hence, their detection in subsequently-erupting regions could be precursor activity. This premise and the indications from models that the pre-eruptive magnetic field configuration is evolving as the system is driven toward loss of equilibrium, have spurred several efforts to identify radio CME precursors (for a discussion on CME precursors in other regimes see section 3.9 in Webb and Howard, 2012).

The promising candidates are Type-I noise storms, type-III bursts and certain radio continuum signatures. Type-I storms are thought to indicate energetic processes within closed magnetic loops. These may be high-rising loops, as the storms occur below 300 MHz generally. The emission usually arises from loop systems above magnetically-strong active regions and is well-associated with flux emergence. Its relation to flaring and erupting activity is more tenuous. There have been a few studies since 2005 (see Vourlidas 2004 for a review of earlier studies). Willson (2005b) discusses radio brightness changes in a Type-I storm ahead of a flare but in another case, they find no connection between the two (Willson, 2005a). Kathiravan et al. (2007) undertook a large-scale study of noise storms imaged with the Nançay Radioheliograph. They investigate only noise storms with start times *after* the onset of a CME. They identified 196 events (out of a total of 340) in 1997–2004, with an average delay of 13 h since the appearance of a CME in the LASCO coronagraph field of view. Ramesh et al. (2012a) analyzed a single noise storm imaged with the Gauribidanur Radioheliograph (GRH) in the 50–109 MHz range (corresponding to heights below 1.5 Rs for quiescent coronal density models) during a solar eclipse (**Figure 2b**). The storm was concurrent with the CME but it was located almost 180° from the CME position angle in the LASCO coronagraph. Neither of these studies provided any conclusive evidence for the relation between CMEs and noise storms and they certainly did not indicate that noise storms can be used as precursors. So we have no reason (yet) to change our original conclusion in (Vourlidas, 2004): *"It seems that the two phenomena are somehow interrelated but the details of the relationship (physical, temporal and/or spatial) are still unclear"*.

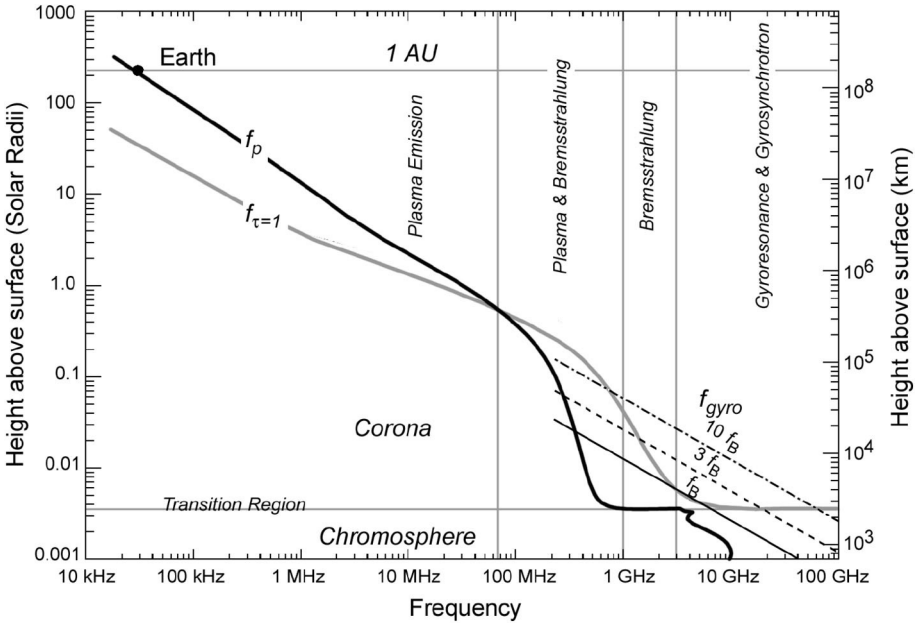

FIGURE 1 | Dominant radio emission mechanism vs. heliocentric distance based on model plasma parameters of temperature, density, and magnetic field strength. f_p are the plasma frequency, f_B is the gyrofrequency, and $f_{\tau=1}$ is the frequency where free-free emission becomes optically think. For details on these quantities and physical mechanisms (see Alissandrakis et al., 2020; Nindos et al., 2020). The plot is available here (Courtesy D. Gary).

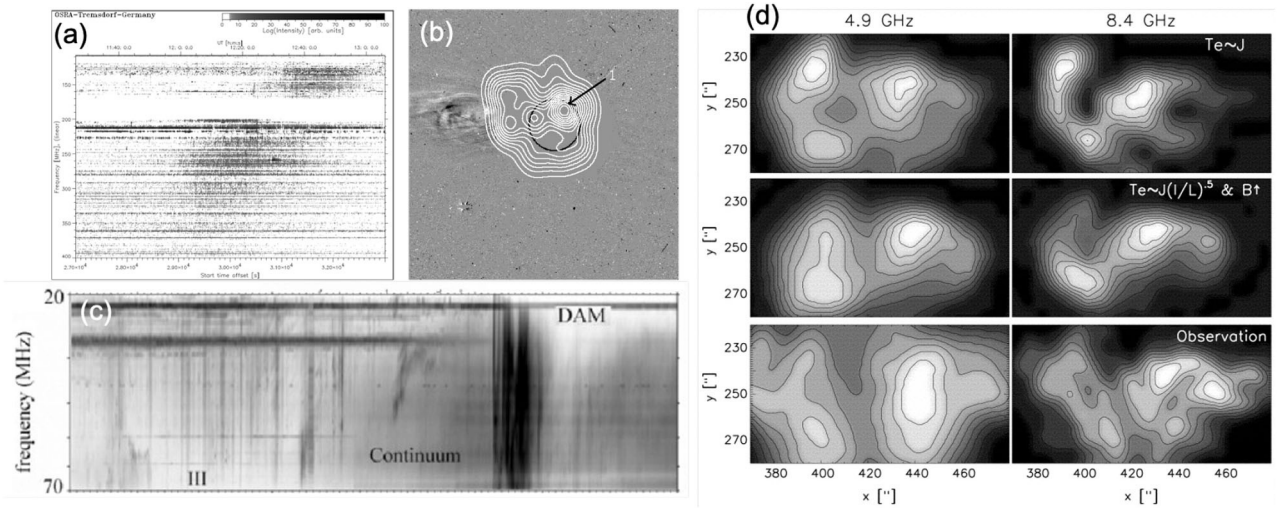

FIGURE 2 | (a) Astrophysical Institute Potsdam spectra showing the faint type IV continuum on May 16 (from Aurass et al., 1999). **(b)** Composite of the GRH 109 MHz radioheliogram (white contours) at 05:00 UT and the SOHO-LASCO C2 image at 05:19 UT on 2010 January 15 showing the CME and Type-I noise storm (from Ramesh et al., 2012b). **(c)** DAM radio spectrum of an outburst following type-III emissions and a continuum increase (from Pick et al., 2005). **(d)** Comparison of model (top two rows) and observed (bottom row) radio intensities at 4.9 and 8.4 GHz (left and right panels, resp.). The key assumption for the dependence of electron temperature to currents is shown at the upper right-hand corner of the right panels. The comparison demonstrates the power of multi-frequency observations in constraining coronal magnetic properties (from Lee et al., 1998). All figures reproduced by permission of the AAS.

Type-III emission is another promising precursor candidate as it arises from outward propagating electron beams and may thus indicate recently opened field lines. Such magnetic field changes are postulated by CME initiation models, such as breakout (Antiochos et al., 1999) and are generally expected as the CME forms and begins to emerge from within the closed fields of active regions. Based on our review of type-IIIs in the low corona in Carley et al. (2020b), we conclude that although such emissions are detected frequently in eruptive events, they tend to occur in close temporal proximity (∼mins) to the flare impulsive phase

and are of little value as a precursor (Pohjolainen et al., 2005; Aurass et al., 2011, 2013). The question, however, remains on whether earlier type-III signatures exist that may have escaped detection because either they are weak and may be masked by other activity or because no one has searched specifically for them.

Finally, there is another type of radio signature, the rising continuum, first proposed as a precursor by Aurass et al. (1999) (**Figures 2a,c**). Detected also 30 min before the large eruption on Oct 28, 2003 (**Figure 2** and Pick et al., 2005), this feature has attracted little attention in the recent years. Detections have been recorded only within the decimetric range, a few 10^5 km above the surface and so may indeed be indications of the rising flux system before eruption. More observations are sorely needed to demonstrate the value of this radio feature.

Fortunately, the deployment of new radio instrumentation looks promising. Mugundhan et al. (2018) reports results on several types of noise storms from a high resolution spectropolarimeter in the 15-85 MHz range at Gauribidanur. McCauley et al. (2019) present similar polarization investigations from the MWA at 80–240 MHz. It is hoped, that as the activity picks up the increased sensitivity and frequency complementarity of these two instruments will shed some light on the relation between noise storms and CME onset (or aftermath, as the case might be).

2.1.2. Predictors: Energy Accumulation in ARs

CMEs are coronal phenomena. They are powered by the release of free magnetic energy and helicity in the corona (Georgoulis et al., 2019). The energy is accumulated and stored in stressed magnetic field and should therefore reveal itself by measuring currents in those fields. Alas, the coronal magnetic field is notoriously difficult to measure (e.g., Casini et al., 2017) and there is currently no monitoring capability as it exists for photospheric magnetic fields. Almost all radio emission mechanisms have a magnetic field diagnostic potential since they tend to arise from electron gyration around magnetic field lines. The potential has been demonstrated numerous times (see White, 2005; Casini et al., 2017; Alissandrakis et al., 2020, and references therein). Spectropolarimetric imaging of gyroresonance emission is one of the most straightforward options for deriving 3D distributions of magnetic field from the upper chromosphere to the corona (e.g., Vourlidas et al., 1997). These studies occasionally uncover kG fields at coronal temperatures within $\sim$3,000 km above the photosphere (e.g., Vourlidas and Bastian, 1996; Vourlidas et al., 2006) suggesting the presence of strong currents at the cores of active regions (Lee et al., 1997, 1998) (**Figure 2d**).

There is, however, a catch. Robust detection and separation of gyroresonance harmonic emission is limited to strong fields (down to $\sim$ 100 G as explained in Casini et al., 2017). In other words, gyroresonance emission as a magnetograph proxy is suitable to active region observations only. This is not necessarily overly restrictive from a SpWx perspective, since the most geoeffective CMEs are expected to originate (and they do) from strongly magnetic active regions.

2.2. During the Eruption

There is a great host of radio emissions during the formation phase of the CME, which we review in Carley et al. (2020b). They are associated with flares, lifting of prominences, and opening of field lines, and can be readily understood within the context of the standard flare-CME model (see Figure 1 in Carley et al., 2020b). In fact, much of that connection has been apparent for a long time and there have been no surprises despite the great improvements in the sensitivity and cadence of radio observations since the 1990's (**Figure 3**). There is a slight exception, however; the detection of "radio" CMEs by the Nancay Radioheliograph (NRH; Kerdraon and Delouis, 1997). The fortuitous coincidence of NRH's imaging capability deployment with LASCO's start of science operations in 1996, led to the discovery of spatially resolved (but faint) radio emission within the white light transient, dubbed "radio" CMEs because of their similar appearance to LASCO CMEs (Bastian et al., 2001). There have been only two such "radio" CME detections (Bastian et al., 2001; Maia et al., 2007) since 1998 despite the rather continual coverage from imaging spectrometers, i.e., NRH, LOFAR, and MWA. We note here that the term "radio" CMEs tends to be broadly applied to events without a clear CME morphology (e.g., Carley et al., 2017; Mondal et al., 2019). The latter are actually more akin to moving Type-IV (mIV) bursts (section 2.2 and Carley et al., 2020b) and may also have a different emission mechanism (plasma rather than gyrosynchrotron). However, "radio" CMEs may just be spatially resolved mIVs but the reason behind the dearth of "radio" CME detections remains unclear. More details can be found in Carley et al. (2020b).

The SpWx relevance of "radio" CMEs and mIVs lies in their emission mechanism. If it is synchrotron, as commonly assumed in the analyses (e.g., Tun and Vourlidas, 2013; Sasikumar Raja et al., 2014; Carley et al., 2017; Mondal et al., 2019), then their detection provides a means to estimate the (total) magnetic field entrained in the CME, while the CME is still in the low corona. Such information could help improve prediction schemes of the geoeffectiveness of the transient when augmented, say, with 3D estimates of the CME volume and its evolution from white light coronagraphs. At the moment, all methods for predicting the CME magnetic field rely on observations and extrapolations of the photospheric field (e.g., Gopalswamy et al., 2017; Savani et al., 2017), which are just proxies. Of particular value is the southward component of the CME entrained magnetic field, B_Z, at 1 AU as it relates directly to the strength of the CME-magnetosphere interaction (see Vourlidas et al., 2019 for a review of the B_Z problem). The radio observations offer a unique way to estimate the total magnetic field (and B_Z if the CME magnetic configuration is assumed or modeled) close to the Sun and issue some sort of forecast with a day (or possibly more) horizon rather than waiting for the transient to cross the Lagrangian L1 point thus restricting the forecast horizon to an hour or less. One should consider the intervening evolution of the CME as interactions with upstream events (some of which have radio signatures, e.g., Gopalswamy et al., 2001) or the ambient solar wind can lead to field erosion or compression depending on the situation (Kilpua et al., 2019).

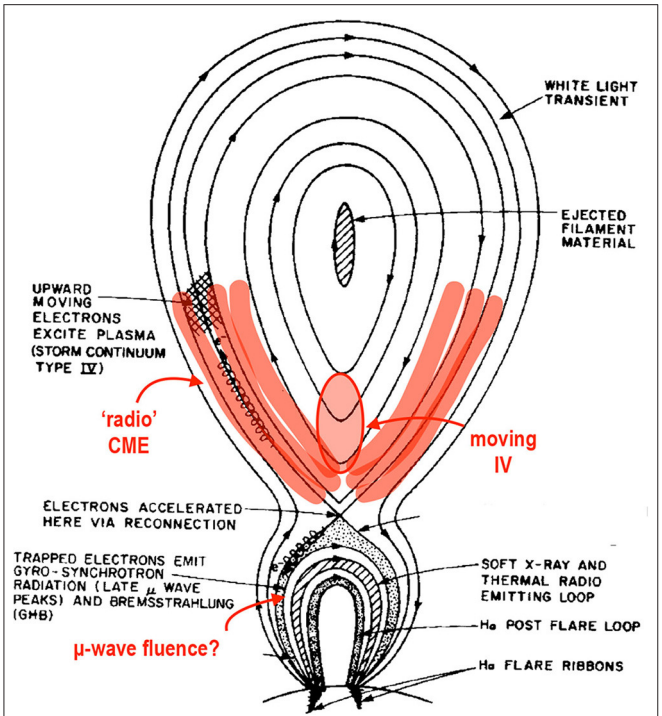

FIGURE 3 | A cartoon representing the flare-CME model from Cliver et al. (1986) showing the origin of various radio emissions. We mark areas impacted by the newer observations. Reproduced by permission of the AAS.

We conclude that spatially-resolved radio observations of CMEs hold a rich, yet unfulfilled, potential for SpWx research and operations. Their sensitivity of radio observations to magnetic field across a wide swath of features, from quiescent active regions to flares to CME internal structures, makes them the ideal method for probing the geo-effectiveness of CMEs right "at birth." But that potential is not restricted to the low corona, as we shall see next.

2.3. After the Eruption: CME Propagation

One of the outstanding issues in SpWx operations is the accurate forecasting of the time-of-arrival (ToA) of a CME at Earth. There are many methods to forecast ToA (most recently reviewed in Vourlidas et al. 2019) varying widely in accuracy. The averaged (over most published research) mean absolute error in ToA currently stands at 9.8 h, which is too large to be useful for many SpWx users. Vourlidas et al. (2019) discusses several reasons for this discrepancy and they largely revolve around our incomplete grasp of the IP kinematic evolution of the CMEs. The speed of CMEs is especially difficult to assess for the most SpWx-relevant events—Earth-directed CMEs—due to severe projection effects in the low corona (EUV) and middle corona (visible) observations. To circumvent these problems, several authors have searched for emission signatures concurrent to CMEs, such as EUV dimmings (Mason et al., 2016), soft X-ray light curves and more recently high frequency (GHz) fluence measurements, to use as proxies by relating their evolution to the CME speed via empirical relationships. Focusing on the radio proxies, Matamoros et al. (2017) have recently demonstrated a correlation between microwave fluence at 9 GHz and CME arrival time at the Earth, using limb CME observations to construct the empirical (linear in this case) relationship. The performance of the method is average and has only been demonstrated with a very small event sample (11 events) so it is unclear if it holds SpWx potential. Further work to increase the event sample and possibly examine other frequencies is necessary.

Once the CME reaches 3–4 R_s, it enters into the radial (open) field corona and effectively starts its outward propagation toward the inner heliosphere. This height range marks a transition in our abilities to observe CMEs in the radio from the ground, as the relevant frequencies dip below 20 MHz and encounter the ionospheric cutoff. Routine lower frequency observations can be made only from space. Space radio spectrometers can use direction finding techniques (Fainberg et al., 1972; Krupar et al., 2012) to track type II sources in 3D via triangulation, when radio spectra from two spacecraft are available (e.g., Magdalenić et al., 2014; Krupar et al., 2016; Mäkelä et al., 2018). As the accuracy of the technique depends on the source signal-to-noise ratio, the instrument cross-calibration and the relatively wide directivity of type-II radio emission, the ensuing localizations are rather broad (of the order of 10–20 R_s) and are generally restricted to near-Sun tracking (MHz frequencies). The complexity of the analysis has restricted the application of radio triangulation to only a handful of events despite the availability of measurements from three spacecraft (STEREO, Wind) since 2007. In any case, the rather large uncertainties in the source location and size limits the Space Weather utility of radio triangulation compared to direct imaging in white light. No radio imaging capability currently exists but there are two space interferometry pathfinders under development. The Cubesat Radio Interferometry Experiment (CURIE, Sundkvist et al., 2016), in development since 2018, aims to demonstrate single-baseline interferometry (0.1–40 MHz) of solar bursts (centroid location and envelope) using 2 cubesats in Low Earth Orbit. The mission is not yet manifested. Recently, NASA selected Sun Radio Interferometer Space Experiment (SUNRISE, Lazio and Kasper, 2018), an imaging interferometry space mission comprising six CubeSats in super-GEO orbit with a launch in late 2023. SUNRISE's aim is to image *and localize* type-II bursts below 25 MHz. While these frequencies can track CMEs only up to 20 R_s, and hence do not provide much additional information beyond what is currently available from coronagraphs, the mission will demonstrate whether solar interferometric imaging is possible in space. We will return to this point in section 3.3.

Before the advent of heliospheric imaging from the Solar-Terrestrial Relations Observatory (STEREO) (Harrison et al., 2018), tracking of CMEs in the outer corona and heliosphere had been possible only from space-borne spectrometers albeit indirectly. The tracking was based on the detection of type-II emission arising from shocks driven by CMEs, not CME themselves (see **Figure 4** and Cane and Erickson, 2005 for more examples). Occasionally, the type-II spectral signatures extend to the local plasma frequency around the detecting spacecraft, hence enabling track to 1 AU. The IP type-II sources, although

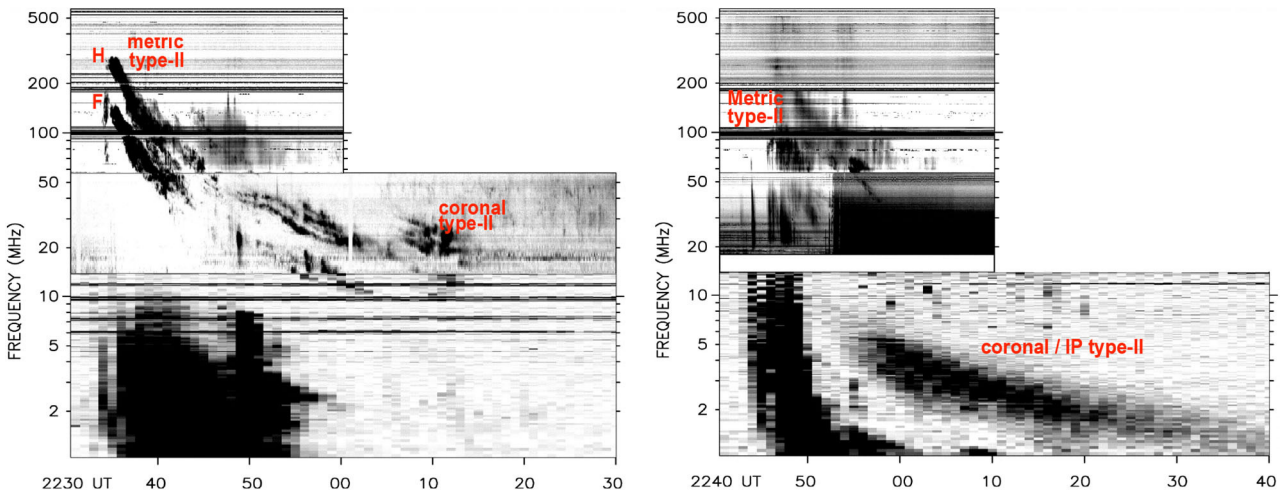

FIGURE 4 | Examples of type-II bursts in the low corona ("metric") outer corona ("coronal") and IP. **Left**: Composite spectrum on 2003 November 1. The WAVES data are below 14 MHz, the BIRS data run from 14 to 57 MHz, and the Culgoora data run from 57 to 570 MHz. Fundamental ("F") and harmonic ("H") bands of the type II are easily seen, along with band-splitting. A short, type II-like feature ("coronal") is seen in the BIRS data between 23:06 and 23:14 UT. There is no indication of an IP counterpart. **Right**: The beginning of an IP type-II on 2003 June 17 22:40 UT. It is apparently unconnected to the metric type-II seen in the higher frequencies. Culgoora data are used between 18 and 57 MHz. Adapted from Cane and Erickson (2005). Reproduced by permission of the AAS.

similar in many respects to their lower corona counterparts, are much longer-lived (hours to days compared to a few minutes) and are unambiguously driven by CMEs (Pick et al., 2006 and references therein). There is long-standing ambiguity regarding the connection between the coronal and IP shocks (Leblanc et al., 2001; Cane and Erickson, 2005; Bougeret and Pick, 2007 and **Figure 4**, right panel) although the differences between metric and IP type-IIs may simply be due to the shocks being produced at different phases of the CME evolution; namely, the metric bursts originate during the over-expansion phase of the CME formation (Patsourakos et al., 2010) while IP type-IIs are due to shocks driven by the largely self-similarly expanding CME (Cane and Erickson, 2005).

The main SpWx benefit of IP type-II observations is the quasi-continuous tracking of the CME *shock* in the outer corona/inner heliosphere. The shock can be variously driven or free-propagating depending on the CME kinematical behavior and the upstream conditions in the ambient medium. Thus, type-IIs should be treated as a (possibly rough) proxy for the actual CME. Unfortunately, such long-lived IP type-II's are uncommon since they require CMEs capable of shock-driving over large parts of their propagation to 1 AU. Gopalswamy et al. (2019) undertook recently a thorough statistical investigation of IP type-IIs detected by the Wind spacecraft since 1995. They find only about 500 events, which correspond to a very small fraction (3.1%) of all CMEs. Only half of those bursts reached below 500 KHz. On the positive side, these bursts are associated with faster CMEs (1,160 km/s average speed), which tend to have higher geoeffective potential. While the radio spectroscopic measurements are unaffected by particle storms that may blind a coronagraph using a traditional CCD detector (this will no longer be the case after the deployment of NOAA's operational coronagraphs at L1 and GEO in 2024) and are straightforward to interpret and to derive a speed, they have some serious impediments for SpWx use. IP type-IIs are not a robust indicator of a fast CME (low association with white light CMEs, not all fast CMEs drive shocks or have radio emissions, Gopalswamy et al., 2010), they track the shock rather than the transient and the tracking is incomplete (only 250 bursts in the last 25 years have reached near 1 AU locations). However, the IP radio observations are highly complementary to heliospheric imaging and provide key information on IP shocks, which constitute SpWx hazards of their own.

Radio observations, offer the only means to probe the CME internal magnetic field during heliospheric propagation via linear polarization measurements (Jackson et al. 2020, and references therein). The linearly polarized emission from an extragalactic (or artificial source, say, a satellite beacon) rotates when crossing magnetized plasma. The effect is called Faraday Rotation (FR) and the degree of rotation, known as Rotation Measure (RM), depends on the total density and magnetic field along the path (e.g., Kooi et al., 2017 and references therein). The left and middle panels of **Figure 5** show recent FR observations by the VLA of not one but two CMEs crossing over the radio source 0843 (Kooi et al., 2017). The modeling was able to disentangle the RM contribution along the line-of-sight of each transient demonstrating that the technique can be successful in estimating the magnetic field of CMEs in the outer corona. As CMEs carry, generally, higher magnetic fields than the ambient heliosphere and intergalactic space, they will be the dominant contributors to the measured FR (**Figure 5**, right and Oberoi and Lonsdale, 2012). If the density of the transient is known, say, from white light measurements, then the total magnetic field within the CME (along a given path) can be estimated. Modeling of the CME magnetic structure can be employed to derive the magnetic field configuration (Jensen et al., 2010; Le Chat et al., 2014),

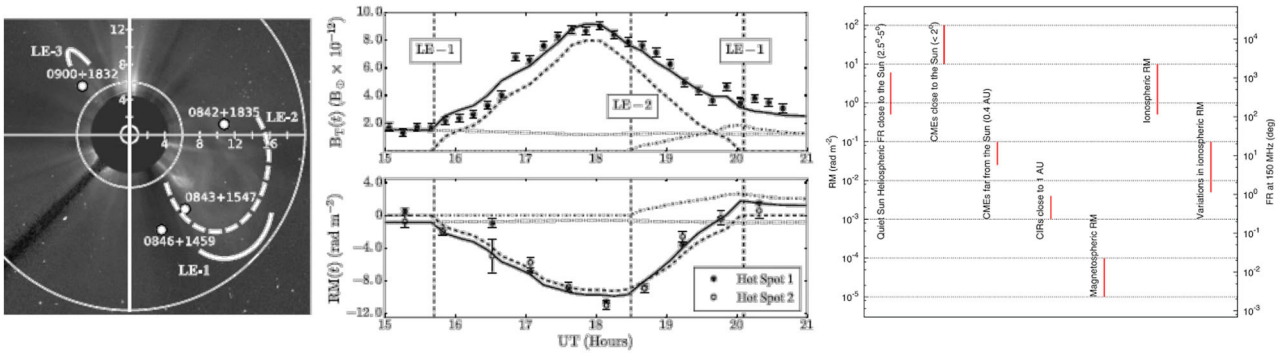

FIGURE 5 | Left: LASCO observations at the time (19:06 UT) of the 0843 radio source occultation by two CMEs (CME-1 and CME-2) on Aug. 2, 2012. **Middle**: Thomson-scattering brightness (top) and coronal RM (bottom) for 0843. The Thomson brightness is given for one line-of-sight to the target source center (see Kooi et al., 2017 for details on Hot Spot 1 and 2). The dotted curve represents the background coronal model, the dashed curve represents the flux-rope model for CME-1, the dash-dotted curve represents the flux-rope model for CME-2, and the solid curve represents the sum of the contributions from all models together. The LE-1 vertical lines mark the times of the radio source occultation by CME-1 (15:42 UT and 20:06 UT, respectively). LE-2 marks the start of CME-2 occultation (18:30 UT) (Adapted from Kooi et al., 2017 with permission by Springer Nature). **Right**: Overview of the RM effects from various plasmas. The corresponding FR (in deg) at 150 MHz is also indicated. A ± range of a factor of 2 has been assumed where needed. Adapted from Oberoi and Lonsdale (2012) with permission by the AGU.

which is actually the critical parameter for SpWx. There are other indirect methods for estimating the CME magnetic field (Kilpua et al., 2019, and references therein) but FR remains the most straightforward technique.

It does, however, have its shortcomings. For one, it requires the presence of a suitable source (i.e., a well-calibrated celestial or artificial source) at the right place to intersect the CME while the radio instrument is operating. This is a set of very strong requirements and it is unsurprising that only a handful of measurements have been recorded since the 1970's (see Kooi et al., 2017 for a historical review). Furthermore, the measurements are biased toward limb CMEs as they provide a wider projection on the sky plane and thus are more likely to intercept a celestial source. The technique applies to Earth-directed CMEs, of course, but those lines of sight will cross the shock sheath as well the magnetic flux rope behind it, increasing the ambiguity in the decoupling of line-of-sight effects and thus relying more on modeling assumptions. In any case, the SpWx potential of this technique has not been demonstrated yet since it would require both continuous coverage from Earth, and a large selection of calibrated sources. No FR measurements have been demonstrated in space. The optimum SpWx location for such a receiver would likely be one of the Lagrange point to monitor CMEs on the sky plane as they propagate toward Earth. A receiver-transmitter system on concurrently-operating satellites at L4/L5 could be the basis for a SpWx-operational system to provide B_z measurements of Earth-bound transients.

3. OUTLOOK

So far, we reviewed CME aspects where radio observations can contribute to problems in SpWx research and operations. Hopefully, our discussion (and the accompanying papers in this ebook) makes clear that solar radio astronomy, particularly spectropolarimetric imaging, has great potential to impact SpWx research by closing several gaps in our knowledge, from the magnetic field distribution in pre-eruptive active regions to the magnetic field and energetic particle content of the transients.

In this last section, we take a strategic look in the near future of radio CME research, always from a SpWx perspective. We first take stock of the available instrumentation, then summarize and assess the relative importance of the various radio emission types for CME SpWx research and close with a brief discussion of some issues to consider for moving the field forward.

3.1. Future Radio Instrumentation Relevant to CME SpWx Studies

Developments in radio instrumentation in the present day and those planned for the near future promise to provide new insight into CME physics. The Expanded Owens Valley Solar Array (EOVSA) is now providing unprecedented imaging-spectroscopy observations of the early stages of energy release and CME formation, low in the corona ($<3\,R_\odot$). The observations tend to focus on the sources of non-thermal electrons associated with the eruption, such as in the current sheet and the associated termination shocks. They are therefore indirectly connected to SpWx concerns on CMEs but they usher a new understanding of the eruptive process as a whole that may provide SpWx benefits down the line.

New instruments such as MingantU SpEctral Radioheliograph (MUSER; Mei et al., 2018) will have an ultrawide bandwidth from 400 MHz to 15 GHz, bridging the gap between the microwave and lower frequency instruments and should provide a more comprehensive view of radio sources associated with both flares and CMEs. Although not specifically geared toward space weather observations, future radio facilities such as the Square Kilometer Array (SKA) will deploy ground-breaking new instrumental capabilities on general flare/CME physics in a wideband observing range from 300 MHz to 14 GHz; see Nindos

et al. (2019) for an overview of solar radio physics from an SKA perspective.

Lower frequency observations from instruments such as the Low Frequency Array (LOFAR; van Haarlem et al., 2013) and the Murchison Widefield Array (MWA; Li et al., 2018) can provide CME diagnostics generally $\leq 3\,R_{\odot}$, via imaging observations of type II, III and IV radio bursts during the acceleration phase of the CME (e.g., Zucca et al., 2018; Mondal et al., 2019; Morosan et al., 2019). Such observations enable an independent measure of ejecta speed while the CME is still in the low corona, where its early stage propagation may be obscured behind the occulting disks of coronagraphs. As we mentioned, if the CME can be directly imaged in the radio domain (which is still a rarity) it may be used to perform CME magnetography. We expand in Carley et al. (2020b) on the necessity of high dynamic range interferometric imaging for observing radio CMEs, and efforts in this regard have recently been demonstrated with MWA leading to spatially resolved diagnostics of magnetic field of the ejecta (Mondal et al., 2019).

Low frequency phased-array interferometers such as LOFAR and MWA attain their most powerful SpWx utility when they are used as beamformers on multiple background sources to perform IPS observations. This requires observation of well-calibrated astrophysical radio sources. Beamformers, such as LOFAR and MWA, can simultaneously observe multiple astrophysical radio sources (potentially hundreds) in many different directions and hence can provide IPS diagnostics over large portions of the inner heliosphere. Hence, IPS can be used to derive density and velocity measurements in the solar wind, including any CME that is passing through the heliosphere, and can therefore be used as a means of estimating the arrival time of Earth directed CMEs (Bisi et al., 2010). This may also be used as boundary conditions in the driving of MHD models of the heliosphere such as ENLIL (Jackson et al., 2015). Apart from MWA and LOFAR, phased arrays are now used to perform routine observations of the heliosphere for space weather purposes e.g., the Mexican Array Radio Telescope (MEXART; Mejia-Ambriz et al., 2010) operating at 140 MHz, KSWC-IPS in Korea (327 MHz), the Solar Terrestrial Environment Laboratory ISEE IPS array (Asai et al., 1995) in Japan (327 MHz), the Big Scanning Array of the Lebedev Physical Institute (Dagkesamanskii, 2009) in Russia (110 MHz), and the Ooty Radio Telescope (ORT; Sukumar et al., 1988) operating at 327 MHz in India. These arrays are grouped together into a consortium of IPS monitors known as Worldwide Interplanetary Scintillation Stations, aiming to provide 24 h space weather monitoring coverage of the heliosphere and any CME passing through it (see Jackson et al., 2020 for details).

Related to IPS are the Faraday rotation (FR) measurements of radio emission passing through the heliosphere (Jensen et al., 2010), as discussed in section 2.3. Studies are currently under way to assess the requirements of modern instrumentation in observing FR, particularly at low radio frequencies where the ionosphere can contribute to the rotation measure significantly (**Figure 5**). A new project known as LOFAR for Space Weather (LOFAR4SW; Carley et al., 2020a) is a design study to upgrade the entire LOFAR system such that it provides routine observation of the Sun, heliosphere, and ionosphere from a space weather science and operations perspective. The upgraded system aims to perform daily imaging spectroscopy of the Sun, including imaging of the radio activity during the early phases of solar eruptions, as well as IPS and FR observations of the solar wind and CMEs propagating throughout the heliosphere.

Finally, space-based radio instrumentation is also entering a new era. The FIELDS instrument (PSP-FIELDS; Bale et al., 2016) on-board the recently launched Parker Solar Probe and Radio and Plasma Waves (RPW; Maksimovic et al., 2007) instrument on Solar Orbiter will provide a new perspective on the observation of radio bursts in the inner-heliosphere from 10 kHz to 20 MHz. However both are primarily research instruments, rather than platforms offering the continuous low-latency observations required by space weather operations. As mentioned above, SUNRISE will also expand upon low radio frequency observations of the heliosphere, offering for the first time the ability to observe radio bursts interferometrically and provide 2D positional information with the constraints discussed in section 2.3.

3.2. An Assessment of Radio CME Observations for SpWx Research

We have presented a relatively large number of radio emission types and studies in this and our companion paper (Carley et al., 2020b). Although they provide important information for physical properties and processes in quiescent and eruptive phenomena, they do not all have the same impact when viewed from a SpWx viewpoint. Some parameters, e.g., CME occurrence or speed, can be provided by other instrumentation, often in a much more continuous and robust way compared to the limited daily operations of most radio observatories. However, other information, such as the CME internal magnetic field can only be derived synoptically through radio observations.

In **Table 1**, we organize the various radio emissions into a SpWx-relevant list. We mark as "essential" the types of observations (column 1) that are unique to radio and provide highly sought-after parameters for SpWx research and operations (columns 2–3). We also assess the top-level instrumental capabilities required to maximize the SpWx benefit (column 4). We consider the required (required: "Y" or not: "N") spectral (Sp), imaging (Img), and polarimetric (Pol) capabilities but we do not discuss any specific frequency range or spatial/spectral resolution requirements. These details, as well as a broader SpWx perspective are summarized in a White Paper by Bastian et al. (2019). The "?" denotes areas where the SpWx value of a particular observation or capability is not obvious at the moment. Further research with a possibly stronger SpWx focus may be useful for those areas.

3.3. Considerations for Moving Forward

With a new solar cycle on the horizon, improvements in ground-based instrumentation and an ever-increasing societal attention to the Space Weather problem, it is time to consider the future of Radio SpWx research. To increase the value of ground- and space-based radio observations to SpWx research and operations, we first need to consider some strategic questions. For example, where do we focus instrument development efforts? which

TABLE 1 | Overview of radio emission types with relevance to SpWx CME research.

Emission type	SpWx concern	SpWx parameters	Instrumental capabilities			Remarks
			Sp	Img	Pol	
AR mapping	Prediction	3D mag. field, coronal currents	Y	Y	Y	Essential capability for assessing AR eruptive potential. SpWx potential
"Radio" CMEs	B_Z	CME mag. field strength	Y	Y	Y	Essential capability for mag. field estimates. SpWx potential
Moving Type-IV	B_Z	CME mag. field strength	Y	Y	Y	Essential capability for mag. field estimates. SpWx potential
Faraday Rotation	B_Z	ICME mag. field strength & configuration	N	N	Y	Essential capability for remote B_Z estimate. SpWx potential.
Type-II	Shock tracking, SEP	Shock speed	Y	?	N	IP type-IIs are useful but no robust association to CMEs
Type-I	Precursor?	CME onset	Y	?	Y	Unclear connection to CME
Microwave fluence	CME Speed	CME ToA	Y	N	N	Promising approach. Needs more research
Flare Continuum	SEP?	CME kinematics?	Y	Y	Y	Unclear connection to CME

science activities are likely to return the most impactful SpWx-relevant results? The answers should come from a community-wide discussion. To get the conversation going we present a few issues (some may be controversial) we derived during the compilation of our two reviews (Carley et al. 2020b and the present manuscript). We note again that the following issues pertain to SpWx aspects of CMEs.

- *Radio as a CME Magnetograph*: We believe that the most important SpWx value of radio observations is their unique ability to estimate magnetic fields both in active regions and inside CMEs. High-frequency arrays (GHz) are best suited for coronal magnetic field mapping, especially for eruption-prone ARs (e.g., δ-spots). Lower frequency arrays (<200 MHz) are ideal for IVM and "radio" CME imaging. High signal-to-noise ratio imaging is paramount (Bastian et al., 2019). The SpWx value can only be realized when those measurements are available *synoptically* and as close to 24 × 7, as possible. Continuous solar coverage is a fundamental need for operational SpWx. Even for research purposes, nearly continuous coverage will greatly increase the numbers of all radio emission types and further their understanding. In other words, we need the deployment of solar-dedicated interferometric arrays with spectropolarimetric capabilities across the globe.
- *How necessary are IP radio observations for CME-specific SpWx issues?* The case is not very strong. As Gopalswamy et al. (2019) show, only a very small fraction of CMEs (3.1 are associated with IP type-II bursts. Those tend to be fast CMEs but it is also clear that a number of fast CMEs either do not drive shocks in the heliosphere or their radio emission is too faint or shocks do not always produce radio emission (Gopalswamy et al., 2008). The bottom line is that type-II bursts cannot be a reliable CME proxy on their own. Of course, this statement refers to CME-specific SpWx issues, such at the CME time-of-arrival, speed and magnetic content (Vourlidas et al., 2019). IP shocks can be a SpWx driver but they are beyond the scope of this review (see Kilpua et al., 2017 and references therein for a broader review on this subject).

  A question arises on whether imaging of IP (or at least of the outer corona) type-IIs has something more to offer on predicting either CMEs or shock properties at 1 AU (Gopalswamy et al., 2010). The problem is that radio sources tend to be very large due to scattering. Therefore, any *imaging* reduces to centroid localization that may or may not be accurate since the type-II emission depends on the ambient microphysics (that are not well-understood, although PSP and Solar Orbiter may shed some light on this). It is unclear (at best) that imaging at low frequencies will provide any SpWx-relevant information that cannot be gleaned by coronagraphs or heliospheric imagers.
- *Are there any radio CME precursors?*: This is an important question for SpWx operations. No reliable precursor to CMEs has been identified so far in any wavelength. Most CME initiation theories require magnetic field line opening above (and/or the sides) of the CME flux rope as it forms and begins to ascend. It is, therefore, expected that these field line openings, resulting from reconnection, would release energetic electrons and hence some radio beaming signature is expected. Recent PSP observations detected weak type-III signatures in association with small surges on the solar disk (Leske et al., 2020). The PSP was located at about 30–40 R_s at the time and in alignment with STEREO-A, which did not detect any radio emission. It is conceivable, then, that CME precursors may exist in the radio but have escaped detection due to the high detection threshold of past instruments. For instance, it would be interesting, to investigate whether such weak radio signatures could arise in radio quiet CMEs (Gopalswamy et al., 2008) or from "stealth" CMEs (Robbrecht et al., 2009) that generally lack low corona signatures in other spectral regimes. On the other hand, there are rare instances where major flares (but no CMEs!) have taken place without any radio emission. Since, however, all of these cases involve non-eruptive flares, they are not relevant for SpWx (except for the flare radiation effects). A search for such precursors may prove more fruitful with MWA and LOFAR in the upcoming maximum.
- *What to do next?*: It seems to us that there is considerable potential for SpWx-relevant studies now by taking advantages of existing ground-based instrumentation and missions. For example, the frequent crossings of PSP and of Solar Orbiter

through the corona provide an excellent opportunity for coordinated Faraday rotation, mIV and "radio" CMEs studies with LOFAR, MWA and EOVSA. Solar radio observatories were the biggest ground-based component in the campaign to support the fourth PSP perihelion in January 2020. Upwards of 20 solar radio observatories participated and results are already being compiled even before the PSP data are processed. We expect that radio observations will play an increasing role in PSP and Solar Orbiter research.

Careful design and planning of SpWx-specific observing programs will maximize the SpWx benefit of radio observations. The LOFAR4SW project mentioned above is an example (Carley et al., 2020a). It comprises a set of observing programs for diverse targets, such as CME Faraday rotation studies, multi-spectral imaging or IPS observations. The coordinated campaigns with PSP perihelia we just mentioned offer another opportunity for developing such programs, which can then be used outside of the PSP or Solar Orbiter perihelia for a more SpWx-minded efforts as the activity picks up.

Radio analyses should also adopt a more SpWx viewpoint. For example, large sample analyses of type-I storms and mIVs or searches for "radio" CMEs and more focus on the derivation of magnetic fields in CMEs may increase the visibility of radio observations within the SpWx community. Further research to identify radio proxies for CME SpWx parameters, such as speed, may prove valuable. Regular availability of well-calibrated radio images at various wavelengths, as it is done by the solar space missions, will help greatly in increasing the community uptake of radio observations from the new instruments. Such capabilities should be in place before the next solar maximum in about 2024 for maximum effect for SpWx research.

In closing, we emphasize once more the great potential of ground-based spectropolarimetric radio imaging for addressing important open questions in SpWx research. Radio imaging of moving Type-IVs and "radio" CMEs with Faraday Rotation measurements in the outer corona, offers a straightforward means to estimate the CME's internal magnetic field and possibly configuration, with the aid of modeling. The construction of a solar-dedicated instrument, such as FASR and further efforts like LOFAR4SW, will energize the international radio community and provide an ideal testbed to refine and expand the SpWx value of radio observations.

AUTHOR CONTRIBUTIONS

EC and NV contributed text and figures. All authors contributed to the initial concept, design of the paper, read and critically revised the paper, approved the final version, and agreed to be accountable for all aspects of the work.

FUNDING

AV was supported by the NASA HSR (NNX16AG86G) and LWS (80NSSC19K0069) programs. EC is a Shrödinger Research Fellow funded by the Dublin Institute for Advanced Studies.

REFERENCES

Alissandrakis, K., et al. (2020). Radio measurements of solar magnetic field.

Antiochos, S. K., DeVore, C. R., and Klimchuk, J. A. (1999). A model for solar coronal mass ejections. *Astrophys. J.* 510, 485–493. doi: 10.1086/306563

Asai, K., Ishida, Y., Kojma, M., Maruyama, K., Misawa, H., and Yoshimi, N. (1995). Multi-station system for solar wind observations using the interplanetary scintillation method. *J. Geomagnet. Geoelectricity* 47, 1107–1112. doi: 10.5636/jgg.47.1107

Aurass, H., Holman, G., Braune, S., Mann, G., and Zlobec, P. (2013). Radio evidence for breakout reconnection in solar eruptive events. *Astron. Astrophys.* 555:A40. doi: 10.1051/0004-6361/201321111

Aurass, H., Mann, G., Zlobec, P., and Karlický, M. (2011). Radio evidence of break-out reconnection? *Astrophys. J.* 730:57. doi: 10.1088/0004-637X/730/1/57

Aurass, H., Vourlidas, A., Andrews, M. D., Thompson, B. J., Howard, R. H., and Mann, G. (1999). Nonthermal radio signatures of coronal disturbances with and without coronal mass ejections. *Astrophys. J.* 511, 451–465. doi: 10.1086/306653

Bale, S. D., Goetz, K., Harvey, P. R., Turin, P., Bonnell, J. W., Dudok de Wit, T., et al. (2016). The FIELDS instrument suite for solar probe plus. Measuring the coronal plasma and magnetic field, plasma waves and turbulence, and radio signatures of solar transients. *Space Sci. Rev.* 204, 49–82. doi: 10.1007/s11214-016-0244-5

Bastian, T., Bain, H., Chen, B., Gary, D. E., Fleishman, G. D., Glesener, L., et al. (2019). Diagnostics of space weather drivers enabled by radio observations. *arXiv [Preprint]. arXiv:1904.05817*.

Bastian, T. S., Pick, M., Kerdraon, A., Maia, D., and Vourlidas, A. (2001). The coronal mass ejection of 1998 April 20: direct imaging at radio wavelengths. *Astrophys. J. Lett.* 558, L65-L69. doi: 10.1086/323421

Bisi, M. M., Breen, A. R., Jackson, B. V., Fallows, R. A., Walsh, A. P., Mikić, Z., et al. (2010). From the Sun to the Earth: the 13 May 2005 coronal mass ejection. *Solar Phys.* 265, 49–127. doi: 10.1007/s11207-010-9602-8

Bougeret, J. L., and Pick, M. (2007). "Solar radio emissions," in *Handbook of the Solar-Terrestrial Environment*, eds Y. Kamide and A. Chian (Berlin; Heidelberg: Springer), 133–151.

Cane, H. V., *and* Erickson, W. C. (2005). Solar type II radio bursts and IP type II events. *Astrophys. J.* 623, 1180–1194. doi: 10.1086/428820

Carley, E. P., Baldovin, C., Benthem, P., Bisi, M. M., Fallows, R. A., Gallagher, P. T., et al. (2020a). Radio observatories and instrumentation used in space weather science and operations. *J. Space Weather Space Clim.* 10:7. doi: 10.1051/swsc/2020007

Carley, E. P., Vilmer, N., Simões, P. J. A., and Ó Fearraigh, B. (2017). Estimation of a coronal mass ejection magnetic field strength using radio observations of gyrosynchrotron radiation. *Astron. Astrophys.* 608:A137. doi: 10.1051/0004-6361/201731368

Carley, E. P., Vilmer, N., and Vourlidas, A. (2020b). Radio observations of coronal mass ejection initiation and development in the low solar corona.

Casini, R., White, S. M., and Judge, P. G. (2017). Magnetic diagnostics of the solar corona: synthesizing optical and radio techniques. *Space Sci. Rev.* 210, 145–181. doi: 10.1007/s11214-017-0400-6

Chen, P. F. (2011). Coronal mass ejections: models and their observational basis. *Living Rev. Solar Phys.* 8:1. doi: 10.12942/lrsp-2011-1

Cliver, E. W., Dennis, B. R., Kiplinger, A. L., Kane, S. R., Neidig, D. F., Sheeley, N. R., et al. (1986). Solar gradual hard X-ray bursts and associated phenomena. *Astrophys. J.* 305, 920–935. doi: 10.1086/164306

Dagkesamanskii, R. D. (2009). The Pushchino Radio Astronomy Observatory of the P N Lebedev Physical Institute Astro Space Center: yesterday, today, and tomorrow. *Phys. Uspekhi* 52, 1159–1167. doi: 10.3367/UFNe.0179.200911i.1225

Fainberg, J., Evans, L. G., and Stone, R. G. (1972). Radio tracking of solar energetic particles through interplanetary space. *Science* 178, 743–745. doi: 10.1126/science.178.4062.743

Fleishman, G., et al. (2020). Coherent emission. this volume.

Gary, D. E. (2020). Solar radio bursts. this volume.

Georgoulis, M. K., Nindos, A., and Zhang, H. (2019). The source and engine of coronal mass ejections. *Philos. Trans. R. Soc. A Math. Phys. Eng. Sci.* 377:20180094. doi: 10.1098/rsta.2018.0094

Gopalswamy, N., Akiyama, S., Yashiro, S., and Xie, H. (2017). A new technique to provide realistic input to CME forecasting models. *Proc. Int. Astron. Union* 13, 258–262. doi: 10.1017/S1743921317011048

Gopalswamy, N., Makela, P., and Yashiro, S. (2019). A catalog of type II radio bursts observed by wind/WAVES and their statistical properties. *arXiv [Preprint]. arXiv:1912.07370*. doi: 10.31401/SunGeo.2019.02.03

Gopalswamy, N., Xie, H., Makela, P., Akiyama, S., Yashiro, S., Kaiser, M. L., et al. (2010). Interplanetary shocks lacking type II radio bursts. *Astrophys. J.* 710, 1111–1126. doi: 10.1088/0004-637X/710/2/1111

Gopalswamy, N., Yashiro, S., Kaiser, M. L., Howard, R. A., and Bougeret, J.-L. (2001). Radio signatures of coronal mass ejection interaction: coronal mass ejection cannibalism? *Astrophys. J. Lett.* 548, L91-L94. doi: 10.1086/318939

Gopalswamy, N., Yashiro, S., Xie, H., Akiyama, S., Aguilar-Rodriguez, E., Kaiser, M. L., et al. (2008). Radio-quiet fast and wide coronal mass ejections. *Astrophys. J.* 674, 560–569. doi: 10.1086/524765

Harrison, R. A., Davies, J. A., Barnes, D., Byrne, J. P., Perry, C. H., Bothmer, V., et al. (2018). CMEs in the heliosphere: I. A statistical analysis of the observational properties of CMEs detected in the heliosphere from 2007 to 2017 by STEREO/HI-1. *Solar Phys.* 293:77. doi: 10.1007/s11207-018-1297-2

Jackson, B. V., et al. (2020). Interplanetary scintillation measurements. this volume.

Jackson, B. V., Odstrcil, D., Yu, H. S., Hick, P. P., Buffington, A., Mejia-Ambriz, J. C., et al. (2015). The UCSD kinematic IPS solar wind boundary and its use in the ENLIL 3-D MHD prediction model. *Space Weather* 13, 104–115. doi: 10.1002/2014SW001130

Jensen, E. A., Hick, P. P., Bisi, M. M., Jackson, B. V., Clover, J., and Mulligan, T. (2010). Faraday rotation response to coronal mass ejection structure. *Solar Phys.* 265, 31–48. doi: 10.1007/s11207-010-9543-2

Kathiravan, C., Ramesh, R., and Nataraj, H. S. (2007). The post-coronal mass ejection solar atmosphere and radio noise storm activity. *Astrophys. J.* 656:L37. doi: 10.1086/512013

Kerdraon, A., and Delouis, J.-M. (1997). "The nançay radioheliograph," in *Coronal Physics from Radio and Space Observations*, Vol. 483, ed G. Trottet (Berlin; Heidelberg: Springer), 192. doi: 10.1007/BFb0106458

Kilpua, E., Lugaz, N., Mays, M. L., and Temmer, M. (2019). Forecasting the structure and orientation of earthbound coronal mass ejections. *Space Weather*. 17, 1–29. doi: 10.1029/2018SW001944

Kilpua, E. K. J., Balogh, A., Steiger, R. V., and Liu, Y. D. (2017). Geoeffective properties of solar transients and stream interaction regions. *Space Sci. Rev.* 212, 1271–1314. doi: 10.1007/s11214-017-0411-3

Klein, K.-L., et al. (2020). Radio observations of solar energetic particles.

Kooi, J. E., Fischer, P. D., Buffo, J. J., and Spangler, S. R. (2017). VLA measurements of faraday rotation through coronal mass ejections. *Solar Phys.* 292:56. doi: 10.1007/s11207-017-1074-7

Krupar, V., Eastwood, J. P., Kruparova, O., Santolik, O., Soucek, J., Magdalenić, J., et al. (2016). An analysis of interplanetary solar radio emissions associated with a coronal mass ejection. *Astrophys. J. Lett.* 823(1):L5. doi: 10.3847/2041-8205/823/1/L5

Krupar, V., Santolik, O., Cecconi, B., Maksimovic, M., Bonnin, X., Panchenko, M., et al. (2012). Goniopolarimetric inversion using SVD: An application to type III radio bursts observed by STEREO. *J. Geophys. Res.* 117:A06101. doi: 10.1029/2011JA017333

Lazio, J., and Kasper, J. (2018). "The sun radio interferometer space experiment (SunRISE) mission concept," in *42nd COSPAR Scientific Assembly* (Big Sky, MT).

Le Chat, G., Kasper, J. C., Cohen, O., and Spangler, S. R. (2014). Diagnostics of the solar corona from comparison between faraday rotation measurements and magnetohydrodynamic simulations. *Astrophys. J.* 789:163. doi: 10.1088/0004-637X/789/2/163

Leblanc, Y., Dulk, G. A., Vourlidas, A., and Bougeret, J.-L. (2001). Tracing shock waves from the corona to 1 AU: Type II radio emission and relationship with CMEs. *J. Geophys. Res.* 106, 25301–25312. doi: 10.1029/2000JA000260

Lee, J., McClymont, A. N., Mikic, Z., White, S. M., and Kundu, M. R. (1998). Coronal currents, magnetic fields, and heating in a solar active region. *Astrophys. J.* 501:853. doi: 10.1086/305851

Lee, J., White, S. M., Gopalswamy, N., and Kundu, M. R. (1997). Signatures of coronal currents in microwave images. *Solar Phys.* 174, 175–190. doi: 10.1023/A:1004956422669

Leka, K. D., Park, S.-H., Kusano, K., Andries, J., Barnes, G., Bingham, S., et al. (2019). A comparison of flare forecasting methods. II. Benchmarks, metrics, and performance results for operational solar flare forecasting systems. *Astrophys. J.* 243:36. doi: 10.3847/1538-4365/ab2e12

Leske, R. A., Christian, E. R., Cohen, C. M. S., Cummings, A. C., Davis, A. J., Desai, M. I., et al. (2020). Observations of the 2019 April 4 solar energetic particle event at the parker solar probe. *Astrophys. J.* 246:35. doi: 10.3847/1538-4365/ab5712

Li, W., Pober, J. C., Hazelton, B. J., Barry, N., Morales, M. F., Sullivan, I., et al. (2018). Comparing redundant and sky-model-based interferometric calibration: a first look with phase II of the MWA. *Astrophys. J.* 863:170. doi: 10.3847/1538-4357/aad3c3

Magdalenić, J., Marqué, C., Krupar, V., Mierla, M., Zhukov, A. N., Rodriguez, L., et al. (2014). Tracking the CME-driven Shock Wave on 2012 March 5 and radio triangulation of associated radio emission. *Astrophys. J.* 791:115. doi: 10.1088/0004-637X/791/2/115

Maia, D. J. F., Gama, R., Mercier, C., Pick, M., Kerdraon, A., and Karlický, M. (2007). The radio-coronal mass ejection event on 2001 April 15. *Astrophys. J.* 660, 874–881. doi: 10.1086/508011

Mäkelä, P., Gopalswamy, N., and Akiyama, S. (2018). Direction-finding analysis of the 2012 July 6 type II solar radio burst at low frequencies. *Astrophys. J.* 867:40. doi: 10.3847/1538-4357/aae2b6

Maksimovic, M., Bale, S. D., Vaivads, A., Krasnoselskikh, V., Chust, T., Balikhin, M., et al. (2007). "A radio and plasma wave experiment for the solar orbiter mission," in *Second Solar Orbiter Workshop* (Noordwijk: ESA Special Publication), 38.

Mason, J. P., Woods, T. N., Webb, D. F., Thompson, B. J., Colaninno, R. C., and Vourlidas, A. (2016). Relationship of EUV irradiance coronal dimming slope and depth to coronal mass ejection speed and mass. *Astrophys. J.* 830:20. doi: 10.3847/0004-637X/830/1/20

Matamoros, C. S., Klein, K. L., and Trottet, G. (2017). Microwave radio emissions as a proxy for coronal mass ejection speed in arrival predictions of interplanetary coronal mass ejections at 1 AU. *J. Space Weather Space Clim.* 7:A2. doi: 10.1051/swsc/2016038

McCauley, P. I., Cairns, I. H., White, S. M., Mondal, S., Lenc, E., Morgan, J., et al. (2019). The low-frequency solar corona in circular polarization. *Solar Phys.* 294:106. doi: 10.1007/s11207-019-1502-y

Mei, Y., Wang, F., Wang, W., Chen, L., Liu, Y., Deng, H., et al. (2018). GPU-based high-performance imaging for Mingantu spectral radioheliograph. *Publ. Astron. Soc. Pac.* 130:014503. doi: 10.1088/1538-3873/aa9608

Mejia-Ambriz, J. C., Villanueva-Hernandez, P., Gonzalez-Esparza, J. A., Aguilar-Rodriguez, E., and Jeyakumar, S. (2010). Observations of interplanetary scintillation (IPS) using the Mexican array radio telescope (MEXART). *Solar Phys.* 265, 309–320. doi: 10.1007/s11207-010-9562-z

Mondal, S., Oberoi, D., and Vourlidas, A. (2019). Estimation of the physical parameters of a CME at high coronal heights using low frequency radio observations. *arXiv [Preprint]. arXiv:1909.12041*. doi: 10.3847/1538-4357/ab7fab

Morosan, D. E., Carley, E. P., Hayes, L. A., Murray, S. A., Zucca, P., Fallows, R. A., et al. (2019). Multiple regions of shock-accelerated particles during a solar coronal mass ejection. *Nat. Astron.* 3, 452–461. doi: 10.1038/s41550-019-0689-z

Mugundhan, V., Ramesh, R., Kathiravan, C., Gireesh, G. V. S., and Hegde, A. (2018). Spectropolarimetric observations of solar noise storms at low frequencies. *Solar Phys.* 293:41. doi: 10.1007/s11207-018-1260-2

Nindos, A., et al. (2020). Incoherent Emission.

Nindos, A., Kontar, E. P., and Oberoi, D. (2019). Solar physics with the Square Kilometre Array. *Adv. Space Res.* 63, 1404–1424. doi: 10.1016/j.asr.2018.10.023

Oberoi, D., and Lonsdale, C. J. (2012). Media responsible for Faraday rotation: a review. *Radio Sci.* 47:RS0K08. doi: 10.1029/2012RS004992

Opgenoorth, H. J., Wimmer-Schweingruber, R. F., Belehaki, A., Berghmans, D., Hapgood, M., Hesse, M., et al. (2019). Assessment and recommendations for a consolidated European approach to space weather—as part of a global space weather effort. *J. Space Weather Space Clim*. 9:A37. doi: 10.1051/swsc/2019033

Patsourakos, S., Vourlidas, A., and Kliem, B. (2010). Toward understanding the early stages of an impulsively accelerated coronal mass ejection. SECCHI observations. *Astron. Astrophys*. 522:100. doi: 10.1051/0004-6361/200913599

Pick, M., Forbes, T. G., Mann, G., Cane, H. V., Chen, J., Ciaravella, A., et al. (2006). Multi-wavelength observations of CMEs and associated phenomena. Report of working group F. *Space Sci. Rev*. 123, 341–382. doi: 10.1007/s11214-006-9021-1

Pick, M., Malherbe, J.-M., Kerdraon, A., and Maia, D. J. F. (2005). On the Disk Hα and radio observations of the 2003 October 28 flare and coronal mass ejection event. *Astrophys. J. Lett*. 631, L97-L100. doi: 10.1086/497137

Pohjolainen, S., Vilmer, N., Khan, J. I., and Hillaris, A. E. (2005). Early signatures of large-scale field line opening. Multi-wavelength analysis of features connected with a "halo" CME event. *Astron. Astrophys*. 434, 329–341. doi: 10.1051/0004-6361:20041378

Ramesh, R., Kathiravan, C., Barve, I. V., and Rajalingam, M. (2012a). High angular resolution radio observations of a coronal mass ejection source region at low frequencies during a solar eclipse. *Astrophys. J*. 744:165. doi: 10.1088/0004-637X/744/2/165

Ramesh, R., Lakshmi, M. A., Kathiravan, C., Gopalswamy, N., and Umapathy, S. (2012b). The location of solar metric type II radio bursts with respect to the associated coronal mass ejections. *Astrophys. J*. 752:107. doi: 10.1088/0004-637X/752/2/107

Robbrecht, E., Patsourakos, S., and Vourlidas, A. (2009). No trace left behind: STEREO observation of a coronal mass ejection without low coronal signatures. *Astrophys. J*. 701, 283–291. doi: 10.1088/0004-637X/701/1/283

Sasikumar Raja, K., Ramesh, R., Hariharan, K., Kathiravan, C., and Wang, T. J. (2014). An estimate of the magnetic field strength associated with a solar coronal mass ejection from low frequency radio observations. *Astrophys. J*. 796:56. doi: 10.1088/0004-637X/796/1/56

Savani, N. P., Vourlidas, A., Richardson, I. G., Szabo, A., Thompson, B. J., Pulkkinen, A., et al. (2017). Predicting the magnetic vectors within coronal mass ejections arriving at Earth: 2. Geomagnetic response. *Space Weather* 15, 441–461. doi: 10.1002/2016SW001458

Schrijver, C. J., Kauristie, K., Aylward, A. D., Denardini, C. M., Gibson, S. E., Glover, A., et al. (2015). Understanding space weather to shield society: a global road map for 2015–2025 commissioned by COSPAR and ILWS. *Adv. Space Res*. 55, 2745–2807. doi: 10.1016/j.asr.2015.03.023

Sukumar, S., Velusamy, T., Pramesh Rao, A., Swarup, G., and Bagri, D. S. (1988). Ooty synthesis radio telescope - design and performance. *Bull. Astron. Soc. India* 16, 93–110.

Sundkvist, D. J., Saint-Hilaire, P., Bain, H. M., Bale, S. D., Bonnell, J. W., Hurford, G. J., et al. (2016). "CURIE: cubesat radio interferometry experiment," in *AGU Fall Meeting Abstracts* (San Fransisco, CA).

Tun, S. D., and Vourlidas, A. (2013). Derivation of the magnetic field in a coronal mass ejection core via multi-frequency radio imaging. *Astrophys. J*. 766:130. doi: 10.1088/0004-637X/766/2/130

van Haarlem, M. P., Wise, M. W., Gunst, A. W., Heald, G., McKean, J. P., Hessels, J. W. T., et al. (2013). LOFAR: The LOw-Frequency ARray. *Astron. Astrophys*. 556:A2. doi: 10.1051/0004-6361/201220873

Vourlidas, A. (2004). "Radio observations of coronal mass ejection4," in *Solar and Space Weather Radiophysics: Current Status and Future Developments, Vol. 314*, eds D. E. Gary and C. U. Keller (Dordrecht: Kluwer Academic Publishers), 223–242. doi: 10.1007/1-4020-2814-8_11

Vourlidas, A., and Bastian, T. S. (1996). Multiband VLA observations of solar active regions: implications for the distribution of coronal plasma. *Astrophys. J*. 466:1039. doi: 10.1086/177574

Vourlidas, A., Bastian, T. S., and Aschwanden, M. J. (1997). The structure of the solar corona above sunspots as inferred from radio, x-ray, and magnetic field observations. *Astrophys. J*. 489:403. doi: 10.1086/304769

Vourlidas, A., Gary, D. E., and Shibasaki, K. (2006). Sunspot gyroresonance emission at 17 GHz: a statistical study. *Publ. Astron. Soc. Japan* 58, 11–20. doi: 10.1093/pasj/58.1.11

Vourlidas, A., Patsourakos, S., and Savani, N. P. (2019). Predicting the geoeffective properties of coronal mass ejections: current status, open issues and path forward. *Philos. Trans. R. Soc. A Math. Phys. Eng. Sci*. 377:20180096. doi: 10.1098/rsta.2018.0096

Webb, D. F., and Howard, T. A. (2012). Coronal mass ejections: observations. *Living Rev. Solar Phys*. 9:3. doi: 10.12942/lrsp-2012-3

White, S. M. (2005). "Coronal magnetic field measurements through gyroresonance emission," in *Solar and Space Weather Radiophysics, Number 314 in Astrophysics and Space Science Library*, eds D. E. Gary and C. U. Keller (Dordrecht: Springer), 89–113. doi: 10.1007/1-4020-2814-8_5

Willson, R. F. (2005a). Collaborative VLA, SOHO and RHESSI observations of evolving sources of energy release in the corona above active regions. *Adv. Space Res*. 35, 1813–1821. doi: 10.1016/j.asr.2005.04.081

Willson, R. F. (2005b). Very large array and SOHO observations of type I noise storms, large-scale loops and magnetic restructuring in the corona. *Solar Phys*. 227, 311–326. doi: 10.1007/s11207-005-1104-8

Zucca, P., Morosan, D. E., Rouillard, A. P., Fallows, R., Gallagher, P. T., Magdalenic, J., et al. (2018). Shock location and CME 3D reconstruction of a solar type II radio burst with LOFAR. *Astron. Astrophys*. 615:A89. doi: 10.1051/0004-6361/201732308

Conflict of Interest: The authors declare that the research was conducted in the absence of any commercial or financial relationships that could be construed as a potential conflict of interest.

frontiers in Astronomy and Space Sciences

REVIEW
published: 24 September 2020
doi: 10.3389/fspas.2020.00056

A Review of Recent Solar Type III Imaging Spectroscopy

*Hamish A. S. Reid**

Mullard Space Science Laboratory, Department of Space and Climate Physics, University College London, Dorking, United Kingdom

Solar type III radio bursts are the most common impulsive radio signatures from the Sun, stimulated by electron beams traveling through the solar corona and solar wind. Type III burst analysis provides us with a powerful remote sensing diagnostic tool for both the electron beams and the plasma they travel through. Advanced radio telescopes like the LOw Frequency ARray (LOFAR), the Murchison Widefield Array (MWA) and the Karl G. Jansky Very Large Array (VLA) are now giving us type III imaging spectroscopy with orders of magnitude better resolution than before. In this review, the recent observational progress provided by the new observations is discussed for type III bursts at GHz and MHz frequencies, including how this enhanced resolution has facilitated study of type III burst fine structure. The new results require more detailed theoretical understanding of how type III bursts are produced. Consequently, recent numerical work is discussed which improves our understanding of how electron beams, Langmuir waves and radio waves evolve through the turbulent solar system plasma. Looking toward the future, some theoretical challenges are discussed that we need to overcome on our quest to understand type III bursts and the electron beams that drive them.

Keywords: solar flares, electron transport, electron acceleration, solar corona, solar type III bursts, beam plasma instabilities

OPEN ACCESS

Edited by:
Nicole Vilmer, Centre National de la Recherche Scientifique (CNRS), France

Reviewed by:
Rohit Sharma, University of Applied Sciences and Arts Northwestern Switzerland, Switzerland
Pierre Henri, UMR7328 Laboratoire de physique et chimie de l'environnement et de l'Espace (LPC2E), France

***Correspondence:**
Hamish A. S. Reid
hamish.reid@ucl.ac.uk

Specialty section:
This article was submitted to Stellar and Solar Physics, a section of the journal Frontiers in Astronomy and Space Sciences

Received: *14 April 2020*
Accepted: *28 June 2020*
Published: *24 September 2020*

Citation:
Reid HAS (2020) A Review of Recent Solar Type III Imaging Spectroscopy. Front. Astron. Space Sci. 7:56. doi: 10.3389/fspas.2020.00056

1. INTRODUCTION

Type III radio bursts are the most common coherent radio emission produced by the Sun. Type III bursts are an indirect signature of energetic electrons propagating through the plasma of the solar corona and the solar wind. A gift of non-linear physics, the more we understand type III bursts, the more we can use them as remote sensing tools for astrophysical plasma. As high energy electron beams propagate through plasma with decreasing background electron densities, and hence decreasing plasma frequency, they emit type III radio emission at correspondingly decreasing radio frequencies. The spatial and spectral evolution of type IIIs thus contains a wealth of plasma dynamics information that has been studied for many decades since their first observational report by Payne-Scott et al. (1947). Analysis of type IIIs can provide insight on astrophysical processes including particle acceleration, charged particle transport through plasma, and the structure of solar system plasma. Space-based observations can detect *in situ* the electron beams, their associated plasma waves and radio spectra. However, we are dependent upon Earth-based telescopes to provide type III imaging, which we obtain above the 10 MHz ionospheric cut-off. These frequencies correspond to electron beams propagating through the solar corona before they reach interplanetary space.

The focus of this review is to cover the advances in type III theory that have arisen due to new high resolution imaging spectroscopy which became available in the last decade. Type III observations in the past were either analyzed spectroscopically or through imaging only at a few discreet frequencies. Now orders of magnitude better spatial, spectral and temporal resolution is allowing the physics of the radio Sun to be examined like never before. The main telescopes that have been facilitating new type III observations of the Sun are (in descending frequency) the upgraded Karl G. Jansky Very Large Array (VLA, Perley et al., 2011), the Mingantu Ultrawide Spectral Radioheliograph (MUSER, Yan et al., 2009), the Murchison Widefield Array (MWA, Lonsdale et al., 2009), the Low Frequency Array (LOFAR, van Haarlem et al., 2013) the Long Wavelength Array (Ellingson et al., 2009). Additionally, imaging at discrete frequencies has been provided by the Nançay Radioheliograph (NRH, Kerdraon and Delouis, 1997) and the Giant Metrewave Radio Telescope (GMRT, Swarup et al., 1991).

This review is not intended to be a historical overview on type III bursts, nor a review of all type III properties. In science we are all "perched on the shoulders of giants" and so readers are encouraged to get a more complete understanding of the field by reading the introductions that are contained within the cited works. There are also many other reviews specifically on type III bursts (Suzuki and Dulk, 1985; Reid and Ratcliffe, 2014) and more generally on solar radio emission (e.g., Dulk, 1985; McLean and Labrum, 1985; Bastian, 1990; Pick and Vilmer, 2008; Gary et al., 2018).

Over the last decade, snapshot synthesis imaging techniques have substantially improved for generating solar radio images. A significant upgrade was made the VLA, described in Perley et al. (2011), where state-of-art receivers and electronics were added, greatly increasing capabilities. There are now a larger number of spectral channels, a larger instantaneous bandwidth for imaging and a faster sampling times, enabling new solar radio observations first documented by Chen et al. (2013). Additionally new radio telescopes like LOFAR, MUSER, and the MWA have been built with large numbers of antenna distributed across large spatial scales. These new telescopes have drastically improved the UV coverage available for making solar imaging spectroscopy, leading to temporal resolution for imaging of 100 ms or better, and for spectroscopy it can go down to microsecond resolution. The increased number of long distance baselines provides orders of magnitude better spatial resolution although radio transport effects limit the use of such high resolution for solar science at MHz frequencies. New and improved telescopes have enhanced spectral resolutions, with low frequencies especially going down to 100s kHz resolution. The latter is particularly significant as previous low frequency imaging spectroscopy has been carried out with spectral resolution of 40 MHz till the 1980s, preventing past imaging spectroscopic analysis of type III fine structure. An example of new imaging techniques using the MWA is given by Mohan and Oberoi (2017).

As well as traditional interferometric techniques, new radio interferometers are able to operate in a coherent tied-array mode that involves combining the collecting area into array beams, or a coherent sum of multiple station beams (see e.g., Stappers et al., 2011, for a description using LOFAR). Hundreds of tied-array beams are pointed at the Sun in a honeycomb pattern that mosaics the solar radio intensity. The advantage of this method of imaging is enhanced spectral resolution of 10s kHz and temporal resolutions of ms, which are particularly important for imaging type III bursts that are short-lived and change significantly with frequency. The disadvantage is a reduced spatial resolution. An early example of tied-array imaging performed by LOFAR is given in **Figure 1**. This example highlights the power of imaging spectroscopy as each pixel has an associated dynamic spectrum. One is able to disentangle each burst from the other via their spatial information which would not have been possible from full-disc integrated dynamic spectra.

With the successful launch of Parker Solar Probe (PSP, Fox et al., 2016) and Solar Orbiter (SolO, Müller et al., 2013) traveling close to the Sun, analysis of coronal magnetic connectivity is hugely important. In particular with PSP, analysis of *in situ* data close to the Sun is dramatically improved once we know where on the solar disc the plasma originated from. Type III imaging spectroscopy from Earth plays a crucial role here as radio bursts can isolate where high energy particles were accelerated and what trajectory they took when escaping the Sun. Despite energetic protons not producing radio emission, they are likely to follow the same magnetic connectivity as the electrons. Similarly, type III bursts can show the trajectory of heated plasma jets, typically observed in UV or X-rays, which can subsequently be observed *in situ*. Type III bursts are also able to ascertain coronal plasma parameters in high regions of the solar corona (around 1 solar radius and above), where UV and X-ray diagnostics are not effective due to the tenuous plasma not emitting enough photons at these wavelengths. Coronal parameters deduced from type III imaging spectroscopy can then be compared with solar wind parameters detected *in situ* to help understand how the solar corona transitions into the solar wind.

This review begins by discussing high frequency radio bursts and the constraints they make for particle acceleration. Recently observed properties of low-frequency bursts are then discussed in the frame of particle propagation through the corona, along with new type III fine structure observations. The type III contribution toward coronal density models is then featured, along with the difficulties that result from radio wave propagation effects. New insights about electron beams, Langmuir waves and radio waves from recent theoretical models are then presented. The review concludes with a summary of some future observatories and scientific questions that type III imaging spectroscopy can help answer.

2. HIGH FREQUENCY BURSTS

Type III bursts observed at high frequencies are signatures of electron transport in the low corona. The term "high frequency" is subjective, and in this context we consider the frequency range of 2–0.2 GHz, with imaging spectroscopy available from the VLA, the NRH and the GMRT. This relates to altitudes lower than roughly 0.5 solar radii from the solar surface (e.g., Newkirk, 1961; Saito et al., 1977) although care must be taken

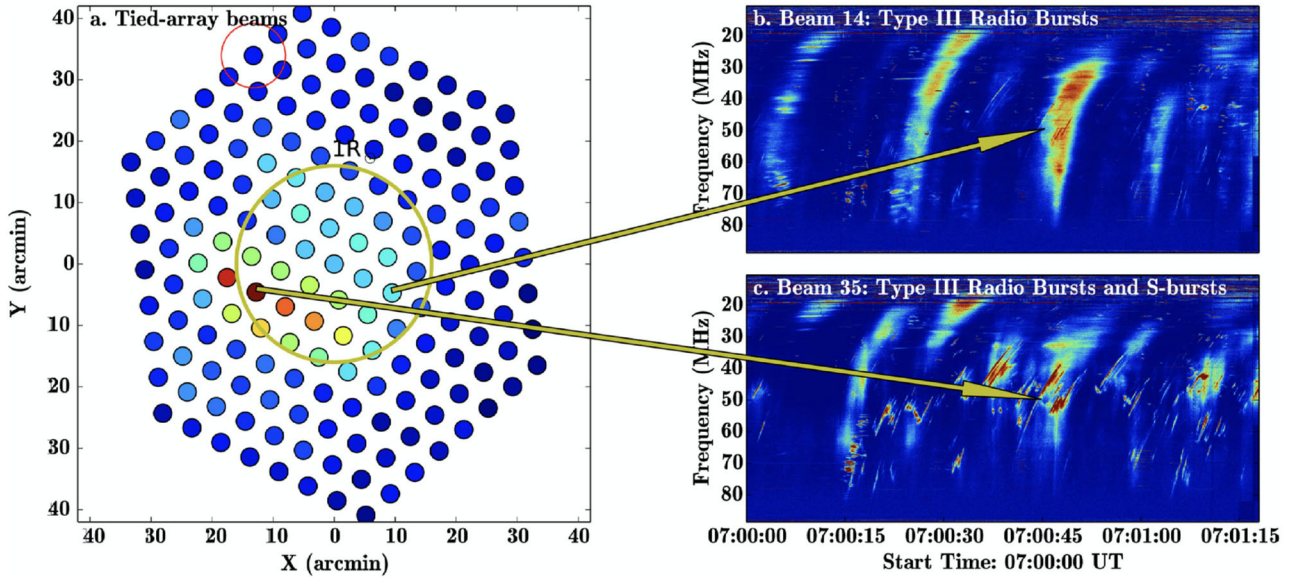

FIGURE 1 | LOFAR tied-array beam observations of Type III radio bursts and solar S bursts. **Left**: The 170 tied-array beams covering a field-of-view of about 1.3 degrees about the Sun. **Right**: Two dynamic spectrum highlighting different solar activity coming from different regions in the solar disc. From Morosan et al. (2015).

when assuming heights from density models. For example, type III bursts can be observed in the GHz frequencies which requires either active Sun coronal density models or some multiplicative of quiet Sun models.

The importance of analyzing type III bursts at high frequencies is that electron beams which produce the emission have not traveled far from their acceleration region. The electron beams have not undergone significant transport effects and so their kinetic profile as deduced from the type III emission is closer to the acceleration region characteristics that generated them. Solar particle acceleration region characteristics are ill-quantified, and a subject of intense study, because the energized particles propagate away before generating significant electromagnetic emission (see e.g., Zharkova et al., 2011, as a review). This makes high frequency type III burst imaging spectroscopy attractive for diagnosing the spatial, energetic and temporal profile of electron acceleration in the corona.

High resolution type III imaging spectroscopy in GHz frequencies have been carried out using observations from the VLA. Type III bursts were imaged in the low corona, in association with coronal jets (Chen et al., 2013; Chen B. et al., 2018). The evolution of type III source location with frequency was used to estimate the background density profile, assuming second harmonic emission due to low polarization degree. Best-fit density scale heights were derived to be 40 Mm (Chen et al., 2013) and 3–17 Mm (Chen B. et al., 2018), or 5–29 Mm taking into account a 60 degree inclination angle. These are very steep density profiles when one considers that the scale height for a 2 MK plasma is 94 Mm, and likely highlight that the flux tubes are far from their hydrostatic state or highly dynamic in nature. Assuming a density model, the electron beam acceleration site was estimated to be 15 Mm below the 2 GHz type III emission detected in Chen et al. (2013). The acceleration site was estimated even closer (1 Mm at closest approach) in Chen B. et al. (2018) using the conjunction of varying straight line trajectory fits through the type III centroids at different frequencies (see **Figure 2**). The different trajectories varied systematically over each 50 ms timestep of the VLA observations and diverged from a compact ($<$600 km^2) region. The authors suggest that the very short acceleration timescales strongly favor a reconnection-driven particle acceleration mechanism (e.g., Drake et al., 2006) and estimate a lower limit of $E > 0.1$ V m^{-1} if a macroscopic DC electric field is responsible. Moreover, by extrapolating their density models back into the acceleration region, a high level ($\Delta n/n > 100\%$) of density inhomogeneity is inferred.

Other high frequency type III imaging observations have been recently analyzed using the GMRT and the NRH. An example using the GMRT found type III emission observed at 610 MHz during a GOES C-class flare (Bisoi et al., 2018). Whilst radio emission was imaged close to the flaring site, a remote source 500 arcsecs away also glowed brightly. The authors confirmed the source was generated by plasma emission and explained the remote source through wave ducting. They also highlighted that a clearer picture could be found if high spectral resolution imaging spectroscopy had been available. An example using the NRH analyzed type III emission before a large coronal mass ejection (Carley et al., 2016). By combining the NRH imaging spectroscopy with radio spectroscopy at higher frequencies, Carley et al. (2016) identified where and when electron acceleration to $>$75 keV took place, deducing either tether-cutting or flux-cancellation type reconnection at the flux rope center. As the flux rope erupted, it caused reconnection to take place in a fan-spine null point above the rope, producing

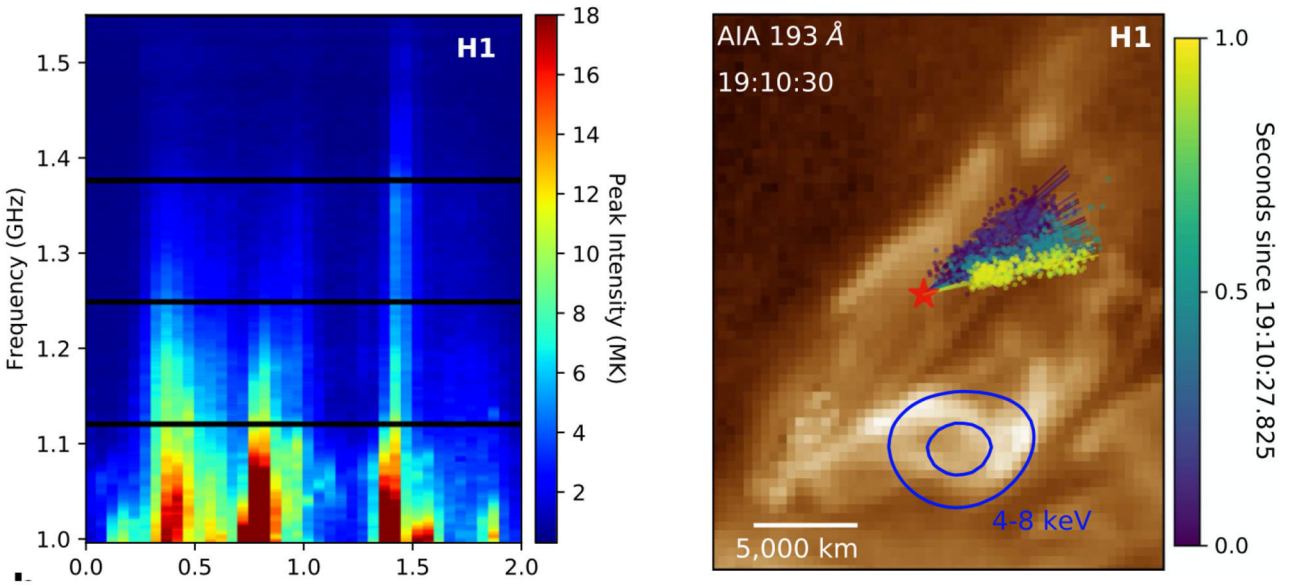

FIGURE 2 | Left: VLA dynamic spectrum of a series of type III radio bursts. **Right**: The electron beam trajectories fit over the type III centroids, showing a systematic change in the spatial motion. All trajectories lead to a common acceleration region, denoted by the red star. Both panels adapted from Chen B. et al. (2018).

many electron beams around 5 keV for a period of 5 min which caused lower-frequency type III bursts.

All the type III studies above have simultaneous X-ray sources, indicating bi-directional electron beam acceleration. When co-temporal images were available, they provided an impression of the locality of the flare acceleration region and a sense of scale, particularly in Chen B. et al. (2018). Simultaneous study of type III radio and X-rays (see e.g., Pick and Vilmer, 2008, as a review) is attractive because electron beam characteristics can be obtained from the X-ray emission (Holman et al., 2011) and applied to the type III producing electron beams by assuming a common acceleration region. As an example, the distance an electron beam must travel before a "bump-on-tail" distribution forms and it becomes unstable to the production of Langmuir waves has been postulated to be $\Delta r \approx d\alpha$, where d is the longitudinal extent of the acceleration region and α is the electron velocity spectral index (Reid et al., 2011). This was shown through a correlation between X-ray spectral index with the type III starting frequency (Reid et al., 2014) such that the "soft-hard-soft" pattern of X-ray spectral index was mirrored by a "low-high-low" pattern in the type III starting frequency. The compact acceleration region of < 600 km^2 estimated from Chen B. et al. (2018) fits this picture if the instability distance is on the scale of megameters. Additionally, the same physical arguments infer that the electron beam instability distance is also connected to the temporal evolution of the flare acceleration, so as to also be dependent upon $\Delta r \approx v\tau\alpha$ for a characteristic beam velocity v, where τ is the characteristic temporal injection time (Reid and Kontar, 2013). The fast type III time profiles on the order of 50 ms shown by Chen B. et al. (2018) infer similar acceleration timescales, which are consistent with the small instability distances of megameters assuming beam velocities around 0.3c. The combined type III and X-ray flare study by Reid et al. (2014) was also able to estimate acceleration region spatial characteristics, with altitudes ranging from 25 to 200 Mm and longitudinal extents ranging from 2 to 13 Mm.

The temporal correlation between hard X-ray (HXR) bursts and type III radio emission is well-established, being shown in many single-event studies and backed up by statistical studies (Kane, 1972; Kane et al., 1982; Hamilton et al., 1990; Aschwanden et al., 1995; Arzner and Benz, 2005; Reid et al., 2014; Reid and Vilmer, 2017). **Figure 3** shows two examples of flares with temporally correlated radio and X-ray emission. Nevertheless, such a correlation is not present in all flares, presumably relating to different magnetic connectivity preventing electron beams to simultaneously stream down into the chromosphere and up into the higher corona. A statistical correlation over 10 years of type III events with co-temporal X-ray flares has been found between the peak type III flux and the peak X-ray count rate using imaging spectroscopy from the NRH to obtain the type III flux profile (Reid and Vilmer, 2017). Whilst a large amount of non-thermal X-ray counts were accompanied by high flux type IIIs, a low amount of non-thermal X-ray counts was accompanied by both high and low flux type IIIs. This result is explained by low density electron beams being able to produce detectable type III bursts via the amplification of coherent waves. Conversely, a high number of hard X-rays counts is dependent upon high beam densities due to the incoherent nature of Bremsstrahlung (Holman et al., 2011; Kontar et al., 2011). The dependency of hard X-rays on the number of high energy electrons naturally explains the notable absence of events with high X-ray intensity and low type III radio flux. This is another reason that co-temporal type III bursts and HXRs are not observed during all flares.

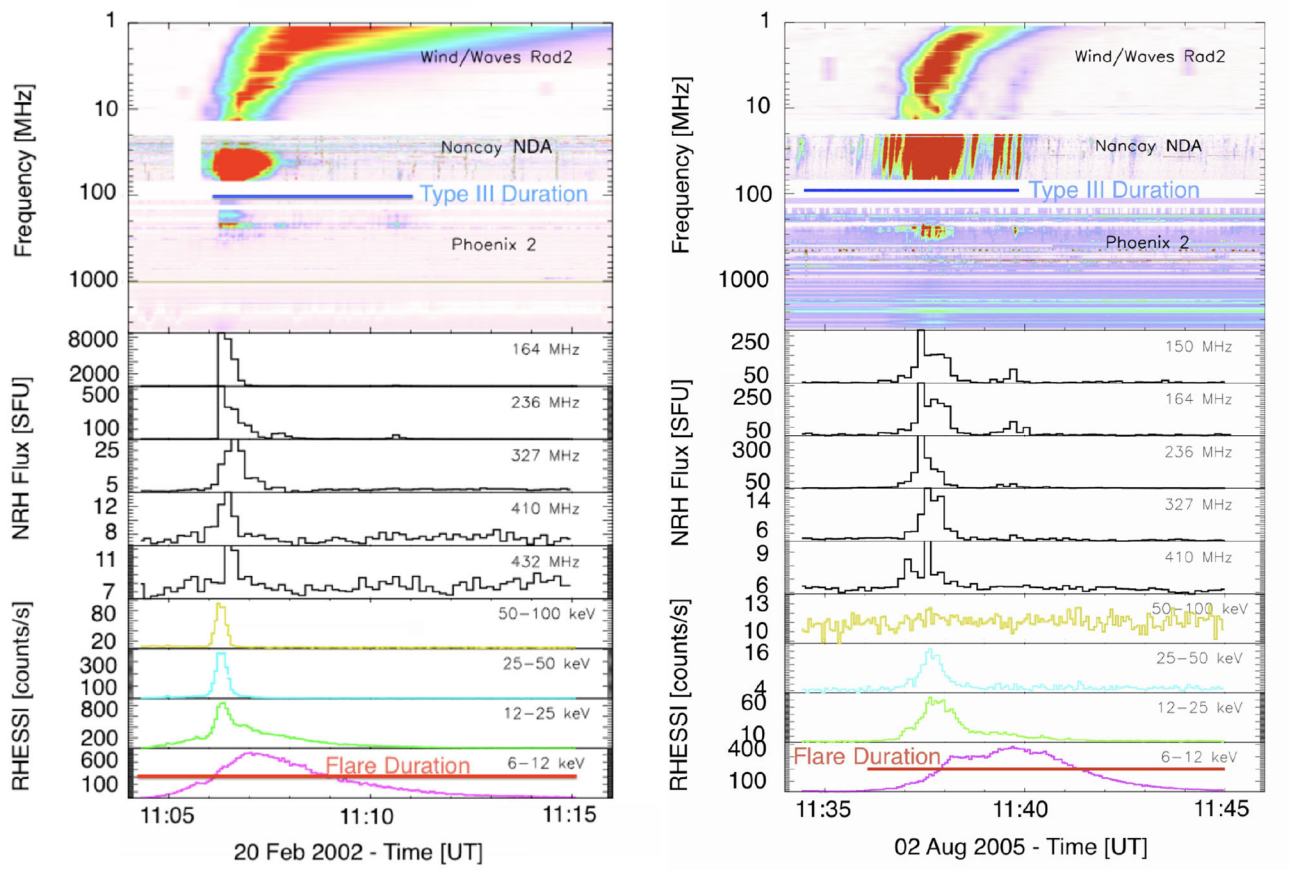

FIGURE 3 | An example of two type III bursts with associated X-ray flares, highlighting the temporal correlation between hard X-rays and type III radio emission. The flare and radio burst durations are indicated, with the longer flare duration defined both by accelerated electrons and cooling bulk plasma. From Reid and Vilmer (2017).

Electron beams that propagate down through the dense corona can also produce reverse type III bursts, which have corresponding positive frequency drift rates and typically start at frequencies >500 *MHz* (Isliker and Benz, 1994; Aschwanden and Benz, 1997). Simultaneous type III and reverse type III events are of particular interest for new-age imaging spectroscopy studies at higher frequencies because the radio positions localize the acceleration region which must be situated between the standard and reverse type IIIs. These bi-directional type III events are a key motivation for simultaneous imaging spectroscopy between 1 GHz and 100 MHz with high frequency resolutions. Currently, it is typical that only one side (normal or reverse) of the bi-directional burst is imaged (e.g., Feng et al., 2016). A wide range of bi-directional type III properties were reported by Tan et al. (2016) using radio spectroscopic observations. Using the full MHD equations and an assumption of a barometric atmosphere, Tan et al. (2016b) devised a model where the electron beam velocity can be estimated using the plasma beta and the type III drift rates. By estimating the plasma temperature (e.g., using soft X-ray line ratios), the upper and lower estimates of electron beam velocity can be used to obtain estimates of the magnetic field at densities corresponding to the start frequencies of the bi-directional type III bursts. The magnetic field of the acceleration region is then simply assumed to be an average of these two values, with estimates found between 50–90 G and 4–18 G for two events (Tan et al., 2016a).

3. LOW FREQUENCY BURSTS

Type III bursts at the low frequencies are signatures of electron beams traveling through the high corona before they reach the solar wind. In this section we define "low frequency" from around 200 MHz down to 10 MHz, the frequency at which Earth's ionosphere becomes opaque to solar radio emission, with imaging spectroscopy results mainly from LOFAR and the MWA.

Low frequency type III radio emission provides diagnostics of electron beams that have propagated into the upper solar corona. The electron beams have undergone more propagation effects than when they produce the high frequency type III components, and so low frequency type IIIs are a key source of electron transport diagnostics. Electron beams that produce low frequency type IIIs are likely to propagate out of the

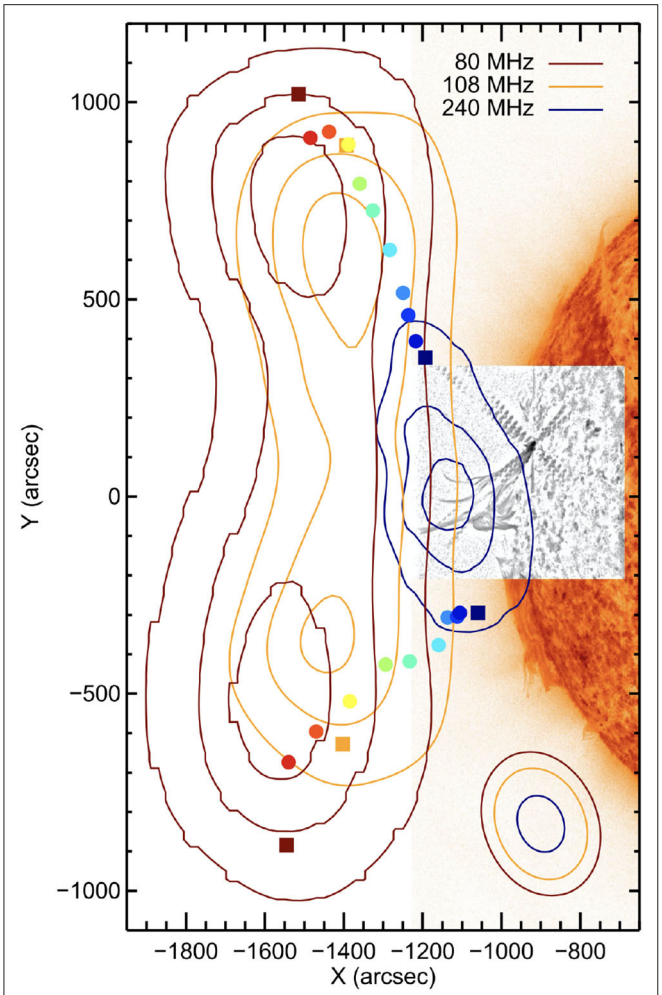

FIGURE 4 | MWA contours at 20, 50, 80% peak flux of a type III burst following a splitting magnetic connectivity above a EUV jet. The background jet structure is highlighted in black and white, over the 304 Angstroms Sun. From McCauley et al. (2017).

solar atmosphere and therefore their presence indicates coronal magnetic field lines open to the solar wind. As such, low frequency type IIIs provide an important diagnostic of magnetic field connectivity for solar wind and space weather studies, provided they are corrected for radio propagation effects. The higher the flux of low-frequency type III emission, as found from NRH imaging spectroscopy at 150 MHz, the more likely that an interplanetary type III burst is observed (Reid and Vilmer, 2017), with almost all sampled type III events with flux greater than 1000 SFU generating interplanetary bursts.

Type IIIs are commonly associated with jets in extreme ultraviolet (EUV) and X-rays (e.g., Bain and Fletcher, 2009; Klassen et al., 2011; Krucker et al., 2011), with electron beams typically following the same path as the jet. A number of studies have analyzed type IIIs using high resolution MWA imaging spectroscopy that occurred co-temporal and co-spatially with jets observed in UV (McCauley et al., 2017; Cairns et al., 2018; Mulay et al., 2019). In all three events the type III emission showed resolved fine temporal structure, consistent with several distinct EUV jet episodes and caused by multiple electron beam injections, explained via energization within magnetic reconnection regions by Cairns et al. (2018). A splitting of the magnetic connectivity was highlighted by McCauley et al. (2017) using MWA imaging spectroscopy of a succession of type III radio bursts. The radio bursts started from a common source around 200 MHz and split into two separate sources, following different magnetic flux tubes. The UV jet traces out a region where the magnetic field connectivity diverges, which appears to facilitate the splitting of the type III into two separate sources, indicated in **Figure 4**. For this event, type III imaging spectroscopy was used to ascertain typical electron beam speeds around 0.2c. Comparing with magnetic field extrapolations, Mulay et al. (2019) found type III radio sources at the flaring site which did not appear at the expected points along magnetic field lines. There was a distinct absence of type III frequency evolution along the field that would be consistent with electron beam propagation. Mulay et al. (2019) concluded this was possibly due to radio wave scattering or the magnetic field extrapolation not including local small scale variations.

Not all electron beams that generate type III bursts are able to escape into the solar wind. Some electron beams travel along loops that are confined to the corona, producing radio emission that forms a J- or U-shape in the dynamic spectrum, known as J/U-bursts (Maxwell and Swarup, 1958). J-bursts can also occur at the same time as coronal jets, with one imaged using LOFAR by Morosan et al. (2017) where the accelerated electron beam traveled along a large magnetic coronal loop. The electron beam can also mirror at the footpoint of magnetic loops forming what is known as an N-burst, with Kong et al. (2016) reporting a well-observed N-burst using the NRH. The bulk of magnetic flux is closed in the corona and so we might expect U-bursts and J-bursts to be observed more often than type III bursts when in fact the converse is true. Using the derived magnetic loop and electron beam parameters from LOFAR imaging spectroscopy, Reid and Kontar (2017a) analyzed the electron beam instability criteria, shown in **Figure 5**. For radio emission to be generated on closed magnetic fields, the loop needs to be long enough for a power-law accelerated electron beam to become Langmuir-wave unstable through time-of-flight. Additionally the beam needs to be dense enough for the timescale of Langmuir wave growth and their successive conversion to radio waves to be shorter than the electron propagation timescale. These conditions result in a stricter set of requirements for electron beams and background loop plasma parameters to produce U/J-burst radio emission over type III radio emission.

One quintessential property of type III radio bursts is the frequency drift rate, typically attributed to the bulk speed of the electron beam traveling through the solar plasma. The enhanced spectral resolution from LOFAR and the MWA allows drift rates to be more accurately measured and has been statistically sampled recently by a number of radio spectroscopic studies by Morosan and Gallagher (2017) and Reid and Kontar (2018a) that used LOFAR, by Zhang et al. (2018) that used the Nançay Decametre Array (NDA, Lecacheux, 2000), and by Stanislavsky

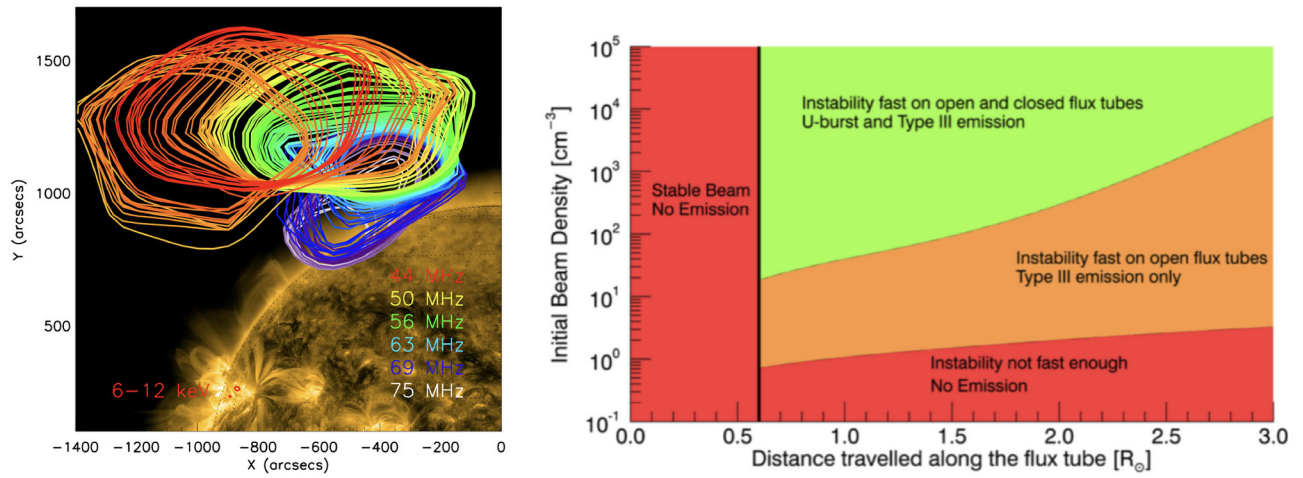

FIGURE 5 | Left: LOFAR contours of a U-burst tracing out a large coronal magnetic loop. The co-temporal X-ray source is shown with a background of the 171 Angstroms Sun. **Right**: A schematic showing how electron beams require long flux tubes and/or high densities to produce J/U-bursts. Adapted from Reid and Kontar (2017a).

et al. (2018) that used the Ukrainian T-shaped Radio telescope (UTR-2, Konovalenko et al., 2016). Similar to Alvarez and Haddock (1973) who compared type III drift rate from 550 MHz to 50 kHz from many studies, the drift rate has been approximated by a power law of the form $\frac{\partial f}{\partial t} = -Af^{\alpha}$. Findings for α were $-1.82 \pm 0.11, -1.63 \pm 0.11, -1.23, -2.11 \pm 0.66$, respectively for the four studies, compared to the value of $\alpha = -1.84$ found by Alvarez and Haddock (1973). It is unsurprising that the power law spectral indices vary because the type III drift rate depends primarily upon the speed of the electron beam exciter (e.g., demonstrated numerically by Reid and Kontar, 2018b), the density gradient of the background plasma, and whether the radio burst was generated via fundamental or second harmonic emission. For fundamental emission, the electron beam travels smaller distances over the same frequency range. Moreover, the fundamental emission is more susceptible to radio wave propagation effects (see section 3.3).

It is noteworthy that Zhang et al. (2018) found such a low spectral index as they sampled nearly 1400 type III bursts over half a solar cycle via an automatic analysis system using a Hough transform. **Figure 6** shows a scatter plot of the frequency drift rates, highlighting the huge spread in values between different radio bursts. If we assume that the background electron density was similar for all studies, as was the proportion of fundamental to harmonic emission then Zhang et al. (2018) observed more electron beams with lower bulk velocities than the other studies. Lower velocity beams take longer to travel from one frequency to another and hence the frequency drift rate is smaller in magnitude. The large number of type IIIs detected by the automated method might have analyzed a greater number of type IIIs with low signal-to-noise ratio, produced by slow, weak beams, which may account for the lower magnitude drift rates observed. A similar study would be beneficial using new type III imaging spectroscopy from telescopes with larger collecting areas to detect very faint type III bursts and make a drift rate comparison between them and the type III bursts with higher fluxes.

The time profile of type III bursts is another property that has undergone recent analysis. At a single frequency, the time profile is influenced by a convolution of processes based upon the plasma emission mechanism including; beam acceleration characteristics, beam velocity dispersion, the radio emission process, radio propagation, and density variation in the solar corona. Characterizing when certain processes are dominant is essential for extracting diagnostic information about the electron beam. The high flux sensitivity and time resolution of new type III imaging spectroscopy makes it ideally suited for analyzing the rise and decay of type III emission at a single frequency. At frequencies between 30-70 MHz, Reid and Kontar (2018a) used LOFAR to analyzed 31 radio bursts, coming to the conclusion that their half-width half-maximum (HWHM) rise and decay was best fit by a Gaussian rise plus a Gaussian decay. This was the first study to analyse the type III HWHM rise time, finding $t_{\rm rise} \propto f^{-0.77\pm0.14}$. The Gaussian decay was in contrast to the exponential decay used in previous works (e.g., Aubier and Boischot, 1972; Barrow and Achong, 1975; Mel'Nik et al., 2011) although similar HWHM decay times were found. The decay time $r_{\rm decay} \propto f^{0.89\pm0.15}$ compares very well with comparisons of decay times all the way down to kHz frequencies, shown by Kontar et al. (2019), that could be fit with a power-law that had a spectral index close to 1. The rise and decay times also showed a very strong correlation, indicating that one process dominates both time scales at LOFAR frequencies.

The explanation put forward by Reid and Kontar (2018a) is that the rise and decay times are primarily caused by the front and back of the electron beam, respectively, separated through velocity dispersion. The front of the electron beam consists of faster particles and so consequently they arrive at a

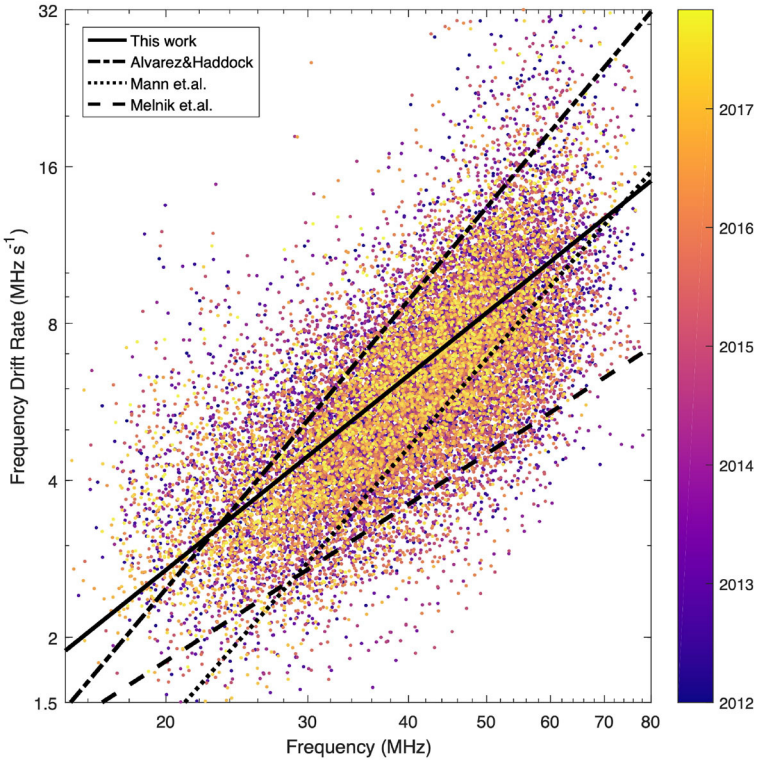

FIGURE 6 | Scatter plot of the frequency drift rate vs. frequency for 1389 simple type III bursts; the data points are color-coded according to the occurrence time of the corresponding event. The black lines indicate fitted results to the data points and from other works. From Zhang et al. (2018).

certain background plasma frequency first. Similarly the back of the electron beam is made up of slower particles and so arrives last. This theory was consistent with the larger and smaller magnitudes of drift rates found using the rise and decay time, respectively (Reid and Kontar, 2018a) and with quasilinear simulations (see section 4). Assuming a coronal density model gave average front and back velocities of 0.2 $\pm$ 0.06c and 0.15 $\pm$ 0.04c. The same conclusion was obtained by Zhang et al. (2019) who used LOFAR imaging spectroscopy to analyse one radio burst. They found the source locations from the rise, peak and decay times were displaced with respect to one another, and followed different paths in the solar atmosphere. Derived velocities from centroid locations were different, with the velocities relating to the front edge, peak and back edge of a type III burst were 0.42c, 0.25c, and 0.16c, respectively. The centroids of the front edge were farther away from the solar disc meaning that the front of the electron beam was propagating along a magnetic flux tube with higher coronal density whilst the back of the beam was propagating along a flux tube with lower coronal density. In seems that whilst the rate of velocity dispersion is governed by the electron beam acceleration characteristics like energy spectral index, the magnetic flux tubes that guide electron beams also influence the type III durations.

Velocity dispersion is not the only effect that contributed to type III durations, and Zhang et al. (2019) estimated the contribution of density turbulence and wave propagation effects. Density variation causes different regions in the solar atmosphere to have the same plasma frequency, and hence contribute to the time profile at any given frequency (Roelof and Pick, 1989). By analyzing the wave frequency distribution of sources observed at the same distance from the solar disc, Zhang et al. (2019) estimated the effect of density variation, finding that it caused an observed duration about 2.2–5.7 times the duration caused by density variations (a lower effect than, Roelof and Pick, 1989). Wave propagation effects were also analyzed using shorter duration type III bursts occurring before the main type III burst. These provided an upper limit on the effect of wave propagation effects of less than half of the observed duration. Whilst the growth rates of radio waves from Langmuir waves are fast, more theoretical study should be carried out to fully explore the effect of the radio emission mechanism on the type III drift rates.

Type III polarization measurements are a strong diagnostic potential for discerning between fundamental and harmonic emission. There has not been much recent works using polarization information in imaging spectroscopy as calibration issues complicate matters. A recent work (Rahman et al., 2020) looked at the polarization of type IIIs using the MWA. They found the degree of circular polarization increased as a function of frequency and was higher at the start of the radio bursts, consistent with previous models that fundamental emission is generated first. The polarization fraction decreased with time, consistent with scattering effects depolarizing the radio emission.

3.1. Fine Structure

One of the most powerful applications of high resolution imaging spectroscopy lies in the analysis of fine structure. For type III bursts this typically takes the form of striae bursts, or type IIIb bursts (de La Noe and Boischot, 1972), fine structure exhibited along a backbone of fundamental emission. The general consensus about the driver is density turbulence in the background plasma (e.g., Takakura and Yousef, 1975) although a formal theoretical treatment of the entire process is yet to be formulated. With previous imaging, the spectral resolution was too sporadic to have multiple images of one stria. A number of studies using LOFAR imaging spectroscopy (Kontar et al., 2017; Chen X. et al., 2018; Kolotkov et al., 2018; Sharykin et al., 2018) have analyzed striae bursts, concentrating on one specific event on the 16 April 2015.

The LOFAR dynamic spectrum and corresponding image is shown in **Figure 7**. Kontar et al. (2017) concentrated on analyzing the spatial information of individual striae. They found that individual striae increased in size at a single frequency, and this rate was different between the fundamental and harmonic emission. They reasoned that the intrinsic source size (the actual size of the source in the corona) is much smaller than the apparent source size (source size derived from radio waves at Earth) and hence the brightness temperature of the sources is orders of magnitude larger than what is estimated using observed source size. The power spectral density of the same type IIIb burst was analyzed by Chen X. et al. (2018). They found that the fluctuations had an almost 5/3 spectral index in wavenumber space, similar to what is normally observed for solar wind density turbulence at 1 AU (Chen, 2016). Interestingly the same spectral index was found for the harmonic emission, possible to obtain due to the sensitivity and the spectral resolution of LOFAR. A characteristic spatial scale of striae was estimated around 700 km, using the Newkirk density model (Newkirk, 1961) rather than spatial positions because the source was located over the solar disc. Sharykin et al. (2018) extended this study to analyse the spatial motion of the individual striae. These structures have an instantaneous bandwidth around 20–100 kHz that increases with increasing central frequency. By fitting each striae with a elliptical Gaussian, they found the striae drift rate around 0-0.3 MHz s^{-1}, increasing with increasing central frequency. The mean striae speed from the drift rate was around 600 km s^{-1}, larger than the typical sound speed of 200 km s^{-1} and smaller than the type III burst speed of 0.2c. Kolotkov et al. (2018) analyzed the same type III event, finding quasi-periodicity in the signal. The authors explained the periodicity by a propagating fast wave train that modulated the radio emission produced by the electron beam.

Spectroscopic observations of type IIIb bursts have been carried out by Tun Beltran et al. (2015) using the LWA. Analyzing a type III storm that displayed both type IIIs and type IIIbs, they concluded that electron beams must travel along magnetic structures with density inhomogeneities present. Moreover, the sudden onset of type IIIb storms from a normal type III storm must be explainable, which could be caused by different electrons propagating along different magnetic field lines with an increased level of density turbulence. Mugundhan et al. (2017) also spectroscopically analyzed a number of type IIIb bursts using the Guribidanur Low Frequency Solar Spectrograph (GLOSS, Kishore et al., 2014). By analyzing numerous striae, they approximated $\Delta n/n$ using the observed value of $\Delta f/f$, finding ranges of 0.006 ± 0.002. Sharykin et al. (2018) made the same assumption and found similar amplitudes of 10^{-3}.

3.2. Coronal Density Models

The advent of high resolution imaging spectroscopy has brought increased interest in using type III bursts to diagnose the density structure of the solar corona. Type III frequencies are associated with a background electron density assuming either fundamental or second harmonic emission. The change in centroid position of the type III sources as a function of frequency thus provides information about how the background coronal density changes with altitude, $n_e(r)$. Altitudes inferred from type IIIs are typically larger than altitudes predicted by standard coronal density models. Previous investigations using spectra and images at a few frequencies explained the enhanced altitudes through type IIIs being generated in over-dense structures (e.g., Wild et al., 1959; Trottet et al., 1982; Kundu et al., 1983) as there were spatially correlated streamers imaged in white light. An alternative explanation is that the enhanced altitudes are not real. Radio source centroids are shifted by scattering of radio waves off density inhomogeneities, which causes their apparent position to be farther away from the Sun (e.g., Riddle, 1974). This theory is currently preferred as many type III bursts are not necessarily observed over dense streamers (e.g., Leblanc and de La Noe, 1977). The reality is likely that both scenarios are possible, with some proportion of type III events occurring on over-dense flux tubes. A nice historical overview on some issues arising from coronal density models derived from type IIIs is given in McCauley et al. (2018).

The initial results from LOFAR imaging spectroscopy were consistent with previous findings that type III sources corresponded to altitudes much higher than standard coronal density models would infer (Morosan et al., 2014), with altitudes extending out to 3 solar radii around 30 MHz. This was significantly farther out than predicted by a density model using white-light data from the same day (Zucca et al., 2014). Further observational studies using the MWA and LOFAR found altitudes deduced from type III observations to be much higher than standard coronal density models predicted (Reid, 2016; Mann et al., 2018; McCauley et al., 2018; Gordovskyy et al., 2019). **Figure 8** shows an example of such a density model being found from type III centroid locations. Whilst it might be possible that type IIIs preferentially travel along over-dense flux tubes, the electron beam velocities that can be deduced from type III bursts must also be consistent with theory. Some deduced velocities from type III bursts observed by LOFAR were found to be superluminal (Reid, 2016; Mann et al., 2018). Such velocity estimates are likely influenced by the spatial and temporal modifications due to radio wave propagation effects (see section 3.3) but other effects may also play a role such as different regions of the electron beam emitting radio waves at different times, creating an apparent speed faster than the beam speed (Reid and Kontar, 2018b). Other deduced velocities by LOFAR and the MWA using imaging spectroscopy have been

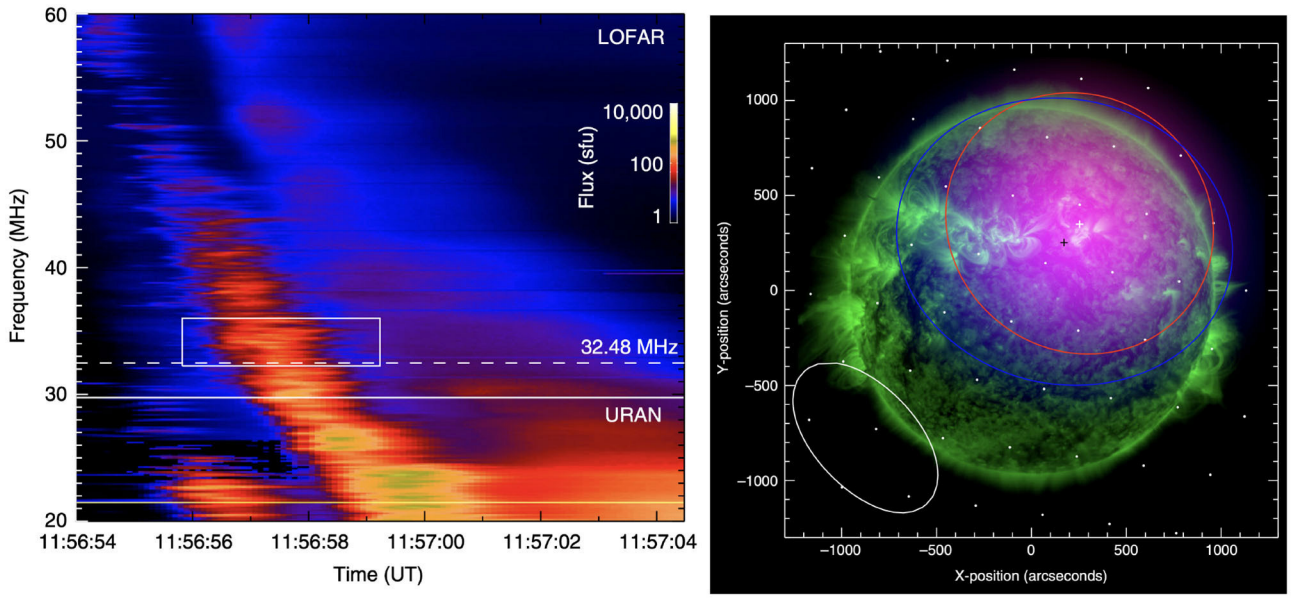

FIGURE 7 | Left: Type IIIb dynamic spectrum showing the fundamental and harmonic pair with significant fine structure observable in the fundamental emission. **Right:** Image of the fine structure component with fundamental in red and harmonic in blue. The background is the EUV Sun. Adapted from Kontar et al. (2017).

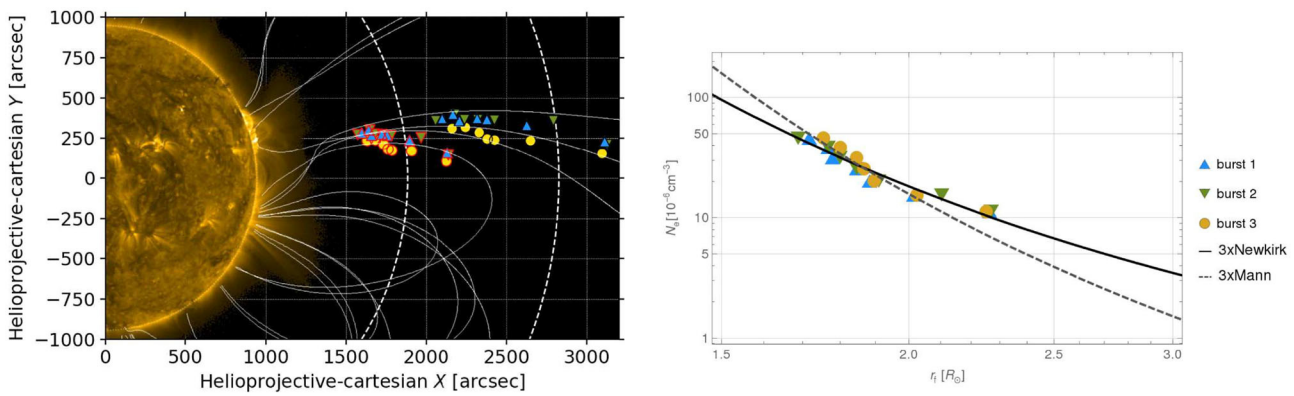

FIGURE 8 | Left: Type III centroids from a number of radio bursts at the fundamental (red outlines) and the harmonic. **Right**: Density models derived from the type III centroids. Adapted from Mann et al. (2018).

higher than the standard 0.1-0.3c velocities typically observed (e.g., Morosan and Gallagher, 2017; McCauley et al., 2018).

Type U and J bursts allow diagnosis of coronal densities within magnetic flux tubes confined to the corona. Using LOFAR, Reid and Kontar (2017a) found the coronal density profile from two J-bursts and one U-burst that occurred in quick succession. Estimating second harmonic emission, the density profile roughly fit enhanced standard density profiles, the 3.0× Baumbach-Allen Model (Allen, 1947), 3.5× Sittler model (Sittler and Guhathakurta, 1999) and 4.5× Saito Model (Saito et al., 1977) density model. However, the lowest frequencies around 40 MHz at the loop apex did not fit any density models as the magnitude of the density gradient became much less at these frequencies. Only by taking into account this change in density gradient obtained through the imaging spectroscopy were realistic burst exciter speeds around 0.2c able to be estimated.

Radio observations taken only from the Earth suffer from projection effects; our limitation of imaging on a 2-dimensional plane without any spatial information on the line-of-sight dimension. Projection effects can only amplify the larger derived electron density altitudes from type III bursts, getting larger the more the electron beam is propagating toward/away from the Earth. The uncertainty is amplified for electron beam source regions that are close to the center of the Sun. An example was shown by Gordovskyy et al. (2019) on how projection effects modify derived density models using LOFAR imaging spectroscopy for four different events at electron beam propagation angles of 90, 60, and 30 degrees from the Sun-Earth

line. Most of the sources were off-disc and so 30 degrees gave widely inaccurate frequency vs. distance estimates. Such small projection angles are more likely to occur for on-disc sources close to Sun center. Whilst radio projection effects amplify the larger derived electron density altitudes, the larger the radio projection effect, the smaller the correction for radio wave propagation from source to observer as more of the scattering will occur along the line of sight and so not affect the 2D radio imaging spectroscopy.

3.3. Radio Wave Propagation

Understanding the propagation of radio waves through the solar system is paramount if we are to make best use of radio imaging spectroscopy at low frequencies. The displacement of sources by scattering was convincingly shown using LOFAR's high resolution imaging spectroscopy of a type III burst displaying both fundamental and harmonic emission (Kontar et al., 2017). A systematic radial displacement of 1.8 arcmin s^{-1} was observed for the fundamental emission. We would expect the fundamental type III emission to be more displaced through scattering off density inhomogeneities because the radio frequency is closer to the local plasma frequency. The radial displacement was found for numerous fundamental emission fine structures (stria) between 32 and 38 MHz. Moreover the areal extent of the fundamental sources increased faster than the harmonic emission at a single frequency, consistent with radio waves scattering off density inhomogeneities. An increase in the area of the burst source was also observed by Mohan et al. (2019) using type III imaging spectroscopy from the MWA. They found a radial expansion around 43 Mm s^{-1}, two orders larger than the local Alfvén speed and so rejected the increase in physical area due to magnetic waves. With LOFAR and MWA showing how important radio wave propagation is to the spatial characteristics of fundamental emission, this opens up the ability to test radio wave propagation models (Robinson, 1983; Arzner and Magun, 1999; Thejappa and MacDowall, 2008) and investigate analysis of the turbulent structure of the solar corona. Analyzing the same type III event as Kontar et al. (2017), Sharykin et al. (2018) found that the source size across the line-of-sight exceeds the size along the line-of-sight, implying that radio wave scattering must be anisotropic. Mohan et al. (2019) used the model by Arzner and Magun (1999) on the analyzed type III bursts to estimate a value of $\Delta n/n = 4 \times 10^{-3}$.

It is attractive to correct for propagation effects so that type III burst source positions can derive more realistic coronal density models. A method proposed by Chrysaphi et al. (2018) treats radio wave propagation like scattering of a charged particle in plasma. They applied this technique to LOFAR imaging spectroscopy of a type II, showing that split-band emission can arise from the same spatial location. The mean scattering rate depends upon the local intensity of density turbulence and the frequency of radio emission. By integrating over regions where the optical depth is greater than one, a radial correction can be approximated. Chrysaphi et al. (2018) found corrections around 0.3 $\mathcal{R}_\odot$ for 40 MHz and 0.6 $\mathcal{R}_\odot$ for 32 MHz. The technique was applied to type III emission by Gordovskyy et al. (2019) showing that it can indeed explain larger than expected heliocentric distances of radio sources. A different correction method was proposed by McCauley et al. (2018) who calculated synthetic radio images using the FORWARD software (Gibson et al., 2016) to find expected Bremsstrahlung and gyroresonance emission from a model atmosphere found using the MAS software (Lionello et al., 2009) to extrapolate coronal magnetic fields and then applying a heating model (Schrijver et al., 2004) to compute density and temperature. The difference between observed type III burst source locations, found using MWA imaging spectroscopy between 80 and 240 MHz, and the synthetic radio images was found to estimate the effect of radio propagation effects. Using three type III radio bursts they found corrections around 0.3 $\mathcal{R}_\odot$ for 80 MHz and 0.1 $\mathcal{R}_\odot$ for 240 MHz, slightly higher than those predicted by Chrysaphi et al. (2018). Applying the corrections to the estimated coronal density models from type III bursts, McCauley et al. (2018) found a better agreement with typical density models, although two type III bursts had unusually steep density profiles. The third type III burst agreed well with a type III density model predicted by Cairns et al. (2009) from type III burst spectra.

The above methods attempt to approximate the effect of radio wave scattering off density fluctuations but to properly understand this effect, ray-tracing simulations are required. There have been a number of ray-tracing studies in the past that have tracked type III burst propagation (Steinberg et al., 1971; Thejappa and MacDowall, 2008; Krupar et al., 2018) which assumed isotropic scattering by small-scale density fluctuations. Krupar et al. (2018) using the STEREO spacecraft and Krupar et al. (2020) using Parker Solar Probe found that from the arrival time, the exponential decay times observed at low frequencies from spacecraft are able to be explained through the scattering of radio waves by density inhomogeneities. Bian et al. (2019) modeled the scattering process using a Fokker-Planck equation and were able to reproduce the time profile but not the inverse frequency dependence of the decay time, which they concluded was down to the exclusion of a large-scale refractive term. Kontar et al. (2019) recently extended the work of Bian et al. (2019) but treated the scattering in the anisotropic domain, with the dominant effect being perpendicular to the heliospheric radial domain (Kontar et al., 2017). As well as explaining temporal profiles, Kontar et al. (2019) used ray-tracing simulations to explain the increase in source sizes, finding a scattering increase in the FWHM around 1.1 $\mathcal{R}_\odot$ at 35 MHz, although this value will depend upon the size of the density fluctuations from event to event. Changing the anisotropy parameter strongly influences source sizes that are off the solar limb and less so at disc center.

4. ELECTRON BEAM PROPAGATION

Electron propagation through plasma is the cause of type III radio bursts and there has been an extensive amount of theoretical work on the subject. Electrons have been simulated propagating through the solar coronal plasma and out into the interplanetary medium. Their propagation is not simply ballistic but is modified by the energy exchange with Langmuir waves as the electron beam becomes unstable during transport. The radio

emission is then believed to be mainly produced through wave-wave processes with ion-sound waves to produce fundamental emission, and with almost oppositely directed Langmuir waves for second harmonic emission.

In this section, the recent theoretical progress is discussed that has been undertaken to explain how type III bursts are generated by propagating electron beams. This theoretical understanding is critical for using type III bursts as remote sensors of electron acceleration and propagation through the solar corona and to maximize the research output that we can obtain from Earth-based imaging spectroscopy. It is beyond the scope of this review to cover all simulations works and so, as indicated in section 1, readers are encouraged to look through the introductions contained within cited works to obtain a more historical overview of the subject. In almost all of the work the electron beam acceleration is taken as an initial condition. This is largely due to the complexity and unanswered questions about which mechanism is responsible for electron acceleration in the corona (e.g., Zharkova et al., 2011).

Assuming electron beam acceleration with a power-law energy spectrum, the beam undergoes an initial period of propagation without becoming unstable to Langmuir waves. This "instability distance" is related to the distance required for velocity dispersion to create the bump-in-tail velocity distribution required for Langmuir wave generation. As discussed in section 2, quasilinear simulations (Reid et al., 2011; Reid and Kontar, 2013) showed that the distance is dependent upon the electron beam velocity spectral index, the size of the acceleration site, and the temporal injection profile. The instability distance is the reason that the starting frequency of type III bursts is not observed at the particle acceleration region. Perhaps the most striking observation that show this are the bi-directional type III bursts where there is a frequency gap, and hence a spatial gap between the forward and reverse type III bursts. The simulations done by Li et al. (2011) show this spatial gap well and highlight the reduced intensity of radio emission generated by electron beams propagating through plasma with a positive density gradient (**Figure 9**). Whilst Li et al. (2011) assumed a 20 MK Gaussian distribution of accelerated electrons, their distribution had a spatial width of 1 Mm which likely influenced the frequency gap between downward and upward propagating electron beams.

Despite electron beams being made up of electrons with a distribution of velocities, type III bursts are typically tracked using one velocity derived by the frequency drift rate. The main theoretical reason behind this pseudo-constant velocity is the beam-plasma structure that is formed by the electron beam wave-particle interactions with Langmuir waves, proposed theoretically (Zheleznyakov and Zaitsev, 1970; Zaitsev et al., 1972; Mel'Nik, 1995) and successfully simulated (Takakura and Shibahashi, 1976; Magelssen and Smith, 1977; Kontar' et al., 1998; Mel'Nik et al., 1999). Electrons travel as an ensemble with roughly the mean velocity of all electrons taking part in the energy exchange between waves and particles. Langmuir waves are generated at the front of the beam and re-absorbed at the back of the beam, allowing propagation over long distances of 1 AU, and avoiding a catastrophic beam energy loss postulated by Sturrock (1964).

The initial properties of the accelerated electron beam play a significant role in how the resultant type III burst evolves through the solar corona. Understanding how these properties modify the radio dynamic spectra is key to using type III imaging spectroscopy as a probe of electron beam transport in the solar corona. Assuming that the injected energy spectra is a power-law, the spectral index of this distribution influences which electrons contribute to the beam-plasma structure and therefore how fast the resultant electron beam propagates through space (e.g., Li and Cairns, 2013; Reid and Kontar, 2018b). When simulated, Li and Cairns (2013) found that smaller spectral indices give rise to faster electron beams, cause type III bursts to have higher magnitude drift rates and result in higher peak values of type III burst fundamental emission. However, the electron beam speed is not just governed by the spectral index but by the initial beam density too as both properties govern the energy density contained with the electron beam. It is this energy density that more completely governs which electrons contribute to the beam plasma structure (Reid and Kontar, 2018b). If the energy density is too small at certain electron energies, the Langmuir wave growth rate will not be high enough and these energies will not contribute to the beam-plasma structure that dictates beam speed. As electron beams expand in the solar wind, their energy density decreases and they stop producing radio emission (Reid and Kontar, 2015). Additionally, Reid and Kontar (2018b) showed that the peak brightness temperature of type III fundamental emission is proportional to the energy density contained within the electron beam. This result is significant as, if proven to be true via *in situ* measurements from PSP or SolO, type III bursts can be used to estimate the energy density of beams traveling through the solar corona. Moreover, with electron beam size estimates using type III imaging spectroscopy by taking into account wave propagation effects, the total energy contained within escaping electron beams during solar eruptive events can be estimated.

As discussed from LOFAR observations in section 3, the drift rates at the front of the beam are faster than the drift rates at the back of the beam, relating to faster and slower velocities, respectively (Reid and Kontar, 2018a; Zhang et al., 2019). This dependence was found using numerical simulations by Reid and Kontar (2018b) using the drift rates from synthetic fundamental emission dynamic spectra. The front of the beam was always faster than the back and could travel over twice as fast. The maximum and minimum electron energies in the beam plasma structure were significantly higher at the front than at the back of the beam, and so average velocities greater than 0.5c were possible. This is in stark contrast to the back of the beam, where the minimum energy was dictated by the temperature of the background plasma and so velocities cannot go higher than 0.5c. Simulations from Li and Cairns (2014) showed that higher beam velocities occur when the background plasma is simulated by a kappa distribution as the minimum energy that contributes toward the beam plasma structure is higher. It remains to be proven whether the solar corona can be described by a kappa distribution like the solar wind. The difference between the electron energies at the front and back of the beam dictate how fast the electron beam elongates in space (expansion velocity).

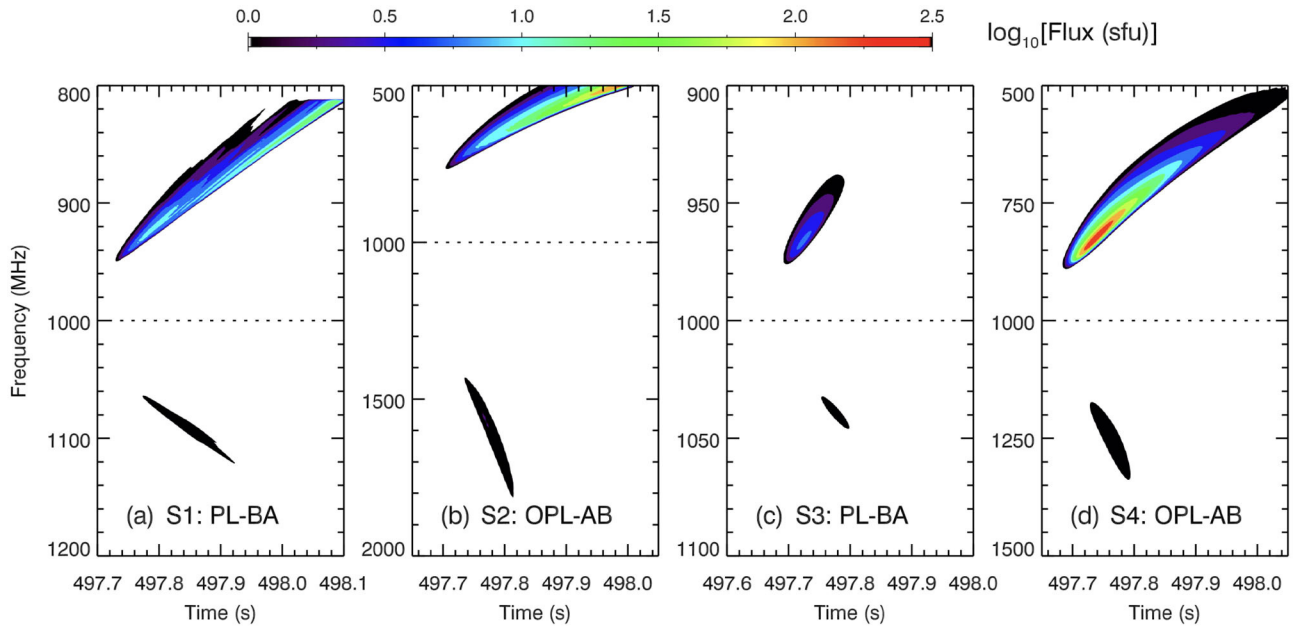

FIGURE 9 | Predicted type III second harmonic dynamic spectrum of a bi-directional electron beam injection using simulations with different ininital conditions. From Li et al. (2011).

This is related to the type III duration at one frequency. However, it should be emphasized again that whilst velocity dispersion likely makes the most significant contribution toward the type III decay time, radio wave propagation effects, density turbulence and the radio emission process will also influence type III durations and derived speeds. As an example, Ratcliffe et al. (2014b) found that using the peak flux to estimate electron beam speeds from a dynamic spectrum of second harmonic emission, the derived exciter speed was more closely related to the region of the beam that produced the peak in back-scattered Langmuir waves, which was slightly farther back in space from where the peak Langmuir waves were generated.

When electron beams become unstable, it has been the focus of many recent theoretical works how density inhomogeneities in the background plasma influence subsequent Langmuir wave growth, electromagnetic emission and the development of the electron distribution function. Studies are typically carried out either in one spatial location (e.g., Ratcliffe and Kontar, 2014; Krafft et al., 2015; Voshchepynets and Krasnoselskikh, 2015; Voshchepynets et al., 2015), in a small spatial box (e.g., Thurgood and Tsiklauri, 2015; Volokitin and Krafft, 2018; Henri et al., 2019; Krafft and Volokitin, 2020) or over distance comparable to the solar corona or longer (e.g., Li et al., 2012; Reid and Kontar, 2013, 2015, 2017b; Loi et al., 2014; Ratcliffe et al., 2014b). Each of these different approaches has their own advantages and disadvantages and are used based upon the focus of the relevant study. Studies in one spatial location are computationally less expensive and are typically used to investigate how wave k-vectors develop over time, taking a static spatial gradient for the background density. Studies in a small spatial box focus on both on wave-particle and wave-wave interactions required to generate radio emission. These studies aim for a more complete treatment of the problem, with the small spatial box and hence restrictive length scales necessary due to the computational overhead. Studies over large distances typically use the quasilinear approximation to reduce the computational overhead and try to capture the large-scale evolution of the beam-plasma system and the fine structure that occurs within the resulting Langmuir waves and radio waves that we detect as type III bursts.

It has been known for decades that density inhomogeneities in the background plasma suppress the generation of beam-induced Langmuir waves by refracting them in phase space, out of resonance with the electron beam. Langmuir waves refracted to low phase velocities (high k-vectors) are eventually re-absorbed by the background plasma. Langmuir waves refracted to high phase velocities can be re-absorbed by the electron beam, accelerating a tail of energetic electrons. The level of Langmuir wave suppression is dependent upon on the characteristic length scale of density inhomogeneities $L \propto \frac{1}{n_e}\frac{\partial n_e}{\partial x}$ (e.g., Kontar, 2001; Reid and Kontar, 2010, 2017b; Voshchepynets et al., 2015; Krafft and Volokitin, 2020) such that if the magnitude of L reaches a certain value, Langmuir waves are suppressed. The level of density inhomogeneities also influence the conversion of Langmuir wave energy into electromagetic energy (e.g., Li et al., 2012; Ratcliffe and Kontar, 2014; Krasnoselskikh et al., 2019).

When electric fields associated with Langmuir waves are measured in the solar wind at the same time as electron beams and type III bursts, they are distributed in spatial clumps (e.g., Vidojevic et al., 2012). This is attributed to aforementioned Langmuir wave suppression from density inhomogeneities. How the distribution of the beam-driven electric field is modified by density inhomogeneities has been simulated both locally

(Voshchepynets et al., 2017; Krafft and Volokitin, 2020), with an electron beam propagation through the solar corona and through the solar wind (Reid and Kontar, 2017b). Without any density fluctuations, the beam-driven electric field distribution is peaked at the highest electric fields. As the intensity of the density fluctuations increases, the logarithm of the electric field becomes more uniformly distributed and the mean field is decreased. When the intensity of the density fluctuations is high, the largest electric field amplitude part of the distribution is better approximated by a power-law or exponential decay. The effect was described probabilistically (Voshchepynets and Krasnoselskikh, 2015; Voshchepynets et al., 2015) and through resonance broadening (Bian et al., 2014). In the resonance broadening description, for homogeneous plasma, wave-particle interactions have a sharp resonance function $\delta(\omega - kv)$. For inhomogeneous plasma, wave particle interactions occur over a range of velocities Δv due to wave refraction and so the growth rate of the beam-plasma instability changes to become a function of the electron beam velocity gradient averaged over Δv. If this width is small then wave growth can still occur but as the width increases the average slope reduces and can even become positive (see **Figure 10**).

The most visible consequence of density inhomogeneities is the type IIIb radio burst fine structure which was discussed in section 3.1. Quasilinear simulations are able to capture the fluctuating Langmuir waves (e.g., Reid and Kontar, 2015) and produce dynamic spectra that are similar to type IIIb bursts (Li et al., 2012; Loi et al., 2014; Ratcliffe et al., 2014b). Indeed, without simulating density inhomogeneities the electron flux at 1 AU does not compare with *in situ* observations (Reid and Kontar, 2013). However, there are still notable discrepancies when comparing synthetic dynamic spectra to observations, particularly using recent high resolution imaging spectroscopy. Whilst the electric fields in the solar corona cannot currently be measured, for events that are also seen at lower frequencies, the *in situ* measurements of the beam-induced electric field from PSP and SolO can be analyzed to see how they change as a function of distance from the Sun. Combining with numerical simulations, the measurements could be used to back-project the beam-induced electric field and infer what was happening in the solar corona, and then compared with the type III imaging spectroscopy of type IIIb striae bursts.

Many of the studies above use a 1D approximation for the propagation of electrons along magnetic field lines. Whilst this simplifies the models and is grounded by observations of electrons with small pitch angles at 1 AU, it is still a major simplification. Recent efforts have been undertaken (Ziebell et al., 2014, 2015, 2016; Tigik et al., 2016) to model the plasma emission process in two velocity dimensions for a single point in space, taking into account all the steps involved in the plasma emission process. In the simulations by Ziebell et al. (2015), fundamental emission was generated by Langmuir waves both with ion-sound waves and by scattering. These processes dominated initially, whilst over time the harmonic emission overtook the fundamental. Taking into account collisions, Tigik et al. (2016) found that a wider plateau was formed in the distribution function and increased the tendency to isotropization.

The bulk of the results documented above use the weak turbulence approximation to simulate electron beam dynamics. However, there has been significant effort to simulate the beam-plasma interaction and the subsequent generation of radio waves using the Zakharov equations (e.g., Zaslavsky et al., 2010; Krafft et al., 2015; Volokitin and Krafft, 2018; Krafft and Volokitin, 2020). This approach is not self-consistent with the electron beam exciter but has produced comparable type III fluxes using parameters in the solar wind. The plasma emission process has also been reproduced using particle-in-cell (PIC) codes (e.g., Thurgood and Tsiklauri, 2015; Henri et al., 2019). Both studies were able to produce electrostatic and electromagnetic waves through plasma instabilities. Henri et al. (2019) found weaker electron beams produced radio waves that were more forward directed at the source, whilst larger beam densities widened the Langmuir wave spectrum, leading to a larger available angular spread of radio emission. The validity of the weak turbulence approximation has been analyzed using PIC code both for 1D (Ratcliffe et al., 2014a) and 2D (Lee et al., 2019) weak turbulence codes. Both studies found a plateau forming in the beam region within comparable timescales, although the weak turbulence code developed a extended tail along the forward direction not seen in the PIC code (Lee et al., 2019). The Langmuir wave spectrum was similar unless the ion temperature was increased to the electron temperature or hotter (Ratcliffe et al., 2014a). In terms of radio emission Lee et al. (2019) found a good agreement, especially for larger beam velocities but it required a high number of particles per cell in the PIC codes.

5. CONCLUSION

5.1. Future Observing

The future is bright for type III imaging spectroscopy. Not only are we now taking advantage of the capability of instruments like the VLA, MWA, and LOFAR but there are numerous new observational platforms that have either recently come online or will be operational very soon.

Starting at the ground, the first notable platform is the Mingantu Ulrawide Spectral Radioheliograph (MUSER, Yan et al., 2009, 2016), based in Inner Mongolia, China. Most relevant for type III bursts is MUSER I that will operate between 0.4 and 2 GHz. MUSER is a solar dedicated radio telescope unlike the astrophysical telescopes like LOFAR which means that it has a much higher chance of catching transient type III bursts when they occur and MUSER I has already observed a radio burst (Yan et al., 2016) around 1 GHz. MUSER I is poised to provide the community with a plethora of type III imaging spectroscopy data that will significantly help to understand the physics behind these radio bursts.

Another platform that will come online soon is the Square Kilometer Array (SKA, see Nindos et al., 2019, for a solar physics overview). Both the SKA1-LOW, observing between 50 and 350 MHz and the SKA1-MID, observing from 0.35 to 15.3 GHz will be relevant for observing type III bursts from different regions within the solar corona. Commissioning of SKA1 is expected to start in 2024. With SKA1-LOW being based in Western Australia it should hopefully be available to pair with

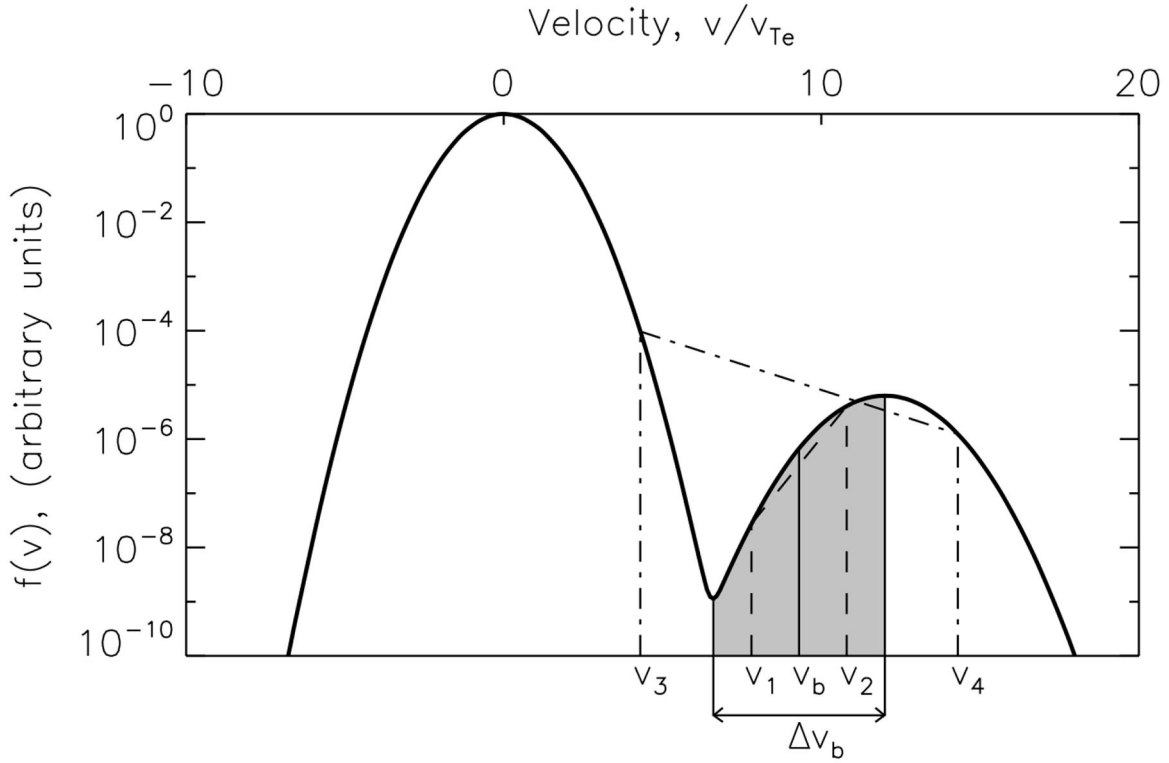

FIGURE 10 | An example of weakening and possible suppression of the beam instability by resonance broadening. The shaded gray corresponds to a positive slope from resonance width $\Delta v = v2 - v1$. If the resonance width is increased to $\Delta v = v4 - v3$ the slope becomes negative and the Langmuir wave instability is suppressed From Bian et al. (2014).

MUSER I for complimentary observations of type III imaging spectroscopy from the low to high corona. Similarly, SKA1-MID is based in the Karoo desert of South Africa and should be able to take complimentary type III observations with LOFAR. Both the sensitivity and angular resolution of SKA will be much better than what has come before and promises to provide major advances on key type III science questions.

Going into space and the launch of Parker Solar Probe and Solar Orbiter has far-reaching implications for type III theory. Both spacecraft are spectroscopically observing type III bursts from 20 MHz and below from changing vantage points around the solar system. They are also taking *in situ* particle measurements at different distances from the Sun that will allow analysis of high energy electrons, solar wind particles and plasma waves. ESAs BepiColombo should provide a third point in the inner solar wind for radio wave and *in situ* plasma measurements when the Mio spacecraft starts science operations.

On the horizon are two NASA space missions that are attempting to break the 10 MHz frequency barrier for type III imaging spectroscopy. CURIE (Sundkvist et al., 2016) is a two-cubesat mission that will formation fly in low-Earth orbit with a few km separation. It will take imaging spectroscopy observations of the Sun from 40 to 0.1 MHz. SunRISE (Alibay et al., 2017) is a six-cubesat mission that will fly slightly above the Geostationary Equatorial Orbit in a passive formation that will allow the formation of an interferometer whilst minimizing operations complexity. SunRISE will take imaging spectroscopy observations of the Sun from 25 to 0.1 MHz. Both missions intend to observe type III bursts. A further mission concept study NOIRE (Cecconi et al., 2018) is being developed in Europe to launch a swarm of nanosatellites for imaging low frequency radio emission targetted toward the astronomical dark ages and planetary radio emissions. Such a venture would certainly be of use for observing type III bursts.

5.2. Outstanding Science Questions

Our new age of type III imaging spectroscopy has already brought us many new observational discoveries. The high frequency VLA observations are showing us the signatures of energetic particles very close to their acceleration site. Low frequency MWA and LOFAR observations are showing us how the particles are escaping the Sun and what the structure of the upper corona is like. However, there are still many challenging science questions that require detailed answers, which type III imaging spectroscopy can help contribute.

Where are the locations of electron acceleration sites and what physical processes accelerate electrons? Electron acceleration properties are generally assumed in type III studies and not self-consistently generated by an acceleration mechanism. There are a few works done in the context of 3D magnetic reconnection,

based on particle-in-cell codes, that focus on the physical mechanisms behind electron acceleration at reconnection sites (e.g., Markidis et al., 2013). Type IIIs regularly appear in groups which is not traditionally simulated, nor the duration of these groups fully understood. As indicated in section 2, we have started to address these issues with the help of high frequency type IIIs (e.g., Chen B. et al., 2018) and combined analysis with other wavelengths (e.g., Reid et al., 2014) but there still remains significant uncertainty on the spatialy characteristics of acceleration sites. For example, are all electron beams that make type III groups accelerated in a compact volume, or spread throughout a larger volume around 1,000 Mm^3? Do they change location in time? Is there size connected with type III burst properties? Type III analysis has provided observational constraints on accelerated electron beam parameters such as characteristic times and electron energies. Electron acceleration can certainly occur at a range of heights in the solar corona, with high frequency type III bursts starting low in the corona and type III noise storm sources probably being accelerated much higher in the corona. Does the same acceleration mechanism produce electron beams that form type III bursts at 10 and 200 Mm? Type III imaging spectroscopy will help by catching the location of the type III starting frequency and the subsequent evolution of position in time. It will also allow the localization of acceleration through the imaging of bi-directional type III bursts.

What physical processes are responsible for the transport of accelerated electrons? Whilst we have a general understanding of how wave-particle interactions affect the propagation of electrons through the solar atmosphere (e.g., Reid and Kontar, 2018b), there are still unknowns about how the 3D phase space properties of these particle beams evolves with time as they propagate away from the acceleration region. Recent numerical studies are not taking into account modeling large spatial scales in three dimensions and we risk missing many details (Harding et al., 2020), in a similar way that 3D magnetic reconnection is different from 2D. Type III imaging spectroscopy has been helping to answer this question about electron transport by analyzing the spatial evolution of different frequencies with time (e.g., Zhang et al., 2019). Such studies can confirm and constrain numerical simulations, with the imaging spectroscopy providing more detailed diagnostics about the spatial location of electron beams with time as they travel out through the solar corona. These studies are only just beginning and there is still much to be analyzed both statistically and using single event studies. The combination of electron beam diagnostics from type III imaging spectroscopy studies with *in situ* measurements from PSP and SolO should provide significant clarity on how electron beams evolve through the solar system and help disentangle transport and acceleration effects.

How does the type III emission mechanism influence observed properties? There are still many open questions about how Langmuir waves undergo wave-wave coupling to produce radio waves, and when fundamental emission dominates over harmonic emission. Analysis of type III fine structures should help answer this question and is an area of type III study that is significantly enhanced by new imaging spectroscopy. There has already been notable advances in the evolution of type III striae (e.g., Sharykin et al., 2018) that are providing us with new insight on small-scale dynamics. Imaging spectroscopy analysis of the location and spatial extent between fundamental and harmonic emission (e.g., Kontar et al., 2017) have been providing observational constraints than can help develop theoretical models (e.g., Li and Cairns, 2013; Ratcliffe et al., 2014b; Krasnoselskikh et al., 2019) that are describing these non-linear processes. Future imaging spectroscopy should be used to further analyse fundamental and harmonic image properties as a function of frequency as their differences diagnose how the distinct wave-wave processes modify the radio burst properties, provided light transport effects are accounted for.

What properties are intrinsic to the type III source and what are caused by light transport effects? There has been a reinvigorated effort recently to understand and model how radio waves travels from the solar corona to Earth. It is apparent that the scattering of waves off density fluctuations significantly affect what we observe at Earth, in particular for low frequency fundamental emission. If we want to fully unlock the benefits of type III imaging spectroscopy we must be able to untangle these effects and significant efforts are already under way (e.g., Kontar et al., 2019). The variation in source parameters as a function of frequency can be used to constrain and improve the ray-tracing models that are being used to describe light transport. However, as with many complex processes, knowledge of light scattering can, and is, providing new diagnostics of the turbulent nature of the solar corona.

What is the structure of the flaring solar corona? Type III studies have been approximating the density structure of the solar corona for some time and directly producing a number of density models (e.g., Cairns et al., 2009; Saint-Hilaire et al., 2013). As discussed in section 3, the validity of these and other density models is something that is being tested by current observations using type IIIs for magnetic loops that extend into the solar wind (e.g., McCauley et al., 2018) and using U-burst observations for magnetic loops confined to the corona (e.g., Reid and Kontar, 2017a). Imaging radio sources at coronal heights around 1 solar radii and above will help to understand the structure of the magnetic field as it evolves from the corona to the solar wind. Despite this, our estimates of source heights are still uncertain and we are yet to have a good handle on source projection effects, something that is likely to ellude us without some future mission that can perform radio interferometric imaging from a spacecarft not near the Earth.

To help answer the above science questions, we must overcome a number of logistical challenges we face in the coming years. The advent of high volume data sets will bring with it significant challenges to store and analyse such large amounts of data. The astrophysical telescopes that are providing some of the new high resolution type III imaging spectroscopy are only observing the Sun sporadically. Whilst there has been numerous successful observing campaigns already on all these telescopes, the limited observing time will miss most type III radio bursts and highlights the benefits of solar monitoring for capturing type

III burst activity from the Sun. Additionally the solar coverage in radio frequencies is not uniform around the globe and we risk missing key information when the Sun provides us with interesting type III events.

What is certain is that our new radio interferometer tools are allowing type III imaging spectroscopy with much higher spatial, spectral and temporal resolution that ever before. Not only are we going to further our understanding of the science questions described above, this new leap in solar radio observing is likely to bring about new discoveries that we have not even thought of yet. Furthering our quest to enable type III bursts as remote sensors of astrophysical plasma.

AUTHOR CONTRIBUTIONS

HR contributed all of the text to the document.

ACKNOWLEDGMENTS

I want to acknowledge all the authors that produced the high-quality research which was reviewed in this article. I also want to acknowledge the support that goes into running the many ground-based radio observatories that provided the data for these studies. Finally I want to acknowledge the helpful and interesting discussions about type III bursts with by colleagues over the years.

REFERENCES

Alibay, F., Kasper, J. C., Lazio, T. J. W., and Neilsen, T. (2017). "Sun radio interferometer space experiment (SunRISE): tracking particle acceleration and transport in the inner heliosphere," in *2017 IEEE Aerospace Conference* (Big Sky, MT), 1–15. doi: 10.1109/AERO.2017.7943789

Allen, C. W. (1947). Interpretation of electron densities from corona brightness. *Mnthly Notices R. Astron. Soc.* 107:426. doi: 10.1093/mnras/107.5-6.426

Alvarez, H., and Haddock, F. T. (1973). Solar wind density model from km-wave type III bursts. *Sol. Phys.* 29, 197–209. doi: 10.1007/BF00153449

Arzner, K., and Benz, A. O. (2005). Temporal correlation of hard x-rays and meter/decimeter radio structures in solar flares. *Sol. Phys.* 231, 117–141. doi: 10.1007/s11207-005-1590-8

Arzner, K., and Magun, A. (1999). Radiowave propagation in a statistically inhomogeneous plasma. *Astron. Astrophys.* 351, 1165–1189.

Aschwanden, M. J., and Benz, A. O. (1997). Electron densities in solar flare loops, chromospheric evaporation upflows, and acceleration sites. *Astrophys. J.* 480, 825–839. doi: 10.1086/303995

Aschwanden, M. J., Montello, M. L., Dennis, B. R., and Benz, A. O. (1995). Sequences of correlated hard X-ray and type III bursts during solar flares. *Astrophys. J.* 440, 394–406. doi: 10.1086/175281

Aubier, M., and Boischot, A. (1972). Exciter of type III bursts and coronal temperature. *Astron. Astrophys.* 19:343–353.

Bain, H. M., and Fletcher, L. (2009). Hard X-ray emission from a flare-related jet. *Astron. Astrophys.* 508, 1443–1452. doi: 10.1051/0004-6361/200911876

Barrow, C. H., and Achong, A. (1975). Solar type III burst profiles at decametre-wave frequencies. I - Observations. II - Exciter. *Sol. Phys.* 45, 459–465. doi: 10.1007/BF00158462

Bastian, T. S. (1990). Radio emission from flare stars. *Sol. Phys.* 130, 265–294. doi: 10.1007/BF00156794

Bian, N. H., Emslie, A. G., and Kontar, E. P. (2019). A Fokker-Planck framework for studying the diffusion of radio burst waves in the solar corona. *Astrophys. J.* 873:33. doi: 10.3847/1538-4357/ab0411

Bian, N. H., Kontar, E. P., and Ratcliffe, H. (2014). Resonance broadening due to particle scattering and mode coupling in the quasi-linear relaxation of electron beams. *J. Geophys. Res.* 119, 4239–4255. doi: 10.1002/2013JA019664

Bisoi, S. K., Sawant, H. S., Janardhan, P., Yan, Y., Chen, L., Awasthi, A. K., et al. (2018). Decimetric emission 500 arcsecs away from a flaring site: possible scenarios from GMRT solar radio observations. *Astrophys. J.* 862:65. doi: 10.3847/1538-4357/aacd07

Cairns, I. H., Lobzin, V. V., Donea, A., Tingay, S. J., McCauley, P. I., Oberoi, D., et al. (2018). Low altitude solar magnetic reconnection, type III solar radio bursts, and x-ray emissions. *Sci. Rep.* 8:1676. doi: 10.1038/s41598-018-19195-3

Cairns, I. H., Lobzin, V. V., Warmuth, A., Li, B., Robinson, P. A., and Mann, G. (2009). Direct radio probing and interpretation of the sun's plasma density profile. *Astrophys. J. Lett.* 706, L265–L269. doi: 10.1088/0004-637X/706/2/L265

Carley, E. P., Vilmer, N., and Gallagher, P. T. (2016). Radio diagnostics of electron acceleration sites during the eruption of a flux rope in the solar corona. *Astrophys. J.* 833:87. doi: 10.3847/1538-4357/833/1/87

Cecconi, B., Dekkali, M., Briand, C., Segret, B., Girard, J. N., Laurens, A., et al. (2018). "NOIRE study report: towards a low frequency radio interferometer in space," in *2018 IEEE Aerospace Conference* (Big Sky, MT), 1–19. doi: 10.1109/AERO.2018.8396742

Chen, B., Bastian, T. S., White, S. M., Gary, D. E., Perley, R., Rupen, M., et al. (2013). Tracing electron beams in the sun's corona with radio dynamic imaging spectroscopy. *Astrophys. J. Lett.* 763:L21. doi: 10.1088/2041-8205/763/1/L21

Chen, B., Yu, S., Battaglia, M., Farid, S., Savcheva, A., Reeves, K. K., et al. (2018). Magnetic reconnection null points as the origin of semirelativistic electron beams in a solar jet. *Astrophys. J.* 866:62. doi: 10.3847/1538-4357/aadb89

Chen, C. H. K. (2016). Recent progress in astrophysical plasma turbulence from solar wind observations. *J. Plasma Phys.* 82:535820602. doi: 10.1017/S0022377816001124

Chen, X., Kontar, E. P., Yu, S., Yan, Y., Huang, J., and Tan, B. (2018). Fine structures of solar radio type III bursts and their possible relationship with coronal density turbulence. *Astrophys. J.* 856:73. doi: 10.3847/1538-4357/aaa9bf

Chrysaphi, N., Kontar, E. P., Holman, G. D., and Temmer, M. (2018). CME-driven shock and type II solar radio burst band splitting. *Astrophys. J.* 868:79. doi: 10.3847/1538-4357/aae9e5

de La Noe, J., and Boischot, A. (1972). The type III B burst. *Astron. Astrophys.* , 20:55.

Drake, J. F., Swisdak, M., Che, H., and Shay, M. A. (2006). Electron acceleration from contracting magnetic islands during reconnection. *Nature* 443, 553–556. doi: 10.1038/nature05116

Dulk, G. A. (1985). Radio emission from the sun and stars. *Annu. Rev. Astron. Astrophys.* 23, 169–224. doi: 10.1146/annurev.aa.23.090185.001125

Ellingson, S. W., Clarke, T. E., Cohen, A., Craig, J., Kassim, N. E., Pihlstrom, Y., et al. (2009). The long wavelength array. *IEEE Proc.* 97, 1421–1430. doi: 10.1109/JPROC.2009.2015683

Feng, S. W., Chen, Y., Song, H. Q., Wang, B., and Kong, X. L. (2016). An imaging study of a complex solar coronal radio eruption. *Astrophys. J. Lett.* 827:L9. doi: 10.3847/2041-8205/827/1/L9

Fox, N. J., Velli, M. C., Bale, S. D., Decker, R., Driesman, A., Howard, R. A., et al. (2016). The solar probe plus mission: humanity's first visit to our star. *Space Sci. Rev.* 204, 7–48. doi: 10.1007/s11214-015-0211-6

Gary, D. E., Bastian, T. S., Chen, B., Fleishman, G. D., and Glesener, L. (2018). "Radio observations of solar flares," in *Astronomical Society of the Pacific Conference Series*, 99.

Gibson, S., Kucera, T., White, S., Dove, J., Fan, Y., Forland, B., et al. (2016). FORWARD: a toolset for multiwavelength coronal magnetometry. *Front. Astron. Space Sci.* 3:8. doi: 10.3389/fspas.2016.00008

Gordovskyy, M., Kontar, E., Browning, P., and Kuznetsov, A. (2019). Frequency-distance structure of solar radio sources observed by LOFAR. *Astrophys. J.* 873:48. doi: 10.3847/1538-4357/ab03d8

Hamilton, R. J., Petrosian, V., and Benz, A. O. (1990). Statistical study of the correlation of hard X-ray and type III radio bursts in solar flares. *Astrophys. J.* 358, 644–653. doi: 10.1086/169017

Harding, J. C., Cairns, I. H., and Melrose, D. B. (2020). Electron-Langmuir wave resonance in three dimensions. *Phys. Plasmas* 27:020702. doi: 10.1063/1.5139068

Henri, P., Sgattoni, A., Briand, C., Amiranoff, F., and Riconda, C. (2019). Electromagnetic simulations of solar radio emissions. *J. Geophys. Res.* 124, 1475–1490. doi: 10.1029/2018JA025707

Holman, G. D., Aschwanden, M. J., Aurass, H., Battaglia, M., Grigis, P. C., Kontar, E. P., et al. (2011). Implications of x-ray observations for electron acceleration and propagation in solar flares. *Space Sci. Rev.* 159, 107–166. doi: 10.1007/978-1-4614-3073-5_4

Isliker, H., and Benz, A. O. (1994). Catalogue of 1-3 GHz solar flare radio emission. *Astron. Astrophys. Suppl. Ser.* 104, 145–160.

Kane, S. R. (1972). Evidence for a common origin of the electrons responsible for the impulsive x-ray and type III radio bursts. *Sol. Phys.* 27, 174–181. doi: 10.1007/BF00151781

Kane, S. R., Benz, A. O., and Treumann, R. A. (1982). Electron acceleration in impulsive solar flares. *Astrophys. J.* 263, 423–432. doi: 10.1086/160514

Kerdraon, A., and Delouis, J.-M. (1997). "The Nançay radioheliograph," in *Coronal Physics from Radio and Space Observations*, ed G. Trottet (Berlin: Springer Verlag), 192. doi: 10.1007/BFb0106458

Kishore, P., Kathiravan, C., Ramesh, R., Rajalingam, M., and Barve, I. V. (2014). Gauribidanur low-frequency solar spectrograph. *Sol. Phys.* 289, 3995–4005. doi: 10.1007/s11207-014-0539-1

Klassen, A., Gómez-Herrero, R., and Heber, B. (2011). Electron spikes, type III radio bursts and EUV jets on 22 February 2010. *Sol. Phys.* 273, 413–419. doi: 10.1007/s11207-011-9735-4

Kolotkov, D. Y., Nakariakov, V. M., and Kontar, E. P. (2018). Origin of the modulation of the radio emission from the solar corona by a fast magnetoacoustic wave. *Astrophys. J.* 861:33. doi: 10.3847/1538-4357/aac77e

Kong, X., Chen, Y., Feng, S., Du, G., Li, C., Koval, A., et al. (2016). Observation of a metric type N solar radio burst. *Astrophys. J.* 830:37. doi: 10.3847/0004-637X/830/1/37

Konovalenko, A., Sodin, L., Zakharenko, V., Zarka, P., Ulyanov, O., Sidorchuk, M., et al. (2016). The modern radio astronomy network in Ukraine: UTR-2, URAN and GURT. *Exp. Astron.* 42, 11–48. doi: 10.1007/s10686-016-9498-x

Kontar, E. P. (2001). Dynamics of electron beams in the inhomogeneous solar corona plasma. *Sol. Phys.* 202, 131–149. doi: 10.1023/A:1011894830942

Kontar, E. P., Brown, J. C., Emslie, A. G., Hajdas, W., Holman, G. D., Hurford, G. J., et al. (2011). Deducing electron properties from hard x-ray observations. *Space Sci. Rev.* 159, 301–355. doi: 10.1007/978-1-4614-3073-5_8

Kontar, E. P., Chen, X., Chrysaphi, N., Jeffrey, N. L. S., Emslie, A. G., Krupar, V., et al. (2019). Anisotropic radio-wave scattering and the interpretation of solar radio emission observations. *Astrophys. J.* 884:122. doi: 10.3847/1538-4357/ab40bb

Kontar', E. P., Lapshin, V. I., and Mel'Nik, V. N. (1998). Numerical and analytical study of the propagation of a monoenergetic electron beam in a plasma. *Plasma Phys. Rep.* 24, 772–776.

Kontar, E. P., Yu, S., Kuznetsov, A. A., Emslie, A. G., Alcock, B., Jeffrey, N. L. S., et al. (2017). Imaging spectroscopy of solar radio burst fine structures. *Nat. Commun.* 8:1515. doi: 10.1038/s41467-017-01307-8

Krafft, C., and Volokitin, A. S. (2020). Electromagnetic radiation from upper-hybrid wave turbulence in inhomogeneous solar plasmas. *Plasma Phys. Controlled Fusion* 62:024007. doi: 10.1088/1361-6587/ab569d

Krafft, C., Volokitin, A. S., and Krasnoselskikh, V. V. (2015). Langmuir wave decay in inhomogeneous solar wind plasmas: simulation results. *Astrophys. J.* 809:176. doi: 10.1088/0004-637X/809/2/176

Krasnoselskikh, V., Voshchepynets, A., and Maksimovic, M. (2019). On the efficiency of the linear-mode conversion for generation of solar type III radio bursts. *Astrophys. J.* 879:51. doi: 10.3847/1538-4357/ab22bf

Krucker, S., Kontar, E. P., Christe, S., Glesener, L., and Lin, R. P. (2011). Electron acceleration associated with solar jets. *Astrophys. J.* 742:82. doi: 10.1088/0004-637X/742/2/82

Krupar, V., Maksimovic, M., Kontar, E. P., Zaslavsky, A., Santolik, O., Soucek, J., et al. (2018). Interplanetary type III bursts and electron density fluctuations in the solar wind. *Astrophys. J.* 857:82. doi: 10.3847/1538-4357/aab60f

Krupar, V., Szabo, A., Maksimovic, M., Kruparova, O., Kontar, E. P., Balmaceda, L. A., et al. (2020). Density fluctuations in the solar wind based on type III radio bursts observed by parker solar probe. *Astrophys. J. Suppl. Ser.* 246:57. doi: 10.3847/1538-4365/ab65bd

Kundu, M. R., Gergely, T. E., Turner, P. J., and Howard, R. A. (1983). Direct evidence of type III electron streams propagating in coronal streamers. *Astrophys. J. Lett.* 269, L67–L71. doi: 10.1086/184057

Leblanc, Y., and de La Noe, J. (1977). Solar radio type III bursts and coronal density structures. *Sol. Phys.* 52, 133–139. doi: 10.1007/BF00935796

Lecacheux, A. (2000). *The Nançay Decameter Array: A Useful Step Towards Giant, New Generation Radio Telescopes for Long Wavelength Radio Astronomy*. Washington, DC" American Geophysical Union Geophysical Monograph Series. doi: 10.1029/GM119p0321

Lee, S.-Y., Ziebell, L. F., Yoon, P. H., Gaelzer, R., and Lee, E. S. (2019). Particle-in-cell and weak turbulence simulations of plasma emission. *Astrophys. J.* 871:74. doi: 10.3847/1538-4357/aaf476

Li, B., and Cairns, I. H. (2013). Type III bursts produced by power law injected electrons in Maxwellian background coronal plasmas. *J. Geophys. Res.* 118, 4748–4759. doi: 10.1002/jgra.50445

Li, B., and Cairns, I. H. (2014). Fundamental emission of type III bursts produced in non-Maxwellian coronal plasmas with kappa-distributed background particles. *Sol. Phys.* 289, 951–976. doi: 10.1007/s11207-013-0375-8

Li, B., Cairns, I. H., and Robinson, P. A. (2012). Frequency fine structures of type III bursts due to localized medium-scale density structures along paths of type III beams. *Sol. Phys.* 279, 173–196. doi: 10.1007/s11207-012-0001-1

Li, B., Cairns, I. H., Yan, Y. H., and Robinson, P. A. (2011). Decimetric type III bursts: generation and propagation. *Astrophys. J. Lett.* 738:L9. doi: 10.1088/2041-8205/738/1/L9

Lionello, R., Linker, J. A., and Mikić, Z. (2009). Multispectral emission of the sun during the first whole sun month: magnetohydrodynamic simulations. *Astrophys. J.* 690, 902–912. doi: 10.1088/0004-637X/690/1/902

Loi, S. T., Cairns, I. H., and Li, B. (2014). Production of fine structures in type III solar radio bursts due to turbulent density profiles. *Astrophys. J.* 790:67. doi: 10.1088/0004-637X/790/1/67

Lonsdale, C. J., Cappallo, R. J., Morales, M. F., Briggs, F. H., Benkevitch, L., Bowman, J. D., et al. (2009). The murchison widefield array: design overview. *IEEE Proc.* 97, 1497–1506. doi: 10.1109/JPROC.2009.2017564

Magelssen, G. R., and Smith, D. F. (1977). Nonrelativistic electron stream propagation in the solar atmosphere and type III radio bursts. *Sol. Phys.* 55, 211–240. doi: 10.1007/BF00150886

Mann, G., Breitling, F., Vocks, C., Aurass, H., Steinmetz, M., Strassmeier, K. G., et al. (2018). Tracking of an electron beam through the solar corona with LOFAR. *Astron. Astrophys.* 611:A57. doi: 10.1051/0004-6361/201629017

Markidis, S., Henri, P., Lapenta, G., Divin, A., Goldman, M., Newman, D., et al. (2013). Kinetic simulations of plasmoid chain dynamics. *Phys. Plasmas* 20:082105. doi: 10.1063/1.4817286

Maxwell, A., and Swarup, G. (1958). A new spectral characteristic in solar radio emission. *Nature* 181, 36–38. doi: 10.1038/181036a0

McCauley, P. I., Cairns, I. H., and Morgan, J. (2018). Densities probed by coronal type III radio burst imaging. *Sol. Phys.* 293:132. doi: 10.1007/s11207-018-1353-y

McCauley, P. I., Cairns, I. H., Morgan, J., Gibson, S. E., Harding, J. C., Lonsdale, C., et al. (2017). Type III solar radio burst source region splitting due to a quasi-separatrix layer. *Astrophys. J.* 851:151. doi: 10.3847/1538-4357/aa9cee

McLean, D. J., and Labrum, N. R. (1985). *Solar Radiophysics: Studies of Emission from the Sun at Metre Wavelengths*. Cambridge University Press.

Mel'Nik, V. N. (1995). "Gas-dynamic" expansion of a fast-electron flux in a plasma. *Plasma Phys. Rep.* 21, 89–91.

Mel'Nik, V. N., Konovalenko, A. A., Rucker, H. O., Boiko, A. I., Dorovskyy, V. V., Abranin, E. P., et al. (2011). Observations of powerful type III bursts in the frequency range 10-30 MHz. *Sol. Phys.* 269, 335–350. doi: 10.1007/s11207-010-9703-4

Mel'Nik, V. N., Lapshin, V., and Kontar, E. (1999). Propagation of a monoenergetic electron beam in the solar corona. *Sol. Phys.* 184, 353–362. doi: 10.1023/A:1005191910544

Mohan, A., Mondal, S., Oberoi, D., and Lonsdale, C. J. (2019). Evidence for super-Alfvénic oscillations in solar type III radio burst sources. *Astrophys. J.* 875:98. doi: 10.3847/1538-4357/ab0ae5

Mohan, A., and Oberoi, D. (2017). 4D data cubes from radio-interferometric spectroscopic snapshot imaging. *Sol. Phys.* 292:168. doi: 10.1007/s11207-017-1193-1

Morosan, D. E., and Gallagher, P. T. (2017). "Characteristics of type III radio bursts and solar S bursts," in *Planetary Radio Emissions VIII*, eds G. Fischer, G. Mann,

M. Panchenko, and P. Zarka (Vienna: Austrian Academy of Sciences Press), 357–368.

Morosan, D. E., Gallagher, P. T., Fallows, R. A., Reid, H., Mann, G., Bisi, M. M., et al. (2017). The association of a J-burst with a solar jet. *Astron. Astrophys.* 606:A81. doi: 10.1051/0004-6361/201629996

Morosan, D. E., Gallagher, P. T., Zucca, P., Fallows, R., Carley, E. P., Mann, G., et al. (2014). LOFAR tied-array imaging of Type III solar radio bursts. *Astron. Astrophys.* 568:A67. doi: 10.1051/0004-6361/201423936

Morosan, D. E., Gallagher, P. T., Zucca, P., O'Flannagain, A., Fallows, R., Reid, H., et al. (2015). LOFAR tied-array imaging and spectroscopy of solar S bursts. *Astron. Astrophys.* 580:A65. doi: 10.1051/0004-6361/201526064

Mugundhan, V., Hariharan, K., and Ramesh, R. (2017). Solar type IIIb radio bursts as tracers for electron density fluctuations in the corona. *Sol. Phys.* 292:155. doi: 10.1007/s11207-017-1181-5

Mulay, S. M., Sharma, R., Valori, G., Vásquez, A. M., Del Zanna, G., Mason, H., et al. (2019). Study of the spatial association between an active region jet and a nonthermal type III radio burst. *Astron. Astrophys.* 632:A108. doi: 10.1051/0004-6361/201936369

Müller, D., Marsden, R. G., St. Cyr, O. C., and Gilbert, H. R. (2013). Solar orbiter. Exploring the sun-heliosphere connection. *Sol. Phys.* 285, 25–70. doi: 10.1007/s11207-012-0085-7

Newkirk, G. Jr. (1961). The solar corona in active regions and the thermal origin of the slowly varying component of solar radio radiation. *Astrophys. J.* 133:983. doi: 10.1086/147104

Nindos, A., Kontar, E. P., and Oberoi, D. (2019). Solar physics with the square kilometre array. *Adv. Space Res.* 63, 1404–1424. doi: 10.1016/j.asr.2018.10.023

Payne-Scott, R., Yabsley, D. E., and Bolton, J. G. (1947). Relative times of arrival of bursts of solar noise on different radio frequencies. *Nature* 160, 256–257. doi: 10.1038/160256b0

Perley, R. A., Chandler, C. J., Butler, B. J., and Wrobel, J. M. (2011). The expanded very large array: a new telescope for new science. *Astrophys. J. Lett.* 739:L1. doi: 10.1088/2041-8205/739/1/L1

Pick, M., and Vilmer, N. (2008). Sixty-five years of solar radioastronomy: flares, coronal mass ejections and Sun Earth connection. *Astron. Astrophys. Rev.* 16, 1–153. doi: 10.1007/s00159-008-0013-x

Rahman, M. M., Cairns, I. H., and McCauley, P. I. (2020). Spectropolarimetric imaging of metric type III solar radio bursts. *Sol. Phys.* 295:51. doi: 10.1007/s11207-020-01616-0

Ratcliffe, H., Brady, C. S., Che Rozenan, M. B., and Nakariakov, V. M. (2014a). A comparison of weak-turbulence and particle-in-cell simulations of weak electron-beam plasma interaction. *Phys. Plasmas* 21:122104. doi: 10.1063/1.4904065

Ratcliffe, H., and Kontar, E. P. (2014). Plasma radio emission from inhomogeneous collisional plasma of a flaring loop. *Astron. Astrophys.* 562:A57. doi: 10.1051/0004-6361/201322263

Ratcliffe, H., Kontar, E. P., and Reid, H. A. S. (2014b). Large-scale simulations of solar type III radio bursts: flux density, drift rate, duration, and bandwidth. *Astron. Astrophys.* 572:A111. doi: 10.1051/0004-6361/201423731

Reid, H. A. S. (2016). *Solar Type III Bursts Observed with LOFAR*. URSI Asia-Pacific Radio Science Conference (URSI AP-RASC). doi: 10.1109/URSIAP-RASC.2016.7601384

Reid, H. A. S., and Kontar, E. P. (2010). Solar wind density turbulence and solar flare electron transport from the Sun to the Earth. *Astrophys. J.* 721, 864–874. doi: 10.1088/0004-637X/721/1/864

Reid, H. A. S., and Kontar, E. P. (2013). Evolution of the solar flare energetic electrons in the inhomogeneous inner heliosphere. *Sol. Phys.* 285, 217–232. doi: 10.1007/s11207-012-0013-x

Reid, H. A. S., and Kontar, E. P. (2015). Stopping frequency of type III solar radio bursts in expanding magnetic flux tubes. *Astron. Astrophys.* 577:A124. doi: 10.1051/0004-6361/201425309

Reid, H. A. S., and Kontar, E. P. (2017a). Imaging spectroscopy of type U and J solar radio bursts with LOFAR. *Astron. Astrophys.* 606:A141. doi: 10.1051/0004-6361/201730701

Reid, H. A. S., and Kontar, E. P. (2017b). Langmuir wave electric fields induced by electron beams in the heliosphere. *Astron. Astrophys.* 598:A44. doi: 10.1051/0004-6361/201629697

Reid, H. A. S., and Kontar, E. P. (2018a). Solar type III radio burst time characteristics at LOFAR frequencies and the implications for electron beam transport. *Astron. Astrophys.* 614:A69. doi: 10.1051/0004-6361/201732298

Reid, H. A. S., and Kontar, E. P. (2018b). Spatial expansion and speeds of type III electron beam sources in the solar corona. *Astrophys. J.* 867:158. doi: 10.3847/1538-4357/aae5d4

Reid, H. A. S., and Ratcliffe, H. (2014). A review of solar type III radio bursts. *Res. Astron. Astrophys.* 14, 773–804. doi: 10.1088/1674-4527/14/7/003

Reid, H. A. S., and Vilmer, N. (2017). Coronal type III radio bursts and their X-ray flare and interplanetary type III counterparts. *Astron. Astrophys.* 597:A77. doi: 10.1051/0004-6361/201527758

Reid, H. A. S., Vilmer, N., and Kontar, E. P. (2011). Characteristics of the flare acceleration region derived from simultaneous hard X-ray and radio observations. *Astron. Astrophys.* 529:A66. doi: 10.1051/0004-6361/201016181

Reid, H. A. S., Vilmer, N., and Kontar, E. P. (2014). The low-high-low trend of type III radio burst starting frequencies and solar flare hard X-rays. *Astron. Astrophys.* 567:A85. doi: 10.1051/0004-6361/201321973

Riddle, A. C. (1974). On the Determination of coronal temperature from the decay of type III radio bursts. *Sol. Phys.* 34, 181–184. doi: 10.1007/BF00149609

Robinson, R. D. (1983). Scattering of radio waves in the solar corona. *Proc. Astron. Soc. Austral.* 5, 208–211. doi: 10.1017/S132335800001688X

Roelof, E. C., and Pick, M. (1989). Type III radio bursts in a fibrous corona. *Astron. Astrophys.* 210, 417–424.

Saint-Hilaire, P., Vilmer, N., and Kerdraon, A. (2013). A decade of solar type III radio bursts observed by the Nançay radioheliograph 1998-2008. *Astrophys. J.* 762:60. doi: 10.1088/0004-637X/762/1/60

Saito, K., Poland, A. I., and Munro, R. H. (1977). A study of the background corona near solar minimum. *Sol. Phys.* 55, 121–134. doi: 10.1007/BF00150879

Schrijver, C. J., Sandman, A. W., Aschwanden, M. J., and De Rosa, M. L. (2004). The coronal heating mechanism as identified by full-sun visualizations. *Astrophys. J.* 615, 512–525. doi: 10.1086/424028

Sharykin, I. N., Kontar, E. P., and Kuznetsov, A. A. (2018). LOFAR observations of fine spectral structure dynamics in type IIIb radio bursts. *Sol. Phys.* 293:115. doi: 10.1007/s11207-018-1333-2

Sittler, E. C. Jr., and Guhathakurta, M. (1999). Semiempirical two-dimensional magnetohydrodynamic model of the solar corona and interplanetary medium. *Astrophys. J.* 523, 812–826. doi: 10.1086/307742

Stanislavsky, A. A., Konovalenko, A. A., Abranin, E. P., Dorovskyy, V. V., Lecacheux, A., Rucker, H. O., et al. (2018). Revisiting the frequency drift rates of decameter type III solar bursts observed in July - August 2002. *Sol. Phys.* 293:152. doi: 10.1007/s11207-018-1374-6

Stappers, B. W., Hessels, J. W. T., Alexov, A., Anderson, K., Coenen, T., Hassall, T., et al. (2011). Observing pulsars and fast transients with LOFAR. *Astron. Astrophys.* 530:A80. doi: 10.1051/0004-6361/201116681

Steinberg, J. L., Aubier-Giraud, M., Leblanc, Y., and Boischot, A. (1971). Coronal scattering, absorption and refraction of solar radiobursts. *Astron. Astrophys.* 10:362.

Sturrock, P. A. (1964). Type III solar radio bursts. *NASA Spcl Publ.* 50:357.

Sundkvist, D. J., Saint-Hilaire, P., Bain, H. M., Bale, S. D., Bonnell, J. W., Hurford, G. J., et al. (2016). "CURIE: cubesat radio interferometry experiment," in *AGU Fall Meeting Abstracts*.

Suzuki, S., and Dulk, G. A. (1985). *Bursts of Type III and Type V*. Cambridge University Press.

Swarup, G., Ananthakrishnan, S., Kapahi, V. K., Rao, A. P., Subrahmanya, C. R., and Kulkarni, V. K. (1991). The giant metre-wave radio telescope. *Curr. Sci.* 60:95.

Takakura, T., and Shibahashi, H. (1976). Dynamics of a cloud of fast electrons travelling through the plasma. *Sol. Phys.* 46, 323–346. doi: 10.1007/BF00149860

Takakura, T., and Yousef, S. (1975). Type IIIb radio bursts - 80 MHz source position and theoretical model. *Sol. Phys.* 40, 421–438. doi: 10.1007/BF00162389

Tan, B., Mészárosová, H., Karlický, M., Huang, G., and Tan, C. (2016). Microwave type III pair bursts in solar flares. *Astrophys. J.* 819:42. doi: 10.3847/0004-637X/819/1/42

Tan, B.-L., Karlický, M., Mészárosová, H., and Huang, G.-L. (2016b). Diagnosing physical conditions near the flare energy-release sites from

observations of solar microwave type III bursts. *Res. Astron. Astrophys.* 16:82. doi: 10.1088/1674-4527/16/5/082

Tan, B.-L., Karlický, M., Mészárosová, H., Kashapova, L., Huang, J., Yan, Y., et al. (2016a). Diagnosing the source region of a solar burst on 26 September 2011 by using microwave type-III pairs. *Sol. Phys.* 291, 2407–2418. doi: 10.1007/s11207-016-0986-y

Thejappa, G., and MacDowall, R. J. (2008). Effects of scattering on radio emission from the quiet sun at low frequencies. *Astrophys. J.* 676, 1338–1345. doi: 10.1086/528835

Thurgood, J. O., and Tsiklauri, D. (2015). Self-consistent particle-in-cell simulations of fundamental and harmonic plasma radio emission mechanisms. *Astron. Astrophys.* 584:A83. doi: 10.1051/0004-6361/201527079

Tigik, S. F., Ziebell, L. F., Yoon, P. H., and Kontar, E. P. (2016). Two-dimensional time evolution of beam-plasma instability in the presence of binary collisions. *Astron. Astrophys.* 586:A19. doi: 10.1051/0004-6361/201527271

Trottet, G., Pick, M., House, L., Illing, R., Sawyer, C., and Wagner, W. (1982). An association between coronal structures and type III burst sources. *Astron. Astrophys.* 111, 306–311.

Tun Beltran, S. D., Cutchin, S., and White, S. (2015). A new look at type-III bursts and their use as coronal diagnostics. *Sol. Phys.* 290, 2423–2437. doi: 10.1007/s11207-015-0760-6

van Haarlem, M. P., Wise, M. W., Gunst, A. W., Heald, G., McKean, J. P., Hessels, J. W. T., et al. (2013). LOFAR: The LOw-Frequency ARray. *Astron. Astrophys.* 556:A2. doi: 10.1051/0004-6361/201220873

Vidojevic, S., Zaslavsky, A., Maksimovic, M., Atanackovic, O., Hoang, S., and Drazic, M. (2012). Statistical analysis of Langmuir waves associated with type III radio bursts. *Publ. Astron. Soc. Rudjer Boskovic* 11, 343–349.

Volokitin, A. S., and Krafft, C. (2018). Electromagnetic wave emissions from a turbulent plasma with density fluctuations. *Astrophys. J.* 868:104. doi: 10.3847/1538-4357/aae7cc

Voshchepynets, A., and Krasnoselskikh, V. (2015). Probabilistic model of beam-plasma interaction in randomly inhomogeneous solar wind. *J. Geophys. Res.* 120:10. doi: 10.1002/2015JA021705

Voshchepynets, A., Krasnoselskikh, V., Artemyev, A., and Volokitin, A. (2015). Probabilistic model of beam-plasma interaction in randomly inhomogeneous plasma. *Astrophys. J.* , 807:38. doi: 10.1088/0004-637X/807/1/38

Voshchepynets, A., Volokitin, A., Krasnoselskikh, V., and Krafft, C. (2017). Statistics of electric fields amplitudes in Langmuir turbulence: a numerical simulation study. *J. Geophys. Res.* 122, 3915–3934. doi: 10.1002/2017JA023898

Wild, J. P., Sheridan, K. V., and Neylan, A. A. (1959). An investigation of the speed of the solar disturbances responsible for Type III radio bursts. *Austral. J. Phys.* 12:369. doi: 10.1071/PH590369

Yan, Y., Chen, L., and Yu, S. (2016). "First radio burst imaging observation from Mingantu Ultrawide Spectral Radioheliograph," in *Solar and Stellar Flares and their Effects on Planets*, eds A. G. Kosovichev, S. L. Hawley, and P. Heinzel (Cambridge University Press), 427–435. doi: 10.1017/S174392131600051X

Yan, Y., Zhang, J., Wang, W., Liu, F., Chen, Z., and Ji, G. (2009). The Chinese spectral radioheliograph-CSRH. *Earth Moon Planets* 104, 97–100. doi: 10.1007/s11038-008-9254-y

Zaitsev, V. V., Mityakov, N. A., and Rapoport, V. O. (1972). A dynamic theory of type III solar radio bursts. *Sol. Phys.* 24, 444–456. doi: 10.1007/BF00153387

Zaslavsky, A., Volokitin, A. S., Krasnoselskikh, V. V., Maksimovic, M., and Bale, S. D. (2010). Spatial localization of Langmuir waves generated from an electron beam propagating in an inhomogeneous plasma: applications to the solar wind. *J. Geophys. Res.* 115:A08103. doi: 10.1029/2009JA014996

Zhang, P., Yu, S., Kontar, E. P., and Wang, C. (2019). On the source position and duration of a solar type III radio burst observed by LOFAR. *Astrophys. J.* 885:140. doi: 10.3847/1538-4357/ab458f

Zhang, P. J., Wang, C. B., and Ye, L. (2018). A type III radio burst automatic analysis system and statistic results for a half solar cycle with Nançay Decameter Array data. *Astron. Astrophys.* 618:A165. doi: 10.1051/0004-6361/201833260

Zharkova, V. V., Arzner, K., Benz, A. O., Browning, P., Dauphin, C., Emslie, A. G., et al. (2011). Recent advances in understanding particle acceleration processes in solar flares. *Space Sci. Rev.* 159, 357–420. doi: 10.1007/s11214-011-9803-y

Zheleznyakov, V. V., and Zaitsev, V. V. (1970). Contribution to the theory of type III solar radio bursts. I. *Soviet Ast.* 14:47.

Ziebell, L. F., Petruzzellis, L. T., Yoon, P. H., Gaelzer, R., and Pavan, J. (2016). Plasma emission by counter-streaming electron beams. *Astrophys. J.* 818:61. doi: 10.3847/0004-637X/818/1/61

Ziebell, L. F., Yoon, P. H., Gaelzer, R., and Pavan, J. (2014). Plasma emission by weak turbulence processes. *Astrophys. J. Lett.* 795:L32. doi: 10.1088/2041-8205/795/2/L32

Ziebell, L. F., Yoon, P. H., Petruzzellis, L. T., Gaelzer, R., and Pavan, J. (2015). Plasma emission by nonlinear electromagnetic processes. *Astrophys. J.* 806:237. doi: 10.1088/0004-637X/806/2/237

Zucca, P., Carley, E. P., Bloomfield, D. S., and Gallagher, P. T. (2014). The formation heights of coronal shocks from 2D density and Alfvén speed maps. *Astron. Astrophys.* 564:A47. doi: 10.1051/0004-6361/201322650

Conflict of Interest: The author declares that the research was conducted in the absence of any commercial or financial relationships that could be construed as a potential conflict of interest.

frontiers in Astronomy and Space Sciences

REVIEW
published: 22 October 2020
doi: 10.3389/fspas.2020.574460

Structure of the Solar Atmosphere: A Radio Perspective

*Costas E. Alissandrakis**

Department of Physics, University of Ioannina, Ioannina, Greece

Solar radio emission has been providing information about the Sun for over half a century. In order to fully exploit this information, one needs to have a broader view of the solar atmosphere, which cannot be provided by radio observations alone. The purpose of this review is to present this background information, which is necessary to understand the physical processes that determine the solar radio emission and to link the radio domain with the rest of the electromagnetic spectrum. Both classic and modern results are presented in a concise manner. After a brief discussion of the solar interior, the basic physics of the solar atmosphere and some elements of radiative transfer are presented. Subsequently the atmospheric structure as a function of height is examined and one-dimensional models of the photosphere, the chromosphere, the transition region and the corona are presented and discussed. An introduction to basic magnetohydrodynamics precedes the discussion of the rich fine structure of the solar atmosphere as a 3D object. Active regions are briefly discussed in a separate section, and this is followed by a section on the problem of heating of the chromosphere and the corona. I finish with some thoughts on what to expect from the new instruments currently under development.

Keywords: sun, solar radio emission, photoshere, chromosphere, corona, quiet sun, active regions

OPEN ACCESS

Edited by:
Dale E. Gary,
New Jersey Institute of Technology, United States

Reviewed by:
Divya Oberoi,
Tata Institute of Fundamental Research, India
Ramesh Chandra,
Kumaun University, India
Eoin Carley,
Trinity College Dublin, Ireland

***Correspondence:**
Costas E. Alissandrakis
calissan@uoi.gr

Specialty section:
This article was submitted to Stellar and Solar Physics, a section of the journal Frontiers in Astronomy and Space Sciences

Received: *19 June 2020*
Accepted: *28 August 2020*
Published: *22 October 2020*

Citation:
Alissandrakis CE (2020) Structure of the Solar Atmosphere: A Radio Perspective. Front. Astron. Space Sci. 7:574460. doi: 10.3389/fspas.2020.574460

1. INTRODUCTION

By definition, the atmosphere of a star is the region from which photons can escape and reach the observer. Photons are not our only source of information for the Sun; important information can also be obtained from particles originating on the Sun and reaching the vicinity of the Earth, both in the form of the quasi-steady flow of the solar wind and during energetic events. The magnetic field carried by the solar wind plasma is also an important carrier of information. Last but not least, neutrinos and global oscillations have provided us with a wealth of information on the solar interior. Still, the bulk of what we know about the Sun comes from photons, thus in this review we will restrict ourselves to the results obtained from the analysis of the solar electromagnetic emission, in an attempt to compile a concise, but still comprehensive picture of the structure of the solar atmosphere; we will also try to give a historical perspective, as far as possible. More details can be found in a number of monographs on the Sun (Kuiper, 1953; Zirin, 1966, 1988; Priest, 1987, 2014; Durrant, 1988; Foukal, 2004; Stix, 2004; Aschwanden, 2004; Engvold et al., 2019) and on solar radio astronomy (Kundu, 1965; Zheleznyakov, 1970; Krueger, 1979; McLean and Labrum, 1985; Gary and Keller, 2004). There are also reviews on the Quiet Sun radio emission that the reader might be interested in (Alissandrakis, 1994; Gary, 1996; Alissandrakis and Einaudi, 1997; Lantos, 1999; Shibasaki, 1999; Keller and Krucker, 2004 and Shibasaki et al., 2011). Also of interest to the readers will be the reviews on *Coherent Emission Mechanisms* (Nindos, 2020) and on *Radio Measurements of the Magnetic field* (Alissandrakis and Gary, 2020), included in this special research topic collection.

As a rule, the term *structure* refers to the description of physical parameters as a function of position (in three dimensions) and time. As far as the time scale is concerned, solar phenomena are divided in three groups: the Quiet Sun (QS), the slowly varying component and the sporadic component. This grouping also reflects the energy associated with the phenomena, with the sporadic emission being the most energetic. Here we will not discuss sporadic phenomena, but we will only consider the Quiet Sun and, briefly, the slowly varying component that form the background for the more energetic phenomena.

It is important to stress that, as the solar emission extends over a wide spectral range, from γ-rays to radio waves, no single spectral window can provide complete information on solar phenomena. Yet, for reasons that have to do with the instrumentation and the effects of the earth's atmosphere, astronomical observations refer to particular spectral windows. Each spectral window offers unique information, radio being no exception. Addressing an audience of solar radio astronomers, we will try to emphasize what this spectral range has offered to our understanding of the Sun and to integrate radio data with data from other spectral ranges.

Although this chapter is about the Sun's atmosphere, we will start with a brief section on its interior, which plays the role of the source for all atmospheric phenomena. We will continue with a discussion of the radial structure of the solar atmosphere and then with its horizontal structure. We will then pass to active regions and we will finish with a discussion of the heating problem.

2. FROM THE CORE TO THE SOLAR ATMOSPHERE

Until a few decades ago, we had no direct information about the interior of the Sun; what we knew was based on the theory of stellar structure, which produced the so called *standard model* of the solar interior. The most important conclusion, apart from the fact that conditions in the solar core are appropriate for the fusion of hydrogen to helium through the proton-proton cycle, is that the interior of the Sun is radiative up to $\sim 0.71 R_\odot$, where convection starts and operates up to the subphotospheric layers. The convection zone has huge implications on the solar dynamo (Ossendrijver, 2003; Charbonneau, 2010), producing the magnetic field observed in the atmospheric layers and governing their structure.

The detection of neutrinos produced by nuclear fusion reactions in the solar core opened up a new area of research (Davis, 2003). However, it turned out that neutrino astronomy gave us more information about the properties of neutrinos such as neutrino oscillations (Ahmad et al., 2002), rather than the solar interior. Real observational information about the interior of the Sun came with helioseismology (see reviews by Christensen-Dalsgaard, 2002, Basu, 2016, García and Ballot, 2019).

Helioseismological spectral data are as rich in spectral lines as the optical solar spectrum or even richer, and their inversion allows us to measure quantities such as the speed of sound and the speed of rotation in the solar interior. The most impressive results are the excellent agreement with the standard model (see Figure 6 in Basu et al., 1997) and the rigid rotation of the solar interior (see Figure 18 in Christensen-Dalsgaard, 2002) below the convection zone.

Acoustic (p) modes cannot probe the deep solar interior; g modes, for which gravity (buoyancy) is the restoring force, are much better in this respect (see review by Appourchaux et al., 2010). However, gravity waves cannot propagate in a convectively unstable medium, such as the convection zone; they are evanescent there and are expected to come out in the photosphere with a much reduced, amplitude. A recent report on the detection of g-modes (Fossat et al., 2017) has been contested by Appourchaux and Corbard (2019).

With the advent of time-distance seismology, we have also been able to map the structure of the solar interior in the sub-photospheric layers (see review by Gizon et al., 2010; also Kosovichev, 2011). Impressive results have been obtained on the subphotospheric structure of sunspots (Gizon et al., 2009; Zhao et al., 2010) and supergranular flows (Jackiewicz et al., 2008). We can even detect active regions on the far side of the solar disk (see the recent article by Zhao et al., 2019), with data routinely available at http://jsoc.stanford.edu/data/farside/.

3. ATMOSPHERIC STRUCTURE

3.1. Elementary Physics of the Solar Atmosphere

Part of energy radiated by the Sun reaches the earth and it can be measured. From the value of the *solar constant* (the energy per unit area per unit time at 1 AU), together with the solar radius and the sun-earth distance, the effective temperature of the visible layer of the solar atmosphere (the *photosphere*) can be computed. Its value of 5,800 K gives us a measure of the photospheric temperature, and this is very important information.

Let us note further that in visible light the Sun appears as a disk with a sharp limb. From this elementary remark we can infer that the photospheric density decreases very fast with height. Let us start from the equation of hydrostatic equilibrium,

$$\frac{dP}{dz} = -g\rho \tag{1}$$

where P is the pressure, g the gravity (assumed constant), ρ is the density, and z the height. We can further express the pressure in terms of the density, using the equation of state,

$$P = Nk_BT = \frac{\rho}{\mu_{mol} m_H} k_BT \tag{2}$$

where N is the number density of particles, μ_{mol} is the mean molecular weight (= 1 for an atmosphere of neutral Hydrogen, 0.5 for fully ionized Hydrogen, 0.61 for 10% Helium), m_H the hydrogen mass, k_B the Boltzmann constant and T the temperature. Integrating (1), under the (crude) isothermal approximation, we obtain:

$$\rho = \rho_o e^{-z/H} \tag{3}$$

where ρ_o is the density at $z = 0$ and

$$H = \frac{kT}{g\mu_{mol}m_H} \tag{4}$$

is the isothermal scale height. Expressions similar to (3) hold for the pressure and for the number density. For the effective temperature of the photosphere, the scale height is a mere 175 km, i.e., just 0.0025 $R_\odot$, which tells us that the photosphere is very thin and, at the same time, explains why the optical limb is so sharp.

Another well-known fact is that, during total eclipses of the Sun and at the time that the moon has covered completely the photosphere, a bright red-colored crescent appears, the *chromosphere*. Its extent is certainly greater than that of the photosphere and this, following the argument about the scale height, implies that it has a higher temperature; indeed, more precise measurements give chromospheric temperatures of 10 to 20×10^3 K. The fact that it is much fainter than the photosphere, indicates that it has also a much lower density. Finally, much more extended, faint and diffuse than the chromosphere is the *corona*, which appears when the chromosphere has been covered by the moon. It has a scale height that indicates million-degree temperature and, of course, is much less dense than the chromosphere. Last but not least, the huge temperature difference between the chromosphere and the corona (2×10^4 to 10^6 K) requires a *chromosphere-corona Transition Region* (TR) to bridge the two.

Thus, using simple physical arguments, we have discovered the principal layers of the solar atmosphere and we have come across a basic problem of solar physics: that of the heating of the chromosphere and the corona, which we will discuss further in section 7.

3.2. Extracting the Information

In order to go beyond the elementary arguments of the previous section, we have to know how the physical conditions influence the production and transport of photons. The electromagnetic radiation that comes to us is rich in information about the physical conditions in the region of its formation, such as the electron temperature, the electron density and pressure, the magnetic field, the velocity of flow, the abundance of elements etc. It is the astrophysicist's task to extract this information and the main tool for this is the theory of radiative transfer (Mihalas, 1970; Rutten, 2003). Without going into the details, let us remind the reader that the specific intensity, I_ν, observed at the frequency, ν, that reaches the observer from a stellar atmosphere is given by the formal solution of the transfer equation for a plane-parallel, semi-infinite atmosphere:

$$I_\nu(\tau_\nu = 0, \mu) = \int_0^\infty S_\nu e^{-\tau_\nu/\mu}\, d\tau_\nu/\mu \tag{5}$$

Here the integration is carried along the vertical (radial) direction, z, which forms an angle θ with the path of the radiation (i.e., with the line of sight, in the absence of refraction), hence the presence of $\mu = \cos\theta$ in (5), θ being the heliocentric angle; the position along the vertical is expressed in terms of the optical depth, τ_ν, which is related to the geometrical height, z, and the opacity of the material through:

$$d\tau_\nu = -k_\nu \rho dz \tag{6}$$

where ρ is the density of the material and k_ν is the absorption coefficient. The minus sign is because the optical depth is measured from the observer to the star, while z is measured in the opposite direction. Furthermore, S_ν in (5) is the *source function*, which is the ratio of the coefficients of emission, j_ν, and absorption, k_ν,

$$S_\nu = \frac{j_\nu}{k_\nu} \tag{7}$$

and expresses the emissivity of the material; it is equal to the Plank function, $B_\nu(T)$, under conditions of Local Thermodynamic Equilibrium (LTE).

From the very form of (5), we can see that the specific intensity carries information about all atmospheric layers and that the contribution of each layer is weighted by the local value of the source function and reduced by the absorption of overlying layers. It is easy to prove that, in first order, the observed specific intensity corresponds to the value of the source function at $\tau_\nu = \mu$ (Eddington-Barbier relation); thus at the center of the disk we see at $\tau_\nu \simeq 1$.

In practice, we can probe the atmosphere by two means. One is by varying μ, which can be done by measuring the variation of the specific intensity from the center of the solar disk ($\mu = 1$) to the limb ($\mu = 0$). It is easy to show that, if the temperature decreases with height, the intensity at the limb is lower than at the disk center (limb darkening); in the opposite case the limb is brighter. **Figure 1**, top row, shows three full disk solar images. Two of them, in the optical range, show limb darkening (more in the blue than in the red part of the spectrum), which proves that the temperature is decreasing with height in the region of formation of the radiation (photosphere); the third, in the microwave range, shows signs of limb brightening, which indicates that the temperature is rising above the photosphere, where the radiation is formed.

The second method for probing the atmosphere is by varying the frequency of observation, which changes the opacity. As shown in the bottom row of **Figure 1**, this allows us to probe a height range of $\sim$ 600 km, where the temperature ranges from $\sim$ 4,500 to $\sim$ 6,700 K, in the spectral range from sub-mm λ to the far ultraviolet.

It follows from the above discussion that, in principle, one could invert (5) and recover the information on the physical conditions. This is the basis for the computation of *empirical* atmospheric models (see Chapter 6.10 in Zirin, 1988). Things are not simple though, because of the complex dependence of the absorption coefficient on the physical conditions and due to departures from LTE in the upper solar atmosphere. The situation is better in the radio range, thanks to the Rayleigh-Jeans approximation to the Planck function and the fact that electrons, which are responsible for the thermal emission, are always in LTE. Under these circumstances, the solution of the

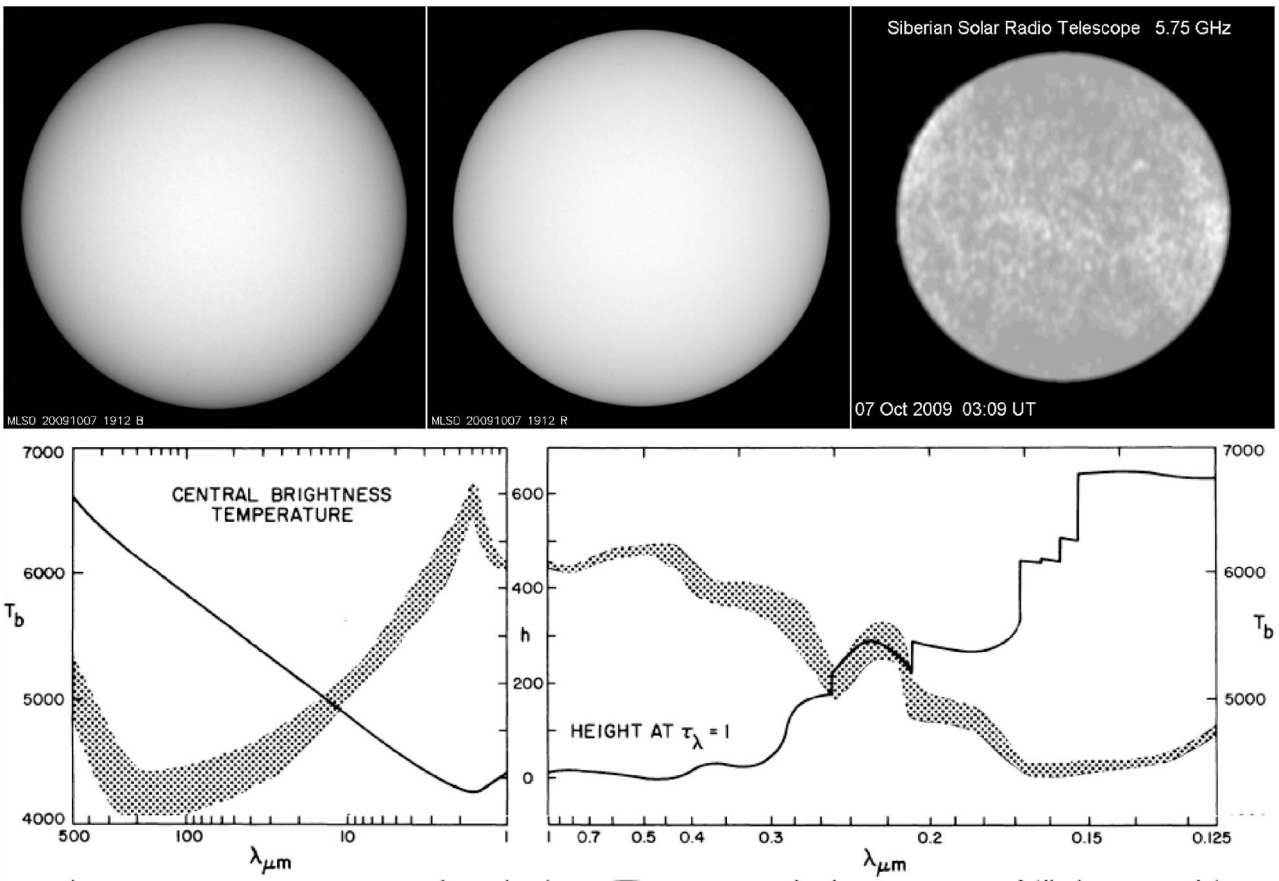

FIGURE 1 | (Top) Solar images on October 7, 2009 in the blue part of the spectrum (left) in the red (middle) from the Mauna Loa Solar Observatory (MLSO) and at $\lambda = 5.2$ cm from the Siberian Solar Radio Telescope (SSRT); images selected by the author. **(Bottom)** Observed continuum brightness temperature at the center of the solar disk as a function of wavelength (shaded band) and the approximate height of formation of the radiation (black line); from Vernazza et al. (1976), © AAS, reproduced with permission.

transfer equation takes the form:

$$T_b = \int_0^\infty T_e e^{-\tau_\nu/\mu}\, d\tau_\nu/\mu \tag{8}$$

which links the electron temperature, T_e, to the observed brightness temperature, T_b, defined so that

$$I_\nu = \frac{2kT_b}{\lambda^2} \tag{9}$$

We will finish the section by considering the emission of a homogeneous slab of material (cloud), overlying a background of specific intensity $I_{\nu o}$:

$$I_\nu = I_{\nu o} e^{-\tau_\nu} + S_\nu (1 - e^{-\tau_\nu}) \tag{10}$$

or, for the radio range,

$$T_b = T_{bo} e^{-\tau_\nu} + T_e (1 - e^{-\tau_\nu}) \tag{11}$$

An important consequence of these relations is that, if the slab is optically thick, a measurement of the brightness temperature gives us directly the value of the electron temperature ($T_b \simeq T_e$, for $\tau_\nu >> 1$). If, on the contrary, the slab is optically thin ($\tau_\nu << 1$) and there is no background emission, its brightness temperature is lower than its electron temperature:

$$T_b = \tau T_e. \tag{12}$$

4. RADIAL STRUCTURE OF THE SOLAR ATMOSPHERE

In the previous section we implicitly assumed that solar parameters vary only in the radial direction. However, anyone who has seen solar images will agree that the Sun is extremely rich in structure in the non-radial direction (horizontal structure) and that inhomogeneities become more prominent as we move from the photosphere to the chromosphere and the corona. Moreover, as the spatial resolution of our instruments increases, we become more and more aware of the importance of horizontal structures.

Under these circumstances, it is rather surprising that one-dimensional models which, in addition to treating the physical

parameters as a function of height only, also assume hydrostatic equilibrium, have any resemblance to the observations at all. The physical reason behind the success of such models is gravity, which produces a strong radial stratification in the solar atmosphere; as a consequence, the radial density gradient is much larger than the horizontal, at least in the lower atmospheric layers.

4.1. Empirical Models for the Low Atmosphere

There is a long tradition of 1-D empirical solar models. Early models did not extend beyond the chromosphere, stopping around $T_e \simeq 10^4$ K, which is too low for brightness computations beyond the cm radio wavelength range. Subsequent models went higher, with that of Fontenla et al. (2002) reaching 1.2×10^6 K, in the upper TR. These models also developed further the multi-component approach, first introduced in Vernazza et al. (1981), to represent different quiet and active regions on the Sun. Note that multi-component models are not really 3-D, since radiative transfer in the horizontal direction is ignored. More details can be found in Shibasaki et al. (2011).

With the advent of fast numerical computations, a number of sophisticated tools, such as the *bifrost* radiative magnetohydrodynamics (rMHD) code (Gudiksen et al., 2011) and the *STockholm inversion Code* (STic, de la Cruz Rodríguez et al., 2019) have been developed for solar atmospheric modeling. Nevertheless, the classic models still provide a comprehensive picture of the solar atmosphere.

In order to compute brightness spectra at longer wavelengths, one has to add a coronal contribution. Zirin et al. (1991) found that their measurements, which extended up to 21 cm, could simply be reproduced by a two-component model: an optically thick chromosphere and an isothermal corona (see further discussion in section 4.3.2). Selhorst et al. (2005) used a hybrid model (combination of models for the photosphere, chromosphere, and corona) to reproduce the observed features in Nobeyama Radioheliograph (NoRH) images at 17 GHz. To obtain acceptable brightness temperature values and the observed solar radius, they had to include absorbing chromospheric structures, such as spicules (see section 5.3) into the model, as had been done in the past (e.g., Lantos and Kundu, 1972), in order to explain why the observed center-to-limb variation shows less brightening than the homogeneous models predict, or even shows darkening.

Solar observations with the *Atacama Large mm and sub-mm Array* (ALMA) are providing new information on the structure of the low atmosphere. Alissandrakis et al. (2017, 2020) used the center-to-limb variation of the brightness temperature from ALMA full-disk data at 1.25 and 3 mm and data from Bastian et al. (1993) at 0.85 mm to invert the transfer equation and obtained the electron temperature as a function of the optical depth (**Figure 2**). Their results were close (5% lower) to the predictions of the Fontenla et al. (1993) average QS model C.

4.2. Emission Measure and Differential Emission Measure

Several authors have used direct information from the EUV part of the spectrum to compute the radio brightness in the microwave range, which is reasonable since the radiation in both wavelength ranges is formed in the same atmospheric layers. In one approach the emission measure, *EM*, which is a measure of the electron density, N_e, along the line of sight, is used:

$$EM = \int_0^L N_e^2 d\ell \tag{13}$$

This quantity appears both in the expression for the integrated intensity of EUV lines and the radio brightness temperature, provided that the emission is optically thin and the plasma isothermal (see Shibasaki et al., 2011 for details). This fact led to the well-known practice of using two EUV lines or X-ray continuum bands for an estimate of the plasma temperature and the emission measure. Zhang et al. (2001) used three EIT images, at 171, 195, and 284 Å, to derive the emission measure in a two-temperature model. They further computed the emission at 6 and

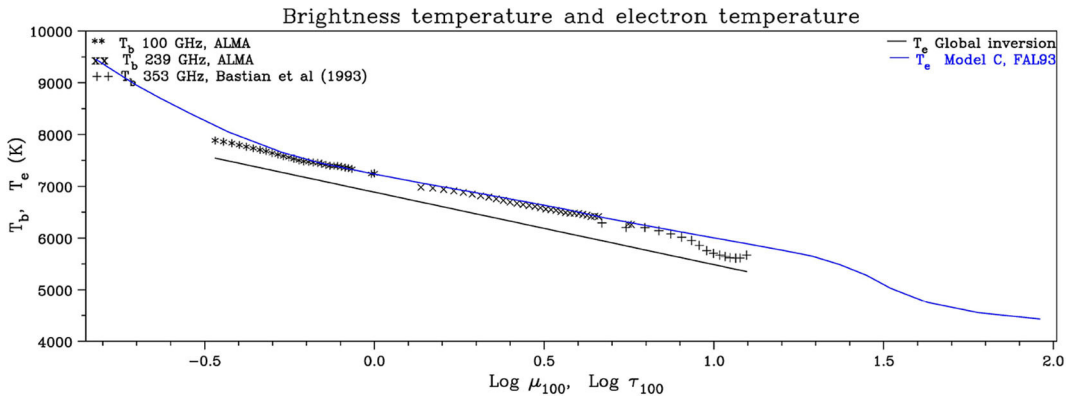

FIGURE 2 | Observed brightness temperature in the mm-λ range, T_b as a function of the cosine of heliocentric angle, μ_{100}, reduced to 100 MHz (symbols). The same plot shows the computed electron temperature, T_e as a function of the optical depth, τ_{100}, (black line), again reduced to 100 GHz. The blue line gives $T_e(\tau_{100})$ predicted by model C of Fontenla et al. (1993). Note that increasing τ corresponds to decreasing altitude in the atmosphere. Adapted from Alissandrakis et al. (2017), reproduced with permission © ESO.

20 cm wavelengths, which they compared with their *Very Large Array* (VLA) observations. Although the model image looks very much like the observed, the computed brightness temperature was twice the observed at both wavelengths; at 6 cm the model gave $\sim 170 \times 10^3$ K vs. the observed $\sim 85 \times 10^3$ K, whereas at 20 cm the values were $\sim 1.5 \times 10^6$ K and $\sim 0.8 \times 10^6$ K respectively (see their **Figure 4**). They attributed the discrepancy to errors in the coronal abundances used to infer the radio flux from the EIT data.

The differential emission measure (DEM) is even better than the emission measure; it is defined as

$$\varphi(T_e) = N_e^2 \frac{d\ell}{dT_e} \tag{14}$$

and represents the distribution of electron density over a temperature range, dropping the isothermal assumption. Obviously, one needs many EUV lines, formed over the appropriate temperature range, to make good use of the DEM.

Landi and Chiuderi Drago (2003) used the DEM values derived from UV and EUV spectral line intensities observed by SUMER and CDS, and showed that a TR model *for the cell interior*—excluding any network contribution—could give an agreement with the observed radio brightness temperatures (see section 5.2 for explanations of the network and the cell interior). In a subsequent work, (Landi and Chiuderi Drago, 2008), they showed that radio observations provide a much more reliable diagnostic tool for the determination of the DEM than UV and EUV lines at $T < 30\,000$ K, since the latter are optically thick. Moreover, they extended the DEM down to 5,600 K using the radio spectrum from 1.5 to 345 GHz, and obtained very good agreement with the radio data.

Useful as it may be, the DEM cannot be used to compute the emission in optically thick cases, in which case both T_e and N_e are required to integrate (8). Still, in a recent work, Alissandrakis et al. (2019) developed a method for the computation of the electron temperature and density along the line of sight from the DEM, under the assumptions of stratification and hydrostatic equilibrium and used it to compute the cm-λ emission from active regions.

4.3. Coronal and Transition Region Models

As we move from the microwave to the metric range, the height of formation of the radiation increases due to the increase of the absorption and, eventually, we reach the corona. This leads to an increase of the solar radius with wavelength (see, e.g., Figure 5 of Menezes and Valio, 2017), although this quantity is not the most accurate way to measure the formation height due to structures beyond the limb and other effects. Hence, in order to understand the radio emission at dm-λ and beyond, it is important to discuss the information obtained for the layers above the chromosphere from other spectral ranges.

4.3.1. Models From Optical Data

As mentioned already in section 3.1, the extent of the corona indicates a large scale height and a high temperature. Emission lines in the optical spectrum (the emission line or *E-corona*), also provide evidence for a hot corona. These lines, originally attributed to an unknown element (coronium), turned out to be due to forbidden transitions of highly ionized species, such as FeX (the red line at 6374 Å), FeXIV (the green line at 5303 Å) and CaXV (the yellow line at 5494 Å); they were identified thanks to the work of Grotrian (1939) and of Edlén (1943). The issue of their formation temperature was not settled, until dielectronic recombination was taken into account (for a vivid account see Chapters 6.3 and 7.3 in Zirin's 1966 book).

Due to the difficulties in the interpretation of the line emission, coronal models are based on the continuum white light corona, which is due to Thomson scattering of photospheric photons on the free electrons of the coronal plasma (van de Hulst, 1950). This emission is linearly polarized and constitutes the *K corona (kontinuierlich)*; there is also unpolarized emission (the *F corona*), which is due to Rayleigh scattering of the Fraunhofer spectrum in dust and small particles between the Sun and the Earth.

Assuming spherical symmetry, a number of models have been produced (Allen, 1947; van de Hulst, 1950; Newkirk, 1961; Saito et al., 1970) from K corona data. In spite of the fact that the corona is highly inhomogeneous, some of them, namely the Newkirk (1961) and Saito et al. (1970) models, were quite successful in describing the coronal density and are still in use. They are very useful in modeling the radio emission and in estimating the height of metric burst sources. In such cases the emission is at the plasma frequency, f_p:

$$f_p\ [\mathrm{MHz}] = 8.978 \times 10^{-3} \sqrt{N_e[\mathrm{cm}^{-3}]} \tag{15}$$

or the second harmonic; the height of the emission is then derived from the observed frequency and the density model.

The Newkirk model predicts a variation of the electron density, N_e, with the distance, r, from the center of the Sun that has the form:

$$N_e = 4.2 \times 10^4\ 10^{4.32 R_\odot / r} = 4.2 \times 10^4\ e^{9.95 R_\odot / r} \qquad [\mathrm{cm}^{-3}] \tag{16}$$

where $R_\odot$ is the solar radius. This is hydrostatic, since the solution of the hydrostatic equilibrium equation (1) in spherical coordinates, taking into account the variation of gravity with height, is:

$$N_e = N_{eo} e^{-\frac{R_\odot}{H_\odot} + \frac{R_\odot}{H_\odot} \frac{R_\odot}{r}} \tag{17}$$

where $H_\odot$ is the scale height at the base of the corona. A comparison with (16) gives,

$$N_{eo} = 8.8 \times 10^8\ \mathrm{cm}^{-3} \tag{18}$$

$$H_\odot = 0.1005 R_\odot = 70\,000\ \mathrm{km} \tag{19}$$

this value of the scale height corresponds to a coronal temperature of $T = 1.41 \times 10^6$ K.

The Saito model allows for density variations with latitude, φ:

$$N_e = \frac{3.09 \times 10^8 (1 - 0.95 \sin\varphi)}{(r/R_\odot)^{16}} + \frac{1.58 \times 10^8 (1 - 0.5 \sin\varphi)}{(r/R_\odot)^6}$$

$$+\ \frac{0.0251\times10^8(1-\sqrt{\sin\varphi})}{(r/R_\odot)^{2.5}}\qquad[\mathrm{cm}^{-3}]\tag{20}$$

The Saito polar corona reflects coronal hole conditions, but coronal holes were not known at the time. The model is close to hydrostatic; the best fit in the range of 1 to $2\,R_\odot$ gives a scale height of $0.103\,R_\odot$ (coronal temperature $T_c = 1.44\times10^6$ K). At $r = R_\odot$ the model predicts lower base densities than the Newkirk model: $4.7\times10^8\,\mathrm{cm}^{-3}$ at the equator and $9.5\times10^7\,\mathrm{cm}^{-3}$ at the poles.

Far from the photosphere, the hydrostatic model is not valid; indeed, (17) predicts a finite density at infinity, $n_o\exp(R_\odot H_\odot)$, which is five orders of magnitude above the density of the interplanetary medium. This means nothing else but that the corona cannot be in hydrostatic equilibrium and we know very well that it is not, as the supersonic, superalfvénic *solar wind* sets up, with the sonic point located near $\sim 3\,R_\odot$, making the sun an integral part of the *heliosphere* which extends beyond the limits of our solar system. The fall of the measured electron density below the values predicted by the hydrostatic model is clearly seen in plots of the electron density as a function of distance, such as that in **Figure 3** (see also Figure 4 of Koutchmy, 1994).

At large distances from the sun, the density is expected to go like r^{-2}, and this is expressed in the model of Leblanc et al. (1998):

$$N_e = 3.3\times10^5(r/R_\odot)^{-2} + 4.1\times10^6(r/R_\odot)^{-4} + 8\times10^7(r/R_\odot)^{-6}\tag{21}$$

which was based on observations of interplanetary type III bursts and is normalized to the average solar wind density at 1 AU, during solar minimum. Subsequently, Mann et al. (1999) developed a heliospheric density model as a special solution of Parker's wind equation which covers a range from the low corona up to 5 AU.

Among the above models, Newkirk's is by far the most popular for the low and middle corona, mainly due to its simple mathematical expression. More often than not, in estimates of metric burst heights, authors multiply the model's density by a factor of 2–4, justified by the fact that in the burst environment the coronal density is higher than in the quiet sun.

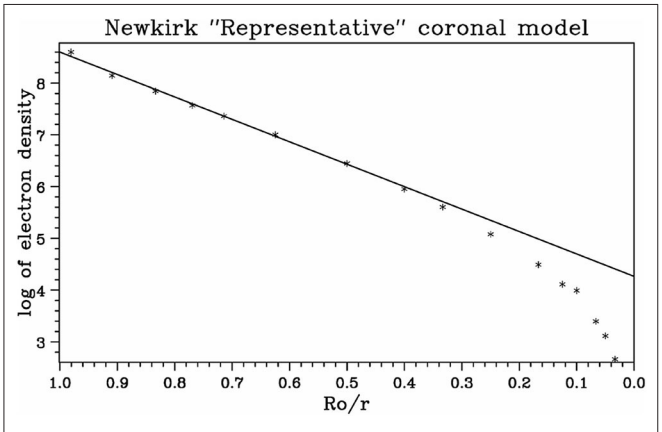

FIGURE 3 | Equatorial "representative" coronal density at minimum, after Table 1 of Newkirk (1967), as a function of the inverse distance from the center of the Sun, up to $30\,R_\odot$. The solid line represents a hydrostatic fit up to $r = 2R_\odot$.

4.3.2. Emission From the Transition Region

Between the chromosphere and the corona there is a thin Transition Region, where the temperature rises fast from $\sim 10^4$ to $\sim 10^6$ K. Many ions have ionization states in this temperature range and emit spectral lines in the extreme ultraviolet range (EUV) of the spectrum. Early space observations of these lines (Dupree and Goldberg, 1967; Athay, 1971) indicated that the temperature structure of the TR is such that the conductive flux, from the corona to the chromosphere, is constant; this can be explained in terms of the thinness of the TR, due to which very little energy is radiated and there is no convection in any case. Under the constant conductive flux assumption, the temperature gradient is given by:

$$\frac{dT}{dz} = \frac{F_c}{A}T^{-5/2}\tag{22}$$

where F_c is the conductive flux and A is a constant with the value of 1.1×10^{-6} cgs units. Integration gives:

$$T(z) = \left[T_o^{7/2} + \frac{7}{2}\frac{F_c}{A}(z-z_o)\right]^{2/7}\tag{23}$$

where T_o is the temperature at the reference height, z_o, which could be at any point within the TR.

Solving the hydrostatic equilibrium equation we get for the electron density:

$$N_e(T) = N_{eo}\frac{T_o}{T}\exp[-8.9\times10^{-11}(T^{5/2} - T_o^{5/2})/F_c]\tag{24}$$

Under the assumption of constant conductive flux, we can compute the optical depth of the TR in the radio range by first expressing Equation (6) in terms of the temperature gradient (Alissandrakis et al., 1980); we then get, using (22) and the standard expression for the absorption coefficient, k:

$$d\tau = -k\frac{dz}{dT}dT = -\Gamma\frac{dT}{T}\tag{25}$$

where $\Gamma = \xi A p^2/f^2F_c$, $p = N_eT_e$ is proportional to the pressure, f is the frequency of observation, ξ is a slowly varying parameter and refraction has been ignored. Since the TR is very thin, the pressure can be assumed constant and, ignoring also the small variation of ξ with temperature, Alissandrakis et al. (1980) obtained:

$$T_{b,TR} = \frac{\Gamma}{\Gamma+1}T_2\left[1-\left(\frac{T_1}{T_2}\right)^{\Gamma+1}\right]\tag{26}$$

where $T_{b,TR}$ is the brightness temperature of the TR, and T_1 and T_2 are the temperatures at the lower and upper part of the TR. For the optically thin case $\Gamma << 1$, and (26) gives:

$$T_{b,TR} \simeq \Gamma(T_2 - T_1)\tag{27}$$

A similar computation can be done for an isothermal, hydrostatic corona. If the variation of the scale height with z is ignored, which is not a bad assumption for the microwave range where the coronal contribution comes from the lower layers, we get for the coronal optical depth, τ_c, and brightness temperature, $T_{b,c}$:

$$\tau_c = 0.5\, k_c\, H \tag{28}$$

$$T_{b,c} = \tau_c\, T_c \tag{29}$$

Putting everything together, if we have a corona on the top of a transition region and a region with brightness temperature T_{bo} at the bottom, the observed brightness is, in the optically thin approximation:

$$T_b = T_{bo} + \Gamma(T_c - T_1) + \tau_c\, T_c \tag{30}$$

The second term in the rhs of Equation (30), which represents the TR contribution, has the same form of frequency dependence ($\Gamma \propto f^{-2}$) as the third term, which represents the coronal contribution ($\tau_c \propto f^{-2}$). It is therefore not surprising that Zirin et al. (1991) could not distinguish between the transition region and the corona in their spectral measurements.

4.3.3. Refraction and Scattering in the Corona

Not only does the formation height of the emission increase as we move from the cm to the meter range, but also the index of refraction departs from unity, as the observing frequency approaches the plasma frequency; hence the rays are refracted and eventually suffer total reflection (**Figure 4**, left panel). As a result of refraction and reflection, the lower part of the corona is inaccessible at long metric wavelengths. Moreover, the observed position of a localized source will be displaced toward the disk center, an effect which is stronger near the limb; a source may even appear in two places, if the optical depth along the path of the refracted ray is small. In any case, both the radiative transfer and the ray tracing equations (Snell's law) should be taken into account in model computations (see, e.g., Vocks et al., 2018).

Refraction effects are important when the optical depth between the observer and the point of total reflection is small. This is illustrated in the right panel of **Figure 4**, where the height of reflection, the optical depth up to reflection and the resulting brightness temperature are plotted as a function of frequency for the center of the solar disk. For frequencies higher than ∼125 MHz the reflection point is inside the TR (between the dashed lines at the bottom of the figure). Moreover, radiation from the reflection point does not reach the observer because is absorbed by the overlaying layers which are optically thick; thus the brightness temperature increases with decreasing frequency, as the effective level of formation moves up through the TR toward the corona. At longer wavelengths the rays are reflected before they accumulate sufficient optical depth and the brightness temperature decreases, remaining below the coronal electron temperature (dashed line, top panel of the figure).

The above predictions are verified by observations at long (metric) wavelengths, where there is a marked departure of the brightness temperature below the coronal electron temperature, with the brightness temperature showing a maximum of $\leq 10^6$ K near 2–3 m (see Table 1 and Figure 4 of Lantos, 1999).

In addition to refraction, scattering by random density fluctuations also plays a role (Aubier et al., 1971; Hoang and Steinberg, 1977; Thejappa and Kundu, 1992, 1994; Bastian, 1994; Thejappa and MacDowall, 2008). Scattering smooths sources of

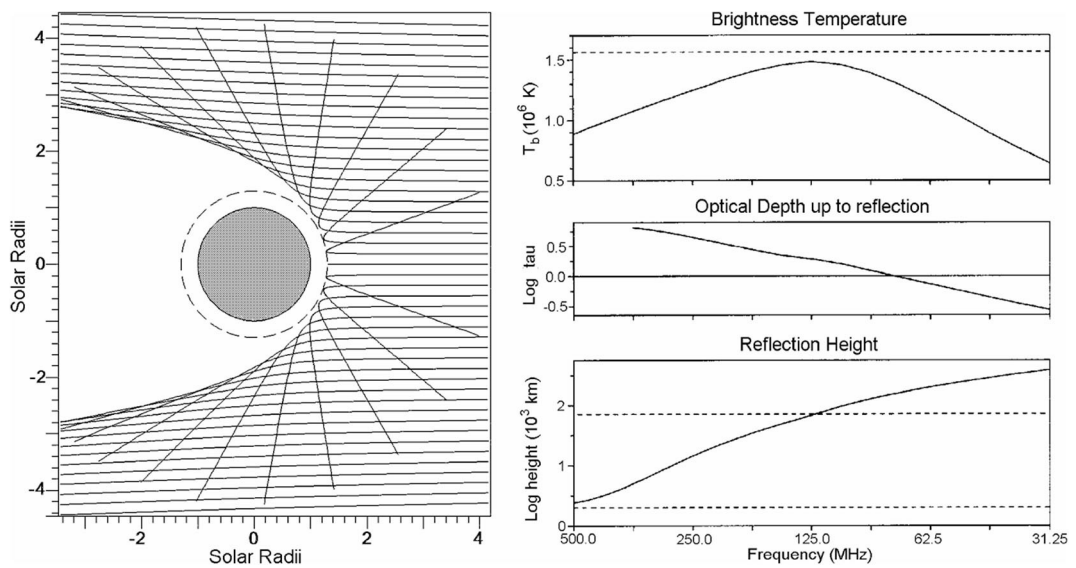

FIGURE 4 | (Left) Ray paths at metric wavelengths, showing the effects of refraction and total reflection; figure prepared by the author. **(Right)** The height of reflection, the optical depth up to the reflection point and the brightness temperature as a function of frequency for the center of the solar disk. The ray tracing computations were performed for a Saito equatorial density model, with a coronal temperature of 1.52 10^6 K and a constant conductive flux Transition Region with $F_c = 10^5$ erg cm^{-2} s^{-1}. Reprinted from *Advances in Space Reseach*, Vol 14, Alissandrakis, Radio observations of the quiet solar corona, 81–91 (1994), with permission from Elsevier.

small angular size; for example, Mercier et al. (2015) reported sizes no smaller than $\sim$ 30″ for type I bursts, although the nominal resolution of their combined NRH-GMRT observations was 20″. Moreover, anisotropic scattering also displaces sources (Kontar et al., 2019). Finally, scattering can decrease the observed brightness at low frequencies (Thejappa and MacDowall, 2008).

4.4. Interplanetary Scintillation

Interplanetary scintillation (IPS) refers to fluctuations in the emission from distant compact radio sources on timescales of ∼1 s, due to density variations in the solar wind plasma (e.g., Hewish et al., 1964; Jokipii, 1973; Bisi et al., 2010 and references therein). The analysis of IPS observations can provide estimates of the solar wind speed over global spatial scales which complement the *in situ* measurements from spacecraft. On the other hand, IPS is sensitive to turbulent-scale density variations which complements the larger scales accessible by white-light coronagraphs.

Classically, IPS probe the solar wind and the outer corona. However, using the Jansky VLA, information on the inner corona down to 2 $R_\odot$ can be obtained (Kobelski et al., 2019).

5. HORIZONTAL STRUCTURE

5.1. Theoretical Issues

The importance of horizontal structure was pointed out in section 4. A basic question that we will address here is what determines the horizontal structure. In order to answer this question we will resort to plasma physics, magnetohydrodynamics in particular (see also Chapter 2 in Priest, 1987 and Chapter 6 in Aschwanden, 2004). We will start with the MHD equation of momentum transport:

$$\rho\left(\frac{\partial \boldsymbol{V}}{\partial t}+\boldsymbol{V}\cdot\nabla\boldsymbol{V}\right)=\rho\boldsymbol{g}-\nabla P+\frac{\boldsymbol{J}\times\boldsymbol{B}}{c} \tag{31}$$

where $\boldsymbol{V}$ is the plasma flow velocity, $\boldsymbol{B}$ the magnetic field, $\boldsymbol{J}$ the electric current density, P the pressure and g the gravity. The magnetic field acts upon the plasma through the *Lorentz force*, $\boldsymbol{J}\times\boldsymbol{B}/c$, which is perpendicular to the field. Using Ampère's law,

$$\nabla\times\boldsymbol{B}=\frac{4\pi}{c}\boldsymbol{J} \tag{32}$$

we can eliminate the current in the Lorentz force to get:

$$\frac{\boldsymbol{J}\times\boldsymbol{B}}{c}=-\nabla\frac{B^2}{8\pi}+\frac{\boldsymbol{B}\cdot\nabla\boldsymbol{B}}{4\pi} \tag{33}$$

which decomposes the Lorentz force to a *magnetic pressure* term:

$$P_m=\frac{B^2}{8\pi} \tag{34}$$

and a *magnetic tension* term which depends on the curvature of the magnetic field lines; indeed, the second term in the right hand side of (33) can be written as:

$$\frac{\boldsymbol{B}\cdot\nabla\boldsymbol{B}}{4\pi}=\frac{B^2}{4\pi}\frac{\hat{\boldsymbol{n}}}{R_c}+\nabla_\parallel\frac{B^2}{8\pi} \tag{35}$$

where $\nabla_\parallel$ is the component of the gradient parallel to the field, $\hat{\boldsymbol{n}}$ is the unit vector perpendicular to the field and R_c is the curvature of magnetic field lines:

$$\frac{\hat{\boldsymbol{n}}}{R_c}=\hat{\boldsymbol{b}}\cdot\nabla\hat{\boldsymbol{b}} \tag{36}$$

where $\hat{\boldsymbol{b}}$ is the unit vector along the field. Going back to (33), the Lorentz force can be written as:

$$\frac{\boldsymbol{J}\times\boldsymbol{B}}{c}=\nabla_\perp P_m+\frac{B^2}{4\pi}\frac{\hat{\boldsymbol{n}}}{R_c} \tag{37}$$

where $\nabla_\perp$ is the component of the gradient perpendicular to the field; the first term in the rhs is the magnetic pressure and the second is the magnetic tension.

Since the Lorentz force acts perpendicular to the field, parallel to the field we can write from (31):

$$\rho\left(\frac{\partial \boldsymbol{V}_\parallel}{\partial t}+\boldsymbol{V}_\parallel\cdot\nabla\boldsymbol{V}_\parallel\right)=\rho\boldsymbol{g}_\parallel-\nabla_\parallel P \tag{38}$$

which is Bernouli's equation of flow in a flux tube. Moreover, if the plasma motion is slow, i.e.,

$$V\ll\sqrt{\frac{P}{\rho}}=v_s \quad \text{(sound speed)} \tag{39}$$

$$V\ll\frac{B}{\sqrt{4\pi\rho}}=v_A \quad \text{(Alfvén speed)} \tag{40}$$

$$V\ll\sqrt{Lg}\sim v_g \quad \text{(free fall speed)} \tag{41}$$

the velocity terms in the momentum transfer equation can be ignored, and we get the hydrostatic equilibrium equation:

$$\nabla_\parallel P=\rho\boldsymbol{g}_\parallel \tag{42}$$

which is the same as (1) and has the solution:

$$P=P_0e^{-\int_{z_0}^{z}\frac{dz}{H(T)}} \tag{43}$$

where $H(T)=(kT)/(g\mu_{mol}m_H)$ is the scale height (*cf* section 3.1).

The conclusion from the above analysis is that, under the conditions specified by (39)–(41), *each magnetic flux tube has its own atmosphere*, as far as the pressure distribution is concerned. Moreover, since the heat conduction coefficient is much higher along the magnetic field than in the perpendicular direction, each flux tube has its own temperature distribution.

Let us now consider the equation for the time variation of the magnetic field. Starting from Ohm's law:

$$\boldsymbol{E}+\frac{\boldsymbol{V}\times\boldsymbol{B}}{c}=\eta\boldsymbol{J} \tag{44}$$

where $\boldsymbol{E}$ is the electric field, $\boldsymbol{J}$ is the electric current density and η is the resistivity; substituting in Faraday's law,

$$\nabla\times\boldsymbol{E}=-\frac{1}{c}\frac{\partial\boldsymbol{B}}{\partial t} \tag{45}$$

we obtain the *induction equation*:

$$\frac{\partial \boldsymbol{B}}{\partial t} = \frac{\eta c^2}{4\pi}\nabla^2 \boldsymbol{B} + \nabla \times (\boldsymbol{V} \times \boldsymbol{B}) \tag{46}$$

In the case of

$$R_m \equiv \frac{4\pi VL}{\eta c^2} \ll 1, \tag{47}$$

where R_m is the magnetic Reynolds number and L is the spatial scale of the magnetic field, the second term in the right hand side of (46) can be ignored; in this case the time evolution of the field is described by a diffusion equation:

$$\frac{\partial \boldsymbol{B}}{\partial t} = \frac{\eta c^2}{4\pi}\nabla^2 \boldsymbol{B} \tag{48}$$

and magnetic energy eventually goes to thermal energy, through Joule heating. In the opposite case the second term in the right hand side of (46) dominates and the field is *frozen-in*:

$$\frac{\partial \boldsymbol{B}}{\partial t} = \nabla \times (\boldsymbol{V} \times \boldsymbol{B}) \tag{49}$$

Almost everywhere in the solar atmosphere the magnetic Reynolds number is much larger than unity. Thus, in quiescent situations, the behavior of the plasma and the magnetic field depends upon their relative energy density (see also Gary, 2001):

- If the energy density (thermal plus kinetic) of the plasma is much smaller than that of the magnetic field or, equivalently, if the sum of the gas pressure and the dynamic pressure is much smaller than the magnetic pressure, then the magnetic field dominates and the plasma flows along the field lines. This is the case in the chromosphere, the corona and in sunspots.

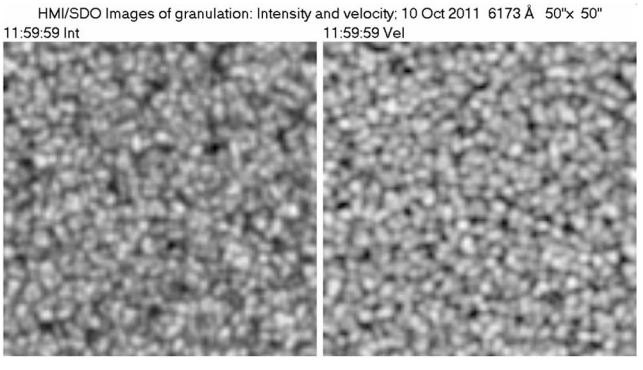

FIGURE 5 | Image of the photospheric granulation at the center of the disk (left), together with an image of the line of sight velocity (white toward the observer). The velocity image has been averaged over 5 min to reduce the effect of oscillations. In this and subsequent figures the field of view is marked in the figure title. Images produced by the author, using data from the *Helioseismic and Magnetic Imager* (HMI) aboard the *Solar Dynamics Observatory* (SDO).

- In the opposite case the plasma dominates and will drag and deform the field. This happens in the photosphere (outside sunspots) and in the solar wind.

The situation is quite different when large amounts of energy are impulsively released, in which case both the plasma and the magnetic field are restructured.

As we will see further on in this review, this simple argument can explain qualitatively almost everything that we see on the Sun. Of course there are phenomena that require a more sophisticated approach, such as kinetic plasma theory. Today we have at our disposal both powerful computers and efficient codes for solving numerically the MHD equations and we have seen spectacular results of simulations that can hardly be distinguished from real observations (see reviews by Solanki et al., 2006; Carlsson, 2007; Nordlund et al., 2009; Moradi et al., 2010, de Wijn et al., 2009; Rempel and Schlichenmaier, 2011; see also the recent review by Carlsson et al., 2019). Still, it is very important to have a sound understanding of the physical principles which are often hidden behind the simulations.

5.2. Photospheric Structure and the Network

From the above discussion we expect plasma motion to dominate in the QS photosphere and drag the magnetic field lines (for an overview of solar magnetic fields see Wiegelmann et al., 2014 and Bellot Rubio and Orozco Suárez, 2019). Indeed, the most prominent photospheric structure is the granulation, with a spatial scale of $\sim$1.5″, and a temporal scale of $\sim$15 min, which is attributed to convection currents (see the classic work by Bray and Loughhead, 1967 for a historic account and the reviews by Nordlund et al., 2009 and Rincon and Rieutord, 2018). As can be seen in **Figure 5**, the intensity and velocity images of the photosphere at the center of the solar disk are practically identical, which proves that hot material in the bright granules ascends, while cooler material in the dark inter-granular lanes descends; the same effect produces the zigzag appearance of photospheric absorption lines (see, e.g., Figure 6.20 in Zirin, 1988). As a matter of fact, the convection zone ends below the photosphere, which is convectively stable; thus, the granulation is an effect of *overshoot* of convection into the stable layers of the photosphere.

The photospheric granulation is not the only convection system on the Sun. A larger scale ($\sim$40″) and long lived ($\sim$20 h) convection system was detected by Leighton et al. (1962), as a horizontal flow pattern; it is better visible far from the center of the disk, where the horizontal flow translates to approaching and receding line of sight velocities. This has been called *supergranulation*. An intermediate scale convection system, the *mesogranulation* has been reported by November et al. (1981), who used correlation tracking to measure horizontal flows. In the older approach, the three scales of convection would be associated with the ionization zones of HI, HeI, and HeII. However, the existence of mesogranulation as distinct scale of convection has been contested; views have been expressed that it is an extension of granulation or even an artifact produced by

the correlation tracking algorithm (see discussion in Nordlund et al., 2009; Rincon and Rieutord, 2018).

The development of time-distance helioseismology has given us some information on the depth of supergranulation, despite the inherent difficulties (Nordlund et al., 2009; Kosovichev, 2011). According to Kosovichev and Duvall (1997), supergranular flows appear down to 2–3 Mm below the surface; however the pattern disappears or is dominated by noise below $\sim$ 5 Mm. Similar results were obtained by Jackiewicz et al. (2008), see Figure 10 of Gizon et al. (2010).

Under the influence of the plasma flows the magnetic field is deformed and dragged at the edge of supergranular boundaries. The compressed magnetic flux tubes appear as tiny bright features in intergranular lanes, best visible in very high resolution photographs taken in the G-band. These were first detected by Dunn and Zirker (1973) and called *filigree* (see, e.g., Hα image in Figure 10, left). Higher up, in the chromosphere, enhanced emission is observed above these regions. The emission is more diffuse there, apparently due to the lateral expansion of the magnetic flux tubes. These regions of enhanced chromospheric emission constitute the well-known *chromospheric network* which, as pointed out by Leighton et al. (1962), coincides with the borders of the supergranules; for the region inside the supergranules the terms *cell interior*, or *internetwork*, or *intranetwork* are used. In spite of its name, the network has its roots in the photosphere, or even lower.

The convective flows not only drag the magnetic field; they also compress it to kilo Gauss strengths, as deduced first by Stenflo (1973), from simultaneous measurements in lines with different Landé factors. Magnetic field of such strength cannot be confined by the plasma pressure alone, thus Parker (1978) proposed that the field is further confined as a result of the adiabatic cooling of the descending plasma. **Figure 6** (left) shows a magnetogram of a quiet region near the center of the solar disk; the strong network field is accompanied with brightenings in the continuum around 1700 Å (center); the strongest magnetic features are associated with persistent downflows (right). The maximum downflow is $\sim$700 m/s, about a factor of 2 stronger than measured by Dara et al. (1987). In spite of the 4 h integration, the velocity image shows signs of granular convective motions, reminiscent of the "persistent" granulation (Baudin et al., 1997).

The fact that the vertical component of the magnetic field is strong at superganular boundaries does not mean either that the internetwork region is devoid of field or that the field orientation is vertical everywhere. As demonstrated by the magnetogram of **Figure 6**, small magnetic elements are practically everywhere (Title and Schrijver, 1998).

The network is easily visible in the microwave radio range. The first high resolution images, obtained by Kundu et al. (1979) at 6 cm with the Westerbork Synthesis Radio Telescope (WSRT) showed a clear association of the microwave emission with the chromospheric network. This conclusion was subsequently verified with VLA observations at 6 and 20 cm by Gary and Zirin (1988), and Gary et al. (1990) at 3.6 cm. In the mid 90's the VLA was used for QS observations in the short cm-range (1.2, 2.0 and 3.6 cm) by a number of authors (Bastian et al., 1996; Benz et al., 1997; Krucker et al., 1997). In a more recent work, Bogod et al. (2015) reported an almost one-to-one correspondence between the microwave structures observed with RATAN-600 and those seen in the 304 Å AIA band, with a somewhat inferior correlation with the 1600 Å band.

In the mm-range, high-resolution images of the QS were first produced by White et al. (2006) and Loukitcheva et al. (2006), with the 10-element Berkeley-Illinois-Maryland Association Array (BIMA), providing $\sim$ 10″ resolution. With the advent of ALMA, a new collection of high-resolution mm-λ images is accumulating, with some of them presented in **Figure 7**. In all cases the chromospheric network, delineated in UV continuum images or photospheric magnetograms, is the dominant structure

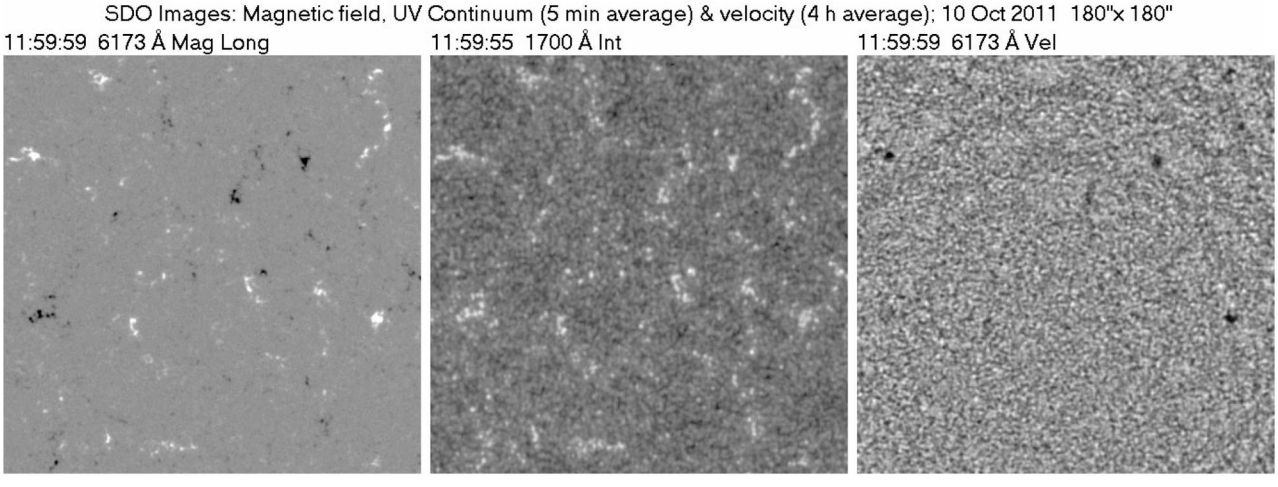

FIGURE 6 | Line of sight magnetic field from HMI/SDO **(Left)**, intensity in the 1700 Å band from AIA/SDO **(Middle)** and line of sight velocity averaged over 4 h from HMI/SDO **(Right)**; downflows are dark, upflows bright. Images produced by the author.

in the quiet sun radio images. The coarse network is also visible in low-resolution full-disk ALMA images, as in Figure 1 of Alissandrakis et al. (2017); at 239 GHz, these authors found best correlation with 1600 Å AIA images.

In addition to the morphology of the radio features, it is important to measure their intensity and size as a function of wavelength. We should note that normal interferometric/synthesis observations cannot measure the background level, which should be provided by other means. Thus, the most appropriate measure of the intensity fluctuations is their amplitude or their rms variation. Such measurements in the cm and mm-λ ranges have been provided by Kundu et al. (1979), Gary and Zirin (1988), Bastian et al. (1996), Benz et al. (1997), Loukitcheva et al. (2009), Nindos et al. (2018), Loukitcheva et al. (2019), and Wedemeyer et al. (2020). In all reported measurements, both the network/cell amplitude and the rms of spatial intensity variations increase with wavelength. Such results can be exploited in multicomponent models (Alissandrakis et al., 2020). Older computations by Chiuderi Drago et al. (1983), based on the Vernazza et al. (1981) model, predicted an increase of brightness difference between network and cell interiors with wavelength, in qualitative agreement with the above results.

5.3. Structure From the Upper Chromosphere to the Low Corona

Above the photosphere, the energy density of the plasma drops fast due to the decrease of the density, whereas the magnetic energy density decreases at a slower rate. Eventually the magnetic field dominates over the plasma in the QS chromosphere and low corona and, as a result, a dramatic change in the morphology of fine structures is observed. Structures of convective origin, such as granules and magnetic bright points give way to elongated structures delineating the lines of force of the magnetic field.

This is illustrated in **Figure 8** where, in addition to the magnetogram of **Figure 6**, images of the same region in the HeII 304 Å and in the FeXII 193 Å lines, formed in the upper chromosphere/low transition region and in the corona respectively, are shown. In addition to the extension of the network, the HeII image shows a multitude of small scale, low-lying loops, mostly in absorption (dark), joining regions of opposite magnetic polarity. Although the appearance of the coronal image is different, loops are still the basic structural element; here they all are in emission (bright), they are not as numerous as in HeII and there is a lot of diffuse emission in between. The latter is probably due to low intensity loops, too thin to be distinguished with the $\sim 1''$, resolving power of the instrument.

Note the absence of any trace of the network in the coronal image. This is well-known from the Skylab era (Reeves et al., 1974): the network becomes diffuse in the upper transition region and disappears in the low corona, apparently as a result of fanning out of the magnetic field and field lines closing at low heights. A similar behavior is expected for the radio network, the main problem here being the variable spatial resolution. However, Bastian et al. (1996) reported no detectable change in the size of network elements between 1.3 and 2 cm, after smoothing the 1.3 cm image to match the 2 cm resolution. There is a lack of imaging observations between 6 and 20 cm; in any case, the few published QS images at 20 cm do not show much of a network (e.g., Gary and Zirin, 1988).

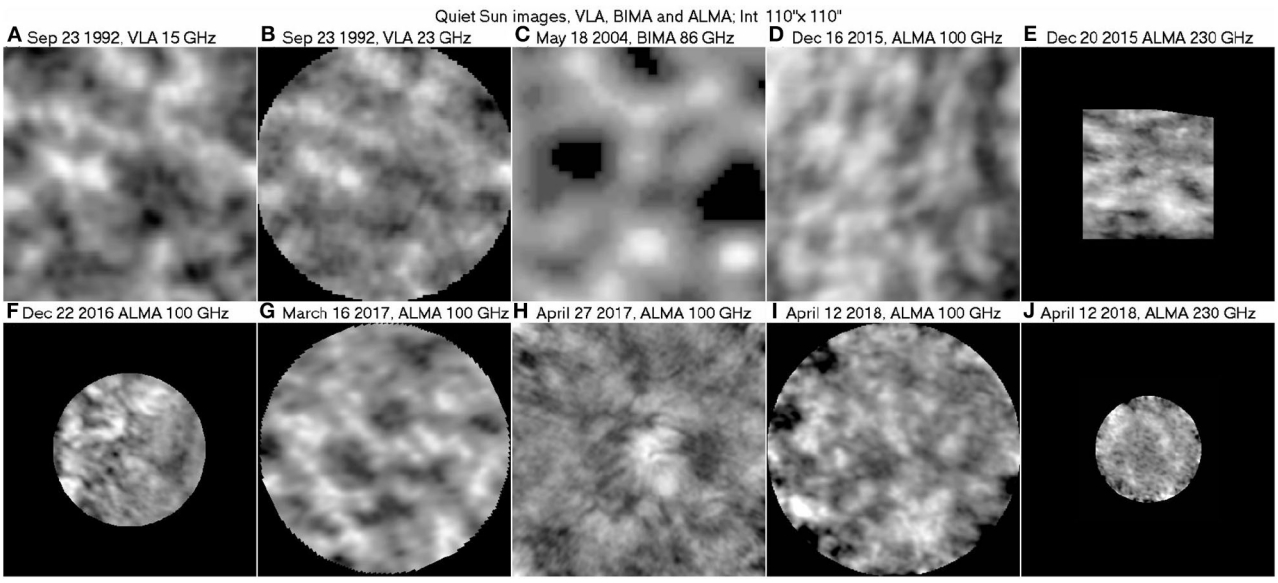

FIGURE 7 | A collection of high-resolution radio images of the quiet Sun from the short cm-λ to the mm-λ range. **(A,B)** are from Bastian et al. (1996), © AAS, reproduced with permission, **(C)** from Loukitcheva et al. (2009), reproduced with permission © ESO, **(D,E)** are from ALMA commissioning, near the East and South limb respectively, **(F)** from Wedemeyer et al. (2020), reproduced with permission © ESO, **(G)** from Nindos et al. (2018), reproduced with permission © ESO, **(H)** from ALMA project 2016.1.00202.S used by Loukitcheva et al. (2019), while **(I,J)** are unpublished, courtesy of A. Nindos. The images have been reprocessed by the author for homogeneity and better visibility.

A more classical picture of the chromospheric fine structure on the disk is shown in the top of **Figure 9**, in the wing and at the center of the Hα line, far from the center of the solar disk. Thin, elongated dark structures, known as *dark mottles*, emerge above the supergranular boundaries. They extend more or less vertically and are best visible in the blue wing of the line, revealing a predominantly upward motion. They are less prominent at the Hα line center where, in addition, fine *bright mottles* appear at their roots.

Seen at the limb, these structures appear as jet-like features (*spicules*, see Secchi, 1875, Beckers, 1968, 1972; Sterling, 2000; Pasachoff et al., 2009, Tsiropoula et al., 2012), well visible in the Hα line and many other chromospheric lines and continua. Spicules have a typical lifetime of ∼10 min; they rise to heights of up to ∼10 000 km with a velocity of ∼ 20 km s^{-1} and then either fall down or diffuse in the corona. A classic spicule image, −1 Å off the Hα line center, is shown in the bottom of **Figure 9**. This was the best image at the time it was taken (1970); today we can have much higher spatial resolution, as evidenced in **Figure 10**, which shows structures as thin as a few tenths of an arc second both on the disk (left) and beyond the limb (right). High resolution imaging from space, together with the improved resolution of ground-based observations, has led to a number of recent investigations both at the limb and on the disk. The new observations revealed the existence of a new type of spicules, *type II spicules* (de Pontieu et al., 2007), which are both faster (∼100 km s^{-1}) and short lived (∼1 min), compared with ordinary spicules. The other domain where new observations

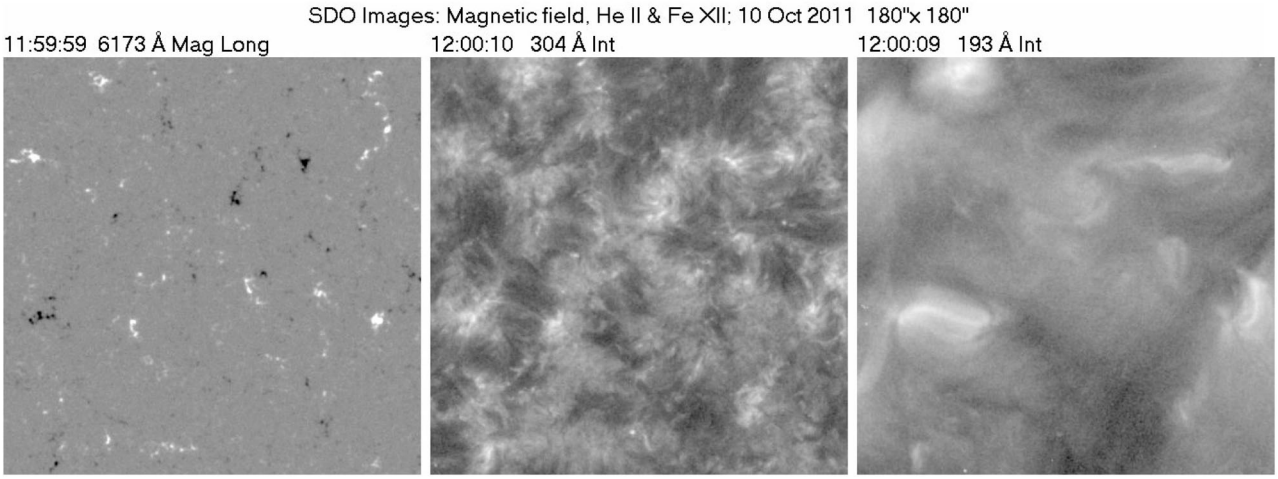

FIGURE 8 | Line of sight magnetic field from HMI/SDO (left), intensity in the HeII 304 Å band (middle) and in the FeXII 193 Å band (right) from AIA/SDO. Same region as in **Figure 6**. Images produced by the author.

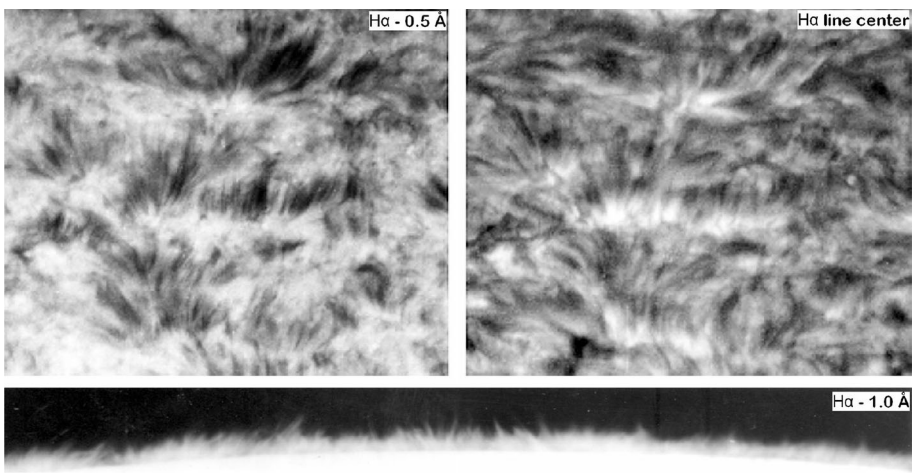

FIGURE 9 | (Top) A chromospheric region far from the center of the solar disk, in the blue wing of Hα (left) and in the center of the line (right). The field of view is 95″ by 80″. Photographs by the author with the 40 cm *Tourelle* refractor at the Pic du Midi Observatory on September 27, 1979. **(Bottom)** Spicules at the limb, in the blue wing the Hα line. Observed by R. D. Dunn with the Vacuum Tower Telescope (now the Dunn Telescope) of the Sacramento Peak Observatory in 1970. Image adapted by the author from a figure published in Lynch et al. (1973).

have had an enormous contribution is spicule oscillations (see Zaqarashvili and Erdélyi, 2009 for details).

Note that the appearance of chromospheric structure in different spectral lines can be quite different, depending on the details of line formation. For example, spicules on the disk are hard to see in any other line except for Hα (see, however, Bose et al., 2019); in other lines and in the EUV continuum one can clearly see the bright emission associated to the network (**Figure 10**, right), as well as *grains*, which represent oscillating elements. Beyond the limb, structures seen in the HeII 304 Å line are much more extended than Hα spicules and are usually referred to as *macrospicules*.

The origin of spicules is still a subject of debate. As disk mottles are clearly associated with the network, a magnetic association is very likely; what is not clear is whether they are a result of reconnection, as suggested a long time ago by Pikel'Ner (1969), see also Samanta et al. (2019), or some other mechanism, such as the leakage of photospheric oscillations expelling plasma along the magnetic field lines, as suggested by De Pontieu et al. (2004). In a recent work, (Martínez-Sykora et al., 2017; see also Carlsson et al., 2019) obtained spicule-like features in a 2.5D radiative MHD simulation. According to these authors, spicules occur when magnetic tension is amplified and transported upward through interactions between ions and neutrals or ambipolar diffusion.

In the pre-ALMA era there has been only one report of structures beyond the limb (Habbal and Gonzalez, 1991) in the microwave range. Still, chromospheric structures have been invoked in the interpretation of the center to limb variation of the intensity, with observations showing less brightening than predicted by homogeneous models. This effect has been interpreted in terms of absorbing features, such as spicules (e.g., Lantos and Kundu, 1972; Selhorst et al., 2005). ALMA observations near the limb (Nindos et al., 2018; Yokoyama et al., 2018; Shimojo et al., 2020) do show spicular structures (**Figure 11**). Although the resolution is still worse than an arc second, such observations are promising for spicule diagnostics. More generally, high resolution images with ALMA can provide excellent diagnostics of the chromosphere, as the observed brightness temperature is directly related to the electron temperature and density.

Another note-worthy observation is that polar regions are brighter than the low-latitude QS at short cm-waves to mm-waves, an effect known as *polar brightening*. We will not discuss this in detail here, but refer the reader to the review by Shibasaki et al. (2011).

5.4. Large Scale Structure of the Corona

The magnetic lines of force of small scale magnetic dipoles, associated with the network magnetic fields, close at relatively low heights (comparable to the distance between the opposite polarities). Thus, the coronal structure is dominated by two types of magnetic configuration: one is the medium and large scale bipolar fields associated with active regions, where the plasma is confined by the magnetic field in medium and large scale loops. The other is the so called *open* magnetic configuration, associated with extended regions of the same polarity; these regions cannot confine the plasma, which expands in the interplanetary medium as the *fast* solar wind and what is left in the corona is just a hole. An example with both closed an open regions in the corona together with the corresponding magnetogram and extrapolated magnetic field lines is presented in **Figure 12**.

As we go to heights where the solar wind attains significant speed, the kinetic energy density of the plasma increases and surpasses the energy density of the magnetic field. Thus, if a closed magnetic configuration extends high enough, the tops of the outer lines of force will be dragged by the solar wind to produce the magnetic configuration of a *streamer* (**Figure 13**, left). Note that an electric current sheet (dashed line in the figure) is formed, separating regions of opposite magnetic polarity (Koutchmy and Livshits, 1992). Streamers are not cylindrically symmetric, as was thought in the past (hence the term *helmet* streamer), but go around the Sun, forming a belt which is often irregular, depending on the complexity of the large scale solar magnetic field; the associated current sheets extends into the interplanetary space, forming the *heliosheet* that separates

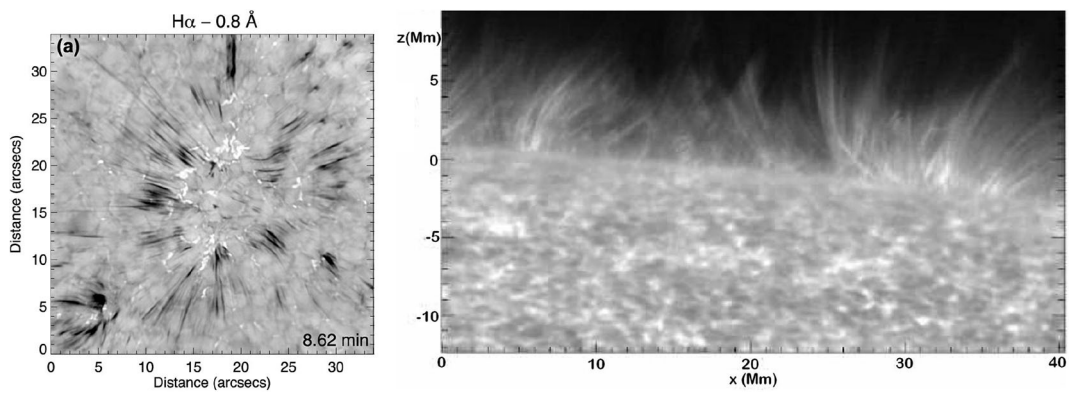

FIGURE 10 | High resolution images of Hα spicules near the center of the disk from the Goode Solar Telescope, Big Bear (left, from Sterling et al., 2020, © AAS, reproduced with permission, based on work by Samanta et al., 2019) and at the limb observed in the CaII H line with the Solar Optical Telescope (SOT) aboard Hinode (right, from Judge and Carlsson, 2010, © AAS, reproduced with permission).

opposite magnetic polarities in the heliosphere. Streamers may also form in more complex (quadrupole) magnetic field configurations (Koutchmy et al., 1994).

The magnetic field lines of force shown in **Figure 12** have been computed under the *current-free assumption*, using the photospheric magnetic field as a lower boundary condition (Schmidt, 1964 in plane geometry; Altschuler and Newkirk, 1969 in spherical geometry and for the entire Sun; see Chapter 5 in Aschwanden, 2004 for a more detailed discussion). In the more general case of the *force free* approximation, the electric current is assumed to flow along the magnetic field, so that Ampère's law, (32), takes the

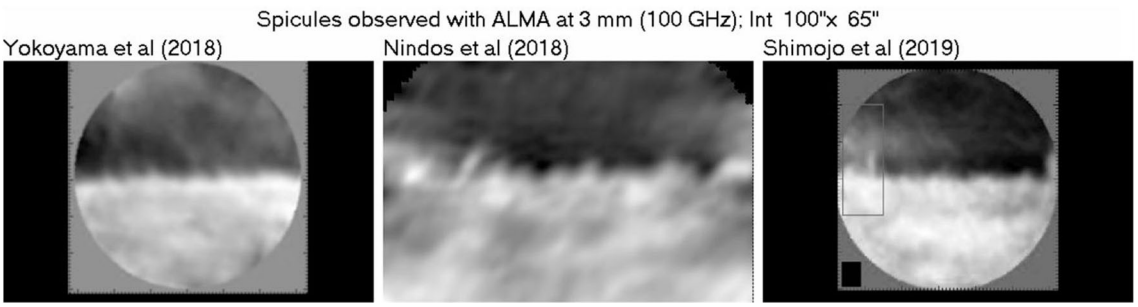

FIGURE 11 | The first ALMA observations of spicules at 100 GHz (3 mm). Images reprocessed by the author for better visibility. The central image is reproduced with permission © ESO, the others are © AAS, reproduced with permission.

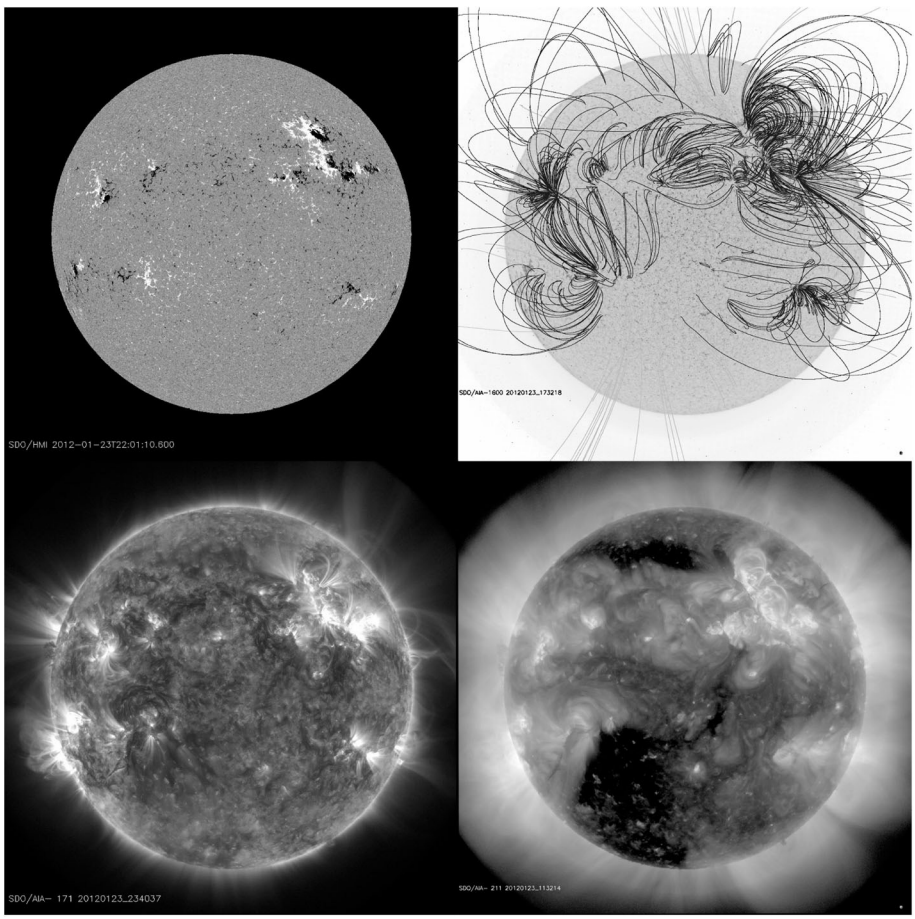

FIGURE 12 | A full disk HMI/SDO magnetogram (top left) with extrapolated magnetic field lines (top right), the upper TR observed in the 171 Å (Fe VIII) band (bottom left) and the corona observed in the 211 Å (Fe XIV) band (bottom right) with AIA/SDO on January 23, 2012. Images adapted from http://suntoday.lmsal.com/suntoday/.

form:

$$\nabla \times \boldsymbol{B} = \alpha \boldsymbol{B} \tag{50}$$

which includes the current-free case ($\alpha = 0$). In this case the Lorentz force vanishes, hence the term force-free. It is easy to prove that α is constant along a magnetic field line, by taking the divergence of (50). If α is assumed constant everywhere, we have the *linear* force free case; this is relatively easy to compute (Alissandrakis, 1981), compared to the non-linear case (Wiegelmann and Sakurai, 2012; Wiegelmann et al., 2017).

One can go further by taking into account the full set of MHD equations, and compute, in addition to the magnetic field, the density of the plasma, as well as the flow velocity in 3 dimensions. An example is shown at the right of **Figure 13**, where the coronal intensity has been computed with the *Magnetohydrodynamic Algorithm outside a Sphere* (MAS) code (Riley et al., 2011; see also Wiegelmann et al., 2017). Despite the fact that the computation is based on magnetic field data over a full solar rotation (26 days), the similarity with the observed corona is remarkable, in particular for large scale structures (such as streamers), which are also long-lived.

The corona is accessible with radio observations in the metric region, but here one has to be content with arc-minute resolution. The first images were obtained with the Culgoora Radioheliograph at 80 MHz (3.75 m) and 160 MHz (1.88 m), followed by the Clark Lake Radioheliograph at 73.8 MHz (4.07 m), 50 MHz (6 m), and 30.9 MHz (9.7 m). The first 2D images from the Nançay Radioheliograph (NRH) were computed by Alissandrakis et al. (1985) at 169 MHz (1.78 m) with 1.2′ by 4.2′ resolution.

The NRH evolved gradually to its present state of 2D synthesis instrument (Kerdraon and Delouis, 1997), providing images at 10 frequencies from 450 to 150 MHz (67 cm to 2 m) with a cadence of 0.25 s. The instantaneous images, however, cannot exploit the full resolution of the system since they only use the densely sampled inner part of the u-v plane. In order to exploit the full resolution one has to resort to full-day synthesis, which improves the resolution by a factor of $\sim$ 2.5. This was done by Marqué (2004) with an emphasis on filament cavities and subsequently by Mercier and Chambe (2009, 2012, 2015), who did a systematic study of the quiet Sun. The NRH covers a broad range of frequencies, the ratio of the maximum to minimum frequency being $\sim$ 3; it can thus probe an altitude range from the upper TR to the low corona. Shibasaki et al., 2011 give some examples of synthesis images from NRH in their **Figure 7**.

Mercier and Chambe (2015) found that the temperature deduced from the hydrostatic scale height (1.5×10^6 K) was too high compared to the brightness temperature of the solar disk (0.60 to 0.65×10^6 K at 150 MHz) and suggested that the electron temperature in the corona (contributing to observed brightness) is lower than the proton temperature (mainly responsible for the hydrostatic scale). More recently, QS images in the decametric range, obtained with the *Low Frequency Array* (LOFAR), were presented by Vocks et al. (2018), in the range of 25 to 79 MHz. They give brightness temperatures of the order of 10^6 K at 54 MHz, which are higher than the values of Mercier and Chambe (2015) and previous measurements given in section 4.3.2; they also deduced high hydrostatic temperatures, up to 2.2×10^6 K. These results show that more work is necessary in order to settle the issue of interpretation of the QS metric-decametric emission. In addition to NRH and LOFAR, the *Murchison Widefield Array* (MWA) have started providing interesting QS data (McCauley et al., 2019; Rahman et al., 2019) with high dynamic range.

Coronal holes are usually observed as brightness depressions in radio wavelengths (e.g., Borovik and Medar, 1999; Lantos and Alissandrakis, 1999). At cm-λ the average brightness temperature in coronal hole regions is not much different from that of the quiet Sun, while at mm-λ it is slightly higher (Gopalswamy et al., 2000), apparently due to the underlying chromosphere and TR, rather than the coronal holes. A number of computations of the coronal hole radio emission (e.g., Borovik et al., 1990; Chiuderi Drago et al., 1999; Pohjolainen, 2000) have been published. Borovik et al. (1990) observed four coronal holes in the wavelength range of 2 to 32 cm with the RATAN-600 telescope and found that the brightness difference between the holes and the QS becomes appreciable at wavelengths longer than $\sim$ 4 cm. In their best-fit models the coronal holes are cooler than the background and less dense by a factor of 2.

The work of Mercier and Chambe (2009) confirmed that, at long dm wavelengths, coronal holes are the most prominent feature; in agreement with previous observations (e.g., Lantos et al., 1987), their contrast decreases at longer wavelengths (see

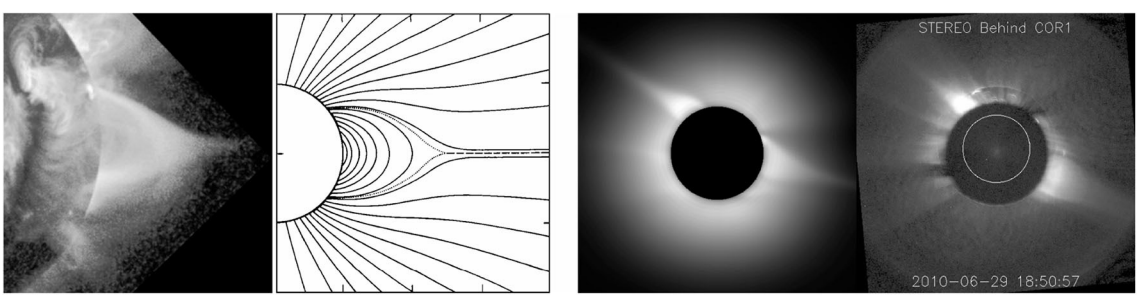

FIGURE 13 | From left to right: A streamer observed with Yohkoh; a schematic drawing of the corresponding magnetic configuration; computed intensity of the corona based on the MAS code; the corresponding image of the COR1 coronograph aboard STEREO-B, on June 29, 2010. From http://www.predsci.com/stereo/home.php.

the hole near the center of the disk in Figure 3 of Mercier and Chambe, 2009). At decameter waves coronal holes are sometimes seen in emission (Dulk and Sheridan, 1974; Lantos et al., 1987; Rahman et al., 2019). A possible interpretation is in terms of refraction effects (Alissandrakis, 1994, *c.f.* Figure 3 of Lantos, 1999) and/or scattering in inhomogeneities; a similar conclusion was reached by Rahman et al. (2019). In addition, these authors computed metric solar images using parameters derived from the MAS code (see above) and found qualitative similarities with high frequency observations, but could not reproduce the dark-to-bright transition at low frequencies. McCauley et al. (2019) measured the polarization of coronal holes and reported values up to 5–8%; they also reported a "bullseye" polarization structure, in which one polarization sense is surrounded by a full or partial ring of the opposite sense (see their **Figure 7**).

In a systematic study of emission sources observed with the NRH at 169 MHz, Lantos and Alissandrakis (1999) came to the conclusion that the large scale emission is dominated by the *coronal plateau*. This is an intermediate brightness region forming a belt around the Sun and surrounding almost all local emission sources (Lantos et al., 1992). It is visible both in daily images and in synoptic charts, and has a close association with enhanced emission of the K-corona, delineating the base of the coronal plasma sheet. The diffuse emission of the *coronal plateau* could be due to a high altitude loop system which overrides the principal neutral line of the general solar magnetic field at the base of the heliosheet, with a possible contribution of loops connecting active regions to surrounding quiet areas.

Coronal streamers are best visible at decametric wavelengths (Lantos, 1999). They are less prominent in the meter and decimeter ranges, where one sees loops at the base of streamers rather than proper streamers, as pointed out in the previous paragraph. From the circularly polarized thermal emission of streamers observed with the Gauribidanur radioheliograph at 77 and 109 MHz, Ramesh et al. (2010) estimated magnetic field strengths in the range of 5 – 6 G at 1.5 – 1.7 $R_\odot$.

5.5. Filaments and Prominences

The configuration of the magnetic field above neutral lines of the magnetic field is such that, under certain topologies, it can sustain clouds of material of chromospheric temperature and density against gravity and thermally isolate them from the hot corona. In chromospheric lines and on the solar disk, these clouds appear in absorption as *filaments*; projected beyond the solar disk, they appear in emission as *prominences* (see reviews by Labrosse et al., 2010 and Mackay et al., 2010).

At decimeter-meter wavelengths (Marqué, 2004), as well as in the mm and cm range (Irimajiri et al., 1995) large filaments are observed as regions of lower brightness temperature on the solar disk. Beyond the limb filaments are seen in emission, projected against the sky; in this case it is possible to calculate electron temperatures and densities using multi-frequency radio observations (Irimajiri et al., 1995). Filaments, filament cavities and prominences show well in full-disk ALMA images at 1.25 and 3 mm (see, e.g., Figure 1 in Alissandrakis et al., 2017).

A set of simultaneous observations of a filament in the microwave range and in the EUV was analyzed by Chiuderi Drago et al. (2001). The authors concluded that the depression at radio wavelengths is due to the lack of coronal emission; the same data favored a prominence model with cool threads embedded in the hot coronal plasma, enveloped by a sheath-like TR, and a filling factor varying from about 3 to 4%.

A systematic study of filaments and their environment in the metric radio range was presented by Marqué (2004). He used NRH observations primarily at 410.5 MHz, pointing out that the visibility of filament associated radio depressions is rather poor at lower frequencies. He concluded that the most likely source of the radio depression is the cavity (electron density depletion) that surrounds the filament. In cm and mm wavelengths contradictory results have been reported on the contribution of the cavity to the observed radio depression (Kundu and McCullough, 1972; Raoult et al., 1979).

6. ACTIVE REGIONS

Active Regions appear in the photosphere as roughly bipolar magnetic regions of intermediate scale ($\sim 0.2 R_\odot$, or $\sim 1.5 \times 10^5$ km). Sunspots, associated with strong magnetic fields (above $\sim$1000 G), are their primary manifestation in the photosphere, bright *plage* emission, associated with intermediate magnetic fields, prevails in the chromospheric layers together with elongated *fibrils* (Foukal, 1971; Kianfar et al., 2020), indicating a more organized magnetic field compared to the QS, while impressive loops mark their presence in the corona. They are accompanied by all sorts of dynamic phenomena, most notably flares and Coronal Mass Ejections (CMEs).

Active regions are the result of emergence of large quantities of magnetic flux from the subphotospheric layers, a result of *magnetic buoyancy* (see, e.g., Parker, 1955; Priest, 1987; Rempel and Schlichenmaier, 2011) and disappear as their magnetic flux is spread out due to convective motions or canceled near polarity inversion lines.

Figure 14 shows images of an active region from the photosphere to the low corona, during its emergence and development phase, as the region crosses the solar disk. Concentrating on the radio emission, we note that in the 17 GHz images of July 30, as well as of August 2 and 4 show the classic two components of sunspot and plage associated emission, identified for the first time by Kundu (1959) with a 2-element interferometer and imaged by Kundu and Alissandrakis (1975) with the Westerbork Synthesis Radio Telescope. Since that time many observations and models have been published (see reviews by Gelfreikh, 1998 and Lee, 2007). It is well-established that the sunspot, or core component of the emission, observed in the microwave range, is due to the gyroresonance process (Kakinuma and Swarup, 1962; Zheleznyakov, 1962; Alissandrakis et al., 1980), whereas the plage, or halo component is due to free-free emission.

Going back to **Figure 14**, note that no sunspot component is visible at 17 GHz on the other days, apparently due to the low value of the sunspot field with regard to the observing frequency. Note also that on July 26 and 28, emission as strong as the sunspot emission is observed, probably associated with hot coronal loops seen in the 335 Å, (FeXVI) band. This is reminiscent of the *neutral line sources* reported by Kundu et al. (1977), see also Uralov et al. (2008) and references therein, and attributed to a quasi-steady, low density population of non-thermal electrons (Alissandrakis et al., 1993).

At longer wavelengths a *decimetric halo component* of non-thermal nature has been reported (Gelfreikh, 1998), while at even longer decimetric and metric wavelengths no sunspot-associated emission is visible, presumably due to the high opacity of the overlaying plasma and refraction effects; we do see, however, non-thermal noise-storm sources in the vicinity of active regions.

The microwave emission of active regions is a powerful diagnostic of the magnetic field in the transition region and the low corona. The magnetic field determines the emissivity of gyroresonance process above sunspots, of the free-free process above plages, as well as the circular polarization inversion higher up. In addition to the magnetic field, sunspot-associated emission can provide information about the temperature and density structure of the sunspot atmosphere (Nindos et al., 1996; Korzhavin et al., 2010; Nita et al., 2018; Stupishin et al., 2018; Alissandrakis et al., 2019). Let us also mention in passing the detection and study of sunspot oscillations (Gelfreikh et al., 1999; Nindos et al., 2002) and refer the reader to the review by Nindos and Aurass (2007) for more details. We also refer the reader to the reviews by Solanki (2003) and by Rempel and Schlichenmaier (2011) for extensive descriptions of sunspots.

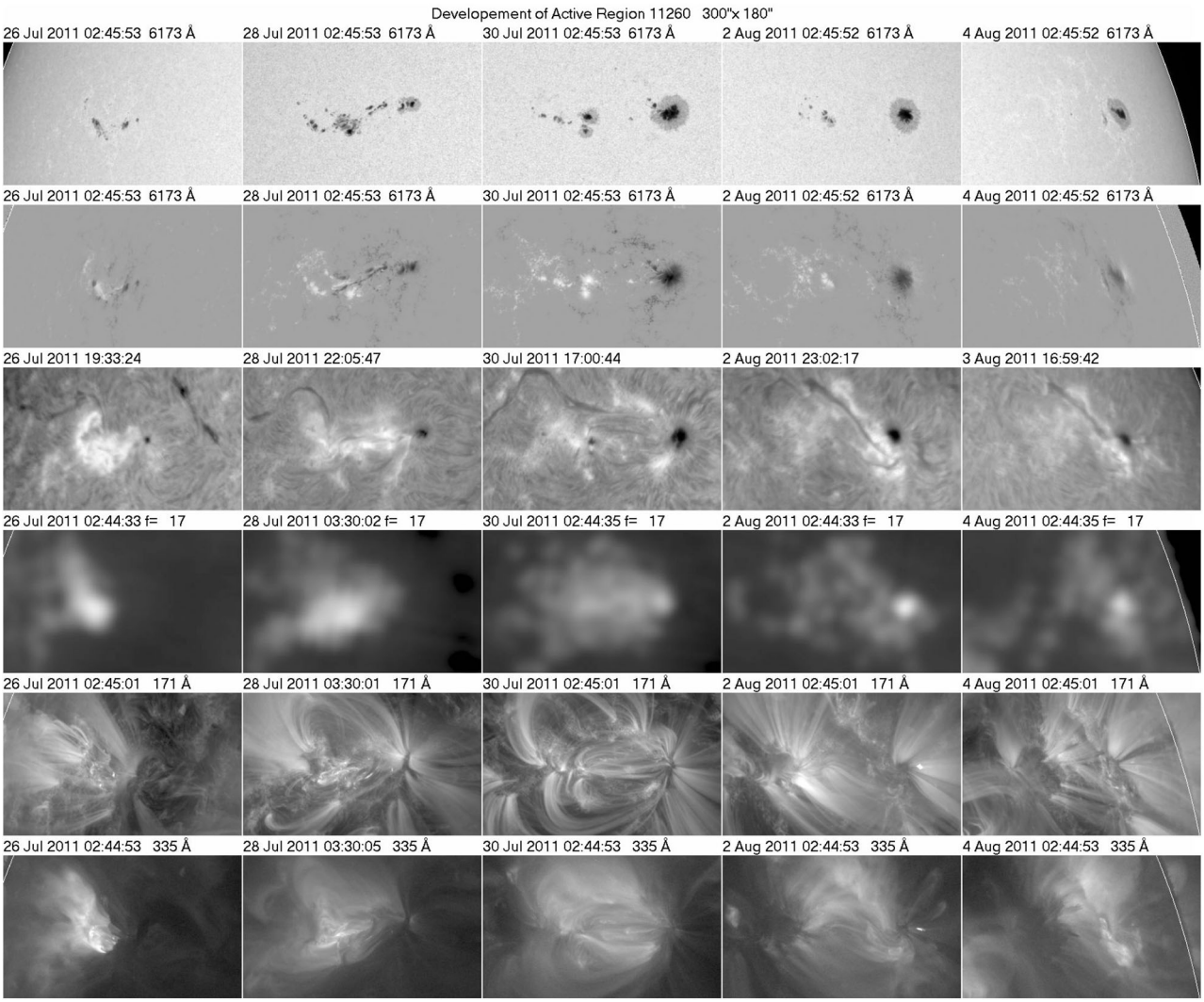

FIGURE 14 | Development of Active Region 11260 during its passage on the solar disk. Sunspots and magnetograms from HMI/SDO, Hα images from Big Bear, Nobeyama images at 17 GHz and AIA/SDO images in the 171 Å (FeIX, log $T \sim 5.8$), and 335 Å (FeXVI, log $T \sim 6.4$) bands. The region crossed the central meridian on July 30, ~9 UT. The white arc marks the photospheric limb. Figure prepared by the author.

7. HEATING OF THE CHROMOSPHERE AND THE CORONA

7.1. The Problem

Elementary thermodynamics tells us that you cannot transfer energy from a cold body to a hot body through radiation, conduction or convection. How do you then explain the temperature minimum and the subsequent temperature rise in the chromosphere and the corona and the energy carried away by the solar wind? The obvious answer is that you have to transport energy from below by mechanical means. As for the amount of energy required, this is of the order of 4×10^6 erg cm^{-2} s^{-1} for the quiet chromosphere and about a factor of 10 lower for the quiet corona (Withbroe and Noyes, 1977).

The first answer to the heating problem was proposed more than 70 years ago, by Schwarzschild (1948) and by Schatzman (1949): the chromosphere and the corona are heated by the dissipation of shock waves, originating as acoustic waves in the noise produced by the granulation and steepened as they propagate upwards in regions of decreasing density. The discovery of the 5-min oscillations gave a boost to this idea, still other ideas, more promising, have been advanced. In what follows we will discuss some concepts and constrains with regard to the heating problem. Obviously, we cannot be exhaustive, so we refer the reader to Chapter 6 of Priest (1987), Chapter 9 of Aschwanden (2004) and reviews by Withbroe and Noyes (1977), Walsh and Ireland (2003), Klimchuk (2006), Erdélyi and Ballai (2007), Cranmer and Winebarger (2019) and Carlsson et al. (2019).

First of all, the question is not that of bulk heating, as the upper solar atmosphere is highly structured (section 5). In the chromosphere, for example, we need to supply more energy to the network, which is brighter, more dense and more dynamic than the internetwork regions. In the corona, each individual flux tube has its own energy requirement. A loop will become visible in a particular spectral line, if it contains enough plasma at the appropriate temperature; this plasma presumably comes from the chromosphere, through evaporation induced by the deposition of energy somewhere in the loop. Open flux tubes in coronal holes must also be heated, both for their own sake and in order to provide energy to the plasma that makes the fast solar wind. Note also that coronal heating requirements vary during the solar cycle, as evidenced by the great variations in X-ray brightness revealed by Yohkoh images (see, e.g., Takeda et al., 2019). Thus, the problem is not just to have an abundance of wave or some other form of mechanical energy, but mainly to transport and dissipate the energy at the proper place and at the proper time.

The magnetic field plays the primary role in determining the structure of the upper atmosphere (section 5); we also expect the magnetic field to influence the propagation of acoustic waves and, in addition, to provide plenty of additional wave modes. Wave heating, which is commonly referred to as *AC heating*, is not the only possibility. At the photospheric level, magnetic flux tubes (section 5.3) are known to be in continuous motion, as shown in **Figure 15**, in response to horizontal convective flows. As a result waves could be excited but, what is probably more important, the magnetic lines of force, which extend up in the chromosphere and the corona, will become tangled, accumulating magnetic energy in innumerable current sheets. This magnetic energy cannot accumulate *in perpetuo*, it will eventually be converted to heat (*DC heating*) in the course of reconnection, either through Joule dissipation (Equation 46), or through collisionless processes. Note that these processes could also accelerate particles that will eventually depose their energy in the plasma; these particles should have observable consequences both in the radio and the hard X-ray range.

Reconnection mechanisms have been invoked to explain energy release in flares, hence the concept of *nanoflare heating*, first proposed by Parker (1988). Nanoflares are impulsive by nature and are expected to occur in elemental flux tubes that are below the resolution limit of present-day instruments. Impulsiveness is not limited to nanoflares, but may characterize AC heating as well (Klimchuk, 2006).

A radically different approach has been advanced by Scudder (1992), that the coronal plasma originates from suprathermal particles in the transition region, which have enough energy to overcome gravity (velocity filtration). However, this model requires a mechanism to produce the suprathermal particles as well as collisionless conditions, of which none is proven.

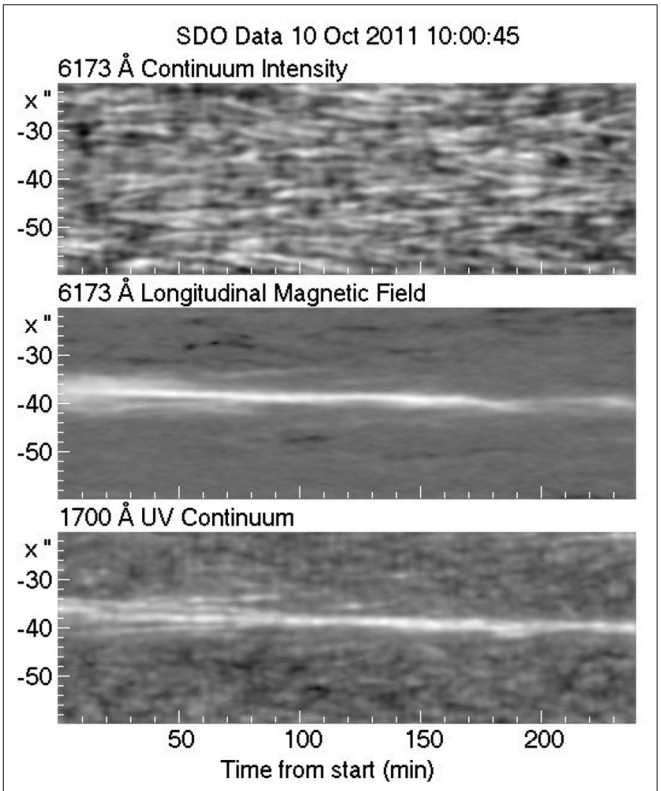

FIGURE 15 | Position (vertical axis) - time (horizontal axis) cuts through a magnetic element. Granular motions are clearly visible in the top panel; the middle and the bottom panels show the motion of the magnetic element and the corresponding bright point in the 1700 Å band. A low pass filter has been applied in the time domain to reduce the effect of the 5 min oscillations. Figure prepared by the author from SDO data.

Although we have plenty of mechanisms, we have no answer yet as to which mechanism(s) may operate and in which case. As a matter of fact, we have plenty of negative answers. It is encouraging that there is sufficient energy associated with the granulation noise, as already pointed out by Schatzman (1949) and also in the random motion of magnetic flux tubes (Alissandrakis and Einaudi, 1997; Klimchuk, 2006), but this is not enough, as pointed up above, since this energy must be directed to the right place at the right time. Nanoflare heating is certainly attractive, but it evades observational confirmation so far. Several authors have computed histograms of the energy distribution in impulsive events, including microflares observed in abundance with RHESSI and other missions (Hannah et al., 2011); the extrapolation to low energies only gave negative results as far as heating is concerned. Acoustic wave heating has been a favorite for the non-magnetic chromosphere, but it appears that the appropriate waves do not carry enough energy (Fossum and Carlsson, 2005). Other types of waves, such as Alfvén waves in the presence of turbulence (van Ballegooijen et al., 2011), might help; in this context, the recently reported kink-backs in the solar wind magnetic field (Kasper et al., 2019) observed by the Parker Solar Probe, might have a bearing.

Let us finally note that, in addition to heating the upper chromosphere, one has to replenish the corona with the mass lost through the solar wind. This is not considered a problem since, as it has been shown a long time ago (Beckers, 1972), spicules that diffuse into the corona carry more mass than is actually required.

7.2. Pertinent Radio Data

We will now summarize radio observations that might have a bearing to the heating problem (see also Alissandrakis and Einaudi, 1997 and Shibasaki et al., 2011). Radio fine structures show time variability comparable to that of the chromospheric network, on time scales of minutes to hours (Erskine and Kundu, 1982; Bastian et al., 1996). Apart from that, it is important to check for oscillatory behavior, which could be a signature of shock waves heating the upper solar atmosphere. White et al. (2006) reported intensity oscillations at 3.5 mm with rms brightness variation of 50–150 K and periods of 3 to 5 min (frequencies of 3.3 to 5.5 mHz). In a recent work with ALMA, Patsourakos et al. (2020) observed oscillations at 3 mm, with frequencies of 4.2 ± 1.7 mHz and rms variation of 55 to 75 K.

A number of authors have looked for impulsive/transient events that might have a bearing on the heating of the upper atmosphere (Gary et al., 1997; Krucker et al., 1997; Benz and Krucker, 1999; Krucker and Benz, 2000). Transient brightenings are observed in microwaves both within and well-away from active regions and both thermal and non-thermal emission mechanisms have been suggested (White et al., 1995; Nindos et al., 1999); it thus seems that electrons are accelerated to non-thermal energies even in the quiet solar atmosphere. There appears to be a continuity between bursts, the radio counterparts of X-ray bright points (see Keller and Krucker, 2004 and references therein), and smaller transient events. In a recent work, Nindos et al. (2020) reported non-impulsive transients from 3 mm ALMA observations, providing $\sim$ 1% of the energy of chromospheric losses. Moreover, Mondal et al. (2020) detected a large number of low intensity impulsive QS emissions with the MWA in the frequency range of 98 to 160 MHz, that might be signatures of heating events.

We may conclude that radio observations can provide important input to the problem of the heating of the chromosphere and the corona, both in the wave and nano-flare heating scenarios. Instruments with dense coverage of the u-v plane as well as improved image reconstruction techniques are necessary, in order to provide accurate instantaneous images of regions with complex structure.

8. FINAL COMMENTS

In addition to being our source of life, the Sun is also the nearest star (hence the stellar prototype) and an immense laboratory of plasma physics. During the last few decades we have accumulated a tremendous amount of knowledge on how the Sun operates and how it affects our daily life, thanks to the development of new instruments, both ground-based and space- borne, and the advances in the theory and numerical simulations.

An important ingredient of the recent progress is the exploitation of information from all spectral ranges. The radio domain is a basic source of information. In this respect, it is in synergy rather than in competition with the EUV and X-ray domains which also provide information about the same layers of the solar atmosphere and for the same phenomena. We should stress, however, that the interpretation of radio data, at least for the Quiet Sun and a good part of active phenomena, is straight forward; it is not plagued by non-LTE effects, uncertainties in excitation and ionization equilibrium and abundances, as are other wavelength ranges. The weakness of radio is the low spatial resolution, but this can be overcome with large synthesis instruments, without having to go to space. There are several such projects under development. Among this new generation of radio instruments, LOFAR has already provided very interesting new results, ALMA is entering dynamically into the field, the *Expanded Owens Valley Solar Array* (EOVSA) has started providing nice spectral imaging data, the MWA is giving interesting QS data, the *Siberian Radioheliograph* (SRH) is starting, the Chinese *Mingantu Ultrawide Spectral Radioheliograph* (MUSER) is in operation, the *next generation VLA* (ngVLA) is under consideration, while the *Square Kilometer Array* (SKA) is not too far below the horizon.

What can we expect to learn about the QS from those new instruments? Here is a partial list, reflecting the views of the author and by no means exhaustive:

- Better diagnostics of the physical conditions in all structures of the solar upper atmosphere.
- Better atmospheric models, both in the classic radial/multi-component approach and in the context of radiative MHD; among others, differences between network and cell interior conditions, as well as conditions in spicules and small-scale dynamic events, will be better measured and understood.
- Measurement of the temperature amplitude of chromospheric oscillations as a function of height.

- Improved understanding and modeling of the large-scale magnetic field in the corona.
- Filaments, filament cavities and prominences will be better diagnosed and modeled.
- Better diagnostics and understanding of the active region atmosphere.
- Better understanding of the QS emission at metric wavelengths and reconciliation with optical data.
- If nanoflares have any bearing to chromospheric/coronal heating, the energetic electrons produced should have observable signatures somewhere in the radio range.
- Last but not least, there will be new, unpredictable, discoveries as is usually the case when novel instruments become operational.

As it is always the case, as we learn more, old questions are answered, at least partially, and new questions emerge. With the new instrumentation currently under development and the continued effort on the theoretical side, we will certainly give important results in the next few years.

AUTHOR CONTRIBUTIONS

The author confirms being the sole contributor of this work and has approved it for publication.

ACKNOWLEDGMENTS

This review is based on a presentation to a CESRA summer school on solar radio physics. The author would like to thank Dr. L. Klein of Meudon observatory for organizing the school and for comments on an early version of the manuscript. This work makes use of the following ALMA data: ADS/JAO.ALMA#2011.0.00020.SV and ADS/JAO.ALMA2016.1.00202.S. ALMA is a partnership of ESO (representing its member states), NSF (USA) and NINS (Japan), together with NRC (Canada) and NSC and ASIAA (Taiwan), and KASI (Republic of Korea), in cooperation with the Republic of Chile. The Joint ALMA Observatory is operated by ESO, AUI/NRAO, and NAOJ. In preparing this review the author used publicly available data from a number of instruments: the *Nobeyama Radioheliograph* (NoRH), the *Siberian Solar Radio Telescope* (SSRT), the *Mauna Loa Solar Observatory* (MLSO), the *Big Bear Solar Observatory* (BBSO), the *Yohkoh* mission, the Solar Terrestrial Environment Observatory (STEREO), the *Helioseismic and Magnetic Imager* (HMI) and the *Atmospheric Imaging Assembly* (AIA) aboard the *Solar Dynamics Observatory* (SDO), the *Predictive Science Inc.* website (http://www.predsci.com/stereo/home.php) and the *Sun Today* website (http://suntoday.lmsal.com/suntoday/). I am grateful to all those that operate these instruments and make their data available to the community.

REFERENCES

Ahmad, Q. R., Allen, R. C., Andersen, T. C., Anglin, J. D., Barton, J. C., Beier, E. W., et al. (2002). Direct evidence for neutrino flavor transformation from neutral-current interactions in the sudbury neutrino observatory. *Phys. Rev. Lett.* 89:011301. doi: 10.1103/PhysRevLett.89.011301

Alissandrakis, C. E. (1981). On the computation of constant alpha force-free magnetic field. *Astron. Astrophys.* 100, 197–200.

Alissandrakis, C. E. (1994). Radio observations of the quiet solar corona. *Adv. Space Res.* 14, 81–91.

Alissandrakis, C. E., Bogod, V. M., Kaltman, T. I., Patsourakos, S., and Peterova, N. G. (2019). Modeling of the sunspot-associated microwave emission using a new method of dem inversion. *Solar Phys.* 294:23. doi: 10.1007/s11207-019-1406-x

Alissandrakis, C. E., and Einaudi, G. (1997). "Radio observations of the quiet sun and their implications on coronal heating," in *Coronal Physics from Radio and Space Observations, Lecture Notes in Physics*, Vol. 483, ed G. Trottet (Springer), 53. doi: 10.1007/BFb0106451

Alissandrakis, C. E., and Gary, D. E. (2020). Radio measurements of the magnetic field in the solar chromosphere and the corona. *Front. Astron. Space Sci.* doi: 10.3389/fspas.2020.591075

Alissandrakis, C. E., Gel'Frejkh, G. B., Borovik, V. N., Korzhavin, A. N., Bogod, V. M., Nindos, A., et al. (1993). Spectral observations of active region sources with RATAN-600 and WSRT. *Astron. Astrophys.* 270, 509–515.

Alissandrakis, C. E., Kundu, M. R., and Lantos, P. (1980). A model for sunspot associated emission at 6 CM wavelength. *Astron. Astrophys.* 82, 30–40.

Alissandrakis, C. E., Lantos, P., and Nicolaidis, E. (1985). Coronal structures observed at metric wavelengths with the Nançay radioheliograph. *Solar Phys.* 97, 267–282.

Alissandrakis, C. E., Nindos, A., Bastian, T. S., and Patsourakos, S. (2020). Modeling the quiet Sun cell and network emission with ALMA. *Astron. Astrophys.* 640:A57. doi: 10.1051/0004-6361/202038461

Alissandrakis, C. E., Patsourakos, S., Nindos, A., and Bastian, T. S. (2017). Center-to-limb observations of the sun with alma. Implications for solar atmospheric models. *Astron. Astrophys.* 605:A78. doi: 10.1051/0004-6361/201730953

Allen, C. W. (1947). Interpretation of electron densities from corona brightness. *Mon. Notices R. Astron. Soc.* 107:426.

Altschuler, M. D., and Newkirk, G. (1969). Magnetic fields and the structure of the solar corona. I: methods of calculating coronal fields. *Solar Phys.* 9, 131–149.

Appourchaux, T., Belkacem, K., Broomhall, A. M., Chaplin, W. J., Gough, D. O., Houdek, G., et al. (2010). The quest for the solar g modes. *Astron. Astrophys. Rev.* 18, 197–277. doi: 10.1007/s00159-009-0027-z

Appourchaux, T., and Corbard, T. (2019). Searching for g modes. II. Unconfirmed g-mode detection in the power spectrum of the time series of round-trip travel time. *Astron. Astrophys.* 624:A106. doi: 10.1051/0004-6361/201935196

Aschwanden, M. J. (2004). *Physics of the Solar Corona. An Introduction*. Chichester; Berlin: Praxis Publishing Ltd.; Springer-Verlag.

Athay, R. G. (1971). "The chromosphere-corona transition region," in *Physics of the Solar Corona, Vol. 27 of Astrophysics and Space Science Library*, ed C. J. Macris (Dordrecht: Reidel), 36. doi: 10.1007/978-90-277-0204-3_4

Aubier, M., Leblanc, Y., and Boischot, A. (1971). Observations of the quiet Sun at decameter wavelengths - Effects of scattering on the brightness distribution. *Astron. Astrophys.* 12:435.

Bastian, T. S. (1994). Angular scattering of solar radio emission by coronal turbulence. *Astrophys. J.* 426:774.

Bastian, T. S., Dulk, G. A., and Leblanc, Y. (1996). High-resolution microwave observations of the quiet solar chromosphere. *Astrophys. J.* 473:539.

Bastian, T. S., Ewell, M. W., J., and Zirin, H. (1993). The center-to-limb brightness variation of the sun at lambda = 850 microns. *Astrophys. J.* 415:364.

Basu, S. (2016). Global seismology of the Sun. *Liv. Rev. Solar Phys.* 13:2. doi: 10.1007/s41116-016-0003-4

Basu, S., Christensen-Dalsgaard, J., Chaplin, W. J., Elsworth, Y., Isaak, G. R., New, R., et al. (1997). Solar internal sound speed as inferred from combined BiSON and LOWL oscillation frequencies. *Mon. Notices R. Astron. Soc.* 292, 243–251.

Baudin, F., Molowny-Horas, R., and Koutchmy, S. (1997). Granulation and magnetism in the solar atmosphere. *Astron. Astrophys.* 326, 842–850.

Beckers, J. M. (1968). Solar Spicules (Invited Review Paper). *Solar Phys.* 3, 367–433.

Beckers, J. M. (1972). Solar Spicules. *Annu. Rev. Astron. Astrophys.* 10:73.

Bellot Rubio, L. and Orozco Suárez, D. (2019). Quiet Sun magnetic fields: an observational view. *Liv. Rev. Solar Phys.* 16:1. doi: 10.1007/s41116-018-0017-1

Benz, A. O., and Krucker, S. (1999). Heating events in the quiet solar corona: multiwavelength correlations. *Astron. Astrophys.* 341, 286–295.

Benz, A. O., Krucker, S., Acton, L. W., and Bastian, T. S. (1997). Fine structure of the X-ray and radio emissions of the quiet solar corona. *Astron. Astrophys.* 320, 993–1000.

Bisi, M. M., Jackson, B. V., Breen, A. R., Dorrian, G. D., Fallows, R. A., Clover, J. M., et al. (2010). Three-dimensional (3-D) reconstructions of EISCAT IPS velocity data in the declining phase of solar cycle 23. *Solar Phys.* 265, 233–244. doi: 10.1007/s11207-010-9594-4

Bogod, V. M., Alissandrakis, C. E., Kaltman, T. I., and Tokhchukova, S. K. (2015). Ratan-600 observations of small-scale structures with high spectral resolution. *Solar Phys.* 290, 7–20. doi: 10.1007/s11207-014-0526-6

Borovik, V. N., Kurbanov, M. S., Livshits, M. A., and Ryabov, B. I. (1990). Coronal holes on the background of the quiet sun - Analysis of RATAN-600 observations in the 2-32-cm range. *Astron. Z.* 67, 1038–1052.

Borovik, V. N., and Medar, V. G. (1999). "Coronal holes at microwaves as based on observations with the RATAN-600 radiotelescope," in *8th SOHO Workshop: Plasma Dynamics and Diagnostics in the Solar Transition Region and Corona*, volume 446 of *ESA Special Publication*, eds J. C. Vial and B. Kaldeich-Schü, 185.

Bose, S., Henriques, V. M. J., Joshi, J., and Rouppe van der Voort, L. (2019). Characterization and formation of on-disk spicules in the Ca II K and Mg II k spectral lines. *Astron. Astrophys.* 631:L5. doi: 10.1051/0004-6361/201936617

Bray, R. J., and Loughhead, R. E. (1967). *The Solar Granulation*. London: Chapman & Hall.

Carlsson, M. (2007). "Modeling the solar chromosphere," in *The Physics of Chromospheric Plasmas*, Vol. 368 of *Astronomical Society of the Pacific Conference Series*, eds P. Heinzel, I. Dorotovič, and R. J. Rutten (San Francisco, CA), 49.

Carlsson, M., De Pontieu, B., and Hansteen, V. H. (2019). New view of the solar chromosphere. *Annu. Rev. Astron. Astrophys.* 57, 189–226. doi: 10.1146/annurev-astro-081817-052044

Charbonneau, P. (2010). Dynamo models of the solar cycle. *Liv. Rev. Solar Phys.* 7:3. doi: 10.12942/lrsp-2010-3

Chiuderi Drago, F., Alissandrakis, C. E., Bastian, T., Bocchialini, K., and Harrison, R. A. (2001). Joint EUV/Radio observations of a solar filament. *Solar Phys.* 199, 115–132. doi: 10.1023/A:1010390726242

Chiuderi Drago, F., Kundu, M. R., and Schmahl, E. J. (1983). Network to cell contrast at microwaves. *Solar Phys.* 85, 237–242.

Chiuderi Drago, F., Landi, E., Fludra, A., and Kerdraon, A. (1999). EUV and radio observations of an equatorial coronal hole. *Astron. Astrophys.* 348, 261–270.

Christensen-Dalsgaard, J. (2002). Helioseismology. *Rev. Mod. Phys.* 74, 1073–1129. doi: 10.1103/RevModPhys.74.1073

Cranmer, S. R., and Winebarger, A. R. (2019). The properties of the solar corona and its connection to the solar wind. *Annu. Rev. Astron. Astrophys.* 57, 157–187. doi: 10.1146/annurev-astro-091918-104416

Dara, H. C., Alissandrakis, C. E., and Koutchmy, S. (1987). Small-scale motions over concentrated magnetic regions of the quiet Sun. *Solar Phys.* 109, 19–29.

Davis, R. (2003). Nobel Lecture: a half-century with solar neutrinos. *Rev. Mod. Phys.* 75, 985–994. doi: 10.1103/RevModPhys.75.985

de la Cruz Rodríguez, J., Leenaarts, J., Danilovic, S., and Uitenbroek, H. (2019). STiC: a multiatom non-LTE PRD inversion code for full-Stokes solar observations. *Astron. Astrophys.* 623:A74. doi: 10.1051/0004-6361/201834464

De Pontieu, B., Erdélyi, R., and James, S. P. (2004). Solar chromospheric spicules from the leakage of photospheric oscillations and flows. *Nature* 430, 536–539. doi: 10.1038/nature02749

de Pontieu, B., McIntosh, S., Hansteen, V. H., Carlsson, M., Schrijver, C. J., Tarbell, T. D., et al. (2007). A tale of two spicules: the impact of spicules on the magnetic chromosphere. *Publ. Astron. Soc. Jpn.* 59:S655. doi: 10.1093/pasj/59.sp3.S655

de Wijn, A. G., Stenflo, J. O., Solanki, S. K., and Tsuneta, S. (2009). Small-scale solar magnetic fields. *Space Sci. Rev.* 144, 275–315. doi: 10.1007/s11214-008-9473-6

Dulk, G. A., and Sheridan, K. V. (1974). The structure of the middle corona from observations at 80 and 160 MHz. *Solar Phys.* 36, 191–202.

Dunn, R. B., and Zirker, J. B. (1973). The Solar Filigree. *Solar Phys.* 33, 281–304.

Dupree, A. K., and Goldberg, L. (1967). Solar abundance determination from ultraviolet emission lines. *Solar Phys.* 1, 229–241.

Durrant, C. J. (1988). *The Atmosphere of the Sun*. Bristol: Hilger.

Edlén, B. (1943). Die Deutung der Emissionslinien im Spektrum der Sonnenkorona. Mit 6 Abbildungen. *Z. Astrophys* 22:30.

Engvold, O., Vial, J.-C., and Skumanich, A. (2019). *The Sun as a Guide to Stellar Physics*. Elsevier. doi: 10.1016/C2017-0-01365-4

Erdélyi, R., and Ballai, I. (2007). Heating of the solar and stellar coronae: a review. *Astron. Nachrichten* 328, 726–733. doi: 10.1002/asna.200710803

Erskine, F. T., and Kundu, M. R. (1982). Time variability and structure of quiet sun sources at 6-CM wavelength. *Solar Phys.* 76, 221–237.

Fontenla, J. M., Avrett, E. H., and Loeser, R. (1993). Energy balance in the solar transition region. III. Helium emission in hydrostatic, constant-abundance models with diffusion. *Astrophys. J.* 406:319.

Fontenla, J. M., Avrett, E. H., and Loeser, R. (2002). Energy balance in the solar transition region. IV. Hydrogen and helium mass flows with diffusion. *Astrophys. J.* 572, 636–662. doi: 10.1086/340227

Fossat, E., Boumier, P., Corbard, T., Provost, J., Salabert, D., Schmider, F. X., et al. (2017). Asymptotic g modes: evidence for a rapid rotation of the solar core. *Astron. Astrophys.*, 604:A40. doi: 10.1051/0004-6361/201730460

Fossum, A., and Carlsson, M. (2005). High-frequency acoustic waves are not sufficient to heat the solar chromosphere. *Nature* 435, 919–921. doi: 10.1038/nature03695

Foukal, P. (1971). Morphological relationships in the chromospheric Hα fine structure. *Solar Phys.* 19, 59–71.

Foukal, P. V. (2004). *Solar Astrophysics. 2nd Revised ed.* Wiley-VCH.

García, R. A., and Ballot, J. (2019). Asteroseismology of solar-type stars. *Liv. Rev. Solar Phys.* 16:4. doi: 10.1007/s41116-019-0020-1

Gary, D. E. (1996). "Imaging spectroscopy of the non-flaring sun," in *Radio Emission from the Stars and the Sun*, volume 93 of *Astronomical Society of the Pacific Conference Series*, eds A. R. Taylor and J. M. Paredes (San Francisco, CA), 387.

Gary, D. E., Hartl, M. D., and Shimizu, T. (1997). Nonthermal radio emission from solar soft X-ray transient brightenings. *Astrophys. J.* 477, 958–968.

Gary, D. E., and Keller, C. U. (2004). *Solar and Space Weather Radiophysics - Current Status and Future Developments*, Vol. 314. Dordrecht: Kluwer Academic Publishers.

Gary, D. E., and Zirin, H. (1988). Microwave structure of the quiet sun. *Astrophys. J.* 329:991.

Gary, D. E., Zirin, H., and Wang, H. (1990). Microwave structure of the quiet sun at 8.5 GHz. *Astrophys. J.* 355:321.

Gary, G. A. (2001). Plasma beta above a solar active region: rethinking the paradigm. *Solar Phys.* 203, 71–86. doi: 10.1023/A:1012722021820

Gelfreikh, G. B. (1998). "Three-dimensional structure of the magnetospheres of solar active regions from radio observations (Invited review)," in *Three-Dimensional Structure of Solar Active Regions, Volume 155 of* Astronomical Society of the Pacific Conference Series, eds C. E. Alissandrakis and B. Schmieder (San Francisco, CA), 110.

Gelfreikh, G. B., Grechnev, V., Kosugi, T., and Shibasaki, K. (1999). Detection of periodic oscillations in sunspot-associated radio sources. *Solar Phys.* 185, 177–191.

Gizon, L., Birch, A. C., and Spruit, H. C. (2010). Local helioseismology: three-dimensional imaging of the solar interior. *Annu. Rev. Astron. Astrophys.* 48, 289–338. doi: 10.1146/annurev-astro-082708-101722

Gizon, L., Schunker, H., Baldner, C. S., Basu, S., Birch, A. C., Bogart, R. S., et al. (2009). Helioseismology of sunspots: a case study of NOAA Region 9787. *Space Sci. Rev.* 144, 249–273. doi: 10.1007/s11214-008-9466-5

Gopalswamy, N., Shibasaki, K., and Salem, M. (2000). Microwave enhancement in coronal holes: statistical propeties. *J. Astrophys. Astron.* 21:413. doi: 10.1007/BF02702435

Grotrian, W. (1939). Zur Frage der Deutung der Linien im Spektrum der Sonnenkorona. *Naturwissenschaften* 27, 214.

Gudiksen, B. V., Carlsson, M., Hansteen, V. H., Hayek, W., Leenaarts, J., and Martínez-Sykora, J. (2011). The stellar atmosphere simulation code Bifrost. Code description and validation. *Astron. Astrophys.* 531:A154. doi: 10.1051/0004-6361/201116520

Habbal, S. R., and Gonzalez, R. D. (1991). First observations of macrospicules at 4.8 GHz at the solar limb in polar coronal holes. *Astrophys.J. Lett.* 376:L25.

Hannah, I. G., Hudson, H. S., Battaglia, M., Christe, S., Kašparová, J., Krucker, S., et al. (2011). Microflares and the statistics of X-ray flares. *Space Sci. Rev.* 159, 263–300. doi: 10.1007/s11214-010-9705-4

Hewish, A., Scott, P. F., and Wills, D. (1964). Interplanetary scintillation of small diameter radio sources. *Nature* 203, 1214–1217.

Hoang, S., and Steinberg, J. L. (1977). About the computed meter-wavelength thermal radiation from coronal streamers and coronal holes. *Astron. Astrophys.* 58, 287–290.

Irimajiri, Y., Takano, T., Nakajima, H., Shibasaki, K., Hanaoka, Y., and Ichimoto, K. (1995). Simultaneous multifrequency observations of an eruptive prominence at millimeter wavelengths. *Solar Phys.* 156, 363–375.

Jackiewicz, J., Gizon, L., and Birch, A. C. (2008). High-resolution mapping of flows in the solar interior: fully consistent OLA inversion of helioseismic travel times. *Solar Phys.* 251, 381–415. doi: 10.1007/s11207-008-9158-z

Jokipii, J. R. (1973). Turbulence and scintillations in the interplanetary plasma. *Annu. Rev. Astron. Astrophys.* 11:1.

Judge, P. G., and Carlsson, M. (2010). On the solar chromosphere observed at the LIMB with hinode. *Astrophys. J.* 719, 469–473. doi: 10.1088/0004-637X/719/1/469

Kakinuma, T., and Swarup, G. (1962). A model for the sources of the slowly varying component of microwave solar radiation. *Astrophys. J.* 136:975.

Kasper, J. C., Bale, S. D., Belcher, J. W., Berthomier, M., Case, A. W., Chandran, B. D. G., et al. (2019). Alfvénic velocity spikes and rotational flows in the near-Sun solar wind. *Nature* 576, 228–231. doi: 10.1038/s41586-019-1813-z

Keller, C. U., and Krucker, S. (2004). "Radio observations of the quiet sun," in *Astrophysics and Space Science Library*, Vol. 314, eds D. E. Gary and C. U. Keller (Springer Science + Business Media, Inc.), 287. doi: 10.1007/1-4020-2814-8_14

Kerdraon, A., and Delouis, J.-M. (1997). "The nançay radioheliograph," in *Coronal Physics from Radio and Space Observations, Lecture Notes in Physics*, Vol. 483, ed G. Trottet (Springer), 192. doi: 10.1007/BFb0106458

Kianfar, S., Leenaarts, J., Danilovic, S., de la Cruz Rodríguez, J., and José Díaz Baso, C. (2020). Physical properties of bright Ca II K fibrils in the solar chromosphere. *Astron. Astrophys.* 637:A1. doi: 10.1051/0004-6361/202037572

Klimchuk, J. A. (2006). On solving the coronal heating problem. *Solar Phys.* 234, 41–77. doi: 10.1007/s11207-006-0055-z

Kobelski, A., Bastian, T. S., and Vourlidas, A. (2019). "Radio propagation diagnostics of the inner heliosphere in the era of the parker solar probe," in *American Astronomical Society Meeting Abstracts #234, Vol. 234 of American Astronomical Society Meeting Abstracts*. Available online at: https://ui.adsabs.harvard.edu/abs/

Kontar, E. P., Chen, X., Chrysaphi, N., Jeffrey, N. L. S., Emslie, A. G., Krupar, V., et al. (2019). Anisotropic radio-wave scattering and the interpretation of solar radio emission observations. *Astrophys. J.* 884:122. doi: 10.3847/1538-4357/ab40bb

Korzhavin, A. N., Opeikina, L. V., and Peterova, N. G. (2010). Transition region above sunspots inferred from microwave observations. *Astrophys. Bull.* 65, 60–74. doi: 10.1134/S1990341310010062

Kosovichev, A. G. (2011). "Advances in global and local helioseismology: an introductory review," in *The Pulsations of the Sun and the Stars, Lecture Notes in Physics*, Vol. 832 (Berlin; Heidelberg: Springer-Verlag), 3. doi: 10.1007/978-3-642-19928-8_1

Kosovichev, A. G., and Duvall, T. L., J. (1997). "Acoustic tomography of solar convective flows and structures," in *SCORe'96 : Solar Convection and Oscillations and their Relationship*, volume 225 of *Astrophysics and Space Science Library*, eds F. P. Pijpers, J. Christensen-Dalsgaard, and C. S. Rosenthal, 241–260. doi: 10.1007/978-94-011-5167-2_26

Koutchmy, S. (1994). Coronal physics from eclipse observations. *Adv. Space Res.* 14, 29–39.

Koutchmy, S., Koutvitsky, V. A., Molodensky, M. M., Solov'iev, L. S., and Koutchmy, O. (1994). Magnetic configuration of coronal streamers and threads. *Space Sci. Rev.* 70, 283–288.

Koutchmy, S., and Livshits, M. (1992). Coronal streamers. *Space Sci. Rev.* 61, 393–417.

Krucker, S., and Benz, A. O. (2000). Are heating events in the quiet solar corona small flares? Multiwavelength observations of individual events. *Solar Phys.* 191, 341–358. doi: 10.1023/A:1005255608792

Krucker, S., Benz, A. O., Bastian, T. S., and Acton, L. W. (1997). X-ray network flares of the quiet sun. *Astrophys. J.* 488, 499–505.

Krueger, A. (1979). *Introduction to Solar Radio Astronomy and Radio Physics*. Geophysics and Astrophysics Monographs, Dordrecht: Reidel.

Kuiper, G. P. (1953). *The Sun*. University of Chicago Press.

Kundu, M. R. (1959). Structures et propriétés des sources d'activité solaire sur ondes centimétriques. *Ann. Astrophys.* 22:1.

Kundu, M. R. (1965). *Solar Radio Astronomy*. New York, NY: Interscience Publication.

Kundu, M. R., and Alissandrakis, C. E. (1975). Observations at 6 CM of the solar active region. *Nature* 257, 465–467.

Kundu, M. R., Alissandrakis, C. E., Bregman, J. D., and Hin, A. C. (1977). 6 centimeter observations of solar active regions with 6" resolution. *Astrophys. J.* 213, 278–295.

Kundu, M. R., and McCullough, T. P. (1972). Polarization of solar active regions at 9.5 mm wavelength. *Solar Phys.* 24, 133–141.

Kundu, M. R., Rao, A. P., Erskine, F. T., and Bregman, J. D. (1979). High-resolution observations of the quiet sun at 6 centimeters using the Westerbork Synthesis Radio Telescope. *Astrophys. J.* 234, 1122–1136.

Labrosse, N., Heinzel, P., Vial, J. C., Kucera, T., Parenti, S., Gunár, S., et al. (2010). Physics of solar prominences: I—Spectral diagnostics and non-LTE modelling. *Space Sci. Rev.* 151, 243–332. doi: 10.1007/s11214-010-9630-6

Landi, E., and Chiuderi Drago, F. (2003). Solving the discrepancy between the extreme-ultraviolet and microwave observations of the quiet sun. *Astrophys. J.* 589, 1054–1061. doi: 10.1086/374811

Landi, E., and Chiuderi Drago, F. (2008). The quiet-sun differential emission measure from radio and UV measurements. *Astrophys. J.* 675, 1629–1636. doi: 10.1086/527285

Lantos, P. (1999). "Low frequency observations of the quiet sun: a review," in *Proceedings of the Nobeyama Symposium*, eds T. S., Bastian, N. Gopalswamy, and K. Shibasaki, 11–24.

Lantos, P., and Alissandrakis, C. E. (1999). Analysis of coronal emissions observed at meter wavelengths. *Astron. Astrophys.* 351, 373–381.

Lantos, P., Alissandrakis, C. E., Gergely, T., and Kundu, M. R. (1987). Quiet sun and slowly varying component at meter and decameter wavelengths. *Solar Phys.* 112, 325–340.

Lantos, P., Alissandrakis, C. E., and Rigaud, D. (1992). Quiet-sun emission and local sources at meter and decimeter wavelengths and their relationship with the coronal neutral sheet. *Solar Phys.* 137, 225–256.

Lantos, P., and Kundu, M. R. (1972). The quiet sun brightness distributions at millimeter wavelengths and chro mospheric inhomogeneities. *Astron. Astrophys.* 21, 119–124.

Leblanc, Y., Dulk, G. A., and Bougeret, J.-L. (1998). Tracing the electron density from the corona to 1au. *Solar Phys.* 183, 165–180.

Lee, J. (2007). Radio emissions from solar active regions. *Space Sci. Rev.* 133, 73–102. doi: 10.1007/s11214-007-9206-2

Leighton, R. B., Noyes, R. W., and Simon, G. W. (1962). Velocity fields in the solar atmosphere. I. Preliminary report. *Astrophys. J.* 135:474.

Loukitcheva, M., Solanki, S. K., and White, S. (2006). The dynamics of the solar chromosphere: comparison of model predictions with millimeter-interferometer observations. *Astron. Astrophys.* 456, 713–723. doi: 10.1051/0004-6361:20053171

Loukitcheva, M., Solanki, S. K., and White, S. M. (2009). The relationship between chromospheric emissions and magnetic field strength. *Astron. Astrophys.* 497, 273–285. doi: 10.1051/0004-6361/200811133

Loukitcheva, M. A., White, S. M., and Solanki, S. K. (2019). Alma detection of dark chromospheric holes in the quiet sun. *Astrophys.J. Lett.* 877:L26. doi: 10.3847/2041-8213/ab2191

Lynch, D. K., Beckers, J. M., and Dunn, R. B. (1973). A Morphological study of solar spicules. *Solar Phys.* 30, 63–70.

Mackay, D. H., Karpen, J. T., Ballester, J. L., Schmieder, B., and Aulanier, G. (2010). Physics of solar prominences: II—Magnetic structure and dynamics. *Space Sci. Rev.* 151, 333–399. doi: 10.1007/s11214-010-9628-0

Mann, G., Jansen, F., MacDowall, R. J., Kaiser, M. L., and Stone, R. G. (1999). A heliospheric density model and type III radio bursts. *Astron. Astrophys.* 348, 614–620.

Marqué, C. (2004). Radio metric observations of quiescent filament cavities. *Astrophys. J.* 602, 1037–1050. doi: 10.1086/381085

Martínez-Sykora, J., De Pontieu, B., Hansteen, V. H., Rouppe van der Voort, L., Carlsson, M., and Pereira, T. M. D. (2017). On the generation of solar spicules and Alfvénic waves. *Science* 356, 1269–1272. doi: 10.1126/science.aah5412

McCauley, P. I., Cairns, I. H., White, S. M., Mondal, S., Lenc, E., Morgan, J., and Oberoi, D. (2019). The low-frequency solar corona in circular polarization. *Solar Phys.* 294:106. doi: 10.1007/s11207-019-1502-y

McLean, D. J., and Labrum, N. R. (1985). *Solar Radiophysics : Studies of Emission From the Sun at Metre Wavelengths*. New York, NY : Cambridge University Press.

Menezes, F., and Valio, A. (2017). Solar radius at subterahertz frequencies and its relation to solar activity. *Solar Phys.* 292:195. doi: 10.1007/s11207-017-1216-y

Mercier, C., and Chambe, G. (2009). High dynamic range images of the solar corona between 150 and 450 MHz. *Astrophys.J. Lett.* 700, L137–L140. doi: 10.1088/0004-637X/700/2/L137

Mercier, C., and Chambe, G. (2012). Morphology of the quiet Sun between 150 and 450 MHz as observed with the Nançay radioheliograph. *Astron. Astrophys.* 540:A18. doi: 10.1051/0004-6361/201118163

Mercier, C., and Chambe, G. (2015). Electron density and temperature in the solar corona from multifrequency radio imaging. *Astron. Astrophys.* 583:A101. doi: 10.1051/0004-6361/201425540

Mercier, C., Subramanian, P., Chambe, G., and Janardhan, P. (2015). The structure of solar radio noise storms. *Astron. Astrophys.* 576:A136. doi: 10.1051/0004-6361/201321064

Mihalas, D. (1970). *Stellar Atmospheres*. San Francisco, CA: Freeman.

Mondal, S., Oberoi, D., and Mohan, A. (2020). First radio evidence for impulsive heating contribution to the quiet solar corona. *Astrophys.J. Lett.* 895:L39. doi: 10.3847/2041-8213/ab8817

Moradi, H., Baldner, C., Birch, A. C., Braun, D. C., Cameron, R. H., Duvall, T. L., et al. (2010). Modeling the subsurface structure of sunspots. *Solar Phys.* 267, 1–62. doi: 10.1007/s11207-010-9630-4

Newkirk, G. J. (1961). The solar corona in active regions and the thermal origin of the slowly varying component of solar radio radiation. *Astrophys. J.* 133:983.

Newkirk, G. J. (1967). Structure of the solar corona. *Annu. Rev. Astron. Astrophys.* 5:213.

Nindos, A. (2020). Incoherent solar radio emission. *Front. Astron. Space Sci.*

Nindos, A., Alissandrakis, C. E., Bastian, T. S., Patsourakos, S., De Pontieu, B., Warren, H., et al. (2018). "First high-resolution look at the quiet sun with alma at 3mm," in *The High Energy Solar Corona: Waves, Eruptions, Particles, Lecture Notes in Physics,* Vol. 725 (Berlin; Heidelberg: Springer-Verlag), 251. doi: 10.1051/0004-6361/201834113

Nindos, A., Alissandrakis, C. E., Gelfreikh, G. B., Bogod, V. M., and Gontikakis, C. (2002). Spatially resolved microwave oscillations above a sunspot. *Astron. Astrophys.* 386, 658–673. doi: 10.1051/0004-6361:20020252

Nindos, A., Alissandrakis, C. E., Gelfreikh, G. B., Borovik, V. N., Korzhavin, A. N., and Bogod, V. M. (1996). Two-dimensional mapping of the Sun with the RATAN-600. *Solar Phys.* 165, 41–59.

Nindos, A., Alissandrakis, C. E., Patsourakos, S., and Bastian, T. S. (2020). Transient brightenings in the quiet Sun detected by ALMA at 3 mm. *Astron. Astrophys.* 638:A62. doi: 10.1051/0004-6361/202037810

Nindos, A., and Aurass, H. (2007). *Pulsating Solar Radio Emission*, Vol. 725, 251.

Nindos, A., Kundu, M. R., and White, S. M. (1999). A study of microwave-selected coronal transient brightenings. *Astrophys. J.* 513, 983–989.

Nita, G. M., Viall, N. M., Klimchuk, J. A., Loukitcheva, M. A., Gary, D. E., Kuznetsov, A. A., et al. (2018). Dressing the coronal magnetic extrapolations of active regions with a parameterized thermal structure. *Astrophys. J.* 853:66. doi: 10.3847/1538-4357/aaa4bf

Nordlund, Å., Stein, R. F., and Asplund, M. (2009). Solar surface convection. *Liv. Rev. Solar Phys.* 6:2. doi: 10.12942/lrsp-2009-2

November, L. J., Toomre, J., Gebbie, K. B., and Simon, G. W. (1981). The detection of mesogranulation on the sun. *Astrophys.J. Lett.* 245, L123–L126.

Ossendrijver, M. (2003). The solar dynamo. *Astron. Astrophys. Rev.* 11, 287–367. doi: 10.1007/s00159-003-0019-3

Parker, E. N. (1955). The formation of sunspots from the solar toroidal field. *Astrophys. J.* 121:491.

Parker, E. N. (1978). Hydraulic concentration of magnetic fields in the solar photosphere. VI. Adiabatic cooling and concentration in downdrafts. *Astrophys. J.* 221, 368–377.

Parker, E. N. (1988). Nanoflares and the solar X-ray corona. *Astrophys. J.* 330:474.

Pasachoff, J. M., Jacobson, W. A., and Sterling, A. C. (2009). Limb spicules from the ground and from space. *Solar Phys.* 260, 59–82. doi: 10.1007/s11207-009-9430-x

Patsourakos, S., Alissandrakis, C. E., Nindos, A., and Bastian, T. S. (2020). Observations of solar chromospheric oscillations at 3 mm with ALMA. *Astron. Astrophys.* 634:A86. doi: 10.1051/0004-6361/201936618

Pikel'Ner, S. B. (1969). A mechanism for the formation of chromospheric spicules. *Astron. Z.* 46:328.

Pohjolainen, S. (2000). On the origin of polar radio brightenings at short millimeter wavelengths. *Astron. Astrophys.* 361, 349–358.

Priest, E. (2014). *Magnetohydrodynamics of the Sun*. Cambridge: Cambridge University Press.

Priest, E. R. (1987). *Solar Magneto-Hydrodynamics*. Dordrecht: D. Reidel.

Rahman, M. M., McCauley, P. I., and Cairns, I. H. (2019). On the relative brightness of coronal holes at low frequencies. *Solar Phys.* 294:7. doi: 10.1007/s11207-019-1396-8

Ramesh, R., Kathiravan, C., and Sastry, C. V. (2010). Estimation of magnetic field in the solar coronal streamers through low frequency radio observations. *Astrophys. J.* 711, 1029–1032. doi: 10.1088/0004-637X/711/2/1029

Raoult, A., Lantos, P., and Fuerst, E. (1979). Prominences at centrimetric and millimetric wavelengths. I. Size and spectrum of the radio filaments. *Solar Phys.* 61, 335–343.

Reeves, E. M., Foukal, P. V., Huber, M. C. E., Noyes, R. W., Schmahl, E. J., Timothy, J. G., Vernazza, J. E., et al. (1974). Observations of the chromospheric network: initial results from the apollo telescope mount. *Astrophys.J. Lett.* 188:L27.

Rempel, M., and Schlichenmaier, R. (2011). Sunspot modeling: from simplified models to radiative MHD simulations. *Liv. Rev. Solar Phys.* 8:3. doi: 10.12942/lrsp-2011-3

Riley, P., Lionello, R., Linker, J. A., Mikic, Z., Luhmann, J., and Wijaya, J. (2011). Global MHD modeling of the solar corona and inner heliosphere for the whole heliosphere interval. *Solar Phys.* 274, 361–377. doi: 10.1007/s11207-010-9698-x

Rincon, F., and Rieutord, M. (2018). The Sun's supergranulation. *Liv. Rev. Solar Phys.* 15:6. doi: 10.1007/s41116-018-0013-5

Rutten, R. J. (2003). *Radiative Transfer in Stellar Atmospheres*. Lecture Notes Utrecht University.

Saito, K., Makita, M., Nishi, K., and Hata, S. (1970). A non-spherical axisymmetric model of the solar K corona of the minimum type. *Ann. Tokyo Astron. Observ.* 12, 51–173.

Samanta, T., Tian, H., Yurchyshyn, V., Peter, H., Cao, W., Sterling, A., et al. (2019). Generation of solar spicules and subsequent atmospheric heating. *Science* 366, 890–894. doi: 10.1126/science.aaw2796

Schatzman, E. (1949). The heating of the solar corona and chromosphere. *Ann. Astrophys.* 12:203.

Schmidt, H. U. (1964). *On the Observable Effects of Magnetic Energy Storage and Release Connected With Solar Flares*, Vol. 50, 107.

Schwarzschild, M. (1948). On noise arising from the solar granulation. *Astrophys. J.* 107:1.

Scudder, J. D. (1992). Why all stars should possess circumstellar temperature inversions. *Astrophys. J.* 398:319.

Secchi, A. (1875). *Le Soleil*. Paris : Gauthier-Villars.

Selhorst, C. L., Silva, A. V. R., and Costa, J. E. R. (2005). Solar atmospheric model with spicules applied to radio observation. *Astron. Astrophys.* 433, 365–374. doi: 10.1051/0004-6361:20042043

Shibasaki, K. (1999). "Microwave observations of the quiet sun," in *Proceedings of the Nobeyama Symposium*, eds T. S. Bastian, N. Gopalswamy, and K. Shibasaki, 1–9.

Shibasaki, K., Alissandrakis, C. E., and Pohjolainen, S. (2011). Radio emission of the quiet sun and active regions (Invited Review). *Solar Phys.* 273, 309–337. doi: 10.1007/s11207-011-9788-4

Shimojo, M., Kawate, T., Okamoto, T. J., Yokoyama, T., Narukage, N., Sakao, T., et al. (2020). Estimating the temperature and density of a spicule from 100 GHz data obtained with ALMA. *Astrophys.J. Lett.* 888:L28. doi: 10.3847/2041-8213/ab62a5

Solanki, S. K. (2003). Sunspots: an overview. *Astron. Astrophys. Rev.* 11, 153–286. doi: 10.1007/s00159-003-0018-4

Solanki, S. K., Inhester, B., and Schüssler, M. (2006). The solar magnetic field. *Rep. Prog. Phys.* 69, 563–668. doi: 10.1088/0034-4885/69/3/R02

Stenflo, J. O. (1973). Magnetic-field structure of the photospheric network. *Solar Phys.* 32, 41–63.

Sterling, A. C. (2000). Solar spicules: a review of recent models and targets for future observations - (Invited Review). *Solar Phys.* 196, 79–111. doi: 10.1023/A:1005213923962

Sterling, A. C., Moore, R. L., Samanta, T., and Yurchyshyn, V. (2020). Possible production of solar spicules by microfilament eruptions. *Astrophys.J. Lett.* 893:L45. doi: 10.3847/2041-8213/ab86a5

Stix, M. (2004). *The Sun : An Introduction*. Berlin: Springer.

Stupishin, A. G., Kaltman, T. I., Bogod, V. M., and Yasnov, L. V. (2018). Modeling of solar atmosphere parameters above sunspots using RATAN-600 microwave observations. *Solar Phys.* 293:13. doi: 10.1007/s11207-017-1228-7

Takeda, A., Acton, L., and Albanese, N. (2019). Solar cycle variation of coronal temperature, emission measure, and soft X-ray irradiance observed with Yohkoh soft X-ray telescope. *Astrophys. J.* 887:225. doi: 10.3847/1538-4357/ab53e3

Thejappa, G., and Kundu, M. R. (1992). Unusually low coronal radio emission at the solar minimum. *Solar Phys.* 140, 19–39.

Thejappa, G., and Kundu, M. R. (1994). The effects of largescale and smallscale density structures on the radio emission from coronal streamers. *Solar Phys.* 149, 31–49.

Thejappa, G., and MacDowall, R. J. (2008). Effects of scattering on radio emission from the quiet sun at low frequencies. *Astrophys. J.* 676, 1338–1345. doi: 10.1086/528835

Title, A. M., and Schrijver, C. J. (1998). "The Sun's magnetic carpet," in *Cool Stars, Stellar Systems, and the Sun, Vol. 154 of Astronomical Society of the Pacific Conference Series*, eds R. A. Donahue and J. A. Bookbinder (San Francisco, CA), 345.

Tsiropoula, G., Tziotziou, K., Kontogiannis, I., Madjarska, M. S., Doyle, J. G., and Suematsu, Y. (2012). Solar fine-scale structures. I. spicules and other small-scale, jet-like events at the chromospheric level: observations and physical parameters. *Space Sci. Rev.* 169, 181–244. doi: 10.1007/s11214-012-9920-2

Uralov, A. M., Grechnev, V. V., Rudenko, G. V., Rudenko, I. G., and Nakajima, H. (2008). Microwave neutral line associated source and a current sheet. *Solar Phys.* 249, 315–335. doi: 10.1007/s11207-008-9183-y

van Ballegooijen, A. A., Asgari-Targhi, M., Cranmer, S. R., and DeLuca, E. E. (2011). Heating of the solar chromosphere and corona by Alfvén wave turbulence. *Astrophys. J.* 736:3. doi: 10.1088/0004-637X/736/1/3

van de Hulst, H. C. (1950). The electron density of the solar corona. *Bull. Astron. Inst. Netherlands* 11:135.

Vernazza, J. E., Avrett, E. H., and Loeser, R. (1976). Structure of the solar chromosphere. II. The underlying photosphere and temperature-minimum region. *Astrophys.J. Suppl.* 30, 1–60.

Vernazza, J. E., Avrett, E. H., and Loeser, R. (1981). Structure of the solar chromosphere. III. Models of the EUV brightness components of the quiet sun. *Astrophys.J. Suppl.* 45, 635–725.

Vocks, C., Mann, G., Breitling, F., Bisi, M. M., Dabrowski, B., Fallows, R., et al. (2018). LOFAR observations of the quiet solar corona. *Astron. Astrophys.* 614:A54. doi: 10.1051/0004-6361/201630067

Walsh, R. W., and Ireland, J. (2003). The heating of the solar corona. *Astron. Astrophys. Rev.* 12, 1–41. doi: 10.1007/s00159-003-0021-9

Wedemeyer, S., Szydlarski, M., Jafarzadeh, S., Eklund, H., Guevara Gomez, J. C., Bastian, T., et al. (2020). The Sun at millimeter wavelengths. I. Introduction to ALMA Band 3 observations. *Astron. Astrophys.* 635:A71. doi: 10.1051/0004-6361/201937122

White, S. M., Kundu, M. R., Shimizu, T., Shibasaki, K., and Enome, S. (1995). The radio properties of solar active region soft X-ray transient brightenings. *Astrophys. J.* 450:435.

White, S. M., Loukitcheva, M., and Solanki, S. K. (2006). High-resolution millimeter-interferometer observations of the solar chromosphere. *Astron. Astrophys.* 456, 697–711. doi: 10.1051/0004-6361:20052854

Wiegelmann, T., Petrie, G. J. D., and Riley, P. (2017). Coronal magnetic field models. *Space Sci. Rev.* 210, 249–274. doi: 10.1007/s11214-015-0178-3

Wiegelmann, T., and Sakurai, T. (2012). Solar force-free magnetic fields. *Liv. Rev. Solar Phys.* 9:5. doi: 10.12942/lrsp-2012-5

Wiegelmann, T., Thalmann, J. K., and Solanki, S. K. (2014). The magnetic field in the solar atmosphere. *Astron. Astrophys. Rev.* 22:78. doi: 10.1007/s00159-014-0078-7

Withbroe, G. L., and Noyes, R. W. (1977). Mass and energy flow in the solar chromosphere and corona. *Annu. Rev. Astron. Astrophys.* 15, 363–387.

Yokoyama, T., Shimojo, M., Okamoto, T. J., and Iijima, H. (2018). ALMA observations of the solar chromosphere on the polar limb. *Astrophys. J.* 863:96. doi: 10.3847/1538-4357/aad27e

Zaqarashvili, T. V., and Erdélyi, R. (2009). Oscillations and waves in solar spicules. *Space Sci. Rev.* 149, 355–388. doi: 10.1007/s11214-009-9549-y

Zhang, J., Kundu, M. R., White, S. M., Dere, K. P., and Newmark, J. S. (2001). Reconciling extreme-ultraviolet and radio observations of the Sun's corona. *Astrophys. J.* 561, 396–405. doi: 10.1086/323212

Zhao, J., Hing, D., Chen, R., and Hess Webber, S. (2019). Imaging the Sun's far-side active regions by applying multiple measurement schemes on multiskip acoustic waves. *Astrophys. J.* 887:216. doi: 10.3847/1538-4357/ab5951

Zhao, J., Kosovichev, A. G., and Sekii, T. (2010). High-resolution helioseismic imaging of subsurface structures and flows of a solar active region observed by hinode. *Astrophys. J.* 708, 304–313. doi: 10.1088/0004-637X/708/1/304

Zheleznyakov, V. V. (1962). The Origin of the slowly varying component of solar radio emission. *Soviet Astron.* 6:3.

Zheleznyakov, V. V. (1970). *Radio Emission of the Sun and Planets*. New York, NY: Pergamon Press.

Zirin, H. (1966). *The Solar Atmosphere*. Waltham, MA: Blaisdell.

Zirin, H. (1988). *Astrophysics of the sun*. Cambridge: University Press.

Zirin, H., Baumert, B. M., and Hurford, G. J. (1991). The microwave brightness temperature spectrum of the quiet sun. *Astrophys. J.* 370:779.

Conflict of Interest: The author declares that the research was conducted in the absence of any commercial or financial relationships that could be construed as a potential conflict of interest.

frontiers in Astronomy and Space Sciences

REVIEW
published: 30 October 2020
doi: 10.3389/fspas.2020.551558

Radio Observations of Coronal Mass Ejection Initiation and Development in the Low Solar Corona

Eoin P. Carley[1]*, *Nicole Vilmer*[2,3] *and Angelos Vourlidas*[4]

[1]School of Cosmic Physics, Astronomy and Astrophysics Section, Dublin Institute for Advanced Studies, Dublin, Ireland, [2]LESIA, Observatoire de Paris, Université PSL, CNRS, Sorbonne Université, Université de Paris, Meudon, France, [3]Station de Radioastronomie de Nançay, Observatoire de Paris, PSL Research University, CNRS, Univ, Orléans, France, [4]The Johns Hopkins University Applied Physics Laboratory, Laurel, MD, USA

Coronal mass ejections (CMEs) are large eruptions of plasma and magnetic field from the low solar corona into the heliosphere. These eruptions are often associated with energetic electrons that produce various kinds of radio emission. However, there is ongoing investigation into exactly where, when, and how the electron acceleration occurs during flaring and eruption, and how the associated radio emission can be exploited as a diagnostic of both particle acceleration and CME eruptive physics. Here, we review past and present developments in radio observations of flaring and eruption, from the destabilization of flux ropes to the development of a CME and the eventual driving of shocks in the corona. We concentrate primarily on the progress made in CME radio physics in the past two decades and show how radio imaging spectroscopy provides the ability to diagnose the locations and kinds of electron acceleration during eruption, which provides insight into CME eruptive models in the early stages of their evolution ($< 10\ R_{\odot}$). We finally discuss how new instrumentation in the radio domain will pave the way for a deeper understanding of CME physics in the near future.

Keywords: radio, coronal mass ejection, solar flare, imaging spectroscopy, particle acceleration

OPEN ACCESS

Edited by:
Dipankar Banerjee, Indian Institute of Astrophysics, India

Reviewed by:
Nariaki V. Nitta, Lockheed Martin Solar and Astrophysics Laboratory (LMSAL), United States
Abhishek Kumar Srivastava, Indian Institute of Technology (BHU), India

***Correspondence:**
Eoin P. Carley
eoin.carley@dias.ie

Specialty section:
This article was submitted to Stellar and Solar Physics, a section of the journal Frontiers in Astronomy and Space Sciences

Received: *13 April 2020*
Accepted: *15 September 2020*
Published: *30 October 2020*

Citation:
Carley EP, Vilmer N and Vourlidas A (2020) Radio Observations of Coronal Mass Ejection Initiation and Development in the Low Solar Corona. Front. Astron. Space Sci. 7:551558. doi: 10.3389/fspas.2020.551558

1. INTRODUCTION

Coronal mass ejections (CMEs) are large eruptions of plasma and magnetic field from the low solar corona into the heliosphere, often associated with flares—radiative signature of hot plasmas and energetic particles at the origin of the eruption. Both phenomena are powered by the release of magnetic energy and are almost always accompanied by the acceleration of electrons that emit across the electromagnetic spectrum, from X-rays to radio waves. Observation in the radio domain can provide remote diagnostic tools in flare/CME physics, from identifying the sites of electron acceleration to estimating CME bulk plasma properties such density, temperature, and magnetic field strength (see Vourlidas (2004) and Pick (2004) for previous reviews of radio emissions associated with CMEs). Radio observations therefore enjoy a unique position in their ability to diagnose both kinetic-scale plasma physics and large-scale CME and flare physics, which, in turn, provide a means of testing particular models of eruptive phenomena in the solar corona. Here, we provide a review of CME observations from a radio perspective, in particular detailing the progress that has been made from modern developments in radio imaging and spectroscopy.

There exists a long legacy of radio observations of flares and CMEs, for example, from the very first examples of type II, III, and IV solar radio bursts (Reber, 1944; Hey, 1946; Wild et al., 1954, 1959;

Boischot, 1957, 1958; Pick-Gutmann, 1961) right up to imaging and spectroscopic observation of such phenomena in present day studies (Pick and Vilmer (2008) provide an extensive review of flares and CME radio observations over the past 6 decades.) In recent years, there has been an emergence of new observational capability using advanced radio imaging spectrometers such as the Low-Frequency Array (LOFAR; van Haarlem et al., 2013), the Murchison Widefield Array (MWA; Li et al., 2018), the Karl G. Jansky Very Large Array (JVLA; Perley et al., 2011), the Mingantu Ultrawide Spectral Radioheliograph (MUSER; Yan et al., 2016), and the Expanded Owens Valley Solar Array (EOVSA; ovsa.njit.edu). These instruments, as well as legacy facilities such the Nançay Radioheliograph (NRH; Kerdraon and Delouis, 1997), have shown that radio is an integral part of flare and CME development studies. Modern radio telescopes have opened up previously unexplored regions of parameter space in flare/CME observations, particularly with their ability to provide extremely high time-resolution (from seconds to milliseconds) imaging spectroscopy observations of the plasma and energetic electron physics at play during the eruption.

The advances in radio instrumentation have also been augmented by new space-based extreme ultraviolet (EUV) imagers such as the Atmospheric Imaging Assembly (AIA; Lemen et al., 2012), Sun Watcher using Active Pixel System Detector and Image Processing (SWAP; Berghmans et al., 2006) instrument, and the Solar Ultraviolet Imager (SUVI; Seaton and Darnel, 2018). These instruments have much improved spatial resolution, temporal resolutions (on the order of seconds), and fields of view compared to their precursors, and can better compare with the high-temporal resolution observations of radio imaging spectrometers. In addition to the improved EUV imaging, recent white-light coronagraphs, such as STEREO COR1 and COR2 (Howard et al., 2008), have provided a new means of observing the 3D development and propagation of CMEs and their relationship to radio observations. The above progress in radio, EUV, and white-light instrumentation makes a review of flare/CME radio physics timely, especially while considering the upcoming deployment of new facilities from microwave to decametric wavelengths (see Carley et al. (2020) for a review of radio instruments in a space weather context).

In this article, we review the developments of radio observation of flare/CMEs, concentrating on the sites and mechanisms of electron acceleration at play during eruption initiation as well as on the early stage CME development in $< 10\ R_{\odot}$ corona. Although CMEs are primarily defined to be a white-light phenomenon, here we focus on radio activity associated with all large-scale eruptive events in the early stages of eruption evolution observed from EUV to white light. We primarily concentrate on advances made since past reviews of CME observations in a radio context, for example, Vourlidas (2004) and Pick (2004), demonstrating how radio, in combination with a variety of other instruments, has led to new insights into flare/CME eruptive physics. We conclude by discussing the potential of radio instruments for advancing our understanding of CMEs beyond the current state of the art in the near future.

2. THE STANDARD MODEL OF CORONAL MASS EJECTIONS AND RADIO EMISSION MECHANISMS

Large-scale white-light CMEs are usually thought to contain a twisted magnetic structure known as a flux rope (Vourlidas et al., 2013). There is a wealth of magnetohydrodynamic (MHD) modeling that now supports the flux rope theory (see, e.g., Chen (2011) for a review). In light of this, much of our description of radio emission associated with CME initiation and development will refer back to the standard model of CMEs, shown in **Figure 1B**. It shows a schematic of the standard model of flare and flux rope eruption from Ko et al. (2003), including the presence of flare loops and the current sheet, where reconnection and electron acceleration take place. We have added in some of the regions (labeled 1–7) where we may expect energetic electrons to be observed as radio sources. Throughout this article, we will refer back to **Figure 1** in the context of radio observations and the evidence they offer for the standard model of CMEs.

There is a variety of radio emission mechanisms associated with nearly all stages of CME eruptions. These emissions may be either incoherent or coherent radiations from electrons of a variety of energy ranges, distribution functions, and different plasma environments. These emissions may thus provide diagnostic tools for many different particle and plasma conditions during eruption. Some examples of radio emission types that are encountered in CME observations, and those that we will discuss in this review, are thermal bremsstrahlung (Gopalswamy and Kundu, 1993), gyrosynchrotron or synchrotron emission (Bastian et al., 2001; Carley et al., 2017), or plasma emission (Robinson and Stewart, 1985; Pick, 1986). For the physical details and diagnostic capabilities of these emission types, we refer the reader to detailed overviews, for example, those of Ramaty (1969), Dulk (1985), and Melrose (1986, 2017), or to reviews of emission mechanisms in this Research Topic issue, for example, Nindos and et al. (2020).

In what follows, we will discuss these different radio emissions in combination with EUV, SXR, or white-light observations of CMEs. We note here that white-light CMEs may have a variety of morphologies such as the usual "three-part structure," loop-like structures, outflows, jets, and failed eruptions (see Vourlidas et al. (2013) for a review and references therein), or those with extended and complex prominence morphologies (Mishra et al., 2018). Here, we concentrate on radio observations in association with large-scale eruptions, and we do not make distinction among these different types of CME morphology unless it is pertinent to the radio observations and related phenomena.

3. CORONAL MASS EJECTION INITIATION AND ACCELERATION

As mentioned above, there is a wealth of evidence from MHD modeling supporting the flux rope theory of CMEs. However, the origin of the flux rope structure in the low corona remains

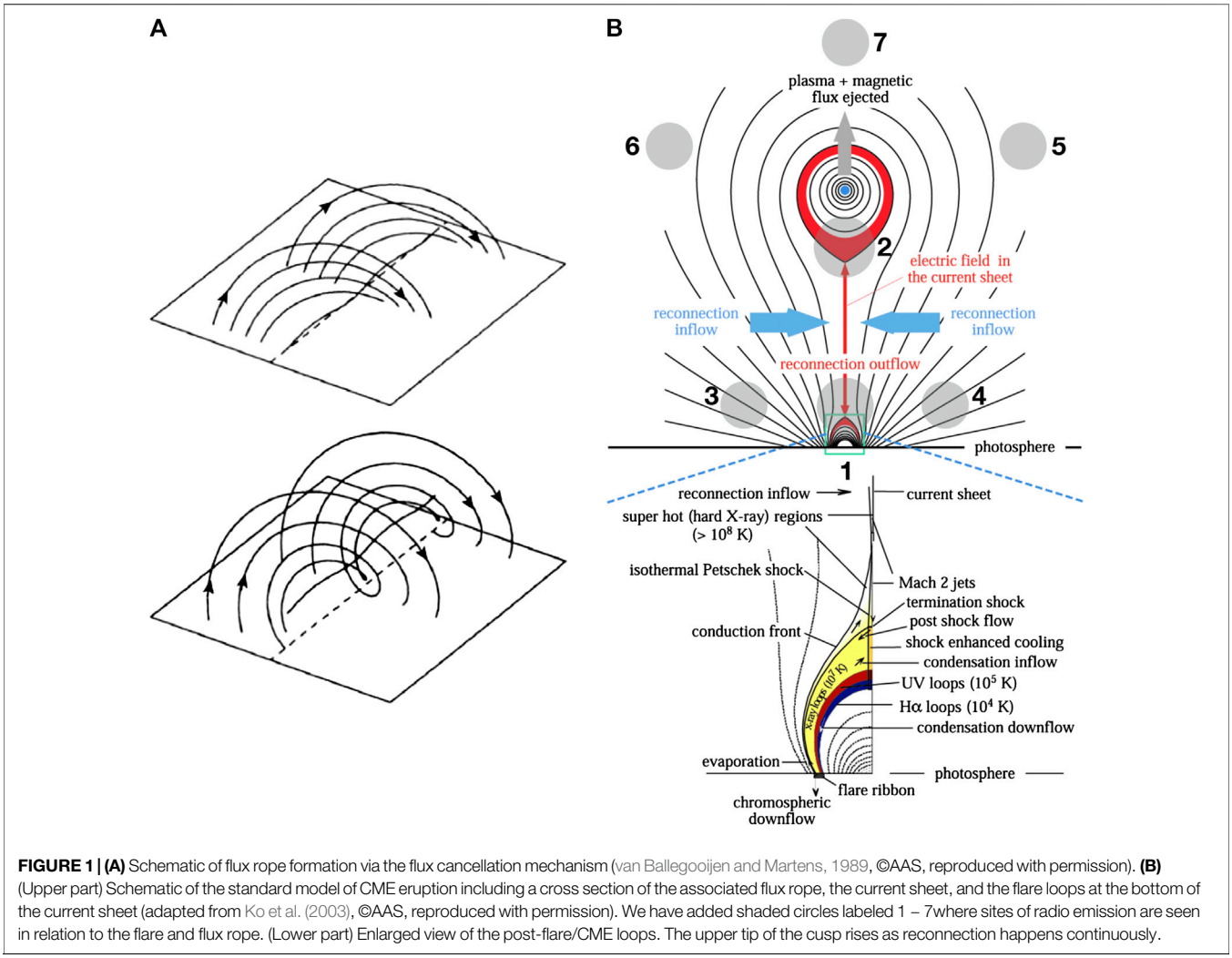

FIGURE 1 | (A) Schematic of flux rope formation via the flux cancellation mechanism (van Ballegooijen and Martens, 1989, ©AAS, reproduced with permission). **(B)** (Upper part) Schematic of the standard model of CME eruption including a cross section of the associated flux rope, the current sheet, and the flare loops at the bottom of the current sheet (adapted from Ko et al. (2003), ©AAS, reproduced with permission). We have added shaded circles labeled 1 – 7where sites of radio emission are seen in relation to the flare and flux rope. (Lower part) Enlarged view of the post-flare/CME loops. The upper tip of the cusp rises as reconnection happens continuously.

uncertain. It may be either a pre-existing magnetic flux rope which becomes destabilized via an ideal process such as the toroidal (Aulanier et al., 2010; Zuccarello et al., 2015) and kink instabilities (Török et al., 2004), or one formed from a sheared arcade through catastrophic loss of equilibrium (Forbes and Priest, 1995), tether-cutting reconnection (see **Figure 1A**), or breakout reconnection (Antiochos et al., 1999). Each of these processes has characteristic signatures of where and when one might expect to observe energetic electrons during the destabilization process (most likely due to magnetic reconnection). Given that radio observations provide direct observations of the sites of such electron acceleration, they can provide a means of testing the validity of model predictions, especially when combined with EUV or SXR imaging of the eruption. Such observations provide images of the low corona where flux rope formation and eruption initiation begin. In the following subsections, we discuss some of the latest multiwavelength observational advances and the understanding this provides us on CME precursor triggering and subsequent eruption initiation.

3.1. Coronal Mass Ejection Precursors and Eruption Initiation

Observations of the low corona can provide insight into the nascent CME structure and its early stage initiation and acceleration, for example, CME precursors such as filaments and prominences (primarily observed in Hα; Parenti, 2014) and related hot loops and sigmoid structure (primarily in EUV and SXR; Parenti, 2014; Sterling, 2000). The time evolution of such structures gives insight into CME initiation and potential triggers to the eruption, but few studies in the past have combined this with imaging of radio sources simultaneously. Previous observations relied upon relatively low cadence (several minutes) imaging observations of the erupting structure in EUV or SXR combined with images of nonthermal radio emission sources, indicative of electron acceleration (to tens or hundreds of keV) in the early stages of eruption, for example, Marqué et al. (2002) and Klassen et al. (2003). While the early multiwavelength studies showed evidence for reconnection in the initiation phases of erupting sigmoids and filaments, the low-cadence imaging of the EUV and SXR images

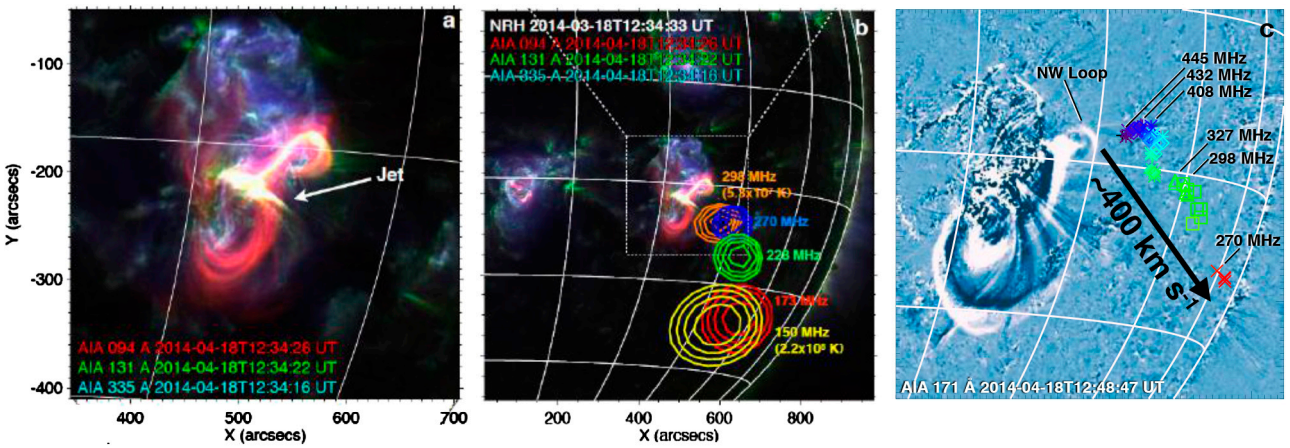

FIGURE 2 | Observations of nonthermal radio sources during the eruption of a sigmoid observed in EUV (adapted from Carley et al. (2016), ©AAS, reproduced with permission). **(A)** A brightening and jet occur at the center of the sigmoid, at the same time a beam of electrons (type III burst) emerges from this region, as seen in panel **(B)**. This is an indicator of reconnection taking place at the center of the sigmoid, followed by rapid acceleration of the emerging flux rope. Such a reconnection site would agree with the tether-cutting model of flux rope eruptive triggering. **(C)** During the acceleration phase of the eruption, a series of nonthermal radio sources propagate above the sigmoid at 400 km s^{-1}, indicative of breakout-style reconnection.

generally hindered comparison to the radio observations, which have imaging time resolutions of seconds or less.

With the launch of AIA onboard the Solar Dynamics Observatory (SDO; Pesnell et al., 2012), the cadence of EUV imaging approached the same order of magnitude available in the radio, allowing for a much more detailed comparison of the eruptive dynamics and sites of electron acceleration during initiation. AIA has a temperature coverage of 1–10 MK, arc-second spatial resolution, and cadence of 12 s, and provides routine evidence for structures in the corona that have the hallmarks of flux ropes (hot plasma in twisted magnetic field lines which become destabilized and accelerate rapidly; Zhang et al., 2012; Hannah and Kontar, 2013; Chintzoglou et al., 2015; Nindos et al., 2015). Such observations in combination with radio now have the ability to determine the sites of energetic electrons (and by inference magnetic reconnection) during flux rope destabilization and acceleration. Carley et al. (2016) recently observed a plasma jet in AIA 94, 131, and 335 Å occurring simultaneously with a type III radio burst observed with NRH from 150 to 298 MHz, indicating electron beam acceleration to ~ 30 keV at the time of the jet. The beam and jet were observed to originate near the center of a sigmoid at the time of eruption initiation see **Figure 2**, which was interpreted as evidence for the flux cancellation or tether-cutting mechanisms during the initiation phase (similar to that illustrated in **Figure 1A**, although the presence of a jet is not a standard component of these mechanisms). This corroborated the same findings using UV spectroscopic analysis of the same event (Joshi et al., 2015). During the CME acceleration phase, Carley et al. (2016) also showed nonthermal radio sources at successively lower frequencies propagating above the flux rope as it erupted, with its northern apex traveling ~ 400 km s^{-1} (see **Figure 2C**). While the position of these radio sources is indicative of a breakout-style reconnection, it was unclear from the observations if this reconnection was responsible for flux rope release or, conversely, driven by the erupting body in the early stages of eruption. Aurass et al. (2013) also showed radio imaging observations of coronal plasma emissions at altitudes of 290 Mm in the early stages of an eruptive flare, interpreted as evidence for near-relativistic electrons accelerated during breakout reconnection. Similarly, James et al. (2017) used a combination of AIA, the Heliospheric Magnetic Imager (HMI; Scherrer et al., 2012), and NRH to show the locations of nonthermal radio sources from 150 to 445 MHz during the slow-rise phase of a flux rope, concluding that as the rope slowly expands, it continuously reconnects with the overlying ambient magnetic field of the corona (although destabilization was attributed to the torus instability rather than breakout). Also using the NRH, Huang et al. (2011) showed observations of a 432-MHz nonthermal radio emission co-spatial with the footpoint of a flux rope at the time of eruption initiation, interpreted as a signature of coronal reconnection that led to reduction in magnetic tension on the rope and subsequent eruption.

The above studies show that low-frequency radio observations provide important insight into the sites of nonthermal electrons (to tens of keV), indicative of the sites of reconnection during eruption initiation. At higher frequencies, radio observations have led to direct imaging of the destabilization and eruption of prominences in the microwave domain (Srivastava et al., 2000; Kundu et al., 2004; Wu et al., 2016; Kallunki and Tornikoski, 2017). For example, Huang et al. (2019) recently used the Nobeyama Radioheliograph (NoRH) to image the spatial and temporal variability of thermal bremsstrahlung emission from plasma in an erupting prominence (see **Figure 3**), revealing localized heating to $(1-2)\times10^4$ K on a background plasma temperature of $(0.5-1)\times10^4$ K. This was interpreted as small-scale release of magnetic energy in the twisted magnetic structure of the prominence during the eruption. Microwave imaging of prominence eruption has also been compared directly to

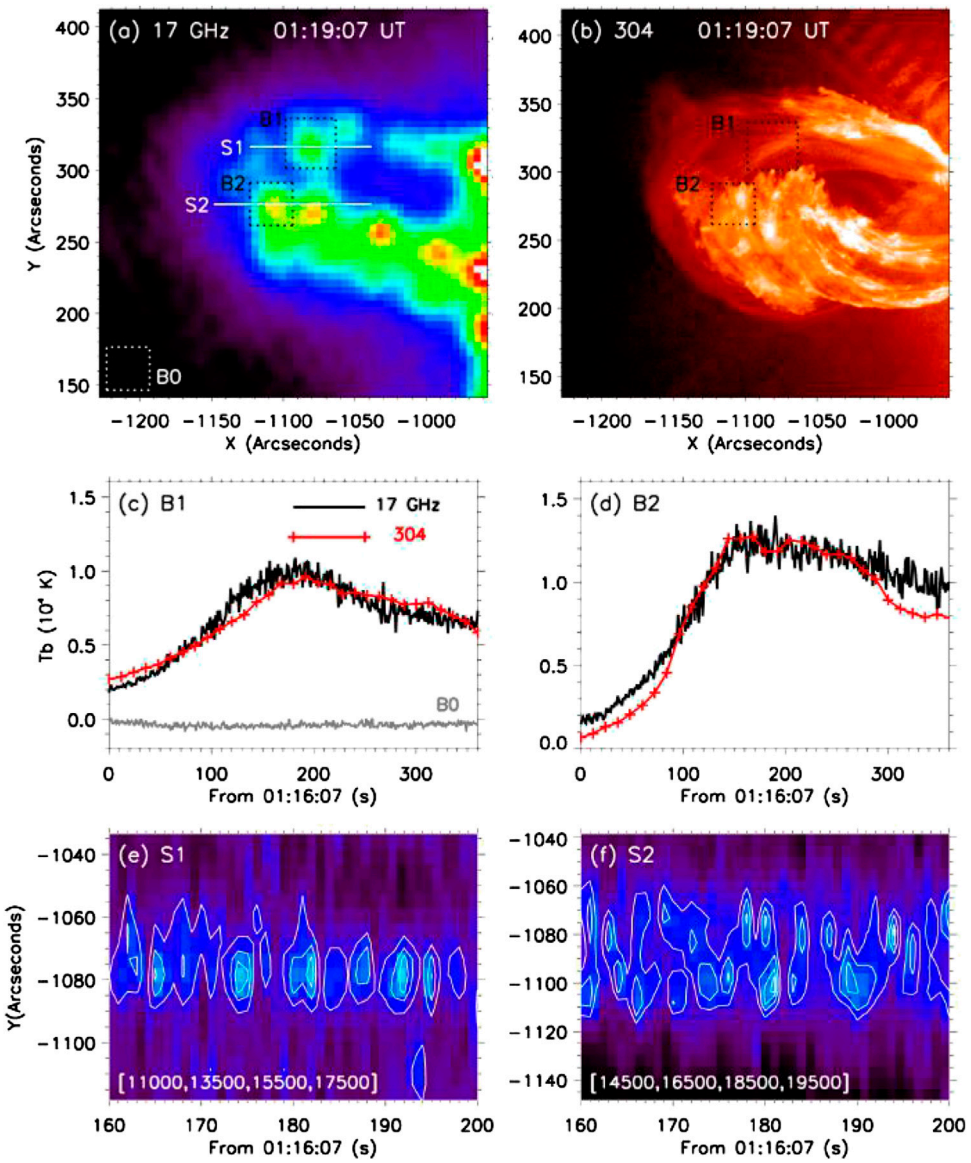

FIGURE 3 | Prominence eruption on 2015 May 9 observed in **(A)** microwave imaging from NoRH at 17 GHz, and **(B)** EUV imaging from SDO AIA 304 Å. **(C–D)** The mean brightness temperature and mean intensity in boxes B1 and B2 (indicated in the microwave and EUV images) showing a rise–peak–decay time profile. **(E–F)** Brightness temperature time–distance plots from S1 and S2 in the 17-GHz image showing spatially localized and intermittent enhancements in temperature, interpreted to be localized heating events during prominence eruption (adapted from Huang et al. (2019), ©AAS, reproduced with permission).

numerical models, with Kliem et al. (2010) finding that the dynamics of one such event was best accounted for using numerical modeling of the kink instability.

Despite improvements in our ability to observe flux rope signatures in EUV (or microwave) and the associated reconnection sites in low-frequency radio, these multiwavelength observations remain relatively rare. That said, with the development of new radio imaging spectrometers and the growing archive of EUV observations, there are increasing opportunities to study nascent CME structure and its eruption initiation in the context of the standard model and MHD model predictions.

3.2. Coronal Mass Ejection Acceleration and Flare Impulsive Phases

The early phase development of the nascent flux rope is best imaged in EUV and SXR, and radio observations provide a unique diagnostic on where electron acceleration (and inferred reconnection) occurs during the triggering of the eruption. The next stage of development is the acceleration phase of the CME, during which time flare emissions (HXRs and nonthermal microwaves) are usually observed (Zhang et al., 2001; Berkebile-Stoiser et al., 2012). The rapid CME development in the low corona during this phase strongly correlates with the associated flare activity.

Figure 1B, adapted from Ko et al. (2003), shows a 2D schematic diagram of magnetic configurations formed in an eruptive process. Such a configuration has now been observed in EUV with SDO/AIA instruments for the eruptive X8.2 flare associated with a CME on 2017 September 10 (Yan et al., 2018). **Figure 1B** illustrates the close relationship between flares and CMEs as well as the different electron acceleration sites (shaded gray circles) which can be found in the flare/CME development. Radio imaging observations provide one of the best means of detecting nonthermal electrons associated with the flare and CME development at these sites since they may be sensitive (e.g., through plasma emissions) to a smaller number of energetic electrons in the corona than what is usually required to produce strong chromospheric HXR emissions. In the following, we discuss the radio signatures of the flare–CME evolution in terms of where, when, and how electrons are energized during the CME acceleration and flare impulsive phases.

3.2.1. Electron Acceleration Sites and Reconnecting Current Sheets

Joint spectral and multifrequency imaging radio observations provide evidence for electron acceleration associated with magnetic reconnection in the various current sheets developed during the evolution of the flare/CME in the low corona. A lot of HXR and radio observational evidence for electron acceleration in reconnecting current sheets has been spectroscopic, revealing bursty or quasiperiodic electron energization to tens of keV, interpreted as a signature of tearing mode instabilities in the current sheet connecting the flare loops to the ejected plasmoid (Kliem et al., 2000; Karlický et al., 2005). This combination of spectral and imaging observations at several radio frequencies has provided direct evidence on the formation of reconnecting current sheets behind ejected flux ropes and on the acceleration and radiation of energetic electrons in these current sheets. That was evidenced by observations of long duration broadband continuum (type IV bursts) drifting to low frequencies and modulated by fast sporadic bursts. The radio emissions were found to originate from two sources: a quasi-stationary and a fast moving source (around 400 km s^{-1} around 400 MHz). Both radio sources were located close to a rising EUV loop (at a speed of 540 km s^{-1}) overlying the flare. The stationary and moving radio sources are presumably on either end of the current sheet behind the erupting flux rope (e.g., regions one and two on **Figure 1B**). A further study by Benz et al. (2011) investigating the positions of decimetric pulsations with respect to coronal hard X-ray sources in the range of 18–100 keV pointed to the acceleration and radiation of electrons in the current sheet above the coronal X-ray source. Finally, production of energetic electrons in the current sheet behind a rising flux rope is commonly observed in the late flare phase since stationary sources of type IV bursts (in particular sources of flare continua) are found to be co-spatial with post-eruption flare loops (see, e.g., Carley et al., 2016; Morosan et al., 2019b).

Recent studies using EOVSA observations beautifully demonstrate the link between EUV, radio sources in the GHz regime, and the standard model of solar eruptions (Gary et al., 2018; Karlický et al., 2020), as depicted in **Figure 1B**. EUV and X-ray diagnostics of this system were also provided by Yan et al. (2018). Early in the flare, at the time of drifting pulsation structures observed in the 1–2 GHz range with the Ondrejov radio spectrograph, the EOVSA imaging spectroscopy captured the fast evolution of a radio source below 4 GHz (bifurcation of the radio source seen in **Figures 4A,B**) in connection with the tearing and ejection of the filament seen in EUV (Karlický et al., 2020). These observations suggest that the radio pulsations are signatures of suprathermal electrons trapped in the rising magnetic rope and flare arcade when flare magnetic reconnection starts.

Figure 4C shows the configuration of microwave sources at the onset of the flare main phase. While source A (observed mainly at < 5 GHz) is co-spatial with the rising flux rope, source B corresponds to the nonthermal electrons in the flare arcade. Source B (at frequencies above 5 GHz) is also closely related to an extended nonthermal HXR source in the 30–100 keV range, as was observed using a combination of RHESSI and EOVSA images in Gary et al. (2018) (see **Figure 5**). The sources at lower frequencies are distributed along a line connecting the EUV bright loops and the fast rising flux rope, potentially corresponding to the reconnecting current sheet. This strongly suggests the acceleration of energetic electrons in this reconnecting current sheet with HXR and radio emissions in the 10 GHz range being produced by electrons ejected downward (region one of **Figure 1B**) from the current sheet and radio emissions below 5 GHz being produced by electrons ejected upward (region two of **Figure 1B**).

Two more distinct sources (C and D) are seen at high frequencies and are associated with the legs of a much larger loop associated with the coronal mass ejection. This is consistent with regions three and four in **Figure 1B** and with earlier observations at lower frequencies and higher in the corona of nonthermal radio sources at the base of CME legs, as reported in Maia et al. (1999), Carley et al. (2016), and Morosan et al. (2020). At the flare peak phase, the weaker flank sources are no longer detected and the main microwave source B associated with the flare arcade continues to rise together with the flare arcade seen in EUV and the nonthermal 35–60 keV source observed by RHESSI (**Figures 5C,D**). In a later phase of the event, an elongated current sheet is seen above the limb in EUV with nonthermal HXR sources (35–50 keV) at the base of the current sheet and located between the microwave sources now positioned at the rising EUV bright loops (**Figures 5E,F**). In total, the combination of EUV, HXR, and microwave imaging matches completely the expectations of the standard model as in **Figure 1B**. Indeed, Chen et al. (2020) recently showed that the variety of observed microwave sources during the 2017 September 10 event can be explained by the magnetic topology and the associated energy release scenario expected of the standard model in three dimensions.

Another output of microwave imaging spectroscopy is the possibility to deduce (from gyrosynchrotron emission) the spatially resolved values of the spectral index of nonthermal electrons and of the magnetic field. For the same 2017-September-10 event discussed above, the spatially resolved magnetic field at the base of the current sheet was

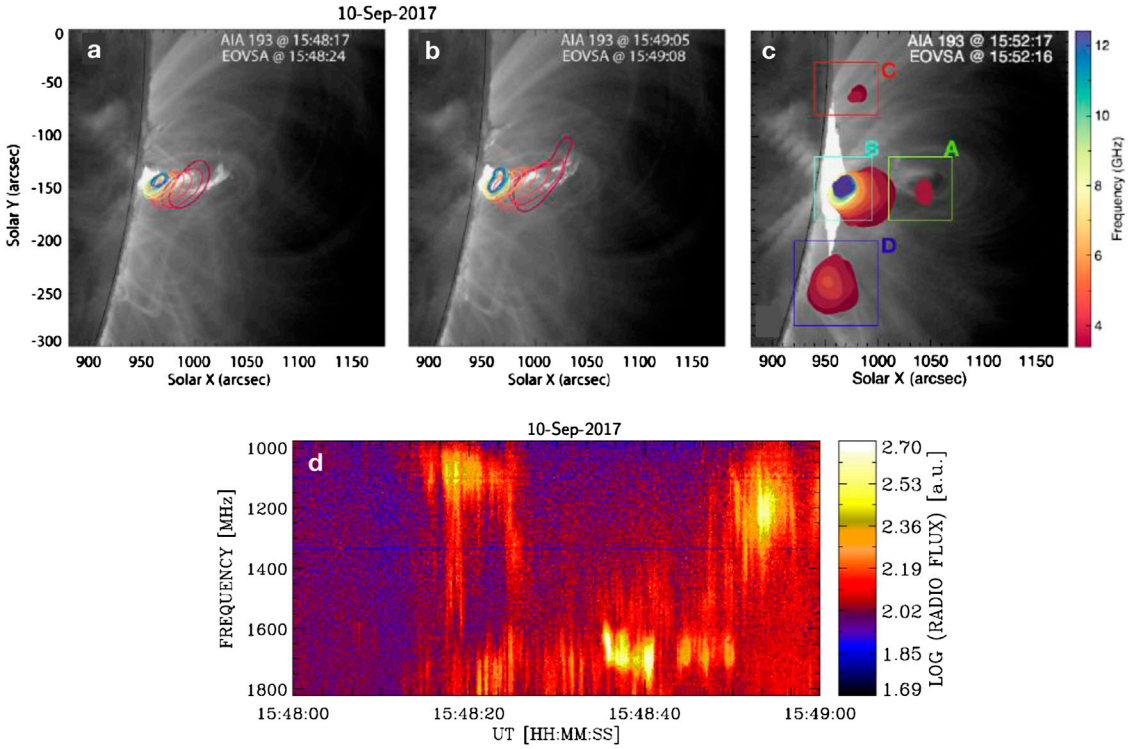

FIGURE 4 | (A–B) EOVSA sources (contours) at 15:48:24 and 15:49:08 UT during the 2017 September 10 flare overlaid on the observations of the tearing of the ejected filament. **(C)** EOVSA spectral imaging observations of the microwave sources in the 3.4–12.4 GHz frequency range at 15:52:16 UT. **(D)** Detail of the radio dynamic spectrum in the 1,000–1800 MHz range observed at the very beginning of the flare at 15:48–15:49 UT. The pulsations appear mainly in two frequency bands (1,000–1,300 MHz and 1,600–1,800 MHz), which are interconnected by fast drifting bursts (adapted from Karlický et al. (2020), ©AAS, reproduced with permission).

found to be between 200 and 900 G and decay at a rate of 5 G s^{-1} for up to 2 min (Fleishman et al., 2020). This kind of diagnostic is of major importance in flare/CME physics and space weather applications; for example, spatially resolved magnetic field measurements could be used to diagnose the energy source and driver of the flare/CME eruption. Such diagnostics remain a rarity at present, but modern radio imaging spectroscopy, like that provided by EOVSA, hold great promise for more regular observations of the all-important eruption magnetic field (see also **Section 5**).

3.2.2. Reconnection Outflow Jets and Termination Shocks

One by-product of magnetic reconnection is the formation of jets and termination shocks. Soft X-ray ejecta were extensively studied at the time of Yohkoh observations, and it had been shown that the jets can be related to the production of electron beams and their associated type III bursts (Raulin et al., 1996). Nowadays, EUV jets are imaged with AIA, and this can be readily compared with imaging of the associated type III radio bursts (see **Figures 2A,B**).

According to the standard eruption model, outflows from the reconnection region interact with the underlying flare arcade and with the bottom part of the rising magnetic rope. This generates termination shocks (Cargill and Priest, 1983) which were identified for the first time in 300 – 400 MHz radio observations as a zero-drift type II burst with a characteristic herringbone fine structure and a band split (Aurass et al., 2002). A simultaneous zero-drift type II burst was later reported at 40 – 80 MHz (Aurass and Mann, 2004) and identified as the termination shock from the upper reconnection outflow during the rise of a flare-associated CME (region two on **Figure 1B**). More recently, high-cadence imaging spectroscopy observations at higher frequencies (1–1.8 GHz) by the VLA identified signatures of a solar flare termination shock lower in the corona (Chen et al., 2015, see **Figure 6**). VLA images revealed localized radio sources, nearly co-spatial with the HXR loop-top source at 15–25 keV, corresponding to short-lived and narrow-frequency bandwidth radio spikes produced at the termination shock, as suggested by the numerical simulations of a reconnection outflow seen edge-on. These observations provide strong evidence that the acceleration mechanisms for energetic electrons are associated with flare/CME termination shocks.

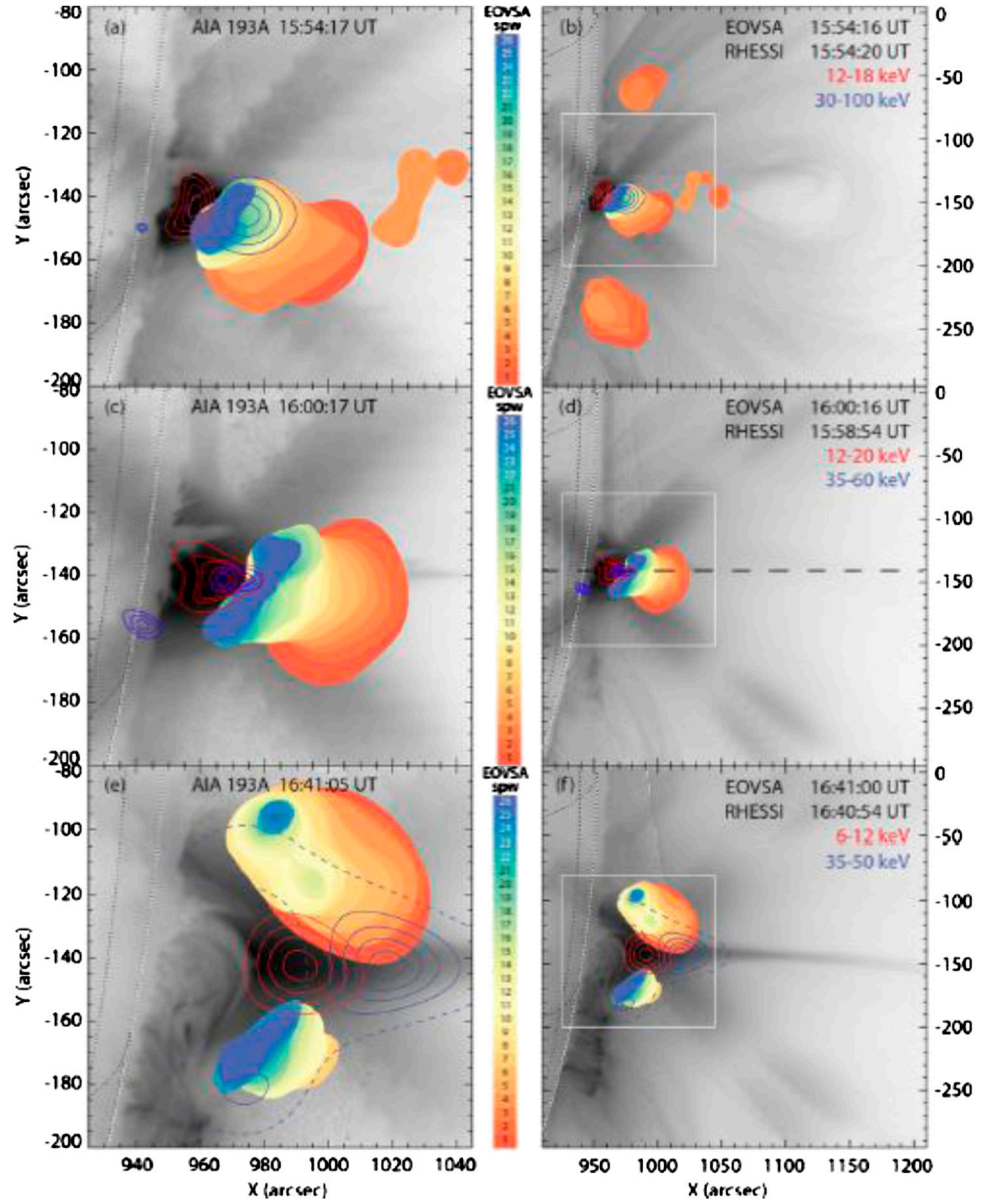

FIGURE 5 | Overlay of AIA, RHESSI, and EOVSA images. 50% contours of EOVSA at 26 spectral windows are plotted with hues shown in the color bar. RHESSI HXR 30%, 50%, 70%, and 90% contours are also superposed for two energy ranges: **(A, C, E)** zoomed fields of view of the limb flare, with larger field of views in **(B, D, F)** (adapted from Gary et al. (2018), ©AAS, reproduced with permission).

4. CORONAL MASS EJECTION FORMATION AND RECONNECTION WITH THE CORONAL ENVIRONMENT

The current sheet that forms between the flare loops and erupting structure is responsible for electron acceleration and resulting radio sources near the current sheet. This occurs at the main acceleration phase of the erupting flux rope, and during this phase, sources may also appear on the boundaries of the flux rope (e.g., region 5, six, or seven in **Figure 1B**), providing evidence that electron energization is taking place from the interaction of the flux rope with the external coronal environment.

Démoulin et al. (2012) presented an example of propagating radio sources at the boundaries of an erupting structure (also directly imaged as a radio CME), where such radio sources were believed to be plasma emission from energetic electrons due to reconnection of the erupting structure with the coronal environment. These radio sources are often type IIIs, indicating that reconnection between the erupting structure and ambient open fields can lead to particle escape into the heliosphere, as had previously been reported by Maia and Pick (2004). Pick et al. (2016) showed an example of a flux rope propagating nonradially and interacting with ambient coronal magnetic loops during this propagation. The interactions result in

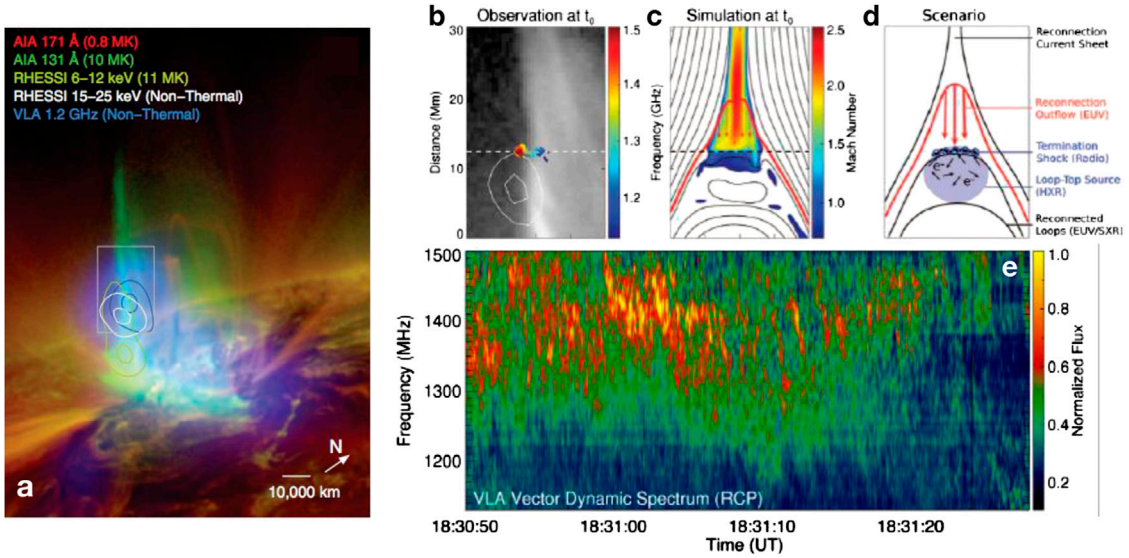

FIGURE 6 | (A) Radio source (blue contours at 1.2 GHz) observed with VLA at the top of hot flaring loops (10 MK). This radio source is nearly co-spatial with a nonthermal HXR source (white contours) at 15–25 keV observed with RHESSI. **(B–D)** Observation and simulation of the dynamic termination shock. **(B)** The termination shock appears as a dynamic surface with many unresolved radio sources, each of which corresponding to a radio spike in the dynamic spectrum. White contours show the coronal HXR source at 15–25 keV. **(C)** The termination shock is seen in the MHD simulation as a sharp layer of velocity discontinuity at the loop top. The fast-mode magnetosonic Mach number is shown in color and overlaid with magnetic field lines. **(D)** Physical scenario of emission processes near the termination shock. Radio spikes are emitted as accelerated electrons impinge on density fluctuations at the shock (blue circles). These electrons also produce a HXR source in the shock downstream region (blue-shadowed region). **(E)** VLA radio spectrum showing the spike bursts. Figure adapted from Chen et al. (2015) and reproduced under AAAS copyright.

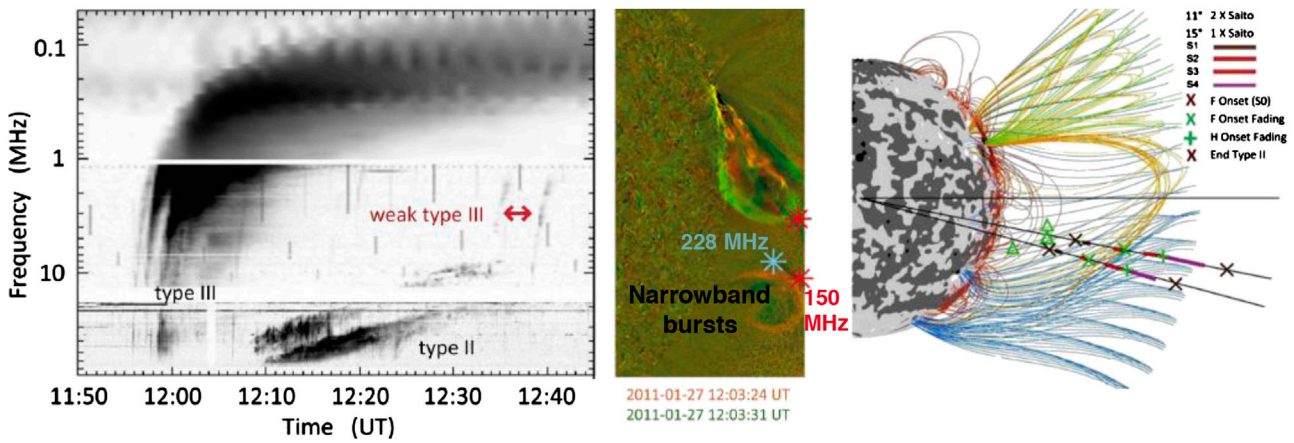

FIGURE 7 | (A) Type III and type II radio bursts observed for an eruptive event on 2011-01-27. **(B)** These radio bursts were associated with the non-radial propagation of an erupting flux rope and its subsequent interaction with the coronal environment to produce various radio sources. **(C)** The radio sources are due to electron acceleration in both open and closed field environments. Figure adapted from Pick et al. (2016), ©AAS, reproduced with permission.

reconnection between the eruption and ambient magnetic field, resulting in electron acceleration and the observation of type III and narrow-band bursts (**Figure 7**). Carley et al. (2016) also reported 150–445 MHz imaging observations of multiple type III bursts for a 5-min duration during the early stages of flux rope eruption. This was attributed to reconnection and electron beam acceleration to 5 keV above the flux rope as it erupts. This is similar to the MHD modeling scenario of solar energetic particles (originally trapped in the flux rope) being released onto open field lines from a breakout-style reconnection during flux rope eruption (Masson et al., 2013, 2019). Similar observations have been used to explain secondary episodes of electron acceleration that result in the delayed arrival of energetic electrons (from several tens to hundreds of keV) detected *in situ* (Klein et al., 2005; Dresing et al., 2018). Salas-Matamoros et al. (2016) also showed type III sources near open fields at an eruption boundary,

thought to be due to electron acceleration to 45 keV via a betatron mechanism or magnetic reconnection related to the passing of a EUV wave across open magnetic field lines. Recently, Duan et al. (2019) also concluded that an interplanetary type III radio burst observed with Wind/WAVES during a jet-like CME eruption was due to reconnection of the erupting structure with the ambient coronal environment and subsequent escape of energetic electrons into the heliosphere.

There is much evidence of reconnection at flux rope boundaries as they erupt. However, it remains unclear if this reconnection is an inherent part of the flux rope formation (i.e., part of the "on-the-fly" formation, as it erupts) or simply a natural consequence of flux rope motion through the corona, for example, eruption impact on a region of ambient magnetic structures leading to forced reconnection in this region, as reported in Srivastava et al. (2019).

5. TYPE IV BURSTS AND RADIO CORONAL MASS EJECTIONS

In this section, we discuss sources of radio emission believed to be from energetic electrons radiating from within the erupting flux rope, namely, type IV radio bursts and the related phenomenon of radio CMEs.

5.1. Type IV Radio Bursts

Boischot (1957) first identified a rare type of radio burst occurring after a solar flare and characterized by a radio emission source moving outward with speeds of several hundred kilometers per second, which he named a type IV radio burst. Boischot (1958) and Boischot and Daigne (1968) proposed that this emission is due to synchrotron radiation of 2.5–3 MeV electrons trapped in moving coronal magnetic structures with field strength on the order of 1 G. However, observations during this era also revealed the existence of similar broadband post-flare emissions without any systematic motions of the radio source (Pick-Gutmann, 1961). Type IV bursts have thus been subcategorized over the years into stationary and moving (see historical overviews from Robinson and Stewart (1985), Pick (1986), and Pick and Vilmer (2008)), with the moving component now attributed to energetic electrons trapped in the CME, emitting plasma emission (Duncan, 1980; Gary et al., 1985), gyrosynchrotron or synchrotron (Dulk and Altschuler, 1971; Bain et al., 2014; Carley et al., 2017), or sometimes electron cyclotron maser emission (Liu et al., 2018; Morosan et al., 2019a). If the emission mechanism can be readily identified, type IV bursts can therefore provide diagnostics of electron density, characteristics of the electron energy distribution (e.g., spectral index and maximum energy), or magnetic field strength in the CME flux rope.

Furthermore, type IV radio sources can be located at different parts of the erupting structure, such as in the CME core (Tun and Vourlidas, 2013; Bain et al., 2014; Carley et al., 2017) or at the CME legs (Carley et al., 2016; Dresing et al., 2016; Gary et al., 2018), and can therefore provide plasma diagnostic at various parts of the CME structure. For example, Bain et al. (2014) determined type IV emission in the range 150–360 MHz from a CME to be optically thin gyrosynchrotron, enabling a calculation of a magnetic field strength of $\sim$3–5 G in the CME core at a heliocentric distance of $\sim$1.5 $R_{\odot}$(see **Figure 8A**). Similarly, Carley et al. (2017) found type IV emission to be gyrosynchrotron produced internally to the CME from energetic electrons $>$1 MeV in a 4.4-G magnetic field at $\sim$1.3 R$\odot$ (see **Figure 8B**). Generally, CME magnetic field strengths have been found to range from $\sim$0.6 to 15 G at heliocentric distances $<$4 R$\odot$ (Stewart et al., 1982; Gary et al., 1985; Bastian et al., 2001; Maia et al., 2007; Tun and Vourlidas, 2013; Sasikumar Raja et al., 2014). Energetic electrons at the core and front of the CME were also recently shown to be responsible for plasma emission (Hariharan et al., 2016; Vasanth et al., 2019), while Morosan et al. (2019b) showed that type IV emission mechanisms can also vary within a single event, ranging from plasma to gyrosynchrotron emission (and potentially ECM). Type IV bursts are therefore one of the most powerful diagnostic tools of the plasma conditions within a CME, provided that the emission mechanism can be unambiguously identified. That said, they have a low occurrence rate compared to type II and III bursts, with only 5% of CMEs having an associated type IV radio burst (Gergely, 1986, although a modern statistical analysis in this regard is lacking).

With respect to the standard model of **Figure 1B**, type IV radio emissions can be located at several regions. For example, a stationary type IV could be located at the flare site (region 1). A moving type IV could belong to region 2, or potentially anywhere within the flux rope body where energetic electrons may become trapped and radiate.

5.2. Radio Coronal Mass Ejections

Type IV radio bursts may be observed as radio sources that are closely associated with a CME and indicate the presence of energetic electrons in the internal magnetic structure of the flux rope. Energetic electrons trapped in the flux rope can also sometimes lead to a spatially resolved image of a "radio CME" (**Figure 9**). Of the many tens of thousands of CMEs observed in white light, only a handful have ever been imaged at radio wavelengths. A few were attributed to spatially resolved gyrosynchrotron sources (Bastian et al., 2001; Maia et al., 2007; Démoulin et al., 2012; see **Figure 9**). Other radio CMEs were interpreted as plasma emission (Maia et al., 2000; Carley et al., 2016) or even thermal bremsstrahlung emission (Gopalswamy and Kundu, 1993). Thermal bremsstrahlung emission from a CME, however, has never been corroborated with newer more sensitive instruments (see section 2.1 in Vourlidas, 2004). Mondal et al. (2020) recently used MWA to image a radio CME, showing such observations can be used to make spatially resolved diagnostics of the magnetic field, with the regions labeled by the blue circles in **Figure 9D** ranging in field strength from 7 to 12.6 G.

Despite their diagnostic potential, type IV bursts and radio CMEs remain understudied in the modern era, perhaps due to more attention being focused on type II bursts or due to a relative lack of observations of type IVs. This has left many open questions on the phenomenon. For example, given that the

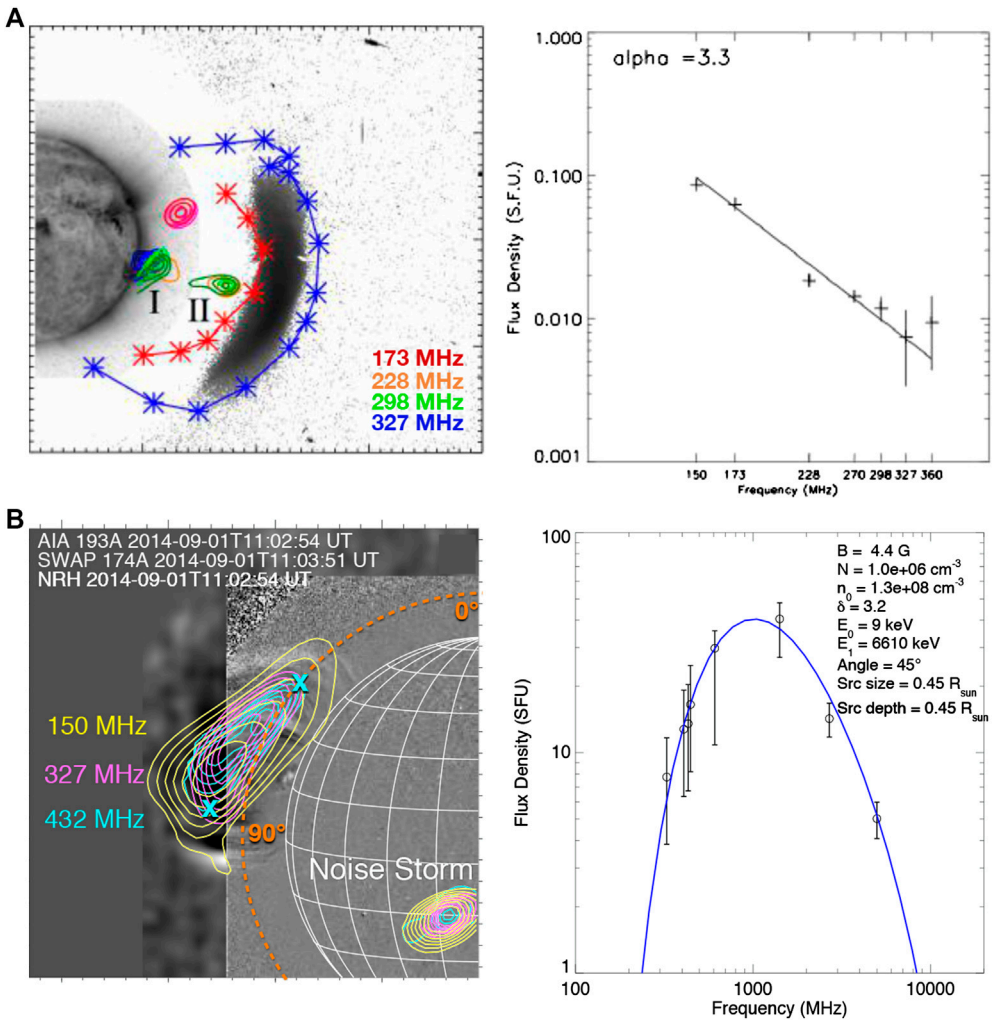

FIGURE 8 | Magnetic field diagnostics of CMEs. **(A)** Type IV emission sources at the core of a CME with a flux density spectrum representative of the optically thin gyrosynchrotron emission (adapted from Bain et al. (2014), ©AAS, reproduced with permission). **(B)** Type IV sources likely associated with the CME core, again showing a gyrosynchrotron flux density spectrum (Carley et al., 2017) (reproduced with permission from *Astronomy and Astrophysics*© ESO). Observations such as these provide one of the few means of determining CME magnetic field strengths.

emission is from energetic electrons (from tens to thousands of keV) internal to the CME structure (at the core, flanks, or legs), how are such electrons injected onto the magnetic field of the flux rope and where are they accelerated? As mentioned, Masson et al. (2013, 2019) indicated that energetic particles may enter the flux rope body via the magnetic reconnection in the underlying current sheet; for example, reconnected field lines from the current sheet wrap around the flux rope, building it up further and carrying energetic particles into the flux rope structure. Evidence for energetic electrons spreading into the erupting volume was found by radio imaging of nonthermal sources using NRH in combination with flux rope eruption imaging in the EUV (Huang et al., 2011). This may explain the observation of moving type IV radio sources often bifurcating and breaking away from the stationary source, as observed in Pick and Maia (2005). Some of the energetic electrons accelerated in the current sheet may be carried away to produce radio emission from within the plasmoid. If the electrons spread throughout the flux rope, they may allow it to be spatially resolved as an image of a "radio CME."

The big picture question is, however, why spatially resolved radio emission of CMEs is so rare. It could indicate a special configuration between the flux rope and flare such that energetic electrons are carried away by the eruption. Or it may be an instrumental issue. The emission from radio CMEs exhibits extremely weak flux densities, for example, ~1–10 SFU in Carley et al. (2017) and as low as 10^{-2} SFU in Mondal et al. (2020). This emission can be co-temporal with other types of radio bursts, which can reach up to 10^6 SFU in extreme cases (Gary, 2019). Hence, many instruments may not possess the sensitivity or dynamic range required to observe both types of emissions simultaneously. Bastian and Gary (1997) originally modeled the thermal bremsstrahlung radio emission expected from a CME, which helps in determining the dynamic range and

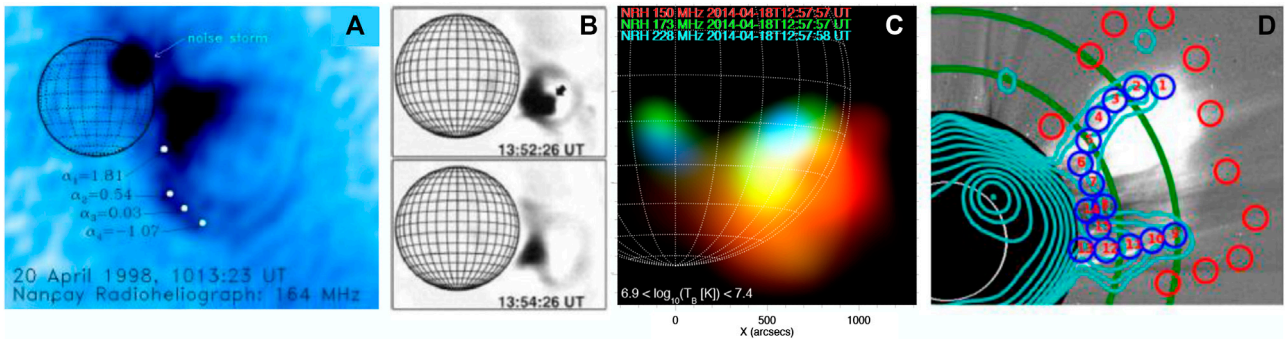

FIGURE 9 | Examples of CMEs observed in radio imaging. **(A)** An example of a spatially resolved radio CME observed using the NRH. The emission mechanism was determined to be synchrotron emission, enabling magnetic field diagnostics (Bastian et al., 2001). **(B)** A similar example of gyrosynchrotron emission from an erupting plasmoid (Maia et al., 2007). **(C)** A "radio bubble" believed to be plasma emission from an erupting CME (Carley et al., 2016). **(D)** MWA observations of weak (10^{-2} SFU) gyrosynchrotron emission at several different locations in the CME, hence leading to spatially resolved magnetic field measurements (Mondal et al., (2020), ©AAS, reproduced with permission).

sensitivity required of radio observations. Recent advances by Moschou et al. (2018) to model CME thermal emission using MHD simulations have also helped in this regard, and the authors highlight the future need for modeling thermal and nonthermal radio emissions simultaneously. Overall, modern instrumentation should aspire to high dynamic range and sensitive observations of eruptive coronal phenomena, as routine imaging of radio CMEs has the potential to revolutionize CME physics, primarily due to the spatially resolved magnetic field measurements that such observations can offer.

6. ERUPTION-DRIVEN SHOCKS

Although CMEs were discovered only with the advent of space-based white-light observations in the 1970s with the OSO-7 satellite (Tousey, 1973), evidence for solar eruptions first came from the radio domain in the 1940s. In observations of a time series of single frequencies at 60 MHz, 100 MHz, and 200 MHz, Payne-Scott et al. (1947) noted that the delay in onset time of the burst from high to low frequency may suggest "the excitation of radiation at successive levels by an agency traveling at finite velocity," at the time estimated to be a few hundreds of kilometers per second. Wild et al. (1954) and Wild et al. (1959) identified the emission to be generated at the coronal plasma oscillation frequency and its first harmonic, with Uchida (1960) and others attributing the emission to a shock traveling through the corona. This type of radio burst was named "type II" and is now widely believed to be due to the generation of radio emission by energetic electrons accelerated in a shock as it propagates into the corona (Nelson and Melrose, 1985).

Type II bursts generally start below 150 MHz (Mann et al., 1996), and some may continue on to be observed at decametric and hectometric wavelengths with space-based instruments as interplanetary (IP) type II bursts (a more detailed description of IP type IIs is provided in Vourlidas et al. (2020), this research topic issue). Decametric to hectometric type II bursts are generally attributed to shocks driven by CMEs in the corona and heliosphere. However, several examples of type II bursts exist with starting frequencies in the decimetric range (Vrsnak et al., 1995; Cho et al., 2013; Cairns et al., 2020), and the origin of such "high-frequency" type II bursts is somewhat debated. They may be from blast waves due to impulsive heating by flares low in the corona (Magdalenić et al., 2012), driven by the shock of eruptive bubbles, or potentially due to strong lateral expansion (associated with EUV waves) during early-phase flux rope eruption (Patsourakos and Vourlidas, 2012; Nitta et al., 2014).

We concentrate here on the metric or decimetric type II bursts. They exhibit drift rates from −0.1 to −0.4 MHz s^{-1} and last on the order of 10 min. They usually show two emission bands with a 2:1 ratio, with each band having a bandwidth of $\Delta f/f = 0.3$ (Mann and Classen, 1996; Aguilar-Rodriguez et al., 2005). Observational studies have been used to derive shock kinematics: for example, Gopalswamy et al. (2013) used STEREO EUVI to show that the typical height of eruptions at the start time of metric or decimetric type II bursts is between 1.2 and 2 $R_\odot$. Vršnak et al. (2002) used the frequency drift of 18 metric type II bursts to show their exciter speeds were in the range of $\sim$ 500–1,500 km s^{-1}. Theoretical models have also successfully explained the characteristic features of type II bursts using 3D MHD simulations of coronal shocks in combination with kinetic simulations of radio emission from energetic electrons produced via the shock-drift acceleration mechanism (Knock and Cairns, 2005; Schmidt and Cairns, 2012; Schmidt et al., 2013; Cairns and Schmidt, 2015).

Type II bursts provide their most powerful diagnostics when they are directly imaged in radio, and the recent advances in high-cadence EUV imaging have allowed for observation of where type II radio sources (and hence shocks) are located with respect to eruptive structures in the early phases of evolution. For example, Dauphin et al. (2006), Bain et al. (2012), Zimovets et al. (2012), and Zucca et al. (2014a) have shown excellent radio imaging observations of type II sources in association with EUV and/or SXR erupting structures (**Figure 10**). The location of the radio sources is often found at the driver apex (region seven in

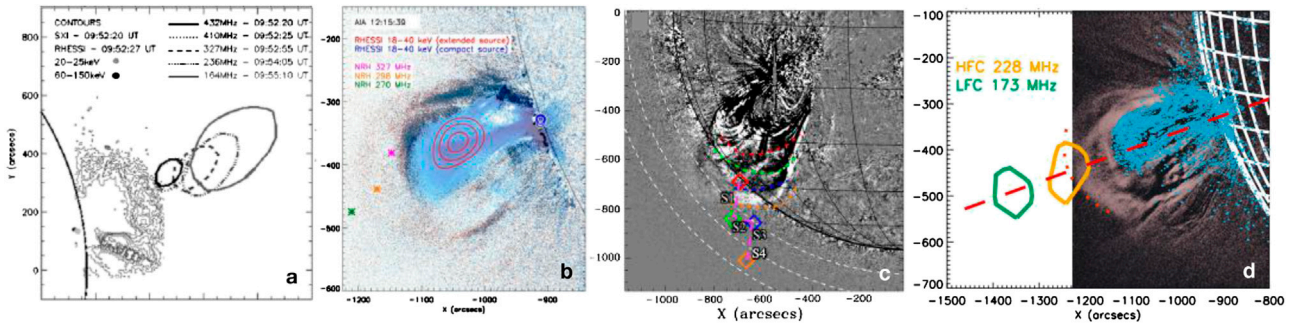

FIGURE 10 | Images of type II radio sources in association with eruptive activity observed in EUV or SXR from **(A)** Dauphin et al. (2006), **(B)** Bain et al. (2012), **(C)** Zucca et al. (2014b), and **(D)** Zimovets et al. (2012). Such examples indicate that type II radio sources may originate from shocks driven close to the apex of erupting structures in the corona. Figures AAS, reproduced with permission, and ©ESO reproduced with permission from *Astronomy and Astrophysics*.

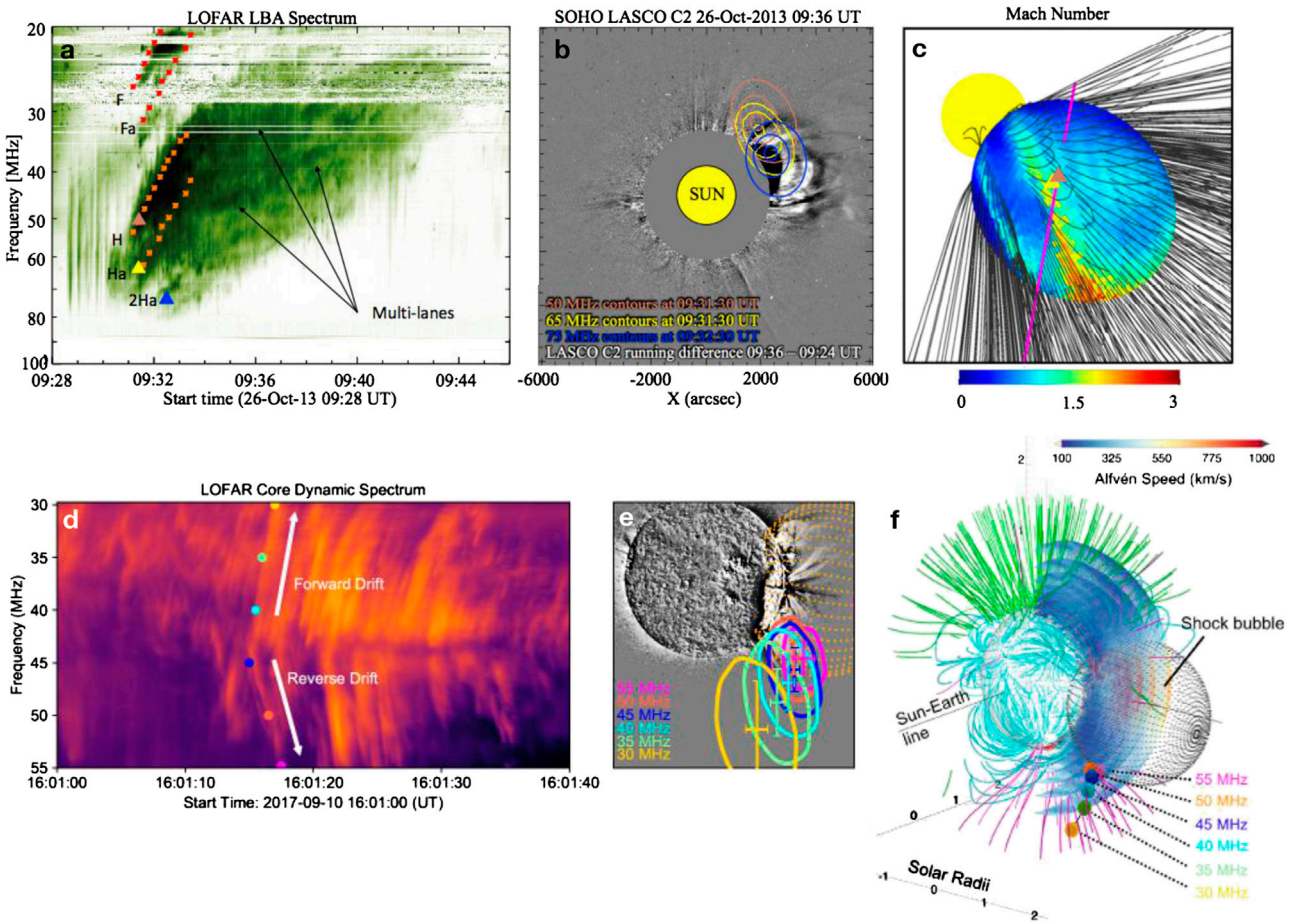

FIGURE 11 | 3D reconstructions of the shock and plasma environment in which type II radio sources are produced. **(A–C)** Zucca et al. (2018) used LOFAR tied-array imaging to show that the radio sources originated at the northern flank of a CME, and applied 3D modelling to estimate the shock Mach number at the radio source locations. Reproduced with permission from Astronomy & Astrophysics ©ESO. **(D–F)** Morosan et al. (2019a) again used LOFAR tied-array imaging and 3D modelling of the coronal environment, this time showing the location of type II herringbone radio bursts, which are direct signatures of electron beams being accelerated by a shock. Figure reproduced with permission from original authors.

Figure 1B). Some studies have shown the radio sources can originate at the eruption flanks (region five or six of **Figure 1**; Cho et al., 2007; Carley et al., 2013; Zucca et al., 2014a; Rouillard et al., 2016; Morosan et al., 2019a) and are likely associated with the same MHD disturbance that creates the large-scale propagating disturbances observed in EUV known as "EUV waves," "EIT

waves," or "coronal bright fronts" (Grechnev et al., 2011; Nitta et al., 2014; Long et al., 2017). In rare instances, such propagating fronts have been directly imaged in the radio domain (Maia et al., 2000; Pohjolainen et al., 2001).

The most recent studies of type IIs have attempted to reconstruct the environment that resulted in shock-accelerated electrons and subsequent radio emission. Both Zucca et al. (2018) and Morosan et al. (2019a) used LOFAR tied-array imaging and data-driven modeling to locate the CME-driven shock in 3D space (**Figure 11**). Both cases found that electrons were accelerated in a low Alfvénic speed environment at the CME flanks. Similar results were reached with 3D geometrical reconstructions (Kozarev et al., 2015; Rouillard et al., 2016; Plotnikov et al., 2017; Mancuso et al., 2019) and with 3D radio triangulation techniques, known as goniopolarimetry, which identified radio sources at both the nose and flanks of the CME (Magdalenić et al., 2014).

While type II radio bursts have helped greatly in understanding coronal shocks, questions on their spectral features remain, particularly with regard to their fine spectral structure. As mentioned above, type II bursts are often observed as two bands of emission, with a 2:1 ratio widely interpreted as originating at the fundamental plasma frequency and its first harmonic. These two bands can be further split into sub-bands, known as band-splitting. The band-splitting has long been postulated to represent the emission from the upstream and downstream regions of the shock (Smerd et al., 1974; Vršnak et al., 2001; Maguire et al., 2020) and, hence, could be used to diagnose the shock compression and Alvén Mach number, which typically have values $\chi < 1.5$ and $M_A = 1.1 - 2$ (Vršnak et al., 2002, although the authors highlight the compression and Mach depend on assumptions about the plasma-beta value, typically assumed to be $\beta \ll 1$, and the shock orientation, assumed to be quasi-perpendicular). Images of the two sources of the band-splitting are rare, but some cases have supported the upstream–downstream hypothesis (Zimovets et al., 2012; Zimovets and Sadykov, 2015). However, Du et al. (2015) showed that the band-split frequency ratio (which should be related to the shock compression ratio) does not correlate with shock speed, which the authors claim does not support the upstream–downstream hypothesis. Split-band sources have also been observed at different locations, which may be unexpected given the small spatial scale of the shock surface. Explanations for this involve multiple sources of radio emission at spatially separated sections of the shock surface (Holman and Pesses, 1983), radio wave refraction and scattering producing a radio source shifted from its original location (Chrysaphi et al., 2018), and the radio source of the higher frequency band being located downstream in the shock sheath (Zimovets et al., 2012). As of now, the origin of the phenomenon remains debated.

Perhaps the most intriguing, yet unexplained, feature of type II radio bursts is the observations of herringbones (Cairns and Robinson, 1987; Cane and White, 1989; Carley et al., 2015). The herringbone burst envelope has similar morphology to type II bursts. However, herringbone fine structure within this envelope is composed of a repetitive signature of forward- and reverse-drift radio bursts that are narrow in time and frequency, for example, **Figure 11D**. These bursts are rare, with only 20% of type II bursts exhibiting these structures (Cairns and Robinson, 1987), but they have been interpreted as direct observations of a CME-driven shock producing "bursty" acceleration of electron beams to energies in the range 0.2–80 keV (Mann and Klassen, 2005), with the beam speeds or energies being deduced from the herringbone drift rates in dynamic spectra. The fact that they drift toward both low and high frequencies simultaneously means they are bidirectional in space, for example, drifting simultaneously toward and away from the Sun from a common origin in the corona. The "bursty," or quasiperiodic, nature of the herringbones extends over timescales of seconds (Mann and Classen, 1995; Mann and Klassen, 2005), and they are believed to be the result of the shock drift acceleration (SDA) process (Miteva and Mann, 2007). They have been directly imaged and shown to be located near shocks driven at CME flanks (Carley et al., 2013; Morosan et al., 2019a). However, their origin, particularly the cause of the bursty and quasiperiodic nature of electron acceleration, remains unknown. This impulsiveness has been attributed to inhomogeneity on the shock front and may be a signature of the so-called wavy or rippled shock (Zlobec et al., 1993; Guo and Giacalone, 2010; Vandas and Karlický, 2011), but such hypotheses remain unconfirmed.

7. RADIO-QUIET CORONAL MASS EJECTIONS AND STEALTH CORONAL MASS EJECTIONS

In general, given that CMEs are inherently linked to the acceleration of electrons to a variety of energies and via multiple mechanisms, radio emission should be a natural consequence of the coronal eruptive process. However, we now dedicate a short section to radio-quiet CMEs, including the related phenomenon of "stealth CMEs" (Robbrecht et al., 2009), which are those eruptions that have no low coronal signature, for example, no associated flare, filament eruption, or activity usually associated with the eruption (Ma et al., 2010; D'Huys et al., 2014; Lynch et al., 2016).

Gopalswamy et al. (2008) reported a statistical study of 461 fast (> 900 km s^{-1}) and wide ($> 60^\circ$) CMEs, showing 41% to be "radio-quiet." In this instance, radio-quiet means no discernible deca- to hectometric (DH) type II activity, but there may still be type III or other types of radio bursts. The authors attribute the absence of radio to either the location of the eruption or to the generally smaller speeds of the radio-quiet CMEs in their sample; for example, even at speeds > 900 km s^{-1}, the Alfvén speed may not be surpassed. Similarly, Sheeley et al. (1984) reported on CMEs without metric type II radio bursts, stating that "fast" eruptions (> 450 km s^{-1} in their sample) may not produce shock-producing super-Alfvénic speeds until they leave the low corona. Michalek et al. (2007) also showed that radio-quiet CMEs (those without metric or decametric type IIs) have smaller widths than their radio-loud counterparts. All of this points to the CME speed and expansion, as well as the ambient medium, playing a role in

the eruption's ability to drive a shock and produce electron acceleration and radio bursts.

We have already discussed the open question of why so few CMEs (~ 5%) are associated with type IV radio activity (Gergely, 1986). It may take a special eruption configuration for electrons to be trapped at the flare or within the CME. A similar assertion can be made for the absence of type III radio bursts in some events. For example, Cairns et al. (2020) recently showed an interesting study of three events on the same day, only one of which showed significant type III activity. Those events with no type III bursts were from the same active region, and perhaps provided no means of electron beam escape into the heliosphere, which points to the special configuration of the ambient coronal environment in producing such radio bursts. In the case of flares, several authors have highlighted the necessity of favorable magnetic configurations in producing escaping particles and type III bursts (Hofmann and Ruždjak, 2007; Klein et al., 2011).

Finally, there are those CMEs which appear to have no discernible activity in the low corona, the so-called stealth CMEs. These eruptions have no associated signature in X-ray, EUV, radio, or any other waveband that permits observation of the eruption origin. The majority of reported stealth CMEs in the literature provide little mention of radio activity (see Howard and Harrison (2013) and references therein). This is perhaps not a surprise, given the lack of flare, EUV, or other low coronal signatures during stealth CME eruption; this likely means no energetic electrons were accelerated (or too few to observe). However, O'Kane et al. (2019) recently showed very weak, short-duration bursts at 150 MHz by NRH in association with one stealth CME, which may be an indicator of small levels of electron acceleration during the stealth eruption. Radio is perhaps best placed to observe such small levels of electron acceleration, given that fewer numbers of energetic electrons are required to produce coherent radio emission than would be required for EUV or X-ray emission.

The absence of nonthermal or coherent radio emission may also be an opportunity to observe the often very weak CME thermal bremsstrahlung or gyroemission (Gopalswamy and Kundu, 1993; Bastian and Gary, 1997); for example, stealth CMEs may allow for direct radio imaging of the thermal emission from CMEs at times when it would otherwise be obscured by the large fluxes of nonthermal radio sources. To our knowledge, no study has been performed in this regard.

8. CONCLUSIONS

In this article, we reviewed the recent advances that have been made in radio observation of the flare/CME development in the low corona. The availability of new radio imaging spectrometers from metric to microwave wavelengths, in combination with new EUV instrumentation, has led to new insight into the sites and mechanisms of electron acceleration at play during eruption initiation, as well as on the early stage CME development in the corona at heliocentric distances $< 10\ R_{\odot}$.

In the initiation stages of the eruption, observations of flux rope destabilization and acceleration can now be observed using instruments such as AIA, SUVI, or SWAP. During this eruption, the high-time resolution imaging and spectroscopy observations provided by radio facilities now give the ability to discern where, when, and how electron acceleration takes place during flux rope eruption initiation. Such observations can be used to find evidence for particular eruptive models; for example, observational results from a combination of NRH and AIA have indicated electron acceleration sites that would be expected of tether-cutting and breakout reconnection during the early phases of eruption (Carley et al., 2016), while comparisons of numerical simulations to direct imaging of a filament eruption using NoRH provided evidence of the kink instability (Kliem et al., 2010).

During acceleration phases, high-time resolution imaging spectroscopy provided at microwave wavelengths from VLA has been combined with AIA to show evidence for current sheets and associated termination shocks (Chen et al., 2015), while AIA and EOVSA provided the most striking evidence to date for the standard model of solar eruptions (Gary et al., 2018; Chen et al., 2020).

The high-resolution imaging spectroscopy observations provided by new low-frequency phased-array technologies such as LOFAR and MWA are now providing remarkable new insight into the physics of CME-driven shocks and, in some cases, direct spatially resolved imaging of the radio emission from the CME itself. LOFAR has shown that high-time resolution imaging observations provided by its tied-array mode can directly image type II fine structures such as band-splitting and herringbones (Chrysaphi et al., 2018; Morosan et al., 2019a). Efforts to push the boundaries of high sensitivity and dynamic range in imaging observations with MWA have led to a rare spatially resolved diagnostic of a CME magnetic field (Mondal et al., 2020). MWA, as well as legacy instruments such as NRH, have shown that radio instruments provide the most promising means of determining spatially resolved CME magnetic field strength. Such a diagnostic remains one of the most important yet illusive properties in CME observations, and next-generation phased-array technologies have demonstrated they may be capable of advancing these observations and provide routine diagnostics of CME magnetic fields.

The recent results of legacy and new radio technology have shown the groundbreaking new insight the radio domain can offer to CME observations. Instruments such as NRH and NoRH have had a long history of such observations, and the capabilities of current facilities such as VLA, EOVSA, MWA, and LOFAR are now providing a unique means of observing CMEs and their related phenomena. Looking to the future, Nindos et al. (2019) recently provided an overview of solar radio physics (including CME radio observations) in the context of the capabilities that will be provided by the Square Kilometer Array (SKA). There are also upcoming and dedicated solar observing facilities such as the MUSER that will have the ability to perform imaging spectroscopy measurements from 400 MHz to 15 GHz. An overview of the observational capability of these and other radio domain instruments in the context of space weather science and operations was recently provided by Carley et al.

(2020), which also describes the current LOFAR for Space Weather (LOFAR4SW) design study. LOFAR4SW aims to upgrade the entire LOFAR network, allowing it to make routine observations of space weather phenomena.

Progress in CME physics is of course not dependent on radio observations alone, and a host of new multiwavelength observations will be available with new and upcoming space-based missions. Imaging of the inner corona from coronagraphs such as Metis (Antonucci et al., 2019) on Solar Orbiter, the Association of Spacecraft for Polarimetric and Imaging Investigation of the Corona of the Sun (ASPIICS; Galy et al., 2015) onboard PROBA-3, the Visible Emission Line Coronagraph (VELC; Prasad et al., 2017) onboard Aditya-L1, as well as from EUV imagers such as SUVI and the Extreme Ultraviolet Imager (EUI; Rochus et al., 2020) on Solar Orbiter will provide excellent synergies alongside the radio instrumentation described above. Radio and multiwavelength studies can provide powerful diagnostics in CME physics from the CME nascent stages to eruption and eventual propagation into the heliosphere and promise to make significant advances in the understanding of this phenomenon in the near future and beyond.

AUTHOR CONTRIBUTIONS

EC, NV, and AV each wrote sections of this article.

FUNDING

EC is a Schrödinger Research Fellow funded by the Dublin Institute for Advanced Studies. AV contribution was supported by the NASA HSR (NNX16AG86G) and LWS (80NSSC19K0069) programs.

REFERENCES

Aguilar-Rodriguez, E., Gopalswamy, N., MacDowall, R., Yashiro, S., and Kaiser, M. L. (2005). A universal characteristic of type II radio bursts. *J. Geophys. Res.: Space Physics.* 110. A12S08. doi:10.1029/2005JA011171

Antiochos, S. K., DeVore, C. R., and Klimchuk, J. A. (1999). A Model for Solar Coronal Mass Ejections. *Astrophys. J.* 510, 485–493. doi:10.1086/306563

Antonucci, E., Romoli, M., Andretta, V., Fineschi, S., Heinzel, P., Moses, J. D., et al. (2019). Metis: the Solar Orbiter visible light and ultraviolet coronal imager. *Astron. Astrophys.* 642, 41. doi:10.1051/0004-6361/201935338

Aulanier, G., Török, T., Démoulin, P., and DeLuca, E. E. (2010). Formation of Torus-Unstable Flux Ropes and Electric Currents in Erupting Sigmoids. *Astrophys. J.* 708, 314–333. doi:10.1088/0004-637X/708/1/314

Aurass, H., Holman, G., Braune, S., Mann, G., and Zlobec, P. (2013). Radio evidence for breakout reconnection in solar eruptive events. *Astron. Astrophys.* 555, A40. doi:10.1051/0004-6361/201321111

Aurass, H., and Mann, G. (2004). Radio Observation of Electron Acceleration at Solar Flare Reconnection Outflow Termination Shocks. *Astrophys. J.* 615, 526–530. doi:10.1086/424374

Aurass, H., Vršnak, B., and Mann, G. (2002). Shock-excited radio burst from reconnection outflow jet? *Astron. Astrophys.* 384, 273–281. doi:10.1051/0004-6361:20011735

Bain, H. M., Krucker, S., Glesener, L., and Lin, R. P. (2012). Radio Imaging of Shock-accelerated Electrons Associated with an Erupting Plasmoid on 2010 November 3. *Astrophys. J.* 750, 44. doi:10.1088/0004-637X/750/1/44

Bain, H. M., Krucker, S., Saint-Hilaire, P., and Raftery, C. L. (2014). Radio Imaging of a Type IVM Radio Burst on the 14th of August 2010. *Astrophys. J.* 782, 43. doi:10.1088/0004-637X/782/1/43

Bastian, T. S., and Gary, D. E. (1997). On the feasibility of imaging coronal mass ejections at radio wavelengths. *J. Geophys. Res.* 102, 14031–14040. doi:10.1029/97JA00483

Bastian, T. S., Pick, M., Kerdraon, A., Maia, D., and Vourlidas, A. (2001). The Coronal Mass Ejection of 1998 April 20: Direct Imaging at Radio Wavelengths. *Astrophys. J. Lett.* 558, L65–L69. doi:10.1086/323421

Benz, A. O., Battaglia, M., and Vilmer, N. (2011). Location of Decimetric Pulsations in Solar Flares. *Sol. Phys.* 273, 363–375. doi:10.1007/s11207-011-9760-3

Berghmans, D., Hochedez, J. F., Defise, J. M., Lecat, J. H., Nicula, B., Slemzin, V., et al. (2006). SWAP onboard PROBA 2, a new EUV imager for solar monitoring. *Adv. Space Res.* 38, 1807–1811. doi:10.1016/j.asr.2005.03.070

Berkebile-Stoiser, S., Veronig, A. M., Bein, B. M., and Temmer, M. (2012). Relation between the Coronal Mass Ejection Acceleration and the Non-thermal Flare Characteristics. *Astrophys. J.* 753, 88. doi:10.1088/0004-637X/753/1/88

Boischot, A. (1957). Caractères d'un type d'émission hertzienne associé à certaines éruptions chromosphériques. *Academie des Sciences Paris Comptes Rendus* 244, 1326–1329.

Boischot, A. (1958). Étude du rayonnement radioélectrique solaire sur 169 MHz é l'aide d'un grand interféromètre à réseau. *Annales d'Astrophysique* 21, 273.

Boischot, A., and Daigne, G. (1968). Sur quelques caractéristiques des sursauts de type IV. II. *Annales d'Astrophysique* 31, 531.

Cairns, I. H., Kozarev, K. A., Nitta, N. V., Agueda, N., Battarbee, M., Carley, E. P., et al. (2020). Comprehensive Characterization of Solar Eruptions with Remote and In-Situ Observations, and Modeling: The Major Solar Events on 4 November 2015. *Sol. Phys.* 295, 32. doi:10.1007/s11207-020-1591-7

Cairns, I. H., and Robinson, R. D. (1987). Herringbone bursts associated with type II solar radio emission. *Sol. Phys.* 111, 365–383. doi:10.1007/BF00148526

Cairns, I. H., and Schmidt, J. M. (2015). Testing a theory for type II radio bursts from the Sun to near 0.5 AU. *Journal of Physics Conference Series.* 642, 012004. doi:10.1088/1742-6596/642/1/012004

Cane, H. V., and White, S. M. (1989). On the Source Conditions for Herringbone Structure in Type-II Solar Radio Bursts. *Sol. Phys.* 120, 137–144. doi:10.1007/BF00148539

Cargill, P. J., and Priest, E. R. (1983). The heating of postflare loops. *Astrophys. J.* 266, 383–389. doi:10.1086/160786

Carley, E. P., Baldovin, C., Benthem, P., Bisi, M. M., Fallows, R. A., Gallagher, P. T., et al. (2020). Radio observatories and instrumentation used in space weather science and operations. *Journal of Space Weather and Space Climate.* 10, 7. doi:10.1051/swsc/2020007

Carley, E. P., Long, D. M., Byrne, J. P., Zucca, P., Bloomfield, D. S., McCauley, J., et al. (2013). Quasiperiodic acceleration of electrons by a plasmoid-driven shock in the solar atmosphere. *Nat. Phys.* 9, 811–816. doi:10.1038/nphys2767

Carley, E. P., Reid, H., Vilmer, N., and Gallagher, P. T. (2015). Low frequency radio observations of bi-directional electron beams in the solar corona. *Astron. Astrophys.* 581, A100. doi:10.1051/0004-6361/201526251

Carley, E. P., Vilmer, N., and Gallagher, P. T. (2016). Radio Diagnostics of Electron Acceleration Sites During the Eruption of a Flux Rope in the Solar Corona. *Astrophys. J.* 833, 87. doi:10.3847/1538-4357/833/1/87

Carley, E. P., Vilmer, N., Simões, P. J. A., and Ó Fearraigh, B. (2017). Estimation of a coronal mass ejection magnetic field strength using radio observations of gyrosynchrotron radiation. *Astron. Astrophys.* 608, A137. doi:10.1051/0004-6361/201731368

Chen, B., Bastian, T. S., Shen, C., Gary, D. E., Krucker, S., and Glesener, L. (2015). Particle acceleration by a solar flare termination shock. *Science.* 350, 1238–1242. doi:10.1126/science.aac8467

Chen, B., Yu, S., Reeves, K. K., and Gary, D. E. (2020). Microwave Spectral Imaging of an Erupting Magnetic Flux Rope: Implications for the Standard Solar Flare Model in Three Dimensions. *Astrophys. J. Lett.* 895, L50. doi:10.3847/2041-8213/ab901a

Chen, P. F. (2011). Coronal Mass Ejections: Models and Their Observational Basis. *Living Rev. Sol. Phys.* 8, 1. doi:10.12942/lrsp-2011-1

Chintzoglou, G., Patsourakos, S., and Vourlidas, A. (2015). Formation of Magnetic Flux Ropes during a Confined Flaring Well before the Onset of a Pair of Major Coronal Mass Ejections. *Astrophys. J.* 809, 34. doi:10.1088/0004-637X/809/1/34

Cho, K. S., Gopalswamy, N., Kwon, R. Y., Kim, R. S., and Yashiro, S. (2013). A High-frequency Type II Solar Radio Burst Associated with the 2011 February 13 Coronal Mass Ejection. *Astrophys. J.* 765, 148. doi:10.1088/0004-637X/765/2/148

Cho, K. S., Lee, J., Moon, Y. J., Dryer, M., Bong, S. C., Kim, Y. H., et al. (2007). A study of CME and type II shock kinematics based on coronal density measurement. *Astron. Astrophys.* 461, 1121–1125. doi:10.1051/0004-6361:20064920

Chrysaphi, N., Kontar, E. P., Holman, G. D., and Temmer, M. (2018). CME-driven Shock and Type II Solar Radio Burst Band Splitting. *Astrophys. J.* 868, 79. doi:10.3847/1538-4357/aae9e5

Dauphin, C., Vilmer, N., and Krucker, S. (2006). Observations of a soft X-ray rising loop associated with a type II burst and a coronal mass ejection in the 03 November 2003 X-ray flare. *Astron. Astrophys.* 455, 339–348. doi:10.1051/0004-6361:20054535

Démoulin, P., Vourlidas, A., Pick, M., and Bouteille, A. (2012). Initiation and Development of the White-light and Radio Coronal Mass Ejection on 2001 April 15. *Astrophys. J.* 750, 147. doi:10.1088/0004-637X/750/2/147

D'Huys, E., Seaton, D. B., Poedts, S., and Berghmans, D. (2014). Observational Characteristics of Coronal Mass Ejections without Low-coronal Signatures. *Astrophys. J.* 795, 49. doi:10.1088/0004-637X/795/1/49

Dresing, N., Gómez-Herrero, R., Heber, B., Hidalgo, M. A., Klassen, A., Temmer, M., et al. (2016). Injection of solar energetic particles into both loop legs of a magnetic cloud. *Astron. Astrophys.* 586, A55. doi:10.1051/0004-6361/201527347

Dresing, N., Gómez-Herrero, R., Heber, B., Klassen, A., Temmer, M., and Veronig, A. (2018). Long-lasting injection of solar energetic electrons into the heliosphere. *Astron. Astrophys.* 613, A21. doi:10.1051/0004-6361/201731573

Du, G., Kong, X., Chen, Y., Feng, S., Wang, B., and Li, G. (2015). An Observational Revisit of Band-split Solar Type-II Radio Bursts. *Astrophys. J.* 812, 52. doi:10.1088/0004-637X/812/1/52

Duan, Y., Shen, Y., Chen, H., and Liang, H. (2019). The Birth of a Jet-driven Twin CME and Its Deflection from Remote Magnetic Fields. *Astrophys. J.* 881, 132. doi:10.3847/1538-4357/ab32e9

Dulk, G. A. (1985). Radio emission from the sun and stars. *Rev. Astron. Astrophys.* 23, 169–224. doi:10.1146/annurev.aa.23.090185.001125

Dulk, G. A., and Altschuler, M. D. (1971). A Moving Type IV Radio Burst and Its Relation to the Coronal Magnetic Field. *Sol. Phys.* 20, 438–447. doi:10.1007/BF00159777

Duncan, R. A. (1980). The emission mechanism of solar moving Type IV metre-wave radio sources. *Proc. Astron. Soc. Aust.* 4, 67–70. doi:10.1017/S1323358000018828

Fleishman, G. D., Gary, D. E., Chen, B., Kuroda, N., Yu, S., and Nita, G. M. (2020). Decay of the coronal magnetic field can release sufficient energy to power a solar flare. *Science.* 367, 278–280. doi:10.1126/science.aax6874

Forbes, T. G., and Priest, E. R. (1995). Photospheric Magnetic Field Evolution and Eruptive Flares. *Astrophys. J.* 446, 377. doi:10.1086/175797

Galy, C., Fineschi, S., Galano, D., Howard, R. A., Kintziger, C., Kirschner, V., et al. (2015). "Design and modelisation of ASPIICS optics," In Solar Physics and Space Weather Instrumentation VI, Editors S. Fineschi and J. Fennelly (Bellingham, WA: International Society for Optics and Photonics (SPIE), Vol. 9604, 71–82. doi:10.1117/12.2188404

Gary, D. E. (2019). "Cause and extent of the extreme radio flux density reached by the solar flare of 2006 December 06.," Proceedings of the 2008 Ionospheric Effects Symposium; Alexandria VA; Editor J. M. Goodman (JMG Associates Ltd: Sheridan Books)

Gary, D. E. Chen, B., Dennis, B. R., Fleishman, G. D., Hurford, G. J., Krucker, S., et al. (2018). Microwave and Hard X-Ray Observations of the 2017 September 10 Solar Limb Flare. *Astrophys. J.* 863, 83. doi:10.3847/1538-4357/aad0ef

Gary, D. E., Dulk, G. A., House, L. L., Illing, R., Wagner, W. J., and Mclean, D. J. (1985). The type IV burst of 1980 June 29, 0233 UT - Harmonic plasma emission?. *Astron. Astrophys.* 152, 42–50.

Gergely, T. E. (1986). Type-Iv Bursts and Coronal Mass Ejections. *Sol. Phys.* 104, 175–178. doi:10.1007/BF00159959

Gopalswamy, N., and Kundu, M. R. (1993). Thermal and nonthermal emissions during a coronal mass ejection. *Sol. Phys.* 143, 327–343. doi:10.1007/BF00646491

Gopalswamy, N., Xie, H., Mäkelä, P., Yashiro, S., Akiyama, S., Uddin, W., et al. (2013). Height of shock formation in the solar corona inferred from observations of type II radio bursts and coronal mass ejections. *Adv. Space Res.* 51, 1981–1989. doi:10.1016/j.asr.2013.01.006

Gopalswamy, N., Yashiro, S., Xie, H., Akiyama, S., Aguilar-Rodriguez, E., Kaiser, M. L., et al. (2008). Radio-Quiet Fast and Wide Coronal Mass Ejections. *Astrophys. J.* 674, 560–569. doi:10.1086/524765

Grechnev, V. V., Uralov, A. M., Chertok, I. M., Kuzmenko, I. V., Afanasyev, A. N., Meshalkina, N. S., et al. (2011). Coronal Shock Waves, EUV Waves, and Their Relation to CMEs. I. Reconciliation of "EIT Waves", Type II Radio Bursts, and Leading Edges of CMEs. *Sol. Phys.* 273, 433–460. doi:10.1007/s11207-011-9780-z

Guo, F., and Giacalone, J. (2010). The Effect of Large-scale Magnetic Turbulence on the Acceleration of Electrons by Perpendicular Collisionless Shocks. *Astrophys. J.* 715, 406–411. doi:10.1088/0004-637X/715/1/406

Hannah, I. G. and Kontar, E. P. (2013). Multi-thermal dynamics and energetics of a coronal mass ejection in the low solar atmosphere. *Astron. Astrophys.* 553, A10. doi:10.1051/0004-6361/201219727

Hariharan, K., Ramesh, R., Kathiravan, C., and Wang, T. J. (2016). Simultaneous Near-Sun Observations of a Moving Type IV Radio Burst and the Associated White-Light Coronal Mass Ejection. *Sol. Phys.* 291, 1405–1416. doi:10.1007/s11207-016-0918-x

Hey, J. S. (1946). Solar Radiations in the 4-6 Metre Radio Wave-Length Band. *Nature.* 157, 47–48. doi:10.1038/157047b0

Hofmann, A., and Ruždjak, V. (2007). Favourable Magnetic Field Configurations for Generation of Flare-Associated Meter-Wave Type III Radio Bursts. *Sol. Phys.* 240, 107–119. doi:10.1007/s11207-006-0228-9

Holman, G. D. and Pesses, M. E. (1983). Solar type II radio emission and the shock drift acceleration of electrons. *Astrophys. J.* 267, 837–843. doi:10.1086/160918

Howard, R. A. Moses, J. D., Vourlidas, A., Newmark, J. S., Socker, D. G., Plunkett, S. P., et al. (2008). Sun Earth Connection Coronal and Heliospheric Investigation (SECCHI). *Space Sci. Rev.* 136, 67–115. doi:10.1007/s11214-008-9341-4

Howard, T. A., and Harrison, R. A. (2013). Stealth Coronal Mass Ejections: A Perspective. *Sol. Phys.* 285, 269–280. doi:10.1007/s11207-012-0217-0

Huang, J., Démoulin, P., Pick, M., Auchère, F., Yan, Y. H., and Bouteille, A. (2011). Initiation and Early Development of the 2008 April 26 Coronal Mass Ejection. *Astrophys. J.* 729, 107. doi:10.1088/0004-637X/729/2/107

Huang, J., Tan, B., Masuda, S., Cheng, X., Bisoi, S. K., and Melnikov, V. (2019). Localized Microwave and EUV Bright Structures in an Eruptive Prominence. *Astrophys. J.* 874, 176. doi:10.3847/1538-4357/ab0e80

James, A. W., Green, L. M., Palmerio, E., Valori, G., Reid, H. A. S., Baker, D., et al. (2017). On-Disc Observations of Flux Rope Formation Prior to Its Eruption. *Sol. Phys.* 292, 71. doi:10.1007/s11207-017-1093-4

Joshi, N. C., Liu, C., Sun, X., Wang, H., Magara, T., and Moon, Y. J. (2015). The Role of Erupting Sigmoid in Triggering a Flare with Parallel and Large-scale Quasi-circular Ribbons. *Astrophys. J.* 812, 50. doi:10.1088/0004-637X/812/1/50

Kallunki, J., and Tornikoski, M. (2017). Eruptive Solar Prominence at 37 GHz. *Sol. Phys.* 292, 84. doi:10.1007/s11207-017-1110-7

Karlický, M., Bárta, M., Mészárosová, H., and Zlobec, P. (2005). Time scales of the slowly drifting pulsating structure observed during the April 12, 2001 flare. *Astron. Astrophys.* 432, 705–712. doi:10.1051/0004-6361:20041551

Karlický, M., Chen, B., Gary, D. E., Kašparová, J., and Rybák, J. (2020). Drifting Pulsation Structure at the Very Beginning of the 2017 September 10 Limb Flare. *Astrophys. J.* 889, 72. doi:10.3847/1538-4357/ab63d0

Kerdraon, A., and Delouis, J.-M. (1997). The Nançay Radioheliograph. Coronal Physics from Radio and Space Observations 483. 192–201. doi:10.1007/BFb0106458

Klassen, A., Pohjolainen, S., and Klein, K. L. (2003). Type II radio precursor and X-ray flare emission. *Sol. Phys.* 218, 197–210. doi:10.1023/B:SOLA.0000013034.61996.c4

Klein, K. L., Krucker, S., Trottet, G., and Hoang, S. (2005). Coronal phenomena at the release of solar energetic electron events. *Astron. Astrophys.* 431, 1047–1060. doi:10.1051/0004-6361:20041258

Klein, K. L., Trottet, G., Samwel, S., and Malandraki, O. (2011). Particle Acceleration and Propagation in Strong Flares without Major Solar

Energetic Particle Events. *Sol. Phys.* 269, 309–333. doi:10.1007/s11207-011-9710-0

Kliem, B., Karlický, M., and Benz, A. O. (2000). Solar flare radio pulsations as a signature of dynamic magnetic reconnection. *Astron. Astrophys.* 360, 715–728.

Kliem, B., Linton, M. G., Török, T., and Karlický, M. (2010). Reconnection of a Kinking Flux Rope Triggering the Ejection of a Microwave and Hard X-Ray Source II. Numerical Modeling. *Sol. Phys.* 266, 91–107. doi:10.1007/s11207-010-9609-1

Knock, S. A. and Cairns, I. H. (2005). Type II radio emission predictions: Sources of coronal and interplanetary spectral structure. *J. Geophys. Res. B.* 110, A01101. doi:10.1029/2004JA010452

Ko, Y.-K., Raymond, J. C., Lin, J., Lawrence, G., Li, J., and Fludra, A. (2003). Dynamical and Physical Properties of a Post-Coronal Mass Ejection Current Sheet. *Astrophys. J.* 594, 1068–1084. doi:10.1086/376982

Kozarev, K. A., Raymond, J. C., Lobzin, V. V., and Hammer, M. (2015). Properties of a Coronal Shock Wave as a Driver of Early SEP Acceleration. *Astrophys. J.* 799, 167. doi:10.1088/0004-637X/799/2/167

Kundu, M. R., White, S. M., Garaimov, V. I., Manoharan, P. K., Subramanian, P., Ananthakrishnan, S., et al. (2004). Radio Observations of Rapid Acceleration in a Slow Filament Eruption/Fast Coronal Mass Ejection Event. *Astrophys. J.* 607, 530–539. doi:10.1086/383217

Lemen, J. R., Title, A. M., Akin, D. J., Boerner, P. F., Chou, C., Drake, J. F., et al. (2012). The Atmospheric Imaging Assembly (AIA) on the Solar Dynamics Observatory (SDO). *Sol. Phys.* 275, 17–40. doi:10.1007/s11207-011-9776-8

Li, W., Pober, J. C., Hazelton, B. J., Barry, N., Morales, M. F., Sullivan, I., et al. (2018). Comparing Redundant and Sky-model-based Interferometric Calibration: A First Look with Phase II of the MWA. *Astrophys. J.* 863, 170. doi:10.3847/1538-4357/aad3c3

Liu, H., Chen, Y., Cho, K., Feng, S., Vasanth, V., Koval, A., et al. (2018). A Solar Stationary Type IV Radio Burst and Its Radiation Mechanism. *Sol. Phys.* 293, 58. doi:10.1007/s11207-018-1280-y

Long, D. M., Bloomfield, D. S., Chen, P. F., Downs, C., Gallagher, P. T., Kwon, R.-Y., et al. (2017). Understanding the Physical Nature of Coronal "EIT Waves". *Sol. Phys.* 292, 7. doi:10.1007/s11207-016-1030-y

Lynch, B. J., Masson, S., Li, Y., DeVore, C. R., Luhmann, J. G., Antiochos, S. K., et al. (2016). A model for stealth coronal mass ejections. *J. Geophys. Res. B.* 121, 10677–10697. doi:10.1002/2016JA023432

Ma, S., Attrill, G. D. R., Golub, L., and Lin, J. (2010). Statistical Study of Coronal Mass Ejections With and Without Distinct Low Coronal Signatures. *Astrophys. J.* 722, 289–301. doi:10.1088/0004-637X/722/1/289

Magdalenić, J., Marqué, C., Krupar, V., Mierla, M., Zhukov, A. N., Rodriguez, L., et al. (2014). Tracking the CME-driven Shock Wave on 2012 March 5 and Radio Triangulation of Associated Radio Emission. *Astrophys. J.* 791, 115. doi:10.1088/0004-637X/791/2/115

Magdalenić, J., Marqué, C., Zhukov, A. N., Vršnak, B., and Veronig, A. (2012). Flare-generated Type II Burst without Associated Coronal Mass Ejection. *Astrophys. J.* 746, 152. doi:10.1088/0004-637X/746/2/152

Maguire, C. A., Carley, E. P., McCauley, J., and Gallagher, P. T. (2020). Evolution of the Alfvén Mach number associated with a coronal mass ejection shock. *Astron. Astrophys.* 633, A56. doi:10.1051/0004-6361/201936449

Maia, D. J. F., Gama, R., Mercier, C., Pick, M., Kerdraon, A., and Karlický, M. (2007). The Radio-Coronal Mass Ejection Event on 2001 April 15. *Astrophys. J.* 660, 874–881. doi:10.1086/508011

Maia, D. J. F., and Pick, M. (2004). Revisiting the Origin of Impulsive Electron Events: Coronal Magnetic Restructuring. *Astrophys. J.* 609, 1082–1097. doi:10.1086/386319

Maia, D., Pick, M., Vourlidas, A., and Howard, R. (2000). Development of Coronal Mass Ejections: Radio Shock Signatures. *Astrophys. J. Lett.* 528, L49–L51. doi:10.1086/312421

Maia, D., Vourlidas, A., Pick, M., Howard, R., Schwenn, R., and Magalhães, A. (1999). Radio signatures of a fast coronal mass ejection development on November 6, 1997. *J. Geophys. Res.* 104, 12507–12514. doi:10.1029/1999JA900033

Mancuso, S., Frassati, F., Bemporad, A., and Barghini, D. (2019). Three-dimensional reconstruction of CME-driven shock-streamer interaction from radio and EUV observations: a different take on the diagnostics of coronal magnetic fields. *Astron. Astrophys.* 624, L2. doi:10.1051/0004-6361/201935157

Mann, G., and Classen, H. T. (1995). Electron acceleration to high energies at quasi-parallel shock waves in the solar corona. *Astron. Astrophys.* 304, 576.

Mann, G., and Klassen, A. (2005). Electron beams generated by shock waves in the solar corona. *Astron. Astrophys.* 441, 319–326. doi:10.1051/0004-6361:20034396

Mann, G., Klassen, A., Classen, H. T., Aurass, H., Scholz, D., MacDowall, R. J., et al. (1996). Catalogue of solar type II radio bursts observed from September 1990 to December 1993 and their statistical analysis. *Astronomy and Astrophysics, Supplement.* 119, 489–498. doi:10.1051/aas:1996261

Marqué, C., Lantos, P., and Delaboudinière, J. P. (2002). Multi wavelength investigation of the eruption of a sigmoidal quiescent filament. *Astron. Astrophys.* 387, 317–325. doi:10.1051/0004-6361:20020309

Masson, S., Antiochos, S. K., and DeVore, C. R. (2013). A Model for the Escape of Solar-flare-accelerated Particles. *Astrophys. J.* 771, 82. doi:10.1088/0004-637X/771/2/82

Masson, S., Antiochos, S. K., and DeVore, C. R. (2019). Escape of Flare-accelerated Particles in Solar Eruptive Events. *Astrophys. J.* 884, 143. doi:10.3847/1538-4357/ab4515

Melrose, D. B. (1986). *Instabilities in Space and Laboratory Plasmas.* Cambridge, UK: Cambridge University Press, 288.

Melrose, D. B. (2017). Coherent emission mechanisms in astrophysical plasmas. *Reviews of Modern Plasma Physics.* 1, 5. doi:10.1007/s41614-017-0007-0

Michalek, G., Gopalswamy, N., and Xie, H. (2007). Width of Radio-Loud and Radio-Quiet CMEs. *Sol. Phys.* 246, 409–414. doi:10.1007/s11207-007-9062-y

Mishra, S. K., Singh, T., Kayshap, P., and Srivastava, A. K. (2018). Evolution of Magnetic Rayleigh-Taylor Instability into the Outer Solar Corona and Low Interplanetary Space. *Astrophys. J.* 856, 86. doi:10.3847/1538-4357/aaae03

Miteva, R., and Mann, G. (2007). The electron acceleration at shock waves in the solar corona. *Astron. Astrophys.* 474, 617–625. doi:10.1051/0004-6361:20066856

Mondal, S., Oberoi, D., and Vourlidas, A. (2020). Estimation of the Physical Parameters of a CME at High Coronal Heights Using Low-frequency Radio Observations. *Astrophys. J.* 893, 28. doi:10.3847/1538-4357/ab7fab

Morosan, D. E., Carley, E. P., Hayes, L. A., Murray, S. A., Zucca, P., Fallows, R. A., et al. (2019a). Multiple regions of shock-accelerated particles during a solar coronal mass ejection. *Nature Astronomy.* 3, 452–461. doi:10.1038/s41550-019-0689-z

Morosan, D. E., Kilpua, E. K. J., Carley, E. P., and Monstein, C. (2019b). Variable emission mechanism of a Type IV radio burst. *Astron. Astrophys.* 623, A63. doi:10.1051/0004-6361/201834510

Morosan, D. E., Palmerio, E., Pomoell, J., Vainio, R., Palmroth, M., and Kilpua, E. K. J. (2020). Three-dimensional reconstruction of multiple particle acceleration regions during a coronal mass ejection. *Astron. Astrophys.* 635, A62. doi:10.1051/0004-6361/201937133

Moschou, S.-P., Sokolov, I., Cohen, O., Drake, J. J., Borovikov, D., Kasper, J. C., et al. (2018). Synthetic Radio Imaging for Quiescent and CME-flare Scenarios. *Astrophys. J.* 867, 51. doi:10.3847/1538-4357/aae58c

Nelson, G. J., and Melrose, D. B. (1985). "Type II bursts," in Solar radiophysics: Studies of emission from the sun at metre wavelengths (A87-13851 03-92). Cambridge and New York, Cambridge University Press, 333–359.

Nindos, A., et al. (2020). Incoherent Emission. *Frontiers in Astronomy and Space Sciences this.* volume

Nindos, A., Kontar, E. P., and Oberoi, D. (2019). Solar physics with the Square Kilometre Array. *Adv. Space Res.* 63, 1404–1424. doi:10.1016/j.asr.2018.10.023

Nindos, A., Patsourakos, S., Vourlidas, A., and Tagikas, C. (2015). How Common Are Hot Magnetic Flux Ropes in the Low Solar Corona? A Statistical Study of EUV Observations. *Astrophys. J.* 808, 117. doi:10.1088/0004-637X/808/2/117

Nitta, N. V., Liu, W., Gopalswamy, N., and Yashiro, S. (2014). The Relation Between Large-Scale Coronal Propagating Fronts and Type II Radio Bursts. *Sol. Phys.* 289, 4589–4606. doi:10.1007/s11207-014-0602-y

O'Kane, J., Green, L., Long, D. M., and Reid, H. (2019). Stealth Coronal Mass Ejections from Active Regions. *Astrophys. J.* 882, 85. doi:10.3847/1538-4357/ab371b

Parenti, S. (2014). Solar Prominences: Observations. *Living Rev. Sol. Phys.* 11, 1. doi:10.12942/lrsp-2014-1

Patsourakos, S., and Vourlidas, A. (2012). On the Nature and Genesis of EUV Waves: A Synthesis of Observations from SOHO, STEREO, SDO, and Hinode (Invited Review). *Sol. Phys.* 281, 187–222. doi:10.1007/s11207-012-9988-6

Payne-Scott, R., Yabsley, D. E., and Bolton, J. G. (1947). Relative Times of Arrival of Bursts of Solar Noise on Different Radio Frequencies. *Nature.* 160, 256–257. doi:10.1038/160256b0

Perley, R. A., Chandler, C. J., Butler, B. J., and Wrobel, J. M. (2011). The Expanded Very Large Array: A New Telescope for New Science. *Astrophys. J. Lett.* 739, L1. doi:10.1088/2041-8205/739/1/L1

Pesnell, W. D., Thompson, B. J., and Chamberlin, P. C. (2012). The Solar Dynamics Observatory (SDO). *Sol. Phys.* 275, 3–15. doi:10.1007/s11207-011-9841-3

Pick, M. (1986). Observations of Radio Continua and Terminology. *Sol. Phys.* 104, 19–32. doi:10.1007/BF00159942

Pick, M. (2004). Overview of Solar Radio Physics and Interplanetary Disturbances. *Solar and Space Weather Radiophysics.* Springer, Dordrecht: *Astrophysics and Space Science Library*. 314, 17–45. doi:10.1007/1-4020-2814-8_2

Pick, M., and Maia, D. (2005). Origin of complex type III-L events and electron acceleration. *Adv. Space Res.* 35, 1876–1881. doi:10.1016/j.asr.2005.01.076

Pick, M., Stenborg, G., Démoulin, P., Zucca, P., and Lecacheux, A. (2016). Homologous Solar Events on 2011 January 27: Build-up and Propagation in a Complex Coronal Environment. *Astrophys. J.* 823, 5. doi:10.3847/0004-637X/823/1/5

Pick, M., and Vilmer, N. (2008). Sixty-five years of solar radioastronomy: flares, coronal mass ejections and Sun Earth connection. *Astron. AstroPhys. Rev.* 16, 1–153. doi:10.1007/s00159-008-0013-x

Pick-Gutmann, M. (1961). Évolution des émissions radioélectriques solaires de type IV et leur relation avec d'autres phénomènes solaires et géophysiques. *Annales d'Astrophysique* 24, 183.

Plotnikov, I., Rouillard, A. P., and Share, G. H. (2017). The magnetic connectivity of coronal shocks from behind-the-limb flares to the visible solar surface during γ-ray events. *Astron. Astrophys.* 608, A43. doi:10.1051/0004-6361/201730804

Pohjolainen, S., Maia, D., Pick, M., Vilmer, N., Khan, J. I., Otruba, W., et al. (2001). On-the-Disk Development of the Halo Coronal Mass Ejection on 1998 May 2. *Astrophys. J.* 556, 421–431. doi:10.1086/321577

Prasad, B., Banerjee, D., Singh, J., Subramanya, N., Kumar, A., Kamath, P., et al. (2017). Visible emission line coronagraph on aditya-l1. *Curr. Sci.* 113, 613–615. doi:10.18520/cs/v113/i04/613-615

Ramaty, R. (1969). Gyrosynchrotron Emission and Absorption in a Magnetoactive Plasma. *Astrophys. J.* 158, 753. doi:10.1086/150235

Raulin, J. P., Kundu, M. R., Hudson, H. S., Nitta, N., and Raoult, A. (1996). Metric Type III bursts associated with soft X-ray jets. *Astron. Astrophys.* 306, 299.

Reber, G. (1944). Cosmic Static. *Astrophys. J.* 100, 279. doi:10.1086/144668

Robbrecht, E., Patsourakos, S., and Vourlidas, A. (2009). No Trace Left Behind: STEREO Observation of a Coronal Mass Ejection Without Low Coronal Signatures. *Astrophys. J.* 701, 283–291. doi:10.1088/0004-637X/701/1/283

Robinson, R. D., and Stewart, R. T. (1985). A Positional Comparison Between Coronal Mass Ejection Events and Solar Type-II Bursts. *Sol. Phys.* 97, 145–157. doi:10.1007/BF00152984

Rochus, P., Auchère, F., and Berghmans, D. (2020). The solar orbiter eui instrument: The extreme ultraviolet imager. *Astron. Astrophys.* 642, A8. doi:10.1051/0004-6361/201936663

Rouillard, A. P., Plotnikov, I., Pinto, R. F., Tirole, M., Lavarra, M., Zucca, P., et al. (2016). Deriving the Properties of Coronal Pressure Fronts in 3D: Application to the 2012 May 17 Ground Level Enhancement. *Astrophys. J.* 833, 45. doi:10.3847/1538-4357/833/1/45

Salas-Matamoros, C., Klein, K.-L., and Rouillard, A. P. (2016). Coronal mass ejection-related particle acceleration regions during a simple eruptive event. *Astron. Astrophys.* 590, A135. doi:10.1051/0004-6361/201528015

Sasikumar Raja, K., Ramesh, R., Hariharan, K., Kathiravan, C., and Wang, T. J. (2014). An Estimate of the Magnetic Field Strength Associated with a Solar Coronal Mass Ejection from Low Frequency Radio Observations. *Astrophys. J.* 796, 56. doi:10.1088/0004-637X/796/1/56

Scherrer, P. H., Schou, J., Bush, R. I., Kosovichev, A. G., Bogart, R. S., Hoeksema, J. T., et al. (2012). The Helioseismic and Magnetic Imager (HMI) Investigation for the Solar Dynamics Observatory (SDO). *Sol. Phys.* 275, 207–227. doi:10.1007/s11207-011-9834-2

Schmidt, J. M., and Cairns, I. H. (2012). Type II radio bursts: 1. New entirely analytic formalism for the electron beams, Langmuir waves, and radio emission. *J. Geophys. Res. B.* 117, A04106. doi:10.1029/2011JA017318

Schmidt, J. M., Cairns, I. H., and Hillan, D. S. (2013). Prediction of Type II Solar Radio Bursts by Three-dimensional MHD Coronal Mass Ejection and Kinetic Radio Emission Simulations. *Astrophys. J. Lett.* 773, L30. doi:10.1088/2041-8205/773/2/L30

Seaton, D. B., and Darnel, J. M. (2018). Observations of an Eruptive Solar Flare in the Extended EUV Solar Corona. *Astrophys. J. Lett.* 852, L9. doi:10.3847/2041-8213/aaa28e

Sheeley, J., N. R., Howard, R. A., Michels, D. J., Robinson, R. D., Koomen, M. J., and Stewart, R. T. (1984). Associations between coronal mass ejections and metric type II bursts. *Astrophys. J.* 279, 839–847. doi:10.1086/161954

Smerd, S. F., Sheridan, K. V., and Stewart, R. T. (1974). "On Split-Band Structure in Type II Radio Bursts from the Sun (presented by S.F. Smerd)," In Coronal Disturbances, Editor G. A. Newkirk (Vienna, Austria: IAU Symposium), Vol. 57, 389.

Srivastava, A. K., Mishra, S. K., Jelínek, P., Samanta, T., Tian, H., Pant, V., et al. (2019). On the Observations of Rapid Forced Reconnection in the Solar Corona. *Astrophys. J.* 887, 137. doi:10.3847/1538-4357/ab4a0c

Srivastava, N., Schwenn, R., Inhester, B., Martin, S. F., and Hanaoka, Y. (2000). Factors Related to the Origin of a Gradual Coronal Mass Ejection Associated with an Eruptive Prominence on 1998 June 21-22. *Astrophys. J.* 534, 468–481. doi:10.1086/308749

Sterling, A. C. (2000). Sigmoid CME source regions at the Sun: some recent results. *J. Atmos. Sol. Terr. Phys.* 62, 1427–1435. doi:10.1016/S1364-6826(00)00089-4

Stewart, R. T., Dulk, G. A., Sheridan, K. V., House, L. L., Wagner, W. J., Illing, R., et al. (1982). Visible light observations of a dense plasmoid associated with a moving Type IV solar radio burst. *Astron. Astrophys.* 116, 217–223.

Török, T., Kliem, B., and Titov, V. S. (2004). Ideal kink instability of a magnetic loop equilibrium. *Astron. Astrophys.* 413, L27–L30. doi:10.1051/0004-6361:20031691

Tousey, R. (1973). "The solar corona," In Space Research XIII, Editors M. J. Rycroft and S. K. Runcorn. Berlin: Akademie Verlag, Vol. 2, 713–730

Tun, S. D., and Vourlidas, A. (2013). Derivation of the Magnetic Field in a Coronal Mass Ejection Core via Multi-frequency Radio Imaging. *Astrophys. J.* 766, 130. doi:10.1088/0004-637X/766/2/130

Uchida, Y. (1960). On the Exciters of Type II and Type III Solar Radio Bursts. *PASJ.* 12, 376.

van Ballegooijen, A. A., and Martens, P. C. H. (1989). Formation and Eruption of Solar Prominences. *Astrophys. J.* 343, 971–984. doi:10.1086/167766

van Haarlem, M. P., Wise, M. W., Gunst, A. W., Heald, G., McKean, J. P., Hessels, J. W. T., et al. (2013). LOFAR: The LOw-Frequency ARray. *Astron. Astrophys.* 556, A2. doi:10.1051/0004-6361/201220873

Vandas, M., and Karlický, M. (2011). Electron acceleration in a wavy shock front. *Astron. Astrophys.* 531, A55. doi:10.1051/0004-6361/201016135

Vasanth, V., Chen, Y., Lv, M., Ning, H., Li, C., Feng, S., et al. (2019). Source Imaging of a Moving Type IV Solar Radio Burst and Its Role in Tracking Coronal Mass Ejection from the Inner to the Outer Corona. *Astrophys. J.* 870, 30. doi:10.3847/1538-4357/aaeffd

Vourlidas, A. (2004). "Radio Observations of Coronal Mass Ejection4," in Solar and Space Weather Radiophysics: Current Status and Future Developments. Editors D. E. Gary and C. U. Keller (Dordrecht: Springer), Vol. 314, 223–242. doi:10.1007/1-4020-2814-8_11

Vourlidas, A., Lynch, B. J., Howard, R. A., and Li, Y. (2013). How Many CMEs Have Flux Ropes? Deciphering the Signatures of Shocks, Flux Ropes, and Prominences in Coronagraph Observations of CMEs. *Sol. Phys.* 284, 179–201. doi:10.1007/s11207-012-0084-8

Vourlidas, A., Carley, E. P., and Vilmer, N. (2020). Radio observations of coronal mass ejections: space weather aspects. *Front. Astron. Space Sci. 7, id.43.* doi:10.3389/fspas.2020.00043

Vršnak, B., Aurass, H., Magdalenić, J., and Gopalswamy, N. (2001). Band-splitting of coronal and interplanetary type II bursts. I. Basic properties. *Astron. Astrophys.* 377, 321–329. doi:10.1051/0004-6361:20011067

Vršnak, B., Magdalenić, J., Aurass, H., and Mann, G. (2002). Band-splitting of coronal and interplanetary type II bursts. II. Coronal magnetic field and Alfvén velocity. *Astron. Astrophys.* 396, 673–682. doi:10.1051/0004-6361:20021413

Vrsnak, B., Ruzdjak, V., Zlobec, P., and Aurass, H. (1995). Ignition of MHD Shocks Associated with Solar Flares. *Sol. Phys.* 158, 331–351. doi:10.1007/BF00795667

Wild, J. P., Murray, J. D., and Rowe, W. C. (1954). Harmonics in the Spectra of Solar Radio Disturbances. *Aust. J. Phys.* 7, 439. doi:10.1071/PH540439

Wild, J. P., Sheridan, K. V., and Trent, G. H. (1959). "The transverse motions of the sources of solar radio bursts," In URSI Symp. 1: Paris Symposium on Radio Astronomy. Editor R. N. Bracewell (Vienna, Austria: IAU Symposium), Vol. 9, 176.

Wu, Z., Chen, Y., Huang, G., Nakajima, H., Song, H., Melnikov, V., et al. (2016). Microwave Imaging of a Hot Flux Rope Structure during the Pre-impulsive Stage of an Eruptive M7.7 Solar Flare. *Astrophys. J. Lett.* 820, L29. doi:10.3847/2041-8205/820/2/L29

Yan, X. L., Yang, L. H., Xue, Z. K., Mei, Z. X., Kong, D. F., Wang, J. C., et al. (2018). Simultaneous Observation of a Flux Rope Eruption and Magnetic Reconnection during an X-class Solar Flare. *Astrophys. J. Lett.* 853, L18. doi:10.3847/2041-8213/aaa6c2

Yan, Y., Chen, L., and Yu, S. (2016). "First radio burst imaging observation from Mingantu Ultrawide Spectral Radioheliograph,". In Solar and Stellar Flares and their Effects on Planets. Editors A. G. Kosovichev, S. L. Hawley, and P. Heinzel (Vienna, Austria: IAU Symposium), Vol. 320, 427–435. doi:10.1017/S174392131600051X

Zhang, J., Cheng, X., and Ding, M.-D. (2012). Observation of an evolving magnetic flux rope before and during a solar eruption. *Nat. Commun.* 3, 747. doi:10.1038/ncomms1753

Zhang, J., Dere, K. P., Howard, R. A., Kundu, M. R., and White, S. M. (2001). On the Temporal Relationship between Coronal Mass Ejections and Flares. *Astrophys. J.* 559, 452–462. doi:10.1086/322405

Zimovets, I., Vilmer, N., Chian, A. C. L., Sharykin, I., and Struminsky, A. (2012). Spatially resolved observations of a split-band coronal type II radio burst. *Astron. Astrophys.* 547, A6. doi:10.1051/0004-6361/201219454

Zimovets, I. V., and Sadykov, V. M. (2015). Spatially resolved observations of a coronal type II radio burst with multiple lanes. *Adv. Space Res.* 56, 2811–2832. doi:10.1016/j.asr.2015.01.041

Zlobec, P., Messerotti, M., Karlicky, M., and Urbarz, H. (1993). Fine Structures in Time Profiles of Type-II Bursts at Frequencies above 200-MHZ. *Sol. Phys.* 144, 373–384. doi:10.1007/BF00627601

Zucca, P., Carley, E. P., Bloomfield, D. S., and Gallagher, P. T. (2014a). The formation heights of coronal shocks from 2D density and Alfvén speed maps. *Astron. Astrophys.* 564, A47. doi:10.1051/0004-6361/201322650

Zucca, P., Morosan, D. E., Rouillard, A. P., Fallows, R., Gallagher, P. T., Magdalenic, J., et al. (2018). Shock location and CME 3D reconstruction of a solar type II radio burst with LOFAR. *Astron. Astrophys.* 615, A89. doi:10.1051/0004-6361/201732308

Zucca, P., Pick, M., Démoulin, P., Kerdraon, A., Lecacheux, A., and Gallagher, P. T. (2014b). Understanding Coronal Mass Ejections and Associated Shocks in the Solar Corona by Merging Multiwavelength Observations. *Astrophys. J.* 795, 68. doi:10.1088/0004-637X/795/1/68

Zuccarello, F. P., Aulanier, G., and Gilchrist, S. A. (2015). Critical Decay Index at the Onset of Solar Eruptions. *Astrophys. J.* 814, 126. doi:10.1088/0004-637X/814/2/126

Conflict of Interest: The authors declare that the research was conducted in the absence of any commercial or financial relationships that could be construed as a potential conflict of interest.

The reviewer NN declared a past co-authorship with one of the authors EC to the handling editor.

frontiers in Astronomy and Space Sciences

REVIEW
published: 02 November 2020
doi: 10.3389/fspas.2020.00057

Incoherent Solar Radio Emission

*Alexander Nindos**

Physics Department, University of Ioannina, Ioannina, Greece

Incoherent solar radio radiation comes from the free-free, gyroresonance, and gyrosynchrotron emission mechanisms. Free-free is primarily produced from Coulomb collisions between thermal electrons and ions. Gyroresonance and gyrosynchrotron result from the acceleration of low-energy electrons and mildly relativistic electrons, respectively, in the presence of a magnetic field. In the non-flaring Sun, free-free is the dominant emission mechanism with the exception of regions of strong magnetic fields which emit gyroresonance at microwaves. Due to its ubiquitous presence, free-free emission can be used to probe the non-flaring solar atmosphere above temperature minimum. Gyroresonance opacity depends strongly on the magnetic field strength and orientation; hence it provides a unique tool for the estimation of coronal magnetic fields. Gyrosynchrotron is the primary emission mechanism in flares at frequencies higher than 1–2 GHz and depends on the properties of both the magnetic field and the accelerated electrons, as well as the properties of the ambient plasma. In this paper we discuss in detail the above mechanisms and their diagnostic potential.

Keywords: Sun, solar radio emission, chromosphere, corona, quiet Sun, active regions, flares

OPEN ACCESS

Edited by:
Dale E. Gary,
New Jersey Institute of Technology,
United States

Reviewed by:
Victor F. Melnikov,
Pulkovo Observatory (RAS), Russia
Juan Carlos Martínez Oliveros,
University of California, Berkeley,
United States

***Correspondence:**
Alexander Nindos
anindos@uoi.gr

Specialty section:
This article was submitted to Stellar and Solar Physics, a section of the journal Frontiers in Astronomy and Space Sciences

Received: *13 June 2020*
Accepted: *28 July 2020*
Published: *02 November 2020*

Citation:
Nindos A (2020) Incoherent Solar Radio Emission. Front. Astron. Space Sci. 7:57. doi: 10.3389/fspas.2020.00057

1. INTRODUCTION

The Sun produces radiation across virtually the entire electromagnetic spectrum. Radio frequencies offer valuable diagnostic potential because two of the natural frequencies of the atmosphere of the Sun, the electron plasma frequency and the electron gyrofrequency, belong to the radio band.

In the Sun there are no significant spectral lines, either in emission or absorption, from millimeter to meter wavelengths (but see Dravskikh and Dravskikh, 1988, for a possible detection); pressure broadening is so high that makes such lines undetectable. In the Sun the free electrons dominate the radio emission mechanisms. Solar radio emission is produced from electrons with either a thermal or a non-thermal distribution, and the emission can be either incoherent or coherent. In incoherent mechanisms, no back-reaction of the emission on the electron distribution is present, and the emitted photons show no phase association while their number is proportional to the number of electrons. In coherent mechanisms, all electrons exhibit acceleration in phase; they act together to generate photons that are in phase.

Coherent radiation due to wave-particle and wave-wave interactions plays an important role in transient phenomena at frequencies below 1–2 GHz. Coherent emission mechanisms are discussed elsewhere in this issue by Fleishman.

There are two classes of incoherent emission mechanisms that are important on the Sun: free-free (or bremsstrahlung) and gyromagnetic. At radio frequencies free-free emission is primarily produced from collisions between ions and thermal electrons and dominates the radio emission of the quiet Sun. Furthermore it contributes significantly to the radio emission of non-flaring active regions and of certain flares during their decay phase. Erupting prominences and coronal mass ejections (CMEs) may also produce free-free emission. Gyromagnetic radiation is produced from electrons that are accelerated in the presence of magnetic fields. It is called gyroresonance emission when it is produced by thermal

electrons with energies that correspond to temperatures of the non-flaring corona (about 10^6 K). Gyroresonance plays an important role in the emission above sunspots at microwaves. Gyromagnetic emission is called gyrosynchrotron when it is produced by mildly relativistic electrons having either non-thermal or thermal electron energy distributions. Gyrosynchrotron is the principle incoherent emission mechanism in flares.

There are several textbooks and review articles devoted to incoherent solar radio emission. The classical textbooks by Kundu (1965), Zheleznyakov (1970), and Krüger (1979) are valuable sources of information. More recent textbooks include the volume edited by Gary and Keller (2004), as well as Aschwanden's (Aschwanden, 2004) book on the solar corona. A historical account of solar radio astronomy together with recent developments has been given in the review by Pick and Vilmer (2008). A review about the radio emission of the quiet Sun has been published by Shibasaki et al. (2011) while reviews about gyroresonance have been provided by White and Kundu (1997) and Lee (2007). Transient incoherent solar radio emission has been discussed by Bastian et al. (1998) and Nindos et al. (2008). A more recent book about incoherent microwave emission from flaring loops has been written by Huang et al. (2018).

The structure of this paper is as follows. In section 2, we give a short introduction on radiative transfer and propagation of radio emission. In section 3, we discuss free-free emission, and in section 4 the different types of gyromagnetic emission are outlined briefly. Section 5 and section 6 are devoted to gyroresonance and gyrosynchrotron radiation, respectively. We present concluding remarks in section 7.

2. RADIATIVE TRANSFER AND PROPAGATION OF RADIO EMISSION

2.1. Radiative Transfer Basics

Radiation is always intimately related to material through emission and absorption processes. When both emission and absorption are considered, the intensity, I_ν, inside a plasma slab of thickness dl changes by

$$\frac{dI_\nu}{dl} = j_\nu \rho - k_\nu \rho I_\nu \tag{1}$$

where j_ν and k_ν are the emission and absorption coefficients, respectively, which are defined by

$$dI_\nu = j_\nu \rho dl \tag{2}$$

and

$$dI_\nu = -k_\nu \rho I_\nu dl \tag{3}$$

where ρ is the plasma density. The above discussion is only valid for thermal plasma radiation. For non-thermal electron distributions these formulas hold if ρ describes the concentration of non-thermal electrons.

It is convenient to discuss radiative transfer in terms of the optical depth, τ_ν, which is defined by:

$$d\tau_\nu = -k_\nu \rho dl \tag{4}$$

Using the optical depth, Equation (1) becomes

$$\frac{dI_\nu}{d\tau_\nu} = I_\nu - S_\nu \tag{5}$$

where $S_\nu = j_\nu/k_\nu$ is the source function. Equation (5) is called radiative transfer equation (RTE). Its typical solution (i.e., the intensity at the observer where $\tau_\nu = 0$) is

$$I_\nu(\tau_\nu = 0) = \int_0^\infty S_\nu e^{-t_\nu} dt_\nu \tag{6}$$

Therefore the intensity at the observer results from the contribution of all layers of a stellar atmosphere, with each layer contributing proportionally to its emissivity, attenuated by the absorption of the overlying layers, e^{-t_ν}.

From the RTE, we obtain for a finite slab of constant source function:

$$I_\nu = S_\nu(1 - e^{-\tau_\nu}) \tag{7}$$

In the optically thin case (i.e., transparent slab; $\tau_\nu \ll 1$), Equation (7) yields

$$I_\nu = \tau_\nu S_\nu \tag{8}$$

while for the optically thick case (i.e., opaque slab; $\tau_\nu \gg 1$), we obtain

$$I_\nu = S_\nu \tag{9}$$

Thermal solar radio emission originates from local thermodynamic equilibrium (LTE) conditions (i.e., the temperature, T, does not change much with respect to the mean free path of photons and free electrons, and the anisotropy of the radiation field is small). In LTE, the emission and absorption coefficients are not independent, but the source function is equal to the Planck function. At radio frequencies the inequality $h\nu/k_BT \ll 1$ holds, (k_B is the Boltzmann constant), and the Planckian simplifies to the Rayleigh-Jeans law. Then it is convenient to define a brightness temperature, T_b, as the equivalent temperature a black body would have in order to be as bright as the observed brightness:

$$I_\nu = B_\nu(T_b) = \frac{2\nu^2}{c^2} k_B T_b \tag{10}$$

Similarly, we can define an effective temperature, T_{eff}:

$$S_\nu = \frac{j_\nu}{k_\nu} = \frac{2\nu^2}{c^2} k_B T_{eff} \tag{11}$$

Using our definitions of brightness temperature and effective temperature the RTE can be expressed as:

$$\frac{dT_b}{d\tau_\nu} = T_b - T_{eff} \tag{12}$$

Similar to Equation (5), for an homogeneous source, the solution is:

$$T_b = T_{eff}(1 - e^{-\tau_\nu}), \tag{13}$$

For the optically thin and optically thick cases, Equation (13) yields

$$T_b = \tau_\nu T_{eff} \tag{14}$$

and

$$T_b = T_{eff} \tag{15}$$

respectively. When the emission is incoherent, T_{eff} is the kinetic temperature in the case of thermal emission or corresponds to the mean energy, E, of the emitting electrons (i.e., $T_{eff} = E/k_B$) when the emission is non-thermal. Therefore for an incoherent emission, T_b is limited by the mean energy of the radiating particles. Since the rest energy of the electron corresponds to $T_b = 0.6 \times 10^{10}$ K, we conclude that sources with $T_b \gg 10^{10}$ K cannot be due to incoherent emission from non-relativistic or mildly relativistic electrons. Incoherent emission by highly relativistic electrons is dominated by synchrotron emission (see section 4), which is limited to $T_b \leq 10^{12}$ K by Compton scattering (Kellermann and Pauliny-Toth, 1969).

2.2. Propagation of Radio Emission

In most cases, the corona can be described as a cold magnetized plasma, and the magnetoionic theory (e.g., Melrose, 1980, volume 1, chapter 2) is used to study the propagating electromagnetic modes. These are the extraordinary (x-), ordinary (o-), z-, and whistler mode. Only the x- and o- mode waves can propagate from the source to the observer, whereas the z- and whistler mode waves cannot due to stopbands in the refractive index. For most applications in solar radiophysics, the propagation of the x- and o-mode waves can be described by either the quasi-longitudinal (QL) or the quasi-transverse (QT) approximation (propagation almost parallel and almost perpendicular to the magnetic field, respectively).

For observational purposes it is easier to describe radiation using the Stokes parameters I, Q, U, and V. Under conditions of QL propagation, we get $Q = U = 0$, and the x- and o-mode waves are circularly polarized in opposite senses. Thus we obtain $V = I_x - I_o$, and the polarization is circular having the sense of the dominant mode. In the case of QT propagation, we obtain $Q = I_x - I_o$ and $U = V = 0$, and the polarization is linear. However, because the Faraday rotation in the corona is large, we can detect linear polarization only if we use receivers of much narrower bandwidth than those currently available. There is only one observation of linear polarization at microwaves from active regions; it was accomplished by Alissandrakis and Chiuderi-Drago (1994) who used a multichannel spectral line receiver of very small bandwidth.

Under the approximation of geometrical optics (not very low values for the magnetic field and electron density) when conditions change along the radiation path, the polarization of the x- and o-mode waves will change accordingly. Therefore when a transverse field region is crossed, the sense of polarization changes because of the change of the sign of the longitudinal magnetic field. This is valid when the coupling between the x- and o-mode waves is weak (i.e., they propagate independently). However, as both the coronal magnetic field and density decrease with height, the differences between the characteristics of the x- and o-mode waves decrease, and hence their mutual coupling increases. In the strong coupling regime, the waves are not independent and the polarization does not change along the path but attains a limiting value, even if a transverse field region is crossed (e.g., Cohen, 1960; Zheleznyakov, 1970). Therefore, data of circular polarization do not necessarily reflect the polarity of the magnetic field at the source of radiation (e.g., Alissandrakis and Preka-Papadema, 1984; Alissandrakis et al., 1993b; Shain et al., 2017).

The refractive index of the unmagnetized plasma is $n = [1 - (\nu_p/\nu)^2]^{1/2}$ where ν_p is the electron plasma frequency. At low frequencies it can become much smaller than unity which could trigger refraction and total reflection effects. Total reflection of the radio waves will occur when $\nu = \nu_p$. Refraction modifies the ray paths and also decreases the brightness because the rays move away from regions of high density and the optical depth becomes less than unity (Alissandrakis, 1994). Generally, refraction is not important unless the optical depth between the region of total reflection and the observer is small. Its effect becomes more serious when large-scale density inhomogeneities are present in the corona and inner heliosphere (e.g., coronal holes, streamers, slow or fast solar wind streams). This can result in distorions and/or apparent position offsets of the radio sources (e.g., Duncan, 1979; Lecacheux et al., 1989). Ionospheric refraction can also significantly modify the apparent position of radio sources, sometimes more than several minutes of arc in the metric range (e.g., Mercier, 1996).

When small-scale inhomogeneities are present between the observer and the radio source, several scattering phenomena may take place. These include spectral and angular broadenings that cause frequency-dependent blurring in radio structures (e.g., Bastian, 1994) and decrease of the detected brightness temperature at low frequencies (Thejappa and MacDowall, 2008). Furthermore, anisotropic scattering displaces radio sources (Kontar et al., 2019).

3. FREE-FREE EMISSION

3.1. Emissivity and Absorption Coefficient

3.1.1. Electron-ion Free-Free Mechanism

From the middle chromosphere upward, the free-free emission (or bremsstrahlung) exclusively originates from electrons that are diverted in the Coulomb field of ambient ions because they are accelerated by the Coulomb force. The term "free-free" is due to the state of the electrons; they are free both before and after the interaction.

In the classical limit, the radiation of free accelerated charged particles is described by Larmor's formula:

$$\frac{dP}{d\Omega} = \frac{q^2 a^2}{4\pi c^2} \sin^2\theta \tag{16}$$

where P is the power emitted within the solid angle $d\Omega$ by a particle of charge q, mass m, and acceleration a in the direction θ relative to the acceleration vector. The total radiated power is

obtained after integration over solid angle:

$$P = \frac{2q^2a^2}{3c^2} \tag{17}$$

Since $a \propto 1/m$, the power is $\propto 1/m^2$ and the proton radiation can be ignored because it is much smaller than that of electrons. This conclusion holds for all radio emission processes. Interaction between identical charges also does not produce much radiation because radiation power is proportional to the second derivative of the dipole moment of the system of charged particles, which does not change when two identical particles interact. Consequently, only electron-ion collisions are relevant, and significant radiation is produced by the electrons only.

In a binary encounter between an electron of speed v and an ion of charge Z, the electron deviates from its straight line path by an angle θ, which depends on its speed and the distance of the encounter, called impact parameter, b. In the corona there is a large number of particles inside the Debye sphere and hence the ratio of small-to-large angle encounters is $\approx \lambda_D/r_c$, where λ_D is the Debye length and r_c is the impact parameter that produces a 90° deflection (e.g., see Raulin and Pacini, 2005). Consequently, small-angle collisions dominate and the path of an incoming electron is determined primarily by multiple interactions that yield small deflections, and therefore low energy (radio, that is) photons are produced. In large-angle encounters, high energy electrons may undergo large deflections that yield the emission of high energy (X-ray, that is) photons. Large-angle encounters become more important as we move to cooler and denser deeper layers of the solar atmosphere, because the size of the Debye sphere decreases.

The calculation of the emission from free-free interactions is given in detail by Rybicki and Lightman (1979); here, we only outline the procedure. Since we are interested in the radio emission, the small-angle approximation is appropriate for which the deflection of electrons can be neglected, and therefore we assume the motion takes place along a straight line where the electron and ion are separated by $r = \sqrt{b^2 + v^2t^2}$. We further use the dipole approximation to obtain the net acceleration along the path, and therefore for a single collision an electron emits:

$$\frac{dW(b)}{d\omega} = \frac{8Z^2e^6}{3\pi c^3 m_e^2 v^2 b^2} \quad \text{for} \quad b \ll v/\omega \tag{18}$$

(collisions at a given b lead to emission only at $\omega < v/b$). The total incoming flux of electrons with speed v is $(n_e v)(2\pi b db)$, where n_e is the electron number density. Then the free-free emissivity (i.e., emission per unit time, volume, and frequency) is:

$$\frac{dW}{dtdVd\omega} = n_e n_i 2\pi v \int_{b_{min}}^{b_{max}} \frac{dW(b)}{d\omega} b db \tag{19}$$

where n_i is the ion number density. The limits of integration are determined by $b_{min} = 4Ze^2/(\pi m_e v^2)$ corresponding to a 90° deflection, and $b_{max} = v/\omega$, above which the emitted power is negligible. When we combine Equations (18) and (19), we obtain:

$$\frac{dW}{dtdVd\omega} = \frac{16e^6 n_e n_i Z^2}{3c^3 m_e^2 v} \int_{b_{min}}^{b_{max}} \frac{db}{b} = \frac{16e^6 n_e n_i Z^2}{3c^3 m_e^2 v} \ln\left(\frac{b_{max}}{b_{min}}\right) \tag{20}$$

Usually the above equation is written as

$$\frac{dW}{dtdVd\omega} = \frac{16\pi e^6}{3^{3/2} c^3 m_e^2 v} n_e n_i Z^2 G_{ff}(v,\omega) \tag{21}$$

where $G_{ff}(v,\omega)$ is the Gaunt factor (Karzas and Latter, 1961).

The next step is to integrate Equation (21) over the velocity distribution of the electrons. In radio astronomy, a thermal distribution is used in most cases, and the calculation yields

$$\eta_\nu = \frac{2^5\pi e^6}{3m_e c^3}\left(\frac{2\pi}{3m_e k_B T_e}\right)^{1/2} n_e n_i Z^2 G_{ff}(T_e,\nu) \tag{22}$$

where the emissivity is now denoted by η_ν, and T_e is the electron temperature. The emissivity is proportional to the product of the electron number density with the ion number density. The decrease of emissivity with increasing temperature comes from the decrease of $dW(b)/d\omega$ with increasing relative speed v of the electron-ion pairs (Equation 18).

Using the emissivity and the Rayleigh-Jeans law, $B_\nu(T_e) = 2k_B T_e \nu^2/c^2$, we obtain the absorption coefficient:

$$k_\nu = \frac{1}{3c}\sqrt{\frac{2\pi}{3}}\left(\frac{\nu_p}{\nu}\right)^2 \frac{4\pi e^4 n_e n_i Z^2}{m_e^{1/2}(k_B T)^{3/2}} G_{ff}(T_e,\nu) \tag{23}$$

which is also written as

$$k_\nu = \frac{9.78\times10^{-3} n_e n_i Z^2}{\nu^2 T_e^{3/2}} \times \begin{cases} 18.2 + \ln T_e^{3/2} - \ln\nu & (T_e < 2\times10^5 K) \\ 24.5 + \ln T_e - \ln\nu & (T_e > 2\times10^5 K) \end{cases} \tag{24}$$

where two expressions for the Gaunt factor have been used for conditions relevant to the solar atmosphere (Dulk, 1985).

3.1.2. H^- Free-Free Mechanism

Free-free absorption can result not only from interactions between ions and free electrons but also from free-free transitions of electrons in the field of hydrogen atoms. The latter mechanism is often referred to as H^- absorption. Stallcop (1974) has provided analytical expressions for the H^- absorption coefficient, k_{H^-}, from which we obtain:

$$k_{H^-} = 1.2754\times10^{-11}\frac{n_e n_H\sqrt{T}}{\nu^2} e^{-\zeta(2.065K)} \tag{25}$$

where n_H is the hydrogen density and

$$K = 2.517\times10^{-3}\sqrt{T} \tag{26}$$

and

$$\zeta(2.065K) = 4.862K(1 - 0.2096K + 0.0170K^2 - 0.00968K^3) \tag{27}$$

The contribution of H^- absorption becomes non-negligible at wavelengths shorter than about 1 mm, where radiation is formed in cooler layers. Alissandrakis et al. (2017) have estimated that at around electron temperature of 6,000 K, the H^- opacity is about 10% of the total opacity (see also Wedemeyer et al., 2016).

3.2. Polarization

With the above treatment we did not take into account the magnetic field and we also assumed that the index of refraction n is unity. If we relax these assumptions, we obtain equations which are more complicated than Equations (22) and (24). However, simplifications are often used (e.g., Kundu, 1965), which yield a simpler expression for the absorption coefficient:

$$k_\nu = \xi \frac{n_e^2}{n\nu^2 T_e^{3/2}} \frac{1}{(\nu \pm \nu_{ce}|\cos\theta|)^2} \tag{28}$$

where ξ is a slowly varying function of T_e and n_e, ν_{ce} is the electron gyrofrequency, and θ the angle between the magnetic field and the line of sight. The plus sign in Equation (28) corresponds to the *o*-mode emission while the minus sign corresponds to the *x*-mode wave. Therefore the *x*- and o-mode opacities are slightly larger and smaller, respectively, than that of the unmagnetized situation. The radiation forms in regions where the temperature increases with height, and so does the brightness temperature. Consequently, we expect weak polarization in the sense of the *x*-mode.

For uniform thermal material and using Equation (28), we derive that the degree of circular polarization ρ_c of the optically thin free-free emission is:

$$\rho_c = \frac{V}{I} = \frac{2\nu_{ce}\cos\theta}{\nu} \tag{29}$$

where the longitudinal component of the magnetic field, $B\cos\theta$, is involved because $\nu_{ce} = eB/(2\pi m_e c)$. However, one should take into a count that the density and magnetic field are not constant along the line of sight, and that the emission should not necessarily be optically thin. However, in the weak field limit Grebinskij et al. (2000) and Gelfreikh (2004) have shown that one may nevertheless constrain the coronal magnetic field from spectrally resolved data of free-free radiation.

3.3. Observations of Free-Free Emission

At most frequencies and locations (exceptions include regions with strong coronal magnetic fields observed at microwaves, see section 5), the non-flaring Sun produces radio emission via the free-free mechanism. At low frequencies the corresponding emission is optically thick in the corona (though refraction may bring τ_ν below unity at metric wavelengths), while at higher frequencies there is a mixture of optically thick radiation from cool chromospheric plasmas together with contributions from hot coronal plasmas (can be either optically thin or thick) in active regions.

3.3.1. Spectrum

A model of the spectrum of the microwave brightness temperature of free-free emission is presented in the left column of **Figure 1** (from Gary and Hurford, 1994). The calculation was performed for coronal conditions ($T_e \approx 1.5\times10^6$ K, fully ionized H and 10% He) neglecting magnetic field and assuming that the index of refraction is 1. Then by using Equation (28) and the definition of optical depth, τ_ν, we obtain

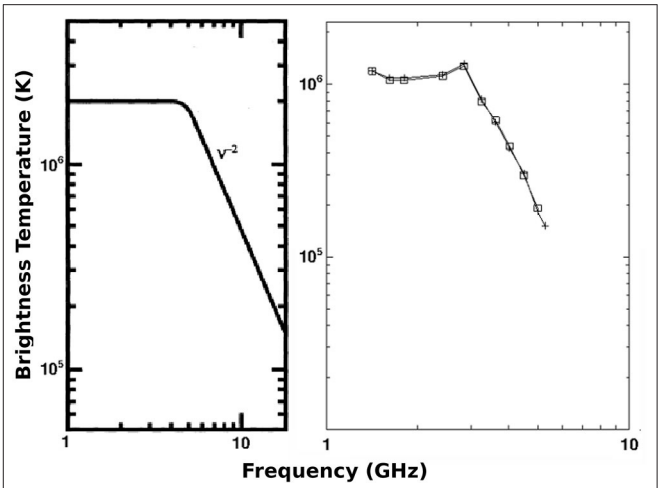

FIGURE 1 | Left: Model of the microwave brightness temperature spectrum of free-free emission (adapted from Gary and Hurford, 1994). ©AAS. Reproduced with permission. **Right**: Brightness temperature spectrum of part of an active region, with crosses and boxes representing left-hand and right-hand circular polarization, respectively. The observations were obtained with the OVSA at 16 frequencies in the range 1.4–8 GHz (adapted from Gary and Hurford, 1987). ©AAS. Reproduced with permission.

$$\tau_\nu \approx 0.2 \frac{\int n_e^2 dl}{\nu^2 T_e^{3/2}} \tag{30}$$

The spectrum is flat where the emission is optically thick and the corresponding T_b is merely the electron temperature of the corona (see Equation 15). At high frequencies, the coronal radiation becomes optically thin and the brightness temperature decreases as $T_b \propto \nu^{-2}$ (see Equations 14 and 30). The brightness temperature spectrum we show in the right panel of **Figure 1** comes from observations obtained with the Owens Valley Solar Array (OVSA) at 16 frequencies in the range 1.4–8 GHz (Gary and Hurford, 1987) and is consistent with the above interpretation. More recent observations by Saint-Hilaire et al. (2012) have confirmed the above results.

Recently, Rodger and Labrosse (2018) and Rodger et al. (2019) have shown that the spectral gradient of millimeter free-free emission can be used for the diagnosis of the optical depth of either isothermal or multithermal material provided a correction is introduced to compensate for the change of the Gaunt factor over the observed frequency range.

There is a long tradition of comparisons of brightness temperature spectra of the free-free emission that span a wide range of frequencies (from sub-mm to microwaves) with either standard one-dimensional atmospheric models or with the computed radio brightness resulted from EUV observations. The reader is referred to the review by Shibasaki et al. (2011) and to

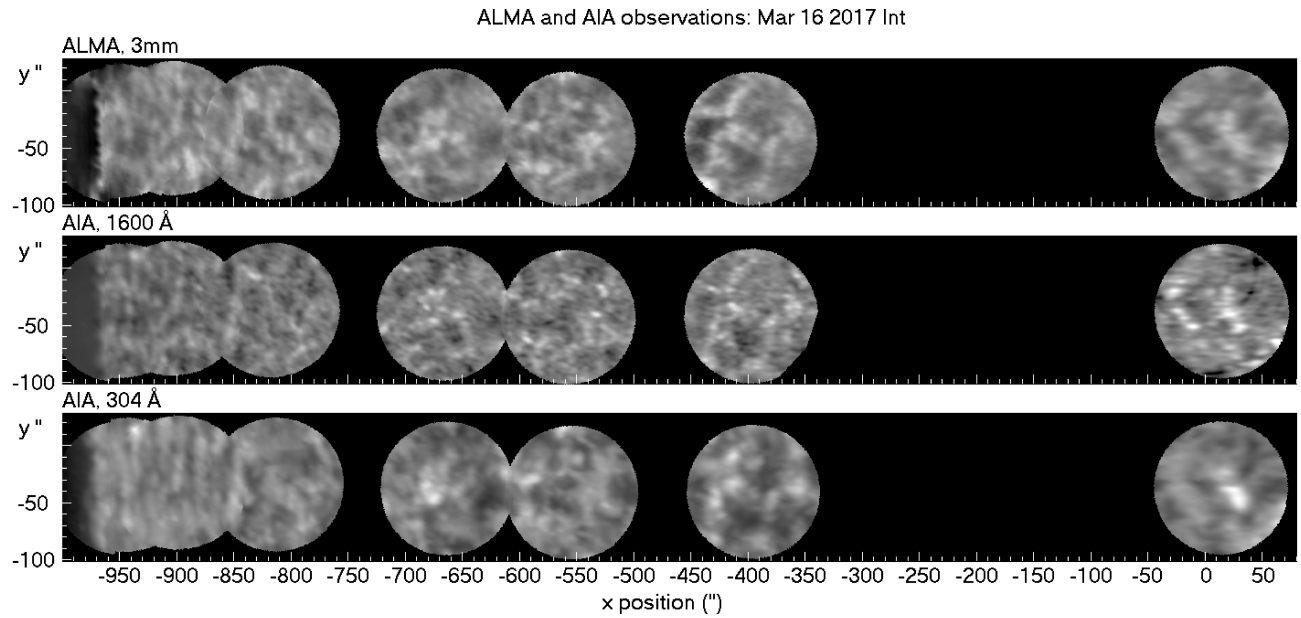

FIGURE 2 | The top row shows a composite (oriented in the south-east direction with respect to solar north) of seven 3 mm average ALMA images (each one computed from visibilities of duration 10 min) while the second and third rows show composites of AIA 1,600 and 304 Å average images for the same fields of view and time intervals as the ALMA images. The AIA images have been convolved with the ALMA beam (from Nindos et al., 2018). Reproduced with permission ©ESO.

the paper about the solar atmosphere written by Alissandrakis in this issue for a detailed discussion of the subject.

3.3.2. Imaging Observations of the Non-flaring Sun

The quiet Sun radio emission comes from the free-free mechanism. At frequencies $\gtrsim$ 20 GHz the corona is optically thin everywhere and radio emission probes the chromosphere. The first high-resolution images of the quiet Sun in the millimeter range were obtained by White et al. (2006) and Loukitcheva et al. (2006) who used the Berkeley-Illinois-Maryland Association Array (BIMA) to obtain $\sim$ 10″ resolution. With the advent of ALMA a new generation of high-resolution millimeter-wavelength images has been forming (e.g., Bastian et al., 2017; Shimojo et al., 2017a,b; Nindos et al., 2018; Yokoyama et al., 2018; Jafarzadeh et al., 2019; Loukitcheva et al., 2019; Molnar et al., 2019; Patsourakos et al., 2020; Wedemeyer et al., 2020) and an example is presented in **Figure 2**. The figure indicates that the chromospheric network, delineated in the AIA 1,600 Å image, is the dominant structure in the radio images. The AIA images of **Figure 2** have been degraded to the resolution of the ALMA images hence the size of the network is similar in all three wavelengths. The chromospheric network is also visible at microwaves (Kundu et al., 1979; Gary and Zirin, 1988; Gary et al., 1990). Subsequent observations (e.g., Bastian et al., 1996; Benz et al., 1997; Krucker et al., 1997) confirmed that result.

In active regions, free-free emission is produced by the plage and coronal loops. At high microwave frequencies ($\nu > 3$ GHz), the active region free-free emission is optically thin (for an example see the 17 GHz image of **Figure 3**); at such high frequencies the only regions of the non-flaring corona that are optically thick are those with strong magnetic fields (> 400 G) where gyroresonance opacity is significant. White (1999) points out that large active regions almost always contain optically thick regions at 1.5 GHz due to free-free opacity, but their free-free opacity is never optically thick at 5 GHz.

The observed brightness temperature of the free-free emission may fall below the coronal electron temperature not only at microwaves, but also at metric wavelengths. The corresponding fall of the optical depth below unity at metric wavelengths is attributed to scattering and refraction effects (see section 2.2). Note, however, that the recent analysis of quiet Sun images obtained with the Low Frequency Array (LOFAR) in the range 25–79 MHz indicates the presence of higher brightness temperatures, of the order of 1 MK (Vocks et al., 2018).

Figure 3 (see also Mercier and Chambe, 2009, 2012) shows images of the Sun at 150–432 MHz obtained with the Nançay Radioheliograph (NRH). These frequencies probe altitudes from the upper transition region to the low corona. At the highest frequencies (327–432 MHz) the most prominent feature is a coronal hole that appears as a depression south of the disk center. Its contrast decreases at lower frequencies in agreement with previous (e.g., Lantos et al., 1987; Lantos and Alissandrakis, 1999) and more recent observations (Rahman et al., 2019). However, the dark-to-bright transition at low frequencies cannot be easily reproduced in model computations (Rahman et al., 2019). Furthermore McCauley et al. (2019) reported values up to 8% for the polarization of coronal holes.

Figure 3 also shows that the similarity of the soft X-ray image with the radio images decreases with frequency. This is not due to spatial resolution differences only. Apart from radio refraction effects, the optical depth of the radio emission is larger than that of the X-ray emission which is always optically thin.

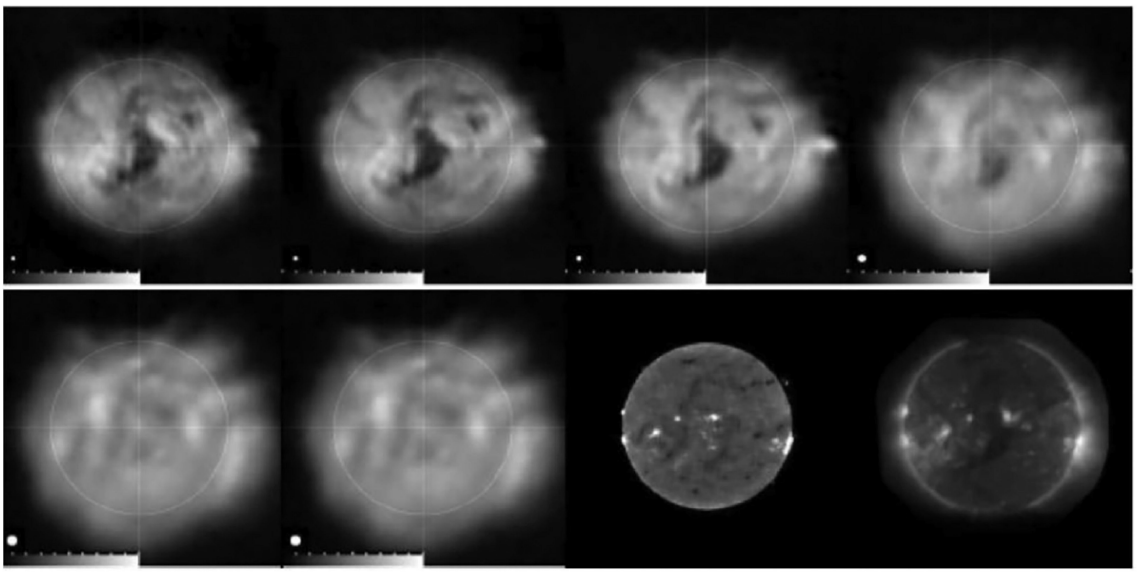

FIGURE 3 | Solar images on 2004 June 27. From left to right and from top to bottom: NRH images obtained at 432, 410, 327, 236, 164, and 150 MHz, NoRH image at 17 GHz, and soft X-rays image obtained from the Solar X-Ray Imager (SXI) on board GOES12 (from Mercier and Chambe, 2009). ©AAS. Reproduced with permission.

Consequently the radio images probe higher coronal layers and lower-lying structures that emit soft X-rays are obscured by dense overlying material. With similar arguments one can interpret the little resemblance between the NRH images and the Nobeyama Radioheliograph (NoRH) image at 17 GHz.

3.3.3. Imaging Observations of Flares and CMEs

The hot soft-X-ray-emitting coronal material that fills flaring loops is expected to produce optically thin free-free emission at millimeter wavelengths and in the decay phase of microwave flares (e.g., Kundu and Vlahos, 1982; Hanaoka, 1999). Thermal free-free emission has also been detected in weak transient brightenings observed at microwaves (White et al., 1995) and millimeter wavelengths (Nindos et al., 2020). For the sake of completeness we note that (i) non-thermal emissions have occasionally also been reported in the decay phase of flares (e.g., Kundu et al., 2001a, 2004a), and (ii) sub-THz emission may originate from optically thick and relatively hot free-free sources located at the chromospheric footpoints of flaring loops (Kontar et al., 2018; Morgachev et al., 2018, 2020).

CME material is also expected to radiate optically thin free-free emission. Ideally, one anticipates that the free-free-emitting structures will be similar to those appearing in coronagraphs because both are associated with multi-thermal plasmas and depend on the electron emission measure (radio frequencies) or column density (white-light data). But the free-free emission of CMEs should be weak because of their low densities and high temperatures (see Equation 30) and often obscured by stronger non-thermal emissions. The published reports on thermal free-free CME emissions at low frequencies are rare. The reader is referred to the articles by Sheridan et al. (1978) and Gopalswamy and Kundu (1992) for early detections with the extinct Culgoora Radioheliograph. Maia et al. (2000) imaged CME fronts at frequencies between 164 and 450 MHz. The radio source motions matched those of white-light CME fronts and their brightness temperature ($\sim 10^4$ K) implied thermal emission. However, their spectral characteristics and polarization were not consistent with such interpretation. Thermal emission from CMEs has also been reported at 109 MHz by Kathiravan et al. (2002) and Ramesh et al. (2003) (Gauribidanur Radioheliograph observations). The thermal free-free CME emission, when detected, can be used for the calculation of the CME mass. Such calculations provide results similar to those obtained from white-light data (Gopalswamy and Kundu, 1992).

Prominences can be observed not only in Hα but also in radio. The Hα emission strongly depends on the plasma temperature but since prominence material is dense ($\sim 10^{10} - 10^{11}$ cm^{-3}) and cool ($\sim$ 8,000 K), it produces optically thick thermal free-free microwave emission (e.g., Gopalswamy and Hanaoka, 1998), which can be easily detected beyond the disk. But quiescent filaments, i.e., quiet prominence seen on the disk, are associated with brightness depressions in the microwave range (e.g., Chiuderi-Drago et al., 2001) and sometimes at decimeter-meter wavelengths (e.g., Marqué et al., 1999; Marqué, 2004). At microwaves, the angular resolution is not as good as in Hα but, thanks to the continuum nature of the free-free emission, the microwave data have the ability to probe the prominence material even at relatively high temperatures which is not always possible in Hα. From the radio data one can calculate the prominence mass (e.g., Gopalswamy and Hanaoka, 1998), but such estimates ignore possible downflows of plasma from the rising prominence. Several events of prominence eruptions at microwaves (see **Figure 4** for an example) have been reported (e.g Hanaoka et al., 1994; Gopalswamy et al., 1996a, 2003; Hori, 2000;

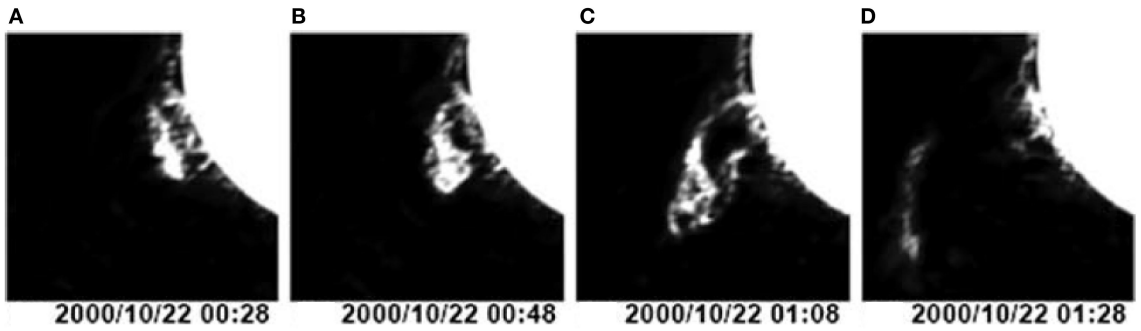

FIGURE 4 | (A–D) 17-GHz images of an eruptive prominence obtained by the NoRH (from Gopalswamy et al., 2003). ©AAS. Reproduced with permission.

Uralov et al., 2002; Grechnev et al., 2006b; Alissandrakis et al., 2013; Fedotova et al., 2018; Huang et al., 2019). In most cases the eruptive prominence detected in radio eventually evolves into the core of the white-light CME.

4. TYPES OF GYROMAGNETIC EMISSION

Gyromagnetic emission is generated when free electrons are accelerated or/and change their velocity direction in a magnetic field due to the influence of the magnetic component of the Lorentz force (in solar plasmas, there are no macroscopic electric fields, except probably in current sheets). An electron with velocity components $v_{\parallel}$ and $v_{\perp}$ parallel and perpendicular to the magnetic field, respectively, will be accelerated perpendicular to both $v_{\perp}$ and B. Its acceleration, a, is:

$$a = \omega_{ce} v_{\perp} \tag{31}$$

where ω_{ce} is the electron gyrofrequency

$$\omega_{ce} = \frac{eB}{m_e c} \tag{32}$$

For non-relativistic speeds, the total power emitted by the electron is provided by the Larmor formula (Equation 17) which yields:

$$P = \frac{2e^2}{3c^2} \omega_{ce}^2 v_{\perp}^2 \tag{33}$$

This expression requires modification when the electron speed is not small compared to the speed of light, c. Then the power of the electron is given by the relativistic Larmor formula:

$$P = \frac{2e^2}{3c^2} \gamma^2 \omega_{ce}^2 v_{\perp}^2 \tag{34}$$

where γ is the Lorentz factor.

It is straightforward to prove that the total emitted power, P, is Lorentz invariant. However, its angular distribution $dP/d\Omega$ is not. In the electron rest frame, the radiated power per solid angle is given by Equation (16) and the radiation pattern is the classical dipole pattern which shows two lobes with power proportional to $\sin^2\theta$. We assume that the relative velocity between the electron rest frame and the observer rest frame is along the x-axis, and we use spherical coordinates such that the angle θ is measured with respect to x-axis while the angle ϕ is the angle between the acceleration and the projection of the line from the charge to the observer onto the plane that is perpendicular to the velocity. Then for the emitted power per solid angle in the rest frame of the observer, the calculations give:

$$\frac{dP}{d\Omega} = \frac{e^2 a^2}{4\pi c^2} \frac{1}{(1-\beta\cos\theta)^4} \left[1 - \frac{\sin^2\theta\cos^2\phi}{\gamma^2(1-\beta\cos\theta)^2}\right] \tag{35}$$

where $\beta = v/c$. There is a strong dependence on the $1-\beta\cos\theta$ factor in the denominator which dominates when $\theta \to 0$ and $\beta \to 1$. In other words, the observer detects strong radiation in the forward direction with respect to the motion of the electron; this is called relativistic beaming. Therefore, in the relativistic case, we obtain strongly beamed emission along the direction of motion which, in turn, is perpendicular to the acceleration. The width of the beam where the emission is concentrated is $2/\gamma$. This means that the signal detected by the observer appears more and more sharply pulsed as the energy of the electron increases. Beaming plays important role in the observed spectrum emitted by a single electron.

The above discussion is valid for an electron radiating in vacuo. In the presence of ambient plasma, we should take into account the influence of the index of refraction n on radiation. In that case, the width of the emission beam is $\theta = 2(1 - n^2\beta^2)^{1/2}$. If $n \approx 1$ we return to the vacuum case. But if $n \ll 1$, then for the ultra-relativistic case ($\beta \sim 1$) we obtain $\theta = 2(1-n^2)^{1/2} = 2\nu_p/\nu$ for a cold plasma. Therefore at low frequencies, the medium quenches wave propagation and plasma effects dominate beaming effects. The decrease in beaming takes place because the electron cannot "catch up" to the wave it just emitted to reinforce it with yet another emission wave.

In the limit of non-relativistic speed (see left column of **Figure 5**), the electron gyrates with frequency equal to the classical gyrofrequency (Equation 32) which is independent of the speed. An observer will detect a sinusoidally varying electric field which has a period of $2\pi/\omega_{ce}$. In that case, the power spectrum is a single line (cyclotron line) at the gyrofrequency. When the electron energy increases, mild beaming is initiated

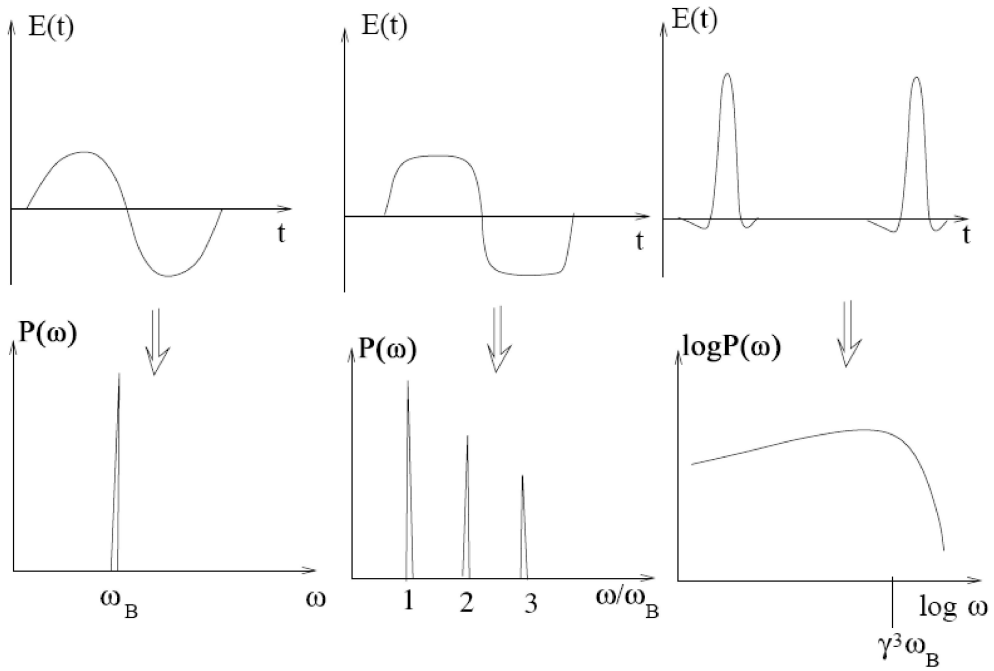

FIGURE 5 | Top: Schematic time variability of the detected electric field that has been produced by a gyrating electron in the cases of small speed (left panel), thermal speed (middle panel) and relativistic speed (right panel). **Bottom**: Schematic power spectra resulted from the cases of the top row.

and the observed temporal variation of the electric field becomes non-sinusoidal. In such circumstances, when the electron energy corresponds to quiescent solar coronal temperatures ($\sim 10^6$ K; see middle column of **Figure 5**), the power spectrum consists of lines at frequencies equal to small integer multiples (called harmonics) of the gyrofrequency. In that case, gyromagnetic emission is called gyroresonance emission. For a mildly relativistic electron (energy of a few tens of keV to a few MeV) there is even more beaming, and there is power in a wide frequency range at harmonics of the gyrofrequency from about 10 to 100. Now the lines exhibit Doppler broadening and start blending together. This type of gyromagnetic emission is called gyrosynchrotron emission. Finally, when the electron is highly relativistic (right column of **Figure 5**) the electric field's temporal variation becomes highly non-sinusoidal and there is power at a large number of harmonics, up to more than $s \sim \gamma^3$, which overlap to yield continuum emission. The frequency $\nu = \gamma^3 \nu_{ce}$ that corresponds to the maximum synchrotron emission of a single electron (see **Figure 5**) is sometimes referred to as the "characteristic frequency of synchrotron emission."

The above discussion is valid for a single electron in the presence of uniform magnetic field. However, in the corona, even along a single line of sight, the magnetic field is not uniform, but generally decreases with height. The non-uniformity of the field together with the spread of the distribution function of the electron energy tend to smear out the spectral lines into an, essentially, continuum emission.

Single expressions for the gyromagnetic emission and absorption coefficients that are valid for all electron energies are not available. Instead, expressions have been derived for separate electron energy regimes.

- At low, non-relativistic energies ($\gamma - 1 \ll 1$), the electron velocity distribution in the corona is thermal and the resulting gyroresonance emission is the primary emission mechanism above sunspots with strong magnetic fields at microwaves.
- In the case of gyrosynchrotron emission from mildly relativistic electrons ($\gamma - 1 \sim 1 - 5$), both thermal and non-thermal electron energy distributions have been used. Gyrosynchrotron emission is the primary incoherent emission mechanism in solar flares.
- Synchrotron emission comes from ultra-relativistic ($\gamma - 1 \gg 1$) electrons. It is well-known that synchrotron emission is relevant in neutron stars, and some extra-galactic sources. In the Sun, it is debated whether it may contribute to the impulsive submillimeter component of some flares (Trottet et al., 2008).

5. GYRORESONANCE EMISSION

5.1. Optical Depth

Gyroresonance opacity for electrons with a thermal energy distribution has been discussed in several textbooks (e.g., Zheleznyakov, 1970; Melrose, 1980). More recent detailed reviews about the physical mechanism and the properties of gyroresonance emission can be found in White and Kundu (1997) and Lee (2007). The gyroresonance absorption coefficient from non-Maxwellian quasi-steady-state electron distributions

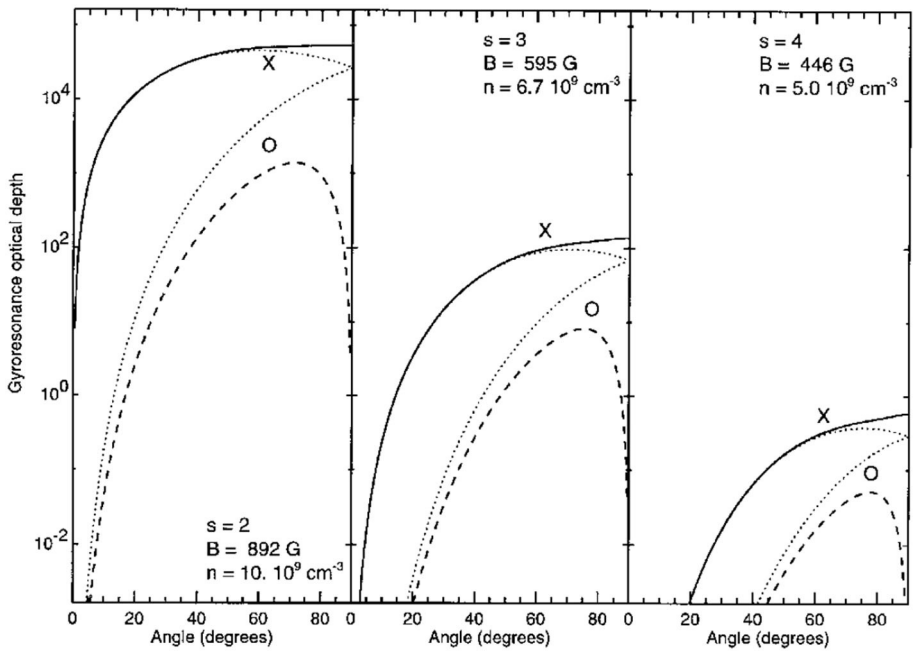

FIGURE 6 | Integrated optical depth, at 5 GHz, of the second, third, and fourth gyroresonance layers (left, middle, and right panels, respectively) as a function of the angle between the magnetic field and the line of sight. The scale height of the magnetic field is 10^9 cm, the electron temperature is 3×10^6 K and the densities are denoted in the figure. The solid and dashed lines correspond to *x*- and *o*-mode exact calculations, respectively. The dotted lines show *x*- and *o*-mode approximate calculations (from White and Kundu, 1997). Reproduced with permission ©Springer Nature.

has been calculated by Fleishman and Kuznetsov (2014) but their predictions have not been tested against observations yet.

The absorption coefficient decreases quickly at frequencies not equal to the resonance frequencies

$$\nu = s\nu_{ce}. \tag{36}$$

where s is the harmonic number. In units of the scale height of the magnetic field, $L_B = B/|\nabla B|$, the frequency width of the resonances is $\sim v/c$, where v is the speed of the emitting electron. In other words, when we observe at a fixed frequency, ν, gyroresonance opacity becomes appreciable only at those points along the line of sight where $\nu_{ce} = \nu/s$. Therefore, the magnetic field, electron density and temperature are almost constant across gyroresonance layers.

The exact expression for the optical depth τ of a gyroresonance layer has been provided by Zheleznyakov (1970) and will not be repeated here. The optical depth depends on many parameters but its most sensitive dependence is on the angle, θ, between the magnetic field and the line of sight.

In **Figure 6**, we show calculations (taken from White and Kundu, 1997) of the optical depth, at 5 GHz, of the second, third, and fourth gyroresonance coronal layers vs. the angle θ. In the figure, the strong dependence of gyroresonance optical depth on θ is evident and shows better at small angles where the opacity drops quickly in both modes. The second and third harmonics are optically thick at most intermediate angles in both *x*- and *o*-mode. The fourth harmonic is optically thin in both polarizations. Harmonics greater than the fourth have negligible opacity. Only *o*-mode emission is possible from the first harmonic, and this can happen if the local cyclotron frequency exceeds the local plasma frequency. The *x*-mode emission from the first harmonic does not propagate out into the corona because the reflecting point of the *x* wave is located higher in the corona (i.e., closer to the observer) than the $s = 1$ layer. At a given harmonic and angle, the *o*-mode opacity is about an order of magnitude smaller than *x*-mode opacity. For a given mode and angle, the transition from harmonic s to harmonic $s+1$ decreases the opacity by about two orders of magnitude.

5.2. Structure of Gyroresonance Sources

The structure of gyroresonance sources is determined to a large extent by the number of harmonic layers that lie above the base of the transition region (TR). The magnetic field decreases with height and therefore higher harmonic layers are located above lower ones. In the case of magnetic field decreasing away from the center of a sunspot, the height of a given harmonic layer decreases with the distance from the center.

The brightness temperature of a given harmonic layer depends on the electron temperature at the height where it is located and on its optical depth. Let us consider the case of a symmetric sunspot. When the harmonic layer is optically thick, the brightness temperature will peak around the center of the spot. Away from the spot center, the electron temperature decreases, at first slowly and then fast as the harmonic layer reaches regions with higher gradient of electron temperature. Consequently, the source will have a flat top and sharp borders. When the source is away from disk center the maximum intensity is located toward the limb because the angle θ attains its highest values there.

Furthermore, projection effects will result in a faster drop of the brightness temperature in the direction of the limb and a smoother drop toward disk center.

Due to the strong dependence of the gyroresonance opacity on the angle θ, a harmonic layer can become optically thick or thin at a given frequency and heliocentric distance, depending on the position within the source. The opacity is zero at $\theta = 0$, thus there is always a region around $\theta = 0$ where the harmonic layer is optically thin. This region can have considerable effects on the structure of the source: it shows up as a region of small intensity and it can result to a ring-shaped or a crescent-shaped harmonic. When the spot is at disk center, this zero-θ region is located at the center of the source, but as the source moves toward the limb, the zero-θ region is displaced. In the current-free case, where the field lines project radially on the photosphere, this displacement is toward the disk center. On the other hand, when the field is not potential, the twist of the field lines introduces an additional displacement in the direction perpendicular to the direction of the center. Thus a microwave source associated with a non-potential field will appear rotated with respect to a source associated with a potential field.

Since the opacity is significantly greater in the *x*-mode than in the *o*-mode, the same source may appear very different in the two modes, and therefore such differences will be prominent in the circular polarization maps. In general, the source is essentially unpolarized in regions where both modes are optically thick but circular polarization may go near the 100% level if the *x*-mode is optically thick and the *o*-mode is optically thin.

To illustrate the structure of microwave gyroresonance sources, we will present model computations of both the gyroresonance and free-free emission resulted from a dipole magnetic field. The magnetic moment of the dipole is 8×10^{30} erg/G and is located vertically below the photospheric disk center at a depth of 2×10^4 km. With these parameters, the value of the maximum field at the photosphere is 2,000 G.

For the computation of the *x*- and *o*-mode emissions, we also need to know the electron temperature, T_e, and density, n_e, in the TR and the low corona. We have used the same approach as in Alissandrakis et al. (1980): both the electron temperature and density change only with height; the temperature is determined by constant conductive flux, F_c, and the density by hydrostatic equilibrium. The model is specified by an $F_c = 2 \times 10^6$ erg cm^{-2} s^{-1} and a density of 10^{10} cm^{-3} at $T_e = 10^5$ K; the 10^5 K level is located at a height of 2000 km above the chromosphere. Below 10^5 K and down to 2×10^4 K, the temperature is determined by the model of Cheng and Moe (1977), while above 2.6×10^6 K it is taken as constant. Models of gyroresonance emission can be found in several other publications (e.g., Zlotnik, 1968a,b; Gelfreikh and Lubyshev, 1979; Alissandrakis et al., 1980; Alissandrakis and Kundu, 1984; Holman and Kundu, 1985; Krüger et al., 1985; Hurford, 1986; Brosius and Holman, 1989; Lee et al., 1993, 1998, 1999; Gopalswamy et al., 1996b; Nindos et al., 1996, 2002; Vourlidas et al., 1997; Tun et al., 2011; Kaltman et al., 2012; Wang et al., 2015; Nita et al., 2018).

Figure 7 shows the *x*- and *o*-mode brightness temperature as a function of distance from the center of the model sunspot that results from the dipole field. **Figure 8** shows the resulted *I* and *V* emission. The positions at which the harmonic layers cross the base of the TR are marked on the figures, so that the contribution of each harmonic can be identified. At the highest frequency, 11.2 GHz, only the fourth and third harmonic layers are above the base of the TR. Moreover, only the third has some contribution and this is at the *x*-mode only. Here we can clearly see the zero-θ region near the center of the source.

The second harmonic shows up at 7.5 GHz, but it is optically thick only in the *x*-mode; the third harmonic has still a small optical depth and the source in the *x*-mode appears like a disk, surrounded by a ring. Both the disk and the ring have sharp borders, a consequence of the steep TR as noted above. The *o*-mode emission is very weak, which results in a circular polarization of almost 100%.

At 5 GHz the third harmonic becomes optically thick at the *x*-mode and the source has the shape of a disk. On the contrary this as well as the second harmonic show extended zero θ regions in the *o*-mode emission, which appears as a bright ring surrounded by a weaker one. The ring structure is also present in the total intensity while the circular polarization has a disk-ring structure. Contrary to the distribution at 7.5 GHz, the minimum in the polarization does not occur just outside of the second harmonic, but it is located at the region of maximum brightness of the ordinary emission.

At frequencies lower than 5 GHz, there is contribution from the first harmonic, as well. This has practically no effect on the *x*-mode (see the relevant comments in section 5.1), but it serves to fill the gap of the zero-θ region in the *o*-mode (the local cyclotron frequency was larger than the local plasma frequency, therefore *o*-mode emission from the first harmonic was possible). Thus the disk part of the circular polarization becomes progressively lower as the frequency decreases. The ring part is preserved still at 1.5 GHz due to the contribution of the fourth harmonic in the *x*-mode. In general, the circular polarization has a maximum around 5 GHz decreasing toward higher frequencies due to the decrease of the brightness temperature of both modes and toward lower frequencies due to the decrease of opacity difference of the modes. The brightness temperature in total intensity increases as the frequency decreases due to the increase of both the opacity and the height of the harmonic layers.

5.3. Observations of Gyroresonance Emission

The expected properties of gyroresonance sources discussed above, have been confirmed by both high spatial resolution observations at a few frequencies (e.g., Kundu et al., 1977; Alissandrakis et al., 1980; Alissandrakis and Kundu, 1982, 1984; Lang and Wilson, 1982; Kundu and Alissandrakis, 1984; Gopalswamy et al., 1996b; Nindos et al., 1996, 2002; Vourlidas and Bastian, 1996; Zlotnik et al., 1996; Vourlidas et al., 1997; Lee et al., 1998, 1999; Brosius and White, 2004, 2006; Tun et al., 2011; Nita et al., 2018) as well as multi-frequency spectral observations (e.g., Akhmedov et al., 1982; Alissandrakis et al., 1993a, 2019; Lee et al., 1993; Gary and Hurford, 1994; Tun et al., 2011; Kaltman et al., 2012; Stupishin et al., 2018).

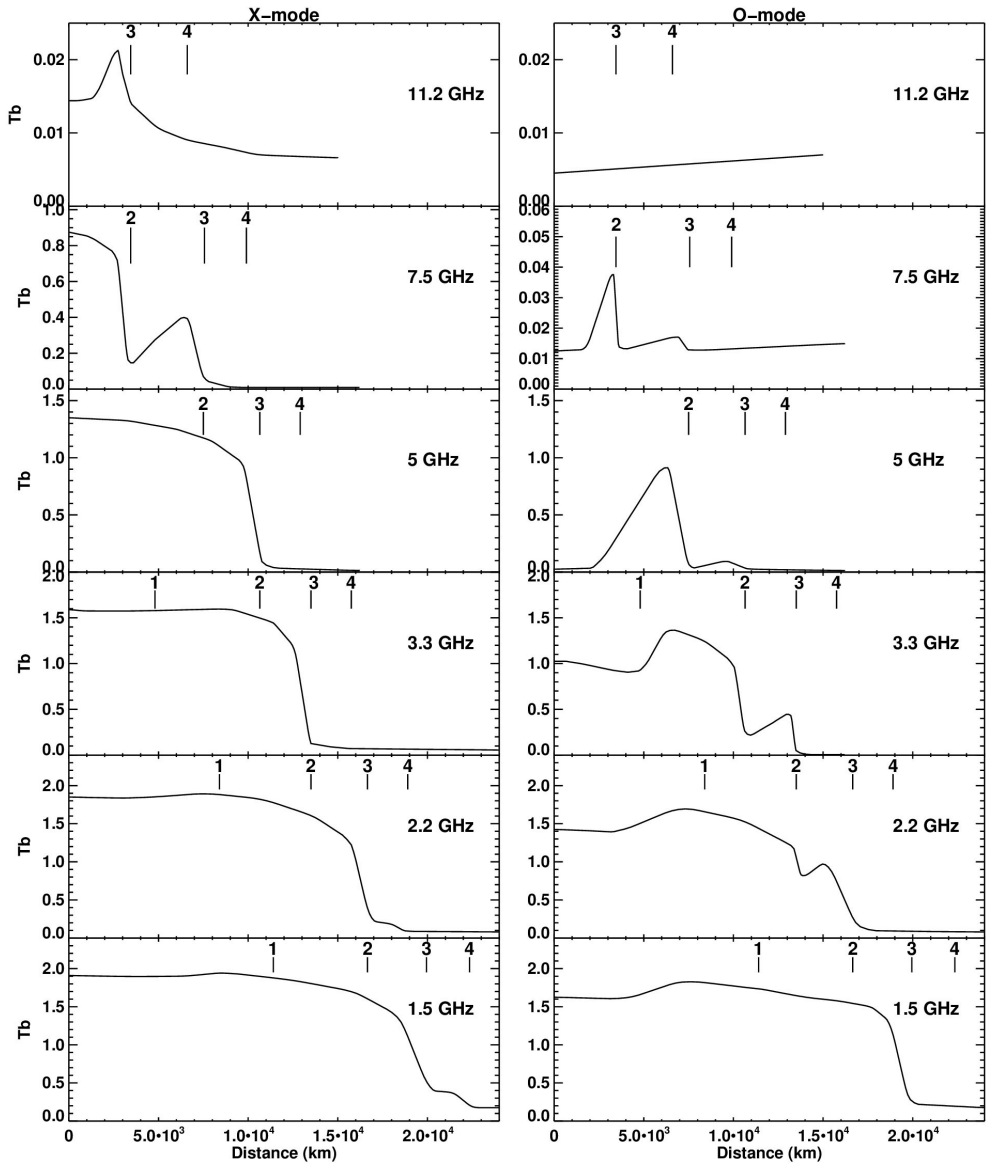

FIGURE 7 | Brightness temperature (in units of million degrees Kelvin) of the *x*-mode **(left)** and *o*-mode **(right)** emission as a function of distance from the center of a dipole sunspot model at several frequencies (see text for details). The position at which the harmonic layers cross the base of the TR are marked with vertical straight lines.

5.3.1. Modeling of a Well-Observed Sunspot Source

An example of a well-observed gyroresonance source associated with a simple sunspot near disk center is provided in **Figures 9**, **10**. Active region 4682 was observed with the RATAN-600 and the Very Large Array (VLA). The RATAN-600 observations provided one-dimensional scans of the Sun at several microwave frequencies, while the VLA provided high-resolution maps at 5 and 1.5 GHz. The flux density spectra of the sunspot source in *R* and *L* appear in **Figure 9**. In the same figure, we also present model flux density spectra in *R* and *L* (the magnetic polarity of the sunspot was negative and therefore the model *o*- and *x*-mode emissions correspond to *R* and *L* polarizations, respectively).

The model we used was the same as the one described in section 5.2 with the exceptions that (i) the magnetic field was computed through extrapolations of the photospheric field provided by a vector magnetogram, and (ii) pressure data in the TR from O IV lines were available for part of the sunspot region. The comparison of the observed and computed flux density spectra allowed us to estimate the conductive flux, F_c and the height, h_0, of the base of the TR: we found $F_c = 6 \times 10^6$ erg cm^{-2} s^{-1} and $h_0 = 2,000$ km.

Figure 9 shows that at 11.1 GHz there is weak *o*-mode emission and significant *x*-mode emission and the source is almost 100% polarized. Consequently, the third harmonic is

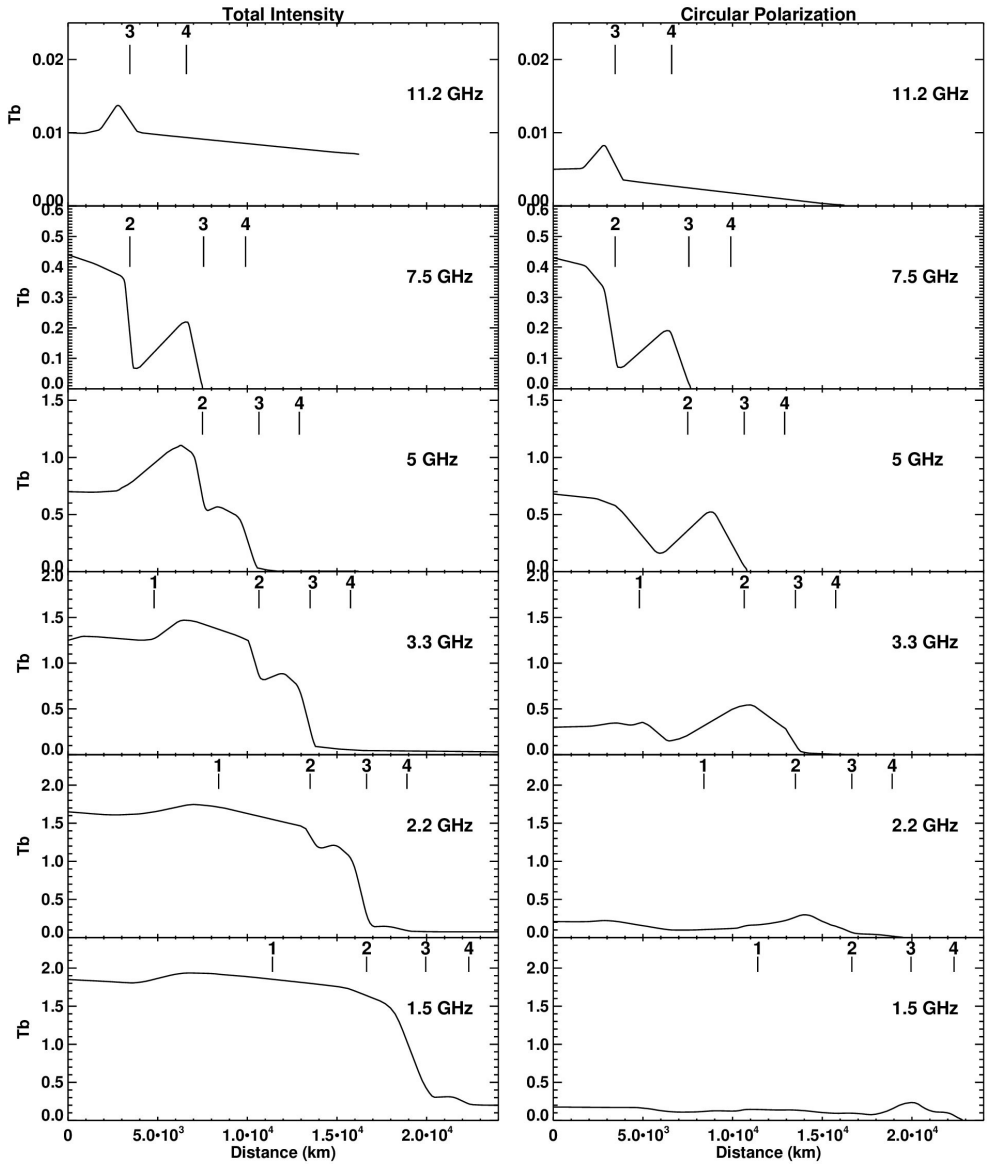

FIGURE 8 | Brightness temperature (in units of million degrees Kelvin) in *I* **(left)** and *V* **(right)** as a function of distance from the center of the dipole sunspot model of **Figure 7**, calculated from the radio models of **Figure 7**.

located in the low TR. The *x*-mode model fluxes increase from 15 to 7.5 GHz (note that the RATAN 7.5 GHz *L* data were not reliable) and reach a maximum around 7.5 to 4.3 GHz, whereas the *o*-mode fluxes increase from 11.1 to 4.8 GHz and reach maximum around 3.7 GHz. At frequencies lower than $\sim$ 3.7 GHz there is contribution to the emission from the plage. However, both the *L* and *R* fluxes decrease because the second and third harmonics have entered the upper part of the TR where the temperature gradient is not large and cannot compensate the effect of the ν^2 factor which is involved in the computation of the spatially integrated flux density spectra.

The above discussion indicates that the third harmonic enters the TR at $\nu \geq 11.1$ GHz and reaches the upper part of the TR at about 7.5 GHz. The corresponding frequencies for the second harmonic are about 9.4 and 4.8 GHz. The combination of these results yields a lower limit of 1,400 G and an upper limit of 1,800 G for the magnetic field strength at the base of the TR. In the upper TR and low corona the field is $\sim$ 900 G.

In **Figure 10** (top four panels), we present the 5 GHz VLA maps in *I*, *V*, *R*, and *L*. The *I* and *R* maps and to some extent the *L* map feature a crescent-shaped source which was rather asymmetric with larger brightness temperatures toward the south. There is also a region of weak intensity in the *I* and

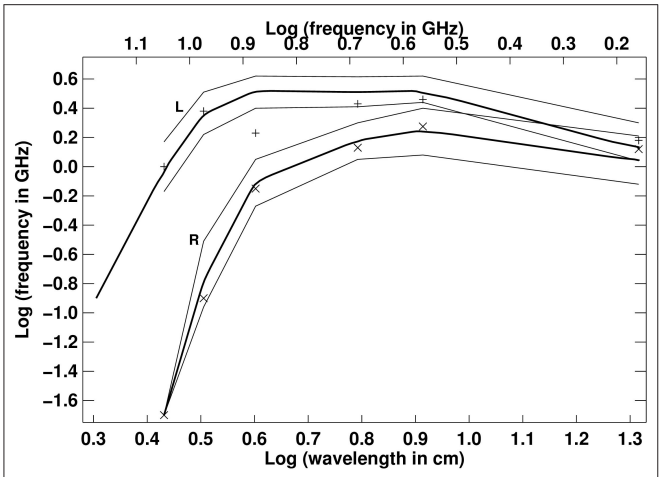

FIGURE 9 | Model flux density spectra in *L* and *R* polarizations (*x*- and *o*-mode, respectively), computed from magnetic field extrapolations for the cases: (i) $h_0 = 2,000$ km, $F_c = 6 \times 10^6$ erg cm^{-2} s^{-1}, (thick lines), (ii) $h_0 = 2,000$ km, $F_c = 3 \times 10^6$ erg cm^{-2} s^{-1}, (iii) $h_0 = 2,000$ km, $F_c = 1.2 \times 10^7$ erg cm^{-2} s^{-1}. In case (i) the flux was computed at frequencies from 2 to 15 GHz while in cases (ii) and (iii) it was computed for 1.5, 3.7, 4.8, 7.5, 9.4, and 11.1 GHz. The observed flux density spectra in *R* (×) and *L* (+) are also given (from Nindos et al., 1996). Reproduced with permission ©Springer Nature.

R maps, which is attributed to the zero-θ region; it does not appear exactly at the sunspot center but is displaced northward. The maxima of the *I*, *R*, and *L* maps show some clockwise rotation with respect to the limb direction. These features can be explained in the framework of non-potential magnetic fields (see the discussion in section 5.2). The *V* map indicates that there is little circular polarization where the total intensity is high. It also shows three distinct maxima: one is associated with the "zero-θ" region and the others occur west and east of the *I* maximum, in locations where only the third harmonic was in the corona.

In the bottom four panels of **Figure 10** we present the best-fit models to the VLA observations. The models were calculated using the F_c and h_0 values deduced from the spectral modeling and allowing the force-free parameter, α, used for the magnetic field extrapolations to take different values for the *x*-mode and *o*-mode computations. This was consistent with the analysis of the vector magnetograms which revealed that α was not constant over the active region. The effect of pressure variations into the computed models was not important at 5 GHz, and this confirms that the magnetic field is the dominant contributor to the emission. A comparison of the observations and models of **Figure 10** shows that the models reproduce key features of the microwave morphology: the zero-θ and crescent shape of the *R* and *I* maps, the clockwise rotation of the maximum intensity with respect to the limb derection, and the three local maxima of the *V* map.

5.3.2. Gyroresonance vs. Free-Free Emission

In active regions, at microwaves, gyroresonance opacity is competing with free-free opacity. Free-free emission is ubiquitous in the corona (see section 3.3) but whenever sunspot-associated microwave sources of coronal brightness temperature or/and high degree of circular polarization appear, they can be safely attributed to gyroresonance emission. In these cases, the sunspot's photospheric magnetic field should be strong enough to bring harmonic layers of the gyrofrequency above the base of the TR. On the other hand, microwave free-free emission is spatially extended, its brightness temperature is smaller (because it is optically thin) and its degree of polarization is small. This situation is illustrated in **Figure 11** where the spatial scale of the 1.5 GHz emission is consistent with the spatial scale of the soft X-ray loops and the plage and comes primarily from free-free emission. Gyroresonance emission may have some contribution to the two bright sources of the 1.5 GHz image, but the rest of the 1.5 GHz emission (including the band of lower emission which is more or less orthogonal to the soft X-ray loops near the loop tops) should come exclusively from free-free emission. On the other hand, the 4.5 GHz image is radically different: it shows localized bright emission above the sunspot due to gyroresonance in the strong magnetic fields there. Note, however, that some weak free-free emission can be traced east of the sunspot source even at 4.5 GHz. Multi-frequency observations of active regions allowed Gary and Hurford (1987) to observe the change in emission mechanism from gyroresonance to predominantly free-free at about 3 GHz.

The highest frequencies where gyroresonance emission has been detected lie in the range of 15–17 GHz (e.g., Akhmedov et al., 1982; White et al., 1991; Alissandrakis et al., 1993a; Shibasaki et al., 1994; Nindos et al., 2000a; Vourlidas et al., 2006). At even higher frequencies, the results are not conclusive because only a few imaging observations have been reported. We note that an active-region 34-GHz emission has been modeled as purely free-free by Selhorst et al. (2008). At decimetric and metric wavelengths, we cannot trace any sunspot-associated sources because the free-free opacity is so high that all the emission comes from regions well above sunspots.

5.3.3. Gyroresonance as a Tool to Study Coronal Magnetic Fields

From Equation (36), we get that the magnetic field (in G) can be written as a function of the harmonic number and frequency of observations through

$$B = 357 \frac{1}{s} \frac{\nu}{1 \text{ GHz}} \tag{37}$$

and once we identify the harmonics which produce the emission, it is easy to constrain the field strength in the TR and low corona. This technique is especially powerful when multi-frequency data are available and was demonstrated in section 5.3.1 (see also e.g., Akhmedov et al., 1982; Alissandrakis et al., 1993a; Lee et al., 1993; Gary and Hurford, 1994; Korzhavin et al., 2010; Tun et al., 2011; Wang et al., 2015; Nita et al., 2018). When only a single frequency is available, we may identify the size of the region, at the base of the TR, in which the field strength exceeds the value that corresponds to the frequency of observations: at 15 GHz (e.g., White et al., 1991) and 17 GHz (e.g., Shibasaki et al., 1994; Nindos et al., 2000a; Vourlidas et al., 2006) field strengths of at

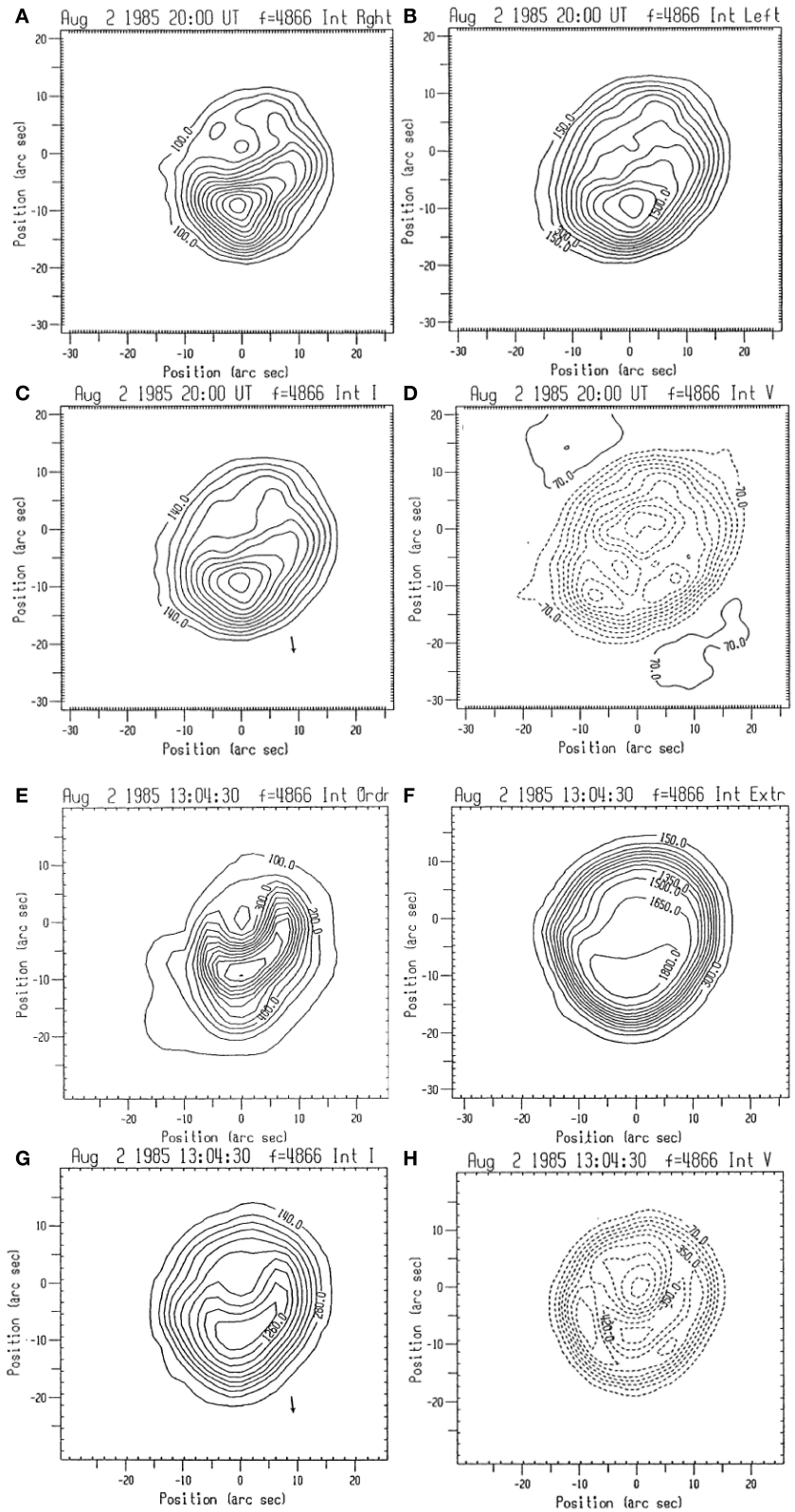

FIGURE 10 | Maps of active region 4862 observed with the VLA at 5 GHz in Stokes *I*, *V* (**C,D**, respectively) and in *R* and *L* polarization (**A,B**, respectively). The contours are in brightness temperature steps of 1.4×10^5, 0.7×10^5, 1.5×10^5, and 10^5 K, respectively. Dashed contours indicate negative values. Panels **(E,F)** show models of active region 4862 at 5 GHz in *R* and *L* which were computed with $\alpha = -2.4 \times 10^{-5}$ km^{-1} and $\alpha = 2.4 \times 10^{-5}$ km^{-1}, respectively. Panels **(G,H)** show model *I* and *V* maps, respectively, calculated from the models of panels **(E,F)**. The arrow in panels **(C,G)** shows the direction of the limb (adapted from Nindos et al., 1996). Reproduced with permission ©Springer Nature.

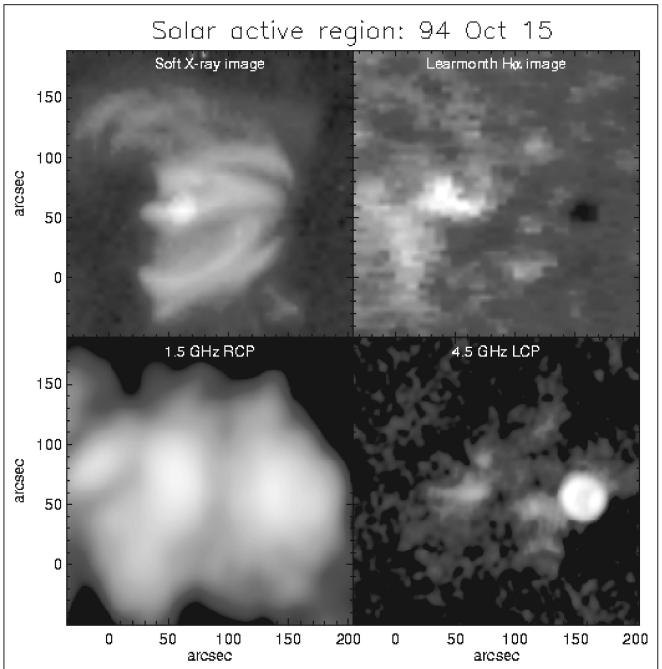

FIGURE 11 | Images of an active region. **Top left**: soft X-ray image obtained by Yohkoh Soft X-ray Telescope (SXT). **Top right**: Hα image from Learmonth Observatory. **Bottom left**: 1.5 GHz VLA image in right circular polarization. **Bottom right**: 4.5 GHz VLA image in left circular polarization (image credit: S.M. White).

least 1,800 and 2,000 G, respectively, have been measured. Details on the subject are given in this issue in the papers about coronal magnetic field measurements by Alissandrakis and Bastian.

6. GYROSYNCHROTRON EMISSION

6.1. General Remarks

Gyrosynchrotron emission may arise in quite diverse solar environments:

(1) Solar flares. Gyrosynchrotron radiation from electrons that gyrate in the magnetic field with energies of tens to hundreds of keV is the basic emission mechanism at microwaves. The literature is vast and selected references will be provided in sections 6.2–6.4, primarily for publications that link modeling of gyrosynchrotron emission with observations. Gyrosynchrotron radiation can also be detected at millimeter wavelengths and is produced by electrons with energies of more than 1 MeV (e.g., White and Kundu, 1992; Kundu et al., 1994; Silva et al., 1996; Raulin et al., 1999; Silva and Valio, 2016; Tsap et al., 2018).

(2) Weak transient brightenings, when observed at microwaves, may sometimes show emission consistent with the properties of gyrosynchrotron radiation (e.g., Gary et al., 1997; Krucker et al., 1997; Nindos et al., 1999; Kundu et al., 2006).

(3) Gyrosynchrotron emission has been detected in a small number of CMEs at decimetric and metric wavelengths (Bastian et al., 2001; Maia et al., 2007; Tun and Vourlidas, 2013; Bain et al., 2014; Carley et al., 2017; Mondal et al., 2019).

In what follows we will put emphasis on the microwave gyrosynchrotron emission from flares because it is a mature topic that has attracted most of the attention on the subject, and because it demonstrates nicely the properties of the gyrosynchrotron mechanism. More on gyrosynchrotron emission from CMEs can be found in this issue in the paper about radio CMEs by Vourlidas.

Both the free-free (e.g., Bastian et al., 2007) and gyroresonance (e.g., Preka-Papadema and Alissandrakis, 1988) emissions produced by ambient thermal electrons should be taken into account when discussing incoherent emission of microwave bursts. Compared to gyrosynchrotron, they both have negligible effects in the emission, but they are important because they may increase the optical depth in the chromosphere and the low corona.

Gyrosynchrotron emission can be produced by electrons with either a non-thermal or a thermal distribution; in the latter case (e.g., Gary and Hurford, 1989 and for more recent examples see Fleishman et al., 2015; Wang et al., 2017) they could be electrons heated due to the flare. Usually the emission is first computed for a single electron radiating in cold plasma (e.g., Ramaty, 1969, the "parent" of all modeling papers), while for the thermal case, Gershman (1960) considered small fluctuations in the thermal equilibrium of a magnetized plasma described by the linearized Vlasov equation. The resulting formulas for the emission and absorption coefficients for an ensemble of electrons involve integration over the distribution function and summation over harmonics.

Simplified expressions have been provided by Petrosian (1981) and Dulk and Marsh (1982). They have a limited range of validity but they are useful in some applications. The model of Petrosian (1981) is valid at harmonic numbers below 10. But it only deals with emissivity, which means that it can only be applied to high frequencies. Klein (1987) extended this model to the absorption coefficient. The agreement with Ramaty's numerical calculations was quite good, starting at low harmonic numbers. By construction Klein's model completely smears out the lines, and it is devised for an isotropic electron population. Furthermore, it does not provide handy formulas for analytical calculations.

The model by Dulk and Marsh (1982) is valid above the tenth harmonic of the gyrofrequency (consequently if the magnetic field is 500 G it cannot be used at frequencies lower than 15 GHz), for a spectral index δ of an isotropic power-law distribution of radiating electrons with $2 \leq \delta \leq 7$, and for angles θ between the magnetic field and the line of sight with $\theta \geq 20°$. At high harmonics (above the 50th), the synchrotron approximation can be used in cases where the effects of high energy cut-off can be neglected.

The flux spectrum is divided into an optically thick part (flux rises with frequency) and an optically thin part (flux falls with frequency). Spectral maximum corresponds to the frequency defined by $\tau_\nu \sim 1$, and usually occurs at low harmonics of the gyrofrequency. The optically thin component of the spectrum

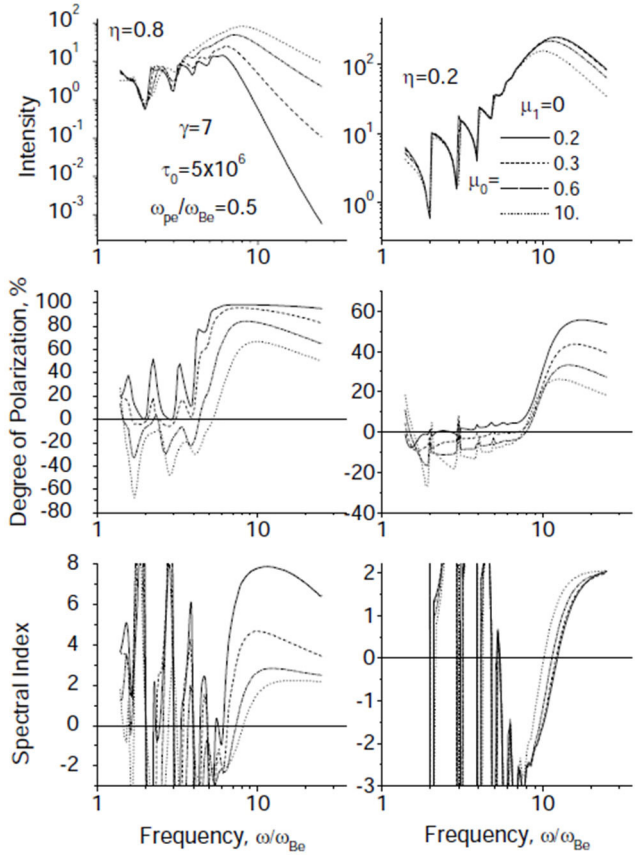

FIGURE 12 | Gyrosynchrotron intensity, degree of polarization and spectral index as a function of frequency for various values of μ_0 in the Gaussian loss-cone type pitch-angle distribution $f \propto \exp[-\mu^2/\mu_0^2]$. The computations presented in the left and right columns have been made for $\eta = 0.8$ and 0.2, respectively, where η is the cosine of the angle between the magnetic field and the line of sight (from Fleishman and Melnikov, 2003a). ©AAS. Reproduced with permission.

is mostly shaped by the energy distribution of the electrons. In the synchrotron approximation the spectral index α in the high-frequency part of the spectrum is

$$\alpha = \frac{\delta - 1}{2} \tag{38}$$

For mildly relativistic electrons, the approximation given by Dulk and Marsh (1982) is often used:

$$\alpha = 0.90\delta - 1.22 \tag{39}$$

A comparison of Equations (38) and (39) indicates that the emission decrease with frequency is steeper at mildly than at ultra relativistic energies. This is because a highly relativistic electron radiates over a broader frequency range than a mildly relativistic electron.

The optically thick part of the spectrum is influenced primarily by the effects of the ambient plasma and radiative transfer. For large ambient densities the refractive index reaches zero at low frequencies (see the discussion in section 4) and both the absorption and emission coefficients are suppressed. This leads to intensity suppression at low frequencies and the shift of the spectral maximum toward higher frequencies. This effect is known as the Razin effect (Razin, 1960; Klein, 1987; Belkora, 1997; Melnikov et al., 2008; Song et al., 2016; Fleishman et al., 2018). Furthermore, if the optical depth of the emitting electrons is larger than unity, as it often happens at low frequencies, the intensity spectrum falls below the emission coefficient spectrum. This is the self-absorption effect which makes gyrosynchrotron radiation to fall off steeply with decreasing frequency.

The *x*-mode is associated with higher emission coefficient than the *o*-mode while the inverse holds for the source function. Therefore, the sense of polarization corresponds to *x*-mode in an optically thin region and to *o*-mode in an optically thick region. The degree of polarization increases with the angle θ between the magnetic field and the line of sight.

For the above discussion we assumed that the pitch-angle (i.e., angle between the velocity of the electron and the magnetic field) distribution of the radiating electrons was isotropic. This can be achieved by collisions or by wave-particle interactions. But in a flaring loop there is little emission from electrons with small pitch angles, so the emissions produced by different electrons, some with large and some with small pitch angles, can be significantly different. Fleishman and Melnikov (2003b) and Fleishman and Melnikov (2003a) have discussed how pitch-angle anisotropies affect gyrosynchrotron emission. It is known (see Fleishman and Mel'nikov, 1998, and references therein) that when anisotropic pitch-angle distributions prevail, the absorption coefficient can become negative and coherent electron cyclotron maser emission is produced. In flares such emission has a typical timescale of the order of tens of milliseconds which is much shorter than that of gyrosynchrotron emission (order of tens of seconds). Therefore, these two types of emission can be distinguished from their different duration. Moreover, there are cases that although the pitch-angle anisotropy significantly reduces the absorption coefficient, the latter remains positive (Fleishman and Melnikov, 2003b).

Fleishman and Melnikov (2003b) and Fleishman and Melnikov (2003a) showed that the changes to the gyrosynchrotron spectrum due to pitch-angle anisotropy are larger for small values of the angle, θ, between the magnetic field and the line of sight (compare the two top panels of **Figure 12**). The degree of polarization increases as the anisotropy of the pitch-angle distribution becomes larger and may approach the 100% level in the optically thin limit (see middle row of **Figure 12**). A similar trend is registered for the spectral index of the optically thin part of the spectrum (see bottom row of **Figure 12**) when the angle θ is small.

6.2. Gyrosynchrotron Emission From Model Flaring Loops

We will present calculations of the gyrosynchrotron emission in a model flaring loop to illustrate the properties of gyrosynchrotron radiation. The models have been published by Kuznetsov et al.

(2011) and are based on the codes developed by Fleishman and Kuznetsov (2010). Similar models have been developed by Simões and Costa (2010) and Osborne and Simões (2019). The magnetic field of the model loop is produced by a dipole below the solar surface. The loop is located at the solar equator and its orientation is characterized by a heliographic longitude of 20° and an angle of 60° between the magnetic dipole and the equatorial plane. The height of the loop is 10″, its radius at the top is 2″, and the footpoint separation is 11.5″. The magnetic field strength at the footpoints and the top of the loop is 800 G and 75 G, respectively. The loop is filled with uniform ambient thermal plasma with a density of 10^{10} cm^{-3} and a temperature of 2×10^7 K.

The energetic electrons have a power-law index of $\delta = 4$ and low- and high-energy cutoffs of 100 keV and 10 MeV, respectively. The pitch-angle distribution can be either isotropic or a loss cone modeled by

$$g_\mu \sim \begin{cases} 1, & \text{for } |\mu| < \mu_c \\ \exp\left[-\frac{(|\mu|-\mu_c)^2}{\Delta\mu^2}\right], & \text{for } |\mu| \geq \mu_c \end{cases} \quad (40)$$

where $\mu_c = \cos\alpha_c$, α_c is the boundary of the loss cone, and $\Delta\mu$ controls how sharp this boundary is. In the models of **Figure 13**, $\Delta\mu = 0.2$. The spatial distribution of energetic electrons along the loop is given by

$$n_e \sim \exp[-\epsilon^2(\phi - \pi/2)^2] \quad (41)$$

where n_e is the number density, ϕ is the magnetic latitude, and ϵ is a dimensionless parameter controlling the degree of spatial inhomogeneity of n_e along the loop (for $\epsilon = 0$ the distribution is homogeneous).

The gyrosynchrotron emission from the model loop is shown in **Figure 13** for the cases of (i) energetic electrons with isotropic pitch-angle distribution and constant number density, $n_e = 3 \times 10^6$ cm^{-3}, along the loop, (ii) same as (i) but with a loss-cone pitch-angle distribution, and (iii) same as (ii) but with a spatially inhomogeneous energetic electron distribution which is controlled by $\epsilon = 4$ and by a loop-top number density of 2.8×10^8 cm^{-3}. These parameters yield a footpoint number density equal to the number density used in cases (i) and (ii).

Let us have a closer look at the models with homogeneous and isotropic electron distribution (see **Figure 13A**). Similar models have been published by Preka-Papadema and Alissandrakis (1992), Bastian et al. (1998), Nindos et al. (2000b), Kundu et al. (2004b), Simões and Costa (2006), and Costa et al. (2013). At 3.75 GHz, the source is optically thick and traces out the spatial extent of magnetic volume accessible to energetic electrons. At 9.4–34 GHz, the emission is optically thin and shows compact sources associated with the footpoints of the loop.

This picture agrees well with the properties of gyrosynchrotron emission. The magnetic field is larger near the footpoints and smaller at the loop top. At a fixed frequency, the harmonic number varies from lower values at the footpoints to higher values at the loop top. The mean energy of the emitting electrons is proportional to the effective temperature, T_{eff} which in turn is (according to the simplified expressions by Dulk and Marsh, 1982) proportional to $s^{0.5+0.085\delta}$. Therefore, higher energy electrons emit at the loop top, while lower energy electrons emit at the footpoints. In other words, the strong field near the footpoints favors the higher frequencies. Decreasing the observing frequency has approximately the same effect for the gyrosynchrotron emission as increasing the magnetic field. Consequently when the observing frequency decreases, we anticipate to obtain emission not only from the footpoints but also from a large part of the flaring loop.

In the models with homogeneous and isotropic electron distributions, changes to the model parameters have the following effects.

Magnetic field strength. A large magnetic field strength increases the opacity and therefore decreases the electron number density required to obtain the same optically thin flux. Furthermore it decreases the harmonic at which the electrons radiate at a given frequency. A larger field than that of the model is required to make the 9.4-34 GHz emissions optically thick and produce extended emission there.

Loop thickness. Changing the loop thickness increases the opacity proportionally, and that effect increases the optically thin flux without changing the optically thick flux significantly.

Electron number density. In the optically thin case, the optical depth increases with the column density of the energetic electrons. Changing the number density has little effect in the optically thick case, but it affects the frequency where the spectral maximum occurs.

Electron energy cutoffs. A decrease of the upper limit to the electron energies suppresses radiation at high frequencies which requires very energetic electrons if the magnetic field is not large. An increase of the lower energy cutoff does not affect much the high-frequency emission because the low energy electrons do not radiate at high frequencies, but it increases the mean energy of the electrons producing the 3.75 GHz optically thick emission and makes it stronger.

Viewing angle. The viewing angle changes when we change the orientation and location of the loop. In many cases, the changes affect the microwave morphology significantly, because the gyrosynchrotron mechanism depends strongly on the angle between the line of sight and the magnetic field.

When there is a homogeneous density profile of energetic electrons along the loop, the morphologies of the sources are similar in both the isotropic and the loss-cone pitch-angle distribution cases (compare **Figures 13A**,**B**). However, there are differences in intensity which show better in the spatially integrated spectra of row (c) of the figure: at the optically thin frequencies, the emission from the loss-cone distribution is lower than the emission from the isotropic electrons by a factor of ∼ 2–6 (note also the differences in maximum brightness temperatures between the maps, at a given frequency, of **Figures 13A,B**). Furthermore, at 17 and 34 GHz, the emission from the anisotropic population is more evenly distributed along the loop than the emission from the isotropic population. On the other hand, at the optically thick frequencies the corresponding intensities are almost identical.

The interpretation of the above differences is as follows. The model loop is located relatively close to disk center, where

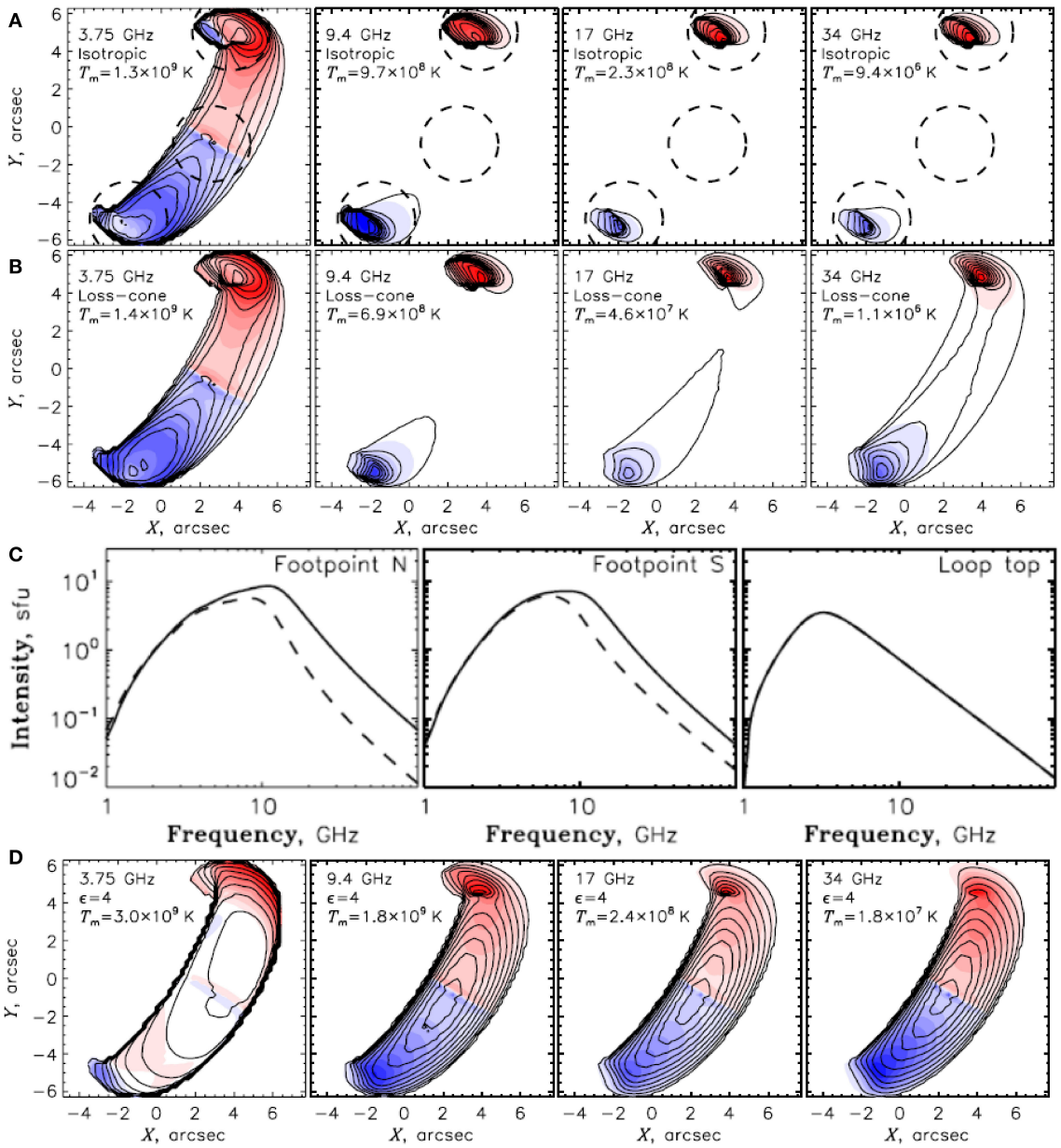

FIGURE 13 | Brightness temperature maps of the gyrosynchrotron emission from a model loop for an isotropic electron pitch-angle distribution **(A)**, and a loss-cone pitch-angle distribution **(B)**. In both cases the density of the accelerated electrons is constant along the loop. **(C)** Flux density spectra of the northern footpoint source (left), southern footpoint source (middle) and loop top source (right) resulted from the models of rows **(A,B)** (solid lines and dashed lines, respectively). These spectra were computed in the areas defined by the dashed circles of row **(A)**. **(D)** Same as row **(B)** but with an inhomogeneous spatial profile of the electron density along the loop. In rows **(A,B,D)**, the contours denote intensities evenly distributed from zero to the maximum brightness temperature which is given in each panel. The red and blue colors denote the circular polarization (right and left sense, respectively). Adapted from Kuznetsov et al. (2011). ©AAS. Reproduced with permission.

the angle θ between the magnetic field and the line of sight is small near the footpoints, whereas near the loop top θ is large. When θ is small, the intensity at low frequencies is not sensitive to the pitch-angle anisotropy because the low-energy electrons contribute most of the emission. The beaming effect (see section 4) for a single low-energy electron is not large and therefore, the actual angular distribution is not so important for the low-frequency emission.

The beaming effect becomes more prominent as the energy of the emitting electrons increases, which results in the suppression of higher frequency emission from the loss-cone distribution when θ is small (we remind that close to the footpoints, the electrons with loss-cone distribution are concentrated around a pitch angle of 90° whereas the model field is almost parallel to the line of sight). When the distribution is anisotropic, this effect results in the decrease of the footpoint emission which makes the

difference between the footpoint and looptop emission smaller than that of the isotropic distribution.

When θ is large (i.e., near the loop top), the loss-cone boundary, α_c, falls to $\sim 20^\circ$ and therefore the loss-cone distribution does not differ much from the isotropic one. Consequently, both distributions will produce very similar emissions.

The emission from electrons with loss-cone pitch-angle distribution and inhomogeneous spatial profile of the electron density along the loop (see **Figure 13D**) shows significant differences from the cases discussed so far. The emission at 9.4, 17, and 34 GHz is optically thin (the turnover frequency of the spectrum occurs at 7.6 GHz) but it peaks close to the loop top, and so does the emission at 3.75 GHz which is optically thick. This change is attributed to the larger concentration of energetic electrons at the loop top. Since the relative contribution of the electrons close to the footpoints decreases, the effect of the anisotropy discussed previously becomes less prominent.

Modeling of gyrosynchrotron emission has gone a long way from the pioneering publications by Klein and Trottet (1984) and Alissandrakis and Preka-Papadema (1984). In recent years it received a major boost with the development of the "GX_Simulator," an interactive IDL application which implements the fitting scheme developed by Fleishman et al. (2009) and the code by Kuznetsov et al. (2011) and allows the user to produce spatially-resolved radio or X-ray spectra using realistic inputs for the magnetic field and the properties of both the energetic and ambient electrons (Nita et al., 2015). Results have appeared in several publications; some of them have already been cited while references for others will be provided below.

A final note about the determination of the magnetic field of flaring loops is in place here. The diagnostic strength of gyrosynchrotron, albeit significant, is not as straightforward as that of gyroresonance; for meaningful results one needs to combine observations (ideally spectroscopic imaging ones) with detailed modeling. In spite of all the complications, modeling of individual flares (e.g., Nindos et al., 2000b; Kundu et al., 2004a; Tzatzakis et al., 2008; Gary et al., 2013, 2018; Kuznetsov and Kontar, 2015; Fleishman et al., 2016b,c, 2018; Kuroda et al., 2018) showed that the magnetic field may lie from less than 200 G (loop top) to about 1700 G (footpoints). Probably the most spectacular result was obtained by Fleishman et al. (2020) who modeled spectroscopic imaging observations from Expanded OVSA (EOVSA) and found that the magnetic field decayed at a rate of about 5 G s^{-1} for 2 min.

6.3. Observational Examples

Actual microwave observations of flares do not always show the simple loop configuration used in the models of section 6.2. First of all, in some cases the spatial structure of the emission may not be resolved in the radio maps. Furthermore, microwave sources may arise from pairs of interacting loops of widely differing scales (Hanaoka, 1997; Nishio et al., 1997; Grechnev et al., 2006a). Configurations involving more complex loop systems have also been revealed (e.g., Kundu et al., 1982, 2004a). Pre-eruptive flux rope configurations have also been imaged at microwaves (Wu et al., 2016; Chen et al., 2020) with their emission coming, at least partly, from the gyrosynchrotron mechanism.

The comparison between observations and models of the gyrosynchrotron emission becomes possible in events with single-loop morphology. As an example of such events, we consider a microwave flaring loop (Nindos et al., 2000b) observed by the VLA at 5 and 15 GHz (see **Figure 14**, top panel). Additional spectral data were obtained from the OVSA at several frequencies between 2 and 15 GHz; they revealed that the turnover frequency was 5.4 GHz. At 15 GHz, the emission was optically thin and was produced at the footpoints of the flaring loop, while the 5 GHz emission outlined the loop with most of it being optically thick with a maximum close to the loop top. In the middle and bottom panels of **Figure 14**, we compare the observations with computations of gyrosynchrotron emission from a model magnetic loop in order to diagnose the conditions in the flaring loop. The best fit to the data was reached with a model flaring loop with photospheric footpoint magnetic field of 870 G. The thickness of the model loop was much smaller than its footpoint separation. The energetic electrons were characterized by an energy spectral index of 3.7, number density of 7.9×10^7 cm^{-3} as well as low- and high-energy cutoffs of 8 and 210 keV, respectively. In this model, the 5 GHz emission comes from low harmonics of the gyrofrequency (3-7), while the lack of electrons with energies higher than 210 keV was necessary to interpret the absence of emission from the loop top at 15 GHz. That model [which is consistent with the models presented in **Figure 13A**] reproduced well both the high-frequency part of the OVSA spectrum and the basic spatial structure of the VLA *I* maps (propagation effects, see section 2.2, affected the structure of the *V* maps, and therefore its comparison with the model was not straightforward).

Observations show that in several cases the electrons that produce gyrosynchrotron emission have often anisotropic and/or inhomogeneous distributions. Such examples are the limb events presented by Kundu et al. (2001b). These flares were imaged by the NoRH at 17 and 34 GHz, and the emission at both frequencies was extended and peaked close to the top of the loop. On the other hand, spectral data from the Nobeyama Polarimeter revealed that both the 17 and 34 GHz emissions were optically thin. A similar event was studied by White et al. (2002). Tzatzakis et al. (2008) found that 36% of the events of an extended database of single-loop limb flares observed by the NoRH showed optically thin emission with maximum close to the loop top. The morphology of these events is not consistent with the morphology of optically thin sources from homogeneous distributions of electrons.

Melnikov et al. (2002) found that optically thin sources with loop-top maxima can result from enhanced concentrations of accelerated electrons at the loop top due to the transverse pitch-angle anisotropy of the injected particles. When the pitch-angle distribution of the injected population is either beam-like (i.e., injection along magnetic field lines) or isotropic, the resulted microwave emission peaks above the footpoints. Melnikov et al. (2002) noted that another possible reason for the concentration of energetic electrons near the loop top is the enhanced losses of electrons close to the footpoints. This

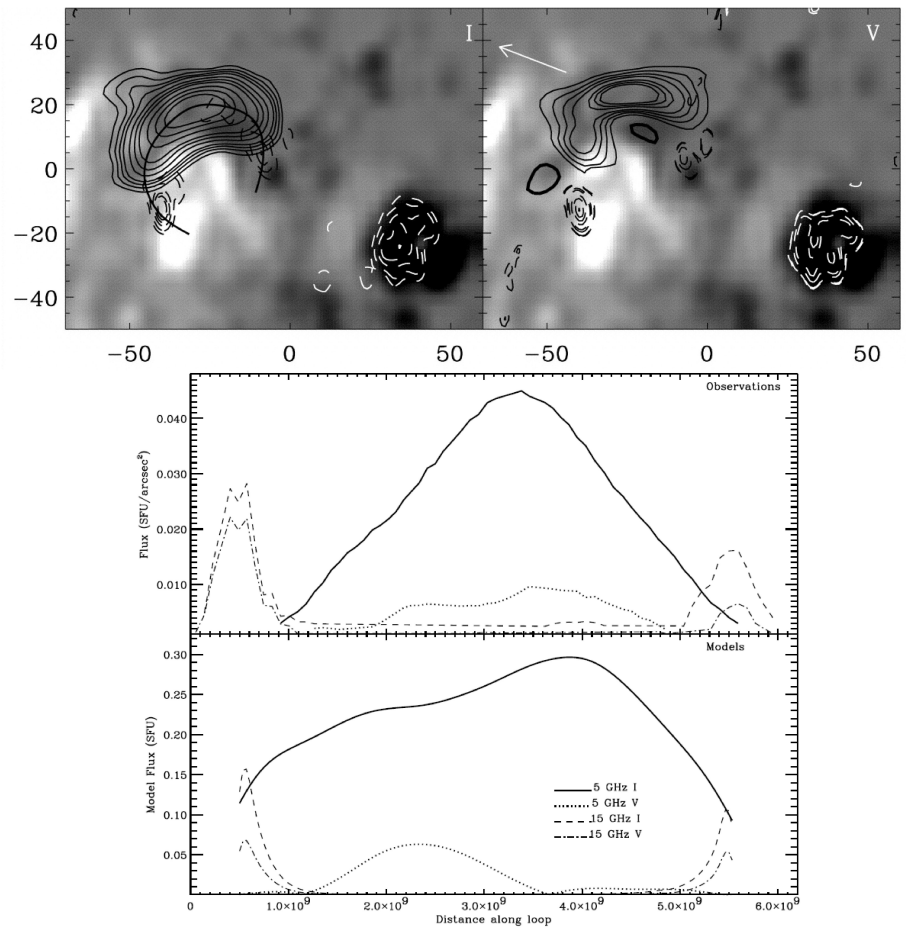

FIGURE 14 | Top row: The 1992 July 1 flare. Contour plots of the flare radio emission maximum observed by the VLA. The gray-scale background is a photospheric magnetogram. The *I* maps are on the left, and the *V* maps on the right. The solid and dashed contours show 5 and 15 GHz emission, respectively. In the 5 GHz *V* map, the thick contours represent positive brightness temperatures. In both images the white contours show emission from the sunspot at 15 GHz. The arrow shows the direction of the limb. **Middle row**: One-dimensional profiles of the flare computed along the black curve of the top left panel. **Bottom row**: spatial profiles of the gyrosynchrotron models (see text for details) as a function of the distance along the loop. For comparison with the observations, the profiles have been computed after the models were convolved with the appropriate VLA beam. In both panels the absolute values of the *V* profiles are presented (adapted from Nindos et al., 2000b). ©AAS. Reproduced with permission.

possibility may occur either from Coulomb collisions if in the lower part of the loop the plasma density is higher or from stronger turbulence there. Stepanov et al. (2007) reported that strong scattering of electrons by whistler waves can reproduce the evolution of collimated streams of non-thermal electrons observed by Yokoyama et al. (2002). Kuznetsov and Kontar (2015) observed an optically-thin loop-top source and argued that the strong concentration of electrons near the loop top reflected the localized particle injection process accompanied by trapping and scattering.

Other publications that report pitch-angle anisotropies of the electrons that emit gyrosynchrotron emission include Lee and Gary (2000), Lee et al. (2000), Fleishman et al. (2003); Fleishman (2006), Altyntsev et al. (2008, 2019), Tzatzakis et al. (2008), Reznikova et al. (2009), and Charikov et al. (2017). Generally speaking, when pitch-angle anisotropy is present it is not correct to derive the energy spectrum of the energetic electrons from the slope of the optically thin part of the gyrosynchrotron spectrum (see Fleishman and Melnikov, 2003a,b, and the discussion in section 6.1). Instead, one needs to resort to either forward fitting (e.g., Gary et al., 2013) or 3D modeling (e.g., Tzatzakis et al., 2008; Nita et al., 2015) in order to obtain meaningful electron diagnostics from the radio emission.

The study of the dynamics of flare microwave gyrosynchrotron emission can provide important information about the kinematics of accelerated electrons in flaring loops. For example, analysis of the dynamics of the spatial distribution of emission intensity, circular polarization and frequency spectrum allows one to determine the localization of the electron acceleration/injection region in a flare loop, as well as the type of electron pitch-angle distribution in different parts of the flare loop (e.g., Reznikova et al., 2009; Melnikov et al., 2012; Morgachev et al., 2015). Furthermore, the measured spectral dynamics of the microwave emission in the optically thin part of

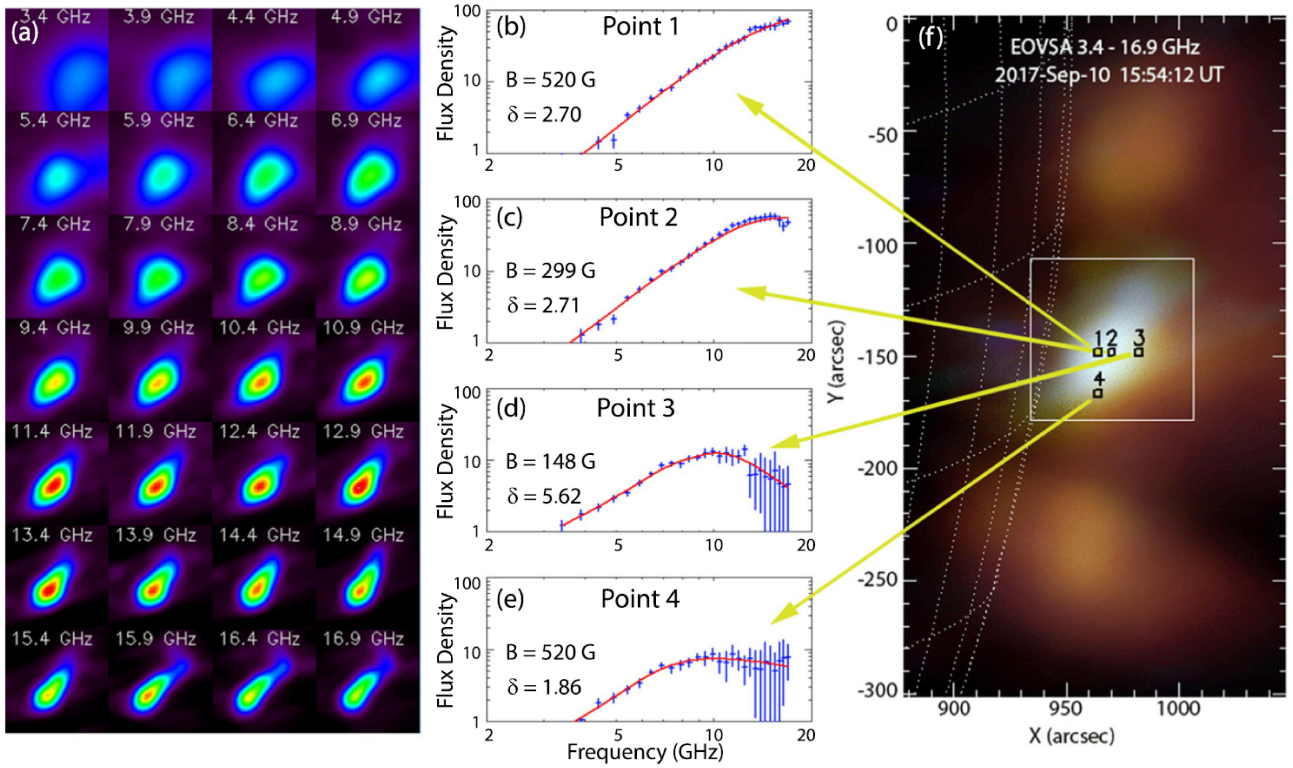

FIGURE 15 | (a) Images of the microwave emission from a partially occulted limb flare obtained at 28 frequencies with EOVSA. The field of view of the images corresponds to the white box of panel **(f)**. **(b–e)** Flux density spectra in those pixels of the images of panel **(a)** that correspond to points 1–4 of panel **(f)**, together with model spectral fits (red lines). **(f)** True-color display of the EOVSA dataset after combining images at the 28 frequencies that are marked in panel **(a)**. From Gary et al. (2018). ©AAS. Reproduced with permission.

the spectrum may provide important information on the whistler turbulence in the flare loop (Filatov and Melnikov, 2017).

Imaging spectroscopy can provide additional information to the study of gyrosynchrotron emission and this is highlighted in **Figure 15** (Gary et al., 2018) where imaging observations from the Expanded OVSA (EOVSA) of a partially occulted flare at 28 frequencies are presented. **Figure 15a** shows the diversity of source morphologies: as the frequency increases the marginally resolved cusp-like source at frequencies between 7.4 and 8.9 GHz gradually evolves toward a loop-like source while at frequencies below 5 GHz two additional sources appear (see **Figure 15f**), presumably associated with the footpoints of a larger loop. The spectral modeling presented in **Figures 15b–e** yields the magnetic field and spectral index of the electron energy distribution at the points marked in **Figure 15f**. This example shows that the combination of spatially resolved radio spectra with realistic modeling can provide detailed estimates of the dynamically evolving parameters in the flare configuration.

6.4. Electron Acceleration and Transport

In sections 6.2 and 6.3, we discussed gyrosynchrotron emission primarily at a fixed time (presumably at the peak of the emission). However, flares are dynamic phenomena, and there is a large literature on the dynamics of flare microwave emission with emphasis on the processes of electron acceleration and transport. Details are given elsewhere in this issue, thus this topic will be only touched on here.

The study of the dynamics of flare microwave gyrosynchrotron emission can provide important information about the kinematics of accelerated electrons in flaring loops

The combination of microwave and hard X-ray observations of flares with state-of-the-art 3D modeling provides a powerful diagnostic of accelerated electrons (e.g., Fleishman et al., 2016a; Kuroda et al., 2018). In the former study several flares were analyzed which, instead of showing the usual broad-band gyrosynchrotron emission produced by electrons trapped in flaring loops, they showed narrow-band gyrosynchrotron spectra (see also Fleishman et al., 2011, 2013). The relationship of these bursts with hard X-rays together with spectral modeling revealed that the trapped electron population was negligible and the radio emission originated directly from the acceleration sites which featured rather strong magnetic fields and densities. In the Kuroda et al. (2018) study the microwave and hard X-ray observations were successfully fitted with a broken power-law spectrum that reproduced the main characteristics of both emissions.

The most popular model for the study of electron transport during flares is the "direct precipitation/trap plus precipitation" (DP/TPP) model (see Bastian et al., 1998; Aschwanden, 2002, 2004; White et al., 2011, and references therein). Energetic

electrons with small pitch angles traveling along appropriate magnetic field lines approach the chromosphere where they are stopped by its dense and cool material. Most of their energy heats the chromosphere, but a smaller fraction is emitted in hard X-rays through the non-thermal thick-target free-free mechanism. The coronal magnetic field traps electrons with large pitch angles inside the flaring loop where they emit gyrosynchrotron radiation. However, eventually they will be scattered into the loss cone under the influence of either Coulomb collisions or wave-particle interactions and will precipitate into the chromosphere emitting additional hard X-ray radiation.

Using the TPP scenario one can study the effect of Coulomb collisions on the energy of electrons (see Aschwanden, 2004, and references therein). The more energetic the electrons, the fewer collisions they undergo, and therefore the longer their lifetimes in the loop. In this way we can interpret the frequency-dependent delays among microwave maxima, the usual lag of microwave emission with respect to the hard X-ray emission, and the slower decay of microwaves than hard X-rays.

Microwave emissions from either directly precipitating electrons (Kundu et al., 2001c; Lee et al., 2002) or from electrons that have been efficiently scattered (Musset et al., 2018) have also been detected. The microwave emission from these populations does not have the same emissivity as the trapped electrons because their pitch-angle distributions are different. Hard X-rays do not come exclusively from precipitated electrons; of course the thick-target emission is more efficient, but trapped electrons also emit free-free radiation, and this has been used to interpret long-duration hard X-ray bursts (Vilmer et al., 1982; Bruggmann et al., 1994). On the other hand, microwave emission is also sensitive to the entire distribution of electrons (both trapped and DP components), but the trapped component will dominate the emission at a given frequency.

7. CONCLUDING REMARKS

Incoherent solar radio emission is provided by the free-free, gyroresonance, and gyrosynchrotron processes. Free-free radiation dominates the quiet Sun and non-flaring active region emissions with the exception of regions of strong fields above sunspots where gyroresonance emission is large at microwaves. Gyrosynchrotron is the most important incoherent mechanism in flares.

Free-free opacity favors cool, dense plasmas, but if the density is high enough then hot material can also produce bright radiation. Since free-free emission is ubiquitous in the Sun, it can be used to probe the non-flaring solar atmosphere above temperature minimum. For this task, the free-free emission has the advantage that it can be observed from the ground and that it is not sensitive to processes affected by ionization equilibrium which characterize the EUV and X-ray observations.

Gyroresonance opacity depends strongly on the magnetic field strength and orientation. The emission is generated in thin layers above the base of the TR that have practically constant magnetic field strength which is determined by the condition that the observing frequency is equal to low harmonics of the gyrofrequency. Coronal magnetic fields cannot be measured from the Zeeman effect; consequently multi-frequency microwave imaging observations of gyroresonance sources provide a unique tool for the determination of the three-dimensional structure of sunspot coronal magnetic field.

Unlike EUV and X-ray coronal emissions which are optically thin everywhere, coronal radio emission can become optically thick due to gyroresonance above regions of strong fields or due to free-free at low frequencies. This means that radio data may allow us to probe different layers in the solar atmosphere by observing at different frequencies. On the other hand, it is fair to say that radio images cannot reach the spatial resolution and crispness of the images obtained with some modern EUV instruments, for example the Atmospheric Imaging Assembly aboard Solar Dynamics Observatory.

Gyrosynchrotron radiation is emitted at microwaves and millimeter wavelengths from accelerated electrons of mildly relativistic energies (i.e., from a few tens of keV to a few MeV) as they move in the coronal magnetic field. Gyrosynchrotron provides powerful diagnostics of physical conditions in flaring sources, because it depends on the properties of both the magnetic field and the accelerated electrons, as well as the properties of the ambient plasma.

The diagnostic potential of the emission mechanisms discussed in this paper has not been fully exploited yet. The basic reason is that until relatively recently there was no instrument capable of performing imaging spectroscopy over a wide frequency range. However, things have been changing with the upgrade of both solar-dedicated (Owens Valley Solar Array, and Siberian Solar Radio Telescope, now named Expanded Owens Valley Solar Array and Siberian Radioheliograph, respectively) and general-purpose interferometers (Very Large Array) as well as the design of new interferometers, either solar-dedicated like the Chinese Mingantu Ultrawide Spectral Radioheliograph (MUSER) or for general astronomical use (e.g., LOFAR and ALMA) while "first light" from the Square Kilometre Array (SKA) is expected in the mid-2020s. The upgraded/new instrumentation combined with the continuous operation of other important facilities (e.g., Nançay Radioheliograph and RATAN-600) and the efforts on the modeling side promise exciting new results in the years to come.

AUTHOR CONTRIBUTIONS

The author confirms being the sole contributor of this work and has approved it for publication.

ACKNOWLEDGMENTS

I thank Dr. K.-L. Klein for his valuable comments on an earlier version of this manuscript. I also thank Prof. C.E. Alissandrakis for his valuable comments on the manuscript.

REFERENCES

Akhmedov, S. B., Gelfreikh, G. B., Bogod, V. M., and Korzhavin, A. N. (1982). The measurement of magnetic fields in the solar atmosphere above sunspots using gyroresonance emission. *Solar Phys.* 79, 41–58. doi: 10.1007/BF00146972

Alissandrakis, C. E. (1994). Radio observations of the quiet solar corona. *Adv. Space Res.* 14:81. doi: 10.1016/0273-1177(94)90167-8

Alissandrakis, C. E., Bogod, V. M., Kaltman, T. I., Patsourakos, S., and Peterova, N. G. (2019). Modeling of the sunspot-associated microwave emission using a new method of DEM inversion. *Solar Phys.* 294:23. doi: 10.1007/s11207-019-1406-x

Alissandrakis, C. E., and Chiuderi-Drago, F. (1994). Detection of linear polarization in the microwave emission of solar active regions. *Astroph. J. Lett.* 428, L73–L76. doi: 10.1086/187396

Alissandrakis, C. E., Gelfreikh, G. B., Borovik, V. N., Korzhavin, A. N., Bogod, V. M., Nindos, A., et al. (1993a). Spectral observations of active region sources with RATAN-600 and WSRT. *Astron. Astrophys.* 270, 509–515.

Alissandrakis, C. E., Kochanov, A. A., Patsourakos, S., Altyntsev, A. T., Lesovoi, S. V., and Lesovoya, N. N. (2013). Microwave and EUV observations of an erupting filament and associated flare and coronal mass ejections. *Publ. Astron. Soc. Japan* 65:8. doi: 10.1093/pasj/65.sp1.S8

Alissandrakis, C. E., and Kundu, M. R. (1982). Observations of ring structure in a sunspot associated source at 6 centimeter wavelength. *Astroph. J. Lett.* 253, L49–L52. doi: 10.1086/183734

Alissandrakis, C. E., and Kundu, M. R. (1984). Center-to-limb variation of a sunspot-associated microwave source. *Astron. Astrophys.* 139, 271–284.

Alissandrakis, C. E., Kundu, M. R., and Lantos, P. (1980). A model for sunspot associated emission at 6 CM wavelength. *Astron. Astrophys.* 82, 30–40.

Alissandrakis, C. E., Nindos, A., and Kundu, M. R. (1993b). Evidence for ordinary mode emission from microwave bursts. *Solar Phys.* 147, 343–358. doi: 10.1007/BF00690724

Alissandrakis, C. E., Patsourakos, S., Nindos, A., and Bastian, T. S. (2017). Center-to-limb observations of the Sun with ALMA. Implications for solar atmospheric models. *Astron. Astrophys.* 605:A78. doi: 10.1051/0004-6361/201730953

Alissandrakis, C. E., and Preka-Papadema, P. (1984). Microwave emission and polarization of a flaring loop. *Astron. Astrophys.* 139, 507–511.

Altyntsev, A. T., Fleishman, G. D., Huang, G.-L., and Melnikov, V. F. (2008). A broadband microwave burst produced by electron beams. *Astroph. J.* 677, 1367–1377. doi: 10.1086/528841

Altyntsev, A. T., Meshalkina, N. S., Lysenko, A. L., and Fleishman, G. D. (2019). Rapid variability in the SOL2011-08-04 flare: implications for electron acceleration. *Astroph. J.* 883:38. doi: 10.3847/1538-4357/ab3808

Aschwanden, M. J. (2002). Particle acceleration and kinematics in solar flares. *Space Sci. Rev.* 101, 1–227. doi: 10.1007/978-94-017-2541-5

Aschwanden, M. J. (2004). *Physics of the Solar Corona. An Introduction*. Berlin: Praxis Publishing Ltd.

Bain, H. M., Krucker, S., Saint-Hilaire, P., and Raftery, C. L. (2014). Radio imaging of a type IVM radio burst on the 14th of August 2010. *Astroph. J.* 782:43. doi: 10.1088/0004-637X/782/1/43

Bastian, T. S. (1994). Angular scattering of solar radio emission by coronal turbulence. *Astroph. J.* 426, 774–781. doi: 10.1086/174114

Bastian, T. S., Benz, A. O., and Gary, D. E. (1998). Radio emission from solar flares. *Ann. Rev. Astron. Astrophys*. 36, 131–188. doi: 10.1146/annurev.astro.36.1.131

Bastian, T. S., Chintzoglou, G., De Pontieu, B., Shimojo, M., Schmit, D., Leenaarts, J., et al. (2017). A first comparison of millimeter continuum and Mg II ultraviolet line emission from the solar chromosphere. *Astroph. J. Lett.* 845:L19. doi: 10.3847/2041-8213/aa844c

Bastian, T. S., Dulk, G. A., and Leblanc, Y. (1996). High-resolution microwave observations of the quiet solar chromosphere. *Astroph. J.* 473:539. doi: 10.1086/178165

Bastian, T. S., Fleishman, G. D., and Gary, D. E. (2007). Radio spectral evolution of an x-ray-poor impulsive solar flare: implications for plasma heating and electron acceleration. *Astroph. J.* 666, 1256–1267. doi: 10.1086/520106

Bastian, T. S., Pick, M., Kerdraon, A., Maia, D., and Vourlidas, A. (2001). The coronal mass ejection of 1998 April 20: direct imaging at radio wavelengths. *Astroph. J. Lett.* 558, L65–L69. doi: 10.1086/323421

Belkora, L. (1997). Time evolution of solar microwave bursts. *Astroph. J.* 481:532. doi: 10.1086/304052

Benz, A. O., Krucker, S., Acton, L. W., and Bastian, T. S. (1997). Fine structure of the X-ray and radio emissions of the quiet solar corona. *Astron. Astrophys.* 320, 993–1000.

Brosius, J. W., and Holman, G. D. (1989). The structure of the microwave emission from sunspot magnetic fields. *Astroph. J.* 342, 1172–1186. doi: 10.1086/167674

Brosius, J. W., and White, S. M. (2004). Close association of an extreme-ultraviolet sunspot plume with depressions in the sunspot radio emission. *Astroph. J.* 601, 546–558. doi: 10.1086/380394

Brosius, J. W., and White, S. M. (2006). Radio measurements of the height of strong coronal magnetic fields above sunspots at the solar limb. *Astroph. J. Lett.* 641, L69–L72. doi: 10.1086/503774

Bruggmann, G., Vilmer, N., Klein, K.-L., and Kane, S. R. (1994). Electron trapping in evolving coronal structures during a large gradual hard X-ray/radio burst. *Solar Phys.* 149, 171–193. doi: 10.1007/BF00645188

Carley, E. P., Vilmer, N., Simões, P. J. A., and Ó Fearraigh, B. (2017). Estimation of a coronal mass ejection magnetic field strength using radio observations of gyrosynchrotron radiation. *Astron. Astrophys.* 608:A137. doi: 10.1051/0004-6361/201731368

Charikov, Y. E., Shabalin, A. N., and Kuznetsov, S. A. (2017). Modeling of physical processes by analysis of hard x-ray and microwave radiations in the solar flare of November 10, 2002. *Geomagnet. Aeronomy* 57, 1009–1017. doi: 10.1134/S0016793217080060

Chen, B., Yu, S., Reeves, K. K., and Gary, D. E. (2020). Microwave spectral imaging of an erupting magnetic flux rope: implications for the standard solar flare model in three dimensions. *Astroph. J. Lett.* 895:L50. doi: 10.3847/2041-8213/ab901a

Cheng, C.-C., and Moe, K. O. (1977). Emission measures and structure of the transition region of a sunspot from emission lines in the far ultraviolet. *Solar Phys.*, 52, 327–335. doi: 10.1007/BF00149649

Chiuderi-Drago, F., Alissandrakis, C. E., Bastian, T., Bocchialini, K., and Harrison, R. A. (2001). Joint EUV/radio observations of a solar filament. *Solar Phys.* 199, 115–132. doi: 10.1023/A:1010390726242

Cohen, M. H. (1960). Magnetoionic mode coupling at high frequencies. *Astroph. J.* 131:664. doi: 10.1086/146878

Costa, J. E. R., Simões, P. J. D. A., Pinto, T. S. N., and Melnikov, V. F. (2013). Solar burst analysis with 3D loop models. *Publ. Astron. Soc. Japan* 65:5. doi: 10.1093/pasj/65.sp1.S5

Dravskikh, A. F., and Dravskikh, Z. V. (1988). Expected detection of the 2(2)P3/2-2(2)S1/2 hydrogen line in the radio emission spectrum of the quiet sun. *Astron. Zh.* 65, 199–202.

Dulk, G. A. (1985). Radio emission from the sun and stars. *Ann. Rev. Astron. Astrophys*. 23, 169–224. doi: 10.1146/annurev.aa.23.090185.001125

Dulk, G. A., and Marsh, K. A. (1982). Simplified expressions for the gyrosynchrotron radiation from mildly relativistic, nonthermal and thermal electrons. *Astroph. J.* 259, 350–358. doi: 10.1086/160171

Duncan, R. A. (1979). Wave ducting of solar metre-wave radio emission as an explanation of fundamental/harmonic source coincidence and other anomalies. *Solar Phys.* 63, 389–398. doi: 10.1007/BF00174543

Fedotova, A., Altyntsev, A., Kochanov, A., Lesovoi, S., and Meshalkina, N. (2018). Observation of eruptive events with the Siberian Radioheliograph. *Solar Terrestrial Phys*. 4, 13–19. doi: 10.12737/stp-43201802

Filatov, L. V., and Melnikov, V. F. (2017). Influence of whistler turbulence on fast electron distribution and their microwave emissions in a flare loop. *Geomagnet. Aeronomy* 57, 1001–1008. doi: 10.1134/S0016793217080084

Fleishman, G. D. (2006). "Radio emission from anisotropic electron distributions," in *Solar Physics with the Nobeyama Radioheliograph*, ed K. Shibasaki (Nobeyama: NSRO Report 1), 51–62.

Fleishman, G. D., Gary, D. E., Chen, B., Kuroda, N., Yu, S., and Nita, G. M. (2020). Decay of the coronal magnetic field can release sufficient energy to power a solar flare. *Science* 367, 278–280. doi: 10.1126/science.aax6874

Fleishman, G. D., Gary, D. E., and Nita, G. M. (2003). Decimetric spike bursts versus microwave continuum. *Astroph. J.* 593, 571–580. doi: 10.1086/376362

Fleishman, G. D., Kontar, E. P., Nita, G. M., and Gary, D. E. (2011). A cold, tenuous solar flare: acceleration without heating. *Astroph. J. Lett.* 731:L19. doi: 10.1088/2041-8205/731/1/L19

Fleishman, G. D., Kontar, E. P., Nita, G. M., and Gary, D. E. (2013). Probing dynamics of electron acceleration with radio and x-ray spectroscopy,

imaging, and timing in the 2002 April 11 solar flare. *Astroph. J.* 768:190. doi: 10.1088/0004-637X/768/2/190

Fleishman, G. D., and Kuznetsov, A. A. (2010). Fast gyrosynchrotron codes. *Astroph. J.* 721, 1127–1141. doi: 10.1088/0004-637X/721/2/1127

Fleishman, G. D., and Kuznetsov, A. A. (2014). Theory of gyroresonance and free-free emissions from non-maxwellian quasi-steady-state electron distributions. *Astroph. J.* 781:77. doi: 10.1088/0004-637X/781/2/77

Fleishman, G. D., Loukitcheva, M. A., Kopnina, V. Y., Nita, G. M., and Gary, D. E. (2018). The coronal volume of energetic particles in solar flares as revealed by microwave imaging. *Astroph. J.* 867:81. doi: 10.3847/1538-4357/aae0f6

Fleishman, G. D., and Mel'nikov, V. F. (1998). REVIEWS OF TOPICAL PROBLEMS: millisecond solar radio spikes. *Phys. Uspekhi* 41, 1157–1189. doi: 10.1070/PU1998v041n12ABEH000510

Fleishman, G. D., and Melnikov, V. F. (2003a). Gyrosynchrotron emission from anisotropic electron distributions. *Astroph. J.* 587, 823–835. doi: 10.1086/368252

Fleishman, G. D., and Melnikov, V. F. (2003b). Optically thick gyrosynchrotron emission from anisotropic electron distributions. *Astroph. J.* 584, 1071–1083. doi: 10.1086/345849

Fleishman, G. D., Nita, G. M., and Gary, D. E. (2009). Dynamic magnetography of solar flaring loops. *Astroph. J. Lett.* 698, L183–L187. doi: 10.1088/0004-637X/698/2/L183

Fleishman, G. D., Nita, G. M., and Gary, D. E. (2015). Energy partitions and evolution in a purely thermal solar flare. *Astroph. J.* 802:122. doi: 10.1088/0004-637X/802/2/122

Fleishman, G. D., Nita, G. M., Kontar, E. P., and Gary, D. E. (2016a). Narrowband gyrosynchrotron bursts: probing electron acceleration in solar flares. *Astroph. J.* 826:38. doi: 10.3847/0004-637X/826/1/38

Fleishman, G. D., Pal'shin, V. D., Meshalkina, N., Lysenko, A. L., Kashapova, L. K., and Altyntsev, A. T. (2016b). A cold flare with delayed heating. *Astroph. J.* 822:71. doi: 10.3847/0004-637X/822/2/71

Fleishman, G. D., Xu, Y., Nita, G. N., and Gary, D. E. (2016c). Validation of the coronal thick target source model. *Astroph. J.* 816:62. doi: 10.3847/0004-637X/816/2/62

Gary, D. E., Chen, B., Dennis, B. R., Fleishman, G. D., Hurford, G. J., Krucker, S., et al. (2018). Microwave and hard x-ray observations of the 2017 September 10 solar limb flare. *Astroph. J.* 863:83. doi: 10.3847/1538-4357/aad0ef

Gary, D. E., Fleishman, G. D., and Nita, G. M. (2013). Magnetography of solar flaring loops with microwave imaging spectropolarimetry. *Solar Phys.* 288, 549–565. doi: 10.1007/s11207-013-0299-3

Gary, D. E., Hartl, M. D., and Shimizu, T. (1997). Nonthermal radio emission from solar soft x-ray transient brightenings. *Astroph. J.* 477:958. doi: 10.1086/303748

Gary, D. E., and Hurford, G. J. (1987). Multifrequency observations of a solar active region during a partial eclipse. *Astroph. J.* 317, 522–533. doi: 10.1086/165296

Gary, D. E., and Hurford, G. J. (1989). A simple solar microwave burst observed with high spectral resolution. *Astroph. J.* 339:1115. doi: 10.1086/167366

Gary, D. E., and Hurford, G. J. (1994). Coronal temperature, density, and magnetic field maps of a solar active region using the Owens Valley Solar Array. *Astroph. J.* 420, 903–912. doi: 10.1086/173614

Gary, D. E., and Keller, C. U. (eds.). (2004). "Solar and space weather radiophysics - current status and future developments," in *Astrophysics and Space Science Library* (Berlin: Springer), 1–400. doi: 10.1007/1-4020-2814-8

Gary, D. E., and Zirin, H. (1988). Microwave structure of the quiet sun. *Astroph. J.* 329, 991–1001. doi: 10.1086/166443

Gary, D. E., Zirin, H., and Wang, H. (1990). Microwave structure of the quiet sun at 8.5 GHz. *Astroph. J.* 355, 321–328. doi: 10.1086/168766

Gelfreikh, G. B. (2004). "Coronal magnetic field measurements through bremsstrahlung emission," in *Astrophysics and Space Science Library*, eds D. E. Gary and C. U. Keller (Berlin: Springer), 115. doi: 10.1007/1-4020-2814-8_6

Gelfreikh, G. B., and Lubyshev, B. I. (1979). Structure of local sources of the s-component of solar radio emission. *Soviet Astron.* 23:316.

Gershman, B. N. (1960). Gyromagnetic resonance absorption of electromagnetic waves in a plasma. *Zh. Eksperim. Teor. Fiz.* 38:912.

Gopalswamy, N., and Hanaoka, Y. (1998). Coronal dimming associated with a giant prominence eruption. *Astroph. J. Lett.* 498:L179. doi: 10.1086/311330

Gopalswamy, N., and Kundu, M. R. (1992). Estimation of the mass of a coronal mass ejection from radio observations. *Astroph. J. Lett.* 390, L37–L39. doi: 10.1086/186366

Gopalswamy, N., Kundu, M. R., Hanaoka, Y., Enome, S., Lemen, J. R., and Akioka, M. (1996a). Yohkoh/SXT observations of a coronal mass ejection near the solar surface. *N. Astron.* 1, 207–213. doi: 10.1016/S1384-1076(96)00016-4

Gopalswamy, N., Raulin, J.-P., Kundu, M. R., Hildebrandt, J., Krüger, A., and Hofmann, A. (1996b). Observations and model calculations of sunspot ring structure at 8.46 GHz. *Astron. Astrophys.* 316, L25–L28.

Gopalswamy, N., Shimojo, M., Lu, W., Yashiro, S., Shibasaki, K., and Howard, R. A. (2003). Prominence eruptions and coronal mass ejection: a statistical study using microwave observations. *Astroph. J.* 586, 562–578. doi: 10.1086/367614

Grebinskij, A., Bogod, V., Gelfreikh, G., Urpo, S., Pohjolainen, S., and Shibasaki, K. (2000). Microwave tomography of solar magnetic fields. *Astron. Astrophys. Suppl.* 144, 169–180. doi: 10.1051/aas:2000202

Grechnev, V. V., Kundu, M. R., and Nindos, A. (2006a). A study of accelerated electrons in solar flares using microwave and x-ray observations. *Publ. Astron. Soc. Japan* 58, 47–54. doi: 10.1093/pasj/58.1.47

Grechnev, V. V., Uralov, A. M., Zandanov, V. G., Baranov, N. Y., and Shibasaki, K. (2006b). Observations of prominence eruptions with two radioheliographs, SSRT, and NoRH. *Publ. Astron. Soc. Japan* 58, 69–84. doi: 10.1093/pasj/58.1.69

Hanaoka, Y. (1997). Double-loop configuration of solar flares. *Solar Phys.* 173, 319–346. doi: 10.1023/A:1004953003558

Hanaoka, Y. (1999). "Long duration events observed with the Nobeyama radioheliograph," in *Proceedings of the Nobeyama Symposium*, eds T. S. Bastian, N. Gopalswamy, and K. Shibasaki, 153–158.

Hanaoka, Y., Kurokawa, H., Enome, S., Nakajima, H., Shibasaki, K., Nishio, M., et al. (1994). Simultaneous observations of a prominence eruption followed by a coronal arcade formation in radio, soft X-rays, and H(alpha). *Publ. Astron. Soc. Japan* 46, 205–216.

Holman, G. D., and Kundu, M. R. (1985). The microwave structure of hot coronal loops. *Astroph. J.* 292, 291–296. doi: 10.1086/163159

Hori, K. (2000). Origin of helical coronal disturbances from the sun. *Astroph. J.* 543, 1011–1015. doi: 10.1086/317162

Huang, G., Melnikov, V. F., Ji, H., and Ning, Z. (2018). *Solar Flare Loops: Observations and Interpretations*. Berlin: Springer. doi: 10.1007/978-981-10-2869-4

Huang, J., Tan, B., Masuda, S., Cheng, X., Bisoi, S. K., and Melnikov, V. (2019). Localized microwave and EUV bright structures in an eruptive prominence. *Astroph. J.* 874:176. doi: 10.3847/1538-4357/ab0e80

Hurford, G. J. (1986). "High-spectral resolution solar microwave observations," in *Solar Flares and Coronal Physics Using P/OF as a Research Tool*, eds E. Tandberg, R. M. Wilson, and R. M. Hudson (Washington, DC: NASA), 191–200.

Jafarzadeh, S., Wedemeyer, S., Szydlarski, M., De Pontieu, B., Rezaei, R., and Carlsson, M. (2019). The solar chromosphere at millimetre and ultraviolet wavelengths. I. Radiation temperatures and a detailed comparison. *Astron. Astrophys.* 622:A150. doi: 10.1051/0004-6361/201834205

Kaltman, T. I., Bogod, V. M., Stupishin, A. G., and Yasnov, L. V. (2012). The altitude structure of the coronal magnetic field of AR 10933. *Astron. Rep.* 56, 790–799. doi: 10.1134/S1063772912100022

Karzas, W. J., and Latter, R. (1961). Electron radiative transitions in a Coulomb field. *Astroph. J. Suppl.* 6:167. doi: 10.1086/190063

Kathiravan, C., Ramesh, R., and Subramanian, K. R. (2002). Metric radio observations and ray-tracing analysis of the onset phase of a solar eruptive event. *Astroph. J. Lett.* 567, L93–L95. doi: 10.1086/339801

Kellermann, K. I., and Pauliny-Toth, I. I. K. (1969). The spectra of opaque radio sources. *Astroph. J. Lett.* 155:L71. doi: 10.1086/180305

Klein, K.-L. (1987). Microwave radiation from a dense magneto-active plasma. *Astron. Astrophys.* 183, 341–350.

Klein, K. L., and Trottet, G. (1984). Gyrosynchrotron radiation from a source with spatially varying field and density. *Astron. Astrophys.* 141, 67–76.

Kontar, E. P., Chen, X., Chrysaphi, N., Jeffrey, N. L. S., Emslie, A. G., Krupar, V., et al. (2019). Anisotropic radio-wave scattering and the interpretation of solar radio emission observations. *Astroph. J.* 884:122. doi: 10.3847/1538-4357/ab40bb

Kontar, E. P., Motorina, G. G., Jeffrey, N. L. S., Tsap, Y. T., Fleishman, G. D., and Stepanov, A. V. (2018). Frequency rising sub-THz emission from solar flare ribbons. *Astron. Astrophys.* 620:A95. doi: 10.1051/0004-6361/201834124

Korzhavin, A. N., Opeikina, L. V., and Peterova, N. G. (2010). Transition region above sunspots inferred from microwave observations. *Astrophys. Bull.* 65, 60–74. doi: 10.1134/S1990341310010062

Krucker, S., Benz, A. O., Bastian, T. S., and Acton, L. W. (1997). X-ray network flares of the quiet sun. *Astroph. J.* 488:499. doi: 10.1086/304686

Krüger, A. (1979). *Introduction to Solar Radio Astronomy and Radio Physics*. Dordrecht: Reidel.

Krüger, A., Hildebrandt, J., and Fuerstenberg, F. (1985). A working model of the solar S-component radio emission. *Astron. Astrophys.* 143, 72–76.

Kundu, M. R. (1965). *Solar Radio Astronomy*. New York, NY: Interscience.

Kundu, M. R., and Alissandrakis, C. E. (1984). Structure and polarization of active region microwave emission. *Solar Phys.* 94, 249–283. doi: 10.1007/BF00151317

Kundu, M. R., Alissandrakis, C. E., Bregman, J. D., and Hin, A. C. (1977). 6 centimeter observations of solar active regions with 6 SEC resolution. *Astroph. J.* 213, 278–295. doi: 10.1086/155155

Kundu, M. R., Garaimov, V. I., White, S. M., and Krucker, S. (2004a). Nobeyama Radioheliograph and RHESSI Observations of the X1.5 Flare of 2002 April 21. *Astroph. J.* 600, 1052–1060. doi: 10.1086/379876

Kundu, M. R., Nindos, A., and Grechnev, V. V. (2004b). The configuration of simple short-duration solar microwave bursts. *Astron. Astrophys.* 420, 351–359. doi: 10.1051/0004-6361:20034461

Kundu, M. R., Nindos, A., Vilmer, N., Klein, K. L., Shibata, K., and Ohyama, M. (2001a). Metric radio emission associated with x-ray plasmoid ejections. *Astroph. J.* 559, 443–451. doi: 10.1086/322301

Kundu, M. R., Nindos, A., White, S. M., and Grechnev, V. V. (2001b). A multiwavelength study of three solar flares. *Astroph. J.* 557, 880–890. doi: 10.1086/321534

Kundu, M. R., Rao, A. P., Erskine, F. T., and Bregman, J. D. (1979). High-resolution observations of the quiet sun at 6 centimeters using the Westerbork Synthesis Radio Telescope. *Astroph. J.* 234, 1122–1136. doi: 10.1086/157596

Kundu, M. R., Schmahl, E. J., Grigis, P. C., Garaimov, V. I., and Shibasaki, K. (2006). Nobeyama radio heliograph observations of RHESSI microflares. *Astron. Astrophys.* 451, 691–707. doi: 10.1051/0004-6361:20053987

Kundu, M. R., Schmahl, E. J., Vlahos, L., and Velusamy, T. (1982). Radio imaging of solar flares using the very large array - New insights into flare process. *Astron. Astrophys.* 108, 188–194.

Kundu, M. R., and Vlahos, L. (1982). Solar microwave bursts - A review. *Space Sci. Rev*. 32, 405–462. doi: 10.1007/BF00177449

Kundu, M. R., White, S. M., Gopalswamy, N., and Lim, J. (1994). Millimeter, microwave, hard X-ray, and soft X-ray observations of energetic electron populations in solar flares. *Astroph. J. Suppl.* 90, 599–610. doi: 10.1086/191881

Kundu, M. R., White, S. M., Shibasaki, K., Sakurai, T., and Grechnev, V. V. (2001c). Spatial structure of simple spiky bursts at microwave/millimeter wavelengths. *Astroph. J.* 547, 1090–1099. doi: 10.1086/318422

Kuroda, N., Gary, D. E., Wang, H., Fleishman, G. D., Nita, G. M., and Jing, J. (2018). Three-dimensional forward-fit modeling of the hard x-ray and microwave emissions of the 2015 June 22 M6.5 Flare. *Astroph. J.* 852:32. doi: 10.3847/1538-4357/aa9d98

Kuznetsov, A. A., and Kontar, E. P. (2015). Spatially resolved energetic electron properties for the 21 May 2004 flare from radio observations and 3D simulations. *Solar Phys.* 290, 79–93. doi: 10.1007/s11207-014-0530-x

Kuznetsov, A. A., Nita, G. M., and Fleishman, G. D. (2011). Three-dimensional simulations of gyrosynchrotron emission from mildly anisotropic nonuniform electron distributions in symmetric magnetic loops. *Astroph. J.* 742:87. doi: 10.1088/0004-637X/742/2/87

Lang, K. R., and Wilson, R. F. (1982). Polarized horseshoes around sunspots at 6 centimeter wavelength. *Solar Phys.* 255, L111–L114. doi: 10.1086/183780

Lantos, P., and Alissandrakis, C. E. (1999). Analysis of coronal emissions observed at meter wavelengths. *Astron. Astrophys.* 351, 373–381.

Lantos, P., Alissandrakis, C. E., Gergely, T., and Kundu, M. R. (1987). Quiet sun and slowly varying component at meter and decameter wavelengths. *Solar Phys.* 112, 325–340. doi: 10.1007/BF00148787

Lecacheux, A., Steinberg, J.-L., Hoang, S., and Dulk, G. A. (1989). Characteristics of type III bursts in the solar wind from simultaneous observations on board ISEE-3 and Voyager. *Astron. Astrophys.* 217, 237–250.

Lee, J. (2007). Radio emissions from solar active regions. *Space Sci. Rev*. 133, 73–102. doi: 10.1007/s11214-007-9206-2

Lee, J., and Gary, D. E. (2000). Solar microwave bursts and injection pitch-angle distribution of flare electrons. *Astroph. J.* 543, 457–471. doi: 10.1086/317080

Lee, J., Gary, D. E., Qiu, J., and Gallagher, P. T. (2002). Electron transport during the 1999 August 20 flare inferred from microwave and hard x-ray observations. *Astroph. J.* 572, 609–625. doi: 10.1086/340311

Lee, J., Gary, D. E., and Shibasaki, K. (2000). Magnetic trapping and electron injection in two contrasting solar microwave bursts. *Astroph. J.* 531, 1109–1120. doi: 10.1086/308511

Lee, J., McClymont, A. N., Mikic, Z., White, S. M., and Kundu, M. R. (1998). Coronal currents, magnetic fields, and heating in a solar active region. *Astroph. J.* 501:853. doi: 10.1086/305851

Lee, J., White, S. M., Kundu, M. R., Mikic, Z., and McClymont, A. N. (1999). A test for coronal magnetic field extrapolations. *Astroph. J.* 510, 413–421. doi: 10.1086/306556

Lee, J. W., Hurford, G. J., and Gary, D. E. (1993). Microwave emission from a sunspot. I - Implications for the sunspot magnetic structure. *Solar Phys.* 144, 45–57. doi: 10.1007/BF00667981

Loukitcheva, M., Solanki, S. K., and White, S. (2006). The dynamics of the solar chromosphere: comparison of model predictions with millimeter-interferometer observations. *Astron. Astrophys.* 456, 713–723. doi: 10.1051/0004-6361:20053171

Loukitcheva, M. A., White, S. M., and Solanki, S. K. (2019). ALMA detection of dark chromospheric holes in the quiet sun. *Astroph. J. Lett.* 877:L26. doi: 10.3847/2041-8213/ab2191

Maia, D., Pick, M., Vourlidas, A., and Howard, R. (2000). Development of coronal mass ejections: radio shock signatures. *Astroph. J. Lett.* 528, L49–L51. doi: 10.1086/312421

Maia, D. J. F., Gama, R., Mercier, C., Pick, M., Kerdraon, A., and Karlicky, M. (2007). The radio-coronal mass ejection event on 2001 April 15. *Astroph. J.* 660, 874–881. doi: 10.1086/508011

Marqué, C. (2004). Radio metric observations of quiescent filament cavities. *Astroph. J.* 602, 1037–1050. doi: 10.1086/381085

Marqué, C., Lantos, P., Delouis, J. M., and Alissandrakis, C. E. (1999). "Metric and decimetric observations of the quiet solar corona," in *8th SOHO Workshop: Plasma Dynamics and Diagnostics in the Solar Transition Region and Corona*, eds J.-C. Vial and B. Kaldeich-Schü (ESA Special Publication), 483.

McCauley, P. I., Cairns, I. H., White, S. M., Mondal, S., Lenc, E., Morgan, J., et al. (2019). The low-frequency solar corona in circular polarization. *Solar Phys.* 294:106. doi: 10.1007/s11207-019-1502-y

Melnikov, V. F., Gary, D. E., and Nita, G. M. (2008). Peak frequency dynamics in solar microwave bursts. *Solar Phys.* 253, 43–73. doi: 10.1007/s11207-008-9275-8

Melnikov, V. F., Pyatakov, N. P., and Shibasaki, K. (2012). "Constraints for electron acceleration models in solar flares from microwave observations with high spatial resolution," in *Hinode-3: The 3rd Hinode Science Meeting*, eds T. Sekii, T. Watanabe, and T. Sakurai, 321.

Melnikov, V. F., Shibasaki, K., and Reznikova, V. E. (2002). Loop-top nonthermal microwave source in extended solar flaring loops. *Astroph. J. Lett.* 580, L185–L188. doi: 10.1086/345587

Melrose, D. B. (1980). Plasma astrohysics. Nonthermal processes in diffuse magnetized plasmas - Vol.1: The emission, absorption and transfer of waves in plasmas; Vol.2: Astrophysical applications. New York, NY: Gordon and Breach.

Mercier, C. (1996). Some characteristics of atmospheric gravity waves observed by radio-interferometry. *Ann. Geoph.* 14, 42–58. doi: 10.1007/s00585-996-0042-6

Mercier, C., and Chambe, G. (2009). High dynamic range images of the solar corona between 150 and 450 MHz. *Astroph. J. Lett.* 700, L137–L140. doi: 10.1088/0004-637X/700/2/L137

Mercier, C., and Chambe, G. (2012). Morphology of the quiet Sun between 150 and 450 MHz as observed with the Nançay radioheliograph. *Astron. Astrophys.* 540:A18. doi: 10.1051/0004-6361/201118163

Molnar, M. E., Reardon, K. P., Chai, Y., Gary, D., Uitenbroek, H., Cauzzi, G., et al. (2019). Solar chromospheric temperature diagnostics: a joint ALMA-Hα analysis. *Astroph. J.* 881:99. doi: 10.3847/1538-4357/ab2ba3

Mondal, S., Oberoi, D., and Vourlidas, A. (2019). Estimation of the physical parameters of a CME at high coronal heights using low frequency radio observations. *arXiv preprint arXiv:1909.12041*. doi: 10.3847/1538-4357/ab7fab

Morgachev, A. S., Kuznetsov, S. A., Melnikov, V. F., and Simões, J. A. (2015). Modeling the distribution of circular polarization degree of microwave emission along the flare loops in event July 19, 2012. *Geomagnet. Aeron.* 55, 1118–1123. doi: 10.1134/S0016793215080228

Morgachev, A. S., Tsap, Y. T., Smirnova, V. V., and Motorina, G. G. (2018). Simulation of subterahertz emission from the April 2, 2017 solar flare based on the multiwavelength observations. *Geomagnet. Aeron.* 58, 1113–1122. doi: 10.1134/S001679321808011X

Morgachev, A. S., Tsap, Y. T., Smirnova, V. V., and Motorina, G. G. (2020). On the source of sub-terahertz radiation of the solar flare on April 2, 2017. *Geomagnet. Aeron.* 59, 1114–1120. doi: 10.1134/S0016793219080140

Musset, S., Kontar, E. P., and Vilmer, N. (2018). Diffusive transport of energetic electrons in the solar corona: x-ray and radio diagnostics. *Astron. Astrophys.* 610:A6. doi: 10.1051/0004-6361/201731514

Nindos, A., Alissandrakis, C. E., Bastian, T. S., Patsourakos, S., De Pontieu, B., Warren, H., et al. (2018). First high-resolution look at the quiet Sun with ALMA at 3mm. *Astron. Astrophys.* 619:L6. doi: 10.1051/0004-6361/201834113

Nindos, A., Alissandrakis, C. E., Gelfreikh, G. B., Bogod, V. M., and Gontikakis, C. (2002). Spatially resolved microwave oscillations above a sunspot. *Astron. Astrophys.* 386, 658–673. doi: 10.1051/0004-6361:20020252

Nindos, A., Alissandrakis, C. E., Gelfreikh, G. B., Kundu, M. R., Dere, K. P., Korzhavin, A. N., et al. (1996). A model for active region emission at centimeter wavelengths. *Solar Phys.* 166, 55–87. doi: 10.1007/BF00179356

Nindos, A., Alissandrakis, C. E., Patsourakos, S., and Bastian, T. S. (2020). Transient brightenings in the quiet Sun detected by ALMA at 3 mm. *Astron. Astrophys.* 638:A62. doi: 10.1051/0004-6361/202037810

Nindos, A., Aurass, H., Klein, K.-L., and Trottet, G. (2008). Radio emission of flares and coronal mass ejections. Invited review. *Solar Phys.* 253, 3–41. doi: 10.1007/s11207-008-9258-9

Nindos, A., Kundu, M. R., and White, S. M. (1999). A study of microwave-selected coronal transient brightenings. *Astroph. J.* 513, 983–989. doi: 10.1086/306886

Nindos, A., Kundu, M. R., White, S. M., Shibasaki, K., and Gopalswamy, N. (2000a). Soft x-ray and gyroresonance emission above sunspots. *Astroph. J. Suppl.* 130, 485–499. doi: 10.1086/317355

Nindos, A., White, S. M., Kundu, M. R., and Gary, D. E. (2000b). Observations and models of a flaring loop. *Astroph. J.* 533, 1053–1062. doi: 10.1086/308705

Nishio, M., Yaji, K., Kosugi, T., Nakajima, H., and Sakurai, T. (1997). Magnetic field configuration in impulsive solar flares inferred from coaligned microwave/x-ray images. *Astroph. J.* , 489:976. doi: 10.1086/304793

Nita, G. M., Fleishman, G. D., Kuznetsov, A. A., Kontar, E. P., and Gary, D. E. (2015). Three-dimensional radio and x-ray modeling and data analysis software: revealing flare complexity. *Astroph. J.* 799:236. doi: 10.1088/0004-637X/799/2/236

Nita, G. M., Viall, N. M., Klimchuk, J. A., Loukitcheva, M. A., Gary, D. E., Kuznetsov, A. A., et al. (2018). Dressing the coronal magnetic extrapolations of active regions with a parameterized thermal structure. *Astroph. J.* 853:66. doi: 10.3847/1538-4357/aaa4bf

Osborne, C. M. J., and Simões, P. J. A. (2019). Thyr: a volumetric ray-marching tool for simulating microwave emission. *MNRAS* 485, 3386–3397. doi: 10.1093/mnras/stz660

Patsourakos, S., Alissandrakis, C. E., Nindos, A., and Bastian, T. S. (2020). Observations of solar chromospheric oscillations at 3 mm with ALMA. *Astron. Astrophys.* 634:A86. doi: 10.1051/0004-6361/201936618

Petrosian, V. (1981). Synchrotron emissivity from mildly relativistic particles. *Astroph. J.* 251, 727–738. doi: 10.1086/159517

Pick, M., and Vilmer, N. (2008). Sixty-five years of solar radioastronomy: flares, coronal mass ejections and Sun Earth connection. *Astron. Astrophys. Rev.* 16, 1–153. doi: 10.1007/s00159-008-0013-x

Preka-Papadema, P., and Alissandrakis, C. E. (1988). Spatial and spectral structure of a solar flaring loop at centimeter wavelengths. *Astron. Astrophys.* 191, 365–373.

Preka-Papadema, P., and Alissandrakis, C. E. (1992). Two-dimensional model maps of flaring loops at cm-wavelengths. *Astron. Astrophys.* 257, 307–314.

Rahman, M. M., McCauley, P. I., and Cairns, I. H. (2019). On the relative brightness of coronal holes at low frequencies. *Solar Phys.* 294:7. doi: 10.1007/s11207-019-1396-8

Ramaty, R. (1969). Gyrosynchrotron emission and absorption in a magnetoactive plasma. *Astroph. J.* 158:753. doi: 10.1086/150235

Ramesh, R., Kathiravan, C., Narayanan, A. S., and Ebenezer, E. (2003). Metric observations of transient, quasi-periodic radio emission from the solar corona in association with a "halo" CME and an "EIT wave" event. *Astron. Astrophys.* 400, 753–758. doi: 10.1051/0004-6361:20030019

Raulin, J.-P., and Pacini, A. A. (2005). Solar radio emissions. *Adv. Space Res.* 35, 739–754. doi: 10.1016/j.asr.2005.03.138

Raulin, J.-P., White, S. M., Kundu, M. R., Silva, A. V. R., and Shibasaki, K. (1999). Multiple components in the millimeter emission of a solar flare. *Astroph. J.* 522, 547–558. doi: 10.1086/322974

Razin, V. A. (1960). On the spectrum of nonthermal cosmic radio emission. *Izv. Vys. Ucheb. Zav. Radiofiz.* 3:584.

Reznikova, V. E., Melnikov, V. F., Shibasaki, K., Gorbikov, S. P., Pyatakov, N. P., Myagkova, I. N., et al. (2009). 2002 August 24 limb flare loop: dynamics of microwave brightness distribution. *Astroph. J.* 697, 735–746. doi: 10.1088/0004-637X/697/1/735

Rodger, A. S., and Labrosse, N. (2018). Spectral gradient of the thermal millimetre continuum as a diagnostic for optical thickness in the solar atmosphere. *Astron. Astrophys.* 617:L6. doi: 10.1051/0004-6361/201833848

Rodger, A. S., Labrosse, N., Wedemeyer, S., Szydlarski, M., Simões, P. J. A., and Fletcher, L. (2019). First spectral analysis of a solar plasma eruption using ALMA. *Astroph. J.* 875:163. doi: 10.3847/1538-4357/aafdfb

Rybicki, G. B., and Lightman, A. P. (1979). *Radiative Processes in Astrophysics*. New York, NY: Wiley.

Saint-Hilaire, P., Hurford, G. J., Keating, G., Bower, G. C., and Gutierrez-Kraybill, C. (2012). Allen telescope array multi-frequency observations of the sun. *Solar Phys.* 277, 431–445. doi: 10.1007/s11207-011-9906-3

Selhorst, C. L., Silva-Válio, A., and Costa, J. E. R. (2008). Solar atmospheric model over a highly polarized 17 GHz active region. *Astron. Astrophys.* 488, 1079–1084. doi: 10.1051/0004-6361:20079217

Shain, A. V., Melnikov, V. F., and Morgachev, A. S. (2017). The role of quasi-transverse propagation in observed polarization of flare loop microwave radiation. *Geomagnet. Aeron.* 57, 988–995. doi: 10.1134/S0016793217080217

Sheridan, K. V., Jackson, B. V., McLear, D. J., and Dulk, G. A. (1978). Radio observations of a massive, slow moving ejection of coronal material. *Proc. Astron. Soc. Australia* 3, 249–250. doi: 10.1017/S1323358000015423

Shibasaki, K., Alissandrakis, C. E., and Pohjolainen, S. (2011). Radio emission of the quiet sun and active regions (invited review). *Solar Phys.* 273, 309–337. doi: 10.1007/s11207-011-9788-4

Shibasaki, K., Enome, S., Nakajima, H., Nishio, M., Takano, T., Hanaoka, Y., et al. (1994). A purely polarized S-component at 17 GHz. *Publ. Astron. Soc. Japan* 46, L17–L20.

Shimojo, M., Bastian, T. S., Hales, A. S., White, S. M., Iwai, K., Hills, R. E., et al. (2017a). Observing the Sun with the Atacama Large Millimeter/submillimeter Array (ALMA): high-resolution interferometric imaging. *Solar Phys.* 292:87. doi: 10.1007/s11207-017-1095-2

Shimojo, M., Hudson, H. S., White, S. M., Bastian, T. S., and Iwai, K. (2017b). The first ALMA observation of a solar plasmoid ejection from an x-ray bright point. *Astroph. J. Lett.* 841:L5. doi: 10.3847/2041-8213/aa70e3

Silva, A. V. R., White, S. M., Lin, R. P., de Pater, I., Shibasaki, K., Hudson, H. S., et al. (1996). First images of a solar flare at millimeter wavelengths. *Astroph. J. Lett.* 458:L49. doi: 10.1086/309918

Silva, D. F., and Valio, A. B. M. (2016). "Millimeter observation of solar flares with polarization," in *Astronomical Society of the Pacific Conference Series*, 55.

Simões, P. J. A., and Costa, J. E. R. (2006). Solar bursts gyrosynchrotron emission from three-dimensional sources. *Astron. Astrophys.* 453, 729–736. doi: 10.1051/0004-6361:20054665

Simões, P. J. A., and Costa, J. E. R. (2010). Gyrosynchrotron emission from anisotropic pitch-angle distribution of electrons in 3-D solar flare sources. *Solar Phys.* 266, 109–121. doi: 10.1007/s11207-010-9596-2

Song, Q. W., Nakajima, H., Huang, G. L., Tan, B. L., Huang, Y., and Wu, Z. (2016). Turnover frequency in solar microwave bursts with an extremely flat optically thin spectrum. *Solar Phys.* 291, 3619–3635. doi: 10.1007/s11207-016-1004-0

Stallcop, J. R. (1974). Absorption of infrared radiation by electrons in the field of a neutral hydrogen atom - I. *Astroph. J.* 187, 179–184. doi: 10.1086/152607

Stepanov, A. V., Yokoyama, T., Shibasaki, K., and Melnikov, V. F. (2007). Turbulent propagation of high-energy electrons in a solar coronal loop. *Astron. Astrophys.* 465, 613–619. doi: 10.1051/0004-6361:20066573

Stupishin, A. G., Kaltman, T. I., Bogod, V. M., and Yasnov, L. V. (2018). Modeling of solar atmosphere parameters above sunspots using RATAN-600 microwave observations. *Solar Phys.* 293:13. doi: 10.1007/s11207-017-1228-7

Thejappa, G., and MacDowall, R. J. (2008). Effects of scattering on radio emission from the quiet sun at low frequencies. *Astroph. J.* 676, 1338–1345. doi: 10.1086/528835

Trottet, G., Krucker, S., Lüthi, T., and Magun, A. (2008). Radio Submillimeter and γ-Ray observations of the 2003 October 28 solar flare. *Astroph. J.* 678, 509–514. doi: 10.1086/528787

Tsap, Y. T., Smirnova, V. V., Motorina, G. G., Morgachev, A. S., Kuznetsov, S. A., Nagnibeda, V. G., et al. (2018). Millimeter and x-ray emission from the 5 July 2012 solar flare. *Solar Phys.* 293:50. doi: 10.1007/s11207-018-1269-6

Tun, S. D., Gary, D. E., and Georgoulis, M. K. (2011). Three-dimensional structure of a solar active region from spatially and spectrally resolved microwave observations. *Astroph. J.* 728:1. doi: 10.1088/0004-637X/728/1/1

Tun, S. D., and Vourlidas, A. (2013). Derivation of the magnetic field in a coronal mass ejection core via multi-frequency radio imaging. *Astroph. J.* 766:130. doi: 10.1088/0004-637X/766/2/130

Tzatzakis, V., Nindos, A., and Alissandrakis, C. E. (2008). A statistical study of microwave flare morphologies. *Solar Phys.* 253, 79–94. doi: 10.1007/s11207-008-9263-z

Uralov, A. M., Lesovoi, S. V., Zandanov, V. G., and Grechnev, V. V. (2002). Dual-filament initiation of a coronal mass ejection: observations and model. *Solar Phys.* 208, 69–90. doi: 10.1023/A:1019610614255

Vilmer, N., Kane, S. R., and Trottet, G. (1982). Impulsive and gradual hard X-ray sources in a solar flare. *Astron. Astrophys.* 108, 306–313.

Vocks, C., Mann, G., Breitling, F., Bisi, M. M., Dabrowski, B., Fallows, R., et al. (2018). LOFAR observations of the quiet solar corona. *Astron. Astrophys.* 614:A54. doi: 10.1051/0004-6361/201630067

Vourlidas, A., and Bastian, T. S. (1996). Multiband VLA observations of solar active regions: implications for the distribution of coronal plasma. *Astroph. J.* 466:1039. doi: 10.1086/177574

Vourlidas, A., Bastian, T. S., and Aschwanden, M. J. (1997). The structure of the solar corona above sunspots as inferred from radio, x-ray, and magnetic field observations. *Astroph. J.* 489:403. doi: 10.1086/304769

Vourlidas, A., Gary, D. E., and Shibasaki, K. (2006). Sunspot gyroresonance emission at 17 GHz: a statistical study. *Publ. Astron. Soc. Japan* 58, 11–20. doi: 10.1093/pasj/58.1.11

Wang, H., Liu, C., Ahn, K., Xu, Y., Jing, J., Deng, N., et al. (2017). High-resolution observations of flare precursors in the low solar atmosphere. *Nat. Astron.* 1:0085. doi: 10.1038/s41550-017-0085

Wang, Z., Gary, D. E., Fleishman, G. D., and White, S. M. (2015). Coronal magnetography of a simulated solar active region from microwave imaging spectropolarimetry. *Astroph. J.* 805:93. doi: 10.1088/0004-637X/805/2/93

Wedemeyer, S., Bastian, T., Brajša, R., Hudson, H., Fleishman, G., Loukitcheva, M., et al. (2016). Solar science with the Atacama large millimeter/submillimeter Array-A new view of our sun. *SSRv* 200, 1–73. doi: 10.1007/s11214-015-0229-9

Wedemeyer, S., Szydlarski, M., Jafarzadeh, S., Eklund, H., Guevara Gomez, J. C., Bastian, T., et al. (2020). The Sun at millimeter wavelengths. I. Introduction to ALMA Band 3 observations. *Astron. Astrophys.* 635:A71. doi: 10.1051/0004-6361/201937122

White, S. M. (1999). Radio versus EUV/x-ray observations of the solar atmosphere. *Solar Phys.* 190, 309–330. doi: 10.1007/978-94-017-3429-5_20

White, S. M., Benz, A. O., Christe, S., Fárník, F., Kundu, M. R., Mann, G., et al. (2011). The relationship between solar radio and hard x-ray emission. *SSRv* 159, 225–261. doi: 10.1007/s11214-010-9708-1

White, S. M., and Kundu, M. R. (1992). Solar observations with a millimeter-wavelength array. *Solar Phys.* 141, 347–369. doi: 10.1007/BF00155185

White, S. M., and Kundu, M. R. (1997). Radio observations of gyroresonance emission from coronal magnetic fields. *Solar Phys.* 174, 31–52.

White, S. M., Kundu, M. R., Garaimov, V. I., Yokoyama, T., and Sato, J. (2002). The physical properties of a flaring loop. *Astroph. J.* 576, 505–518. doi: 10.1086/341621

White, S. M., Kundu, M. R., and Gopalswamy, N. (1991). Strong magnetic fields and inhomogeneity in the solar corona. *Astroph. J. Lett.* 366, L43–L46. doi: 10.1086/185905

White, S. M., Kundu, M. R., Shimizu, T., Shibasaki, K., and Enome, S. (1995). The radio properties of solar active region soft x-ray transient brightenings. *Astroph. J.* 450:435. doi: 10.1086/176153

White, S. M., Loukitcheva, M., and Solanki, S. K. (2006). High-resolution millimeter-interferometer observations of the solar chromosphere. *Astron. Astrophys.* 456, 697–711. doi: 10.1051/0004-6361:20052854

Wu, Z., Chen, Y., Huang, G., Nakajima, H., Song, H., Melnikov, V., et al. (2016). Microwave imaging of a hot flux rope structure during the pre-impulsive stage of an eruptive M7.7 solar flare. *Astroph. J. Lett.* 820:L29. doi: 10.3847/2041-8205/820/2/L29

Yokoyama, T., Nakajima, H., Shibasaki, K., Melnikov, V. F., and Stepanov, A. V. (2002). Microwave observations of the rapid propagation of nonthermal sources in a solar flare by the nobeyama radioheliograph. *Astroph. J. Lett.* 576, L87–L90. doi: 10.1086/343098

Yokoyama, T., Shimojo, M., Okamoto, T. J., and Iijima, H. (2018). ALMA observations of the solar chromosphere on the polar limb. *Astroph. J.* 863:96. doi: 10.3847/1538-4357/aad27e

Zheleznyakov, V. V. (1970). *Radio Emission of the Sun and Planets*. Oxford: Pergamon Press.

Zlotnik, E. Y. (1968a). The theory of the slowly changing component of solar radio emission. II. *Soviet Astron.* 12:464.

Zlotnik, E. Y. (1968b). Theory of the slowly changing component of solar radio emission. I. *Soviet Astron.* 12:245.

Zlotnik, E. Y., Kundu, M. R., and White, S. M. (1996). A model of the atmosphere above a sunspot from radio observations. *Radiophys. Quant. Electron.* 39, 255–267. doi: 10.1007/BF02144449

Conflict of Interest: The author declares that the research was conducted in the absence of any commercial or financial relationships that could be construed as a potential conflict of interest.

frontiers in Astronomy and Space Sciences

ORIGINAL RESEARCH
published: 25 November 2020
doi: 10.3389/fspas.2020.568429

Iterative Tomography: A Key to Providing Time-Dependent 3-D Reconstructions of the Inner Heliosphere and the Unification of Space Weather Forecasting Techniques

Bernard V. Jackson[1], Andrew Buffington[1], Lucas Cota[1], Dusan Odstrcil[2,3], Mario M. Bisi[4], Richard Fallows[3] and Munetoshi Tokumaru[6]*

[1]Center for Astrophysics and Space Sciences, University of California, San Diego, La Jolla, CA, United States, [2]Department of Physics and Astronomy, George Mason University, Fairfax, VA, United States, [3]NASA-Goddard Spaceflight Center, Greenbelt, MD, United States, [4]United Kingdom Research and Innovation–Science and Technology Facilities Council–RAL Space, Rutherford Appleton Laboratory, Oxfordshire, United Kingdom, [5]ASTRON-The Netherlands Institute for Radio Astronomy, Dwingeloo, Netherlands, [6]Institute for Space-Earth Environmental Research (ISEE), Nagoya University, Furo-cho, Japan

OPEN ACCESS

Edited by:
Nicole Vilmer,
Centre National de la Recherche Scientifique (CNRS), France

Reviewed by:
Rui F. Pinto,
UMR5277 Institut de recherche en astrophysique et planétologie (IRAP), France
Keiji Hayashi,
Stanford University, United States

***Correspondence:**
Bernard V. Jackson
bvjackson@ucsd.edu

Specialty section:
This article was submitted to Stellar and Solar Physics, a section of the journal Frontiers in Astronomy and Space Sciences

Received: 01 June 2020
Accepted: 31 August 2020
Published: 25 November 2020

Citation:
Jackson BV, Buffington A, Cota L, Odstrcil D, Bisi MM, Fallows R and Tokumaru M (2020) Iterative Tomography: A Key to Providing Time-Dependent 3-D Reconstructions of the Inner Heliosphere and the Unification of Space Weather Forecasting Techniques. Front. Astron. Space Sci. 7:568429. doi: 10.3389/fspas.2020.568429

Over several decades, UCSD has developed and continually updated a time-dependent iterative three-dimensional (3-D) reconstruction technique to provide global heliospheric parameters—density, velocity, and component magnetic fields. For expediency, this has used a kinematic model as a kernel to provide a fit to either interplanetary scintillation (IPS) or Thomson-scattering observations. This technique has been used in near real time over this period, employing Institute for Space-Earth Environmental Research, Japan, IPS data to predict the propagation of these parameters throughout the inner heliosphere. We have extended the 3-D reconstruction analysis to include other IPS Stations around the Globe in a Worldwide Interplanetary Scintillation Stations Network. In addition, we also plan to resurrect the Solar Mass Ejection Imager Thomson-scattering analysis as a basis for 3-D analysis to be used by the latest NASA Small Explorer heliospheric imagers of the Polarimeter to Unify the Corona and Heliosphere mission, the All Sky Heliospheric Imager, and other modern wide-field imagers. Better data require improved heliospheric modeling that incorporates non-radial transport of heliospheric flows, and shock processes. Looking ahead to this, we have constructed an interface between the 3-D reconstruction tomography and 3-D MHD models and currently include the ENLIL model as a kernel in the reconstructions to provide this fit. In short, we are now poized to provide all of these innovations in a next step: to include them for planned ground-based and spacecraft instruments, all to be combined into a truly global 3-D heliospheric system which utilizes these aspects in their data and modeling.

Keywords: sun, coronal mass ejections, corotating structures, heliosphere, space weather, interplanetary scintillation

INTRODUCTION

The bulk of the particles within the solar wind, a hot, strongly turbulent plasma produced by the Sun, are accelerated up to speeds of about 400 km s^{-1} or more. On average, it takes about 4 days for individual features in the solar wind to travel 1 AU from the Sun to reach the Earth. Transient structures such as Coronal Mass Ejections (CMEs) are usually thousands of times larger than Earth at 1 AU and often travel several times faster than 400 km s^{-1}. A few reach Earth in less than one day. These transient heliospheric phenomena can strongly perturb the geomagnetic field in the near-Earth environment by means of magnetic reconnection and storm triggering when they arrive at 1 AU. They can also accelerate solar energetic particles (SEPs) as well as affect their transport in the heliosphere. In particular, CMEs can modify the surrounding medium by introducing changes in the direction and strength of the interplanetary magnetic field (IMF). The so-called ambient solar wind is not without structure; its features emanate primarily from specific locations on the Sun. Solar locations where magnetic fields open outward have solar winds that are accelerated about twice as fast as the ecliptic average. At times of solar minimum, winds that emanate from the solar poles that are open are also twice as fast and can extend down across the ecliptic. As the Sun rotates, these different features move out primarily radially to provide a spiral structure with faster plasma that merges with generally denser and slower moving portions causing Stream Interaction Regions (SIRs).

Remotely sensed interplanetary scintillation (IPS) data (Hewish et al., 1964) to study the inner heliosphere was pioneered in Cambridge, England (e.g., Houminer 1971; Hewish and Bravo, 1986; Behannon et al., 1991). IPS data from radio observatories near the University of California, San Diego (UCSD), and those from the Solar-Terrestrial Environment Laboratory (STELab), now the Institute for Space-Earth Environmental Research (ISEE), at Nagoya University, Japan, enabled robust studies of the heliospheric solar wind speeds in the early 1970s through to the 1980s. In the 1990s, studies of large-scale corotating heliospheric structures, using two different three-dimensional (3-D) iterative tomographic reconstruction techniques, were developed simultaneously in a collaboration between UCSD (Jackson et al., 1997; Jackson et al., 1998) and Nagoya University (Kojima et al., 1997; Kojima et al., 1998). These analyses provided heliospheric structure boundaries more precisely than previously.

Updates to the UCSD modeling resulted in a time-dependent tomographic model utilizing either IPS data or Thomson-scattered white light from the Helios spacecraft, or a combination of both, to provide visualization and characterization of SIRs (Jackson and Hick, 2002) and CMEs (Jackson et al., 2001; Jackson et al., 2003). These analyses were employed from 2003 onward for the Solar Mass Ejection Imager (SMEI: Eyles et al., 2003; Jackson et al., 2004), to provide 3-D heliospheric reconstructions of its data (Jackson et al., 2006; Jackson et al., 2008a; Jackson et al., 2008b; Jackson et al., 2011b). In its simplest form, this system uses a kinematic model that preserves mass and mass flux, enabling the information of structures lower in the heliosphere to be related to those more distant, thus providing a perspective view of heliospheric plasma in density and velocity as these structures move outward and evolve.

In the mid-2000s, these analyses added magnetic field information (Dunn et al., 2005) so that solar surface fields could be extrapolated outward using Parker (1958) equations from the IPS-derived velocity fields and the kinematic modeling. Here, the IPS analyses are combined with the Current Sheet Source Surface (CSSS) model (Zhao and Hoeksema, 1995), usually using data from ground-based National Solar Observatory (NSO) Synoptic Optical Long-term Investigations of the Sun (SOLIS), or Global Oscillation Network Group (GONG) magnetograms as input. This modeling determines slowly varying solar surface magnetic field components throughout the inner heliosphere (Jackson et al., 2012a; Jackson et al., 2012b; Jackson et al., 2016b) that are combined with the UCSD time-dependent tomography. In the mid-2010s, we found that the 3-component fields derived through this technique could be interpreted at Earth on a daily basis to provide Geocentric Solar Magnetospheric (GSM) Bz fields to enable a several-day future prediction of minor to moderate Geomagnetic Storms (Jackson et al., 2019).

In recent years, in both research and heliospheric forecasting, numerical solar wind models based on magnetohydrodynamic (MHD) equations have been foremost in attempts to reproduce heliospheric structures and propagate them outward from the solar surface. Early MHD models simply replicated energy inputs into the low corona (e.g., Steinolfson et al., 1975; Dryer et al., 1978; Wu et al., 1983), and these have given way to more sophisticated 3-D MHD modeling versions (e.g., Riley et al., 2008). Although MHD is only an approximation to actual plasma behavior, these models have successfully simulated many important space-plasma processes. They provide hope that someday a complete description of plasma propagation and interaction from the solar surface to 1 AU and beyond will be possible if only the physical inputs can be completely defined. In the interim, many approximate 3-D MHD modeling efforts, not discussed later in this article, are important to mention. Usually these models; COIN-TVD (Shen et al., 2014), SIP-CESE-MHD (Feng et al., 2015), SUSANOO-CME (Shiota and Kataoka, 2016), and EUHFORIA (Pomoell and Poedets, 2018), assume velocity inputs to the solar wind governed by magnetic field expansion observed near the solar surface (Wang and Sheeley, 1990). These analyses usually provide additional inputs of energy distributed at the inner MHD boundary to simulate CMEs. Experiments using IPS velocities also show that solar wind speeds can be used to provide background solar wind velocity inputs to 3-D MHD models (Hayashi et al., 2003; Hayashi et al., 2016). IPS scintillation-level measurements have also been shown to allow modification of 3-D MHD heliospheric modeling using velocity inputs from solar surface magnetic fields and energy inputs near the solar surface to make better fits to CME observations with SUSANOO-CME (Iwai et al., 2019).

The UCSD tomographic analyses with a kinematic modeling kernel and ISEE IPS data quickly iterate to update the basic heliospheric plasma parameters, density, velocity, and magnetic field. The ENLIL 3-D MHD model (Odstrcil and Pizzo, 1999a; Odstrcil and Pizzo, 1999b) has also been operated at many of these same universities and space-weather prediction centers worldwide including the following: at UCSD, George Mason University (GMU), Virginia, the NASA Goddard Community Coordinated Modeling Center (CCMC), Maryland, the UKRI STFC Rutherford Appleton Laboratory, United Kingdom, and the Korean Space Weather Center (KSWC), Jeju, South Korea. In 2014, a hybrid model was initiated in most of these locations whereby the tomographic IPS analysis is used to drive ENLIL; this allows shock processes and non-radial heliospheric transport of both SIRs, and CMEs in the heliospheric modeling. With colleagues, we have also used the same kinematic modeling to drive the MS-FLUKSS 3-D MHD Model (Kim et al., 2012, Kim et al., 2014), and the H3D-MHD NRL Model (Yu et al., 2015; Wu et al., 2016). UCSD, GMU, and KSWC operate the ENLIL IPS-driven system in near real time using ISEE, Japan, IPS data.

The ISEE IPS array system has served well for many years and was refurbished in 2010 to provide year-round scintillation observations (Tokumaru et al., 2011). However, it is confined to a single small area on Earth and operates as a transit instrument (which only observes radio sources as they pass overhead due to Earth's rotation). Thus, ISEE data are basically available once a day spread throughout times near the Sun and as much as 24 h can go by without new information from that same area of the sky. Each line of sight (LOS) has a limit to its accuracy and requires that structures be traced in outward motion or at least be present once to provide a perspective view. The fastest features can occasionally slip past a single site on Earth without being viewed, especially if their transient features are mostly Earth directed. In the past, we have been lucky in that some of the first large and fast CMEs were observed well on their way toward Earth. This included the July 14, 2000, "Bastille Day" event (Jackson et al., 2003), and the October 28, 2003, "Halloween storm" event (Tokumaru et al., 2007; Jackson et al., 2011a). ISEE was not so lucky in observations of the extremely fast July 23, 2012, CME event off the west limb of the Sun that occurred just following ISEE observations in that portion of the sky. ISEE observations of this CME were nearly 20 h later, at which time only the fast remnants behind the main portion of the CME remained.

Frequently obtained data are generally not a difficulty with Thomson scattering visible light imaging, since these data are usually available much more often than the travel time of features through enough of the field of view (FOV) needed to provide a perspective view of different heliospheric structures transiting the inner heliosphere. Unlike IPS, Thomson scattering heliospheric observations have the additional advantage in that unlike the IPS, its response is completely optically thin. This is advantageous when determining a brightness relationship to numbers of electrons along the line of sight; using an estimate of the ratio of helium to hydrogen ions (e.g., see Jackson et al., 2006; Jackson et al., 2011b) provides a fairly secure proxy for heliospheric bulk plasma density. Even so, this brightness is a small percentage of other slowly evolving features in successive heliospheric images which include stray light, zodiacal light, and stellar signals; these need to be subtracted for this determination. Separating these effects to get good calibrated images for tomographic reconstruction is difficult and time consuming (e.g., Buffington et al., 2007); additionally, it may be often unnecessary, since imagery in itself provides an intuitive sense of physical processes with only the assumption that the view in the image is the same as that along the LOS. Thomson scattering velocities can be derived by the obvious motion of large bright structures identified from image to image (i.e., Webb and Jackson, 1981). In the iterative tomography, brightness alone can provide a LOS location of bright structures since the modeled outflow can only be present over a limited range of speeds and accelerations. Additionally, there have been other attempts to provide digital velocities from the smaller-scale heliospheric background solar wind features directly (e.g., Jackson et al., 2014; Yu et al., 2014; Yu et al., 2016), and while as yet untried using heliospheric imagery, this information is expected to be used to provide Thomson scattering velocities more directly as is used for the IPS from small-scale features at different LOS locations in these tomographic analyses.

This article describes more of the caveats and some of the results mentioned above. It extends the current tomographic analysis by using an iterative model with a 3-D MHD ENLIL kernel. This kernel provides a refinement to the iterative analysis by including additional physical processes beyond those of radial outflow and the mass and mass flux conservation of the kinematic analysis. Although only IPS data are currently available for 3-D use in real-time space weather forecasting, we show both the IPS and Thomson scattered visible light in order to contrast their possible future use. Section "*IPS and Thomson Scattering*" describes more fully the extent to which these items can be depicted and how each differs in response in their iterative tomographic interpretation. Section "*3-D Reconstructions With an ENLIL Kernel*" describes how the iterative ENLIL tomography is used and the extent to which the MHD analyses can be refined to provide better results than using the solar surface magnetic field data alone. Section "*Advanced Techniques and Summary*" summarizes these results and speculates on different ways forward with more refinements in programming and more abundant data.

IPS AND THOMSON SCATTERING

The UCSD 3-D reconstruction analysis is an iterative system employing a nontraditional tomographic inversion technique on a sparse data set. Observations are LOS data extending through a volume that continually moves outward from the Sun. Were it not for a model that provides a physical representation of the outward flow, it would not be possible to fit these observations and invert them tomographically without assuming a shape for the viewed structure. Without using an iterative system to provide continuity, only a very limited directional capability of outward-moving structures can be depicted from a single point in space. Even observations from a few points in space,

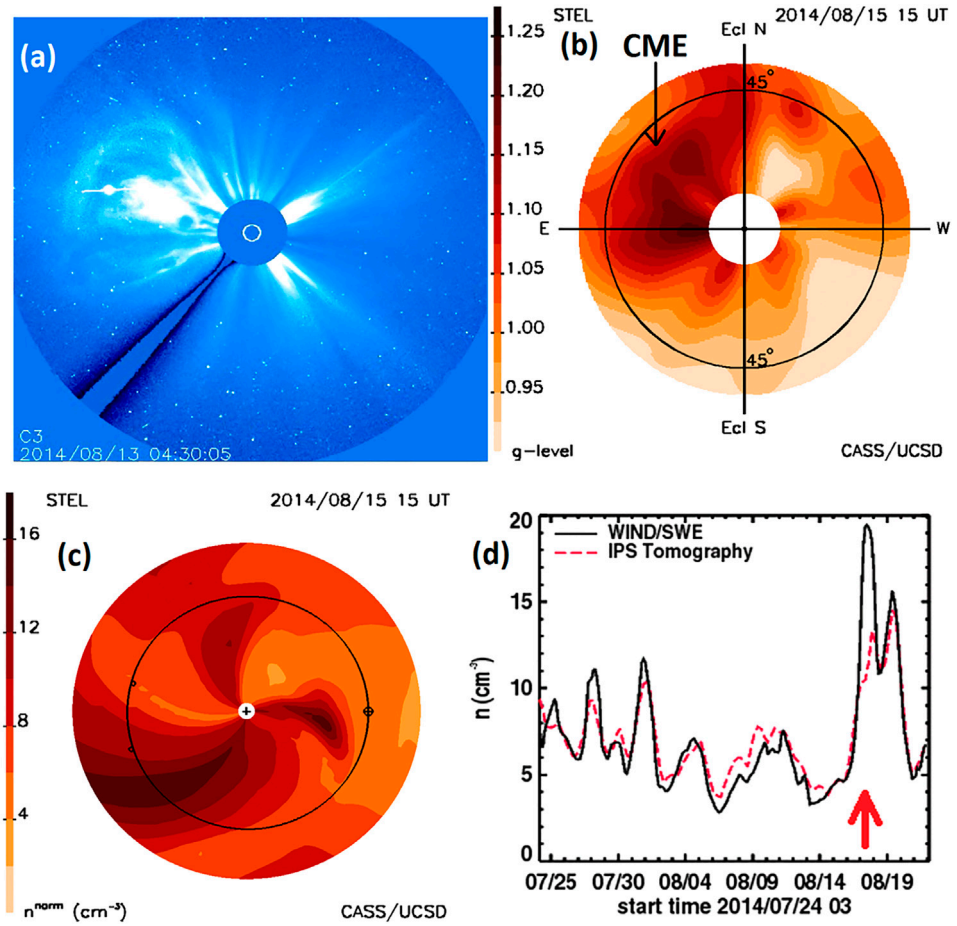

FIGURE 1 | (a) A CME is observed erupting from the Sun in LASCO images beginning on August 12, 2014, at ~21:30 UT. **(b)** This same CME is depicted as reconstructed in the UCSD tomography *g*-level 2½ days later when the CME has reached beyond 45° elongation. **(c)** A reconstructed ecliptic cut of density for the same time period as **(b)** shows the backside CME to the east of the Sun–Earth line as a large spiral-like structure. Additionally, a dense CME-like structure has nearly reached the Earth's position to the right of the image. **(d)** Density time series for a one-month interval during this period from the NASA Wind spacecraft (black line) and the 3-D reconstructed density (red dashed line) showing the time of the CME onset at Earth (red arrow) about 4 days following their solar eruption.

as are available from the two STEREO spacecraft (Kaiser et al., 2008) from the onboard Heliospheric Imager (HI) SECCHI instruments (Howard et al., 2008; Eyles et al., 2009), can provide only simple directional location reconstructions using classical inversion techniques (Barnes, 2020). Stereographic observations can also provide precise locations for some solar erupting features (e.g., Liewer et al., 2009), but only if discretely identifiable points in space can be distinguished from the different viewing directions at nearly the same time.

There are many ways the UCSD 3-D reconstruction analyses can be depicted, and **Figure 1** shows several examples of this in comparison with a coronagraph image. On August 12, 2014, a CME that erupted from the Sun was observed by the NASA space-based Large Angle Space Coronagraph (LASCO) experiment (Brueckner, et al., 1995) onboard the NASA/ESA SOlar and Heliospheric Observatory (SOHO) spacecraft (Domingo et al., 1995). Termed a "partial halo" CME in the LASCO SOHO CME (CDAW) Catalog (Gopalswamy et al., 2009) and "backside" (**Figure 1A**), this event could be seen erupting from behind the Sun by the STEREO A spacecraft, which at that time was situated 162° to the east of the Sun–Earth line. This same CME is shown with the UCSD time-dependent 3-D reconstruction analysis using ISEE IPS data 2½ days later when the CME has reached beyond 45° elongation (**Figure 1B**). Here, *g*-level (defined as the scintillation level divided by its mean value) is displayed as derived from the density model at the time indicated. In this fisheye image, the Sun is in the center, the ecliptic poles are marked, and the 45° elongation circle is shown near the outside edge. The modeled values are the best 18-iteration fit of the IPS kinematic model to the observed *g*-level LOS values (e.g., see Jackson et al., 2010b). The same approximate shape of the backside CME observed in coronagraph brightness is shown to the east of the Sun. Only remnants of this event were visible somewhat later when two additional halo CMEs, not as well observed and not listed in the CDAW catalog, were also viewed by the LASCO coronagraphs shortly thereafter (Leila Mays, private communication, March 27, 2019, NASA Goddard). In **Figure 1C**, the same volume that

reconstructed the IPS *g*-level analysis of **Figure 1B** is shown in density with an r^{-2} falloff imposed so that structures near the Sun have approximately the same density as those farther from it. In this cut viewed from the north through the volume in the ecliptic, the Sun is in the center, the Earth's orbit is shown with Earth to the right, and the two STEREO spacecraft are depicted as small circles to the left near Earth's orbit. This figure also depicts the remnant of the backside halo CME to the east of the Sun–Earth line as a dense spiral. However, this analysis also shows a combination of the two later frontside CMEs headed toward and about to reach the Earth. These are not seen as well in the *g*-level analysis of **Figure 1B** from which they were obtained, but they can be easily discerned in the ecliptic cut. Although the two CMEs are poorly resolved by the tomographic reconstructions as individuals in the ecliptic cut, they fully engulf Earth about five days following their initiation and produce the largest mass increase observed at Earth in Wind *in situ* measurements (Ogilvie and Desch, 1997) for the entire month-long Carrington rotation 2153 time period.

Summaries of how the iterative time-dependent tomography reconstructs the inner heliosphere are found in Jackson and Hick (2005); Hick and Jackson (2004); Jackson et al. (2001); Jackson et al. (2003); Jackson et al. (2006); Jackson et al. (2007); Jackson et al. (2008a); Jackson et al. (2009); and Jackson et al. (2011a). A comprehensive mathematical treatment of the time-dependent IPS and Thomson-scattering tomography is given in Jackson et al. (2008b). The analysis assumes starting values for velocity and density at an inner boundary "source surface". From these initial values, a best fit is reached through iteration. When the LOS integrations through the 3-D solar wind volumes at large solar distances differ from the overall observations, the source-surface values that have been traced back by the outward velocity propagation are inverted tomographically using a least-squares fitting procedure to provide values that reduce the deviations along the LOS. This produces the next set of source-surface values over time that are propagated outward and used to provide new 3-D volumes, and new corrections to the source surface. Iterations are monitored and show that the procedure quickly converges after a few steps. Confirmation of how well the IPS tomography operates with respect to other analysis available at the CCMC is given for seven-month intervals in both 2006 and 2007 by Jian et al. (2015); Jian et al. (2016). Magnetic field extrapolations using the IPS kinematic modeling are presented in a comprehensive effort using over 10 years of data (2006–2016) in Jackson et al. (2016b) and to forecast magnetic field GSM Bz over 11 years of data (2006–2017) in Jackson et al. (2019). Even more recently, the IPS-driven ENLIL programming is explored and contrasted with other models for use in forecasting ICMEs over 6-month periods of data in 2014 and 2016 (Gonzi et al., 2020).

For the IPS tomography, both density and velocity solar wind models are iterated to fit observed values. In this analysis, the small-scale electron density variations (δNe) that provide *g*-level are converted from density by **Eq. 1**.

$$\delta Ne \approx AR^{\alpha}N^{\beta} \quad (1)$$

where A is a constant, R is the radial distance from the Sun, N is the proton bulk density, and the power β is set in our analysis to fit *in situ* proton bulk density at Earth (where electrons are held in neutral equilibrium, primarily with protons and helium atoms in the solar wind). Values of α and β were developed in our analysis of the large variation of bulk proton density observed in the Bastille Day CME event from year 2000 compared with the Advanced Composition Explorer (ACE) spacecraft (Stone et al., 1998) Solar Wind Electron Proton Alpha Monitor (SWEPAM) (McComas et al., 1998), level zero data. These have not been changed since that time but are checked periodically to determine how well they fit current data sets. Constant A is removed by the way *g*-level is defined. The value of $AR^{\alpha}N^{\beta}$ is integrated along the LOS and weighted using the IPS thin scattering theory developed by Young (1971). This LOS weighting is shown for different radio frequencies, and radio source sizes including that of the ISEE 327 MHz observations in **Figure 2**. The weighting, which does not include the different LOS changes in *g*-level, is essentially the same for any direction in the sky but differs according to the frequency of the radio signal and the size of the radio source. In practice, the radio frequency for the observation is well-known, but the source size that varies with this frequency is often poorly determined and can have an irregular shape that depends on the flow of the solar wind across it.

The IPS velocity observations are usually presented relative to the integrated value perpendicular to the LOS. The actual solar wind speed varies with distance along the LOS relative to the radial, and in integration along the LOS this deviation of the solar wind propagation relative to the radial direction is taken into account. In addition, the velocity weighting along the LOS is

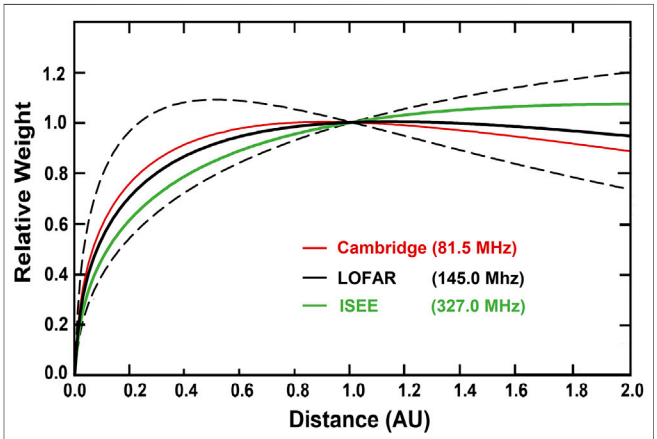

FIGURE 2 | The IPS LOS weighting distribution for different observing frequencies and assumed source sizes relative to distance along the LOS from Earth in the direction to the source. The weights are "normalized" at 1 AU and do not include the different scattering amounts along the LOS including those from the changing amount of scatterers with distance from the Sun. Cambridge, LOFAR, and ISEE source sizes are given at 0.3, 0.2, and 0.1 arcsec, respectively. Dashed lines lower and upper are source sizes at the LOFAR frequency for 0.1 and 0.3 arcsec source sizes, respectively. Frequency and source size need to be accommodated for each radio source observed.

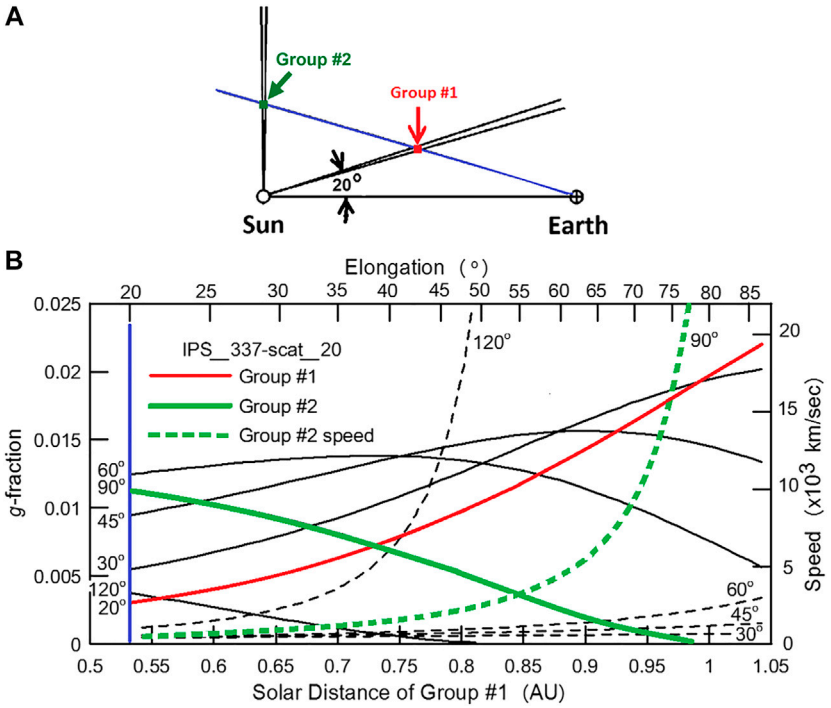

FIGURE 3 | (A) Different groups of plasma, one at 20° and one at 90° angular distance from the Sun–Earth line. Both groups move outward at a constant speed of 400 km s^{-1}. **(B)** Fractional response of IPS *g*-level (left ordinate) for different groups of electrons moving outward at a speed of 400 km s^{-1}. The Group #1 plasma at 20° (red) and the Group #2 plasma at 90° (green) are highlighted. The Group #1 plasma is tracked and moves outward linearly (lower abscissa) at a constant speed (400 km s^{-1}) and is also shown progressing outward in elongation (upper abscissa). Group #1 electrons for the volume packet (solid red line) provide an ever-increasing fractional percentage of the *g*-level response. Group #2 electrons that are viewed along the same LOS as those of Group #1 (solid green line) produce an ever-decreasing fraction of the LOS *g*-level response. Dashed lines show the geometrical speed (right ordinate) that must be present for different groups relative to Group #1 that is tracked outward at constant speed.

usually assumed to be the same as that for small-scale electron density scattering as given in **Eq. 1**. When both velocity and IPS *g*-level are available, they are simultaneously iterated to provide best fits to the *g*-level values that give density variations along the LOS to show density structure, but these also provide weighting along the LOS that give better velocity fits. Likewise, the velocity reconstructions provide more accurate traceback locations for the source surface density spatial and temporal initial positions to provide better fits for the *g*-level observations.

The 3-D reconstructions provide an analysis of the shape of the structures tracked without assuming a predefined shape for them. To indicate how these single-site perspective views using the IPS analysis provide an iterative solution to do this, we present the analysis of small packets of plasma particles in **Figure 3B**. Outward-flowing plasma within the inner heliosphere moves nearly radially outward from the Sun, and the range of different perspectives resulting from this motion iteratively provides the LOS differentiation. This figure illustrates the motion and structure brightness difference from ever-expanding 1° outward-flowing solar wind plasma (group #1 at 20° and group #2 at 90° are highlighted). Here, an IPS LOS to different distant sources sees plasma present in the two outflows, but these appear extremely different to the observer situated at 1 AU. Both 1° flows are assumed to have a value of 5 e^{-} cm^{-3} at 1 AU with an r^{-2} density fall-off with distance from the Sun, as is present in constant-flowing outward solar wind plasma. Group #1 plasma in the near 1° flow are outward-moving at a constant speed of 400 km s^{-1}, as is typical of the background solar wind or a slow CME. The intersection of this solar wind flow is tracked in position angle at the outward moving speed of this 1° flow to ever greater distances from the Sun (depicted on the **Figure 3B** abscissa) by the IPS LOS view to different distant radio sources. As shown in **Figure 3B**, the fractional *g*-level contribution of the Group #1 plasma increases gradually as the material moves outward. The intersected Group #2 electrons of the more distant solar wind falls off significantly in fractional *g*-level response as the LOS moves outward. In addition, the plasma in this distant 1° flow would have had to undergo an unphysical acceleration to extreme speeds over this time interval as shown in **Figure 3B** (green dashed line) to match the motion of the Group 1 plasma. By modeling solar wind flow such that both mass and mass flux are conserved, the distant unrealistic solution to structure flow is quickly eliminated. This plus the greatly different fractional response of the ever-expanding plasma volume along the LOS provides a differentiation of the LOS plasma location using the iterative 3-D reconstruction analysis.

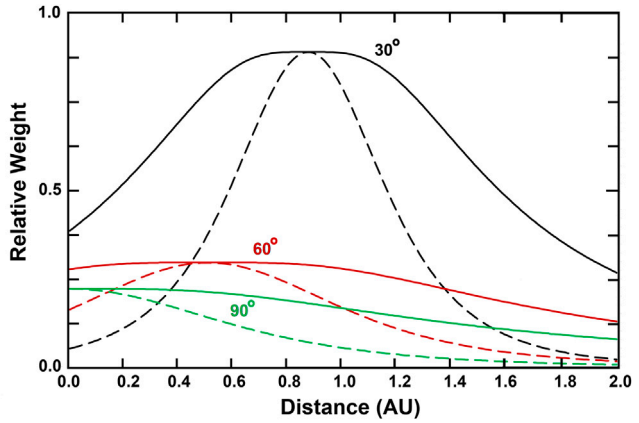

FIGURE 4 | Relative Thomson-scattering LOS brightness weighting from the distance of the observer (in AU) at three different solar elongations. For each elongation labeled, two curves are shown; solid lines are B, dashed lines are pB. Amplitude peaks at small elongations have more weight than those at large elongations because electrons in a one-degree column are closer to the Sun at the same distance from the observer.

The Thomson scattering 3-D reconstruction with views from a single point in space operates in a similar way. This 3-D reconstruction uses well-established electron Thomson-scattering theory (Billings, 1966) to provide its brightness response, and as shown in **Figure 4**, the LOS response to Thomson-scattered light from electrons is significantly different from that of the IPS shown in **Figure 2**. Here, each LOS peaks at the closest point to the Sun, and at elongations greater than 90° this is the location of the observer. Polarization brightness (pB) observations that were used in Helios spacecraft photometer 3-D reconstructions (Jackson et al., 2011a) and that are likely to be used in the Polarimeter to Unify the Corona and Heliosphere (PUNCH) observations are more strongly peaked than those shown for Thomson-scattered brightness (B). SMEI only used brightness in its 3-D reconstructions. A depiction of how single-site perspective views using the Thomson-scattering analysis provide an iterative solution to the LOS response by tracking structures outward from the Sun is illustrated in **Figure 5**. Again, as for the IPS, outward-flowing plasma within the inner heliosphere is shown moving outward radially from the Sun, and the range of different perspectives resulting from this motion provides the LOS differentiation. **Figure 5A** illustrates the motion and structure brightness and polarization brightness differences from two 1° outflows of solar wind plasma. Here, however, a one-degree widening FOV from Earth (expanding lines in **Figure 5A**) sees electrons present in the two identical 1° wide outflows centered on the Sun, but these appear extremely different to the observer situated at 1 AU. Both 1° flows have a 5-electron density r^{-2} fall-off relative to 1 AU with distance from the Sun, and again Group #1 electrons in the near 1° flow are outward-moving at a constant speed of 400 km s^{-1}. As in **Figure 3**, the intersection of this solar wind flow is tracked in position angle at the outward moving speed of this 1° flow to ever greater distances from the Sun (depicted on **Figure 5B** abscissa) by the one-degree FOV. As shown in **Figure 5B**, the brightness of the Group #1 electrons (given in S10 units for the 1°-wide intersected flow) decreases as the material gets closer to the Earth. The 1° intersected Group #2 electron flow of the more distant solar wind falls off with a more extreme brightness decrease. In addition, as for the IPS the electrons in this distant flow would have had to undergo an unphysical acceleration to extreme speeds (as shown by the dashed increasing line) over this time interval to match the motion of the Group #1 electrons. Dotted decreasing lines with distance depict pB for both groups. The Group #1 pB decrease must also fit the observed structure motion, giving even more confirming information about its LOS location and eliminating any duality of the pB value relative to the point of closest approach of the LOS to the Sun. By modeling solar wind flow such that both mass and mass flux are conserved, the distant unrealistic solution to structure flow is quickly eliminated, and this plus the more extreme fall-off of the distant flow provides the basis of 3-D reconstructions using Thomson-scattering brightness.

We note that the above depictions for both the IPS and Thomson scattering are only approximations because outward flow is not uniform over the whole sky, and neither is the density. However, this nonuniformity provides a trackable structure and is used and fit iteratively in the 3-D reconstructions. However, we must remember, both constant and radial outflow are only approximations to actual solar wind conditions. In the UCSD kinematic model, constant flow is modified by mass and mass flux conservation, but only assuming radial outflow. It is well known that other factors can change solar wind flow and enhance plasma density at different locations in the solar wind. These additional factors include solar wind acceleration with distance from the Sun, shock processes, and magnetic fields that interact and modify the solar wind plasma direction and speed. These can be only accommodated in the UCSD 3-D reconstructions by including a better physical model than just radial mass and mass flux conservation. It is for this reason that we include a 3-D MHD kernel as a basis for determining the global solar wind propagation direction and speed as a refinement to our iterative technique.

3-D RECONSTRUCTIONS WITH AN ENLIL KERNEL

Numerical solar wind models based on MHD equations are currently the only self-consistent mathematical descriptions capable of bridging many AU outward from the solar surface to well beyond Earth's orbit. Although MHD is only an approximation to actual plasma behavior, these models have successfully simulated many important space plasma processes and they are utilized by many groups around the world. Several different groups operating MHD analyses have employed the IPS time-dependent tomography boundaries to drive their modeling or have used this IPS modeling to verify their models. These groups include 1) the University of Alabama, Huntsville (UAH) (Kim et al., 2012; Kim et al., 2014; Pogorelov et al., 2012; Yu et al., 2012) who have devised the Multi-Scale FLUid-Kinetic

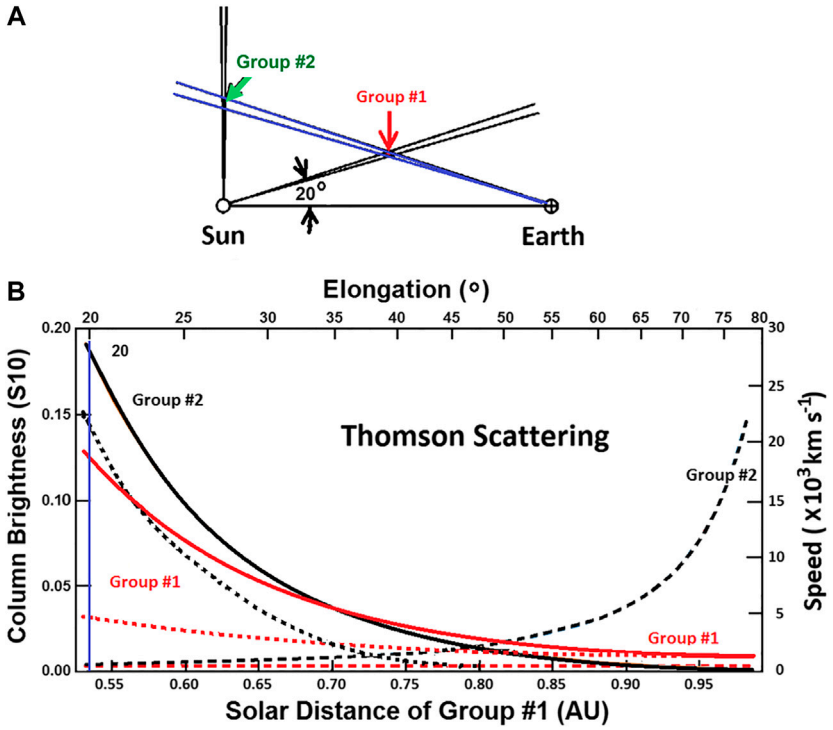

FIGURE 5 | (A) The intersection of a 1° outflow of electrons near the Earth (Group #1) along the same one degree opening angle LOS (blue) as one more distant (Group #2) travels a shorter distance outward from the Sun over the same amount of time. **(B)** Group #1 electrons with a constant speed of 400 km s^{-1} are shown (right ordinate), as well as the necessary increasing speed of the more distant electrons of Group #2) in order that they have the same angular extent of those in the near Group #1. Group #2 electrons must therefore be different material than what was viewed earlier. Additionally, over this same angular extent, the nearer electron outflow decreases far less in surface B or pB over the same distance (lower abscissa) or elongation (upper abscissa) than the more distant electron outflow.

Simulation Suite (MS-FLUKSS) 3-D MHD model; 2) the Naval Research Laboratory group using a model now termed H3D-MHD (Wu et al., 2007; Yu et al., 2015); 3) the University of Michigan group who have developed the BATS-R-US MHD model using the Solar Corona (SC) and Inner Heliosphere (IH) components of the Space Weather Modeling Framework (SWMF) (Meng, 2013; Manchester, 2017; Sachdeva et al., 2019); and; 4) finally, UCSD which has a long-term association with the ENLIL 3-D MHD model and has explored using the IPS boundaries to drive ENLIL since the mid-2000s (Odstrcil et al., 2005b; Odstrcil et al., 2007; Odstrcil et al., 2008; Jackson et al., 2010a; Jackson et al., 2015; Yu et al., 2015).

ENLIL is based on the ideal 3-D MHD description, with two additional continuity equations for tracking the injected CME material and the magnetic field polarity (see Odstrcil and Pizzo, 1999b). Solar wind 3-D MHD modeling often uses photospheric magnetic-field observations (e.g., see Arge and Pizzo, 2000; Arge et al., 2003) and approximates solar wind plasma parameters from these (velocity, density, and temperature) as boundary conditions at the base of the heliosphere and extrapolates these outward. Boundary conditions of transient events, especially velocity and density, are difficult to extract from near-Sun observations and are either "best-guess" approximations to the sources of energy that eject plasma from the Sun or fits to coronagraph data showing the outward speeds of fast-moving structures (CME cone model inputs; Odstrcil and Pizzo, 1999a; Odstrcil et al., 2004; Odstrcil et al., 2005a; Luhmann et al., 2010). Rapidly varying transient CME magnetic-field direct measurements are essentially nonexistent; usually only general background fields are mapped.

The ENLIL 3-D MHD program is exploited by space weather groups for forecasting heliospheric plasma features in advance of their Earth arrival partly because this program is transportable to their institutions. At the KSWC, Jeju, South Korea, this system was operated alongside the UCSD IPS kinematic tomography, which was then modified for use to drive ENLIL in near real time using ISEE IPS data. This system has operated since 2014 by the KSWC in near real time (**Figure 6**). For the IPS-driven 3-D MHD heliospheric modeling, UCSD has prepared their boundaries, including those for the magnetic field, at the height and in the coordinate system (RTN—Radial Tangential, Normal, or Inertial Heliographic—IHG) required by each model. For some of the modeling, these boundaries have been left on UCSD servers to be employed in each 3-D MHD modeling effort. In recent work using these boundaries (**Figure 6**, and as described in Yu et al., 2015 or Jackson et al., 2015), the UCSD kinematic model reproduces the *in situ* record well at the resolutions commensurate with the current IPS data from ISEE. The 3-D MHD models also reproduce the *in situ* record well using these boundaries.

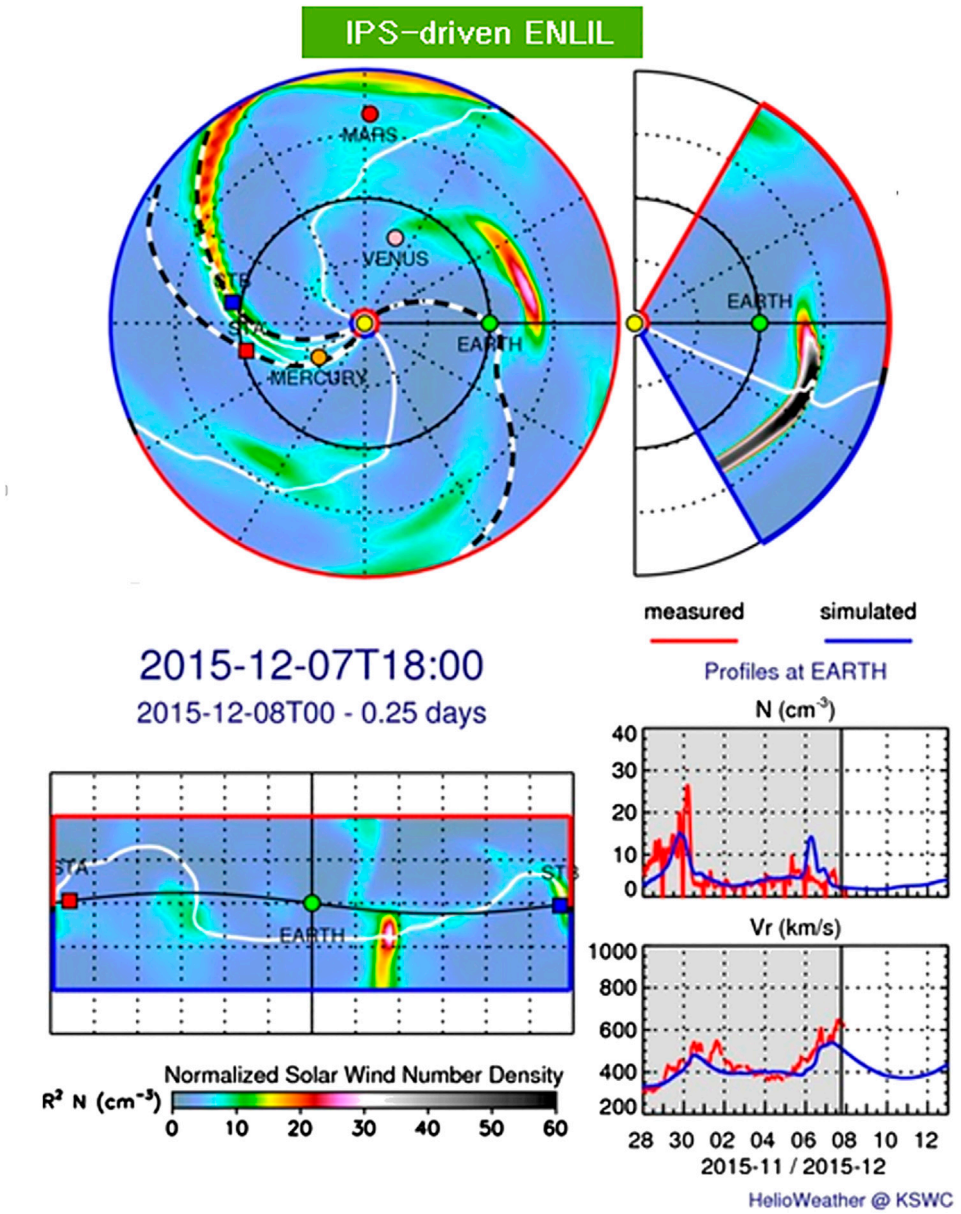

FIGURE 6 | ENLIL 3-D MHD density modeling driven by a UCSD IPS tomography-supplied inner boundary at 21.5 Rs, as provided at the KSWC. The 3-D MHD model sample obtained from http://www.spaceweather.go.kr/models/ipsbdenlil is compared with hour-averaged ACE density and velocity data from 28 November to December 07, 2015 and is depicted in the volumetric data at 2015/12/07 18 UT. Once IPS data become available (at 18:00 UT), these analyses are projected 5 days into the future. The black and white dashed lines in the ecliptic cut show the projections of the 3-D field line trace from Earth, STEREO A, and STEREO B at the time of the observation.

An even more significant advance modifies these analyses so that the 3-D MHD modeling can be updated and fit to the IPS observations as structures move outward in the solar wind. This allows observations to update the location of heliospheric structures during their outward propagation such that mid-course corrections can be applied to changing plasma conditions. The ENLIL modeling now provides this advance as a kernel in the UCSD 3-D reconstruction tomography so that it replaces the current kinematic model (**Figure 7**). In these modeling efforts, we now operate both the kinematic modeling and ENLIL on the same 64-node computer system. ENLIL has been constructed using Fortran MPI and can operate on nodes with different multiples of two; the IPS tomography to date has used only single-string Fortran processing with an IDL system used to output data products. In these initial modeling efforts and for checks, we use a source surface from the kinematic modeling

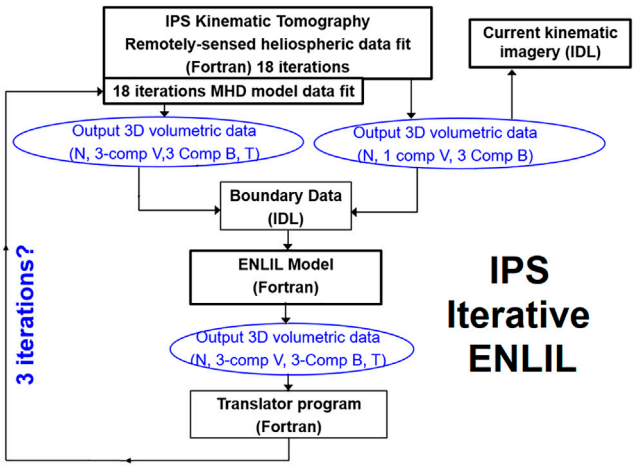

FIGURE 7 | The Iterative IPS-ENLIL process depicted as a flow diagram. The UCSD kinematic tomography begins the process and converges from these inputs after three iterations. A "translator" program converts the ENLIL output coordinate system 3-D files over time to those used by the IPS tomography.

to begin the iterative 3-D reconstructions for the zeroth iteration of the sequence. This enables a kinematic model analysis of the same IPS data set along with IPS-driven modeling at the beginning of the sequence, thus allowing tests to be performed on all three system types at once that are used for checks and updates. The way that this is accomplished using the ENLIL modeling is shown in the **Figure 7** flow diagram. Here, the UCSD kinematic model first provides a full time-dependent 3-D reconstruction of the inner heliosphere. This allows the UCSD IDL visualizations of the inner heliosphere as well as time-dependent ENLIL boundary values extracted from these volumes in velocity, density, and three-component magnetic fields at 21.5 Rs. The ENLIL model is then run using these boundaries to provide an IPS-driven ENLIL model, which provides volumetric data in 3-component velocities, 3-component fields, density, and temperature that is used for plots from the ENLIL run. This ENLIL run provides these same time-dependent volumetric data variables up to 3 AU for use in the IPS iterative tomography. A translator FORTRAN program interpolates these volumetric data from ENLIL as multiple time-dependent boundaries for use as needed in the IPS 3-D reconstruction program. These volumetric data are then returned to the UCSD iterative 3-D reconstruction program where the ENLIL 3-component velocity time-dependent matrix then provides solar surface traceback instructions (see "*IPS and Thomson Scattering*") for its own use. Iterations of this proceed with the UCSD programming providing renewed output boundaries for ENLIL and ENLIL-produced renewed volumetric data for the tomography. So far, we have found that beginning with a completely converged kinematic model as a start, only about three iterations are required for the iterative ENLIL model to produce consistent results. It takes less than 3 h to complete three iterations on our new UCSD 64-core AMD processor using only 16 cores. At the end of this process, a full UCSD run of its volumetric data as well as that from ENLIL is output and displayed to check consistency between the kinematic model results, and the two versions of ENLIL run with the same IPS inputs and *in situ* solar wind data sets. These systems have been tested with archival data sets but are also operated in near real time with a 6-h cadence using ISEE IPS data and are displayed on the UCSD web pages under https://ips.ucsd.edu and compared with *in situ* data available from NOAA, generally from the ACE spacecraft. The real-time display allows checks of all three systems in order to test them under varying input conditions relative to *in situ* data sets. **Figure 8** shows an archival data set comparison using ISEE IPS data and Wind spacecraft *in situ* measurements. In this example, the iterative ENLIL model clearly shows an advantage in providing a better-resolved dense feature that compares well with Wind *in situ* density values on September 10, 2011. Even other large density spikes in the *in situ* sequence on September 2 and September 17 provide a more consistent match between the iterated ENLIL values and Wind. Near real-time comparisons with ACE at current times provide more mixed results, and one of these examples is shown in **Figure 9**. The sequence of images was taken from the UCSD websites shown on the figure and shows a density time series in comparison with NOAA-provided ACE hour-averages, including a Pearson's R correlation (R = 0.953) of the density data set up to the time the observational data were available shown as a dashed vertical line. The analysis beyond this has been extended for another 4 days following the run time and shows density decreasing somewhat following the peak after the time the data were obtained. The density did dip by a few particles cm^{-2} following this to another peak nearly as high from July 31–August 1. Additional imagery includes a density ecliptic cut, a meridional density cut through Earth, a density synoptic map at 1 AU, a velocity ecliptic cut, and a velocity meridional cut through Earth. The bottom analysis shows the exact same sequence of images in the ENLIL format with the exception of the time series data, which was presented from the third iteration of the 3-D reconstruction model from which the boundary data was used for the final ENLIL imagery shown. This time series has a Pearson's R correlation of R = 0.808 for its *in situ* comparison. This additional imagery as well as these is also archived and available for viewing on the two websites presented in **Figure 9**.

These are encouraging results using both the kinematic modeling or the ENLIL systems, but nevertheless they only show general results in low resolution that provide analyses with a cadence of about half a day from archived data and somewhat less than this used in forecast mode as in **Figure 6** or **Figure 9**. While these analyses provide interesting confirmation of CME structure and density, especially where the IPS data LOS are numerous (near Earth), they provide less information globally, i.e., at non-Earth deep-space locations. As time-dependent fits to heliospheric data, and with confirmation detailed daily by comparison with *in situ* measurements, these analyses are unique. They are also prone to the idiosyncrasies of data fits and their statistical properties, which provides excellent results only part of the time. With relatively few parameters to fit in the 3-D reconstruction procedures, improvements can generally be made in the prediction by using different data

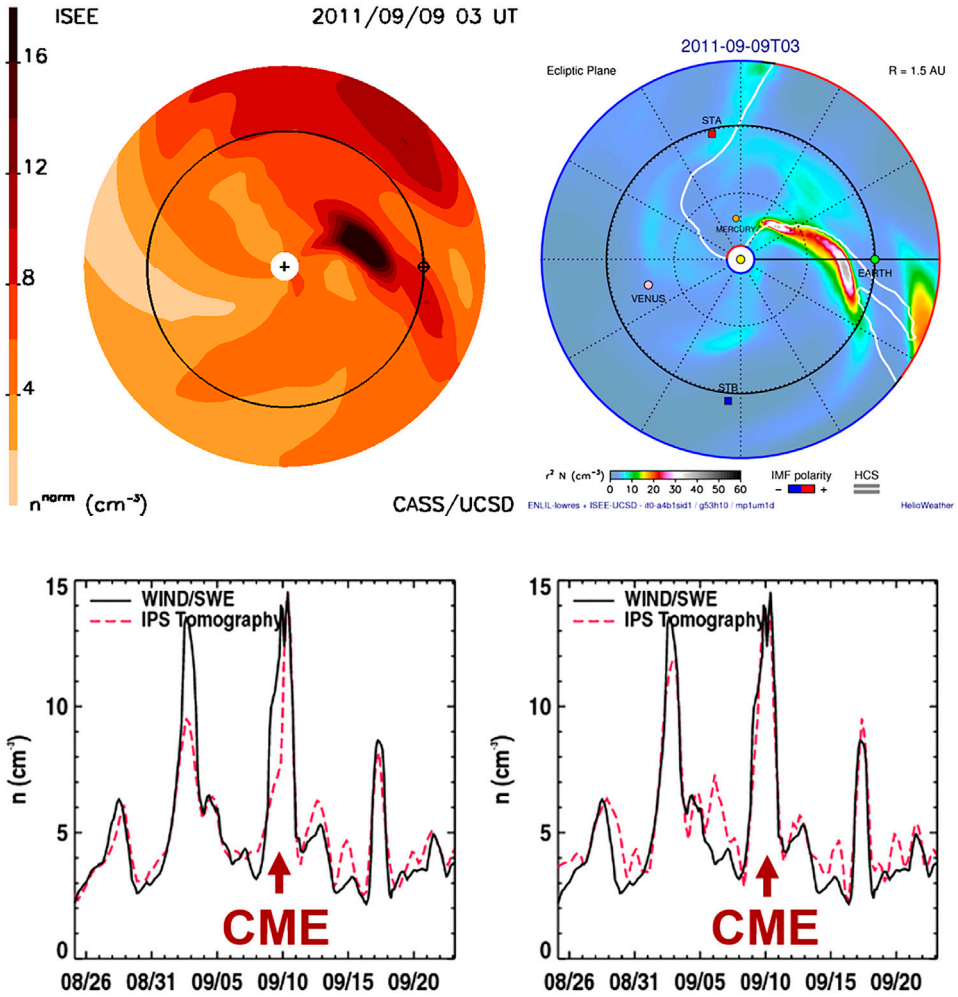

FIGURE 8 | Comparison of the density derived from the iterated kinematic model **(left)** and the iterated model using ENLIL as a kernel **(right)** in the UCSD tomography. The ecliptic cuts **(top)** show the modeling for a CME in 2011 from a tomography-supplied inner boundary at 21.5 Rs. Two bottom plots show the comparison of the kinematic model and the ENLIL model for Carrington rotation 2114 with Wind *in situ* density data that includes this CME. Pearson's R correlations for the overall density time series kinematic and ENLIL analyses are 0.92, and 0.95, respectively.

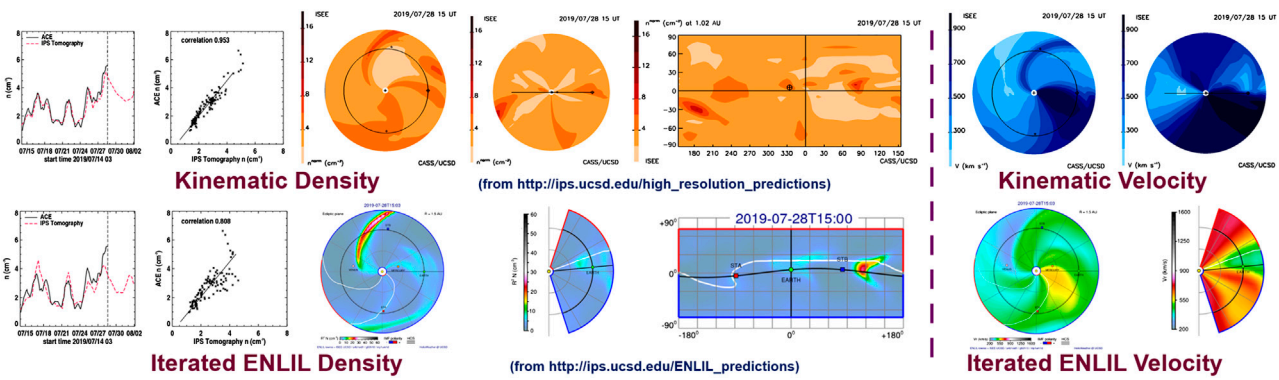

FIGURE 9 | (top) Real-time analyses of density and velocity for the IPS kinematic modeling using the ISEE IPS values on July 28, 2019, at 15 UT. **(bottom)** A third iteration of the 3-D MHD iterative ENLIL model provides similar imagery depicted for this period.

sets and adjusting the parameters to make better fits for specific examples. For the IPS, for instance, the relationship of scintillation level to bulk density shown in, **Eq. 1**, is one of the only parameters possible to adjust. For the iterated ENLIL programming, the ratio of specific heats, and the heating of various plasma structures is essentially unknown; these two parameters can be adjusted to make better fits most of the time and to this date have not been thoroughly explored. For the ENLIL iterative analysis, more iterations do not seem to improve the results substantially for the examples studied. For ENLIL, there is also a matter of resolution whereby the smoothing used in the 3-D reconstruction procedure cannot adequately distinguish the fine details of shocked plasma density.

For Earth onset plasma forecasting, these analyses still only provide low-resolution state-of-the-art temporal CME measurements with a sparse data set, and the obvious solution is to simply provide more and better-quality data. Additionally, as stated previously, current IPS analyses can miss some of the fastest transient structures simply because they are not observed by a single longitude observational facility. Thus, we now describe a way forward for these same analyses that can be used to provide better-resolved and more secure results from a variety of different techniques.

ADVANCED TECHNIQUES AND SUMMARY

As long as space research continues, it will always be important to provide better and more refined analyses globally of this medium through remote-sensing techniques. Such techniques enable an understanding of structures surrounding those that can be measured *in situ*, and although these measurements can be more precise and obtained at higher cadences, there are simply not enough of them or the resources to provide them throughout space to fill in all the locations of interest. Furthermore, the physics of how solar wind structures are accelerated and interact is still only in its infancy as the main premises of Parker Solar Probe (PSP) and Solar Orbiter amply demonstrate. We expect our analyses to fill in the gaps between *in situ* measurements where possible and to provide more continuous representation of the spotty global information currently available as well as a better understanding behind the physical processes that create solar wind outflow and their interactions.

Another benefit for forecasting is that the 3-D reconstruction analyses do not require coronagraph or heliospheric imager inputs to provide their predictions to map oncoming CMEs (see, e.g., Jackson et al., 2015). This is good from the standpoint of an autonomous forecast system especially using a 3-D MHD kernel, since all can be done without human intervention except for maintenance of the systems that provide the data and its modeling. There are several ways to remedy the lack of remote sensing data readily available, and for IPS this is by providing more IPS sites around the globe that can input to the remote sensing observations so that there are fewer data gaps and more available data. Over the years, the UCSD 3-D reconstruction analysis has been operated using single instrument data to provide 3-D structure analyses. These include 1) data from the Cambridge, England, array from the year 1979 (Jackson et al., 1998); 2) data from ISEE (Bisi et al., 2008; Bisi et al., 2009a; Bisi et al., 2010b; Jackson et al., 2003; Jackson et al., 2010b; Jackson et al., 2011a; Jackson et al., 2013); 3) data from the Ooty, India, array (Bisi et al., 2009b; Manoharan, 2010); 4) data from EISCAT in northern Europe (Bisi et al., 2010a; Fallows et al., 2007a; Fallows et al., 2007b); 5) data from the Mexican Array Telescope (Chang et al., 2016); and 6) data from the Pushchino, Russia, Big Scanning Array (BSA) (Jackson et al., 2016a).

In 2016, the Worldwide Interplanetary Scintillation Stations (WIPSS) Network (Bisi et al., 2016a; Bisi et al., 2016b; Bisi et al., 2016c; Jackson et al., 2016c) concept was initiated to indicate a standard way to provide results from observations of IPS and allow a unified combination of IPS instruments around the world. The UCSD tomography program had earlier been modified to accommodate many different IPS systems, sort their data, and combine their outputs. Although all groups providing IPS observations have overwhelmingly agreed to this concept (e.g., Bisi et al., 2016b; Bisi et al., 2017a; Bisi et al., 2017b; Bisi et al., 2017c; Bisi et al., 2017d; Bisi et al., 2017e; Bisi et al., 2017f; Bisi et al., 2017g; Bisi et al., 2018; Jackson et al., 2016c; Jackson et al., 2017), the idea has been difficult to implement. The greatest success to date has come from those working with data from the LOw Frequency ARray (LOFAR) (Van Haarlem et al., 2013) who have recently provided a wealth of multi-site IPS velocities for use from campaign-mode observations from this European system. In **Figures 10** and **11**, we show an analysis in 2019 from an ISEE–LOFAR combined data set during the PSP second close solar pass where only ISEE *g*-level data and LOFAR velocity data were available. **Figure 10** provides IPS *g*-level images as introduced in **Figure 1** presented alongside IPS velocity images. The combined ISEE-LOFAR data of modeled velocities show an integration of the velocity signal perpendicular to the LOS that is a best fit to LOFAR observational velocities. The observed *g*-level and velocity observational values (small round circles) are superimposed on the model within 3 h of the given UT time. The times of the models and observations presented are separated by 6 h and show the bulk of the data sources observed on that day within the 3-h limit of the UT time, at each site. The model times are different because the bulk of the ISEE observed *g*-levels are obtained approximately 9 h earlier than the velocities from LOFAR (the difference in longitude between the measurements obtained in Japan and Europe). The LOS locations are coded with values that provide the level of the observation and are circled by a dark line if the observation is above the modeled value, and by a light value if below that of the model. Although the model is formed by all lines of sight over a period of 8–10 days from global observations, the LOS are instantaneous and thus only show the source contribution to the volume within the 3-h time limit of the model. The ecliptic plots show the instantaneous global values of the density and velocity that are derived from the heliospheric models of these parameters. These are presented at the time of the IPS LOFAR skymap modeled velocity observations. In **Figure 10**, PSP is marked as a small black dot to the left of center and above

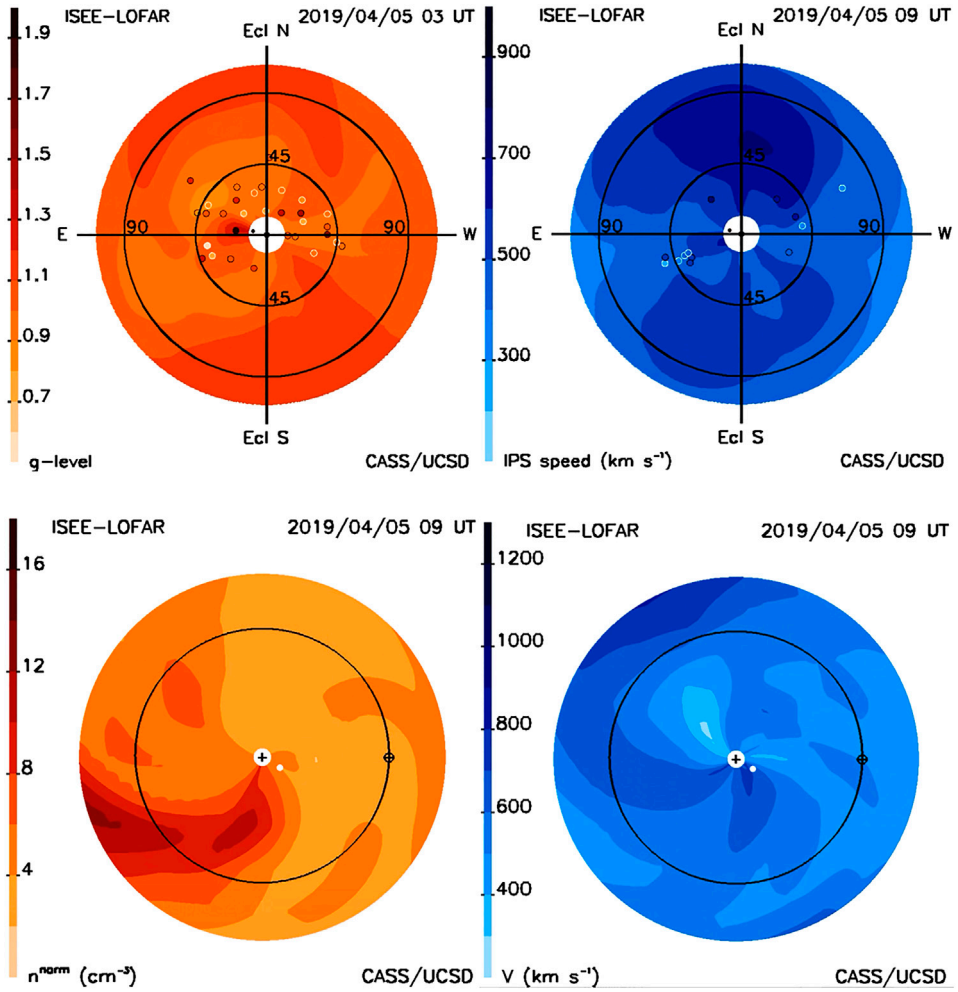

FIGURE 10 | (top) IPS skymap observations out to 110° showing the kinematic model analysis using both systems together near the time of the PSP close solar pass. Observations from ISEE **(left)** and from LOFAR **(right)** are superimposed on the plot as small circles. The Sun is in the center of the image, and the PSP location is marked as a black dot in the images **(bottom)** Ecliptic cuts from the same model volumes show the Sun in the center with Earth to the right on its orbit. PSP is located in the images as a white dot superimposed on the ecliptic plot.

the ecliptic within the white area that marks the region of strong scattering in the skymaps, and as a small white dot within the 3-D-reconstructed ecliptic cuts in the bottom plots. **Figure 11** provides time-series plots at Earth centered on the PSP close solar pass that includes the IPS ACE densities and velocities from NOAA as a weighted input and as compared with *in situ* values in the 3-D reconstructions. Clearly, the **Figure 10** velocity analysis is an advancement because at this time of the year no IPS velocities were available at ISEE to provide global observations. Additionally, with a more careful analysis of these data sets, we find that the IPS LOFAR velocity observations at this time allowed the ISEE data to fit the *in situ* density data better at Earth than the 3-D reconstructions analyzed where no LOFAR velocity observations were added (Jackson et al., 2020a; Jackson et al., 2020b).

Other ways to provide the 3-D time-dependent reconstructions globally include measurement of Thomson scattering like those from the Solar Mass Ejection Imager (SMEI). SMEI was a unique instrument designed to provide heliospheric Thomson-scattering observations from Earth to be used in this same way. Launched in January 2003, initially funded by NASA and the Air Force with some NSF support (Jackson et al., 2004). SMEI was shut down after more than eight years of operation in September 2011 (Howard et al., 2013). Some data analysis from SMEI has continued with studies of solar jetting (Yu et al., 2016). The SMEI data still exist, and recently with advent of NASA funding for the Small Explorer Spacecraft PUNCH, there has been an interest in the resurrection of tests of these data sets for its 3-D reconstruction application with this new system.

Our current computer system has been used with existing SMEI data (**Figure 12**) to provide time series interpolated to 1-h resolutions at Earth, and comparable interpolated time and spatial resolution model analyses. It provides this resolution all the way from the model source surface at 15 Rs from the Sun. This program now can include 1-h ACE or Wind *in situ*

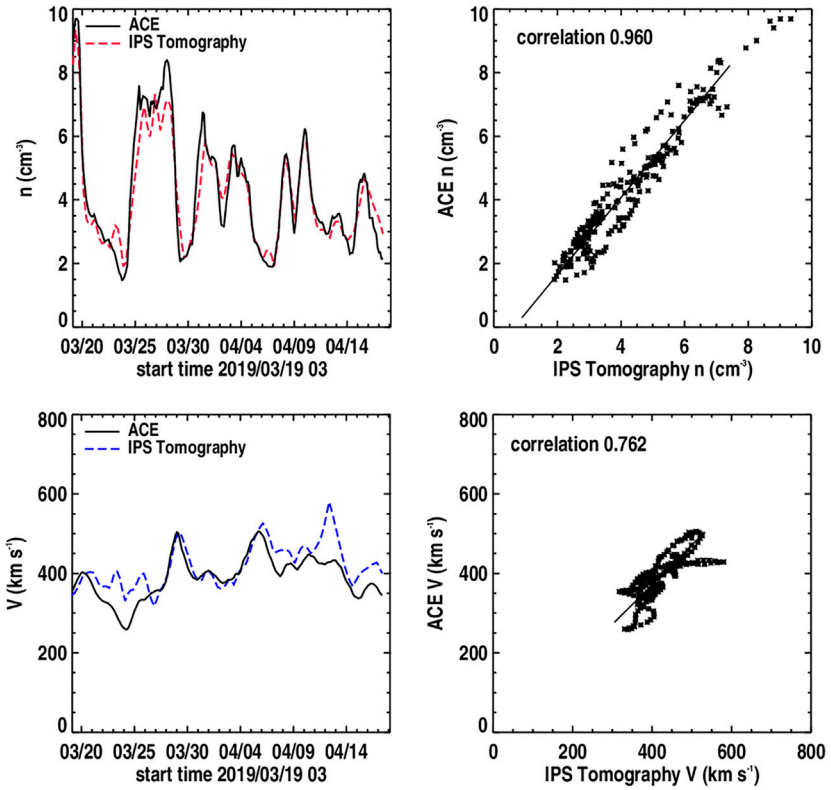

FIGURE 11 | (top) Density and **(bottom)** velocity time series at Earth using ISEE and LOFAR data over Carrington rotation 2215.3 centered on the time period of the PSP second close pass of the Sun.

measurements to help normalize the observations at 1 AU. We show the preliminary analysis of this data set for density the May 30, 2003, CME event sequence (Jackson et al., 2008a), shown in **Figure 12**, which required slightly over 33 h to provide this result on the AMD machine using 14.4% of the 512 Gigabyte memory, and thus this is clearly insufficient as a real-time system at the moment. **Figure 13** shows this same event as a volumetric cut through the ecliptic and the north–south ecliptic meridian along the Sun–Earth line at three different times during the event passage. Although nearly all of the global heliosphere can be filled by this iterative tomography technique, here we show only that portion where at least 10 complete LOS provide the 3-D reconstruction in a given resolution element. In this way, the analysis shows that there is ample LOS information to provide a robust reconstruction over the time of the event passage. The SMEI tomography displayed on the UCSD website http://smei.ucsd.edu provides both an ecliptic cut and an Earth meridional cut of these LOS crossing numbers for the low-resolution SMEI data analyses for years 2003–2011 that are archived on this website. This analysis is encouraging, since it implies that with even better programming perhaps using parallel processing, a relatively small computer might allow an even better result with extant SMEI, or STEREO HI data. Of course, we intend that this tomographic system will be regularly employed using observations from PUNCH or UCSD's own All Sky Heliospheric Imager (ASHI) instrument. The latter is designed specifically for CME and SIR forecasting, as presented to the Space Experiments Review Board for inclusion by the DoD for a Space Test Program flight. As a scientific instrument, this is also very interesting. As an example of this, we note the small peak in density behind the main peak observed in both ACE and Wind *in situ* measurements on May 30 at ~9 UT that we suspect may be a reverse shock (see Liu et al., 2017 and references therein) that has just formed and whose extent we can characterize in 3-D as the CME moves outward past the Earth. In the case of the May 30, 2003, CME event sequence, this will mean that we need to use difference volumetric techniques to explore structure evolution relative to the main outward moving solar wind density features.

CONCLUSION

The preceding text shows how the 3-D reconstructions described can be implemented, combined, and refined to make full use of the planned remote-sensing data imagery that are both ground-based (radio) and available from space-borne instrumentation (Thomson scattered visible light). Utilized in a global 3-D heliospheric system that is refined and used to extend *in situ* data sets, IPS and/or Thomson-scattering data and its modeling will allow the provision of validated 3-D reconstructions of the

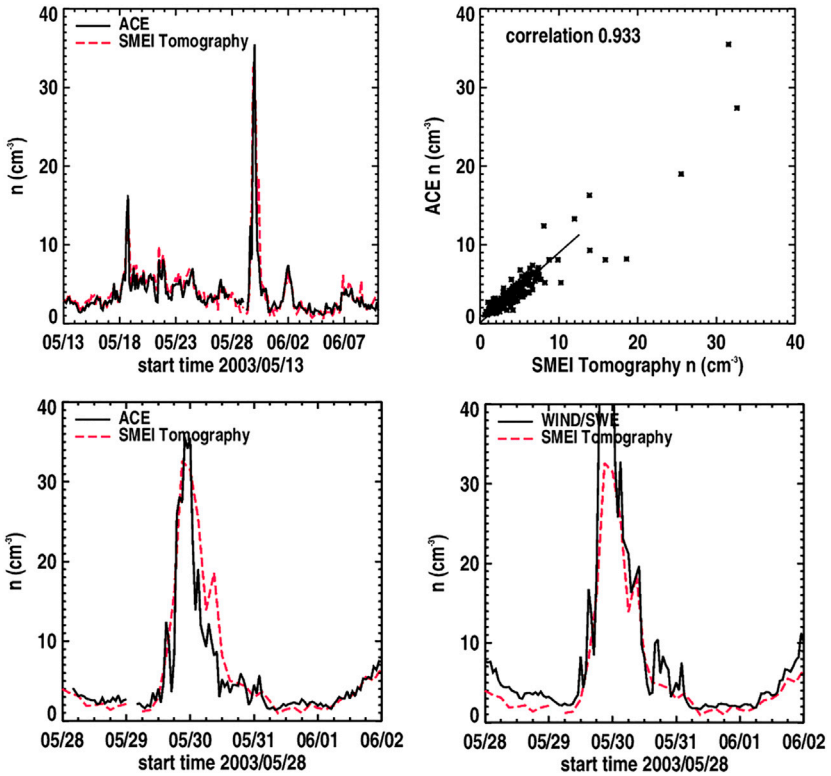

FIGURE 12 | SMEI *in situ* density values plotted with a 1-h cadence. **(top)** Plotted over the full Carrington rotation 2003 data set that begins on May 13, 2003, relative to ACE Level zero data; **(bottom)** relative to the same data set plotted from May 28, 2003, to June 2, 2003, centered on the large density peak at the time of the May 30, 2003, CME and **(left)** relative to the 1-h averaged Wind *in situ* density measurements.

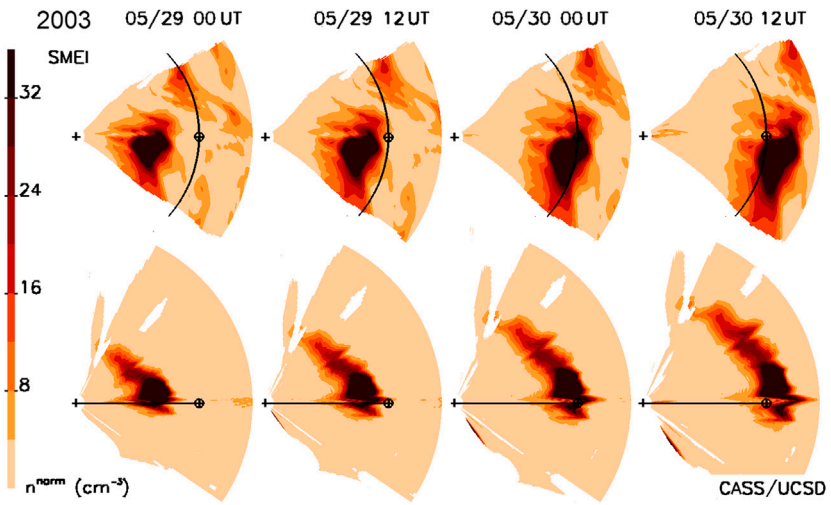

FIGURE 13 | SMEI time-dependent ecliptic **(top)** and meridional **(bottom)** cuts of the May 30, 2003, CME as it propagates outward past the Earth from which the in situ densities of **Figure 12** were obtained. These use the same density color scales as in **Figure 1**, with enhanced values highlighted above the 5 particle cm^{-3} base.

inner heliosphere. This can be used to refine current modeling techniques, including time-dependent 3-D MHD as well as IPS analyses of all ground-based systems. Although we show both 3-D reconstruction techniques here for possible future use, only the IPS analyses are immediately at hand to provide this type of forecasting. It is only with great difficulty, expense, and

uncertainty that space-borne instrumentation will be able to provide similar and supplemental 3-D analyses. Well-calibrated Thomson-scattering data are not as easy to provide, primarily because the signal is small relative to the other many noise sources present, and imagery can be interpreted simply by approximating (or guessing) the LOS extent present in the imagery. Of course, for 3-D reconstructions both systems can be combined and contrasted as shown to provide the best science and forecasting or both. In any case, the best science, and a most exact 3-D reconstruction definition of the heliosphere, will ultimately lead to the best processes employed to provide this.

DATA AVAILABILITY STATEMENT

The datasets presented in this study can be found in online repositories. The names of the repository/repositories and accession number(s) can be found below: https://ips.ucsd.edu.

AUTHOR CONTRIBUTIONS

BJ is the primary person responsible for the Iterative Tomography Technique. He and colleagues AB and LC at UCSD helped in the preparation of this article for publication and in the preparation of some of the figures presented. DO at GMU and NASA Goddard is the main person responsible for developing the ENLIL 3-D MHD program used in the article. MB and RF are the main persons responsible for providing and preparing the LOFAR velocity data for use in the 3-D tomography program. MT at ISEE, Japan and his group have prepared the ISEE IPS data for presentation, and have provided these data for use on their FTP website in Japan.

FUNDING

The work of BJ, AB, and LC acknowledge funding from NASA contracts 80NSSC17K0684, and NNX17AG13G, and AFOSR contract FA9550-19-1-0356 P00001 DEF to the University of California, San Diego. DO acknowledges NASA LWS sub-award 96916956 and MB LWS subcontract RS00963 contract no. 5666 to the University of California, San Diego. MB was also supported by the STFC in-house Research Grant to UKRI STFC RAL Space—Space Physics and Operations Division. The ILT resources have benefitted from the following recent major funding sources: CNRS-INSU, Observatoire de Paris, and Universite d'Orleans, France; BMBF, MIWF-NRW, MPG, Germany; Science Foundation Ireland (SFI), Department of Business, Enterprise and Innovation (DBEI), Ireland; NWO, The Netherlands; The Science and Technology Facilities Council, United Kingdom; and Ministry of Science and Higher Education, Poland.

ACKNOWLEDGMENTS

The authors wish to thank the many persons responsible for this chapter in Frontiers in Solar and Space Weather. Paul Hick, who provided much of the original work on the IPS and SMEI 3-D reconstruction programming, is greatly appreciated for his many contributions to these studies. This paper is based in part on data obtained with the International LOFAR Telescope (ILT) under project code "LT10_001." LOFAR (Van Haarlem et al., 2013) is the Low Frequency Array designed and constructed by ASTRON. It has observing, data processing, and data storage facilities in several countries that are owned by various parties (each with their own funding sources) and that are collectively operated by the ILT foundation under a joint scientific policy.

REFERENCES

Arge, C. N., Odstrcil, D., Pizzo, V. J., and Mayer, L. R. (2003). Improved method for specifying solar wind speed near the Sun. *AIP Conf. Proc.* 679, 190–193. doi:10.1063/1.1618574

Arge, C. N., and Pizzo, V. J. (2000). Improvement in the prediction of solar wind conditions using near-real time solar magnetic field updates. *J. Geophys. Res.* 105, 10465–10479. doi:10.1029/1999ja000262.

Barnes, D. (2020). Remote sensing estimates of CME density in the ecliptic using the STEREO heliospheric imagers. *J. Geophys. Res. Space Phys.* 125(2), 12–27. doi:10.1029/2019JA027175.

Behannon, K. W., Burlaga, L. F., and Hewish, A. (1991). Structure and evolution of compound streams at ≤1 AU. *J. Geophys. Res.* 96(21), 213. doi:10.1029/91ja02267.

Billings, D. E. (1966). *A guide to the solar corona*. New York, NY: Academic Press, 150.

Bisi, M. M., Jackson, B. V., Hick, P. P., Buffington, A., and Clover, J. M. (2008). 3D reconstructions of the early november 2004 CDAW geomagnetic storms: preliminary analysis of STELab IPS speed and SMEI density. *J. Geophys. Res. Space Phys.* 23(113), A00A11. doi:10.1029/2008ja013222

Bisi, M. M., Jackson, B. V., Buffington, A., Clover, J. M., Hick, P. P., and Tokumaru, M. (2009a). Low-resolution STELab IPS 3D reconstructions of the whole heliosphere interval and comparison with in-ecliptic solar wind measurements from STEREO and wind instrumentation. *Sol. Phys.Sol Phys.* 256, 201–217. doi:10.1007/s11207-009-9350-9.

Bisi, M. M., Jackson, B. V., Clover, J. M., Manoharan, P. K., Tokumaru, M., Hick, P. P., et al. (2009b). 3-D reconstructions of the early-November 2004 CDAW geomagnetic storms: analysis of Ooty IPS speed and density data. *Ann. Geophys.* 27, 4479. doi:10.5194/angeo-27-4479-2009.

Bisi, M. M., Jackson, B. V., Breen, A. R., Dorrian, G. D., Fallows, R. A., Clover, J. M., et al. (2010a). Three-dimensional (3-D) reconstructions of EISCAT IPS velocity data in the declining phase of solar cycle 23. *Sol. Phys.* 265, 233–244. doi:10.1007/s11207-010-9594-4.

Bisi, M. M., Breen, A. R., Jackson, B. V., Fallows, R. A., Walsh, A. P., Mikić, Z., et al. (2010b). From the Sun to the Earth: the 13 may 2005 coronal mass ejection. *Sol. Phys. Sol Phys.* 265, 49–127. doi:10.1007/s11207-010-9602-8.

Bisi, M. M., Fallows, R. A., Sobey, C., Eftekhari, T., Jensen, E. A., Jackson, B. V., et al. (2016a). "Worldwide interplanetary scintillation (IPS) and heliospheric Faraday rotation plans and progress," in Oral presentation at the IPSP SANSA space weather research forum, SANSA abstract Hermanus, South Africa, January 20, 2016.

Bisi, M. M., Jackson, B. V., and Webb, D. F. (2016b). "Remote-Sensing observing techniques for improving space-weather science and forecasting," in Oral presentation at the 2016 SHINE conference, SHINE abstract Santa Fe, New Mexico, July 15, 2016.

Bisi, M. M., Gonzalez-Esparza, J. A., Aguilar-Rodriguez, E., Chang, T. O., Jackson, B. V., Yu, H.-S., et al. (2016c). "The worldwide interplanetary scintillation (IPS) stations (WIPSS) Network," ESWW abstract in Presentation at the 13th European space weather week, November 14–18, 2016.

Bisi, M. M., Gonzalez-Esparza, J. A., Jackson, B., Aguilar-Rodriguez, E., Tokumaru, M., Chashei, I., et al. (2017a). "The worldwide interplanetary scintillation (IPS) Stations (WIPSS) Network in support of space-weather science and forecasting," in Paper presented at Geophysical Research Abstracts, EGU General Assembly, Vienna, Austria, April 23–28, 2017.

Bisi, M. M., Fallows, R. A., Jackson, B. V., Tokumaru, M., Yu, H.-S., and Barnes, D. (2017b). ".The worldwide interplanetary scintillation (IPS) stations (WIPSS) Network: October 2016 campaign—LOFAR and ISEE initial Investigations," in Paper presented at space weather workshop, NOAA SWW abstract, Broomfield, CO, May 1–5, 2017.

Bisi, M. M., Gonzalez-Esparza, J. A., Jackson, B. V., Aguilar-Rodriguez, E., Tokumaru, M., Chashei, I., et al. (2017c). "The worldwide interplanetary scintillation (IPS) Stations (WIPSS) Network in Support of space-weather science and forecasting," in Oral presentation at the IAU space weather of the heliosphere conference, IAU abstract, Exeter, UK, July 17–21, 2017.

Bisi, M. M., Fallows, R. A., Jackson, B. V., Tokumaru, M., Yu, H.-S., Morgan, J., et al. (2017d). "The worldwide interplanetary scintillation (IPS) stations (WIPSS) Network October 2016 campaign: LOFAR IPS data analyses," in Poster presentation at the IAU space weather of the heliosphere conference, IAU abstract, Exeter, UK, July 17–21, 2017.

Bisi, M. M., Webb, D. F., Gonzalez-Esparza, J. A., Jackson, B. V., Chashei, I., Tokumaru, M., et al. (2017e). "The worldwide interplanetary scintillation (IPS) stations (WIPSS) Network as a potential future ISWI instrument," in Presentation at the UN/US workshop on the International space weather initiative, UN/US abstract, Boston, MA, July 31–August 4, 2017.

Bisi, M. M., Jackson, B. V., Fallows, R. A., Tokumaru, M., Aguilar-Rodriguez, E., Gonzalez-Esparza, A., et al. (2017f). "The worldwide interplanetary scintillation (IPS) Stations (WIPSS) Network: Initial results from the October 2016 space-weather campaign," in Oral presentation at session 9 at the European space weather week 14, ESWW abstract, Oostende, Belgium, November 27–December, 01, 2017.

Bisi, M. M., Fallows, R. A., Jackson, B. V., Tokumaru, M., Gonzalez-Esparza, A., Morgan, J., et al. (2017g). "The worldwide interplanetary scintillation (IPS) Stations (WIPSS) Network October 2016 observing campaign: initial WIPSS data analyses," in Presentation SH21A-2648, AGU abstract, AGU Fall Meeting, New Orleans, LA, December 11–15, 2017.

Bisi, M. M., Jackson, B. V., Fallows, R. A., Chang, O., Tokumaru, M., Aguilar-Rodriguez, E., et al. (2018). "The worldwide interplanetary scintillation (IPS) stations (WIPSS) Network: recent campaign results including LOFAR and steps towards LOFAR for space weather (LOFAR4SW)," in Poster presentation at the 15th European space weather workshop, ESWW abstract Leuven, Belgium, November 5–9, 2018.

Brueckner, G. E., Howard, R. A., Koomen, M. J., Korendyke, C. M., Michels, D. J., Moses, J. D., et al. (1995). The Large Angle Spectroscopic Coronagraph (LASCO): visible light coronal imaging and spectroscopy. *Sol. Phys.* 162, 357–402. doi:10.1007/bf00733434.

Buffington, A., Morrill, J. S., Hick, P. P., Howard, R. A., Jackson, B. V., and Webb, D. F. (2007). Analysis of the comparative responses of SMEI and LASCO. *Proc. SPIE.* 6689, 66890B1–66890B6. doi:10.1117/12.734658

Chang, O., Jackson, B. V., González-Esparza, A., Yu, H.-S., and Mejia-Ambriz, J. (2016). "Incorporation of MEXART interplanetary scintillation (IPS) data into the UCSD 3-D tomography as part of the worldwide IPS Stations (WIPSS) initiative: enhancing space weather science and forecasting" in Poster presentation, SHINE workshop, Santa Fe, NM, July 11–15.

Domingo, V., Fleck, B., and Poland, A. I. (1995). The SOHO mission: an overview. *Sol. Phys.* 162, 1–37. doi:10.1007/bf00733425.

Dryer, M., Candelaria, C., Smith, Z. K., Steinolfson, R. S., Smith, E. J., Wolfe, J. H., et al. (1978). Dynamic MHD modeling of the solar wind disturbances during the August 1972 events. *J. Geophys. Res.* 83, 532–540. doi:10.1029/ja083ia02p00532.

Dunn, T., Jackson, B. V., Hick, P. P., Buffington, A., and Zhao, X. P., (2005). Comparative analyses of the CSSS calculation in the UCSD tomographic solar observations. *Sol. Phys.* 227, 339–353. doi:10.1007/s11207-005-2759-x.

Eyles, C. J., Harrison, R. A., Davis, C. J., Waltham, N. R., Shaughnessy, B. M., Mapson-Menard, H. C. A., et al. (2009). The heliospheric imagers onboard the STEREO mission. *Sol. Phys.* 254, 387–445. doi:10.1007/s11207-008-9299-0.

Eyles, C. J., Simnett, G. M., Cooke, M. P., Jackson, B. V., Buffington, A., Hick, P. P., et al. (2003). The solar mass ejection imager (SMEI). *Sol. Phys.* 217, 319–347. doi:10.1023/b:sola.0000006903.75671.49.

Fallows, R. A., Breen, A. R., Bisi, M. M., Jones, R. A., and Dorrian, G. D. (2007b). IPS using EISCAT and MERLIN: extremely-long baseline observations at multiple frequencies. Available at: www.prao.ru/conf/Colloquium/pres/Fallows.ppt (Accessed 2007).

Fallows, R. A., Breen, A. R., Bisi, M. M., Jones, R. A., and Dorrian, G. D. (2007a). Interplanetary scintillation using EISCAT and MERLIN: extremely long baselines at multiple frequencies. *Astronom. Astrophys. Trans.* 26(6), 489–500. doi:10.1080/10556790701612197.

Feng, X., Ma, X., and Xiang, C. (2015). Data-driven modeling of the solar wind from 1 Rsto 1 AU. *J. Geophys. Res. Space Phys.* 120, 10159. doi:10.1002/2015JA021911.

Gonzi, S., Weinzierl, M., Bocquet, F.-X., Bisi, M. M., Odstrcil, D., Jackson, B. V., et al. (2020). Impact of inner heliospheric boundary conditions on solar wind predictions at Earth. *Space Weather.* 10, 33–49. doi:10.1029/2020sw002499.

Gopalswamy, N., Yashiro, S., Michalek, G., Stenborg, G., Vourlidas, A., Freeland, S., et al. (2009). The SOHO/LASCO CME catalog. *Earth Moon Planet.* 104, 295–313. doi:10.1007/s11038-008-9282-7.

Hayashi, K., Kojima, M., Tokumaru, M., and Fujiki, K. (2003). MHD tomography using interplanetary scintillation measurement. *J. Geophys. Res.* 108(No. A3), 1102, doi:10.1029/2002JA009567.

Hayashi, K., Tokumaru, M., and Fujiki, K. i. (2016). MHD-IPS analysis of relationship among solar wind density, temperature, and flow speed. *J. Geophys. Res. Space Phys.* 121, 7367–7384. doi:10.1002/2016JA022750.

Hewish, A., and Bravo, S. (1986). The sources of large-scale heliospheric disturbances. *Sol. Phys.* 106, 185–200. doi:10.1007/bf00161362.

Hewish, A., Scott, P. F., and Wills, D. (1964). Interplanetary scintillation of small diameter radio sources. *Nature.* 203, 1214. doi:10.1038/2031214a0.

Hick, P. P., and Jackson, B. V. (2004). Heliospheric tomography: an algorithm for the reconstruction of the 3D solar wind from remote sensing observations. *Proc. SPIE.* 5171, 287–297. doi:10.1117/12.513122

Houminer, Z. (1971). Corotating plasma streams revealed by interplanetary scintillation. *Nat. Phys. Sci.* 231, 165–167. doi:10.1038/physci231165a0.

Howard, R. A., Moses, J. D., Vourlidas, A., Newmark, J. S., Socker, D. G., Plunkett, S. P., et al. (2008). Sun Earth connection coronal and heliospheric investigation (SECCHI). *Space Sci. Rev.* 136, 67. doi:10.1007/s11214-008-9341-4.

Howard, T. A., Bisi, M. M., Buffington, A., Clover, J. M., Cooke, M. P., Eyles, C. J., et al. (2013). The solar mass ejection imager and its heliospheric imaging legacy. *Space Sci. Rev.* 180, 1, doi:10.1007/s11214-013-9992-7.

Iwai, K., Shiota, D., Tokumaru, M., Fujiki, K., Den, M., and Kubo, Y. (2019). Development of a coronal mass ejection arrival time forecasting system using interplanetary scintillation observations. *Earth Planets Space.* 71(1), 39. doi:10.1186/s40623019-1019-5.

Jackson, B. V., and Hick, P. P. (2002). Corotational tomography of heliospheric features using global Thomson scattering data. *Sol. Phys.* 211, 344. doi:10.1023/a:1022409530466.

Jackson, B. V., and Hick, P. P. (2005). "Three-dimensional tomography of interplanetary disturbances, Chapter 17" in *Solar and space weather radiophysics, current status and future developments, Astrophysics and space science library.* Editors D. E. Gary and C. U. Keller (Dordrecht, The Netherlands: Kluwer Academic Publisher), vol. 314, 355–386.

Jackson, B. V., Hick, P. L., Kojima, M., and Yokobe, A. (1997). Heliospheric tomography using interplanetary scintillation observations. *Phys. Chem. Earth.* 22(5), 425. doi:10.1016/s0079-1946(97)00170-5.

Jackson, B. V., Hick, P. L., Kojima, M., and Yokobe, A. (1998). Heliospheric tomography using interplanetary scintillation observations 1. Combined Nagoya and Cambridge data', *J. Geophys. Res.* 103(12), 049. doi:10.1029/97ja02528.

Jackson, B. V., Buffington, A., and Hick, P. P. (2001). "A heliospheric imager for solar orbiter" in Proceedings of the solar encounter: the first solar orbiter workshop, Santa Cruz de Tenerife, Spain, May 14–18, ESA SP-493, 251.

Jackson, B. V., Hick, P. P., Buffington, A., Kojima, T. M., Fujiki, K., et al. (2003). Time-dependent tomography of hemispheric features using interplanetary scintillation (IPS) remote-sensing observations. Solar Wind Ten 679, 75–78. doi:10.1063/1.1618545

Jackson, B. V., Buffington, A., Hick, P. P., Altrock, R. C., Figueroa, S., Holladay, P. E., et al. (2004). The Solar Mass-Ejection Imager (SMEI) Mission. *Sol. Phys.* 225, 177–207. doi:10.1007/s11207-004-2766-3.

Jackson, B. V., Buffington, A., Hick, P. P., Wang, X., and Webb, D. (2006). Preliminary three-dimensional analysis of the heliospheric response to the 28 October 2003 CME using SMEI white-light observations. *J. Geophys. Res.* 111 (A4), A04S91. doi:10.1029/2004ja010942.

Jackson, B. V., Hick, P. P., Buffington, A., Bisi, M. M., Kojima, M., and Tokumaru, M. (2007). "Comparison of the extent and mass of CME events in the interplanetary medium using IPS and SMEI Thomson scattering observations," in *Scattering and scintillation in radio astronomy, astronomical and astrophysical transactions.* Editors I. Chashei and V. Shishov (London, UK: Oxford University Press), 477–487.

Jackson, B. V., Bisi, M. M., Hick, P. P., Buffington, A., Clover, J. M., and Sun, W. (2008a). Solar Mass Ejection Imager 3-D reconstruction of the 27–28 May 2003 coronal mass ejection sequence. *J. Geophys. Res.* 113, A00A15. doi:10.1029/2008JA013224.

Jackson, B. V., Hick, P. P., Buffington, A., Bisi, M. M., Clover, J. M., and Tokumaru, M. (2008b). Solar mass ejection imager (SMEI) and interplanetary scintillation (IPS) 3D-reconstructions of the inner heliosphere. *Adv. Geosci.* 21, 339–366. doi:10.1142/9789812838209_0025

Jackson, B. V., Hick, P. P., Buffington, A., Bisi, M. M., and Clover, J. M. (2009). SMEI direct, 3-D-reconstruction sky maps, and volumetric analyses, and their comparison with SOHO and STEREO observations. *Ann. Geophys.* 27, 4097. doi:10.5194/angeo-27-4097-2009.

Jackson, B. V., Buffington, A., Hick, P. P., Clover, J. M., Bisi, M. M., and Webb, D. F. (2010a). Smei 3D reconstruction of a coronal mass ejection interacting with a corotating solar wind density enhancement: the 2008 April 26 CME. *Astrophys. J.* 724, 829–834. doi:10.1088/0004-637x/724/2/829.

Jackson, B. V., Hick, P. P., Bisi, M. M., Clover, J. M., and Buffington, A. (2010b). Inclusion of in-situ velocity measurements into the UCSD time-dependent tomography to constrain and better-forecast remote-sensing observations. *Sol. Phys.* 265, 245–256. doi:10.1007/s11207-010-9529-0.

Jackson, B. V., Hick, P. P., Buffington, A., Bisi, M. M., Clover, J. M., Tokumaru, M., et al. (2011a). Three-dimensional reconstruction of heliospheric structure using iterative tomography: a review. *J. Atmos. Sol. Terr. Phys.* 73, 1–9. doi:10.1016/j.jastp.2010.10.007.

Jackson, B. V., Hamilton, M. S., Hick, P. P., Buffington, A., Bisi, M. M., Clover, J. M., et al. (2011b). Solar Mass Ejection Imager (SMEI) 3-D reconstruction of density enhancements behind interplanetary shocks: In-situ comparison near Earth and at STEREO. *J. Atmos. Sol. Terr. Phys.* 73, 1317–1329. doi:10.1016/j.jastp.2010.11.023.

Jackson, B. V., Hick, P. P., Buffington, A., Clover, J. M., and Tokumaru, M., (2012a). Forecasting transient heliospheric solar wind parameters at the locations of the inner planets. *Adv. Geosci.* 30, 93–115. doi:10.1142/9789814405744_0007.

Jackson, B. V., Clover, J. M., Hick, P. P., Yu, H.-S., Buffington, A., Bisi, M. M., et al. (2012b). *The 3D global forecast of inner heliosphere solar wind parameters from Remotely-sensed IPS data.* Maui, Hawaii: NSF SHINE abstract, SHINE, June 24–29, 2012.

Jackson, B. V., Clover, J. M., Hick, P. P., Buffington, A., Bisi, M. M., and Tokumaru, M. (2013). Inclusion of real-time in-situ measurements into the UCSD timedependenttomography and its use as a forecast algorithm. Sol. Phys. 258, 151–165. doi:10.1007/s11207-012-0102-x.

Jackson, B. V., Yu, H.-S., Buffington, A., and Hick, P. P. (2014). The dynamic character of the polar solar wind. *Astrophys. J.* 793, 54. doi:10.1088/0004-637X/793/1/54.

Jackson, B. V., Odstrcil, D., Yu, H.-S., Hick, P. P., Buffington, A., Mejia-Ambriz, J. C., et al. (2015). The UCSD kinematic IPS solar wind boundary and its use in the ENLIL 3-D MHD prediction model. *Space Weather.* 13, 104–115. doi:10.1002/2014SW001130.

Jackson, B. V., Yu, H.-S., Chang, O., Hick, P. P., Buffington, A., Tokumaru, M., et al. (2016a). "Space weather forecasting using remotely-sensed heliospheric IPS data sets from around the world—an inclusion of MEXART and BSA Pushchino data into the UCSD STELab IPS tomography," in Presentation at the space weather workshop, NOAA SWW abstract, Boulder, CO, April 25–29, 2016.

Jackson, B. V., Yu, H.-S., Buffington, A., Hick, P. P., Nishimura, N., Nozaki, N., et al. (2016b). Exploration of solar photospheric magnetic field data sets using the UCSD tomography. *Space Weather.* 14 (12), 1107–1124. doi:10.1002/2016SW001481.

Jackson, B. V., Yu, H.-S., Hick, P., Buffington, A., Chang, O., Gonzalez-Esparza, A., et al. (2016c). "Worldwide interplanetary scintillation stations (WIPSS) Use of the UCSD IPS tomography program for space weather forecasting," in Invited presentation at the KSWC space weather workshop, Jeju, South Korea, KSWC abstract, November 24–27, 2016.

Jackson, B., Yu, H.-S., Hick, P., Buffington, A., Tokumaru, M., Fujiki, K., et al. (2017). "*A world interplanetary scintillation stations (WIPSS) tomography program for space weather forecasting.*," in Invited oral presentation at the 2nd PSTEP international symposium, PSTEP 2 abstract, Kyoto, Japan, March 23–24, 2017.

Jackson, B. V., Yu, H. S., Buffington, A., Hick, P. P., Tokumaru, M., Fujiki, K., et al. (2019). A daily determination of Bz using the Russell–McPherron effect to forecast geomagnetic activity. *Space Weather.* 17, 639–652. doi:10.1029/2018SW002098.

Jackson, B. V., Hick, P. P., Yu, H. S., Buffington, A., and Odstrcil, D. (2020a). "Global heliospheric remote sensing: a Brief recent history," in Invited oral presentation at the 4th PSTEP international symposium, PSTEP 4 abstract, Nagoya, Japan, January 27–29, 2020.

Jackson, B. V., Cota, L., Buffington, A., Tokumaru, M., Bisi, M. M., and Fallows, R. (2020b). "ISEE-LOFAR tomography during the second PSP solar passage," in Invited virtual oral presentation at the LOFAR4SW user workshop hosted at Warsaw, Poland and the UK, by the LOFAR4SW consortium, LOFAR4SW abstract, Warsaw, Polland, May 13, 2020.

Jian, L. K., MacNeice, P. J., Taktakishvili, A., Odstrcil, D., Jackson, B., Yu, H.-S., et al. (2015). Validation for solar wind prediction at Earth: comparison of coronal and heliospheric models installed at the CCMC. *Space Weather.* 13, 316. doi:10.1002/2015SW001174.

Jian, L. K., MacNeice, P. J., Mays, M. L., Taktakishvili, A., Odstrcil, D., Jackson, B., et al. (2016). Validation for global solar wind prediction using ulysses comparison: multiple coronal and heliospheric models installed at the community coordinated modeling center. *Space Weather.* 14 (8), 592–611, doi:10.1002/2016sw001435.

Sokolov, M. L., Kucera, T. A., Davila, J. M., St. Cyr, O. C., Guhathakurta, M., and Christian, E. (2008). The STEREO mission: an introduction. *Space Sci. Rev.* 136, 5–16. doi:10.1007/s11214-007-9277-0.

Kim, T. K., Borovikov, S. N., Pogorelov, N. V., Yu, H.-S., Clover, J. M., and Jackson, B. V. (2012). "Time-dependent MHD simulations of the solar wind outflow using interplanetary scintillation observations," in AIP conference proceedings, 1500, space weather: the space radiation environment, 11th annual international astrophysics conference (CSPAR), Palm Springs, CA, March 19–23. Editors Q. Hu, G. Li, G. P. Zank, and X. Ao, 140–146.

Kim, T. K., Pogorelov, N. V., Borovikov, S. N., Jackson, B. V., Yu, H.-S., and Tokumaru, M. (2014). MHD heliosphere with boundary conditions from a tomographic reconstruction using interplanetary scintillation data. *J. Geophys. Res. Space Phys.* 119, 7981. doi:10.1002/2013JA019755.

Kojima, M., Asai, K., Hick, P. L., Jackson, B. V., Tokumaru, M., Watanabe, H., et al. (1997). "Solar wind structure at 0.1–1 AU reconstructed from IPS observations using tomography," in *Robotic exploration close to the Sun: scientific basis.* Editor S. R. Habbal (New York, NY: AIP Press), 97–103.

Kojima, M., Tokumaru, M., Watanabe, H., Yokobe, A., Asai, K., Jackson, B. V., et al. (1998). Heliospheric tomography using interplanetary scintillation observations: 2. Latitude and heliocentric distance dependence of solar wind structure at 0.1–1 AU. *J. Geophys. Res.* 103, 1981. doi:10.1029/97ja02162.

Liewer, P. C., De Jong, E. M., Hall, J. R., Howard, R. A., Thompson, W. T., Culhane, J. L., et al. (2009). Stereoscopic analysis of the 19 may 2007 erupting filament. *Sol. Phys.Sol Phys.* 256, 57–72. doi:10.1007/s11207-009-9363-4.

Liu, Y. D., Hu, H., Zhu, B., Luhmann, J. G., and Vourlidas, A., (2017). Structure, propagation, and expansion of a Cme-driven shock in the heliosphere: a revisit of the 2012 July 23 extreme storm. *Astrophys. J.* 834:158. doi:10.3847/1538-4357/834/2/158.

Luhmann, J. G., Ledvina, S. A., Odstrcil, D., Owens, M. J., Zhao, X.-P., Liu, Y., et al. (2010). Cone model-based SEP event calculations for applications to multipoint observations. *Adv. Space Res.* 46, 1–21. doi:10.1016/j.asr.2010.03.011.

Manchester, W. (2017). "The determination of heliospheric disturbances by simulations and observations," in Poster and oral presentation, SHINE workshop, NSF SHINE abstract, Saint-Sauveur, Canada, July, 23–28, 2017.

Manoharan, P. K. (2010). Ooty interplanetary scintillation—remote-sensing observations and analysis of coronal mass ejections in the heliosphere. *Sol. Phys.* 265, 137–157. doi:10.1007/s11207-010-9593-5.

McComas, D. J., Bame, S. J., Barker, P., Feldman, W. C., Phillips, J. L., Riley, P., et al. (1998). Solar wind electron proton Alpha monitor (SWEPAM) for the advanced composition explorer. *Space Sci. Rev.* 86, 563. doi:10.1023/a:1005040232597.

Meng, X. (2013). Connecting remote-sensing observations and MHD modeling towards a new generation of space weather prediction tools, proposal to the UCAR NASA LWS program.

Ogilvie, K. W., and Desch, M. D. (1997). The wind spacecraft and its early scientific results. *Adv. Space Res.* 20(445), 559–568. doi:10.1016/s0273-1177(97)00439-0.

Odstrcil, D., and Pizzo, V. J. (1999a). Three-dimensional propagation of coronal mass ejections (CMEs) in a structured solar wind flow. 1. CME launched within the streamer belt. *J. Geophys. Res.*, 104 (A1), 483–492. doi:10.1029/1999ja900319.

Odstrcil, D., and Pizzo, V. J. (1999b). Distortion of the interplanetary magnetic field by three-dimensional propagation of coronal mass ejections in a structured solar wind. *J. Geophys. Res.* 104(28), 225–228. doi:10.1029/1999ja900319.

Odstrcil, D., Riley, P., and Zhao, X. P. (2004). Numerical simulation of the 12 May 1997 interplanetary CME event. *J. Geophys. Res.* 109, A02116. doi:10.1029/2003JA010135.

Odstrcil, D., Pizzo, V. J., and Arge, C. N. (2005a). Propagation of the 12 May 1997 interplanetary coronal mass ejection in evolving solar wind structures. *J. Geophys. Res.* 110, A02106, doi:10.1029/2004JA010745.

Odstrcil, D., Pizzo, V. J., Arge, C. N., Jackson, B. V., and Hick, P. P. (2005b). First results from the 3-D MHD heliospheric simulations driven by the SMEI/IPS observations. *Proc. SPIE.* 259 (1–2), 297–309. doi:10.1007/s11207-009-9449-z

Odstrcil, D., Jackson, B. V., and Hick, P. (2007). "3-D numerical simulations of heliospheric disturbances driven by SMEI/IPS observations," in Paper presented at SEC space weather week, NOAA SWW abstract, Boulder, CO, April 24–27, 2007.

Odstrcil, D., Pizzo, V. J., Arge, C. N., Bisi, M. M., Hick, P. P., Jackson, B. V., et al. (2008). Numerical simulations of solar wind disturbances by coupled models. *ASP Conf. Ser. Proc.* 385, 167–173. doi:10.1007/s11207-015-0685-0

Parker, E. N. (1958). Dynamics of the interplanetary gas and magnetic fields. *Astrophys. J.* 128, 664–676. doi:10.1086/146579.

Pogorelov, N., Borovikov, S., Ebert, R., Jackson, B., Kim, T., Linker, J., et al. (2012). "Modeling Heliosheath flow with observational boundary conditions," in Paper presented at the 39th COSPAR scientific assembly, COSPAR abstract, Mysore, India, July 14–22, 2012.

Pomoell, J., and Poedts, S. (2018). EUHFORIA: European heliospheric forecasting information asset. *J. Space Weather Space Clim.* 8, A35. doi:10.1051/swsc/2018020.

Riley, P., Lionello, R., Mikić, Z., and Linker, J. (2008). Using global simulations to relate the three-part structure of coronal mass ejections to in situ signatures. *Astrophys. J.* 672, 1221. doi:10.1086/523893.

Sachedeva, N., van der Holst, B., Manchester, W. B., Toth, G., Chen, Y., Lloveras, D. G., et al., (2019). Validation of the Alfvén Wave Solar Atmosphere Model (AWSoM) with Observations from the Low Corona to 1 au. *Astrophs. J.* 887, 83. doi:10.3847/1538-4357/ab4f5e.

Shen, F., Shen, C., Zhang, J., Hess, P., Wang, Y., Feng, X., et al. (2014). Evolution of the 12 July 2012 CME from the Sun to the Earth: Data-constrained three-dimensional MHD simulations. *J. Geophys. Res. Space Phys.* 119, 7128–7141. doi:10.1002/2014JA020365.

Shiota, D., and Kataoka, R., (2016). Magnetohydrodynamic simulation of interplanetary propagation of multiple coronal mass ejections with internal magnetic flux rope (SUSANOO-CME). *Space Weather.* 14, 56–75. doi:10.1002/2015SW001308.

Steinolfson, R. S., Dryer, M., and Nakagawa, Y., (1975). Numerical MHD simulation of interplanetary shock pairs. *J. Geophys. Res.* 80, 1223–1231. doi:10.1029/ja080i010p01223.

Stone, E. C., Frandsen, A. M., Mewaldt, R. A., Christian, E. R., Margolies, D., Ormes, J. F., et al. (1998). The advanced composition explorer. *Space Sci. Rev.* 86, 1. doi:10.1023/a:1005082526237.

Tokumaru, M., Kojima, M., Fujiki, K. i., Yamashita, M., and Jackson, B. V. (2007). The source and propagation of the interplanetary disturbance associated with the full-halo coronal mass ejection on 28 October 2003. *J. Geophys. Res.* 112, 39. doi:10.1029/2006JA012043.

Tokumaru, M., Kojima, M., Fujiki, K., Maruyama, K., Maruyama, Y., Ito, H., et al. (2011). A newly developed UHF radiotelescope for interplanetary scintillation observations: solar wind imaging facility. *Radio Sci.* 46, RS0F02. doi:10.1029/2011RS004694.

Van Harlem, M. P., Wise, M. W., Gunst, A. W., Heald, G., McKean, J. P., Hessels, J. W., et al. (2013). LOFAR: the low-frequency array. *Astron. Astrophys.* 556, 29. doi:10.1109/iwem.2011.6021486

Wang, Y.-M., and Sheeley, N. R. J. (1990). Solar wind speed and coronal flux-tube expansion. *Astrophys. J.* 355, 726–732. doi:10.1086/168805.

Webb, D. F., and Jackson, B. V. (1981). Kinematical analysis of flare spray ejecta observed in the corona. *Sol. Phys.Sol Phys.* 73, 341–361. doi:10.1007/bf00151686.

Wu, C.-C., Fry, C,D., Wu, S.T., Dryer, M., and Liou, K. (2007). Three-dimensional global simulation of interplanetary coronal mass ejection propagation from the Sun to the heliosphere: Solar event of 12 May 1997. *J. Geophys. Res.* 112, A09104.

Wu, C. C., Liou, K., Vourlidas, A., Plunkett, S., Dryer, M., Wu, S. T., et al. (2016). Global magnetohydrodynamic simulation of the 15 March 2013 coronal mass ejection event-Interpretation of the 30-80 MeV proton flux, *J. Geophys. Res. Space Phys.* 121, 56–76. doi:10.1002/2015JA021051.

Wu, S. T., Dryer, M., and Han, S. M. (1983). Non-planar MHD model for solar flare-generated disturbances in the heliospheric equatorial plane. *Sol. Phys.* 84, 395–418. doi:10.1088/0004-637x/784/2/166.

Young, A. T. (1971). Interpretation of interplanetary scintillations. *Astrophys. J.*, 168, 543–562.

Yu, H.-S., Jackson, B. V., Hick, P. P., Buffington, A., Clover, J. M., et al. (2012). "3-D reconstruction of the inner heliosphere from remote-sensing data: a global solar wind boundary that includes CME transient effects," in AIP conference proceedings, 1500, space weather: the space radiation environment, 11th annual international astrophysics conference (CSPAR), Palm springs, CA, March 19–23. Editors Q. Hu, G. Li, G. P. Zank, and X. Ao, 147–152.

Yu, H.-S., Jackson, B. V., Buffington, A., and Hick, P. P. (2014). The 3D Analysis of *Hinode* Polar Jets Using Images From LASCO C2, the STEREO COR 2 Coronagraphs, and the Solar Mass Ejection Imager (SMEI). *Astrophys. J.*, 784, 166. doi:10.1088/0004-637X/784/2/166.

Yu, H.-S., Jackson, B. V., Hick, P. P., Buffington, A., Odstrcil, D., Wu, C.-C., et al. (2015). 3D reconstruction of interplanetary scintillation (IPS) remote-sensing data: global solar wind boundaries for driving 3D-MHD models. *Sol. Phys.Sol Phys.*, 290, 2519–2538. doi:10.1007/s11207-015-0685-0.

Yu, H.-S., Jackson, B. V., Yang, Y.-H., Chen, N.-H., Buffington, A., and Hick, P. P. (2016). A 17 June 2011 polar jet and its presence in the background solar wind', *J. Geophys. Res. Space Phys.* 121, 4985–4997. doi:10.1002/2016JA022503.

Zhao, X., and Hoeksema, J. T. (1995). Prediction of the interplanetary magnetic field strength. *J. Geophys. Res.* 100, 19–33. doi:10.1029/94ja02266. CrossRef Full Text

Conflict of Interest: The authors declare that the research was conducted in the absence of any commercial or financial relationships that could be construed as a potential conflict of interest.

frontiers in Astronomy and Space Sciences

REVIEW
published: 06 January 2021
doi: 10.3389/fspas.2020.591075

Radio Measurements of the Magnetic Field in the Solar Chromosphere and the Corona

Costas E. Alissandrakis and Dale E. Gary*

Department of Physics, University of Ioannina, Ioannina, Greece

The structure of the upper solar atmosphere, on all observable scales, is intimately governed by the magnetic field. The same holds for a variety of solar phenomena that constitute solar activity, from tiny transient brightening to huge Coronal Mass Ejections. Due to inherent difficulties in measuring magnetic field effects on atoms (Zeeman and Hanle effects) in the corona, radio methods sensitive to electrons are of primary importance in obtaining quantitative information about its magnetic field. In this review we explore these methods and point out their advantages and limitations. After a brief presentation of the magneto-ionic theory of wave propagation in cold, collisionless plasmas, we discuss how the magnetic field affects the radio emission produced by incoherent emission mechanisms (free-free, gyroresonance, and gyrosynchrotron processes) and give examples of measurements of magnetic filed parameters in the quiet sun, active regions and radio CMEs. We proceed by discussing how the inversion of the sense of circular polarization can be used to measure the field above active regions. Subsequently we pass to coherent emission mechanisms and present results of measurements from fiber bursts, zebra patterns, and type II burst emission. We close this review with a discussion of the variation of the magnetic field, deduced by radio measurements, from the low corona up to ∼ 10 solar radii and with some thoughts about future work.

Keywords: sun, solar radio emission, solar magnetic field, solar chromosphere, solar corona

OPEN ACCESS

Edited by:
Xueshang Feng, National Space Science Center (CAS), China

Reviewed by:
Aleksander Stanislavsky, National Academy of Sciences of Ukraine, Ukraine
David Wexler, Massachusetts Institute of Technology, United States

****Correspondence:***
Costas E. Alissandrakis
calissan@uoi.gr

Specialty section:
This article was submitted to Stellar and Solar Physics, a section of the journal Frontiers in Astronomy and Space Sciences

Received: *03 August 2020*
Accepted: *02 September 2020*
Published: *06 January 2021*

Citation:
Alissandrakis CE and Gary DE (2021) Radio Measurements of the Magnetic Field in the Solar Chromosphere and the Corona. Front. Astron. Space Sci. 7:591075. doi: 10.3389/fspas.2020.591075

1. INTRODUCTION

The sun is made up of plasma and magnetic field. The latter affects practically all solar phenomena, in all layers of the solar atmosphere. The structure of the atmospheric layers in particular, is the result of the interaction of the plasma with the magnetic field. Contrary to the photosphere, the magnetic energy density in the chromosphere and the corona is much higher than the energy density of the plasma; consequently, as pointed out in the review of Alissandrakis, 2020 on the solar atmospheric structure in this special research topic collection, it is the magnetic field that gives the chromosphere and the corona their highly structured appearance. Plasma, electric current, heat, all flow along channels provided by the lines of force of the magnetic field. The exception is phenomena that release a large amount of energy, so large that it can completely restructure the ambient magnetic field.

In order to understand how the Sun works, but also in order to predict the effect of solar phenomena near the Earth in the context of space whether, we need quantitative information on the parameters of both the plasma and the magnetic field, with the highest spatial, spectral, and

temporal resolution possible. Since *in situ* measurements are impossible in the solar atmosphere (the *Parker Solar Probe* will not go closer than $\sim$ 10 R$\odot$) and rare in the inner heliosphere, we need to rely on information carried by the electromagnetic radiation. This requires identification of the emission mechanisms and accurate knowledge of the dependence of the characteristics of the radiation on the physical parameters, which affect both the emission and the transfer of the radiation. The magnetic field affects all radiative processes thus, once we can describe quantitatively its influence, we can measure its value.

As the corona is shaped by the magnetic field, qualitative information is easy to obtain: just look at an image in the EUV or soft X-rays (and they are plenty these days thanks to the advancements in space instrumentation) and you will have a map of the topology of the magnetic field lines of force (or at least those with sufficient density to be visible at those wavelengths); you can identify open and closed magnetic configurations, connectivity of magnetic regions, restructuring of the magnetic field by energetic phenomena. Eclipse and coronograph images are equally important, with the limitation of the projection effects and the fact that we can only see above the limb. Images at radio wavelengths (Alissandrakis et al., 1985; Mercier and Chambe, 2009; Gary et al., 2018; Vocks et al., 2018; McCauley et al., 2019) do not have this limitation, and in addition provide measurements in regions that are dark and unobservable at other wavelengths.

Quantitative information on the magnetic field is much more difficult to obtain. The most efficient method of measurement, employing the Zeeman effect on line emission from ions, is extremely difficult to apply because of the weak intensity of coronal lines and their large thermal broadening (Solanki et al., 2006; Cargill, 2009). Many years ago circular polarization in the wings of the CIV line (formed in the transition region at $T \sim 10^5$ K) was observed above sunspots (Henze et al., 1982; Hagyard et al., 1983), giving magnetic field strength of ~1,100–1,400 G. The situation is better in the infrared, e.g., in the Fe XIII 10,747 Å line, which was used by Lin et al. (2000, 2004) to deduce field strengths from a few to $\sim$ 30 G in active regions, 0.12–0.15 R$\odot$ above the solar limb. The disadvantage of such measurements is that they integrate over a large region along the line of sight and they require a long integration time (>60 s). The Hanle effect (Trujillo Bueno, 2010), in which the scattering polarization in a spectral line is modified by the magnetic field, is also a very useful diagnostic, particularly in prominences; however, the associated linear polarization is difficult to observe and to interpret. Finally, oscillations in coronal loops (Stepanov et al., 2012) have provided indirect evidence of magnetic fields of a few tens of G (e.g., Van Doorsselaere et al., 2008).

All the above methods suffer from important observational or theoretical difficulties. As a consequence, the most reliable method for measuring the magnetic field in the corona is through its influence on the radio emission which we will present in this review. As a matter of fact, the magnetic field enters in all processes that produce radio emission, but here we will select those that can better serve as diagnostics. There are some general reviews on the subject such as those of Dulk and McLean (1978), Zlotnik (1994), and White (2005), as well as several others on particular techniques that will be referred to in the relevant sections of this review.

We begin by discussing the influence of the magnetic field on the propagation of radio waves and on the free-free emission mechanism. We proceed with magnetic field measurements based on the gyroresonance and the gyrosynchrotron emission mechanisms and then discuss diagnostics based on wave propagation. We continue with diagnostics from metric burst emission and finish with a summary and a discussion of prospects.

2. BASIC CONCEPTS: WAVE PROPAGATION AND POLARIZATION

Many radio diagnostics of the magnetic field are based on the polarization of the emission. We will therefore devote this section to the propagation of electromagnetic waves in the solar atmosphere, which is well described by the magnetoionic theory of high frequency waves in a cold, collisionless plasma (see, e.g., Chapter VI in Zheleznyakov, 1970). In the presence of magnetic field, the theory predicts two wave modes, the extraordinary (x-mode) and the ordinary (o-mode), which differ in their index of refraction and their polarization The index of refraction, n_j, in the cold collisionless plasma is determined by the plasma frequency parameter, υ, and the electron gyrofrequency parameter, u:

$$n_j^2 = 1 - \frac{2\upsilon(1-\upsilon)}{2(1-\upsilon) - u\sin^2\theta \mp \sqrt{u^2\sin^4\theta + 4u(1-\upsilon)^2\cos^2\theta}} \tag{1}$$

Where $j = 1$ and the upper sign in the denominator corresponds to the extraordinary mode, $j = 2$ and the lower sign corresponds to the ordinary mode; θ is the angle between the magnetic field in the direction of wave propagation (i.e., the line of sight, in the absence or refraction). The dimensionless parameters u and υ are defined as:

$$u = \left(\frac{\omega_{ce}}{\omega}\right)^2 \quad \text{and} \quad \upsilon = \left(\frac{\omega_{pe}}{\omega}\right)^2 \tag{2}$$

where $\omega = 2\pi f$ is the angular frequency of the wave (radians s^{-1}) and f the observing frequency (cycles s^{-1}). Thus u is a measure of the magnetic field, B, through the electron gyrofrequency, ω_{ce}, while the parameter υ expresses the electron density, N_e, through the plasma frequency, ω_{pe}:

$$\omega_{ce} = eB/m_e c \quad \text{and} \quad \omega_{pe}^2 = 4\pi N_e e^2/m_e \tag{3}$$

All equations here are presented in cgs units and the magnetic field strength is given in Gauss (G), with 10,000 G = 1 Tesla.

Some readers may recognize Equation (1) as the Appleton-Hartree or Appleton-Lassen equation, which is usually written in terms of variables $X = \upsilon$ and $Y = \sqrt{u}$ (see Ratcliffe, 1959; Melrose, 1985). Substituting numerical values in Equations (2) and (3), we obtain:

$$f_{pe}\ [\text{MHz}] = 8.978 \times 10^{-3}\sqrt{N_e[\text{cm}^{-3}]}$$
$$\text{and} \quad f_{ce}\ [\text{MHz}] = 2.8B\ [\text{G}] \tag{4}$$

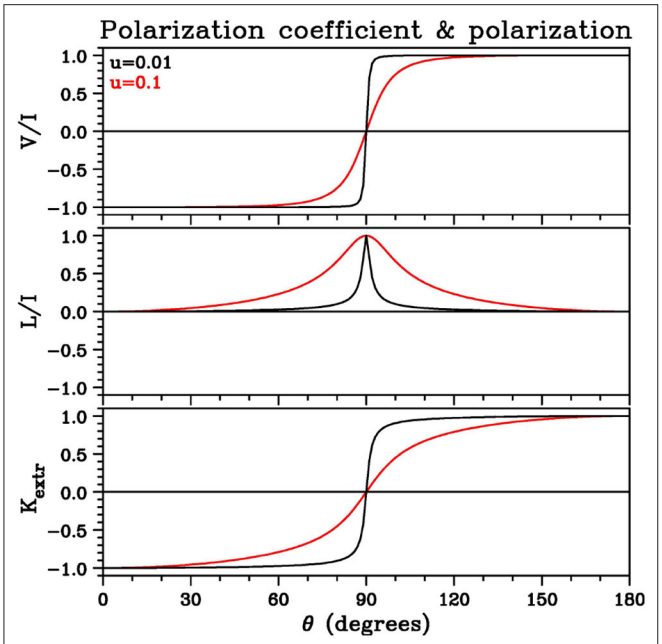

FIGURE 1 | Dependence of the extraordinary mode polarization coefficient, K, as well as of the fraction of linear (L/I) and circular (V/I) polarization, on the angle between the magnetic field and the line of sight, at the limit of small υ and for two values of u.

Note that for frequencies well above the gyrofrequency and the plasma frequency, as is usually the case, both u and υ are much smaller than unity in the optical and the short-λ radio range. The waves do not propagate in regions where $n_j^2 \leq 0$.

Taking a coordinate system with the z-axis in the direction of the wave propagation and the magnetic field in the y-z plane, the polarization of the electromagnetic wave, K_j, is the ratio of the x and y components of the electric field amplitude of the wave, $\tilde{E}$:

$$\frac{\tilde{E}_{yj}}{\tilde{E}_{xj}} = iK_j \tag{5}$$

where i is the imaginary operator. In the general case, the waves will also have an electrostatic component, parallel to the direction of propagation:

$$\frac{\tilde{E}_{zj}}{\tilde{E}_{xj}} = i\Gamma_j \tag{6}$$

The polarization parameters K_j and Γ_j are given by the expressions (Zheleznyakov, 1970):

$$K_j = -\frac{2\sqrt{u}(1-\upsilon)\cos\theta}{u\sin^2\theta \pm \sqrt{u^2\sin^4\theta + 4u(1-\upsilon)^2\cos^2\theta}} \tag{7}$$

and

$$\Gamma_j = -\frac{\sqrt{u}\upsilon\sin\theta + u\upsilon\sin\theta\cos\theta K_j}{1-u-\upsilon+u\upsilon\cos^2\theta} \tag{8}$$

As implied by Equation (5), the x and y components of the wave have a phase difference of 90°, hence in the general case the waves are elliptically polarized with the axes of the ellipse along the x and y axes. Note also that the two waves are polarized in opposite senses, since

$$K_1 K_2 = -1 \tag{9}$$

The sign of K_j determines the sense of polarization; for the x-mode the electric field vector rotates in the same sense as the electrons. The polarization is circular if $K_j = \pm 1$ ($\theta = 0$ or $\theta = 180°$); $K = +1$ is right circular polarization, i.e., counterclockwise rotation in the x-y wave plane if the wave is propagating toward the observer by standard physics convention. $K = -1$ is left circular polarization. The linearly polarized part of the extraordinary mode is perpendicular to magnetic field and that of the ordinary is along the magnetic field. The polarization is linear if $K_j = 0$ or $K_j = \infty$ ($\theta = 90°$). The electrostatic (longitudinal) component of the wave, expressed by the parameter Γ_j, is usually very small.

Figure 1 shows the dependence of the polarization coefficient for the extraordinary mode on the angle between the magnetic field and the line of sight, at the low υ limit, for $u = 0.1$ and $u = 0.01$, which correspond to magnetic field of 570 and 180 G, respectively at 6 cm. The same figure shows the degree of linear and circular polarization ($L/I = \sqrt{Q^2+U^2}/I$ and V/I). Note that, for small υ and u, the polarization is very close to circular for a wide range of propagation angles near zero (*quasi-longitudinal propagation*, QL), whereas it is linear within a limited angle range around 90° (*quasi-transverse propagation*, QT). Thus, in general, solar sources are expected to exhibit circular polarization.

The conditions for QL propagation are (Zheleznyakov, 1970):

$$\frac{u\sin^4\theta}{4\cos^2\theta} << (1-\upsilon)^2, |1-\sqrt{u}\cos\theta| >> \frac{(1+\upsilon)u\sin\theta}{2(1-\upsilon^2)} \tag{10}$$

which lead to the approximate expressions:

$$n_j = 1 - \frac{\upsilon}{1 \mp \sqrt{u}|\cos\theta|} \tag{11}$$

$$K_j = \mp|\cos\theta|/\cos\theta \tag{12}$$

The QT propagation holds when

$$\frac{u\sin^4\theta}{4\cos^2\theta} >> (1-\upsilon)^2, \tan^2\theta >> 1+\upsilon \tag{13}$$

and in this case:

$$n_1 \simeq 1 - \frac{\upsilon(1-\upsilon)}{1-\upsilon-u\sin^2\theta}, n_2 \simeq 1-\upsilon \tag{14}$$

$$K_1 \simeq -\frac{(1-\upsilon)\cos\theta}{\sqrt{u}}, K_2 \simeq -\frac{\sqrt{u}}{(1-\upsilon)\cos\theta} \tag{15}$$

It is important to note that the polarization of the two modes depends only on the properties of the medium in which they propagate and not on the emission mechanism. Therefore, the polarization characteristics are expected to change along the

path of the waves, reflecting the local values of the plasma parameters u and υ as well as the angle θ. This is true as long as the geometrical optics approximation is valid, where the two modes propagate independently of each other (weak coupling) and each mode retains its identity as it propagates toward the observer. There is, however, a region along the path where the coupling of the modes becomes strong and the polarization characteristics lock and change no further; this leads to the concept of limiting polarization.

The observed polarization of the radio emission is determined by two factors: (a) the intensity difference between the oppositely polarized extraordinary and ordinary modes, ($T_{b,1} - T_{b,2}$, in terms of brightness temperature) and (b) the conditions of propagation until the region of limiting polarization is reached. As a consequence, the observed polarization can be quite different from that at the source, in particular if the orientation of the magnetic field reverses along the line of sight.

Going back to the concept of limiting polarization we note that for QL propagation, the condition for strong coupling is (Cohen, 1960; Zheleznyakov, 1970; Bandiera, 1982):

$$C \simeq \frac{1}{2\pi}\frac{1}{\upsilon}\tan^2\theta\frac{\lambda}{L_B} > 1 \tag{16}$$

where C is the coupling coefficient, L_B is the scale of the magnetic field, and λ is the wavelength. Substituting numerical values we conclude that strong coupling occurs for very low values of density, thus coupling is not expected to affect the observed polarization in the QL case. Much more important is the case of QT propagation, which will be treated in section 6.

3. FREE-FREE EMISSION

3.1. Circular Polarization Measurements

Free-free (f-f, bremmstrahlung, see review by Nindos, 2020 in this special research topic collection; see also Gelfreikh, 2004) is the principal emission mechanism for thermal plasma in the absence of gyroresonance emission ($\sqrt{u} \neq 1, 1/2, 1/3, 1/4,...$). The absorption coefficient, k_j, is slightly different for the two wave modes and, in the QL approximation, is given by:

$$k_j = \frac{k}{(1 \mp \sqrt{u} \mid \cos\theta \mid)^2} \tag{17}$$

where k is the absorption coefficient in the unmagnetized case, given by the well-known approximate expression (e.g., Kundu, 1965)

$$k_j(T_e, N_e) = \xi\frac{N_e^2}{n_j f^2 T_e^{3/2}} \tag{18}$$

where ξ depends upon the collision frequency and is a slowly varying function of the electron temperature, T_e, and the electron density, N_e; its approximate value is $\xi \simeq 0.11$ in the chromosphere and $\xi \simeq 0.16$ in the corona (for a more detailed expression see the review by Nindos, 2020 in this special research topic collection). Note that, as pointed out by Chambe and Lantos (1971), for more accurate computations the term N_e^2 should be replaced by $N_e \sum_i N_i z_i$, where N_i and z_i are the ion density and charge and the sum is over all ions; this, for a H/He atmosphere, will increase the value of ξ to 0.14 in the chromosphere and 0.20 in the corona.

Equation (17) implies that the opacity of the plasma in ordinary radiation will be slightly less than that in the extraordinary, hence the ordinary mode emission will come from lower layers of the atmosphere. If the temperature increases with height, i.e., if the radiation is formed above the temperature minimum, as is the case with solar radio emission, the net effect will be weakly polarized emission in the sense of the extraordinary mode. This is a powerful diagnostic of the magnetic field, because we can immediately obtain qualitative information. Polarized emission reveals the presence of magnetic field and its sense gives the direction of the field with respect to the line of sight: right hand circular polarization corresponds to positive magnetic field, left hand circular to negative. We should note however that, far from the center of the disk, the observed circular polarization may be influenced by propagation effects, as we will discuss in section 6.

Quantitative magnetic field information is harder to extract. The simplest case is that of an optically thin uniform slab (cloud model, see Equation 11 in the review of Alissandrakis, 2020 on the solar atmospheric structure in this special research topic collection) above a uniform background. In this case the brightness temperature, T_{bj}, will be:

$$T_{bj} = T_{bo}e^{-\tau_j} + T_e(1 - e^{-\tau_j}) \simeq T_{bo}(1 - \tau_j) + \tau_j T_e \tag{19}$$

where T_{bo} is the background brightness, T_e the electron temperature and τ_j the optical thickness of the slab ($\tau_j \ll 1$ for an optically thin slab). In terms of Stokes parameters I (total intensity, here measured above the background) and V (circular polarization) we have:

$$I = \frac{1}{2}(T_{b,1} + T_{b,2}) - T_{bo} = (\tau_1 + \tau_2)(T_e - T_{bo}) \tag{20}$$

$$V = \frac{1}{2}(T_{b,1} - T_{b,2}) = (\tau_1 - \tau_2)(T_e - T_{bo}) \tag{21}$$

and the fractional polarization, ρ, is:

$$\rho = \frac{V}{I} \simeq \frac{\tau_1 - \tau_2}{\tau_1 + \tau_2} = \frac{k_1 - k_2}{k_1 + k_2} = 2\sqrt{u}\cos\theta \tag{22}$$

Substituting numerical values, Equation (22) gives for the longitudinal component of the magnetic field:

$$B\cos\theta \ [\mathrm{G}] \simeq 5400\frac{\rho}{\lambda\,[\mathrm{cm}]} \tag{23}$$

Thus a 10% polarization at $\lambda = 5$ cm requires a magnetic field of 110 G, while at $\lambda = 1$ cm the required strength is 540 G. An example is given in **Figure 2** which shows I and V images of a facular region obtained with the Nobeyama Radioheliograph (NoRH), together with an MDI magnetogram. We note immediately that the sense of the circular polarization corresponds to the sign of the longitudinal component of the

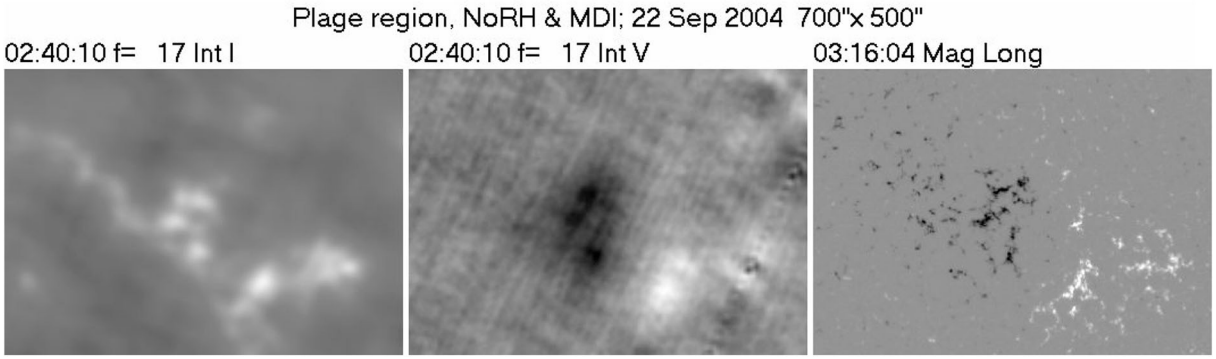

FIGURE 2 | Nobeyama radioheliograph (NoRH) images of a facular region at 17 GHz, in Stokes *I* **(left)** and *V*, **(middle)** together with an MDI magnetogram **(right)**. The NoRH images are full day averages. This region is located near the central meridian in the images shown in **Figure 3**. Images produced by the authors.

photospheric magnetic field. Moreover, the peak values of V are $\sim \pm 90$ K while I is $\sim$ 4, 300 K above the background. Using Equation (23), we obtain a magnetic field in the range of ± 100 G, which compares rather well to the photospheric values which are in the range of ± 350 G, taking into account the lower resolution of the NoRH and the higher altitude of formation of the radiation at 17 GHz. Note that the NoRH does not have the necessary resolution to reveal the small scale magnetic field associated with the chromospheric network, while high resolution observations (e.g., Bastian et al., 1996) with the Very Large Array (VLA) have not been capable of detecting the relatively low polarization signal. Still, in a recent work, Bogod et al. (2015) reported polarization of 1.4–7% and magnetic field in the range of 40–200 G from RATAN-600 observations of the quiet Sun.

Things are more complicated in the general case, where physical conditions vary with height. If spectral observations are available, one can use the approximate expression obtained by Bogod and Gelfreikh (1980) (see also Grebinskij et al., 2000) to estimate the longitudinal component of the magnetic field, B_ℓ:

$$B_\ell \simeq 107 \frac{\rho[\%]}{a\,\lambda[cm]} \tag{24}$$

where a is the spectral index:

$$a = -\frac{\ln T_b}{\ln f} \tag{25}$$

This expression allows for temperature variations in the region of formation of the radiation and its validity is not limited to the optically thin case, but it implicitly assumes constant magnetic field. Using this method, the above authors estimated the magnetic field above a plage to be about 40 G.

Polarization measurements are scarce beyond the cm-λ range. Using RATAN-600 data, Borovik et al. (1999) measured the circular polarization of an isolated equatorial coronal hole and reported values in the range of 0.2% at $\lambda = 9$ cm to 3–4% at 30 cm; using Equation (24), they deduced magnetic field values from $\sim$ 2 G at 2 cm to $\sim$ 10 G at 9 cm, a rather surprising result since one would expect the magnetic field to decrease with height and, hence, with λ. At still longer wavelengths, Ramesh et al. (2010) reported $\sim$ 10% and $\sim$ 15% circular polarization at 109 and 77 MHz, respectively (1.5 and 1.7 $R_\odot$), from Gauribidanur data. They attributed the emission to coronal streamers and estimated field values of 5 and 6 G. Recently, McCauley et al. (2019) measured the polarization of coronal holes and reported values up to 5–8%, but they made no estimates of the magnetic field.

3.2. Faraday Rotation of Celestial Sources

At larger angular distances from the Sun, the magnetic field of structures in the corona and the solar wind can be estimated from the Faraday rotation of linearly polarized celestial radio sources (Spangler, 2005; Bird, 2007). The position angle of the polarization changes by:

$$\Delta\chi = \frac{e^3}{2\pi m_e^2 c^4}\lambda^2 \int_{LOS} N_e \boldsymbol{B}\cdot\boldsymbol{ds} \tag{26}$$

where λ is the observing wavelength and $\boldsymbol{ds}$ the path increment along the line of sight (LOS); this expression contains information both about the magnetic field $\boldsymbol{B}$ and the electron density N_e that has to be untangled (see e.g., Kooi et al., 2014).

Ingleby et al. (2007) reported that the magnitude of the coronal field necessary to reproduce the majority of their Faraday rotation observations was in the range of 46–120 mG, at a reference heliocentric distance of 5 $R_\odot$; however, they could not definitively associate their measurements with any specific coronal structures. Mancuso and Garzelli (2013) used white-light coronograph data to compute the electron density distribution along the line of sight and concluded that, the radial magnetic field, B_r, as a function of the heliocentric distance, R, could be approximated by:

$$B_r = 3.76\left(\frac{R}{R_\odot}\right)^{-2.29} \quad [\mathrm{G}] \tag{27}$$

for heliocentric distances from about 5 to 14 $R_\odot$; this gives 94 mG at 5 $R_\odot$. Kooi et al. (2017) also used white-light information and deduced fields of $\sim$ 11 mG for two CMEs located at heliocentric

distance of around 10 $R_\odot$ and 2.4 mG for a jet-like CME at $\sim$ 8 $R_\odot$.

Faraday rotation measurements of interplanetary space probe signals, such as Helios (e.g., Pätzold et al., 1987; Efimov et al., 2015) and MESSENGER (e.g., Wexler et al., 2019) can provide information on the magnetic field lower in the corona, but this information is highly dependent on electron density models and variations of the magnetic field in the region of closest solar approach. Pätzold et al. (1987) deduced the following relation:

$$B_r = \left(\frac{6}{R^3} + \frac{1.18}{R^2}\right) \quad [\mathrm{G}] \tag{28}$$

valid for R between 2 and 9 solar radii. Wexler et al. (2019) quote values of 1,000–12,000 nT (10–120 mG) at 1.61 $R_\odot$.

4. GYRORESONANCE EMISSION

Gyroresonance (g-r) emission is produced by thermal electrons gyrating around the lines of force of the magnetic field. It is strong in regions where the observing frequency, f, is a low order harmonic (2nd to 4th) of the electron gyrofrequency, $\omega_{ce} = eB/m_e c$; thus, for a given harmonic s, the following numerical relation holds between the wavelength of observation and the magnetic field:

$$B\,[G] = \frac{10700}{s\lambda\,[\mathrm{cm}]} = \frac{360 f\,[\mathrm{GHz}]}{s} \tag{29}$$

Consequently a fairly high magnetic field is necessary (e.g., 600 G for third harmonic emission at 6 cm-λ). Although gyroresonance radiation is emitted at discrete frequencies, it generally gives rise to a continuous spectrum due to the variation of the magnetic field with height; there are some exceptions to this, as will be discussed in section 4.2.

4.1. The Magnetic Field Above Sunspots

Due to their high magnetic field strength, sunspots are an obvious place to look for gyroresonance emission; historically, sources of localized microwave emission were discovered first (Kundu, 1959) and then the emission mechanism was identified (Kakinuma and Swarup, 1962; Zheleznyakov, 1962). The emission is generated in thin layers around iso-Gauss surfaces where the magnetic field strength is such that the observing frequency is equal to a harmonic of the local gyro-frequency; the surfaces of harmonic layers are nicely displayed in Figure 8 of Lee (2007).

The close association of the g-r emission to the magnetic field, makes it a valuable tool for the study of the atmospheric layers above sunspots and for magnetic field measurements (e.g., Gelfreikh, 1998). This has stimulated a large amount of theoretical and observational work over a long period of time, particularly after the first high resolution observations by Kundu and Alissandrakis (1975) and the first detailed modeling by Alissandrakis et al. (1980). Recent works are reviewed by White (2004) and Lee (2007). High-resolution multi-wavelength observations of sunspots can be used to test in detail models of magnetic field extrapolation from measurements at the photosphere (Lee et al., 1998a). In general, observations and modeling can provide valuable diagnostics of the active region atmosphere and magnetic field, in particular if high spatial resolution spectral data are available (e.g., Tun et al., 2011; Nita et al., 2018; Stupishin et al., 2018; Alissandrakis et al., 2019a).

The g-r opacity (Kakinuma and Swarup, 1962; Zheleznyakov, 1962) is a complicated function of the temperature, the density, the intensity of the magnetic field, the wave mode and has a strong dependence on the direction of the field with respect to the line of sight, being zero when these are parallel. It is much greater in the extraordinary mode than in the ordinary, it is also much greater at the second harmonic than at the third; thus, under conditions prevailing in the sunspot atmosphere, in the microwave range the third harmonic is usually opaque in the extraordinary and transparent in the ordinary mode, while the second harmonic is opaque in both modes. Emission from the fundamental is not expected, because it is obscured by the overlying second harmonic layer, while emission at the fourth harmonic can appear at long cm wavelengths (Kaltman and Bogod, 2019).

Measurements of the magnetic field can be obtained without resorting to detailed modeling. We note that if the photospheric field is weak enough (or the frequency is high enough) both the 3rd and the 2nd harmonic layers are below the Transition Region and no strong sunspot-associated emission is expected. For stronger field, or lower frequency, the third harmonic enters into the TR while the second is still in the chromosphere; consequently strong emission is observed, highly polarized in the sense of the extraordinary mode (e.g., Shibasaki et al., 1994). For still higher field strength, the second harmonic also enters the TR; we then have strong emission in the ordinary mode as well as in the extraordinary and the polarization is reduced. Thus, the brightness temperature spectrum of both I and V show a rapid rise at the wavelength where the third harmonic enters into the TR; the magnetic field at the base of the TR can be estimated from the extrapolation of V to zero and the expression (29) with $s = 3$ (Akhmedov et al., 1982). Such measurements are routinely made from RATAN-600 data and are available at http://www.sao.ru/hq/sun/.

The appearance of gyroresonance sources is illustrated in **Figure 3**, which shows radio images of a bipolar active region, obtained by the NoRH and the Siberian Solar Radio Telescope (SSRT), together with a photospheric magnetogram. The photospheric magnetic field is $\sim -3{,}000$ G at the leading sunspot and $\sim 1{,}600$ G at the trailing. There is no trace of sunspot-associated emission at 34 GHz, which means that the 3rd harmonic layer (4,050 G) is below the base of the TR. At 17 GHz we have strong emission from the leading spot in the extraordinary mode (left circular polarization) and no emission in the ordinary mode, which means that the third harmonic level (2,025 G) is already in the low TR; at the same frequency there is no o-mode emission from the leading sunspot, i.e., the second harmonic level (3,040 G) is still below the TR. At 5.7 GHz there is strong emission both in the L and R sense, from which we may deduce that both the second (1,020 G) and third (680 G) harmonics are above the base of the TR. On the basis of

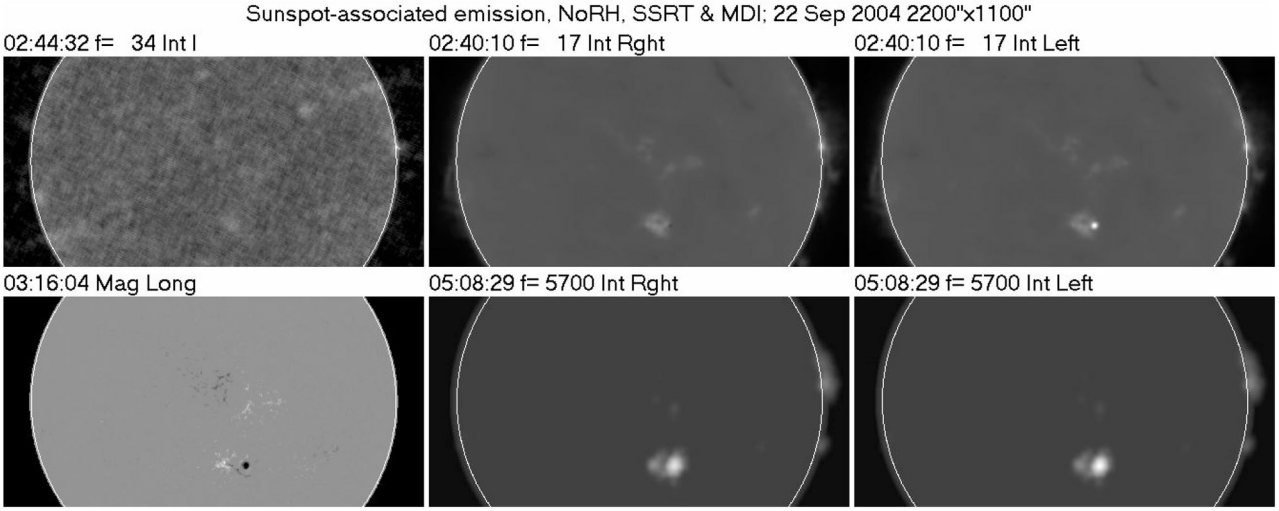

FIGURE 3 | Radio images of an active region. **(Top)** NoRH (34 GHz, Stokes *I* and 17 GHz, R and L polarization). **(Bottom)** MDI magnetogram and SSRT images (5.7 GHz, R and L polarization). White arcs show the photospheric limb. Images produced by the authors.

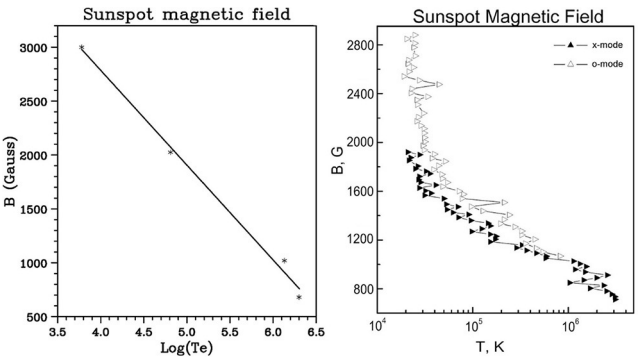

FIGURE 4 | (Left) The variation of the magnetic field strength with temperature for the leading sunspot of **Figure 3**. **(Right)** A similar plot obtained from RATAN-600 spectral data, adapted from Korzhavin et al. (2010); open and filled triangles show results from ordinary and extraordinary mode data, respectively.

this information, and the fact that, when an harmonic layer is opaque, the observed brightness temperature is equal to the local electron temperature, one can reconstruct roughly the variation of the magnetic field strength as a function of temperature (**Figure 4**, left). This is a peculiar magnetogram, in the sense that the temperature, rather than the height plays the role of the independent variable.

More detailed information can be obtained if spectral, rather than single frequency observations are available, such as with the RATAN-600 radio telescope. The right panel of **Figure 4** shows results obtained by Korzhavin et al. (2010). A shortcoming of this method is that, at some wavelengths, both the second and the third harmonic may contribute to the emission in the extraordinary or ordinary mode, as shown by model computations (Alissandrakis et al., 1980).

In order to obtain the magnetic field as a function of height, one has to use a temperature-height model; this, however, is not necessary if the height of the radio emission could be measured by other means. Using a stereoscopic method to measure the height, Bogod et al. (2012) presented results for a number of stable sunspots and compared them with extrapolations of the photospheric magnetic field; they found several cases where the magnetic field intensity measured in this way was greater than the extrapolated one. There have been other indications that the magnetic field above sunspots is rather high; Akhmedov et al. (1982) reported values 80–90% of the photospheric field at the base of the TR, while Brosius and White (2006) reported coronal magnetic field strengths of 1,750 G at a surprisingly large height (8,000 km) above a large sunspot at the west solar limb. In a recent work, Anfinogentov et al. (2019) reported g-r emission at 34 GHz from NoRH data, indicating a magnetic field of at least 4,050 G at the base of the TR; this was associated to a sunspot with a photospheric field above 5,000 G.

Under certain circumstances it is possible to derive not only the magnitude of the magnetic field, but also its orientation. The gyroresonance absorption coefficient has a very strong angular dependence and becomes zero when the magnetic field is parallel to the line of sight. Thus, on a sunspot associated source, there will be a region of low intensity at the location where this condition is fulfilled. This region will be very small (below the instrumental resolution) for x-mode emission but it can be observed in o-mode. Consequently, at that location we will have lower than average intensity and high circular polarization. Alissandrakis and Kundu (1984), using observations with the WSRT were able to identify this low intensity region over a stable sunspot and, using images over six consecutive days, to measure

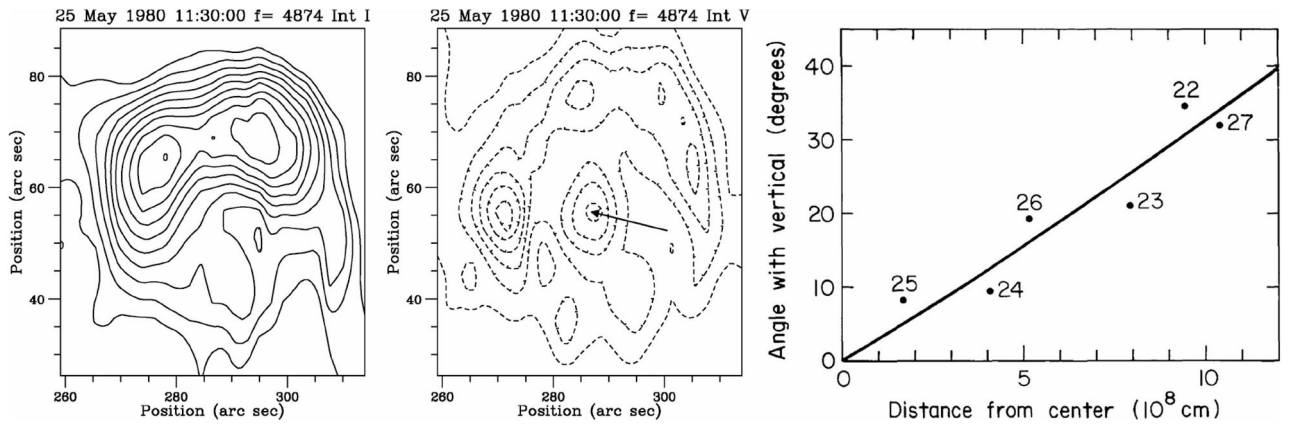

FIGURE 5 | Intensity and polarization maps of a stable sunspot, observed with the Westerbork Synthesis Radio Telescope (WSRT) on May 25, 1980. The arrow points to the region of low intensity and high polarization near the center of the sunspot, where the magnetic field is parallel to the line of sight (from data used in Alissandrakis and Kundu, 1984). The right panel shows the derived inclination of the magnetic field as a function of distance from the sunspot center; data points are marked with the date of observation (May 1980) and the full line is the expected inclination for a force-free field model. From Alissandrakis and Kundu (1984), reproduced with permission © ESO.

the inclination of the magnetic field as a function of distance from the sunspot center (**Figure 5**).

4.2. Cyclotron Lines

As mentioned in section 4.1, the observed spectrum of gyroresonance emission is continuous due to the height variation of the magnetic field. This is true as long as the magnetic field decreases monotonically with height and the electron temperature increases, as is the case above the photosphere of sunspots. However, as pointed out by Zhelezniakov and Zlotnik (1980), if there is a hot structure in the corona (e.g., a hot loop) as shown in the left panel of **Figure 6**, the emission at the frequency corresponding to the third harmonic for the value of the magnetic field at the hot structure will be higher than that of nearby frequencies, giving rise to a *cyclotron* line. The width of the line will depend on the extent of the hot structure and the gradient of the magnetic field, while its polarization will be that of the extraordinary mode if, as expected, $\tau_x > 1$ and $\tau_o < 1$. At the frequency corresponding to the second harmonic the emission will be polarized in the sense of the ordinary mode, because the extraordinary mode will be obscured by the 3rd harmonic layer which is located higher.

Two more configurations that produce cyclotron lines are shown in **Figure 6**. A peak in the magnitude of the magnetic field, as shown in the middle panel, will result in excess o-mode emission near the 3rd harmonic and x-mode emission near the 4th. The bandwidth of the line will be (Zhelezniakov and Zlotnik, 1980):

$$\frac{\delta f}{f} = \sqrt{2}\beta_T \cos\alpha \tag{30}$$

where β_T is the ratio of the thermal electron velocity to the velocity of light and α is the angle between the magnetic field and the line of sight. A current sheet, providing at the same time an inversion of the sign of the magnetic field and energy release to locally heat the corona (**Figure 6**, right panel) will lead to excess emission at the 4th, 3rd, and 2nd harmonics.

It is obvious from the above that cyclotron lines provide a direct measurement of the value of the magnetic field at the location where they are formed while, at the same time, they reveal the particular conditions of their formation, since each case presented above has its own spectral signature.

Cyclotron line detection requires spectrally resolved imaging observations at closely spaced frequencies, with adequate stability of the instrumental gain, thus observational evidence has been scarce: Willson (1985) reported an unpolarized spectral feature with a brightness temperature excess of a factor of ∼2.5 and a spectral width of $\delta f/f \sim 0.1$, in VLA observations at ten frequencies near 20 cm (1,440–1,724 MHz). His interpretation was in terms of a hot loop with a constant magnetic field of ∼145 G for emission at the 4th harmonic. These results were re-analyzed by Zhelezniakov and Zlotnik (1989), in a more realistic approximation of inhomogeneous magnetic field; they obtained a better fit to the data, with emission at the 3rd harmonic ($B =$ 196 G). The absence of polarization was attributed to the high optical thickness of both modes and the spectral width to the variation of the magnetic field. A similar case, again observed with the VLA at the same frequencies, was reported by Lang et al. (1987) and also interpreted in terms of a hot loop.

Evidence of cyclotron lines has been found in 1-dimensional spectral observations with the RATAN-600 radio telescope. A narrow, polarized spectral feature was reported by Bogod et al. (2000) near 8.5 cm, possibly associated with a compact bright source observed at 17 GHz with the Nobeyama radioheliograph. The lack of any other line in the observed spectral range led the authors to identify it with 3rd harmonic emission, implying a magnetic field of ∼400 G; the derived parameters were further constrained by assuming that the 17 GHz source was due to

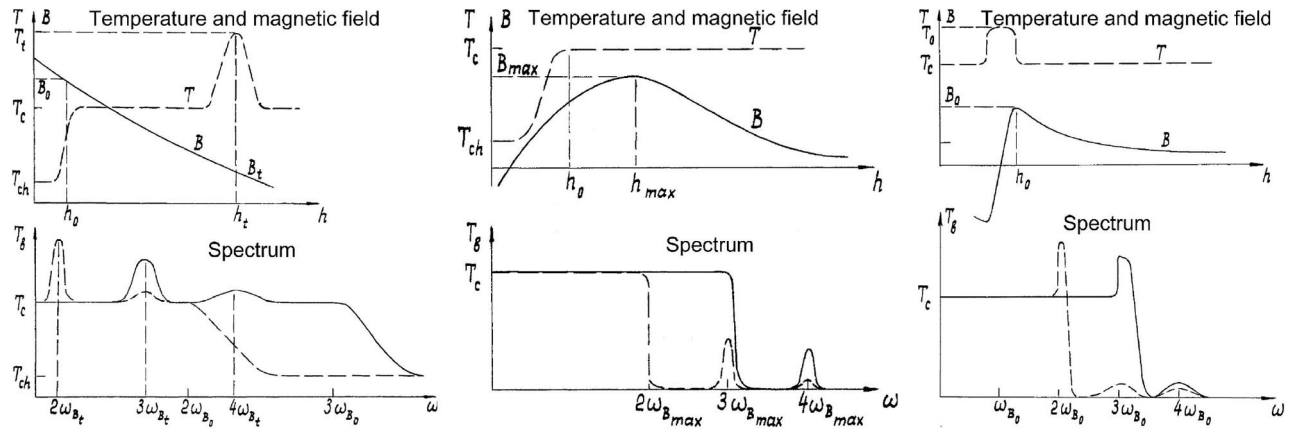

FIGURE 6 | Three configurations that can produce cyclotron lines: A hotter than average structure in the corona **(left)**, a maximum in the magnetic field **(middle)**, and a hot current sheet **(right)**. The top panels show the variation with height of the electron temperature and the magnetic field, bottom panels the expected brightness temperature spectrum in the extraordinary (full lines) and ordinary (dashed lines) mode. T_{ch} is the electron temperature of the chromosphere, T_c of the corona and T_t of the hot structure. Adapted from Zhelezniakov and Zlotnik (1980).

thermal f-f emission from the same hot structure. We should note at this point that peculiarities in spectra, such as a broad minimum in both *I* and *V* have been reported by Yasnov et al. (2011) and interpreted using a model with a hot coronal loop.

5. GYROSYNCHROTRON EMISSION

The characteristics of gyrosynchrotron (g-s) emission from mildly relativistic electrons, trapped in flaring loops, depend strongly on the magnetic field (see the review by Nindos, 2020 in this special research topic collection and the reviews by Bastian et al., 1998 and Nindos et al., 2008). The emission has a quasi-continuous spectrum with maximum in the low harmonics of the gyrofrequency. The peak wavelength of the observed intensity spectrum is mainly determined by opacity effects (self absorption), which shift the peak to the 3rd–4th harmonic (Takakura, 1967). Thus a spectral maximum at 6 cm corresponds to magnetic field strength of 450–600 G; the field is obviously higher in bursts with spectra that peak at shorter wavelengths, sometimes in the millimeter range.

It should be noted that the magnetic field in burst sources is highly inhomogeneous, thus these values should be considered as gross estimates only. Detailed model computations of g-s emission from a homogeneous distribution of energetic electrons in a flaring loop by Preka-Papadema and Alissandrakis (1988) showed that the spectral peak can occur between the second and sixth harmonic; the spectral maximum shifts to shorter wavelengths as we move from the top of the loop to its footpoints, as a result of the variation of the magnetic field strength and direction. Moreover, the emission is expected to peak at the top of the flaring loop in the optically thick case and at the footpoints in the optically thin. Subsequent model computations have treated inhomogeneous and anisotropic distributions of non-thermal electrons, as well as time variations (Fleishman and Melnikov, 2003; Tzatzakis et al., 2008; Simões and Costa, 2010; Nita et al., 2015).

It is obvious from the above discussion that the use of g-s emission for diagnostics of the magnetic field is not as straight forward as in the case of gyroresonance. For reliable diagnostics one requires data with high spatial, spectral, and temporal resolution (i.e., dynamic imaging spectroscopy), as the spectrum will vary from point to point and as a function of time. Homogeneous source models, as well as simplified expressions for the emission are not expected to produce satisfactory results. Simultaneous hard X-ray data are useful in providing independent information about the energy distribution of the accelerated electrons. The observations should be combined with models of all physical parameters that influence the emission, including the magnetic field. In the past, any information on the magnetic field came as a byproduct of the modeling, and not as a more or less direct measurement.

In spite of the difficulties, some results from detailed modeling of observations have been reported. Using VLA *I* and *V* images at 5 and 15 GHz and spectral data from the Owens Valley Radio Observatory at several frequencies between 2 and 15 GHz, Nindos et al. (2000) deduced a magnetic field strength of 870 G at the feet and 270 G at the top of a flaring loop. Values in the same range (1,700–200 G) were obtained from Nobeyama images at 17 and 34 GHz by Kundu et al. (2001, 2004), Tzatzakis et al. (2008), and Kuznetsov and Kontar (2015).

The *Expanded Owens Valley Solar Array* (EOVSA) has provided a breakthrough for measuring magnetic fields and other parameters of flares using g-s emission, by providing high-cadence, spatially-resolved spectra permitting direct spectral fitting. A limb flare was among the first results from EOVSA; images at 30 frequencies from 3.4 to 18 GHz were analyzed by Gary et al. (2018) and preliminary field values from 150 to 520 G were derived. A more thorough analysis of the EOVSA data during the main phase of the event by Fleishman et al. (2020) has provided the first maps of the dynamically decaying magnetic

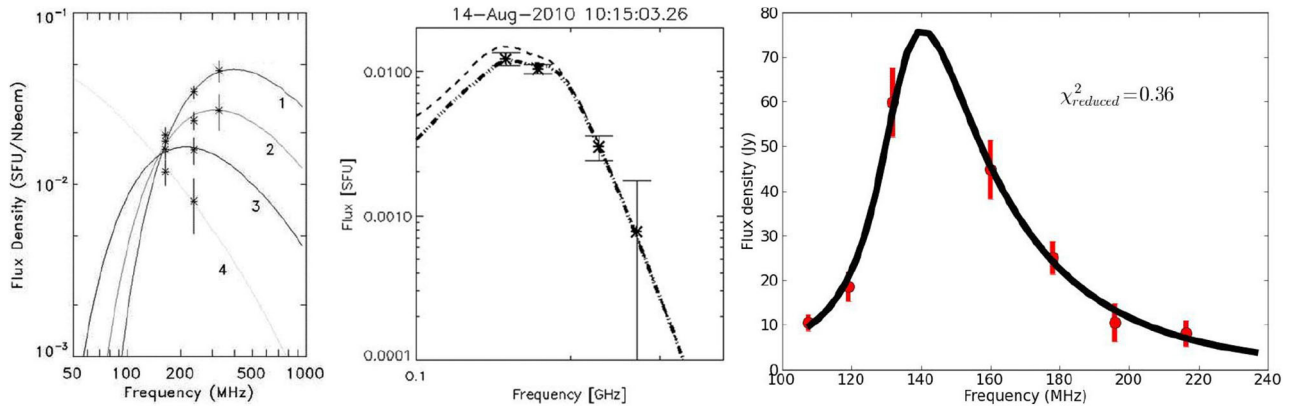

FIGURE 7 | Examples of radio CME spectra and model fits. **(Left)** from Bastian et al. (2001); **(middle)** from Tun and Vourlidas (2013); **(right)** from Mondal et al. (2020). All panels reproduced by permission of the AAS.

field strength in the cusp region of a flare. Additionally, the magnetic field vs. height along the reconnecting current sheet of the early, eruptive stage of the flare was measured and compared with an MHD simulation by Chen et al. (2020).

An important application of g-s emission is in the measurement of the magnetic field in Coronal Mass Ejections (CME), provided that this mechanism rather than plasma emission is the dominant radiation mechanism of the associated type IV metric radio bursts (see also Vourlidas et al., 2020 in this special research topic collection). This distinction can be made on the basis of the low brightness temperature and the spectral shape, which shows a characteristic peak (Klein and Trottet, 1984; see examples in **Figure 7**). Radio CMEs are rare; among the early works, Gopalswamy and Kundu (1987) estimated a magnetic field of ~ 2 G at heliocentric 2.3 $R_\odot$. Subsequent works (Bastian et al., 2001; Maia et al., 2007; Tun and Vourlidas, 2013; Bain et al., 2014; Carley et al., 2017; Mondal et al., 2020) gave a range of values between 0.3 and 23 G in the heliocentric distance range of 1.3–2.7 $R_\odot$, which variation apparently pertains to individual CMEs rather than to the ambient corona. Moreover, all authors used homogeneous source models and simplified expressions for the g-s emissivity.

6. CIRCULAR POLARIZATION INVERSION

We already mentioned in section 3 that, as the physical conditions change along the ray path, the polarization of electromagnetic waves changes accordingly. Consequently, the observed polarization will not be the same as the polarization at the region of formation of radiation. In particular, if the wave crosses a transverse field region (TFR), where the magnetic field is perpendicular to the line of sight, the sense of its polarization will change, since the sign of the longitudinal component of the magnetic field changes. This happens as long as the geometrical optics approximation is valid, i.e., for not too low values of N_e and B. In a more general sense, the situation is described in terms of wave coupling. When the coupling between the x-mode and o-mode waves is weak their polarization properties change along the ray path, whereas when the geometrical optics approximation breaks down the waves are strongly coupled and their polarization remains fixed, even if a TFR is crossed.

The most prominent effect of wave propagation is the inversion of circular polarization as a bipolar active region moves from the eastern to the western limb (Alissandrakis, 1999; Ryabov, 2004). In this section we will discuss how this effect can provide information on the magnetic field in the low corona above active regions.

6.1. Wave Coupling Under QT Propagation

Wave coupling has been studied comprehensively by Cohen (1960) (see also Bandiera, 1982; Zheleznyakov et al., 1996; Segre and Zanza, 2001). In the case of QL propagation, the coupling becomes strong for extremely low values of the density (section 3). Of more practical interest is the case of QT propagation; in this case the coupling coefficient is:

$$C = a\frac{\omega^4}{N_e B^3}\left|\frac{d\theta}{ds}\right| \tag{31}$$

where

$$a = \frac{2\ln 2}{\pi^2}\frac{m_e^4 c^4}{e^5} \tag{32}$$

and the symbols have their usual meaning.

Taking into consideration the effect of wave coupling, the sense of circular polarization does not necessarily change when the waves cross a TFR. In fact, what happens depends on the value of C at the point, along the ray path, where the longitudinal component of the magnetic field, B_ℓ, vanishes:

- If $C \ll 1$ the polarization changes sense (weak coupling)
- If $C = 1$ the polarization becomes linear (critical coupling)
- If $C \gg 1$ the sense of polarization does not change (strong coupling)

Of particular interest is the case of $C \approx 1$, which has been treated by Zheleznyakov and Zlotnik (1963). After the TFR crossing, the

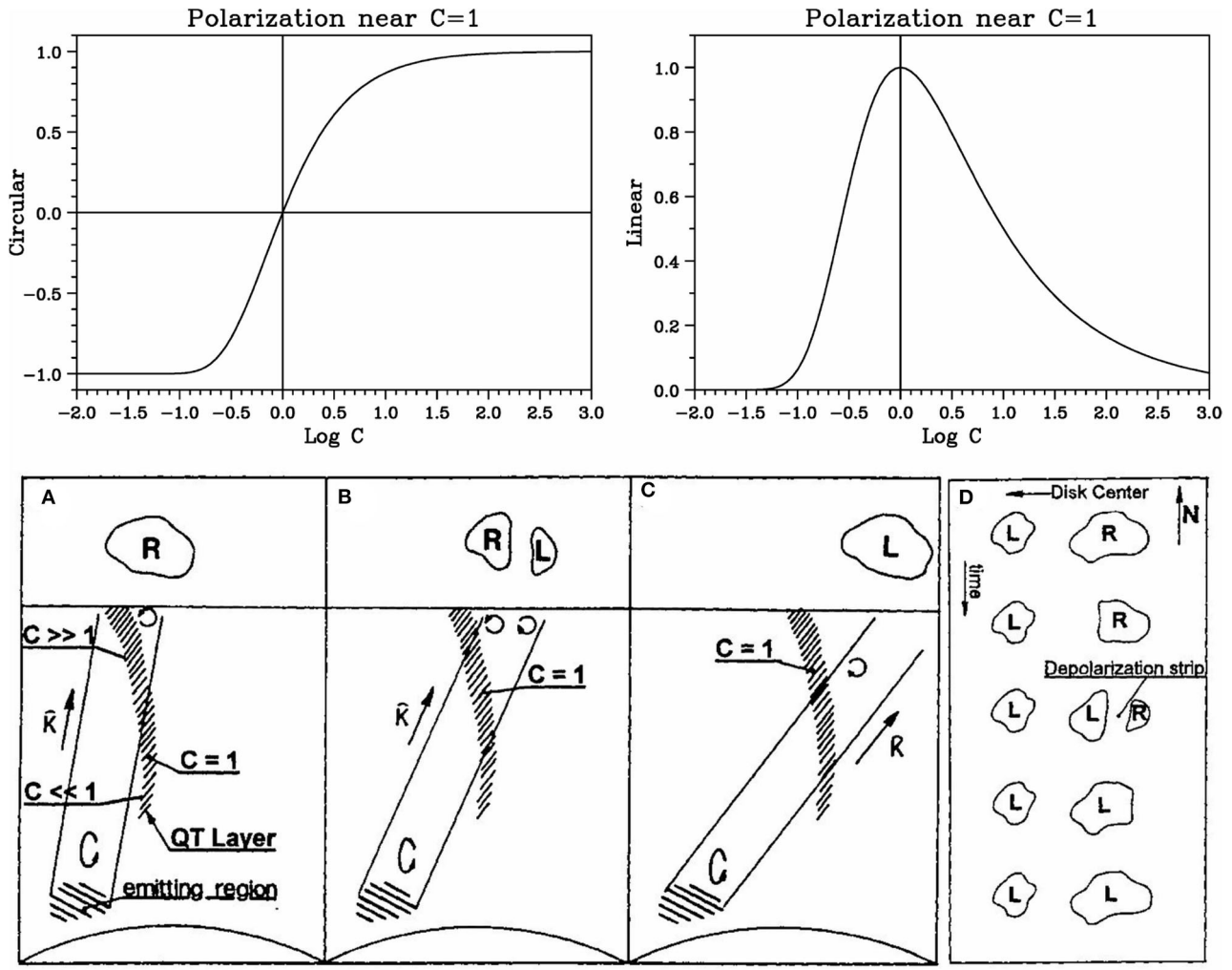

FIGURE 8 | (Top) Circular (left) and linear (right) polarization after TFR crossing, as a function of the coupling coefficient. (Bottom) Geometry of radiation crossing a transverse field region (QT layer); **(A–C)** Polarization inversion of the limbward part of an active region as it rotates from the disk center to the west limb; **(D)** effect on a bipolar active region. (after Bandiera, 1982, reproduced with permission © ESO).

resulting polarization is elliptical, with the degree of circular, ρ_c, and linear, ρ_ℓ polarization given by:

$$\rho_c = -1 + 2\exp\left(-\frac{\ln 2}{C}\right) \tag{33}$$

$$\rho_\ell = 2\exp\left(-\frac{\ln 2}{2C}\right)\sqrt{1-\exp\left(-\frac{\ln 2}{C}\right)} \tag{34}$$

which, for $C = 1$ give $\rho_c = 0$ and $\rho_\ell = 1$; note that $\rho_c = -1$ for $C \ll 1$, while $\rho_c = 1$ for $C \gg 1$; at both limits $\rho_\ell = 0$ (**Figure 8**, top row).

We note here that, with the continuum receivers typically used in past radio observations, the observation of linearly polarized radiation from the Sun was not possible, due to the strong Faraday rotation within the receiver bandwidth. Further difficulties may arise from wave scattering in coronal inhomogeneities (Bastian, 1995). In spite of these difficulties, Alissandrakis and Chiuderi-Drago (1994) reported the detection of linearly polarized radiation and measured the Faraday rotation, using a narrow band ($\Delta f/f = 4 \times 10^{-6}$) spectral line receiver. From their observations, Segre and Zanza (2001) deduced a magnetic field of 12.8–11.2 G and a value of 1.40–2.08×10^{18} cm^{-2} for the product of electron density and the magnetic field scale. It should be noted that due to advances in high-speed signal processing modern radio receivers now routinely provide sufficient spectral resolution to renew interest in the detection of linear polarization. For example, EOVSA has a special narrow-band mode that provides $\Delta f/f = 6 \times 10^{-5}$ at 10 GHz, while the Very Large Array can achieve $\Delta f/f = 5\times10^{-4}$ at 8 GHz.

Even if linear polarization cannot be detected, we can still make use of frequency-dependent spatial patterns in circular polarization to locate the TFR. Let us note from the beginning

that normally only a source located in the limbward part of an active region may suffer polarization inversion, simply because radiation from the diskward part will not cross a TFR. Consider now such a source emitting right circularly polarized radiation, which crosses a TF region on its way to the observer (**Figure 8**, bottom). When the source is near the disk center (**Figure 8** bottom, A), the TFR is crossed high in the corona where the density and the magnetic field are low and the coupling strong, after Equation (31); consequently the observed polarization is the same as the intrinsic. As the region moves toward the West limb (**Figure 8** bottom, B), the radiation crosses the TFR at a lower height, hence the coupling coefficient decreases; at a certain point the radiation from the east part of the source will cross the TFR under conditions of weak coupling, and the sense of its circular polarization will be inverted. Closer to the limb (**Figure 8** bottom, C), the radiation from the entire source will cross the TFR under weak coupling conditions and the observer will see left rather than right circular polarization.

The resulting polarization map of the entire bipolar active region as it moves from the disk center to the west limb, including the unreversed diskward side, is sketched in **Figure 8** bottom, D. The left and right circularly polarized components are separated by the *depolarization strip*, i.e., a region of low circular polarization between the two oppositely polarized sources, which will be displaced with respect to the photospheric neutral line (where $B_\ell = 0$) by an amount which increases as the active region moves toward the limb. Furthermore, the displacement is a function of frequency, generally being larger at lower frequencies although it depends on the detailed shape of the TFR ($C = 1$ layer sketched in **Figure 8**, bottom; e.g. Ryabov, 2004). For a region in the Eastern hemisphere the situation is the reverse: near the limb the observed sense of circular polarization will correspond to the leading magnetic polarity.

6.2. Observations

The inversion of circular polarization in the radio emission of active regions and bursts has been known for several years (Kundu, 1965; Zheleznyakov, 1970). In low resolution observations of active regions where the two polarities are not resolved, the total V is in the sense of the magnetic polarity of the leading part of the region when the source is located in the eastern hemisphere, while the polarization is in the sense of the trailing polarity when the source is in the western hemisphere (e.g., Peterova and Akhmedov, 1974). The effect is better illustrated in high resolution two-dimensional data. An example observed with the WSRT at 6 cm in 1980 is shown in the top four rows of **Figure 9**. Notice that on June 13 (top row), when the Active Region was in the Eastern hemisphere, its trailing part is depolarized; the bipolar structure of the magnetic field is fully revealed on June 16 (fourth row), after the central meridian crossing. Another example, this time from RATAN-600 1-D scans, is shown in the bottom four rows of **Figure 9**; here V is fully inverted in the trailing part of the active region near the E limb (left column) and in the leading part near the W limb (right column).

The position of the depolarization strip (where $V \simeq 0$) depends on wavelength. Equation (31) implies that C is higher at short wavelengths, which means that the region of critical coupling moves lower in the corona; as a result the depolarization strip is closer to the photospheric neutral line (where $B_\ell = 0$). This is illustrated in the RATAN-600 observations in **Figure 9**: note that on August 1, as we go from short to long wavelengths, the depolarization strip moves in the direction of the limb (eastward); the same effect is seen on the August 5 scans, the limb now being in the west. We note in passing that g-r emission from the leading spot starts at shorter wavelengths than from the trailing one, due to the stronger magnetic field of the former (section 4.1).

If we consider the spectrum of Stokes V at a point in the limbward part of an active region, we expect inversion to occur at wavelengths longer than a critical value, where $C \geq 1$ (note that the coupling coefficient goes like λ^{-4}, see Equation 31). In a number of cases a second inversion is observed at longer wavelengths (Bogod et al., 1993; Ryabov, 1998). This can be explained by the radiation crossing two TFRs on its way to the observer, something that may happen under complex morphologies of the magnetic field. The first inversion occurs at the wavelength where $C = 1$ at the lower TFR; in this case the upper TFR will not affect the polarization because the coupling will be strong there, due to the much lower density and field strength. As the coupling decreases with wavelength, the second inversion will occur at longer λ, where both TF regions are crossed under conditions of weak coupling.

Notice that the above discussion is independent of the intrinsic polarization of the wave at the site of its generation. Propagation effects, at longer wavelengths in particular, can change considerably the sense of circular polarization expected on the basis of the emission mechanism. The observations give a picture of the magnetic field polarity *not at the source of the emission, but at the height where* $C = 1$. Therefore one should be careful in inferring the polarity of the magnetic field on the basis of V maps, particularly in regions far from the disk center and at long wavelengths. One more point made by Kundu and Alissandrakis (1984) is that, due to the expected smoother geometry of the coronal magnetic field at large heights, small scale magnetic structures should not be detectable on V maps. Another point raised by Alissandrakis and Preka-Papadema (1984) concerns the identification of the magnetic polarity of microwave burst footpoints, which may also be affected by propagation effects (see Alissandrakis et al., 1993).

The crossing of a TFR is not the only known mechanism of polarization inversion. It has been pointed out (e.g., Zheleznyakov et al., 1996) that the geometrical optics approximation is violated and mode coupling occurs also in the case of radiation crossing plasma current sheets with a weak guide field.

6.3. Diagnostics

Several methods for diagnostics of the magnetic field exist; the choice depends on the available data. For example, if two or one-dimensional information at a single frequency is available over several days, the distance, q, of the depolarization strip from the photospheric $B_\ell = 0$ line can be measured. Using a dipole approximation for the large scale magnetic field of an active

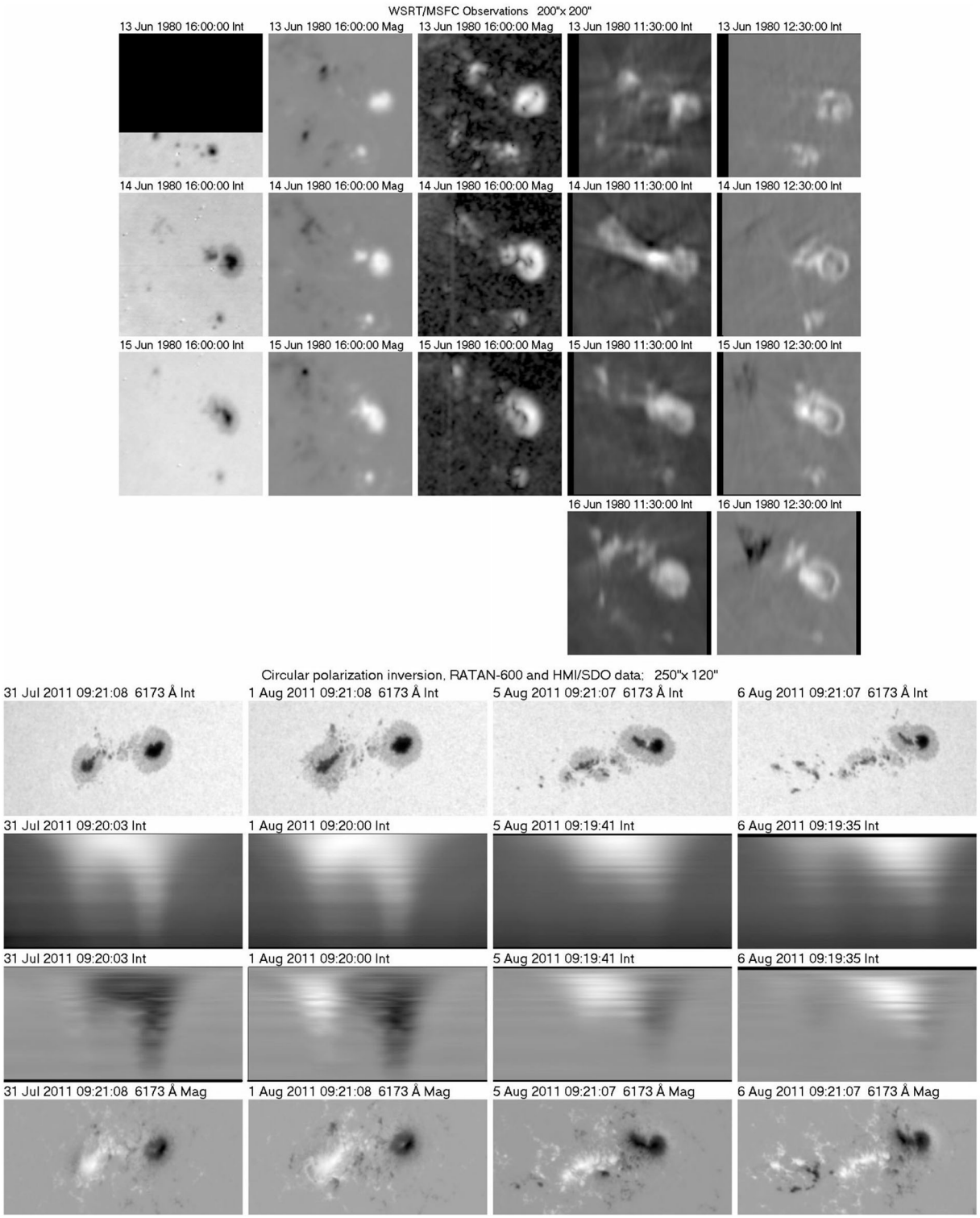

FIGURE 9 | Rows 1–4: WSRT observations of two active regions in total intensity (fourth column) and circular polarization (fifth column), together with white light photographs (first column) and magnetograms (longitudinal: second column, transverse: third column) from the Marshal Space Flight Center. The region was near the East limb on the first day (first row) and had crossed the central meridian on the last day (fourth row). Right hand circular polarization is white. (Images from data used in Chiuderi Drago et al., 1987). Rows 5–8: An active region crossing the solar disk. Row 5: white light images (HMI). Rows 6–7: RATAN-600 one-dimensional scans in Stokes *I* and *V* in the wavelength range 3.65 (bottom of panel) to 8 cm (top of panel). Last row: magnetograms (HMI). The region crossed the central meridian between August 3 and 4. RATAN images constructed from data at ftp://ftp.sao.ru/pub/sun/sun_fits.

TABLE 1 | Coronal parameters from circular polarization inversion.

References	Wavelength (cm)	Height (Mm)	Height ($R_\odot$)	N_e (cm^{-3})	B (G)
Kundu and Alissandrakis (1984)	6.16	110	0.16	10^8	20
		130	0.19	10^8	10
Alissandrakis et al. (1996)	6.16	100	0.14	6.4×10^7	16
Segre and Zanza (2001)	6.16				11.2–12.8
Gelfreikh et al. (1987)	2–4	120	0.17	10^9	16
Nagelis and Ryabov (1992)	2–4	38	0.05		26
Lang et al. (1993)	2–4	50–200	0.07–0.29		50–15
		200–300	0.29–0.43		10–5
Ryabov et al. (1999)	1.76–3.43	57–87	0.08–0.12		65–20
	1.76–3.43	37–64	0.05–0.09		125–30
Ryabov et al. (2005)	5.2	50–90	0.07–0.13		30–10
	1.76	15–38	0.02–0.05		110–50

region, Kundu and Alissandrakis (1984) derived the following expression, extending the work of Bandiera (1982):

$$q = -2\beta \left(\frac{\alpha - \ell}{3} \right)^{7/8} \tag{35}$$

where α is the dipole inclination with respect to the surface, ℓ the longitude, $\beta = (N_e d^3)/(6a\omega^4)$, a is the constant defined in Equation (32) and d is the dipole magnetic moment. They determined β and α by fitting the data, and from those the height of the critical point and the quantity $N_e d^3$. Assuming a reasonable value of N_e they obtained d and furthermore B. The exact value of the electron density is not critical, because the magnetic field is proportional to the cubic root of its value. Their results, together with those of others, are listed in **Table 1**.

Sometimes high resolution data are available for a single day only (Alissandrakis et al., 1996). In this case one can extrapolate the photospheric magnetic field and find the height at which the projection of the $B_\ell = 0$ line matches the position of the depolarization strip. The height of the region of critical coupling as well as the magnetic field parameters are obtained from the extrapolation and the electron density can be computed from the condition $C = 1$. This method, however, does not give a very accurate value of N_e due to its appearance in the third root in the expression, while other uncertainties may arise from the validity of magnetic field extrapolation (Lee et al., 1998b).

Data of V as a function of both the position and the wavelength are readily available thanks to the RATAN-600 radio telescope. The Pulkovo group (e.g., Peterova and Akhmedov, 1974; Gelfreikh et al., 1987; Nagelis and Ryabov, 1992; Lang et al., 1993; Kaltman et al., 2007) have worked extensively with these and some of their results are included in **Table 1**. Note that the RATAN observations extend to short cm-λ, which allows one to access lower heights and stronger magnetic fields.

The diagnostic methods presented so far are based on measurements of the position of the depolarization line in space and/or in frequency. Additional diagnostics can be developed on the basis of the change of the degree of circular polarization as a function of frequency and position, described by Equation (33) and plotted in the left top panel of **Figure 8**; this expression determines, e.g., the width of the depolarization strip as well as the rate of change of polarization in the direction perpendicular to the strip. The work of Gelfreikh et al. (1997) is in that direction; they used Equation (33) to determine the gradient of the magnetic field and obtained typical values in the range of 10^{-9} G/cm a height of 120 Mm, with a single value as high as 2×10^{-5} G/cm at a height of 50 Mm.

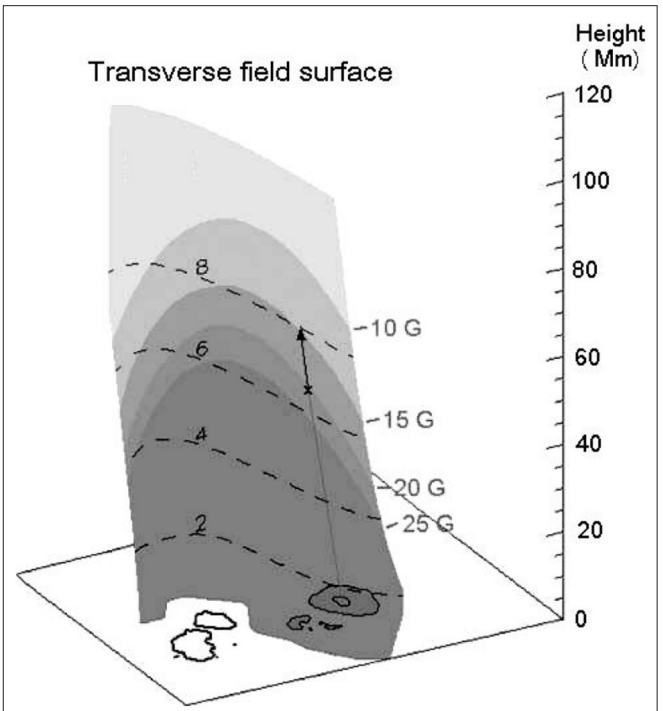

FIGURE 10 | Map of the magnetic field on the transverse field surface above a bipolar active region, deduced from observations of the inversion of circular polarization. Adapted from Ryabov et al. (2005).

If the intrinsic polarization of the waves were known, one could use Equation (33) to obtain a map of the coronal magnetic field in the region where $C \approx 1$. Ryabov et al. (1999) using observations from the Nobeyama Radioheliograph together with RATAN-600 scans, determined the intrinsic polarization on a day without any obvious inversion and subsequently computed the degree of circular polarization for the next day when inversion was observed; in this way they obtained a coronal magnetogram. This appears to be a very powerful method for magnetic field diagnostics, although it is applicable to a rather limited number of cases. More results were obtained by Ryabov et al. (2005), who used combined NoRH and SSRT observations over several days to deduce field strengths of 30 to 10 G at heights of 50–90 Mm and 110–50 G at the heights of 15 to 38 Mm. Their results are shown in **Figure 10**.

The works presented above show an almost perfect agreement between observations and theory. However,

cases of disagreement have also been reported, mainly in the long decimetric and metric range (Gopalswamy et al., 1991; White et al., 1992). Efforts have been made to interpret these results in terms of current sheets (Gopalswamy et al., 1994) or scattering in inhomogeneities (Bastian, 1995).

7. FIBER BURSTS AND ZEBRA PATTERNS

Type IV bursts in the metric and decimetric range are rich in fine structures, embedded in the background continuum emission. Among them, fiber bursts and zebra patterns show periodic maxima and minima in their instantaneous flux spectrum (see reviews by Chernov, 2006, 2011; Nindos and Aurass, 2007). In both cases the frequency of the peaks drifts with time: monotonically toward low frequencies in the case of fibers and in a wavy manner in the case of zebra patterns (**Figure 11**).

Fiber bursts (also known as *intermediate drift bursts*, their frequency drift rate being between those of type II and type III bursts), are commonly attributed to the coalescence of whistler and Langmuir waves formed by a loss cone distribution of non-thermal electrons in post-flare loops (see Kuijpers, 1975, also Mann et al., 1987, 1989). As demonstrated with imaging observations by Alissandrakis et al. (2019b), these loops are considerably higher than microwave and soft X-ray burst loops and probably encompass both the low flaring loops and the CME-associated flux rope. According to this interpretation, each fiber is a whistler wave packet propagating upwards in the loop; the group velocity, v_g, is (Kuijpers, 1975):

$$\upsilon_g = 2\upsilon_{Ae}\sqrt{x(1-x)^3} = 2c\frac{\omega_{ce}}{\omega_{pe}}\sqrt{x(1-x)^3} \tag{36}$$

where

$$\upsilon_{Ae} = \frac{B}{\sqrt{4\pi N_e m_e}} \tag{37}$$

is the *electron* Alfvén velocity, which is about 43 times higher than the usual Alfvén velocity

$$\upsilon_A = \frac{B}{\sqrt{4\pi N_e m_p}} \tag{38}$$

and $x = \omega_w/\omega_{ce}$ is the ratio between the whistler frequency and the electron gyrofrequency.

The group velocity can be retrieved from the frequency drift using a density model. According to Equation (36), υ_g maximizes for $x = 0.25$ and Kuijpers (1975) argued that $0.1 > x > 0.5$, so that υ_g is between 21.5 and 28 υ_A; he used this and the drift velocity to estimate magnetic field strengths of 11.5–15 G at the level of formation of the emission at 900 MHz and 0.51–0.66 G at 160 MHz. An additional diagnostic is provided by the whistler frequency, which is expected to be equal to the separation between the emission and absorption ridges of the fiber, since the radiation is enhanced at $\omega_p + \omega_w$ and reduced at ω_p; taking this into account, Kuijpers (1975) gave field values of 7.2–36 G at 900 MHz and 0.36–1.8 G at 160 MHz. Note, however, that these estimates serve more as a check for the model rather than as magnetic field measurements.

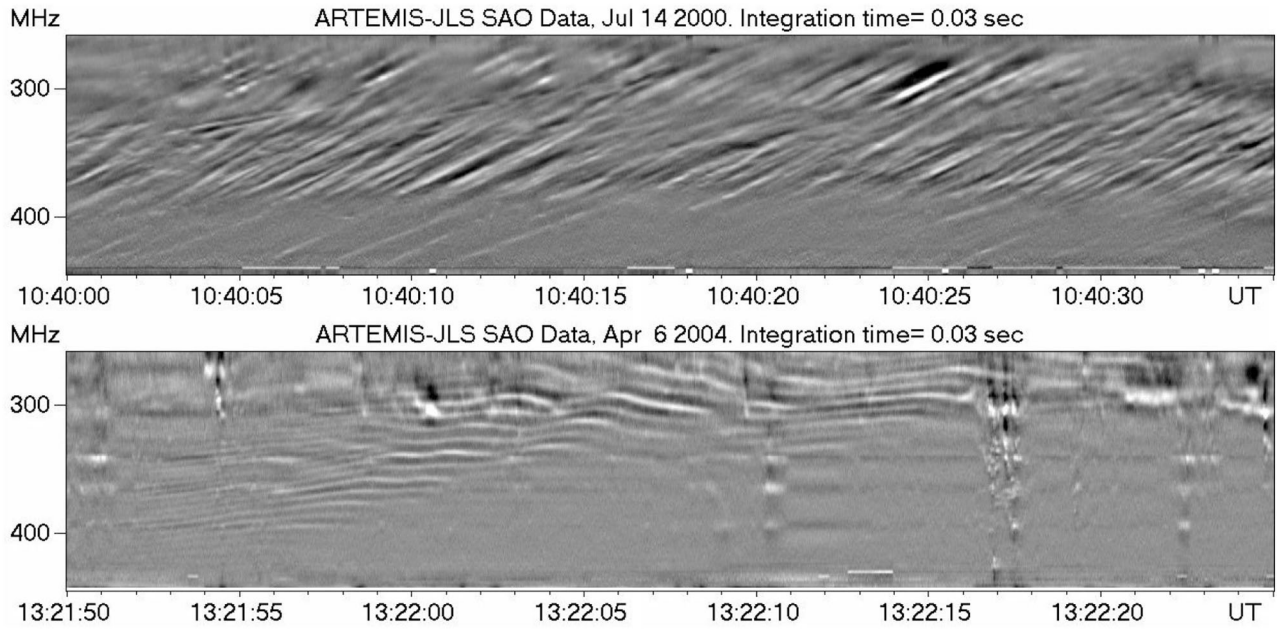

FIGURE 11 | Dynamic spectra of fiber bursts **(top)** and zebra pattern **(bottom)**, observed with the ARTEMIS/JLS radio spectrograph (Kontogeorgos et al., 2006) in the 266–451 MHz range. The spectra have been filtered in time and frequency to improve the visibility of fine structures. Data selected by C. Bouratzis.

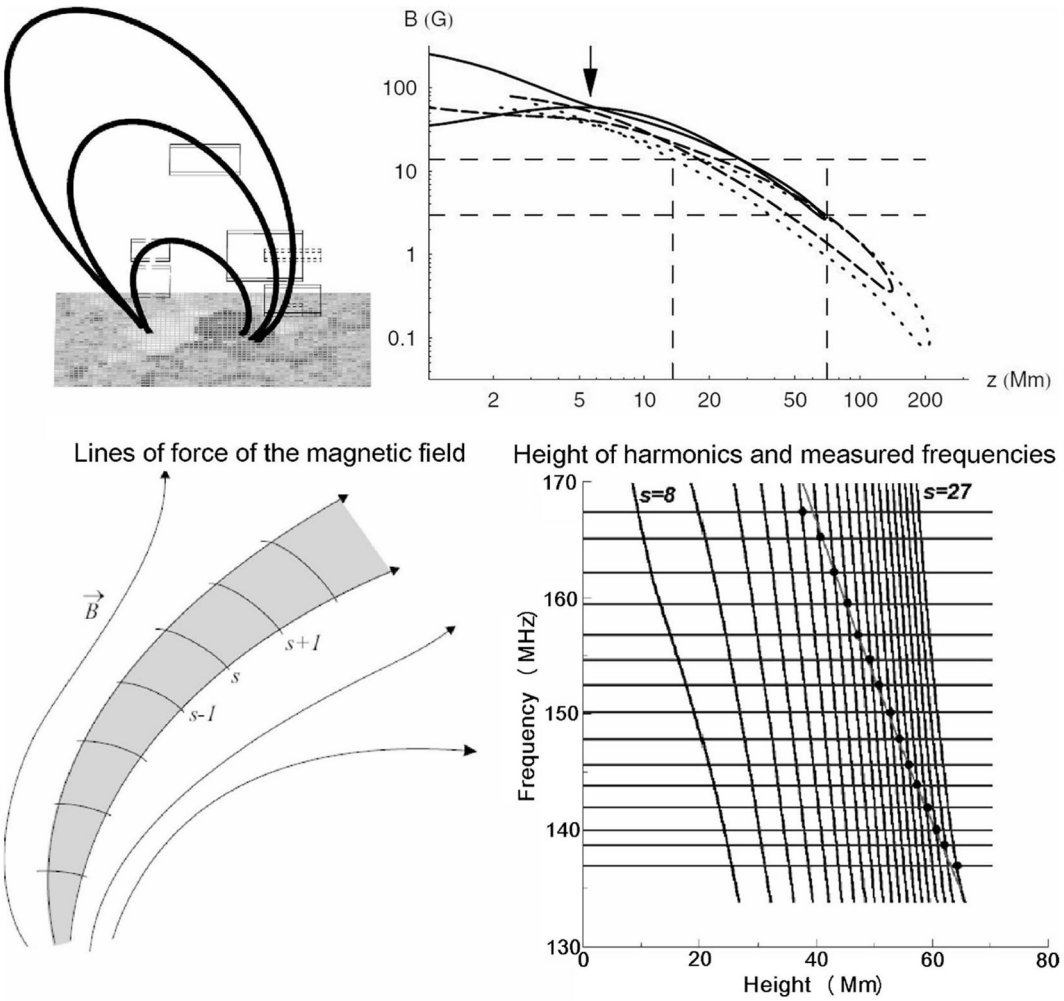

FIGURE 12 | (Top, left) Position of fiber bursts within the associated loops. **(Top, right)** The magnetic field as a function of height for various fiber loops; thin dashed lines show the limits of the region where the bursts were observed. From Aurass et al. (2005), reproduced with permission © ESO. **(Bottom)** Zebra pattern formation due to the double plasma resonance effect. Left: Structure of the source with the harmonic levels marked. Right: Height of the gyrofrequency harmonic levels as a function of frequency; the horizontal lines represent the measured peak frequencies. The points mark the intersections that are consistent with hydrostatic variation of the electron density with height. Adapted from Zlotnik (2009).

Measurements of the frequency drift and the whistler frequency can be combined, in which case Equation (36) gives:

$$\frac{L_N}{c}\frac{1}{f_w}\frac{df}{dt} = \sqrt{\frac{(1-x)^3}{x}} \tag{39}$$

which can be solved for x and hence for B. Here the group velocity has been expressed in terms of the frequency drift rate, df/dt; f_w is the whistler frequency and L_N is the density scale height along the magnetic field lines of the loop which must come from model estimates. For the fibers shown in **Figure 11**, Equation (39) gives 5.6 G at 370 MHz and 4 G at 290 MHz, assuming that $L_N = 100$ Mm. Additional information can be obtained from the derivative of the frequency drift; in this way, Benz and Mann (1998) obtained 212 G at 2 GHz and 5.7 G at 212 MHz for the whistler model, while they got 143 and 14 G, respectively for an alternative model in which the radiation is produced by maser emission at a harmonic of the electron cyclotron frequency and the fiber modulation by an Alfvénic soliton.

In a more elaborate treatment, Aurass et al. (2005) used 2D positions from the Nançay Radioheliograph, together with potential extrapolations of the photospheric magnetic field and a $\alpha \times$ Newkirk density model (Newkirk, 1961) to identify the magnetic loops in which fiber bursts occurred (**Figure 12**, top row). Their best fit was for $\alpha = 3.5$ and they deduced field strengths from 6 to 14 G at 410 MHz (height of 20 Mm) to 3 G higher up, at 100 Mm (236 MHz); the corresponding values of x were 0.41 and 0.21, respectively. A similar analysis was performed by Rausche et al. (2007).

In a recent work, Bouratzis et al. (2019) deduced an average magnetic field of 4.6 G with a dispersion of 1.5 G, from the analysis of a large number of fiber bursts observed with the

ARTEMIS/JLS radiospectrograph between 250 and 470 MHz, assuming whistler origin for the fibers and a hydrostatic coronal model at $T_e = 2 \times 10^6$ K and a base density 4× that of the Newkirk density model. They obtained similar results from the analysis of the tracks on the dynamic spectrum of 38 fiber groups, without assuming any specific density model. Observing at higher frequencies (1–2 GHz) with the VLA, Wang et al. (2017) reported 62 G at 10 Mm and 8 G at 36 Mm.

Let us now consider zebra patterns, which also originate in post-flare loops and for which three principal mechanisms have been proposed (see Zlotnik, 2009 for a review, also Chernov, 2011). In one of them, they are attributed to the coalescence of electrostatic *Bernstein waves* at the harmonics of the electron gyrofrequency, $\omega = s\omega_{ce}$, and plasma waves at the upper hybrid frequency, $\omega_{UH} = \sqrt{\omega_p^2 + \omega_{ce}^2} \simeq \omega_p$ for $\omega_{ce} \ll \omega_p$. The resulting frequency is $\omega = \omega_p + s\omega_{ce}$. The separation of spectral maxima should then be equal to the electron gyrofrequency and this gives directly the magnetic field. Note also that in this model all stripes are produced in the same region, which must be homogeneous; the wavy form of the pattern is attributed to magnetic field variations with time.

As an example of the field values deduced from this model, the frequency separation of the zebra stripes in **Figure 11**, ranging from 5 to 10 MHz, would imply values of 1.8–3.6 G; note, however that the frequency separation at a given time is not constant, as it should be if the stripes were at the harmonics of the gyrofrequency. The low field values that often arise from the Bernstein waves interpretation of zebras is considered as an argument against its validity (Zlotnik, 2009), another one being its inability to account for more than ∼10 stripes.

One alternative, widely accepted interpretation, attributes the zebra pattern to the *double plasma resonance* (see Zheleznyakov and Zlotnik, 1975; Zheleznyakov et al., 2016), in which the emission occurs at locations where the upper hybrid frequency is equal to a harmonic of the gyrofrequency. In this case different stripes are produced in different regions (**Figure 12**, bottom row) and the frequency separation of the stripes is (Zlotnik, 2009):

$$\frac{\Delta\omega}{\omega_{ce}} = \frac{L_B}{|L_N - L_B|} \simeq \frac{L_B}{L_N} \tag{40}$$

where L_N and L_B are the density and magnetic field scales respectively; thus $\Delta\omega$ can be significantly smaller than the gyrofrequency. Another important point is that the growth rate is ∼100 times greater than in the case of Bernstein modes.

In order to extract physical information on the basis of the double plasma resonance process, one has to model both the magnetic field and the density. Zlotnik et al. (2003) used extrapolations of the photospheric magnetic field together with a hydrostatic density variation to fit the observed frequency of the stripes. They deduced harmonic numbers in the range of $s = 13$ at 173 MHz to $s = 27$ at 143 MHz (their **Figure 5**), which correspond to field strengths of 4.9–1.9 G respectively; these are higher by a factor of 2–4 than the values that would be derived from the Bersnstein wave model and the frequency separation of the stripes of 3.3–2.5 MHz, deduced from their **Figure 5** (1.2–0.9 G). However, the temperatures associated with their hydrostatic model were rather low, only $0.8–1.18 \times 10^6$ K.

Further observational evidence in favor of the double plasma resonance has been provided by Chen et al. (2011) for an event observed with the VLA in the 1.2–1.4 MHz range, who found that zebra stripes were at different locations; using the method of Zlotnik et al. (2003), they deduced $s = 8–13$ and $B = 62$ to 35 G at estimated heights of 57–75 Mm, together with $L_N \simeq 140$ Mm and $L_N/L_B \simeq 4.4$. A similar conclusion about the emission mechanism was reached by Altyntsev et al. (2011), from the analysis of 6 events in the microwave range, while Altyntsev et al. (2005) favored the Bernstein wave model for one microwave event. Using the UTR-2 radio telescope in the decametric frequency range (16.5–33 MHz), Stanislavsky et al. (2015) obtained a field value of 0.43 G under the Bernstein mode assumption. At the other end of the radio spectrum (1.4 GHz), Karlický and Yasnov (2018) measured 0.84–37.31 G corresponding to electron densities of 0.026×10^{10} to 16.03×10^{10} cm^{-3}.

A third model attributes zebra patterns to whistler waves (for details see Chernov, 2006, 2011); in this case a magnetic trap is filled with periodic whistler emission zones separated by their absorption zones. Yasnov and Chernov (2020) noted that this model gave a reasonable magnetic field of 4.5 G, whereas the double plasma resonance model gave only 1–1.5 G together with plasma $\beta > 1$, for an event at 183 MHz that they analyzed.

8. TYPE II BURSTS

Type II bursts are due to coherent emission at the plasma frequency and/or its harmonic, excited by shock waves propagating up in the corona with a super-Alfvénic speed (Vršnak and Cliver, 2008). As type II bursts often extend into interplanetary space, they provide a magnetic field diagnostic over a very extended distance range. If the Alfvén Mach number $M_A = \upsilon/\upsilon_A$ could be estimated, the Alfvén speed that contains information about the magnetic field would be deduced from the frequency drift and the density scale.

For emission at the fundamental, under hydrostatic equilibrium with a density scale, L_N, along the shock trajectory, the velocity of the exciter is related to the frequency drift rate, df/dt, through:

$$\upsilon = \frac{2\sqrt{\pi m_e}}{e\sqrt{N_e}} L_N \frac{df}{dt} \tag{41}$$

which, combined with the definition of the Alfvén speed (38) gives:

$$B = 4\pi \frac{\sqrt{m_e m_p}}{e} \frac{L_N}{M_A} \frac{df}{dt} \tag{42}$$

B is a factor of 2 smaller if the emission is at the harmonic. It is obvious that an estimate of L_N along the shock trajectory (which is not necessarily in the vertical direction), is required. Moreover, a density-height model is needed to associate the magnetic field to a particular height in the corona. Thus, if no additional information is available from other observations,

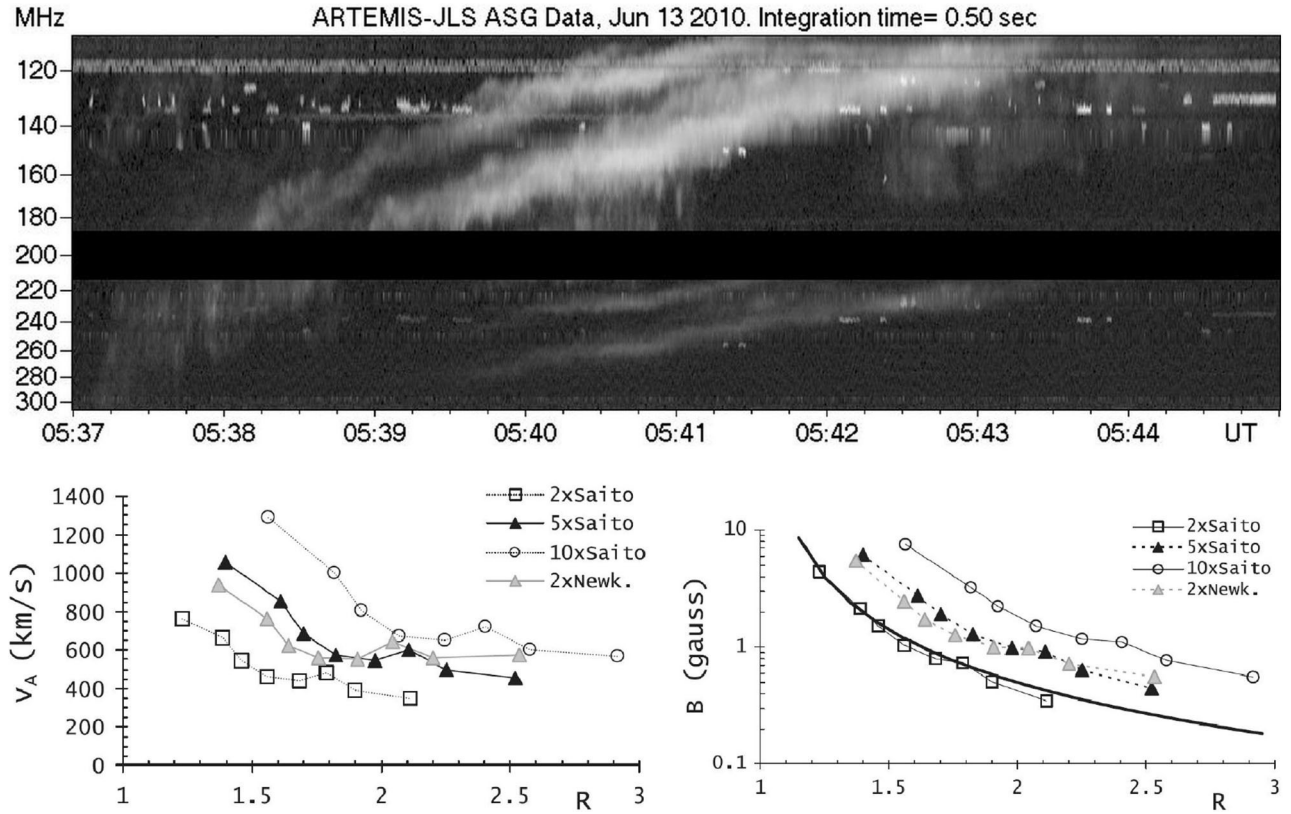

FIGURE 13 | (Top) A Type II burst with band split and fundamental/harmonic structure observed with ARTEMIS/JLS; data selected by S. Armatas. **(Bottom)** Alfvén speed (left) and magnetic field (right) as a function of radial distance in $R_\odot$, computed from type II band splitting by Vršnak et al. (2002), for various coronal density models. The thick line in the right panel shows the empirical relation of Dulk and McLean (1978); reproduced with permission © ESO.

the measurement of the magnetic field using (42) is highly model dependent.

Several decades ago, Takakura (1964) assumed $M_A = 1$ to get estimates of the magnetic field; this is not too bad an assumption since type II shocks are weak, with Mach numbers not too far from unity. The possibility of a more accurate estimate of M_A from the band splitting of certain type II's (**Figure 13**, top) was first proposed by Smerd et al. (1974). Band splitting is interpreted in terms of the density jump at the shock front, i.e., between the uncompressed plasma in front of the shock and the compressed plasma behind it. The Alfvén Mach number, M_A, is related to the compression, X, of the shock through the Rankine-Hugoniot relation which, under the quasi-perpendicular shock approximation and for plasma $\beta << 1$, can be written as (Vršnak et al., 2002):

$$M_A = \sqrt{\frac{X(X+5)}{2(4-X)}} \tag{43}$$

The compression, X, is defined as:

$$X = \frac{N_{e2}}{N_{e1}} = \left(\frac{f_2}{f_1}\right)^2 = \left(\frac{f_2 - f_1}{f_1} + 1\right)^2 \tag{44}$$

here N_{e2} and N_{e1} are the electron densities behind and in front of the shock and f_2 and f_1 the frequencies of the corresponding bands of type II emission.

On the basis of band splitting, Smerd et al. (1974) deduced Mach numbers between 1.2 and 1.5. In an extensive work, Vršnak et al. (2002) investigated 18 low frequency events; their measurements of M_A group around 1.4 and their results on the average Alfvén speed and magnetic field are shown in the bottom panels of **Figure 13** for various coronal density models. In a subsequent work, Vršnak et al. (2004) extended their investigation to events in the km wavelength range, which occur in the interplanetary space out to the Earth and proposed the empirical relation $B \propto R^{-2}$, while Mahrous et al. (2018) reported $\sim$4 G at heliocentric $R \sim 2.6\,R_\odot$ to $\sim$0.62 G at R $\sim 3.77\,R_\odot$.

Other works have employed additional information, together with the band splitting, to reduce model dependent uncertainties. For example, Cho et al. (2007) used MK4 coronameter data to constrain the electron density and deduced magnetic field of 1.3–0.4 G at heights of 1.6–2.1 $R_\odot$. Similarly, Kumari et al. (2017) and Kumari et al. (2019) derived the electron density from white light space born coronograph images and reported 0.47–0.44 G at heliocentric 2.61–2.74 $R_\odot$ and 1.21–0.5 G at heliocentric 1.58–2.15 $R_\odot$, respectively. Gopalswamy et al. (2012), using additional information on the geometry of the shock from SDO/AIA

images, determined the coronal magnetic field to be in the range of 1.3–1.5 G at heliocentric 1.2–1.5 $R_\odot$. Finally, we mention the work of Mancuso et al. (2019), who analyzed metric spectral and imaging observations, together with EUV images of a shock-streamer interaction and concluded that the magnetic field varied as $B(R) = (12.6 \pm 2.5)R^{-4}$ in the heliocentric distance range of 1.11–2.0 $R_\odot$; this gives 8.6 and 0.78 G at the limits of the above range of R.

9. DISCUSSION AND CONCLUSIONS

All things considered, radio observations offer the most reliable quantitative estimates of the magnetic field in the solar TR and the corona. However, there are three aspects that one should bear in mind: (a) That the magnetic field is often measured not over a 2-D field of view as in the photosphere but at particular locations, (b) that the vast majority of the measurements refers to active regions or bursts and not to the quiet Sun, and (c) that some methods require additional information for the computation of the magnetic field, such as the density scale and the height of the emission; this has to be provided by other observations, by models, or even by estimates.

The polarization of f-f emission at short radio λ can provide magnetic field maps over a two-dimensional field of view, which are closest to the concept of photospheric Zeeman magnetograms. Its principal limitation is the instrumental sensitivity to low circular polarization, consequently at present the magnetic field can be measured in plages but not yet in the quiet Sun. As in the case of photospheric magnetograms, the measurements reflect the value of the field over the entire region of formation of radiation which can be quite extended in height, at longer wavelengths in particular. Information about the height variation of the field can be provided by observations at different wavelengths. At longer, metric wavelengths, the situation is more complicated, both due to the difficulties in polarization measurements and the refracted and scattered ray-path geometry of the emission.

Gyro-resonance emission at relatively low heights $\leq 0.1R_\odot$ above sunspots provides directly the magnetic field as a function of temperature, rather than the height, except at the limb where high-resolution imaging can provide direct height measurements. The height variation can be probed by combining radio spectral measurements and magnetic field extrapolations, and efforts are underway to use the radio measurements as constraints to improve such extrapolations (Fleishman et al., 2019). Cyclotron lines can provide important information, but so far only a few cases have been reported. Gyrosyncrotron emission from microwave bursts has long been difficult to use due to its complex dependence on many physical parameters, but recently the method has come into its own with the advent of microwave imaging spectroscopy, both in the case of radio CMEs and in fitting of spatially resolved spectra in the flaring region. Other papers in this special research topic collection are dedicated to covering this new method.

Higher in the corona, from 0.05 to 0.4 $R_\odot$ above the photosphere, the inversion of circular polarization due to propagation effects is a powerful tool for measuring the active region magnetic field. A very important advantage of this method is that it is independent of the emission mechanism. At the same time, the theory of wave propagation gives us a warning not to take at face value the observed circular polarization, as it does not always reflect the properties of its source. The general picture that emerges from these studies is that the magnetic field drops from about 100 G to about 5 Gauss in this height range.

Bursts at metric wavelengths can be used for estimates of the magnetic field in a height range that overlaps that of polarization inversion methods and extends into the interplanetary space. Methods based on fiber bursts, zebra patterns and the band splitting of type II bursts have been discussed in this review. Generated by coherent radiation processes, these emissions are more difficult to model than those that are due to incoherent processes and this has a bearing on their use for magnetic field measurements. Moreover, the results have a high dependency on models of the coronal density.

Going to heliocentric distances of 5 $R_\odot$ and beyond, Faraday rotation of celestial sources or of signals from interplanetary space probes has been employed to diagnose the magnetic field in structures such as CMEs, which is very important information in the context of space weather. The main difficulty here is the untangling of the magnetic field from the electron density, since both contribute to the rotation of the plane of polarization.

Several years ago, Dulk and McLean (1978) combined all radio data available at the time and explored the variation of the magnetic field with height. They derived the following empirical relation, for the range $1.02 \leq R/R_\odot \leq 10$, where R is the heliocentric distance:

$$B = 0.5(R/R_\odot - 1)^{-1.5} \quad \text{G} \tag{45}$$

which fitted the data to about a factor of three. Subsequently, Gopalswamy et al. (1986) assuming that type I bursts are produced by shocks, suggested the following relation, valid for $1.09 \leq R/R_\odot \leq 1.73$:

$$B = 0.41(R/R_\odot - 1)^{-0.89} \quad \text{G} \tag{46}$$

Although it is obviously impossible to describe the complex coronal magnetic field with simple expressions such as the above, it is still instructive to compare them with the more recent observational results. A plot of magnetic field intensity as a function of height from the photosphere, using measurements compiled in this review, is shown in **Figure 14**. Different symbols denote different methods, as explained in the figure and discussed below; we have not included values at low heights from f-f or g-r emission. The thick straight line shows the Dulk-McLean relation; although this relation does not coincide with the linear regression line for this data set, we note that there are points on either side of the line.

The data plotted in **Figure 14** are by no means exhaustive, still they are indicative. Although the decline of the field intensity with height is clear, there is a lot of scatter, sometimes more than a factor of ten at the same height. The set of measurements based on polarization reversal (* in the plot), although made by

different authors and for different active regions, is the most self-consistent set and appears robust. This is not surprising, as the associated processes are well understood and the polarization measurements quite reliable. The free-free measurements of Ramesh et al. (2010) at metric λ (open squares) appear consistent with the polarization inversion measurements.

Most of the scatter in **Figure 14** is due to measurements based on metric bursts, which emit through coherent mechanisms. The majority of the results from zebra patterns and fiber bursts (x and + in the plot), with the exception of those of Chen et al. (2011), are well below the Dulk-McLean curve; these are better fitted by the Gopalswamy et al. (1986) model which, however, is below most other measurements. As for type II split-band results (open circles and dash-dot line), we note that most fall near the Dulk-McLean relation, except for the measurements of Mahrous et al. (2018) in the height range 2-3 $R_\odot$, which are well above. Some radio CME results (diamonds in the figure) are close to the Dulk-McLean curve, while others, in particular those of Mondal et al. (2020), are well above. Finally, the majority of results from Faraday rotation (triangles and the dashed line) fall quite close to the Dulk-McLean line, with the exception of the MESSENGER results of Wexler et al. (2019), which are too low.

In order to explain these differences, one should consider: (a) that physical conditions can be very different above active regions, in bursts and in CMEs and certainly quite different from the quiet Sun, (b) the variety of physical mechanisms that have been proposed for the same type of incoherent emission, (c) that the height ascribed to the measured magnetic field is often computed on the basis of a coronal density model, which may not be applicable to the actual situation; the height problem is also illustrated by the fact that many authors just quote field intensities without specifying the height, and (d) the measurements were carried out at different phases and cycles of solar activity.

What can we hope for the future? The answer is rather trivial: better observations and improved theory will provide more accurate measurements of the coronal magnetic field. Higher spatial resolution and better sensitivity to circular polarization are indispensable for measuring the magnetic field in the chromospheric network, while wide spectral coverage is necessary to follow its evolution till the network fades in the low corona. With sufficient spatial resolution and high sensitivity in V we might even be able to measure the magnetic field in coronal holes and coronal loops at metric wavelengths. High spectral resolution is required for the detection of cyclotron lines, for polarization inversion and, together with narrow band receivers, for linear polarization due to propagation effects. Last but not least, as the perihelion of the Parker Solar Probe comes closer to the Sun, we will have *in situ* measurements in the outer solar corona ($\sim 10\,R_\odot$); results from the first perihelion passage (100 to 36 $R_\odot$) have shown a $1/r^2$ dependence of the background magnetic field, with an intensity of $\sim$80 nT near perihelion (Bale et al., 2019).

Better 2D imaging together with high spectral resolution will provide us with the observational base for a better understanding of microwave, decimetric and metric burst fine structure, and will help us obtain better information on active regions in the TR and low corona. The *Low Frequency Array* (LOFAR), as well as the VLA, EOVSA, and the *Murchison Widefield Array* (MWA) have already opened an exciting new era of imaging spectroscopy. Among the new instruments, the *Siberian Solar Radioheliograph* (SSRH) is starting, a new, solar-dedicated system for the *Owens Valley Radio Observatory-Long Wavelength Array* (OVRO-LWA) is nearing completion, the Chinese *Mingantu Ultrawide Spectral Radioheliograph* (MUSER) is in operation, the *next generation VLA* (ngVLA) is under consideration, while the *Square Kilometer Array* (SKA) is not too far below the horizon. The *Atacama Large mm and sub-mm Array* (ALMA) cannot observe solar circular polarization yet (see Loukitcheva, 2020 in this special research topic collection); when this option becomes available, a 2,000 G sunspot will give an easily measurable polarization of 10% at 3 mm (Equation 23). In addition, the continued operation of existing instruments, such as the Nançay radioheliograph and RATAN-600 must be assured; the shut down of the Nobeyama radioheliograph on March 31, 2020 was a severe loss to the community.

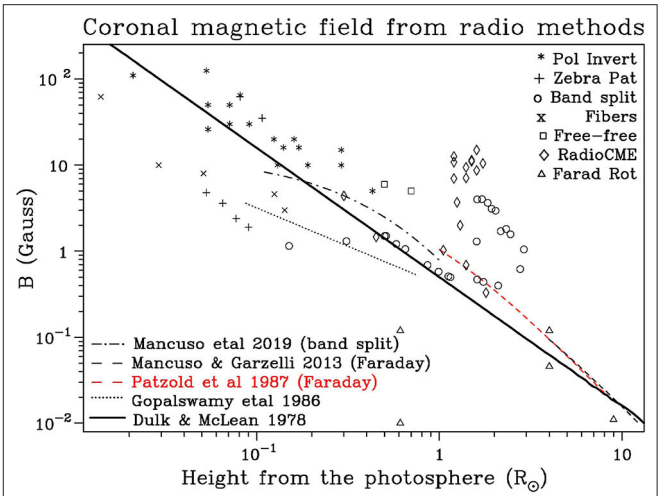

FIGURE 14 | The coronal magnetic field as a function of height, up to 12 $R_\odot$, measured by radio methods, indicated by different symbols. The empirical relations of Mancuso et al. (2019) and Mancuso and Garzelli (2013), Pätzold et al. (1987), Gopalswamy et al. (1986) are plotted as dashed-dotted, dashed, red dashed and dotted lines respectively. The full straight line is the empirical relation of Dulk and McLean (1978).

In the field of theory, modeling has already given impressive results for sunspot associated emission and microwave bursts, but there is always room for more, particularly for bursts. With incoherent mechanisms giving low estimates of the magnetic field, a better understanding of the emission and improved modeling is highly desirable.

AUTHOR CONTRIBUTIONS

Both authors reviewed the literature, selected the material presented in this review, and have approved it for publication.

FUNDING

This work was supported in part by NSF grant AST-1910354 to the New Jersey Institute of Technology.

ACKNOWLEDGMENTS

In preparing this review the authors used publicly available data from a number of instruments: the Nobeyama Radioheliograph (NoRH), the Siberian Solar Radio Telescope (SSRT), the RATAN-600 radio telescope, the Michelson Doppler Imager aboard the Solar and Heliospheric Observatory (SOHO) and the Helioseismic and Magnetic Imager (HMI) aboard the Solar Dynamics Observatory (SDO); dynamic spectra were provided by the ARTEMIS/JLS radio spectrograph group. We are grateful to all those that operate these instruments and make their data available to the community. Comments by Dr. L. Klein of Meudon observatory on an early version of the manuscript are gratefully acknowledged.

REFERENCES

Akhmedov, S. B., Gelfreikh, G. B., Bogod, V. M., and Korzhavin, A. N. (1982). The measurement of magnetic fields in the solar atmosphere above sunspots using gyro-resonance emission. *Solar Phys*. 79, 41–58. doi: 10.1007/BF00146972

Alissandrakis, C. E. (1999). "Magnetic field diagnostics in the low corona from microwave circular polarization inversion," in *Proceedings of the Nobeyama Symposium*, eds T. S. Bastian, N. Gopalswamy, and K. Shibasaki, 53–58.

Alissandrakis, C. E. (2020). Structure of the solar atmosphere: a radio perspective. *Front. Astron. Space Sci.* 7:574460. doi: 10.3389/fspas.2020.574460

Alissandrakis, C. E., Bogod, V. M., Kaltman, T. I., Patsourakos, S., and Peterova, N. G. (2019a). Modeling of the sunspot-associated microwave emission using a new method of dem inversion. *Solar Phys*. 294:23. doi: 10.1007/s11207-019-1406-x

Alissandrakis, C. E., Borgioli, F., Chiuderi Drago, F., Hagyard, M., and Shibasaki, K. (1996). Coronal magnetic fields from microwave polarization observations. *Solar Phys*. 167, 167–179. doi: 10.1007/BF00146335

Alissandrakis, C. E., Bouratzis, C., and Hillaris, A. (2019b). High-resolution observations with artemis-jls and the NRH. III. Spectroscopy and imaging of fiber bursts. *Astron. Astrophys*. 627:A133. doi: 10.1051/0004-6361/201935627

Alissandrakis, C. E., and Chiuderi-Drago, F. (1994). Detection of linear polarization in the microwave emission of solar active regions. *Astrophys. J.* 428:L73. doi: 10.1086/187396

Alissandrakis, C. E., and Kundu, M. R. (1984). Center-to-limb variation of a sunspot-associated microwave source. *Astron. Astrophys*. 139, 271–284.

Alissandrakis, C. E., Kundu, M. R., and Lantos, P. (1980). A model for sunspot associated emission at 6 CM wavelength. *Astron. Astrophys*. 82, 30–40.

Alissandrakis, C. E., Lantos, P., and Nicolaidis, E. (1985). Coronal structures observed at metric wavelengths with the Nançay radioheliograph. *Solar Phys.* 97, 267–282. doi: 10.1007/BF00165990

Alissandrakis, C. E., Nindos, A., and Kundu, M. R. (1993). Evidence for ordinary mode emission from microwave bursts. *Solar Phys*. 147, 343–358. doi: 10.1007/BF00690724

Alissandrakis, C. E., and Preka-Papadema, P. (1984). Microwave emission and polarization of a flaring loop. *Astron. Astrophys*. 139, 507–511.

Altyntsev, A. T., Kuznetsov, A. A., Meshalkina, N. S., Rudenko, G. V., and Yan, Y. (2005). On the origin of microwave zebra pattern. *Astron. Astrophys*. 431, 1037–1046. doi: 10.1051/0004-6361:20048337

Altyntsev, A. T., Lesovoi, S. V., Meshalkina, N. S., Sych, R. A., and Yan, Y. (2011). Radioheliograph observations of microwave bursts with zebra structures. *Solar Phys*. 273, 163–177. doi: 10.1007/s11207-011-9856-9

Anfinogentov, S. A., Stupishin, A. G., Mysh'yakov, I. I., and Fleishman, G. D. (2019). Record-breaking coronal magnetic field in solar active region 12673. *Astrophys. J.* 880:L29. doi: 10.3847/2041-8213/ab3042

Aurass, H., Rausche, G., Mann, G., and Hofmann, A. (2005). Fiber bursts as 3D coronal magnetic field probe in postflare loops. *Astron. Astrophys*. 435, 1137–1148. doi: 10.1051/0004-6361:20042199

Bain, H. M., Krucker, S., Saint-Hilaire, P., and Raftery, C. L. (2014). Radio imaging of a type IVM radio burst on the 14th of august 2010. *Astrophys. J.* 782:43. doi: 10.1088/0004-637X/782/1/43

Bale, S. D., Badman, S. T., Bonnell, J. W., Bowen, T. A., Burgess, D., Case, A. W., et al. (2019). Highly structured slow solar wind emerging from an equatorial coronal hole. *Nature* 576, 237–242. doi: 10.1038/s41586-019-1818-7

Bandiera, R. (1982). Diagnostic of coronal magnetic fields from microwave polarization reversal. *Astron. Astrophys*. 112, 52–60.

Bastian, T. S. (1995). Angular scattering of radio waves: Implications for mode coupling in the solar corona. *Astrophys. J*. 439:494. doi: 10.1086/175190

Bastian, T. S., Benz, A. O., and Gary, D. E. (1998). Radio emission from solar flares. *Annu. Rev. Astron. Astrophys*. 36, 131–188. doi: 10.1146/annurev.astro.36.1.131

Bastian, T. S., Dulk, G. A., and Leblanc, Y. (1996). High-resolution microwave observations of the quiet solar chromosphere. *Astrophys. J.* 473:539. doi: 10.1086/178165

Bastian, T. S., Pick, M., Kerdraon, A., Maia, D., and Vourlidas, A. (2001). The coronal mass ejection of 1998 April 20: direct imaging at radio wavelengths. *Astrophys. J. Lett*. 558, L65–L69. doi: 10.1086/323421

Benz, A. O. and Mann, G. (1998). Intermediate drift bursts and the coronal magnetic field. *Astron. Astrophys*. 333, 1034–1042.

Bird, M. K. (2007). Coronal Faraday rotation of occulted radio signals. *Astron. Astrophys. Trans*. 26, 441–453. doi: 10.1080/10556790701595236

Bogod, V. M., Alissandrakis, C. E., Kaltman, T. I., and Tokhchukova, S. K. (2015). Ratan-600 observations of small-scale structures with high spectral resolution. *Solar Phys*. 290, 7–20. doi: 10.1007/s11207-014-0526-6

Bogod, V. M., Garaimov, V. I., Zheleznyakov, V. V., and Zlotnik, E. Y. (2000). Detection of a cyclotron line in the radio spectrum of a solar active region and its interpretation. *Astron. Rep*. 44, 271–277. doi: 10.1134/1.163850

Bogod, V. M., and Gelfreikh, G. B. (1980). Measurements of the magnetic field and the gradient of temperature in the solar atmosphere above a flocculus using radio observations. *Solar Phys*. 67, 29–46. doi: 10.1007/BF00146680

Bogod, V. M., Gelfreikh, G. B., Ryabov, B. I., and Hafizov, S. R. (1993). "Coronal magnetic fields from the effect of the double inversion of circular polarization of radio emission," in *Astronomical Society of the Pacific Conference Series* (San Francisco, CA), Vol. 46, 302. doi: 10.1017/S0252921100029298

Bogod, V. M., Stupishin, A. G., and Yasnov, L. V. (2012). On magnetic fields of active regions at coronal heights. *Solar Phys*. 276, 61–73. doi: 10.1007/s11207-011-9850-2

Borovik, V. N., Medar', V. G., and Korzhavin, A. N. (1999). First measurements of the magnetic field in a coronal hole from RATAN-600 radio observations of the Sun. *Astron. Lett*. 25, 250–257.

Bouratzis, C., Hillaris, A., Alissandrakis, C. E., Preka-Papadema, P., Moussas, X., Caroubalos, C., et al. (2019). High resolution observations with artemis-jls. ii. type iv associated intermediate drift bursts. *Astron. Astrophys*. 625:A58. doi: 10.1051/0004-6361/201834792

Brosius, J. W., and White, S. M. (2006). Radio measurements of the height of strong coronal magnetic fields above sunspots at the solar limb. *Astrophys. J. Lett*. 641, L69–L72. doi: 10.1086/503774

Cargill, P. J. (2009). Coronal magnetism: difficulties and prospects. *Space Sci. Rev*. 144, 413–421. doi: 10.1007/s11214-008-9446-9

Carley, E. P., Vilmer, N., Simoes, P. J. A., and Ó Fearraigh, B. (2017). Estimation of a coronal mass ejection magnetic field strength using radio observations of gyrosynchrotron radiation. *Astron. Astrophys*. 608:A137. doi: 10.1051/0004-6361/201731368

Chambe, G., and Lantos, P. (1971). Influence of helium and heavy elements on the radio absorption coefficient. *Solar Phys*. 17, 97–98. doi: 10.1007/BF00152864

Chen, B., Bastian, T. S., Gary, D. E., and Jing, J. (2011). Spatially and spectrally resolved observations of a zebra pattern in a solar decimetric radio burst. *Astrophys. J*. 736:64. doi: 10.1088/0004-637X/736/1/64

Chen, B., Shen, C., Gary, D. E., Reeves, K. K., Fleishman, G. D., Yu, S., et al. (2020). Measurement of magnetic field and relativistic electrons along a solar flare current sheet. *arXiv:2005.12757*. doi: 10.1038/s41550-020-1147-7

Chernov, G. (2011). *Fine Structure of Solar Radio Bursts* Berlin: Springer. doi: 10.1007/978-3-642-20015-1

Chernov, G. P. (2006). Solar radio bursts with drifting stripes in emission and absorption. *Space Sci. Rev.* 127, 195–326. doi: 10.1007/s11214-006-9141-7

Chiuderi Drago, F., Alissandrakis, C., and Hagyard, M. (1987). Microwave emission above steady and moving sunspots. *Solar Phys.* 112, 89–105. doi: 10.1007/BF00148490

Cho, K. S., Lee, J., Gary, D. E., Moon, Y. J., and Park, Y. D. (2007). Magnetic field strength in the solar corona from type ii band splitting. *Astrophys. J.* 665, 799–804. doi: 10.1086/519160

Cohen, M. H. (1960). Magnetoionic mode coupling at high frequencies. *Astrophys. J.* 131:664. doi: 10.1086/146878

Dulk, G. A., and McLean, D. J. (1978). Coronal magnetic fields. *Solar Phys.* 57, 279–295. doi: 10.1007/BF00160102

Efimov, A. I., Lukanina, L. A., Rogashkova, A. I., Samoznaev, L. N., Chashei, I. V., Bird, M. K., et al. (2015). Coronal radio occultation experiments with the helios solar probes: correlation/spectral analysis of faraday rotation fluctuations. *Solar Phys.* 290, 2397–2408. doi: 10.1007/s11207-015-0687-y

Fleishman, G., Mysh'yakov, I., Stupishin, A., Loukitcheva, M., and Anfinogentov, S. (2019). Force-free field reconstructions enhanced by chromospheric magnetic field data. *Astrophys. J.* 870:101. doi: 10.3847/1538-4357/aaf384

Fleishman, G. D., Gary, D. E., Chen, B., Kuroda, N., Yu, S., and Nita, G. M. (2020). Decay of the coronal magnetic field can release sufficient energy to power a solar flare. *Science* 367, 278–280. doi: 10.1126/science.aax6874

Fleishman, G. D., and Melnikov, V. F. (2003). Gyrosynchrotron emission from anisotropic electron distributions. *Astrophys. J.* 587, 823–835. doi: 10.1086/368252

Gary, D. E., Chen, B., Dennis, B. R., Fleishman, G. D., Hurford, G. J., Krucker, S., et al. (2018). Microwave and hard x-ray observations of the 2017 September 10 solar limb flare. *Astrophys. J.* 863:83. doi: 10.3847/1538-4357/aad0ef

Gelfreikh, G. (2004) "Coronal magnetic field measurements through bremsstrahlung emission," in *Solar and Space Weather Radiophysics. Astrophysics and Space Science Library*, Vol. 314 (Dordrecht: Springer). doi: 10.1007/1-4020-2814-8_6

Gelfreikh, G. B. (1998). "Three-dimensional structure of the magnetospheres of solar active regions from radio observations (invited review)," in *Three-Dimensional Structure of Solar Active Regions, Vol. 155*, eds C. E. Alissandrakis and B. Schmieder, Astronomical Society of the Pacific Conference Series (San Francisco, CA), 110.

Gelfreikh, G. B., Peterova, N. G., and Riabov, B. I. (1987). Measurements of magnetic fields in solar corona as based on the radio observations of the inversion of polarization of local sources at microwaves. *Solar Phys.* 108, 89–97. doi: 10.1007/BF00152079

Gelfreikh, G. B., Pilyeva, N. A., and Ryabov, B. I. (1997). On the gradient of coronal magnetic fields from radio observations. *Solar Phys.* 170, 253–264. doi: 10.1023/A:1004967202294

Gopalswamy, N., and Kundu, M. R. (1987). Simultaneous radio and white light observations of the 1984 June 27 coronal mass ejection event. *Solar Phys.* 114, 347–362. doi: 10.1007/BF00167350

Gopalswamy, N., Nitta, N., Akiyama, S., Mäkelä, P., and Yashiro, S. (2012). Coronal magnetic field measurement from EUV images made by the solar dynamics observatory. *Astrophys. J.* 744:72. doi: 10.1088/0004-637X/744/1/72

Gopalswamy, N., Thejappa, G., Sastry, C. V., and Tlamicha, A. (1986). Estimation of coronal magnetic fields using type-i emission. *Bull. Astron. Instit. Czechoslov.* 37:115.

Gopalswamy, N., White, S. M., and Kundu, M. R. (1991). Large-scale features of the sun at 20 centimeter wavelength. *Astrophys. J.* 379:366. doi: 10.1086/170512

Gopalswamy, N., Zheleznyakov, V. V., White, S. M., and Kundu, M. R. (1994). Polarization features of solar radio emission and possible existence of current sheets in active regions. *Solar Phys.* 155, 339–350. doi: 10.1007/BF00680599

Grebinskij, A., Bogod, V., Gelfreikh, G., Urpo, S., Pohjolainen, S., and Shibasaki, K. (2000). Microwave tomography of solar magnetic fields. *Astron. Astroph. Suppl. Ser.* 144, 169–180. doi: 10.1051/aas:2000202

Hagyard, M. J., Teuber, D., West, E. A., Tand berg-Hanssen, E., Henze, W., J., Beckers, J. M., et al. (1983). Vertical gradients of sunspot magnetic fields. *Solar Phys.* 84, 13–31. doi: 10.1007/BF00157439

Henze, W., J., Tandberg-Hanssen, E., Hagyard, M. J., West, E. A., Woodgate, B. E., Shine, R. A., et al. (1982). Observations of the longitudinal magnetic field in the transition region and photosphere of a sunspot. *Solar Phys.* 81, 231–244. doi: 10.1007/BF00151299

Ingleby, L. D., Spangler, S. R., and Whiting, C. A. (2007). Probing the large-scale plasma structure of the solar corona with faraday rotation measurements. *Astrophys. J.* 668, 520–532. doi: 10.1086/521140

Kakinuma, T., and Swarup, G. (1962). A model for the sources of the slowly varying component of microwave solar radiation. *Astrophys. J.* 136:975. doi: 10.1086/147450

Kaltman, T. I., and Bogod, V. M. (2019) On detecting the fourth gyrofrequency harmonic in microwave emission spectra above sunspots. *Cosmic Res.* 57, 1-9. doi: 10.1134/S0010952519010040

Kaltman, T. I., Korzhavin, A. N., and Peterova, N. G. (2007). The self-inversion of the sign of circular polarization in "Halo" microwave sources. *Solar Phys.* 242, 125–142. doi: 10.1007/s11207-007-0057-5

Karlický, M., and Yasnov, L. V. (2018). Determination of plasma parameters in radio sources of solar zebra-patterns based on relations between the zebra-stripe frequencies and gyro-harmonic numbers. *Astrophys. J.* 867:28. doi: 10.3847/1538-4357/aae1f8

Klein, K. L., and Trottet, G. (1984). Gyrosynchrotron radiation from a source with spatially varying field and density. *Astron. Astrophys.* 141, 67–76.

Kontogeorgos, A., Tsitsipis, P., Caroubalos, C., Moussas, X., Preka-Papadema, P., Hilaris, A., et al. (2006). The improved Artemis iv multichannel solar radio spectrograph of the University of Athens. *Exp. Astron.* 21, 41–55. doi: 10.1007/s10686-006-9066-x

Kooi, J. E., Fischer, P. D., Buffo, J. J., and Spangler, S. R. (2014). Measurements of coronal faraday rotation at 4.6 $R_\odot$. *Astrophys. J.* 784:68. doi: 10.1088/0004-637X/784/1/68

Kooi, J. E., Fischer, P. D., Buffo, J. J., and Spangler, S. R. (2017). VLA measurements of faraday rotation through coronal mass ejections. *Solar Phys.* 292:56. doi: 10.1007/s11207-017-1074-7

Korzhavin, A. N., Opeikina, L. V., and Peterova, N. G. (2010). Transition region above sunspots inferred from microwave observations. *Astrophys. Bull.* 65, 60–74. doi: 10.1134/S1990341310010062

Kuijpers, J. (1975). Generation of intermediate drift bursts in solar type iv radio continua through coupling of whistlers and Langmuir waves. *Solar Phys.* 44, 173–193. doi: 10.1007/BF00156854

Kumari, A., Ramesh, R., Kathiravan, C., and Wang, T. J. (2017). Strength of the solar coronal magnetic field - A comparison of independent estimates using contemporaneous radio and white-light observations. *Solar Phys.* 292:161. doi: 10.1007/s11207-017-1180-6

Kumari, A., Ramesh, R., Kathiravan, C., Wang, T. J., and Gopalswamy, N. (2019). Direct estimates of the solar coronal magnetic field using contemporaneous extreme-ultraviolet, radio, and white-light observations. *Astrophys. J.* 881:24. doi: 10.3847/1538-4357/ab2adf

Kundu, M. R. (1959). Structures et propriétés des sources d'activit&eacute solaire sur ondes centimétriques. *Ann. d'Astrophys.* 22:1.

Kundu, M. R. (1965). *Solar Radio Astronomy*. New York, NY: Interscience Publication.

Kundu, M. R., and Alissandrakis, C. E. (1975). Observations at 6 CM of the solar active region. *Nature* 257, 465–467. doi: 10.1038/257465a0

Kundu, M. R., and Alissandrakis, C. E. (1984). Structure and polarization of active region microwave emission. *Solar Phys.* 94, 249–283. doi: 10.1007/BF00151317

Kundu, M. R., Nindos, A., and Grechnev, V. V. (2004). The configuration of simple short-duration solar microwave bursts. *Astron. Astrophys.* 420, 351–359. doi: 10.1051/0004-6361:20034461

Kundu, M. R., Nindos, A., White, S. M., and Grechnev, V. V. (2001). A multiwavelength study of three solar flares. *Astrophys. J.* 557, 880–890. doi: 10.1086/321534

Kuznetsov, A. A., and Kontar, E. P. (2015). Spatially resolved energetic electron properties for the 21 May 2004 flare from radio observations and 3D simulations. *Solar Phys.* 290, 79–93. doi: 10.1007/s11207-014-0530-x

Lang, K. R., Willson, R. F., Kile, J. N., Lemen, J., Strong, K. T., Bogod, V. L., et al. (1993). Magnetospheres of solar active regions inferred from spectral-polarization observations with high spatial resolution. *Astrophys. J.* 419:398. doi: 10.1086/173493

Lang, K. R., Willson, R. F., Smith, K. L., and Strong, K. T. (1987). Solar active region physical parameters inferred from a thermal cyclotron line and soft X-ray spectral lines. *Astrophys. J.* 322:1044. doi: 10.1086/165799

Lee, J. (2007). Radio emissions from solar active regions. *Space Sci. Rev*. 133, 73–102. doi: 10.1007/s11214-007-9206-2

Lee, J., McClymont, A. N., Mikić, Z., White, S. M., and Kundu, M. R. (1998a). Coronal currents, magnetic fields, and heating in a solar active region. *Astrophys. J.* 501, 853–865. doi: 10.1086/305851

Lee, J., White, S. M., Kundu, M. R., Mikic, Z., and McClymont, A. N. (1998b). Microwave mode coupling above active regions as a coronal density diagnostic. *Solar Phys*. 180, 193–211. doi: 10.1023/A:1005061416572

Lin, H., Kuhn, J. R., and Coulter, R. (2004). Coronal magnetic field measurements. *Astrophys. J. Lett*. 613, L177–L180. doi: 10.1086/425217

Lin, H., Penn, M. J., and Tomczyk, S. (2000). A new precise measurement of the coronal magnetic field strength. *Astrophys. J. Lett*. 541, L83–L86. doi: 10.1086/312900

Loukitcheva, M. (2020). Measuring magnetic field with atacama large millimeter/submillimeter array. *Front. Astron. Space Sci*. 7:45. doi: 10.3389/fspas.2020.00045

Mahrous, A., Alielden, K., Vršnak, B., and Youssef, M. (2018). Type II solar radio burst band-splitting: measure of coronal magnetic field strength. *J. Atmos. Solar-Terrest. Phys*. 172, 75–82. doi: 10.1016/j.jastp.2018.03.018

Maia, D. J. F., Gama, R., Mercier, C., Pick, M., Kerdraon, A., and Karlický, M. (2007). The radio-coronal mass ejection event on 2001 April 15. *Astrophys. J.* 660, 874–881. doi: 10.1086/508011

Mancuso, S., Frassati, F., Bemporad, A., and Barghini, D. (2019). Three-dimensional reconstruction of CME-driven shock-streamer interaction from radio and EUV observations: a different take on the diagnostics of coronal magnetic fields. *Astron. Astrophys*. 624:L2. doi: 10.1051/0004-6361/201935157

Mancuso, S., and Garzelli, M. V. (2013). Radial profile of the inner heliospheric magnetic field as deduced from Faraday rotation observations. *Astron. Astrophys*. 553:A100. doi: 10.1051/0004-6361/201220319

Mann, G., Baumgaertel, K., Chernov, G. P., and Karlicky, M. (1989). Interpretation of a special fine structure in type-iv solar radio bursts. *Solar Phys*. 120, 383–391. doi: 10.1007/BF00159886

Mann, G., Karlicky, M., and Motschmann, U. (1987). On the intermediate drift burst model. *Solar Phys*. 110, 381–389. doi: 10.1007/BF00206432

McCauley, P. I., Cairns, I. H., White, S. M., Mondal, S., Lenc, E., Morgan, J., et al. (2019). The low-frequency solar corona in circular polarization. *Solar Phys*. 294:106. doi: 10.1007/s11207-019-1502-y

Melrose, D. B. (1985). Elementary theoretical concepts. 89-110.

Mercier, C., and Chambe, G. (2009). High dynamic range images of the solar corona between 150 and 450 MHz. *Astrophys. J. Lett*. 700, L137–L140. doi: 10.1088/0004-637X/700/2/L137

Mondal, S., Oberoi, D., and Vourlidas, A. (2020). Estimation of the physical parameters of a CME at High coronal heights using low-frequency radio observations. *Astrophys. J*. 893:28. doi: 10.3847/1538-4357/ab7fab

Nagelis, J., and Ryabov, B. I. (1992). Energetics of an active region with the microwave interspot component. *Kinemat. Phys. Celest. Bodies* 8, 28–32.

Newkirk, Gordon, J. (1961). The solar corona in active regions and the thermal origin of the slowly varying component of solar radio radiation. *Astron. J.* 133:983. doi: 10.1086/147104

Nindos, A. (2020). Incoherent Solar Radio Emission. *Front. Astron. Space Sci*. 7:57. doi: 10.3389/fspas.2020.00057

Nindos, A., and Aurass, H. (2007). *Pulsating Solar Radio Emission, Vol. 725*, 251. doi: 10.1007/978-3-540-71570-2_12

Nindos, A., Aurass, H., Klein, K. L., and Trottet, G. (2008). Radio emission of flares and coronal mass ejections. *Solar Phys*. 253, 3–41. doi: 10.1007/s11207-008-9258-9

Nindos, A., White, S. M., Kundu, M. R., and Gary, D. E. (2000). Observations and models of a flaring loop. *Astrophys. J.* 533, 1053–1062. doi: 10.1086/308705

Nita, G. M., Fleishman, G. D., Kuznetsov, A. A., Kontar, E. P., and Gary, D. E. (2015). Three-dimensional radio and x-ray modeling and data analysis software: revealing flare complexity. *Astrophys. J.* 799:236. doi: 10.1088/0004-637X/799/2/236

Nita, G. M., Viall, N. M., Klimchuk, J. A., Loukitcheva, M. A., Gary, D. E., Kuznetsov, A. A., et al. (2018). Dressing the coronal magnetic extrapolations of active regions with a parameterized thermal structure. *Astrophys. J*. 853:66. doi: 10.3847/1538-4357/aaa4bf

Pätzold, M., Bird, M. K., Volland, H., Levy, G. S., Seidel, B. L., and Stelzried, C. T. (1987). The mean coronal magnetic field determined from HELIOS Faraday rotation measurements. *Solar Phys*. 109, 91–105. doi: 10.1007/BF00167401

Peterova, N. G., and Akhmedov, S. B. (1974). Influence of transverse magnetic fields on polarized radio emissions from solar local sources. *Soviet Astron*. 17:768.

Preka-Papadema, P., and Alissandrakis, C. E. (1988). Spatial and spectral structure of a solar flaring loop at centimeter wavelengths. *Astron. Astrophys*. 191, 365–373.

Ramesh, R., Kathiravan, C., and Sastry, C. V. (2010). Estimation of magnetic field in the solar coronal streamers through low frequency radio observations. *Astrophys. J*. 711, 1029–1032. doi: 10.1088/0004-637X/711/2/1029

Ratcliffe, J. A. (1959). *The Magneto-Ionic Theory and Its Applications to the Ionosphere*. Cambridge: Cambridge University Press.

Rausche, G., Aurass, H., Mann, G., Karlický, M., and Vocks, C. (2007). On solar intermediate drift radio bursts at decimeter and meter wavelength. *Solar Phys*. 245, 327–343. doi: 10.1007/s11207-007-9036-0

Ryabov, B. (2004). "Coronal magnetic field measurements through quasi-transverse propagation," in *Solar and Space Weather Radiophysics, Vol. 314 of Astrophysics and Space Science Library*, eds D.E. Gary and C. U. Keller (Dordrecht: Springer) 135. doi: 10.1007/1-4020-2814-8_7

Ryabov, B. I. (1998). Analysis of the multiple inversion of the circular polarization of sunspot-associated microwave sources. *Radiophys. Quant. Electron*. 41, 169–176. doi: 10.1007/BF02676534

Ryabov, B. I., Maksimov, V. P., Lesovoi, S. V., Shibasaki, K., Nindos, A., and Pevtsov, A. (2005). Coronal magnetography of solar active region 8365 with the SSRT and Norh radio heliographs. *Solar Phys*. 226, 223–237. doi: 10.1007/s11207-005-2691-0

Ryabov, B. I., Pilyeva, N. A., Alissandrakis, C. E., Shibasaki, K., Bogod, V. M., Garaimov, V. I., et al. (1999). Coronal magnetography of an active region from microwave polarization inversion. *Solar Phys*. 185, 157–175. doi: 10.1023/A:1005114303703

Segre, S. E., and Zanza, V. (2001). Evolution of polarization for radiation crossing a plasma layer of quasi-transverse propagation and the interpretation of radioastronomical measurements. *Astrophys. J*. 554, 408–415. doi: 10.1086/321352

Shibasaki, K., Enome, S., Nakajima, H., Nishio, M., Takano, T., Hanaoka, Y., et al. (1994). A purely polarized S-component at 17 GHz. *Publ. Astron. Soc. Jpn*. 46, L17–L20.

Simões, P. J. A., and Costa, J. E. R. (2010). Gyrosynchrotron emission from anisotropic pitch-angle distribution of electrons in 3-D solar flare sources. *Solar Phys*. 266, 109–121. doi: 10.1007/s11207-010-9596-2

Smerd, S. F., Sheridan, K. V., and Stewart, R. T. (1974). "On split-band structure in type II radio bursts from the sun (presented by S.F. Smerd)," in *Coronal Disturbances, Vol. 57 of IAU Symposium*, ed G. A. Newkirk, Dordecht 389. doi: 10.1017/S0074180900234542

Solanki, S. K., Inhester, B., and Schüssler, M. (2006). The solar magnetic field. *Rep. Prog. Phys*. 69, 563–668. doi: 10.1088/0034-4885/69/3/R02

Spangler, S. R. (2005). The strength and structure of the coronal magnetic field. *Space Sci. Rev*. 121, 189–200. doi: 10.1007/s11214-006-4719-7

Stanislavsky, A. A., Konovalenko, A. A., Koval, A. A., Dorovskyy, V. V., Zarka, P., and Rucker, H. O. (2015). Coronal magnetic field strength from decameter zebra-pattern observations: complementarity with band-splitting measurements of an associated type II burst. *Solar Phys*. 290, 205–218. doi: 10.1007/s11207-014-0620-9

Stepanov, A. V., Zaitsev, V. V., and Nakariakov, V. M. (2012). *Coronal Seismology: Waves and Oscillations in Stellar Coronae Flare Plasma*. Weinheim: Wiley-VCH Verlag GmbH & Co. KGaA. doi: 10.1002/9783527645985

Stupishin, A. G., Kaltman, T. I., Bogod, V. M., and Yasnov, L. V. (2018). Modeling of solar atmosphere parameters above sunspots using RATAN-600 microwave observations. *Solar Phys*. 293:13. doi: 10.1007/s11207-017-1228-7

Takakura, T. (1964). Estimates of the distribution of the sun's magnetic field intensity in the corona using radio bursts measurements. *Publ. Astron. Soc. Jpn*. 16:230.

Takakura, T. (1967). Theory of solar bursts (invited review paper). *Solar Phys*. 1, 304–353. doi: 10.1007/BF00151359

Trujillo Bueno, J. (2010). Recent advances in chromospheric and coronal polarization diagnostics. *Astrophys. Space Sci. Proc*. 19:118. doi: 10.1007/978-3-642-02859-5_9

Tun, S. D., Gary, D. E., and Georgoulis, M. K. (2011). Three-dimensional structure of a solar active region from spatially and spectrally resolved microwave observations. *Astrophys. J*. 728:1. doi: 10.1088/0004-637X/728/1/1

Tun, S. D., and Vourlidas, A. (2013). Derivation of the magnetic field in a coronal mass ejection core via multi-frequency radio imaging. *Astrophys. J*. 766:130. doi: 10.1088/0004-637X/766/2/130

Tzatzakis, V., Nindos, A., and Alissandrakis, C. E. (2008). A statistical study of microwave flare morphologies. *Solar Phys*. 253, 79–94. doi: 10.1007/s11207-008-9263-z

Van Doorsselaere, T., Nakariakov, V. M., Young, P. R., and Verwichte, E. (2008). Coronal magnetic field measurement using loop oscillations observed by Hinode/EIS. *Astron. Astrophys*. 487, L17–L20. doi: 10.1051/0004-6361:200810186

Vocks, C., Mann, G., Breitling, F., Bisi, M. M., Dabrowski, B., Fallows, R., et al. (2018). LOFAR observations of the quiet solar corona. *Astron. Astrophys*. 614:A54. doi: 10.1051/0004-6361/201630067

Vourlidas, A., Carley, E. P., and Vilmer, N. (2020). Radio observations of coronal mass ejections: space weather aspects. *Front. Astron. Space Sci*. 7:43. doi: 10.3389/fspas.2020.00043

Vršnak, B., and Cliver, E. W. (2008). Origin of coronal shock waves. *Solar Phys*. 253, 215–235. doi: 10.1007/s11207-008-9241-5

Vršnak, B., Magdalenić, J., Aurass, H., and Mann, G. (2002). Band-splitting of coronal and interplanetary type ii bursts. II. Coronal magnetic field and alfvén velocity. *Astron. Astrophys*. 396, 673–682. doi: 10.1051/0004-6361:20021413

Vršnak, B., Magdalenić, J., and Zlobec, P. (2004). Band-splitting of coronal and interplanetary type ii bursts. III. Physical conditions in the upper corona and interplanetary space. *Astron. Astrophys*. 413, 753–763. doi: 10.1051/0004-6361:20034060

Wang, Z., Chen, B., and Gary, D. E. (2017). Dynamic spectral imaging of decimetric fiber bursts in an eruptive solar flare. *Astrophys. J*. 848:77. doi: 10.3847/1538-4357/aa8ee5

Wexler, D. B., Hollweg, J. V., Efimov, A. I., Song, P., Jensen, E. A., Lionello, R., et al. (2019). Radio occultation observations of the solar corona over 1.60-1.86 $R_\odot$: faraday rotation and Frequency shift analysis. *J. Geophys. Res*. 124, 7761–7777. doi: 10.1029/2019JA026937

White, S. M. (2004). "Coronal magnetic field measurements through gyroresonance emission," in *Solar and Space Weather Radiophysics. Astrophysics and Space Science Library, Vol. 314*, eds D.E. Gary and C. U. Keller (Dordrecht: Springer), 89. doi: 10.1007/1-4020-2814-8_5

White, S. M. (2005). "Radio measurements of coronal magnetic fields," in *Chromospheric and Coronal Magnetic Fields, Vol. 596 of ESA Special Publication*, eds D. E. Innes, A. Lagg, and S. A. Solanki, 10.1.

White, S. M., Thejappa, G., and Kundu, M. R. (1992). Observations on mode coupling in the solar corona and bipolar noise storms. *Solar Phys*. 138, 163–187. doi: 10.1007/BF00146202

Willson, R. F. (1985). VLA observations of solar active regions at closely spaced frequencies - Evidence for thermal cyclotron line emission. *Astrophys. J*. 298, 911–917. doi: 10.1086/163674

Yasnov, L. V. and Chernov, G. P. (2020). Alternative models of zebra patterns in the event on June 21, 2011. *Solar Phys*. 295:13. doi: 10.1007/s11207-020-1585-5

Yasnov, L. V., Kal'Tman, T. I., and Bogod, V. M. (2011). Peculiarities of polarized radio emission of solar active regions. *Astron. Rep*. 55, 82–90. doi: 10.1134/S1063772910111010

Zhelezniakov, V. V., and Zlotnik, E. I. (1980). "Thermal cyclotron radiation from solar active regions," in *Radio Physics of the Sun, Vol. 86 of IAU Symposium*, eds M. R. Kundu and T. E. Gergely, Dordrecht 87–99. doi: 10.1007/978-94-010-9722-2_10

Zhelezniakov, V. V., and Zlotnik, E. I. (1989). Cyclotron lines in the spectra of solar flares and solar active regions. *Solar Phys*. 121, 449–456. doi: 10.1007/BF00161712

Zheleznyakov, V. V. (1962). The origin of the slowly varying component of solar radio emission. *Astron. Z*. 39:5.

Zheleznyakov, V. V. (1970). *Radio Emission of the Sun and Planets*. New York, NY: Pergamon Press.

Zheleznyakov, V. V., Kocharovsky, V. V., and Kocharovsky, V. V. (1996). Linear mode coupling and polarization features of radiation in current sheets. *Astron. Astrophys*. 308, 685–696.

Zheleznyakov, V. V., and Zlotnik, E. Y. (1963). Polarization of radio waves passing through a transverse magnetic field region in the solar corona. *Astron. Z*. 40:633.

Zheleznyakov, V. V., and Zlotnik, E. Y. (1975). Cyclotron wave instability in the corona and origin of solar radio emission with fine structure. III. Origin of zebra-pattern. *Solar Phys*. 44, 461–470. doi: 10.1007/BF00153225

Zheleznyakov, V. V., Zlotnik, E. Y., Zaitsev, V. V., and Shaposhnikov, V. E. (2016). Double plasma resonance and its manifestations in radio astronomy. *Phys. Uspekhi* 59, 997–1020. doi: 10.3367/UFNe.2016.05.037813

Zlotnik, E. Y. (1994). Measuring magnetic fields in the solar corona by radio emissions. *Radiophys. Quant. Electron*. 37, 533–542. doi: 10.1007/BF01046801

Zlotnik, E. Y. (2009). Origin of zebra pattern in type IV solar radio emission. *Centr. Eur. Astrophys. Bull*. 33, 281–298.

Zlotnik, E. Y., Zaitsev, V. V., Aurass, H., Mann, G., and Hofmann, A. (2003). Solar type IV burst spectral fine structures. II. Source model. *Astron. Astrophys*. 410, 1011–1022. doi: 10.1051/0004-6361:20031250

Conflict of Interest: The authors declare that the research was conducted in the absence of any commercial or financial relationships that could be construed as a potential conflict of interest.

frontiers in Astronomy and Space Sciences

REVIEW
published: 12 February 2021
doi: 10.3389/fspas.2020.580436

Radio Astronomical Tools for the Study of Solar Energetic Particles I. Correlations and Diagnostics of Impulsive Acceleration and Particle Propagation

Karl-Ludwig Klein *

Observatoire de Paris, LESIA and Station de Radioastronomie de Nançay, Univ. PSL, CNRS, Sorbonne Univ., Univ. de Paris, Univ. d'Orléans, Meudon, France

Solar energetic particles (SEPs) are sporadically ejected from the Sun during flares and coronal mass ejections. They are of major astrophysical interest, because the proximity of the Sun allows for detailed multi-messenger studies. They affect space weather due to interactions with electronics, with the Earth's atmosphere, and with humans if they leave the protective shield of the magnetosphere of the Earth. Since early studies in the 1950s, starting with particle detectors on the ground, SEP events have been related to radio bursts. Two subjects are addressed in this chapter: attempts to establish quantitative correlations between SEPs and microwave bursts produced by gyro synchrotron radiation of mildly relativistic electrons, and the information derived from type III radio bursts on impulsive processes of particle acceleration and the coronal and interplanetary propagation. Type III radio bursts produced by electron beams on open magnetic field lines have a wide range of applications, including the identification of acceleration regions, the identification of confined particle acceleration with coronal signatures, but no SEPs, and the paths that the electrons, and energetic charged particles in general, take to travel from the low corona to the Heliosphere in case they escape. Simple scenarios of coronal particle acceleration are confirmed in relatively simple and short events. But the comparison with particle transport models shows that longer and delayed acceleration episodes exist especially in large SEP events. They will be discussed in a companion chapter.

Keywords: acceleration of particles, sun: particle emission, sun: radio emission, sun: flares, sun: coronal mass ejections

OPEN ACCESS

Edited by:
Bin Chen,
New Jersey Institute of Technology, United States

Reviewed by:
Hamish Andrew Sinclair Reid, University College London, United Kingdom
Nat Gopalswamy, Goddard Space Flight Center, National Aeronautics and Space Administration, United States

***Correspondence:**
Karl-Ludwig Klein
ludwig.klein@obspm.fr

Specialty section:
This article was submitted to Stellar and Solar Physics, a section of the journal Frontiers in Astronomy and Space Sciences

Received: *06 July 2020*
Accepted: *23 November 2020*
Published: *12 February 2021*

Citation:
Klein K-L (2021) Radio Astronomical Tools for the Study of Solar Energetic Particles I. Correlations and Diagnostics of Impulsive Acceleration and Particle Propagation. Front. Astron. Space Sci. 7:580436. doi: 10.3389/fspas.2020.580436

1 INTRODUCTION

Solar energetic particles (SEPs) is the term used for energetic particles observed *in situ* in the Heliosphere, which are accelerated during solar flares and coronal mass ejections (CMEs). They are a major element of space weather disturbances (Knipp, 2011; Schwadron et al., 2017; Malandraki and Crosby, 2018), because they interact with space-borne electronics, possibly with airborne electronics, and add to galactic cosmic rays as a source of radiation in the Earth's atmosphere. They are a serious threat for astronauts outside the magnetosphere. From the astrophysicist's viewpoint SEPs are an

illustration of charged particle acceleration in the Universe that can be studied with much detail. Observations in X-rays, EUV and white light trace the plasma dynamics in the corona where particle acceleration takes place. Gamma-ray, hard X-ray and radio observations probe energetic electrons and protons in the solar atmosphere and can be combined with *in situ* measurements to determine the acceleration regions and the processes that govern the propagation of SEPs in the corona and the Heliosphere. All this can be done with time resolutions relevant to the evolution of acceleration and propagation in individual events.

Radio bursts and energetic particles from the Sun were discovered in 1942. Since both are related to non-thermal particles during sporadic events of solar activity, the link between the two phenomena was rapidly established, and radio bursts became a tool to explore the origin of SEPs since the 1950s. At that time the most obvious transient process in the corona were flares and filament eruptions. The advent of space-borne coronagraphs drew attention to the importance of CMEs as drivers of shock waves that can accelerate SEPs in the high corona and the interplanetary medium (e.g., Reames, 1999; Gopalswamy, 2009; Desai and Giacalone, 2016; Schwadron et al., 2017). Different aspects of SEP events were reviewed in Klecker et al. (2006), Reames (2015), Simnett (2017) and Klein and Dalla (2017).

Radio emission provides key information related to the acceleration and propagation of energetic particles. The degree of correlation between SEPs in space and signatures of non-thermal particles in the solar atmosphere can be used to constrain physical relationships between the particle populations. One such signature are microwave bursts (frequency above 1 GHz, wavelengths shorter than 30 cm), produced by mildly relativistic electrons through gyrosnchrotron emission in the low corona. Radio bursts at longer wavelengths are understood to reveal features such as the presence of field lines that connect the corona with the Heliosphere (type III bursts), shock waves (type II bursts), and confined electron populations (type IV bursts), which may all be relevant to understand the connection between eruptive processes in the solar corona and particle populations in space. The reader is referred to other chapters in this volume for presentations of radio bursts (Carley et al., 2020; Reid, 2020; Vourlidas et al., 2020).

This chapter starts with a brief account of the history of joint radio and *in situ* studies of SEPs in **Section 2**, and discusses correlations between quantitative measures of the importance of SEP events and microwave bursts. The use of type III bursts to probe particle acceleration and particle propagation through the corona and interplanetary space is addressed in **Sections 3 and 4**, respectively. Type III radio emission is produced at the electron plasma frequency or its harmonic by electron beams. The electrons are accelerated to energies in the keV to tens of keV range in impulsive processes and injected onto open magnetic field lines that connect the parent active region with the Heliosphere. Tracing the emission through the radio spectrum allows us to follow the electrons from the low corona, at frequencies of about a GHz, to the vicinity of the Earth (frequency near 20 kHz). Time-extended particle acceleration including relativistic energies and its relationship with bursts of types II and IV will be addressed in a companion chapter (Klein, 2021).

2 EMPIRICAL RELATIONSHIPS BETWEEN SOLAR ENERGETIC PARTICLES AND RADIO EMISSION IN THE CORONA

2.1 SEPs and Radio Bursts - A Brief Historical Overview

The first SEP observations were either made from ground, when the SEP spectrum extended to GeV energies, or through the ionospheric absorption due to excess ionization by SEPs at tens of MeV impacting the polar ionosphere of the Earth. Balloon-borne and rocket-borne observations followed. The association between SEPs and solar radio emission was made rapidly when synchrotron emission of relativistic electrons was believed to be the radiation process of type IV bursts, which are broadband emissions at meter wavelengths, sometimes extending up to cm-wavelengths, with durations that may reach several tens of minutes or even hours (see the second panel from top in **Figure 4B**). A physical relationship was supported by the coexistence of two prominent manifestations of solar activity, the estimate of comparable numbers of relativistic electrons in the type IV source and of relativistic protons at Earth (Boischot and Denisse, 1957), and by similar time profiles of the type IV emission at frequencies below 100 MHz and the SEP intensity at energies near 170 MeV (Figure 2 in Boischot and Warwick, 1959). A delay of the type IV onset with respect to the early flare signatures in Hα was considered as an indication of a rising source that connected the chromosphere, where the flare was then supposed to have its origin, with the high corona and the interplanetary space. The first years of research on this topic are reviewed in Section 3.21 of Wild et al. (1963) and in more detail in chapter 14 of Kundu (1965) (see also Section 2.1.3 of Pick and Vilmer, 2008).

An early interpretation of the association between type IV bursts and SEP events (Boischot and Denisse, 1957; Hakura and Goh, 1959) was that the moving type IV burst was the signature of a plasma cloud released from the flaring active region. Relativistic electrons confined within the cloud were to produce the type IV burst by synchrotron emission, while the turbulence within the cloud was to accelerate protons to high energies, which escaped from the cloud when the energy was high enough, and therefore arrived at Earth before the cloud itself. The cloud was supposed to trigger a geomagnetic storm and in some cases a Forbush decrease of galactic cosmic rays. The picture is very close to the present idea that CMEs are a key ingredient in SEP events. The interpretation incorporates a time delay between the start of the flare and the release of accelerated particles into the Heliosphere. Wild et al. (1963) proposed a scenario (their Section 3.23) in two phases, where the first phase, i.e., the impulsive flare phase, was a general counterpart of solar flares, while the second phase, where relativistic electrons and protons were accelerated, occurred only in strong flares, but was directly

triggered by the first phase. They ascribed the second-phase acceleration of relativistic electrons and protons to a MHD shock wave shown by its narrow-band radio emission with slow drift toward lower frequencies (type II burst; two top panels in **Figure 4B**). This picture became very influential later in the discussion on the origin of large SEP events (Reames, 1999). The empirical association between SEP events and type II and type IV bursts is still a tool for the forecasting of SEP events (e.g., Balch, 2008).

2.2 Quantitative Correlation

Correlation studies with radio bursts especially at meter wavelengths remained for some time the basic tool of research on the origin of SEP events. Kundu and Haddock (1960) found that while most SEP events at tens of MeV were accompanied by type IV bursts, a few were only accompanied by type II bursts. However, all were found to have a strong microwave counterpart. Microwave emission in strong bursts is gyro-synchrotron emission from mildly relativistic electrons (see Nindos, 2020) and is therefore a priori a better indicator of particle acceleration than the widely used thermal soft X-rays. The flux density of microwave emission had actually been recognized as a criterion that distinguishes between SEP-events and non-SEP events in the early 1960s (Avignon and Pick-Gutmann, 1959; Kundu and Haddock, 1960; Kundu, 1965). The SEP-associated microwave bursts were found to have long duration (Kundu and Haddock, 1960; Sakurai and Maeda, 1961; Kahler, 1982a), which means that the microwave emission is in general the high-frequency part of a type IV burst. The necessity of both microwave and meter-wave emission, which signals the escape of particles to the high corona, was emphasized by Castelli et al. (1967), Akinyan et al. (1971), and Castelli and Barron (1977).

One may wonder why there should be a relationship between protons and ions in space, and microwaves emitted by non-thermal electrons in the corona. From an empirical viewpoint protons and ions at tens of MeV are strongly correlated with near-relativistic and mildly relativistic electrons in space (Daibog et al., 1989; Posner, 2007; Trottet et al., 2015). The early belief that the acceleration processes of protons and electrons in solar flares were intimately connected was, however, challenged by the RHESSI observation that hard X-rays from near-relativistic electrons and gamma-ray lines from deka-MeV nucleons have slightly, but significantly, different sources (Hurford et al., 2006; Vilmer et al., 2011). But Fomichev and Chertok (1985) and Chertok (1990) demonstrated a correlation between the peak flux of microwave bursts (at 15.4 GHz) and nuclear gamma-ray line peak fluxes in solar flares. Similarly, Shih et al. (2009) found a correlation between hard X-rays from electrons above 300 keV and gamma-ray line intensities. This means that microwave flux densities may be considered as a measure of gamma-ray line intensities, too, and reinforces the interest to use the more abundant microwave measurements in correlation studies with SEP intensities.

Another caveat of using gyrosynchrotron emission as a quantitative measure of electron acceleration is the potential action of self-absorption. It is generally argued that the higher the frequency, the more likely the source is optically thin, so that the flux density is directly related to the number of non-themal electrons. Croom (1971) showed that spectra of SEP-associated microwave bursts have their maximum at higher frequencies than bursts with no SEP-association. Even at the highest microwave frequency that is routinely monitored, 35 GHz[1], only half of the bursts can be considered to be optically thin (Correia et al., 1994). Self-absorption will hence affect a possibly existing relationship between microwaves and SEPs. Nonetheless a number of studies showed that microwave peak fluxes and fluences correlate with SEP peak intensities at tens of MeV (Kahler, 1982b; Chertok, 1990; Daibog et al., 1993; Isaeva et al., 2010; Grechnev et al., 2013; Trottet et al., 2015).

Grechnev et al. (2015) considered SEPs at higher energies than the usual tens of MeV analyzed before. They found that the integral parameters microwave fluence at 35 GHz and proton fluence above 100 MeV are more strongly correlated than the instantaneous parameters microwave peak flux and proton peak intensity. Their interpretation is that the high-energy protons tend to be accelerated by a mechanism that is closely related to the acceleration of the near-relativistic electrons producing the emission at 35 GHz - a process they term flare-acceleration. The authors consider that some proton-rich outliers may reveal predominant acceleration by the CME shock. Cliver (2016) contradicted the conclusion that the outliers could be treated as distinct phenomena, and argued in favor of a general acceleration of SEPs by the CME shock.

Chertok et al. (2009) proposed to use microwaves to predict the hardness of SEP energy spectra. They showed that SEP events with hard proton spectra between 10 and 100 MeV tend to be accompanied by microwave bursts that are particularly strong at high frequencies. They used the two highest frequencies where the flux density is monitored continually, 8.8 and 15.4 GHz (Radio Solar Telescope Network RSTN of the US Air Force). Proton spectra with index <1.5 (hard spectra) are found to be associated with microwave bursts with spectral peak above 8.8 GHz. The ratio of flux densities at the two frequencies, which is an easily observable parameter, correlates with the proton spectral hardness. The correlation has a broad scatter, but could again be confirmed by the SEP events in September 2017 (Chertok, 2018).

The existence of a correlation between two parameters is of course not a sufficient condition to infer a direct physical relationship between the two phenomena. Different eruptive manifestations in the solar corona such as soft X-ray peak flux and fluence, CME kinematics, and microwave peak flux and fluence, are all correlated with each other (Trottet et al., 2015), a phenomenon that Kahler (1982b) termed the 'big flare syndrome'. Multi-parameter statistics could in principle help to remove such internal correlations, but the events are too few to obtain detailed results (Trottet et al., 2015). The representation of SEP events by measurements in a single point is also a problem, although some studies attempt to correct for this. It is unclear whether statistical correlations

[1]Univesity of Berne until 2004, Nobeyama radio observatory.

are unable to decide between an exclusive or dominant acceleration of SEPs in flare-like processes and at CME-driven shocks, or whether they show that such a distinction simply does not exist. It is also important to consider that correlations of SEP parameters with coronal activity may vary with the energy of the SEPs: Dierckxsens et al. (2015) found a higher correlation of SEP intensity with CME speed than with soft X-ray peak flux at SEP energies below 20 MeV, and the inverse at higher energies.

3 TYPE III BURSTS AS TRACERS OF PARTICLE ACCELERATION

Type III bursts are a reference radio emission for SEP studies, because they are frequently observed and because they indicate open magnetic field lines. The advent of space-borne radio spectrographs provided nearly seamless observations from the low solar corona, where the bursts are emitted at decimetric wavelengths (~1 GHz), to the spacecraft, with a typical frequency of 20 kHz (wavelength 15 km). In this section the role of type III bursts as probes of particle acceleration is discussed.

3.1 Radio Emission and SEPs During Simple Impulsive Events

3.1.1 An Illustration: May 1, 2000

The flare of class M1.1 on May 1, 2000 is a showcase event, where different tools combining *in situ* and remote sensing techniques can be combined to get insight into the source region and propagation of energetic particles. **Figures 1A–C** display the time evolution of the radio emission from centimetric (C) to hectometric (A) wavelengths. The light curves (C) show a broadband microwave burst due to gyro-synchrotron emission of electrons of hundreds of keV to perhaps a few MeV. The emission comes from loop structures in the flaring active region (Nindos, 2020). A hard X-ray burst with a photon spectrum up to several hundreds of keV (Figure 1 of Kartavykh et al., 2007) provides complementary evidence on the acceleration of mildly relativistic electrons during this event. The group of type III bursts in the dynamic spectrum at meter-wavelengths (B) demonstrates that electrons escape to the overlying corona. The type III bursts seem to have different start frequencies, but this may also be a threshold effect due to their different flux densities. In the decameter-to-hectometer (henceforth abbreviated DH) range these bursts merge into a few strong type III bursts at frequencies below 14 MHz (**Figure 1A**). The type III bursts in this panel without counterpart above 30 MHz are

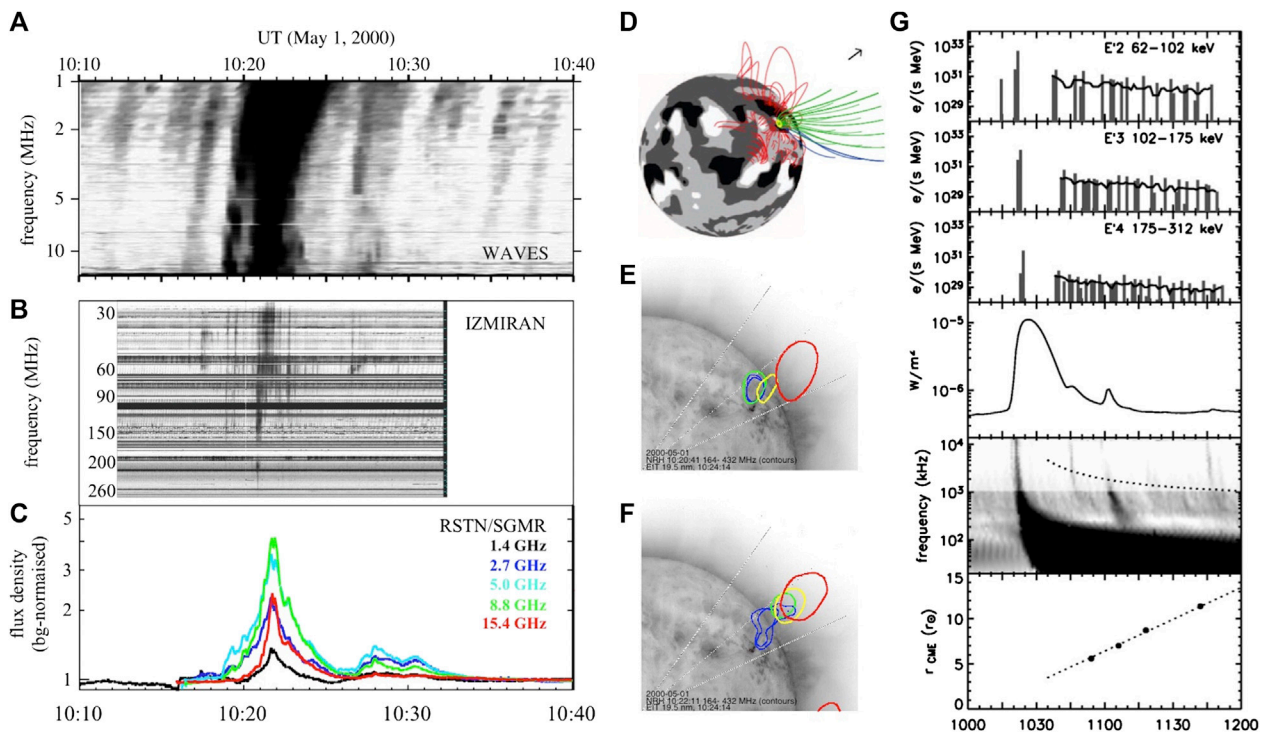

FIGURE 1 | Radio observations, magnetic field mapping, and electron release modeling during the May 1, 2000 flare. Left column: Dynamic spectra at decameter (**(A)**; Maia and Pick, 2004, ©AAS) and meter wavelengths (**(B)**; IZMIRAN, https://www.izmiran.ru/stp/lars/; figure provided by I. Chertok and R. Gorgutsa) and time histories at discrete microwave frequencies (**(C)**; data provided by NGDC, https://www.ngdc.noaa.gov/stp/space-weather/solar-data/solar-features/solar-radio/rstn-1-second/). Middle column: synoptic map of the photospheric magnetic field and field lines extrapolated using a PFSS model (**(D)**; Wang et al., 2006b, ©AAS) and iso-intensity contours of the radio sources during two type III bursts overlaid on an EUV image at 19.5 nm wavelength (**(F)**; after Klein and Posner, 2005, ©ESO). The two radial lines through the disk center delimit the CME as reported by Kahler et al. (2001). Right column **(G)**: Injection functions of electrons in three channels of ACE/EPAM, compared with the soft X-ray time profile (third from bottom), the dynamic radio spectrum in the range 14 MHz–120 kHz (frequency increasing from bottom to top on the vertical axis), and the height-time plot of the CME (bottom). From Agueda et al. (2008), ©AAS. Figures reproduced with permission.

unrelated with the flare under study. This impulsive flare is consistent with a simple scenario of the origin of SEPs: acceleration during a flare in an active region, release to the chromosphere (hard X-rays) and into low coronal loops (microwaves), escape to the Heliosphere along open magnetic field lines. A similar event is discussed in Section 22.3 of Vilmer (2011).

Figure 1D shows the magnetic field configuration around the flaring active region as inferred from a potential field model with a solar wind source surface (Wang et al., 2006b; Nitta et al., 2006). The parent active region has open field lines extending to the ecliptic plane (plotted in blue). The geometry of the radio sources during two type III bursts at meter wavelengths, observed by the Nançay Radioheliograph (NRH), is overlaid in **Figure 1E** and **1F** on an EUV image of the corona taken by SoHO/EIT. The two type III bursts have slightly different sources, showing electrons that travel along different paths in the high corona in different bursts. The open field lines plotted in green do not connect to the ecliptic plane.

Energetic particles observed near 1 AU by the ACE and Wind spacecraft were studied in detail in many publications, and different approaches were used to determine their solar release time. The results are summarized in **Table 1**. The simplest approach to infer the release time at the Sun of the first particles that are detected *in situ* is the ballistic back-projection of the onset time of the electron event at a given energy at the spacecraft, assuming an interplanetary travel distance. This approach is labeled BAL in the third column of the Table. If the electrons are detected in a sufficient number of energy channels, one can use the start time as a function of energy to trace their arrival time at the spacecraft, t_{sc}, to the solar release time, t_{SRT}, using the assumption that electrons of any energy are released at the same point and the same instant in the corona, and that they travel the same distance L: $t_{sc} = t_{SRT} + L/v$. v is the speed of the electrons. This technique is called velocity dispersion analysis (VDA). Both the VDA and BAL techniques replace the complex particle transport in the time-variable interplanetary magnetic field by simple assumptions on the travel path. Both estimate only the release time of the first particles seen at the spacecraft, and tell nothing about the duration of the release. The widths of time intervals for the BAL and VDA techniques are the estimated uncertainties of the initial solar release. Numerical models describe the transport processes, often within the focused transport model, which considers one-dimensional propagation including the focusing of particles along the magnetic field direction by the conservation of the magnetic moment in a Parker-spiral type magnetic field model, and pitch angle scattering by the interplanetary magnetic field. These models are labeled TMod in the Table.

Within the intrinsic uncertainties of the methods the release times of the first electrons in **Table 1** agree with the first type III bursts in **Figure 1**. The most sophisticated approach to determine solar release, using numerical transport models, leads to time-extended release episodes which agree reasonably with the overall timing of the group of type III bursts. One reason that the simple methods estimating the initial electron release work well here is that the pitch-angle scattering is low, as demonstrated by the long mean free paths inferred from the transport models (Kartavykh et al., 2007; Agueda et al., 2008).

Table 1 shows that the first deka-MeV protons and the first heavy ions at energies below 1 MeV/nuc may also be released in the impulsive phase, but within broader uncertainties than the electrons. The modeling of the heavy ions actually uses data with 1 h integration time, so that the inferred timing is less constrained than for the electrons. Remarkably, protons of lower energy seem to be released much later. Figure 7 of Kartavykh et al. (2007) shows that a weak early release is not represented by the model, but the bulk of the protons is clearly released later, at about the time when Agueda et al. (2008) infer a late time-extended electron release (10:36–11:52 UT). This later release is accompanied by a few faint DH type III bursts and weak soft X-ray enhancements (**Figure 1G**), while the flare is still visible in SoHO/EIT images. Judging from the images taken by the NRH (not shown), the burst locations are related with the same active region as the stronger type III bursts in the impulsive phase, but are more widely scattered.

A jet or narrow CME was observed by the SoHO/LASCO coronagraph (Kahler et al., 2001; Wang et al., 2006b) with a speed in the plane of the sky of 1,360 km s^{-1}. From a study of a sample of such events related with impulsive SEP events Wang et al. (2006b) find that the white-light feature propagates along a different path than the accelerated electrons, and that in particular the narrow CME on May 1, 2000 does not intercept field lines connected to the ecliptic plane. The authors therefore discard a role of the narrow CME in the acceleration of energetic particles observed near Earth. Acceleration near the CME front of the first MeV to deka-MeV protons detected near 1 AU is also inconsistent with the timing of the narrow CME and the type III bursts: Klein and Posner (2005) report that the CME front is about half a solar radius above the region where the radio images show the origin of the type III bursts. However, the fast CME provides the possibility of delayed acceleration in the corona, which offers interpretations of the late signatures of energetic electrons and protons detected in the May 1, 2000 event and many others (see **Section 3.2**).

TABLE 1 | Particle release times in the May 1, 2000 ent (with 500 s added to allow for comparison with electromagnetic observations from 1 AU).

Species	Instrument	Method	Release time	References
e 40 keV	ACE/EPAM	TMod	10:14–10:24	Kartavykh et al. (2007)
e 62-312 keV	ACE/EPAM	TMod	10:20–10:24	Agueda et al. (2008)
			10:36–11:52	Agueda et al. (2008)
e 175-312 keV	ACE/EPAM	BAL	10:23 ± 1 min	Maia and Pick (2004)
e 30-500 keV	Wind/3DP	VDA	10:19.5 ± 5.5 min	Klein et al. (2005)
Fe 0.08–0.91 MeV/n	ACE/ULEIS	BAL	10:20 ± 15 min	Mason et al. (2004)
Fe 0.08–0.91 MeV/n	Wind/STEP	TMod	10:14 ± 15 min	Kartavykh et al. (2007)
p 0.72–1.4 MeV	Wind/3DP	TMod	10:50	Kartavykh et al. (2007)
p 4–54 MeV	SoHO/EPHIN	VDA	10:24 ± 3 min	Klein and Posner (2005)

3.1.2 Ambient Density and Location of the Acceleration Region

Through the interpretation of plasma emission the starting frequency of the type III bursts determines the ambient electron density in the region where the beams start to emit (Reid et al., 2014). This is likely a lower limit of the local electron density in the acceleration region. The IZMIRAN spectrum in **Figure 1B** shows that the brightest type III burst starts near or above 270 MHz in the May 1, 2000 event. The NRH sees the type III bursts at 237 and 164 MHz. Their weak polarisation suggests harmonic plasma emission, so the start frequency near 300 MHz implies an electron density of about $3 \cdot 10^8$ cm^{-3}. The type III group studied by Vilmer et al. (2002) and Vilmer (2011) is very similar with a start near 300 MHz. In this event the close connection between the hard X-ray emission in the chromosphere and the decimetric radio emission in the overlying corona was underlined by coordinated changes in the imaged source structure in both spectral ranges. As pointed out, e.g., by Aschwanden (2002), Vilmer (2011), and White et al. (2011), the observations are consistent with the typical scenario of acceleration above the summits of soft X-ray loops in flares, where downward-precipitating electrons yield hard X-ray emission in the dense low atmosphere, while outward-traveling electron beams emit the type III bursts.

In some cases the radio emission comprises bursts with similar behavior as type III bursts, but which drift toward higher frequencies. The straightforward interpretation is that ordinary type III bursts are produced by upward traveling electrons, and bursts with reversed drift by downward propagating electrons, and that the acceleration region is in between. Early results of the technique are summarized in Section 3.6 of Aschwanden (2002). He inferred thermal electron densities that varied from event to event in the range $(1–10) \cdot 10^9$ cm^{-3}. The technique was more recently applied to a sample of nine solar flares by Tan et al. (2016). From burst pairs observed in the impulsive flare phase the authors derived electron densities in the range $(6–28) \cdot 10^9$ cm^{-3}.

Some type III bursts (e.g., Chen et al., 2013) start at higher frequencies, with an inferred thermal electron density of $7 \cdot 10^9$ cm^{-3} at the base of the open field lines. The authors devise a geometric model using the EUV observations of a jet and the position of the hard X-ray source to show the inclination of the open field lines along which the electron beams travel. They conclude that the acceleration region is at a height of about 15–20 Mm above the photosphere. From a completely different approach based on the energy-dependent timing of individual peaks of hard X-ray emission, Aschwanden and coworkers (see Section 3.3 of Aschwanden, 2002, and references therein) inferred a typical height of 44 Mm. These values illustrate a range of heights in different flares, which Reid et al. (2014) find to be between 25 and 180 Mm. Impulsive electron events coming from much higher coronal regions are actually more frequent, since many events show power-law spectra without any turnover down to 1–2 keV (Potter et al., 1980; Lin, 1985; Kahler, 2007). Such a turnover would be created by Coulomb collisions with the ambient electrons if the escaping electrons had traveled through a dense plasma. Lin (1985) concluded that the acceleration region had to be located at least 350 Mm above the photosphere. Evidence for the combined acceleration at low and high ($\sim 1R_\odot$) coronal altitudes was seen in a case study of bidirectional radio bursts at meter wavelengths (Klein et al., 1997), and high-coronal acceleration regions were inferred earlier from observations with the Culgoora Radioheliograph (Wild, 1968). These events of high coronal electron acceleration seem to be the low-energy manifestation of acceleration processes related to flare-like energy conversion, i.e., magnetic reconnection that occurs in fully developed flares, at the release of jets, and during the evolution of coronal streamers (see also the discussion and references in Kahler, 2007).

Since the timing of the initial release of electrons and ions seems consistent in **Table 1**, one can compare these ambient densities with values inferred from the charge states of Fe measured in impulsive SEP events. High charge states of Fe are a characteristic feature of impulsive SEP events, and were for some time attributed to high temperatures, of order 10 MK, thought to be typical for the impulsive flare phase (Reames, 1999). It was later recognized that the charge states depended on energy (Klecker et al., 2007; DiFabio et al., 2008). This can be explained by collisional stripping of the ions during their acceleration (Kocharov et al., 2000, 2001). The process can be modeled, and the measured charge states constrain the product of the ambient particle density n and the residence time in the acceleration region, τ. For the event on May 1, 2000 Kartavykh et al. (2007) infer two acceleration regions, which may be extreme values for a continuum in between: a cool region (10^6 K) where $n\tau = 9 \cdot 10^{10}$ cm^{-3} s, where the bulk of the ions is accelerated, and a minor contribution from a second region with $T = 1.58 \cdot 10^7$ K, $n\tau = 10^{11}$ cm^{-3} s. If these ions were accelerated in the same region as the electrons emitting the type III-bursts, the residence time would be $\tau = 10^{11}/3 \cdot 10^8$ s $\simeq 5$ min. This duration is not inconsistent with the initial release times of the ions in **Table 1**. However, comparative studies of nuclear gamma-ray emission and of hard X-ray emission of electrons usually show that the two particle species evolve together on time scales much closer to 1 s than to 5 min (Forrest and Chupp, 1983; Kane et al., 1986; Vestrand et al., 1999; Kiener et al., 2006; Vilmer et al., 2011). So τ could not be the typical acceleration time, but a trapping time in dense coronal structures, before the ions escape. Since ambient densities as high as 10^{11} cm^{-3} are not common in impulsive flares, although they may be encountered occasionally in coronal thick target hard X-ray sources (Veronig and Brown, 2004; Fletcher et al., 2011), the trapping time would have to exceed by far 5 min.

The frequent occurrence of impulsive ^{3}He-enriched SEP events with electron events that show no bending due to Coulomb collisions led Cliver and Kahler (1991) and Wang et al. (2016) to propose acceleration much higher in the corona, where the time scales of ion acceleration would be much longer. While the detailed independent analyses of the May 1, 2000 event and some others (Pick et al., 2006) give evidence on the coordinated acceleration of electrons from ten to hundreds of keV, ions at (0.1–1) MeV/s, and deka-MeV protons in the corona during the impulsive flare phase, a spectrum of scenarios is probably realized in different events.

3.1.3 Evidence on Fragmented Energy Release and Particle Propagation in a Fibrous Corona

A type III burst at decametric and longer wavelengths is not a simple entity that can be ascribed to an individual electron beam. It has been shown repeatedly that single bursts in this spectral range

result from the merging of several bursts at higher frequencies (e.g., Lin et al., 1973; Poquérusse et al., 1996). Even relatively simply structured type III bursts at DH wavelengths, produced during inconspicuous activity in EUV, result from complex activity in the low corona (Alissandrakis et al., 2015). The type III bursts in **Figure 1** also involved different coronal field lines.

Chen et al. (2013) used dynamical spectroscopic imaging with the VLA for a very detailed analysis of a group of type III bursts at decimeter wavelengths (1.0–1.5 GHz), i.e., lower in the corona than during the May 1, 2000 flare. The bursts accompanied a hard X-ray burst at photon energies 12–25 keV and a jet in EUV, both typical signatures of impulsive energy release in the corona. The source centroids of the bursts are plotted in panel **(A)** of **Figure 2**. The frequencies are coded by colors from red (1.5 GHz) to blue (1.0 GHz). The red contours show the hard X-ray source imaged by RHESSI. Panels **(B)** to **(G)** track one time-resolved type III burst. Panel **(A)** shows clearly that different bursts start at different frequencies and different positions, and that the radio sources follow different paths in the corona in different bursts. These paths do not correspond to any discernible structure in the EUV image. The authors compare the thermal electron density in the flux tubes carrying the electron beams, under the assumption of harmonic plasma emission, with the upper limit of the emission measure in the same regions determined by SDO/AIA. They conclude that individual electron beams propagated along bundles of magnetic field lines that were not larger than 100 km. Chen et al. (2018) find such bundles to diverge from very compact regions, which they identify as reconnection regions around magnetic null points. Models of electron beam propagation in a fibrous corona were developed in the 1990s to understand the dynamic spectra of type III bursts (Roelof and Pick, 1989) or their relationship with type V continua (Raoult et al., 1990). Electron beams injected onto a bundle of field lines propagate or are absorbed depending on the characteristics of the beams, the local plasma conditions, and the magnetic field geometry (Raoult et al., 1990; Reid and Kontar, 2015), so that an apparently simple type III burst observed with low spectral and temporal resolution is resolved into numerous bursts by more powerful instruments. Multiple sources in individual type III burst groups were found by Pick and Ji (1986) at meter wavelengths, spanning a typical angular width of 25° (see also Pick and van den Oord, 1990; Paesold et al., 2001; Ramesh et al., 2020). The new VLA observations allowed for the first time to map the sources in detail and to determine subtelescopic sizes involved in the propagation. The acceleration regions even in simple impulsive flares are multiple and connected to different parts of the high corona. This has bearing on the interpretation of measurements of energetic particles in space, for instance when modeling leads to the conclusion that different acceleration regions supply particles in a given impulsive SEP event, as in Kartavykh et al. (2007).

3.2 Time-Extended and Delayed Acceleration of SEP Events

Type III bursts have become a reference for the release of electrons, and charged particles in general, to the Heliosphere. Timing with respect to the onset of type III groups is used to distinguish different kinds of SEP events.

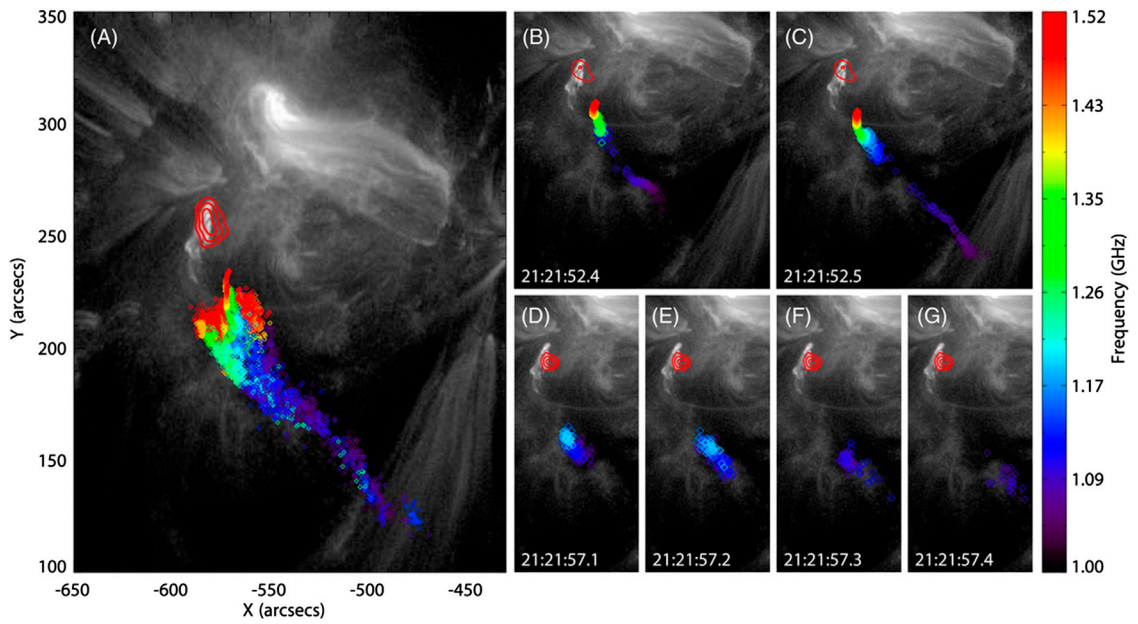

FIGURE 2 | Spectral imaging maps of a group of decimetric type III bursts (panel **(A)**) and an individual burst **(B)–(G)** with the VLA on November 5, 2011 . The centroid positions of the radio source are coded in colors depending on the frequency as shown in the colorbar on the right, and overlaid on an SDO/AIA image at 13.1 nm wavelength. The red contours in **(A)** show the hard X-ray source mapped in the 12–25 keV range by RHESSI. From Chen et al. (2013). ©AAS. Reproduced with permission.

3.2.1 Initial Solar Release Time of Anisotropic/Beamed Electron Events

A detailed study of the initial electron release in simple impulsive events shows subtleties that are not captured by the simple picture of a single initial release time that is independent of energy and particle species. L. Wang and coworkers (Wang et al., 2006a; Wang et al., 2016) studied the release of electrons in impulsive 'scatter-free' events, where the time profile and the ordering of event onset with energy suggest a low rate of pitch-angle scattering. The interplanetary path length inferred from velocity dispersion analysis was found near 1.2 AU. These authors found a systematic ordering of release times, where electrons with energies below some limit near 10 keV started to be released 1–30 min before the start of type III emission at 14 MHz, while electrons above 10 keV (10–300 keV) tended to be released at or a few minutes (0–17 min) after the start of the type III bursts.

The energy of the electron beams emitting type III bursts is inferred indirectly. Identifying the energy of electrons arriving at the time when Langmuir waves started to be observed, Ergun et al. (1998) conclude that type III bursts at km-wavelengths are emitted by electrons of 2–12 keV. Dulk et al. (1987) and Haggerty and Roelof (2006) derived similar typical values of $0.14c$ and ranges of, respectively, $(0.07 - 0.25)c$ and $(0.06 - 0.35)c$ (0.9–34 keV) from the drift rates of the leading edge of type III bursts at frequencies below 1 MHz. Close to the Sun higher exciter speeds are usually estimated from the drift rates of type III bursts at meter wavelengths, by use of a density model for the ambient corona. Exciter speeds above $0.2c$ are often quoted (see Sinclair Reid and Ratcliffe, 2014, and references therein). Reiner and MacDowall (2015) found a range $(0.2 - 0.38)c$ near the Sun, corresponding to energies in the range (10–40) keV, and a lower exciter speed near 1 AU. The exciter speed is the speed where beam electrons resonate with Langmuir waves. The decrease from the corona to interplanetary space does not necessarily reveal an energy loss. Whatever the reason of the decrease, if the electrons producing type III emission close to the Sun are indeed more energetic than those at 1 AU, the electron timing by L. Wang and coworkers is not inconsistent with events like May 1, 2000, where the start of type III bursts near 10 MHz was found to coincide with the initial release of electrons above 20 keV to the Heliosphere.

Krucker et al. (1999) and Haggerty and Roelof (2002) looked in detail into the onset timing of small and large electron events at energies up to some hundreds of keV observed, respectively, by Wind/3DP and ACE/EPAM. Events with a pronounced initial anisotropy were chosen, where one can expect that the onset time is closely related to the electron release at the Sun, rather than being determined by interplanetary propagation. Krucker and coworkers conducted a velocity-dispersion analysis of the onset of 58 events. The energy resolution of EPAM does not allow for such an analysis. Haggerty and Roelof (2002) assumed scatter-free propagation along a standard path length of 1.2 AU to infer the solar release times for more than 100 events. Both papers report that the difference between the solar release times of the electrons and the start times of the type III bursts spans a broad range from zero to about 30 min. Krucker et al. (1999) proposed that they could separate their 58 events into a sample of events with (42 cases) and without (16 cases) delay. The 16 events that were consistent with a common release with the type III bursts tended to have rather low energy, while the high-energy events were in the delayed sample. Results of the velocity-dispersion analysis of three events are shown in **Figure 3**. The vertical axis is the delay of the onset with respect to the start time of the type III emission at 14 MHz. The simultaneous release is illustrated by **(A)**. The delayed sample comprised events where the release of electrons at all energies was delayed **(B)**, as well as events where the low-energy electrons were released together with the first type III bursts, while the high-energy electrons were released later **(C)**. The separation between 'low' and 'high' energy was around 25 keV, similar to Wang et al. (2016). The insets in the three panels show the positions of the parent flares of events in the same category as the plotted one with respect to the meridian 60°W and the ecliptic plane. Krucker et al. (1999) concluded that the events with no delay are small and well-connected, while the delayed events tend to be farther away from the nominal Parker spiral. In the November 6, 1997 event (**Figure 3C**) the parent flare was nominally well-connected in longitude, but not in latitude. Besides, it was observed a few hours before the arrival of an ICME (Wimmer-Schweingruber et al., 1999), i.e., in perturbed interplanetary conditions where the magnetic connection may not be adequately described by the Parker spiral field line. The red bars along the vertical axes in **Figures 3B** and **3C**, which are not part of the original figure, show the approximate duration of the type III groups at 14 MHz. The delayed electron releases in the events in **(B)** and **(C)** started after the end of the type III bursts.

Delayed arrivals of particles near 1 AU were also reported for protons (Krucker and Lin, 2000) and ions (Nitta et al., 2015; Wang et al., 2016) at MeV/nuc energies in simple impulsive events, with delays of order 1 h, different from the May 1, 2000 event in **Section 3.1.1**. The uncertainties of the release times of MeV/nuc ions are rather large, however. Pick et al. (2006) report onset times, within an uncertainty of an hour, that are not inconsistent with a release in the vicinity of energetic electrons.

3.2.2 Evidence on Time-Extended and Delayed Electron Release From Transport Modeling

The interpretation of type III bursts as tracers of individual electron beams suggests to represent the injection function of SEP events as a series of impulsive releases. Agueda and coworkers used this approach to model short and long-lasting anisotropic electron events, in the same way as exposed above for the impulsive May 1, 2000 event. The particles are assumed to be released at a heliocentric distance of $2R_{\odot}$ onto a Parker spiral field line, the shape of which is determined by the solar wind speed measured at the spacecraft. The release height is above the height inferred from radio observations in **Section 3.1.2**, but the difference amounts only to a few seconds for electrons traveling at about $c/3$. Agueda et al. (2009) and Agueda et al. (2014) modeled the intensity and anisotropy of 17 electron events observed by ACE/EPAM and Wind/3DP at energies between about 30 and 300 keV, including impulsive and long-duration events. From the overall duration of the electron release they

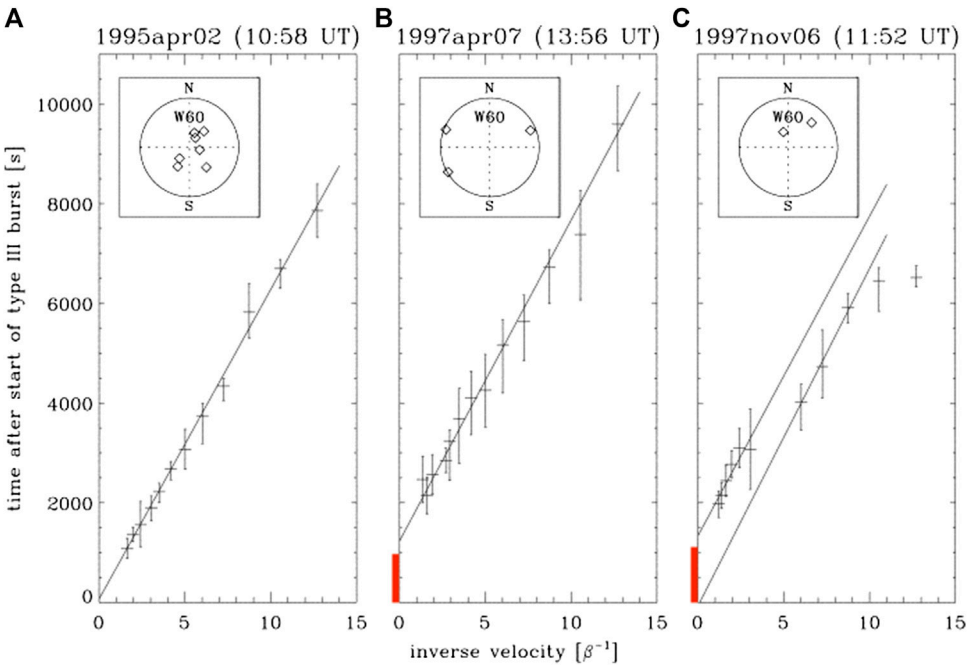

FIGURE 3 | Velocity dispersion analysis of three impulsive electron events showing different timing with respect to the start of the decametric type III bursts. The vertical axis shows the onset delay with respect to the start of the type III burst group: **(A)** simultaneous release of electrons at energies up to 80 keV; **(B)** delayed release of electrons at all energies; **(C)** simultaneous release of low-energy electrons below ~30 keV, and delayed release of electrons at higher energies. The position of the associated flare is shown in the insets with respect to a position in the ecliptic plane at 60°W. From Krucker et al. (1999). ©AAS. Reproduced with permission. The red vertical bars in **(B)** and **(C)** are estimated durations of the type III burst groups, based on the dynamic spectra in Reiner et al. (2000).

distinguished short release episodes, lasting not longer than 15–30 min, and long episodes. Five events had only the short electron release at the time of the DH type III bursts. In six events the short initial release was followed, about 30 min later, by a delayed release lasting in general several hours, as on May 1, 2000. Six events were exclusively produced by a late release. Delayed releases were most often sustained in the sense that the individual impulses produced by the model were densely packed during several hours. Pacheco et al. (2019) applied the same type of analysis to HELIOS SEP observations as close to the Sun as 0.3 AU and found the same separation into short and long release episodes.

Agueda and coworkers noted that the short initial release intervals of electrons up to about 100 keV coincided with hard X-ray emission and type III bursts in the solar atmosphere. In addition to the consistent timing, Agueda et al. (2009) found a correlation between the number of electrons released during this phase and the soft X-ray peak flux. They related these findings to a common acceleration of the interacting and escaping electrons at energies of tens to hundreds of keV during a flare. Similarly, James et al. (2017) found a correlation between spectral indices and numbers of electrons between 38 and at least 103 keV measured near 1 AU (ACE/EPAM) and observed through their hard X-ray emission in the chromosphere (RHESSI). They restricted the analysis to events with weak solar activity, where the soft X-ray emission was at most of importance C1.1 and no CME was observed (six events between 2004 and 2015). The ratio of escaping to interacting electrons ranged from 0.06 to 1.50, assuming a uniform release of electrons into a cone of width 30°. The result differs from the analysis of more energetic events, where the numbers of electrons in space were found to be orders of magnitude below those inferred from the hard X-rays (Krucker et al., 2007).

Dröge and coworkers applied similar 1D models of electron transport to multi-spacecraft observations (Dresing et al., 2012; Dröge et al., 2014; Dröge et al., 2016). Again the start of the electron injection at the Sun (several tens of keV to 100 keV) was found at the time of the DH type III bursts. Delayed onsets were found when the initial rise of the observed intensity profiles had poorly observed anisotropy, and may therefore reveal transport effects (Dresing et al., 2012). The duration of the inferred injection differed between different vantage points in a given event. The different durations in fact reflect the different rise times seen from different vantage points. However, when using 3D models, allowing for transport across the heliospheric magnetic field, they reached agreement of the modeled time profiles of intensity and anisotropy with an injection that started with the DH III bursts and often had similar duration (Dröge et al., 2014; Dröge et al., 2016). The models have a number of free parameters that do not allow to consider this relationship as a firm proof, but they are the most detailed way to infer injection functions at the Sun. Their timing supports the idea that when electrons accelerated during flaring activity in the corona have access to space, the first electrons detected near 1 AU are released with those emitting the DH type III bursts. Delays of the early arrival at the spacecraft can

be due to a poor magnetic connection and the need of cross-field transport to reach the spacecraft.

Only the late, sustained electron release was observed in the large SEP event of December 26, 2001. As shown in the comparison between the modeled electron releases and the type III bursts observed below 14 MHz in **Figure 4A**, ACE detected no electrons above 30 keV from a release at the time of the type III bursts. The parent flare appeared well connected to the Earth (54°W; Grechnev et al., 2017). However, Agueda et al. (2009) noted that the type III burst did not extend downward to the electron plasma frequency at the spacecraft, and explained this by electrons traveling along interplanetary field lines not connected to the spacecraft, as did Cane and Erickson (2003). The electron release to ACE coincided with the start of a type II radio burst. The soft X-ray and radio emissions during the same time interval as in **Figure 4A** are plotted in **Figure 4B**. The type II burst is clearly seen to originate at meter wavelengths, and to continue into the decameter wave range observed by Wind/WAVES. It occurred at the low-frequency edge of a type IV continuum. The emission stands out in the flux density time histories at fixed frequencies up to cm-wavelengths in the second panel from bottom. The type II and type IV radio emissions accompanied the entire time interval of electron release inferred from the transport model. They lasted clearly much longer than the microwave emission from the low corona. Grechnev and coworkers studied the complex evolution of this event in much detail (see Grechnev et al., 2017, and references therein). They identified a succession of two eruptions, and argued that the first, minor one, may have provided particularly favourable conditions for the acceleration of particles by the shock wave witnessed by the type II burst, and their escape to the Heliosphere. However, the type IV continuum is itself a signature of time-extended electron acceleration in the corona, related to the CME that drives the shock. A preferential association of late electron release with the type IV burst was reported in Laitinen et al. (2000).

The sustained late electron releases are in general not accompanied by type III bursts at decametric and longer wavelengths. This is a clear difference with respect to the impulsive flare phase. One possible reason (e.g., Raoult et al., 1990) is that a sustained electron release with a smooth time profile will create a bump-on-the tail distribution only at its start, whereafter the deficit of relatively low-energy electrons is continuously replenished. Similarly, the mutual overtaking of electron beams on the same field line will lead to the suppression of the radio emission (Briand et al., 2014). The absence of type III bursts during the sustained late releases suggests that the late acceleration is not just an extended version of the impulsive phase acceleration.

3.2.3 Type III Bursts and the Initial Solar Release of Major SEP Events

Type III bursts had for some time been considered as a characteristic counterpart of 'impulsive' SEP events (Reames, 1999), as discussed above, which are not particularly energetic.

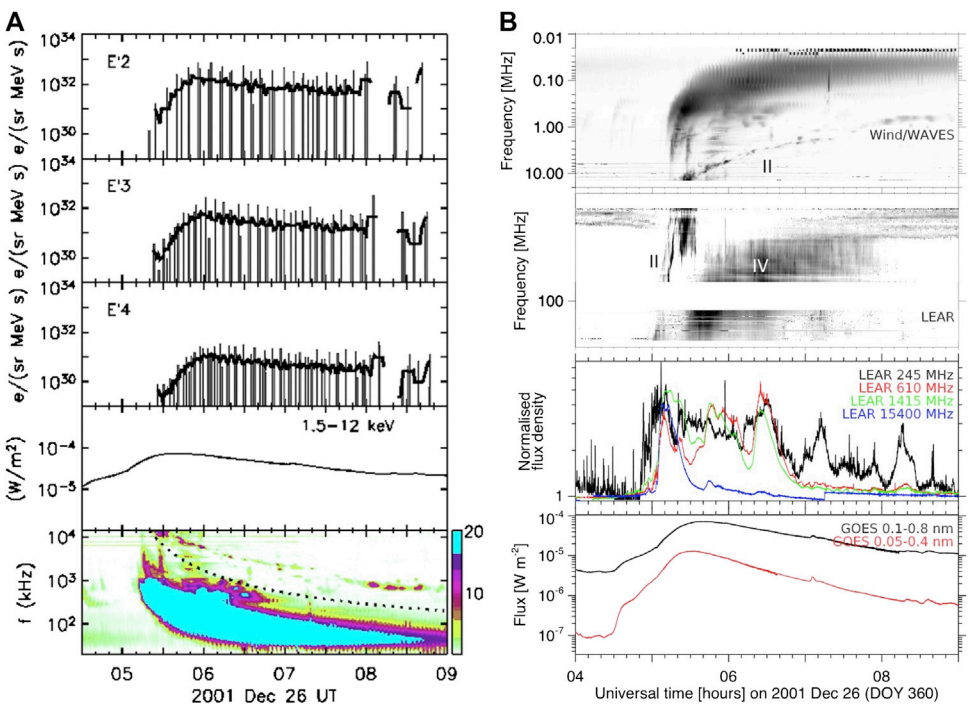

FIGURE 4 | Time histories of electron release, soft X-ray and radio emission during a large SEP event. **(A)** Injection delta-functions derived from the modeling of electrons in three energy channels of ACE/EPAM (three upper panels) compared with the soft X-ray flux (0.1–0.8 nm; second from bottom) and the dynamic radio spectrum between 14 MHz and about 10 kHz (bottom panel; vertical axis shows frequencies, increasing from bottom to top). From Agueda et al. (2009). ©ESO. Reproduced with permission. **(B)** Soft X-ray (bottom) and radio time histories (second from bottom), radio spectrum from 180 MHz to 10 kHz (frequency decreasing from bottom to top). Bursts of types II and IV are marked. Adapted from server. sepserver.eu

Cane et al. (2002), however, demonstrated that groups of type III bursts accompany SEP events in general, occurring at the beginning of 121 of 123 SEP events they analyzed. Similarly, Cane et al. (2010) found that 278 out of 280 SEP events observed above 25 MeV/nuc by IMP 8 and SoHO/ERNE were accompanied by type III bursts at dekametric and longer wavelengths. These type III emissions have a broad range of properties ranging from a few bursts that occur during the impulsive phase to large bright burst groups that continue well after the soft X-ray peak. Some other studies reported lower association rates, but all found similarly that most SEP events are accompanied by type III bursts (Vainio et al., 2013; Richardson et al., 2014; Kouloumvakos et al., 2015; Papaioannou et al., 2016; Miteva et al., 2017; Ameri et al., 2019). The histogram of durations of the burst groups at 14 MHz (Cane et al., 2002) decreases monotonously from the lowest bin, 5–10 min, to the highest, 50–55 min, with a median duration of about 20 min. The large burst groups were initially termed 'shock-accelerated' or 'shock-associated' because of their frequent occurrence on the low-frequency side of type II bursts (Cane et al., 1981; Bougeret et al., 1998; Dulk et al., 2000). Cane et al. (2002) proposed the name type III-*l* bursts, to capture long duration and low frequency in a single letter. Reiner and coworkers (Reiner et al., 2000) called them 'complex type III bursts'. In the following we consider type III bursts collectively. The peculiarities of the complex type III bursts are discussed in Section 2.4 of the companion chapter.

Cane et al. (2010) considered the timing of the DH type III bursts for different categories of SEP events. They showed that SEP events with a relatively high number of electrons (near 500 keV) relative to protons (near 25 MeV) tended to be accompanied by type III bursts during the impulsive phase. This sample comprised 80 out of 201 events that the authors could classify. The 2000 May 01 event is one of them. The events had relatively low intensity, corresponding to the common 'impulsive' SEP events. The other SEP events were accompanied by type III groups that tended to occur in the post-impulsive flare phase (cf. their Figure 13).

Several studies compared the initial release time of SEPs with the start time of the DH type III groups. The large uncertainties of the initial solar release time determination induce considerable uncertainty, with ensuing differences between different event catalogs that were discussed by Miteva et al. (2018). The high energy resolution of the SoHO/ERNE detector allows for a more detailed determination of the initial solar release of SEPs through the velocity-dispersion analysis. Several critical re-evaluations of the analysis methods were presented by Vainio et al. (2013), Kouloumvakos et al. (2015), and Ameri et al. (2019). Vainio et al. (2013) found that the initial release of deka-MeV protons occurred during groups of DH III bursts in 57% of the analyzed cases, and after the end of the type III bursts in 21%, while Ameri et al. (2019) found fractions of 64% and 36%, respectively. The first proton release was in the majority of the events delayed with respect to the start of the type III bursts. These studies did not consider the anisotropy of the SEPs.

3.2.4 Delayed Onsets of Particle Events in Space: Possible Interpretations

The delayed onset of SEP events in space can be explained by different processes including particle propagation in the Heliosphere, particle storage in the corona, and delayed acceleration at the Sun.

The storage of MeV/nuc ions in the corona, already alluded to in **Section 3.1.2**, could explain delays, and the trapping times required to explain the observed charge states are not inconsistent with the reported onset delays. Wang et al. (2016) discard this interpretation, because it does not provide a common description of the escape of electrons and ions. Storage is hard to reconcile with the existence of type III bursts early in the event, and inconsistent with the fast escape of protons at MeV to deka-MeV energies in events such as May 1, 2000.

Cane (2003) argued that the delayed onset of electron events could be explained by interplanetary transport. A possible process is enhanced pitch-angle scattering at energies above about 100 keV, which has been inferred, e.g., from the observed softening of electron spectra with increasing energy (Strauss et al., 2020). It is unclear if the energy dependence is sharp enough to explain a step-increase of the delay such as shown in **Figure 3C**. At the low-energy end of the electron spectrum, below a few tens of keV, the energy loss due to the growth of Langmuir waves, which eventually leads to the type III bursts (Kontar and Reid, 2009; Reid and Kontar, 2013), implies that the electrons had higher energy during part of their travel than when they were detected. The expected flattening of the electron spectrum below a few tens of keV is sometimes observed (Krucker et al., 2007), but not always pronounced (Lin, 1985; Wang et al., 2016). These apparently low-energy electrons would then arrive earlier than expected, consistent with the observations by Wang et al. (2016). However, these authors discard interplanetary propagation as the cause of the delay, because the velocity-dispersion analysis of their events yielded a travel path comparable with a standard Parker spiral, which argues for a scatter-poor propagation at least of the first arriving particles.

Kahler and coworkers (Kahler, 2007; Kahler et al., 2007) envisaged a systematically larger travel path for electrons in delayed events, showing that the onset delays were anti-correlated with solar wind speed, and hence correlated with the length of the Parker spiral. But explaining delays of 10 min and more needs doubling the length of the Parker spiral. This cannot be a general interpretation, although the longitude of the travel path and the pitch angle scattering add to the uncertainties of the interpretation of the observed onset times (e.g., Kahler, 2007). New *in situ* measurements as a function of heliocentric distance will shed more light on the action of these processes.

Whenever the anisotropy of SEPs cannot be observed, the onset may be delayed by interplanetary transport. The possibility of transport across the average heliospheric magnetic field has come into focus again with the multi-spacecraft observations by STEREO. The mechanisms include particle drifts, the meandering of the heliospheric magnetic field lines due to motions of their solar footpoints, and wave-particle

interactions (Dröge et al., 2010; Desai and Giacalone, 2016; Laitinen et al., 2016; Dalla et al., 2020).

However, the most common interpretation of onset delays is a delayed particle release at the Sun, not due to storage, but to a distinct acceleration process. Detailed comparisons of the electron spectra of delayed and prompt electron events corroborate the idea that the different onset times reveal different electron populations: Krucker et al. (2007) found that the prompt events had energy spectral slopes that correlated with those inferred from the hard X-ray emission of electrons in the solar atmosphere, while the spectra of delayed electron events showed a weaker correlation. A similar difference had been reported earlier between electron events of 'short' and 'long' duration, where Dröge (1996) compared rigidity spectra measured *in situ* between about 0.1 and 50 MeV with the associated gamma-ray spectra in the range (0.3–1) MeV. Such differences do not exclude interplanetary transport effects, but are plausible if the prompt and short electron events in space result from a common acceleration with hard X-ray emitting electrons and with the electron beams emitting type III bursts, while the delayed long events come from a different acceleration process. The typical counterparts of sustained delayed particle releases are the long decay of the soft X-ray bursts, type II bursts at meter-to-decameter wavelengths, type IV bursts at centimeter-to-meter wavelengths or a combination of these radio emissions. They are signatures of eruptive solar flares, where CMEs are additional sources of particle acceleration due to their shock waves and the processes of magnetic reconnection in their aftermath. In events where no prompt electron signature is seen, as in **Figure 4**, the interpretation implies that the prompt and delayed acceleration processes release particles onto different field lines, and that only those field lines guiding particles during the delayed release are connected to the spacecraft (cf. Klein et al., 2005).

4 TYPE III BURSTS AS TRACERS OF PARTICLE PROPAGATION IN THE CORONA AND THE HELIOSPHERE

4.1 Confinement Versus Escape of Flare-accelerated Particles

Type III bursts are a frequent manifestation of solar activity (Lin, 1985; Saint-Hilaire et al., 2013). This suggests that the processes of beam instabilities, growth of Langmuir waves, and conversion to escaping radio waves can operate easily, and that the absence of a type III burst conveys also significant information.

For instance, the absence of type III bursts allows one to identify confined flares, which are flares where the magnetic structure surrounding the region of energy release remains intact. Confined flares may be relatively strong: Wang and Zhang (2007) showed that about 10% of the X-class flares in solar cycle 23 were confined, since no CME was observed. Confined flares can be significant electron accelerators, as shown by the associated microwave or hard X-ray bursts (Schmahl et al., 1990; Gopalswamy et al., 1995; Klein et al., 2010; Thalmann et al., 2015). But there are no radio signatures of electrons escaping to the high corona (Gopalswamy et al., 2009; Klein et al., 2010). The GOES particle detectors recorded no excess above background, even when the flare was nominally well-connected to the Earth, although faint signatures may on occasion be detected by more sensitive instruments, as on SoHO and ACE (Klein et al., 2010). The absence of a significant SEP event has two reasons: the absence of a CME, which would have been an alternative source of particle acceleration, and the magnetic confinement of particles accelerated in the low corona, signaled by the absence of radio emission at metric and longer wavelengths.

Particle confinement may evolve during a solar eruptive event. Trottet et al. (1998) and Rieger et al. (1999) studied the radio emission at the times of two strong hard X-ray and gamma-ray flares. The initial hard X-ray and gamma-ray emission had no radio counterpart at frequencies below 1 GHz, and especially no type III emission. In the X15 flare on March 6, 1989 (Rieger et al., 1999) the gamma-rays in this initial phase of 2 min duration extended to above 20 MeV. A type II burst and a strong, long-lasting type IV continuum, indicative of the early CME evolution, appeared after the gamma-ray burst. In the event of Trottet et al. (1998), later gamma-ray peaks were accompanied by new radio sources, including type III emission. It appears from the successive appearance of gamma-ray peaks with new radio sources at dm-m wavelengths that energy release and particle acceleration proceed stepwise from confined magnetic structures in the low corona (below 10^5 km, say) to larger spatial scales, higher in the corona, which then erupt into a CME (see also Chupp et al., 1993; Trottet et al., 1994; Akimov et al., 1996; Laitinen et al., 2000; Klein et al., 2014). The different steps proceed on time scales of tens of seconds to minutes. Radio signatures show that particles may escape from the flaring active region to the Heliosphere since the early onset of the acceleration, one to several minutes later, or not at all, depending on the evolution of the magnetic structure in a given event. Type III bursts at decametric and longer wavelengths are the clearest signatures of the earliest access of particles, not only electrons, to the Heliosphere during an eruptive solar flare.

4.2 The Geometry of Open Magnetic Field Lines in the Corona

When the existence of type III bursts demonstrates the escape of electrons to the high corona, imaging observations can identify those open field lines that are actually taken by the electron beams, and possibly by other species of charged particles. Parker's solar wind model implies that coronal regions around 50°W are best suited to make SEPs reach the Earth. Panels E, F of **Figure 1** illustrate that the May 1, 2000 event is consistent with this expectation. The parent activity of simple impulsive SEP events in general clusters around this longitude (Reames, 1999; Nitta et al., 2006; Wang et al., 2012), albeit with some spread. One reason for this spread is that the Parker spiral as an average field line in interplanetary space makes sense only outside the solar wind source surface, while the geometry between the source surface and the low corona varies (Liewer et al., 2004; Wang et al., 2006b). This is illustrated by **Figure 1D**: open field lines are confined to a narrow region in the low atmosphere by the surrounding closed magnetic flux, but spread out at high altitudes, where the ambient closed flux is lacking, to cover a considerable fraction of the source surface.

Particles accelerated in a flaring active region hence can have access to a wide range of longitudes and latitudes on the solar wind source surface. Klein et al. (2008) used radio images of type III bursts at meter wavelengths in eight impulsive SEP events where the initial solar release occurred during these type III bursts. The maps of type III sources showed that the electron beams propagate along coronal field lines that connect the parent active region to the vicinity of the nominal Parker spiral on the source surface even in a case where the parent active region was as far as 50° away from the longitude of the footpoint of the nominal Parker spiral. Such a divergence of open magnetic field lines was inferred by Dulk et al. (1979) from the broadening of type III sources with decreasing frequency (see Mann et al., 2018, for an illustration using LOFAR). But the fact that the type III sources analyzed by Klein et al. (2008) are smaller than the bundle of open field lines rooted in the parent active region implies that electron beams are only injected onto a fraction, depending on the details of the acceleration region (e.g., Masson et al., 2012). Klassen et al. (2018) obtained a similar result from the analysis of an EUV jet related with an impulsive SEP event.

4.3 The Geometry of the Heliospheric Magnetic Field

Type III bursts at hectometric and kilometric wavelengths can in principle be used to infer the interplanetary trajectories of electron beams, and probe the geometry of field lines that guide particles through the Heliosphere. A number of techniques has been developed, which use the identification of the arrival direction of the radio waves alone or together with information on the density structure of the Heliosphere. The arrival direction can be determined by the modulation of the flux density recorded on a spinning spacecraft (Manning and Fainberg, 1980; Reiner and Stone, 1988, 1989), or by the autocorrelation and cross-correlation of signals recorded by antennas with different orientations on a three-axes stabilized spacecraft (Krupar et al., 2012). Krupar et al. (2020) validated their triangulation method with delay-time measurements of type III bursts between the STEREO A, Wind and Parker Solar Probe spacecraft. The results are found to be consistent with an error of 10–20%.

In the case of type III storms observed during several successive days as the sources pass over the central meridian, an average trajectory can be defined. To the extent that one can assume a rigidly rotating source at a fixed heliocentric distance located in the ecliptic plane, the distance is determined by the time derivative of the measured elongation of the source. The azimuth is determined by the time of meridian passage at individual frequencies. Bougeret et al. (1984) showed that the sources of one such type III storm neatly aligned along a Parker spiral (**Figure 5A**).

Trajectories close to Parker spirals were also found for individual interplanetary type III bursts, often using triangulation from spacecraft at two or three vantage points

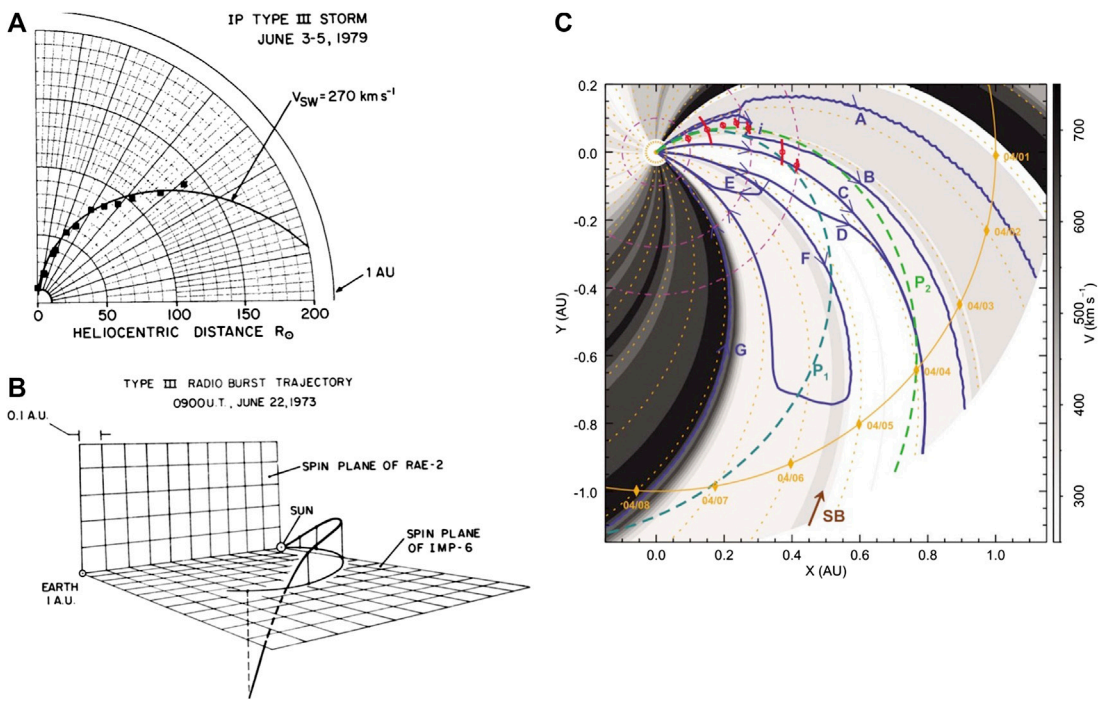

FIGURE 5 | Localization of interplanetary type III bursts; **(A)** Centroid positions of type III sources during a storm, with an overlaid Parker spiral field line for a solar wind speed of 270 km s^{-1} (Bougeret et al., 1984, ©ESO). **(B)** 3D magnetic field line inferred from direction finding and a density model (Fitzenreiter et al., 1977, figure from https://ntrs.nasa.gov/citations/19770005004). **(C)** Type III locations (red arcs, from Reiner et al., 2009) compared with two Parker spiral field lines (P_1, P_2) as proposed by Reiner et al. and an alternative 2D magnetic field model **(A)**–**(D)**, **(F)**, from Li et al. (2016), ©AGU. Figures reproduced with permission.

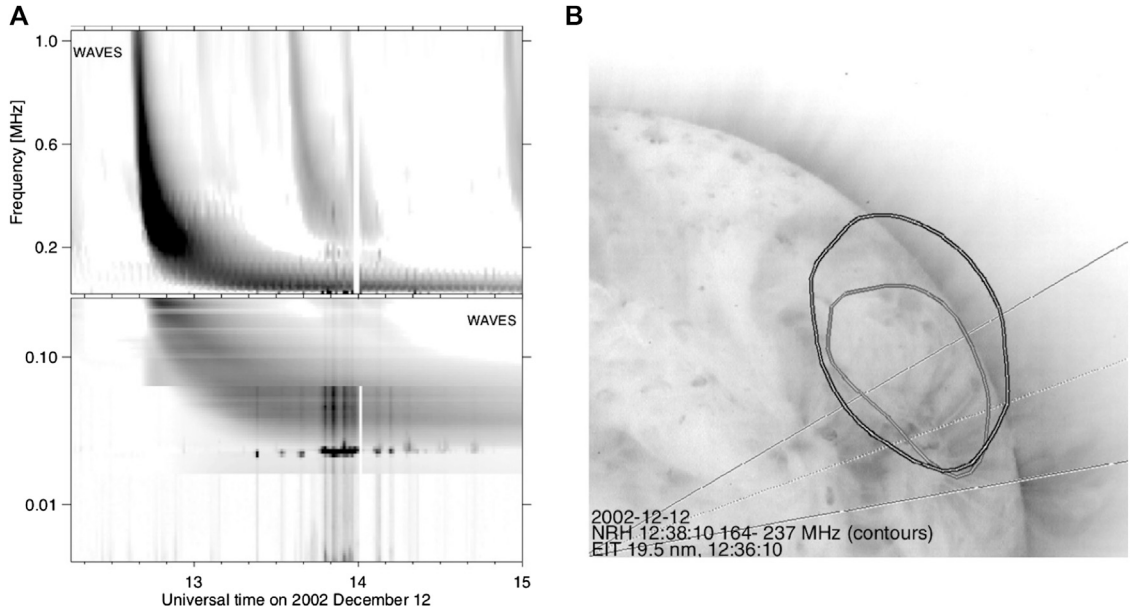

FIGURE 6 | Kilometric type III bursts and Langmuir waves as tracers of magnetic connection to the Sun on December 12, 2002: **(A)** Dynamic spectrum of radio emission between 1 MHz and a few kHz; **(B)** Superposition of radio sources (iso-intensity contours at half maximum) at 164 and 237 MHz on the EUV image (Klein and Posner, 2005). Sharply delimited rectangular gray areas and vertical bars on either side of the intense Langmuir waves in the spectra are instrumental artifacts. ©ESO. Reproduced with permission.

(Fainberg and Stone, 1974; Weber et al., 1977; Reiner and Stone, 1986; Reiner et al., 1995; Reiner et al., 1998; Reiner et al., 2009; Martínez-Oliveros et al., 2012; Krupar et al., 2014). Lin et al. (1973) compared for two events the path lengths of electrons inferred from two methods: 1) the localization of type III bursts using direction finding and an interplanetary density model, 2) a velocity dispersion analysis (VDA) of electrons between about 6 and 50 keV. They found that the lengths of Parker spirals outlined by the type III sources, 1.25 AU in both events, agreed well with those from VDA, 1.4 and 1.68 AU. The difference could be ascribed to the pitch angle scattering of electrons. The event with the longer path length from VDA had indeed a more diffusive time profile, and a lower drift rate of its type III emission than the other.

However, the application of different methods to the same events sometimes yielded substantially different results (Reiner et al., 2009; Martínez-Oliveros et al., 2012). A major source of uncertainty are the huge dimensions of the sources (see Reiner, 2001, and references therein), which makes the hypothesis uncertain that the lines of sight toward the type III source from two widely separated spacecraft point to the same target. Alternative models to a Parker spiral may be more consistent with the observations: Li et al. (2016) compared the positions of a type III burst measured by triangulations from the two STEREO and the Wind spacecraft by Reiner et al. (2009) with the geometry of a Parker spiral and the geometry predicted by a 2D model allowing for a finite azimuthal magnetic field component on the source surface. The comparison is displayed in **Figure 5C**. The Parker spiral P_2 (green dashed line) is consistent with the type III burst locations, but intercepts a sector boundary. Li et al. (2016) conclude that in view of the actually observed interplanetary magnetic field configuration their alternative magnetic field model is more consistent with the type III burst trajectory than a Parker spiral.

Most models assume two-dimensional trajectories in the ecliptic plane, and some statistical studies support this hypothesis (Krupar et al., 2014). However, individual type III bursts may be better represented by 3D field lines. For instance, Fitzenreiter et al. (1977), combining direction finding from two spacecraft with a density model, inferred a trajectory at constant colatitude between the Sun and 0.3 AU, which then curves down to the ecliptic and crosses it at 0.8 AU with an angle of 60° (**Figure 5B**). Further evidence for field lines that rise out of the ecliptic plane near the Sun was provided by Dulk et al. (1986). Using observations from ISEE 3 around solar maximum (1980–81) they found that the latitude distribution of the radio sources near a heliocentric distance of 0.35–0.4 AU increased from the ecliptic plane to a latitude of 10°–15°, comparable to the average latitude of active regions at that time, and then decreased again. The authors concluded that field lines rooted in active regions often have constant latitude out to about 0.3 AU, as predicted by the Parker model, but bend at larger distance and become approximately parallel to the ecliptic plane. No detailed comparison seems to have been undertaken so far with models including a latitudinal component of the heliospheric magnetic field, which have been developed to account for unusual magnetic connections traced by energetic particles (see the reviews by Smith, 2008; Owens and Forsyth, 2013; Lhotka and Narita, 2019).

The Langmuir waves at the origin of type III bursts are only detectable when the spacecraft intercepts the source region, i.e., the electron beam (or one of the electron beams). This is a means to

ascertain that the spacecraft is connected to the source region in the solar corona. On December 12, 2002 an impulsive SEP event occurred in association with a flare at N16 W36. The type III bursts are shown in the decametric-kilometric spectrum in **Figure 6A**. The radio positions at two metric wavelengths are overlaid as contours at half maximum on a nearly simultaneous EUV image in **(B)**. Nitta et al. (2006) and Nitta and DeRosa (2008) noted that in this, like some other apparently simple SEP events, the potential field line extrapolations led to latitudes at the source surface with no connection to the ecliptic plane through a Parker spiral. The type III sources in **Figure 6B** confirm that in the corona the electron beams propagate along field lines that point out of the ecliptic plane, in agreement with the potential-field extrapolations. But Langmuir waves (bright short emissions in the lower panel of **Figure 6A**) accompanied the low-frequency part of the type III burst at the Wind spacecraft. They start at the time when the radio emission approaches the plasma frequency, which confirms that the Langmuir waves are generated by the electron beams producing the type III emission (Hoang et al., 1994). This implies in turn that the open magnetic field lines rooted in the parent active region turned down toward the ecliptic somewhere in the interplanetary medium. The interplanetary magnetic field must hence have had a significant latitudinal component.

Type III bursts seem to be unable to reveal finer details of the interplanetary magnetic field structure. Larson et al. (1997) and Kahler et al. (2011a,b) used the velocity dispersion of electron event onsets to probe the field line lengths in magnetic clouds. All studied electron events were accompanied by type III burst groups at decametric and longer wavelengths. However, the type III spectra do not seem to reflect even substantially different field line lengths. For example, the field line lengths were about 3 AU for an electron event observed shortly after entry into a magnetic cloud, with a type III group at 19:56 UT on October 18, 1995, and about 1.2 AU at 10:28 UT the next day, near the axis of the magnetic cloud. Neither of the papers addresses the details of the type III spectra. Inspection using the 1 min data provided by NASA/GSFC[2] shows that the type III burst with the longer travel path tends to show a slower drift at frequencies near and below 250 kHz than the other one, but the difference is not pronounced and would not be a tool by itself to infer a longer field line. No obvious difference is seen between the type III bursts within and outside a magnetic cloud on 2004 August 30 and 31, respectively, both analyzed by Kahler et al. (2011b). This is probably related to the large sizes of the radio sources in the Heliosphere, usually ascribed to radio wave scattering, and to the possible mixture of fundamental and harmonic emission at a given radio frequency. Saturation of the radio receiver, which is seen in the rectangular brightenings in **Figure 6A** and the fact that an apparently single type III burst at decametric and longer wavelengths is composed of several individual bursts, which may be generated by electron beams on different magnetic field lines, could further confuse the picture. No detailed analysis has been published so far.

[2]https://cdaweb.gsfc.nasa.gov/pub/data/wind/waves/

Type III bursts are indicators of open magnetic field lines, but electron beams may also reveal closed field lines in the corona. In these cases upward-travelling electron beams create a type III-like burst drifting toward lower frequencies, but which turns over toward an opposite drift when the electron beams start to travel sunward after the apex of the loop. The result is a 'type U burst'. In the corona these bursts are well known to be rare phenomena (Aurass and Klein, 1997; Sinclair Reid and Ratcliffe, 2014; Reid and Kontar, 2017), even at decimetric wavelengths, which are emitted in the low corona where closed magnetic field structures dominate. Based on numerical simulations, Reid and Kontar argue especially that the small density gradient near the loop apex reduces the growth rate of Langmuir waves compared with the situation in an open flux tube. Another obvious reason is that the magnetic field divergence along open flux tubes acts to re-focus a beam against pitch-angle diffusion, while during the downward propagation both processes combine to reduce the anisotropy. Leblanc et al. (1999) observed a type U burst with a turnover frequency at 1 MHz, at the time when a CME was observed with apex at $9R_{\odot}$, consistent with plasma emission at the turnover frequency. The interpretation is the propagation of electron beams on the closed magnetic field lines of the CME. Démoulin et al. (2007) reported a burst that started as a type III burst, then turned to the opposite frequency drift, and again to a type III-like drift. The spectral signature resembles the letter *N*. The authors interpreted it as electron beams propagating along a switchback of a magnetic field line that had recently been formed by magnetic reconnection. But such observations of radio emission from sunward-streaming electrons are rare, and were only reported close to the Sun, at frequencies of 1 MHz and above. No such signature has been observed with sunward-streaming electrons near 1 AU. Wang et al. (2011) analyzed an electron event with three successive enhancements at the Wind spacecraft, the first being due to a release of electron beams in the corona, associated with a type III burst, the second to electrons that were back-reflected at an obstacle outside 1 AU, and the third to anti-sunward electrons created by another reflection inside 1 AU. No reverse-drift type III bursts were observed with the second, sunward-propagating electron population. This can probably be explained by the fact that only relatively high-energy electrons (>25 keV) were seen in the reflected electron populations, possibly because the low-energy electrons emitting type III emission in the interplanetary space are strongly focused, and therefore harder to reflect, while the angular distributions of electrons at energies above 15–20 keV are broader (Lin, 1985). Similarly, Martínez Oliveros et al. (2020) analyzed an electron event where the Wind spacecraft observed electrons streaming back from the interplanetary space to the Sun, along the field lines of a magnetic cloud. The associated kilometric radio burst was of type III with no indication of a turnover.

5 SUMMARY

Radio bursts produced by non-thermal electrons in the corona are a unique tool to probe the acceleration and propagation of energetic particles.

The radiative signatures in the low solar atmosphere of mildly relativistic electrons, i.e., hard X-ray bremsstrahlung and microwave gyrosynchrotron emission, have been shown to correlate well with nuclear gamma-ray emission and with different parameters of SEP events, including peak intensity and to some extent spectral hardness. This makes them useful for space weather purposes, especially since relevant data can be acquired with cheap equipment, while ground-based observations are well shielded against adverse space weather. But the interpretation is unclear, because all parameters of eruptive activity correlate with each other. This is especially the case of microwave peak flux and fluence, soft X-ray peak flux and fluence, and CME speed. The validity of statistical correlations therefore remains a subject of debate, with no obvious solution for the time being.

Type III radio bursts trace impulsive electron acceleration and their escape to the high corona and the Heliosphere. The achievement of a nearly seamless connection in radio spectrography combining observations from space and ground provides us with a tool to track electron propagation from the vicinity of the acceleration sites in the corona to the spacecraft. Type III bursts can therefore be used to establish or discard magnetic connections, which they trace in a more reliable way than the nominal interplanetary magnetic field models. The type III bursts show the acceleration regions are complex, and the propagation paths multiple. We have not yet succeeded to relate this to the very broad particle injections that multi-spacecraft measurements reveal. But the radio observations do show that the picture of a simple coronal acceleration region from which particles stream outward to space and downward to the chromosphere is only realized, if at all, in few very simple flares. This is consistent with theoretical expectations, as discussed by Vlahos et al. (2019).

The timing of SEPs gives clear evidence that in many events, especially large ones, electrons and protons are released over much longer durations than type III burst often with some delay. The most common interpretation is that a distinct delayed acceleration process is at work in these events. This subject will be examined in the companion chapter.

AUTHOR CONTRIBUTIONS

The author confirms being the sole contributor of this work and has approved it for publication.

FUNDING

Centre National d'Etudes Spatiales (CNES) CNRS - INSU Observatoire de Paris Institut Polaire Paul-Emile Victor.

ACKNOWLEDGMENTS

This work owes much to the generous data provision of numerous space-borne and ground-based instruments and data bases, especially the SoHO/LASCO CME catalog generated and maintained at the CDAW Data Center by NASA and The Catholic University of America in cooperation with the Naval Research Laboratory, the Radio Monitoring web site at LESIA, Observatoire de Paris, supported by the French Space Agency CNES, the neutron monitor database maintained at the University of Kiel and built within a Framework 7 project of the European Union, and the National Centers for Environmental Information at NOAA. The author acknowledges helpful discussions with many colleagues during the NMDB, SEPSERver and HESPERIA projects funded by the European Union, during several working groups and workshops dedicated to solar energetic particles at the International Space Science Institute (ISSI) in Bern, and during workshops of the Community of European Solar Radio Astronomers (CESRA). He is indebted to the referees for their constructive criticism. This research was supported by the French Polar Institute (IPEV), the French space agency CNES, and the Programme National Soleil-Terre (PNST) of CNRS/INSU.

REFERENCES

Agueda, N., Klein, K.-L., Vilmer, N., Rodríguez-Gasén, R., Malandraki, O. E., Papaioannou, A., et al. (2014). Release timescales of solar energetic particles in the low corona. *Astron. Astrophys.* 570, A5. doi:10.1051/0004-6361/201423549

Agueda, N., Lario, D., Vainio, R., Sanahuja, B., Kilpua, E., and Pohjolainen, S. (2009). Modeling solar near-relativistic electron events. Insights into solar injection and interplanetary transport conditions. *Astron. Astrophys.* 507, 981–993. doi:10.1051/0004-6361/200912224

Agueda, N., Vainio, R., Lario, D., and Sanahuja, B. (2008). Injection and interplanetary transport of near-relativistic electrons: modeling the impulsive event on 2000 May 1. *Astrophys. J.* 675, 1601–1613. doi:10.1086/527527

Akimov, V. V., Ambrož, P., Belov, A. V., Berlicki, A., Chertok, I. M., Karlický, M., et al. (1996). Evidence for prolonged acceleration based on a detailed analysis of the long-duration solar gamma-ray flare of June 15, 1991. *Sol. Phys.* 166, 107–134. doi:10.1007/BF00179358

Akinyan, S. T., Mogilevsky, E. I., Böhme, A., and Krüger, A. (1971). Spectral features of large type IV bursts and interrelation to solar-terrestrial phenomena. *Sol. Phys.* 20, 112–121. doi:10.1007/BF00146102

Alissandrakis, C. E., Nindos, A., Patsourakos, S., Kontogeorgos, A., and Tsitsipis, P. (2015). A tiny event producing an interplanetary type III burst. *Astron. Astrophys.* 582, A52. doi:10.1051/0004-6361/201526265

Ameri, D., Valtonen, E., and Pohjolainen, S. (2019). Properties of high-energy solar particle events associated with solar radio emissions. *Sol. Phys.* 294, 122. doi:10.1007/s11207-019-1512-9

Aschwanden, M. J. (2002). Particle acceleration and kinematics in solar flares. *Space Sci. Rev.* 101, 1–227. doi:10.1023/A:1019712124366

Aurass, H., and Klein, K.-L. (1997). Spectrographic and imaging observations of solar type U radio bursts. *Astron. Astrophys. Suppl.* 123, 279–304. doi:10.1051/aas:1997161

Avignon, Y., and Pick-Gutmann, M. (1959). Relation entre les émissions solaires de rayons cosmiques et les sursauts de type IV. *Acad. des Sci. Paris Comptes Rendus* 249, 2276–2278.

Balch, C. C. (2008). Updated verification of the Space Weather Prediction Center's solar energetic particle prediction model. *Space Weather* 6, S01001. doi:10.1029/2007SW000337

Boischot, A., and Denisse, J.-F. (1957). Les émissions de type IV et l'origine des rayons cosmiques associés aux éruptions chromosphériques. *Acad. des Sci. Paris Comptes Rendus*. 245, 2194–2197.

Boischot, A., and Warwick, J. W. (1959). Radio emission following the flare of August 22, 1958. *J. Geophys. Res*. 64, 683–684. doi:10.1029/JZ064i006p00683

Bougeret, J.-L., Zarka, P., Caroubalos, C., Karlický, M., Leblanc, Y., Maroulis, D., et al. (1998). A shock-associated (SA) radio event and related phenomena observed from the base of the solar corona to 1 AU. *Geophys. Res. Lett*. 25, 2513–2516. doi:10.1029/98GL50563

Bougeret, J. L., Fainberg, J., and Stone, R. G. (1984). Interplanetary radio storms. II - emission levels and solar wind speed in the range 0.05-0.8 AU. *Astron. Astrophys*. 141, 17–24.

Briand, C., Henri, P., and Hoang, S. (2014). Inhibition of type III radio emissions due to the interaction between two electron beams: observations and simulations. *J. Geophys. Res*. 119, 2365–2378. doi:10.1002/2013JA019688

Cane, H. V., and Erickson, W. C. (2003). Energetic particle propagation in the inner heliosphere as deduced from low-frequency (<100 kHz) observations of type III radio bursts. *J. Geophys. Res*. 108, 1203. doi:10.1029/2002JA009488

Cane, H. V., Erickson, W. C., and Prestage, N. P. (2002). Solar flares, type III radio bursts, coronal mass ejections and energetic particles. *J. Geophys. Res*. 107, 1315. doi:10.1029/2001JA000320

Cane, H. V. (2003). Near-relativistic solar electrons and type III radio bursts. *Astrophys. J*. 598, 1403–1408. doi:10.1086/379007

Cane, H. V., Richardson, I. G., and von Rosenvinge, T. T. (2010). A study of solar energetic particle events of 1997-2006: their composition and associations. *J. Geophys. Res*. 115, A08101. doi:10.1029/2009JA014848

Cane, H. V., Stone, R. G., Fainberg, J., Steinberg, J. L., Hoang, S., and Stewart, R. T. (1981). Radio evidence for shock acceleration of electrons in the solar corona. *Geophys. Res. Lett*. 8, 1285–1288. doi:10.1029/GL008i012p01285

Carley, E. P., Vilmer, N., and Vourlidas, A. (2020). Radio observations of coronal mass ejection initiation and development in the low solar corona. *Front. Astron. Space Sci*. 7, 551558. doi:10.3389/fspas.2020.551558

Castelli, J. P., Aarons, J., and Michael, G. A. (1967). Flux density measurements of radio bursts of proton-producing flares and nonproton flares. *J. Geophys. Res*. 72, 5491–5498. doi:10.1029/JZ072i021p05491

Castelli, J. P., and Barron, W. R. (1977). A catalog of solar radio bursts 1966-1976 having spectral characteristics predictive of proton activity. *J. Geophys. Res*. 82, 1275–1278. doi:10.1029/JA082i007p01275

Chen, B., Bastian, T. S., White, S. M., Gary, D. E., Perley, R., Rupen, M., et al. (2013). Tracing electron beams in the Sun's corona with radio dynamic imaging spectroscopy. *Astrophys. J. Lett*. 763, L21. doi:10.1088/2041-8205/763/1/L21

Chen, B., Yu, S., Battaglia, M., Farid, S., Savcheva, A., Reeves, K. K., et al. (2018). Magnetic reconnection null points as the origin of semirelativistic electron beams in a solar jet. *Astrophys. J*. 866, 62. doi:10.3847/1538-4357/aadb89

Chertok, I. M. (2018). Diagnostic analysis of the solar proton flares of September 2017 by their radio bursts. *Geomagn. Aeron*. 58, 457–463. doi:10.1134/S0016793218040035

Chertok, I. M., Grechnev, V. V., and Meshalkina, N. S. (2009). On the correlation between spectra of solar microwave bursts and proton fluxes near the Earth. *Astron. Rep*. 53, 1059–1069. doi:10.1134/S1063772909110110

Chertok, I. M. (1990). On the correlation between the solar gamma-ray line emission, radio bursts and proton fluxes in the interplanetary space. *Astron. Nachr*. 311, 379–381. doi:10.1002/asna.2113110618

Chupp, E. L., Trottet, G., Marschhauser, H., Pick, M., Soru-Escaut, L., Rieger, E., et al. (1993). A study of the evolution of electron and ion acceleration during the 09:09 UT solar flare on 1989 September 9. *Astron. Astrophys*. 275, 602.

Cliver, E., and Kahler, S. (1991). High coronal flares and impulsive acceleration of solar energetic particles. *Astrophys. J*. 366, L91–L94.

Cliver, E. W. (2016). Flare vs. shock acceleration of high-energy protons in solar energetic particle events. *Astrophys. J*. 832, 128. doi:10.3847/0004-637X/832/2/128

Correia, E., Kaufmann, P., and Magun, A. (1994). "The observed spectrum of solar burst continuum emission in the submillimeter spectral range," in *IAU symp. 154: infrared solar Physics*. Editors D. Rabin, J. Jefferies, and C. Lindsey. Dordrecht, Netherlands: Springer, 125–129.

Croom, D. L. (1971). Solar microwave bursts as indicators of the occurrence of solar proton emission. *Sol. Phys*. 19, 152–170. doi:10.1007/BF00148831

Daibog, E. I., Mel'Nikov, V. F., and Stolpovskii, V. G. (1993). Solar energetic particle events from solar flares with weak impulsive phases of microwave emission. *Sol. Phys*. 144, 361–372. doi:10.1007/BF00627600

Daibog, E. I., Stolpovskii, V. G., Melnikov, V. F., and Podstrigach, T. S. (1989). Microwave bursts and the relative abundance of electrons and protons in cosmic-rays from solar flares. *Sov. Astron. Lett*. 15, 432–436.

Dalla, S., de Nolfo, G. A., Bruno, A., Giacalone, J., Laitinen, T., Thomas, S., et al. (2020). 3D propagation of relativistic solar protons through interplanetary space. *Astron. Astrophys*. 639, A105. doi:10.1051/0004-6361/201937338

Démoulin, P., Klein, K.-L., Goff, C. P., van Driel-Gesztelyi, L., Culhane, J. L., Mandrini, C. H., et al. (2007). Decametric N burst: a consequence of the interaction of two coronal mass ejections. *Sol. Phys*. 240, 301–313. doi:10.1007/s11207-006-0259-2

Desai, M., and Giacalone, J. (2016). Large gradual solar energetic particle events. *Living Rev. Sol. Phys*. 13, 3. doi:10.1007/s41116-016-0002-5

Dierckxsens, M., Tziotziou, K., Dalla, S., Patsou, I., Marsh, M. S., Crosby, N. B., et al. (2015). Relationship between solar energetic particles and properties of flares and CMEs: statistical analysis of solar cycle 23 events. *Sol. Phys*. 290, 841–874. doi:10.1007/s11207-014-0641-4

DiFabio, R., Guo, Z., Möbius, E., Klecker, B., Kucharek, H., Mason, G. M., et al. (2008). Energy-dependent charge states and their connection with ion abundances in impulsive solar energetic particle events. *Astrophys. J*. 687, 623–634. doi:10.1086/591833

Dresing, N., Gómez-Herrero, R., Klassen, A., Heber, B., Kartavykh, Y., and Dröge, W. (2012). The large longitudinal spread of solar energetic particles during the 17 January 2010 solar event. *Sol. Phys*. 281, 281–300. doi:10.1007/s11207-012-0049-y

Dröge, W. (1996). "Energetic solar electron spectra and gamma-ray observations," in High energy solar Physics, Greenbelt, MD, August 16–18, 1995. Editors R. Ramaty, N. Mandzhavidze, and X.-M. Hua (Woodbury, NY: American Institute of Physics), 78–85.

Dröge, W., Kartavykh, Y. Y., Dresing, N., Heber, B., and Klassen, A. (2014). Wide longitudinal distribution of interplanetary electrons following the 7 February 2010 solar event: observations and transport modeling. *J. Geophys. Res*. 119, 6074–6094. doi:10.1002/2014JA019933

Dröge, W., Kartavykh, Y. Y., Dresing, N., and Klassen, A. (2016). Multi-spacecraft observations and transport modeling of energetic electrons for a series of solar particle events in August 2010. *Astrophys. J*. 826, 134. doi:10.3847/0004-637X/826/2/134

Dröge, W., Kartavykh, Y. Y., Klecker, B., and Kovaltsov, G. A. (2010). Anisotropic three-dimensional focused transport of solar energetic particles in the inner heliosphere. *Astrophys. J*. 709, 912–919. doi:10.1088/0004-637X/709/2/912

Dulk, G. A., Goldman, M. V., Steinberg, J. L., and Hoang, S. (1987). The speeds of electrons that excite solar radio bursts of type III. *Astron. Astrophys*. 173, 366–374.

Dulk, G. A., Leblanc, Y., Bastian, T. S., and Bougeret, J. L. (2000). Acceleration of electrons at type II shock fronts and production of shock-accelerated type III bursts. *J. Geophys. Res*. 105, 27343–27352.

Dulk, G. A., Melrose, D. B., and Suzuki, S. (1979). Evidence for extreme divergence of open field lines from solar active regions. *Proc. Astron. Soc. Aust*. 3, 375–379.

Dulk, G. A., Steinberg, J. L., Hoang, S., and Lecacheux, A. (1986). "Latitude distribution of interplanetary magnetic field lines rooted in active regions," in *The sun and the heliosphere in three dimensions*. Editor R. G. Marsden (Dordrecht, Netherlands: Springer), 229–233.

Ergun, R. E., Larson, D., Lin, R. P., McFadden, J. P., Carlson, C. W., Anderson, K. A., et al. (1998). Wind spacecraft observations of solar impulsive electron events associated with solar type III radio bursts. *Astrophys. J*. 503, 435–445. doi:10.1086/305954

Fainberg, J., and Stone, R. G. (1974). Satellite observations of type III solar radio bursts at low frequencies. *Space Sci. Rev*. 16, 145–188. doi:10.1007/BF00240885

Fitzenreiter, R. J., Fainberg, J., Weber, R. R., Alvarez, H., Haddock, F. T., and Potter, W. H. (1977). Radio observations of interplanetary magnetic field structures out of the ecliptic. *Sol. Phys*. 52, 477–484. doi:10.1007/BF00149662

Fletcher, L., Dennis, B. R., Hudson, H. S., Krucker, S., Phillips, K., Veronig, A., et al. (2011). An observational overview of solar flares. *Space Sci. Rev*. 159, 19–106. doi:10.1007/s11214-010-9701-8

Fomichev, V. V., and Chertok, I. M. (1985). Relation between gamma-ray emission, radio bursts, and proton fluxes from solar flares. *Sov. Astron*. 29, 554–559.

Forrest, D. J., and Chupp, E. L. (1983). Simultaneous acceleration of electrons and ions in solar flares. *Nature*. 305, 291–292. doi:10.1038/305291a0

Gopalswamy, N., Akiyama, S., and Yashiro, S. (2009). "Major solar flares without coronal mass ejections," in *Universal heliophysical processes*. Editors N. Gopalswamy and D. F. Webb (Paris, France: International Astronomical Union), 283–286. doi:10.1017/S174392130902941X

Gopalswamy, N. (2009). "Coronal mass ejections and space weather," in *Climate and weather of the sun-earth system (CAWSES) selected papers from the 2007 kyoto symposium*. Editors T. Tsuda, R. Fujii, K. Shibata, and M. A. Geller (Tokyo, Japan: TERRAPUB), 77–120.

Gopalswamy, N., Raulin, J.-P., Kundu, M. R., Nitta, N., Lemen, J. R., Herrmann, R., et al. (1995). VLA and YOHKOH observations of an M1.5 flare. *Astrophys. J.* 455, 715–732. doi:10.1086/176618

Grechnev, V., Uralov, A. M., Kiselev, V. I., and Kochanov, A. A. (2017). The 26 December 2001 solar eruptive event responsible for GLE63. II. Multi-loop structure of microwave sources in a major long-duration flare. *Sol. Phys.* 292, 3. doi:10.1007/s11207-016-1025-8

Grechnev, V. V., Kiselev, V. I., Meshalkina, N. S., and Chertok, I. M. (2015). Relations between microwave bursts and near-Earth high-energy proton enhancements and their origin. *Sol. Phys.* 290, 2827–2855. doi:10.1007/s11207-015-0797-6

Grechnev, V. V., Meshalkina, N. S., Chertok, I. M., and Kiselev, V. I. (2013). Relations between strong high-frequency microwave bursts and proton events. *Publ. Astron. Soc. Jpn.* 65, 4. doi:10.1093/pasj/65.sp1.S4

Haggerty, D. K., and Roelof, E. C. (2002). Impulsive near-relativistic solar electron events: delayed injection with respect to solar electromagnetic emission. *Astrophys. J.* 579, 841–853. doi:10.1086/342870

Haggerty, D. K., and Roelof, E. C. (2006). Leading edge and peak flux density exciter speeds for well connected type-III bursts. *Adv. Space Res.* 38, 1001–1006. doi:10.1016/j.asr.2005.09.035

Hakura, Y., and Goh, T. (1959). Pre-SC polar cap ionospheric blackout and type IV solar radio outburst. *J. Radio Res. Lab.* 6, 635–650.

Hoang, S., Dulk, G., and Leblanc, Y. (1994). Interplanetary type III radio bursts that approach the plasma frequency: ulysses observations. *Astron. Astrophys.* 289, 957–971.

Hurford, G. J., Krucker, S., Lin, R. P., Schwartz, R. A., Share, G. H., and Smith, D. M. (2006). Gamma-ray imaging of the 2003 October/November solar flares. *Astrophys. J. Lett.* 644, L93–L96. doi:10.1086/505329

Isaeva, E. A., Melnikov, V. F., and Tsvetkov, L. I. (2010). Dependence of the SCR proton flux estimate on radio burst parameters. *Bull. Crime. Astrophys. Obs.* 106, 26–30. doi:10.3103/S0190271710010043

James, T., Subramanian, P., and Kontar, E. P. (2017). Small electron acceleration episodes in the solar corona. *Mon. Not. Roy. Astron. Soc.* 471, 89–99. doi:10.1093/mnras/stx1460

Kahler, S., Reames, D., and Sheeley, N. (2001). Coronal mass ejections associated with impulsive solar energetic particle events. *Astrophys. J.* 562, 558–565. doi:10.1086/323847

Kahler, S. W., Aurass, H., Mann, G., and Klassen, A. (2007). Solar radio burst and solar wind associations with inferred near-relativistic electron injections. *Astrophys. J.* 656, 567–576. doi:10.1086/510230

Kahler, S. W., Haggerty, D. K., and Richardson, I. G. (2011a). Magnetic field-line lengths in interplanetary coronal mass ejections inferred from energetic electron events. *Astrophys. J.* 736, 106. doi:10.1088/0004-637X/736/2/106

Kahler, S. W., Krucker, S., and Szabo, A. (2011b). Solar energetic electron probes of magnetic cloud field line lengths. *J. Geophys. Res.* 116, A01104. doi:10.1029/2010JA015328

Kahler, S. W. (1982a). Radio burst characteristics of solar proton flares. *Astrophys. J.* 261, 710–719. doi:10.1086/160381

Kahler, S. W. (1982b). The role of the big flare syndrome in correlations of solar energetic proton fluxes and associated microwave burst parameters. *J. Geophys. Res.* 87, 3439–3448. doi:10.1029/JA087iA05p03439

Kahler, S. W. (2007). Solar sources of heliospheric energetic electron events - shocks or flares? *Space Sci. Rev.* 129, 359–390. doi:10.1007/s11214-007-9143-0

Kane, S. R., Chupp, E. L., Forrest, D. J., Share, G. H., and Rieger, E. (1986). Rapid acceleration of energetic particles in the 1982 February 8 solar flare. *Astrophys. J. Lett.* 300, L95–L98. doi:10.1086/184610

Kartavykh, Y. Y., Dröge, W., Klecker, B., Mason, G. M., Möbius, E., Popecki, M., et al. (2007). Evidence of a two-temperature source region in the ^{3}He-rich solar energetic particle event of 2000 May 1. *Astrophys. J.* 671, 947–954. doi:10.1086/522687

Kiener, J., Gros, M., Tatischeff, V., and Weidenspointner, G. (2006). Properties of the energetic particle distributions during the October 28, 2003 solar flare from INTEGRAL/SPI observations. *Astron. Astrophys.* 445, 725–733. doi:10.1051/0004-6361:20053665

Klassen, A., Dresing, N., Gómez-Herrero, R., Heber, B., and Veronig, A. (2018). Strong non-radial propagation of energetic electrons in solar corona. *Astron. Astrophys.* 614, A61. doi:10.1051/0004-6361/201732041

Klecker, B., Kunow, H., Cane, H. V., Dalla, S., Heber, B., Kecskemety, K., et al. (2006). Energetic particle observations. *Space Sci. Rev.* 123, 217–250. doi:10.1007/s11214-006-9018-9

Klecker, B., Möbius, E., and Popecki, M. A. (2007). Ionic charge states of solar energetic particles: a clue to the source. *Space Sci. Rev.* 130, 273–282. doi:10.1007/s11214-007-9207-1

Klein, K.-L., Aurass, H., Soru-Escaut, I., and Kalman, B. (1997). Electron acceleration sites in a large-scale coronal structure. *Astron. Astrophys.* 320, 612–619.

Klein, K.-L., and Dalla, S. (2017). Acceleration and propagation of solar energetic particles. *Space Sci. Rev.* 212, 1107–1136. doi:10.1007/s11214-017-0382-4

Klein, K.-L., Krucker, S., Lointier, G., and Kerdraon, A. (2008). Open magnetic flux tubes in the corona and the transport of solar energetic particles. *Astron. Astrophys.* 486, 589–596. doi:10.1051/0004-6361:20079228

Klein, K.-L., Krucker, S., Trottet, G., and Hoang, S. (2005). Coronal phenomena at the onset of solar energetic electron events. *Astron. Astrophys.* 431, 1047–1060. doi:10.1051/0004-6361:20041258

Klein, K.-L., Masson, S., Bouratzis, C., Grechnev, V., Hillaris, A., and Preka-Papadema, P. (2014). The relativistic solar particle event of 2005 January 20: origin of delayed particle acceleration. *Astron. Astrophys.* 572, A4. doi:10.1051/0004-6361/201423783

Klein, K.-L., and Posner, A. (2005). The onset of solar energetic particle events: prompt release of deka-MeV protons and associated coronal activity. *Astron. Astrophys.* 438, 1029–1042. doi:10.1051/0004–6361:20042607

Klein, K.-L. (2021). Radio astronomical tools for the study of solar energetic particles II. Time-extended acceleration at subrelativistic and relativistic energies. *Front. Astron. Space Sci.* doi:10.3389/fspas.2020.580445

Klein, K.-L., Trottet, G., and Klassen, A. (2010). Energetic particle acceleration and propagation in strong CME-less flares. *Sol. Phys.* 263, 185–208. doi:10.1007/s11207-010-9540-5

Knipp, D. (2011). *Understanding space weather and the physics behind it*. New York, NY: McGraw-Hill. doi:10.1007/978-3-319-43495-7

Kocharov, L. G., Kovaltsov, G. A., and Torsti, J. (2001). Dynamical cycles in charge and energy for iron ions accelerated in a hot plasma. *Astrophys. J.* 556, 919–927. doi:10.1086/321596

Kocharov, L., Kovaltsov, G. A., Torsti, J., and Ostryakov, V. M. (2000). Evaluation of solar energetic Fe charge states: effect of proton-impact ionization. *Astron. Astrophys.* 357, 716–724.

Kontar, E. P., and Reid, H. A. S. (2009). Onsets and spectra of impulsive solar energetic electron events observed near the Earth. *Astrophys. J. Lett.* 695, L140–L144. doi:10.1088/0004-637X/695/2/L140

Kouloumvakos, A., Nindos, A., Valtonen, E., Alissandrakis, C. E., Malandraki, O., Tsitsipis, P., et al. (2015). Properties of solar energetic particle events inferred from their associated radio emission. *Astron. Astrophys.* 580, A80. doi:10.1051/0004-6361/201424397

Krucker, S., Kontar, E. P., Christe, S., and Lin, R. P. (2007). Solar flare electron spectra at the Sun and near the Earth. *Astrophys. J. Lett.* 663, L109–L112. doi:10.1086/519373

Krucker, S., Larson, D. E., Lin, R. P., and Thompson, B. J. (1999). On the origin of impulsive electron events observed at 1 AU. *Astrophys. J.* 519, 864–875. doi:10.1086/307415

Krucker, S., and Lin, R. P. (2000). Two classes of solar proton events derived from onset time analysis. *Astrophys. J.* 542, L61–L64. doi:10.1086/312922

Krupar, V., Maksimovic, M., Santolik, O., Cecconi, B., and Kruparova, O. (2014). Statistical survey of type III radio bursts at long wavelengths observed by the solar terrestrial relations observatory (STEREO)/waves instruments: goniopolarimetric properties and radio source locations. *Sol. Phys.* 289, 4633–4652. doi:10.1007/s11207-014-0601-z

Krupar, V., Santolik, O., Cecconi, B., Maksimovic, M., Bonnin, X., Panchenko, M., et al. (2012). Goniopolarimetric inversion using SVD: an application to type III radio bursts observed by STEREO. *J. Geophys. Res.* 117, A06101. doi:10.1029/2011JA017333

Krupar, V., Szabo, A., Maksimovic, M., Kruparova, O., Kontar, E. P., Balmaceda, L. A., et al. (2020). Density fluctuations in the solar wind based on type III radio bursts observed by Parker Solar Probe. *Astrophys. J. Suppl.* 246, 57. doi:10.3847/1538-4365/ab65bd

Kundu, M. R., and Haddock, F. T. (1960). A relation between solar radio emission and polar cap absorption of cosmic noise. *Nature.* 186, 610–613. doi:10.1038/186610a0

Kundu, M. R. (1965). *Solar radio Astronomy*. New York, NY: Interscience Publishers.

Laitinen, T., Klein, K.-L., Kocharov, L., Torsti, J., Trottet, G., Bothmer, V., et al. (2000). Solar energetic particle event and radio bursts associated with the 1996 July 9 flare and coronal mass ejection. *Astron. Astrophys*. 360, 729–741.

Laitinen, T., Kopp, A., Effenberger, F., Dalla, S., and Marsh, M. S. (2016). Solar energetic particle access to distant longitudes through turbulent field-line meandering. *Astron. Astrophys*. 591, A18. doi:10.1051/0004-6361/201527801

Larson, D. E., Lin, R. P., McTiernan, J. M., McFadden, J. P., Ergun, R. E., McCarthy, M., et al. (1997). Tracing the topology of the October 18-20, 1995, magnetic cloud with ~0.1–10^2 keV electrons. *Geophys. Res. Lett*. 24, 1911–1914. doi:10.1029/97GL01878

Leblanc, Y., Dulk, G. A., Kaiser, M. L., and Bougeret, J. (1999). Type U burst and CME in the solar wind. *Geophys. Res. Lett*. 26, 1089–1092.

Lhotka, C., and Narita, Y. (2019). Kinematic models of the interplanetary magnetic field. *Ann. Geophys*. 37, 299–314. doi:10.5194/angeo-37-299-2019

Li, B., Cairns, I. H., Gosling, J. T., Malaspina, D. M., Neudegg, D., Steward, G., et al. (2016). Comparisons of mapped magnetic field lines with the source path of the 7 April 1995 type III solar radio burst. *J. Geophys. Res*. 121, 6141–6156. doi:10.1002/2016JA022756

Liewer, P. C., Neugebauer, M., and Zurbuchen, T. (2004). Characteristics of active-region sources of solar wind near solar maximum. *Sol. Phys*. 223, 209–229. doi:10.1007/s11207-004-1105-z

Lin, R. P. (1985). Energetic solar electrons in the interplanetary medium. *Sol. Phys*. 100, 537–561.

Lin, R. P., Evans, L. G., and Fainberg, J. (1973). Simultaneous observations of fast solar electrons and type III radio burst emission near 1 AU. *Astrophys. Lett.* 14, 191.

Maia, D., and Pick, M. (2004). Revisiting the origin of impulsive electron events: coronal magnetic restructuring. *Astrophys. J.* 609, 1082–1097. doi:10.1086/386319

Malandraki, O. E., and Crosby, N. B. (2018). "Solar energetic particles and space weather: science and applications," in *Solar particle radiation storms forecasting and analysis: the HESPERIA HORIZON 2020 project and beyond*. Editors O. E. Malandraki and N. B. Crosby (Cham, Switzerland: Springer International Publishing), 1–26. doi:10.1007/978-3-319-60051-2_1

Mann, G., Breitling, F., Vocks, C., Aurass, H., Steinmetz, M., Strassmeier, K. G., et al. (2018). Tracking of an electron beam through the solar corona with LOFAR. *Astron. Astrophys*. 611, A57. doi:10.1051/0004-6361/201629017

Manning, R., and Fainberg, J. (1980). A new method of measuring radio source parameters of a partially polarized distributed source from spacecraft observations. *Space Sci. Instrum*. 5, 161–181.

Martínez Oliveros, J. C., Castillo, S. M. D., Krupar, V., Pulupa, M., Bale, S. D., and Calvo-Mozo, B. (2020). An *in situ* interplanetary "U-burst": observation and results. *Astrophys. J.* 897, 170. doi:10.3847/1538-4357/ab96c3

Martínez-Oliveros, J. C., Lindsey, C., Bale, S. D., and Krucker, S. (2012). Determination of electromagnetic source direction as an eigenvalue problem. *Sol. Phys*. 279, 153–171. doi:10.1007/s11207-012-9998-4

Mason, G. M., Mazur, J. E., Dwyer, J. R., Jokipii, J. R., Gold, R. E., and Krimigis, S. M. (2004). Abundances of heavy and ultraheavy ions in ^{3}He-rich solar flares. *Astrophys. J.* 606, 555–564. doi:10.1086/382864

Masson, S., Aulanier, G., Pariat, E., and Klein, K.-L. (2012). Interchange slip-running reconnection and sweeping SEP beams. *Sol. Phys*. 276, 199–217. doi:10.1007/s11207-011-9886-3

Miteva, R., Samwel, S. W., and Costa-Duarte, M. V. (2018). Solar energetic particle catalogs: assumptions, uncertainties and validity of reports. *J. Atmos. Sol. Terr. Phys*. 180, 26–34. doi:10.1016/j.jastp.2017.05.003

Miteva, R., Samwel, S. W., and Krupar, V. (2017). Solar energetic particles and radio burst emission. *J Space Weather Space Clim*. 7, A37. doi:10.1051/swsc/2017035

Nindos, A. (2020). Incoherent solar radio emission. *Front. Astron. Space Sci*. 7, 57. doi:10.3389/fspas.2020.00057

Nitta, N. V., and DeRosa, M. L. (2008). A comparison of solar open field regions found by type III radio bursts and the potential field source surface model. *Astrophys. J. Lett*. 673, L207. doi:10.1086/527548

Nitta, N. V., Mason, G. M., Wang, L., Cohen, C. M. S., and Wiedenbeck, M. E. (2015). Solar sources of ^{3}He-rich solar energetic particle events in solar cycle 24. *Astrophys. J.* 806, 235. doi:10.1088/0004-637X/806/2/235

Nitta, N. V., Reames, D. V., DeRosa, M. L., Liu, Y., Yashiro, S., and Gopalswamy, N. (2006). Solar sources of impulsive solar energetic particle events and their magnetic field connection to the Earth. *Astrophys. J*. 650, 438–450. doi:10.1086/507442

Owens, M. J., and Forsyth, R. J. (2013). The heliospheric magnetic field. *Living Rev. Sol. Phys*. 10, 5. doi:10.12942/lrsp-2013-5

Pacheco, D., Agueda, N., Aran, A., Heber, B., and Lario, D. (2019). Full inversion of solar relativistic electron events measured by the Helios spacecraft. *Astron. Astrophys*. 624, A3. doi:10.1051/0004-6361/201834520

Paesold, G., Benz, A. O., Klein, K.-L., and Vilmer, N. (2001). Spatial analysis of solar type III events associated with narrow band spikes at metric wavelengths. *Astron. Astrophys*. 371, 333–342. doi:10.1051/0004-6361:20010358

Papaioannou, A., Sandberg, I., Anastasiadis, A., Kouloumvakos, A., Georgoulis, M. K., Tziotziou, K., et al. (2016). Solar flares, coronal mass ejections and solar energetic particle event characteristics. *Journal of Space Weather and Space Climate*. 6, A42. doi:10.1051/swsc/2016035

Pick, M., and Ji, S. (1986). Type III burst sources and electron beam injection. *Sol. Phys*. 107, 159–165. doi:10.1007/BF00155349

Pick, M., Mason, G. M., Wang, Y.-M., Tan, C., and Wang, L. (2006). Solar source regions for ^{3}He-rich solar energetic particle events identified using imaging radio, optical, and energetic particle observations. *Astrophys. J*. 648, 1247–1255. doi:10.1086/505926

Pick, M., and van den Oord, G. H. J. (1990). Observations of beam propagation. *Sol. Phys*. 130, 83–99.

Pick, M., and Vilmer, N. (2008). Sixty-five years of solar radioastronomy: flares, coronal mass ejections and Sun Earth connection. *Astron. Astrophys. Rev*. 16, 1–153. doi:10.1007/s00159-008-0013-x

Poquérusse, M., Hoang, S., Bougeret, J.-L., and Moncuquet, M. (1996). "Ulysses-ARTEMIS radio observation of energetic flare electrons," in *Solar wind eight*. Editors D. Winterhalter, J. Gosling, S. Habbal, W. Kurth, and M. Neugebauer (Melville, NY: Am. Inst. Phys.), 62–65.

Posner, A. (2007). Up to 1-hour forecasting of radiation hazards from solar energetic ion events with relativistic electrons. *Space Weather*. 5, S05001. doi:10.1029/2006SW000268

Potter, D. W., Lin, R. P., and Anderson, K. A. (1980). Impulsive 2-10 keV solar electron events not associated with flares. *Astrophys. J. Lett*. 236, L97–L100. doi:10.1086/183206

Ramesh, R., Mugundhan, V., and Prabhu, K. (2020). New evidence for spatio-temporal fragmentation in the solar flare energy release. *Astrophys. J. Lett*. 889, L25. doi:10.3847/2041-8213/ab6a9c

Raoult, A., Mangeney, A., and Vlahos, L. (1990). An injection model for type III/V bursts in solar flares. *Astron. Astrophys*. 233, 229–234.

Reames, D. V. (1999). Particle acceleration at the sun and in the heliosphere. *Space Sci. Rev*. 90, 413–491.

Reames, D. V. (2015). Solar energetic particles. Cham, Switzerland: Springer.

Reid, H. A. S. (2020). A review of recent solar type III imaging spectroscopy. *Front. Astron. Space Sci*. 7, 56. doi:10.3389/fspas.2020.00056

Reid, H. A. S., and Kontar, E. P. (2013). Evolution of the solar flare energetic electrons in the inhomogeneous inner heliosphere. *Sol. Phys*. 285, 217–232. doi:10.1007/s11207-012-0013-x

Reid, H. A. S., and Kontar, E. P. (2017). Imaging spectroscopy of type U and J solar radio bursts with LOFAR. *Astron. Astrophys*. 606, A141. doi:10.1051/0004-6361/201730701

Reid, H. A. S., and Kontar, E. P. (2015). Stopping frequency of type III solar radio bursts in expanding magnetic flux tubes. *Astron. Astrophys*. 577, A124. doi:10.1051/0004-6361/201425309

Reid, H. A. S., Vilmer, N., and Kontar, E. P. (2014). The low-high-low trend of type III radio burst starting frequencies and solar flare hard X-rays. *Astron. Astrophys*. 567, A85. doi:10.1051/0004-6361/201321973

Reiner, M. (2001). Kilometric type III radio bursts, electron beams, and interplanetary density structures. *Space Sci. Rev*. 97, 129–139. doi:10.1023/A:1011894631803

Reiner, M. J., Fainberg, J., Kaiser, M. L., and Stone, R. G. (1998). Type III radio source located by Ulysses/Wind triangulation. *J. Geophys. Res*. 103, 1923–1932. doi:10.1029/97JA02646

Reiner, M. J., Fainberg, J., and Stone, R. G. (1995). Large-scale interplanetary magnetic field configuration revealed by solar radio bursts. *Science* 270, 461–464. doi:10.1126/science.270.5235.461

Reiner, M. J., Goetz, K., Fainberg, J., Kaiser, M. L., Maksimovic, M., Cecconi, B., et al. (2009). Multipoint observations of solar type III radio bursts from STEREO and Wind. *Sol. Phys.* 259, 255–276. doi:10.1007/s11207-009-9404-z

Reiner, M. J., Karlický, M., Jiřička, K., Aurass, H., Mann, G., and Kaiser, M. L. (2000). On the solar origin of complex type III-like radio bursts observed at and below 1 MHz. *Astrophys. J.* 530, 1049–1060.

Reiner, M. J., and MacDowall, R. J. (2015). Electron exciter speeds associated with interplanetary type III solar radio bursts. *Sol. Phys.* 290, 2975–3004. doi:10.1007/s11207-015-0779-8

Reiner, M. J., and Stone, R. G. (1986). A new method for reconstructing type-III trajectories. *Sol. Phys.* 106, 397–401. doi:10.1007/BF00158504

Reiner, M. J., and Stone, R. G. (1988). Model interpretation of type III radio burst characteristics. I - spatial aspects. *Astron. Astrophys.* 206, 316–335.

Reiner, M. J., and Stone, R. G. (1989). Model interpretation of type III radio burst characteristics. II - temporal aspects. *Astron. Astrophys.* 217, 251–269.

Richardson, I. G., von Rosenvinge, T. T., Cane, H. V., Christian, E. R., Cohen, C. M. S., Labrador, A. W., et al. (2014). >25 MeV proton events observed by the high energy telescopes on the STEREO A and B spacecraft and/or at Earth during the first seven years of the STEREO mission. *Sol. Phys.* 289, 3059–3107. doi:10.1007/s11207-014-0524-8

Rieger, E., Treumann, R. A., and Karlický, M. (1999). The radio-silent start of an intense solar gamma-ray flare. *Sol. Phys.* 187, 59–75.

Roelof, E. C., and Pick, M. (1989). Type III radio bursts in a fibrous corona. *Astron. Astrophys.* 210, 417–424.

Saint-Hilaire, P., Vilmer, N., and Kerdraon, A. (2013). A decade of solar type III radio bursts observed by the Nançay Radioheliograph 1998-2008. *Astrophys. J.* 762, 60. doi:10.1088/0004-637X/762/1/60

Sakurai, K., and Maeda, H. (1961). A relation between solar radio emission and low-energy solar cosmic rays. *J. Geophys. Res.* 66, 1966–1969. doi:10.1029/JZ066i006p01966

Schmahl, E. J., Schmelz, J. T., Saba, J. L. R., Strong, K. T., and Kundu, M. R. (1990). Microwave and X-ray observations of a major confined solar flare. *Astrophys. J.* 358, 654. doi:10.1086/169018

Schwadron, N. A., Cooper, J. F., Desai, M., Downs, C., Gorby, M., Jordan, A. P., et al. (2017). Particle radiation sources, propagation and interactions in deep space, at Earth, the Moon, Mars, and beyond: examples of radiation interactions and effects. *Space Sci. Rev.* 212, 1069–1106. doi:10.1007/s11214-017-0381-5

Shih, A. Y., Lin, R. P., and Smith, D. M. (2009). RHESSI observations of the proportional acceleration of relativistic >0.3 MeV electrons and >30 MeV protons in solar flares. *Astrophys. J. Lett.* 698, L152–L157. doi:10.1088/0004-637X/698/2/L152

Simnett, G. M. (2017). *Energetic particles in the heliosphere*. Cham, Switzerland: Springer.

Sinclair Reid, H. A., and Ratcliffe, H. (2014). A review of solar type III radio bursts. *Res. Astron. Astrophys.* 14, 773. doi:10.1088/1674-4527/14/7/003

Smith, E. (2008). "The global heliospheric magnetic field," in *The heliosphere through the solar activity cycle*. Editors A. Balogh, L. J. Lanzerotti, and S. T. Suess (New York, NY: Springer-Praxis Books), 79–150.

Strauss, R. D., Dresing, N., Kollhoff, A., and Brüdern, M. (2020). On the shape of SEP electron spectra: the role of interplanetary transport. *Astrophys. J.* 897, 24. doi:10.3847/1538-4357/ab91b0

Tan, B., Mészárosová, H., Karlický, M., Huang, G., and Tan, C. (2016). Microwave type III pair bursts in solar flares. *Astrophys. J.* 819, 42. doi:10.3847/0004-637X/819/1/42

Thalmann, J. K., Su, Y., Temmer, M., and Veronig, A. M. (2015). The confined X-class flares of solar active region 2192. *Astrophys. J. Lett.* 801, L23. doi:10.1088/2041-8205/801/2/L23

Trottet, G., Chupp, E. L., Marschhaeuser, H., Pick, M., Soru-Escaut, I., Rieger, E., et al. (1994). A comparison of gamma-ray and radio emissions during the 11:42 UT solar flare on 1982 June 3. *Astron. Astrophys.* 288, 647–655.

Trottet, G., Samwel, S., Klein, K.-L., Dudok de Wit, T., and Miteva, R. (2015). Statistical evidence for contributions of flares and coronal mass ejections to major solar energetic particle events. *Sol. Phys.* 290, 819–839. doi:10.1007/s11207-014-0628-1

Trottet, G., Vilmer, N., Barat, C., Benz, A., Magun, A., Kuznetsov, A., et al. (1998). A multiwavelength analysis of an electron-dominated gamma-ray event associated with a disk solar flare. *Astron. Astrophys.* 334, 1099–1111.

Vainio, R., Valtonen, E., Heber, B., Malandraki, O. E., Papaioannou, A., Klein, K.-L., et al. (2013). The first SEPServer event catalogue ~68-MeV solar proton events observed at 1 AU in 1996-2010. *J. Spa. Wea. Spa. Clim.* 3, A12. doi:10.1051/swsc/2013030

Veronig, A. M., and Brown, J. C. (2004). A coronal thick-target interpretation of two hard X-ray loop events. *Astrophys. J. Lett.* 603, L117–L120. doi:10.1086/383199

Vestrand, W. T., Share, G. H., Murphy, J. R., Forrest, D. J., Rieger, E., Chupp, E. L., et al. (1999). The Solar Maximum Mission atlas of gamma-ray flares. *Astrophys. J. Suppl.* 120, 409–467. doi:10.1086/313180

Vilmer, N. (2011). "Contributions of radioheliograph observations to the understanding of solar flares, coronal mass ejections, electron beams in the corona and in the interplanetary medium," in *The sun, the solar wind, and the Heliosphere*. Editors M. P. Miralles and J. Sánchez Almeida (Cham, Switzerland: Springer), 247

Vilmer, N., Krucker, S., and Lin, R. P.The RHESSI Team (2002). Hard X-ray and metric/decimetric radio observations of the 20 February 2002 solar flare. *Sol. Phys.* 210, 261–272. doi:10.1023/A:1022492414597

Vilmer, N., MacKinnon, A. L., and Hurford, G. J. (2011). Properties of energetic ions in the solar atmosphere from γ-ray and neutron observations. *Space Sci. Rev.* 159, 167–224. doi:10.1007/s11214-010-9728-x

Vlahos, L., Anastasiadis, A., Papaioannou, A., Kouloumvakos, A., and Isliker, H. (2019). Sources of solar energetic particles. *Philos. Trans. R. Soc. London, Ser. A.* 377, 20180095. doi:10.1098/rsta.2018.0095

Vourlidas, A., Carley, E. P., and Vilmer, N. (2020). Radio observations of coronal mass ejections: space weather aspects. *Front. Astron. Space Sci.* 7, 43. doi:10.3389/fspas.2020.00043

Wang, L., Krucker, S., Mason, G. M., Lin, R. P., and Li, G. (2016). The injection of ten electron/^{3}He-rich SEP events. *Astron. Astrophys.* 585, A119. doi:10.1051/0004-6361/201527270

Wang, L., Lin, R. P., Krucker, S., and Gosling, J. T. (2006a). Evidence for double injections in scatter-free solar impulsive electron events. *Geophys. Res. Lett.* 33, L03106. doi:10.1029/2005GL024434

Wang, Y.-M., Pick, M., and Mason, G. M. (2006b). Coronal holes, jets, and the origin of ^{3}He-rich particle events. *Astrophys. J.* 639, 495–509. doi:10.1086/499355

Wang, L., Lin, R. P., and Krucker, S. (2011). Pitch-angle distributions and temporal variations of 0.3-300 keV solar impulsive electron events. *Astrophys. J.* 727, 121. doi:10.1088/0004-637X/727/2/121

Wang, L., Lin, R. P., Krucker, S., and Mason, G. M. (2012). A statistical study of solar electron events over one solar cycle. *Astrophys. J.* 759, 69. doi:10.1088/0004-637X/759/1/69

Wang, Y., and Zhang, J. (2007). A comparative study between eruptive X-class flares associated with coronal mass ejections and confined X-class flares. *Astrophys. J.* 665, 1428–1438. doi:10.1086/519765

Weber, R. R., Fitzenreiter, R. J., Novaco, J. C., and Fainberg, J. (1977). Interplanetary baseline observations of type III solar radio bursts. *Sol. Phys.* 54, 431–439. doi:10.1007/BF00159934

White, S. M., Benz, A. O., Christe, S., Fárník, F., Kundu, M. R., Mann, G., et al. (2011). The relationship between solar radio and hard X-ray emission. *Space Sci. Rev.* 159, 225–261. doi:10.1007/s11214-010-9708-1

Wild, J. P. (1968). Radio evidence of a coronal instability before the onset of a solar flare (9 June 1968). *Proc. Astron. Soc. Aust.* 1, 137–138. doi:10.1017/S1323358000011061

Wild, J. P., Smerd, S. F., and Weiss, A. A. (1963). Solar bursts. *Annu. Rev. Astron. Astrophys.* 1, 291–366. doi:10.1146/annurev.aa.01.090163.001451

Wimmer-Schweingruber, R. F., Kern, O., and Hamilton, D. C. (1999). On the solar wind composition during the November 1997 solar particle events: WIND/MASS observations. *Geophys. Res. Lett.* 26, 3541–3544. doi:10.1029/1999GL010676

Conflict of Interest: The author declares that the research was conducted in the absence of any commercial or financial relationships that could be construed as a potential conflict of interest.

frontiers in Astronomy and Space Sciences

REVIEW
published: 11 March 2021
doi: 10.3389/fspas.2020.580445

Radio Astronomical Tools for the Study of Solar Energetic Particles II.Time-Extended Acceleration at Subrelativistic and Relativistic Energies

Karl-Ludwig Klein *

Observatoire de Paris, LESIA & Station de Radioastronomie de Nançay, University PSL, CNRS, Sorbonne University, University de Paris, University D'Orléans, Meudon, France

OPEN ACCESS

Edited by:
Dale E. Gary, New Jersey Institute of Technology, United States

Reviewed by:
Ian Richardson, University of Maryland, United States
Abhishek Kumar Srivastava, Indian Institute of Technology (BHU), India

***Correspondence:**
Karl-Ludwig Klein
ludwig.klein@obspm.fr

Specialty section:
This article was submitted to Stellar and Solar Physics, a section of the journal Frontiers in Astronomy and Space Sciences

Received: *06 July 2020*
Accepted: *27 October 2020*
Published: *11 March 2021*

Citation:
Klein K-L (2021) Radio Astronomical Tools for the Study of Solar Energetic Particles II.Time-Extended Acceleration at Subrelativistic and Relativistic Energies. Front. Astron. Space Sci. 7:580445. doi: 10.3389/fspas.2020.580445

Solar energetic particle (SEP) events are commonly separated in two categories: numerous "impulsive" events of relatively short duration, and a few "gradual" events, where SEP-intensities may stay enhanced over several days at energies up to several tens of MeV. In some gradual events the SEP spectrum extends to relativistic energies (> 1 GeV), over shorter durations. The two categories are strongly related to an idea developed in the 1960s based on radio observations: Type III bursts, which were addressed in a companion chapter, outline impulsive acceleration of electrons to subrelativistic energies, while the large and the relativistic SEP events were ascribed to a second acceleration process. At radio wavelengths, typical counterparts were bursts emitted by electrons accelerated at coronal shock waves (type II bursts) and by electron populations in large-scale closed coronal structures (type IV bursts). Both burst types are related to coronal mass ejections (CMEs). Type II bursts from metric to kilometric wavelengths tend to accompany large SEP events, which is widely considered as a confirmation that CME-driven shocks accelerate the SEPs. But type II bursts, especially those related to SEP events, are most often accompanied by type IV bursts, where the electrons are rather accelerated in the wake of the CME. Individual event studies suggest that although the CME shock is the most plausible accelerator of SEPs up to some yet unknown limiting energy, the relativistic SEP events show time structure that rather points to coronal acceleration related to type IV bursts. This chapter addresses the question what type II bursts tell us about coronal shock waves and how type II and type IV radio bursts are related with relativistic proton signatures as seen by particle detectors on the Earth and by their gamma-ray emission in the solar atmosphere, focusing on two relativistic SEP events, on 2005 Jan 20 and 2017 Sep 10. The importance of radio emissions as a complement to the upcoming SEP observations from close to the Sun is underlined.

Keywords: acceleration of particles, sun: particle emission, sun: radio emission, sun: flares, sun: coronal mass ejections

1 INTRODUCTION

It has been shown in the companion chapter how radio observations can shed light on processes of impulsive particle acceleration and the propagation of charged particles in the corona and the Heliosphere. But it is clear that many SEP events are much longer than the duration of even the longest groups of type III bursts. Transport models deriving the injection function from electron observations also show that certain events need much longer episodes of particle release.

In their seminal review of early radio observations of the Sun Wild et al. (1963) proposed that two categories of particle accelerators were at work in solar eruptive events. On the one hand numerous flare-related events where non-thermal electrons are accelerated to up to 100 keV in the impulsive flare phase, as demonstrated by hard X-ray and microwave bursts, with direct access to open field lines toward the Heliosphere, as shown by type III bursts. The authors state - erroneously, as seen from today - that there was no evidence for energetic proton acceleration during this phase. On the other hand, in relationship with large flares from complex active regions, relatively rare, and presumably more energetic, events take place when metre-wave type II bursts show the presence of coronal shock waves, and type IV continua the presence of electrons in coronal magnetic structures well after the impulsive phase of the parent flare. Since the idea at that time was that type IV continua are produced by incoherent gyrosynchrotron emission, the radio continuum was taken as evidence of electron acceleration to MeV-energies. The authors noted that it is this category of events where large SEP intensities are observed in the Heliosphere. Wild and coworkers argued that different acceleration processes were needed to explain bursts of second-duration from electron beams in the impulsive flare phase and more smoothly evolving radio emission in the post-impulsive flare phase, and that Fermi acceleration at coronal shocks was the natural candidate in the post-impulsive phase. The later discovery of CMEs and their close association with radio bursts of types II and IV apparently substantiated this conclusion (e.g., Reames, 1999).

In this chapter the relationship of long-lasting SEP events with bursts of types II and IV is investigated. In ***Section 2*** the radio signatures of coronal shock waves associated with type II bursts are examined. The Mach numbers involved are discussed with respect to other observations in the corona and to data-driven models of CMEs. The statistical association between type II bursts and SEP events is then examined. In ***Section 3*** a more detailed investigation of two relativistic SEP events is presented, in order to study how the statistical associations manifest themselves in individual events. The Fermi/LAT telescope observed bursts and long-duration enhancements of gamma-rays produced by the decay of pions, which are themselves due to protons or He nuclei with a minimum energy of about 300 MeV/nucleon. These unique signatures of relativistic protons in the solar atmosphere are ideal counterparts of relativistic SEP events, but few relativistic SEP events could be compared with the gamma-ray observations so far. The gamma-ray observations are confronted with the type II and type IV radio emission in ***Section 4***. The chapter concludes with a short discussion of the role of radio observations in the future studies of SEP events from vantage points close to the Sun.

2 RADIO EVIDENCE OF SHOCK WAVES AND THEIR ROLE IN SEP ACCELERATION

2.1 Type II Radio Bursts

In a dynamic spectrogramme type II bursts appear as one or several narrow bands of emission that gradually drift from high to low frequencies. Examples of such spectra are shown in **Figure 1** of the chapter by Vourlidas et al. In well-developed type II bursts two different bands can be distinguished, with frequency ratio of about 2, which are considered as emission at the plasma frequency (fundamental emission) and its harmonic. *In situ* measurements of electrons and waves at some interplanetary shocks driven by CMEs (Bale et al., 1999; Fitzenreiter et al., 2003; Pulupa and Bale, 2008) confirm the classical picture of type II emission that was inferred from radio observations at metre wavelengths and by analogy with the Earth's bow shock: electrons reflected at the shock form suprathermal beams in the upstream region, where Langmuir waves are also detected. The cospatiality of reflected electrons with Langmuir waves is considered to be a consequence of wave amplification by the bump-on-tail instability. Deficiencies of the beams in the loss cone confirm their origin by reflection at the shock front. The shock geometry is reported to be quasi-perpendicular. This finding is consistent with the observation of energetic electrons at the Earth's bow shock (Burgess, 2007; Cairns, 2011) and with many models of type II burst emission in the corona (Holman and Pesses, 1983; Benz and Thejappa, 1988; Mann et al., 2018). This geometric requirement can explain why coronal radio sources are in general limited in space - a feature that is also suggested by the small (about 30%) relative bandwidth of the fundamental and harmonic bands of the type II burst (Mann et al., 1995).

The electrons generating the type II emission are themselves not very energetic: the measured distribution functions near 1 AU (Bale et al., 1999; Fitzenreiter et al., 2003; Pulupa and Bale, 2008) show beams at velocities of about 4,000 to 10,000 km s^{-1} (energies 25–280 eV), although the observed electron spectra may extend to much higher energies. Using the drift rate of "herringbone" radio bursts excited by electron beams accelerated at type II shocks in the solar corona, Mann and Klassen (2005) estimated the typical energy of the beams as 7 keV, with a broad range up to 80 keV (see also Cairns and Robinson, 1987). The values depend on a coronal density model.

Shock waves giving rise to type II bursts are formed over a broad spatial range from the corona to the interplanetary space. Imaging observations localize high-frequency sources of type II emission (dm-m-wavelengths) within a fraction (~0.3) of a solar radius above the photosphere (Dauphin et al., 2006; Zimovets et al., 2012). The start heights of type II bursts at decametric wavelengths are inferred to lie at or above a solar radius above the photosphere (Gopalswamy et al., 2013; Shanmugaraju et al., 2017).

It is not clear whether the parent shocks have a unique origin, such as the shock wave driven by a fast CME. For long time it has been difficult to understand the relationship between metric type II bursts observed from ground and decametric-to-kilometric bursts observed from space, because of the gap created by the ionosphere between the two spectral domains. The Bruny Island Radio Spectrometer (BIRS) exploited the unique opportunity at its site to observe at frequencies down to 5–10 MHz, creating a seamless coverage of type II spectra from ground to space. In a systematic study Cane and Erickson (2005) distinguished different categories of type II bursts. The coronal type II bursts observed at metre wavelengths were found to have occasional extensions into the decametric range, but to be always limited to emission at heliocentric distances within 10 $R_{\odot}$. Well-defined type II bursts from shocks in the interplanetary medium, on the other hand, were found to start higher in the corona, sometimes at frequencies that were clearly below those of a simultaneous metre-wave type II burst. The "interplanetary" type II bursts had diffuse broad bands of relatively faint emission, and were always associated with particularly fast CMEs. This was confirmed by the follow-up study of Pohjolainen et al. (2013), which showed that among 25 broadband type II bursts 24 were accompanied by CMEs with speeds between 1,200 and 2,600 km s^{-1}. These authors localized the radio source near the CME front in most cases (18/25), and behind the CME front in the remaining cases. This localization relies, however, on a model of the ambient electron density. Using direction-finding techniques from two spacecraft, Magdalenić et al. (2014) and Jebaraj et al. (2020) localized type II sources on the flanks of CMEs, and related them to interactions between the shock waves and streamers.

The most frequent category of low-frequency type II bursts identified by Cane and Erickson (2005) were spectral structures of narrow bandwidth and short duration that were aligned in the dynamic spectra along lines with drift speeds typical of interplanetary shocks. They were also identified in the (1–10) MHz range around the broadband events (Pohjolainen et al., 2013). This variety of features can be ascribed to different shock geometries, different emission processes (Bastian, 2007), and different drivers. Small-scale expanding loops in active regions (Klein et al., 1999b; Klassen et al., 2003; Su et al., 2015), shocks produced by the lateral expansion of CMEs (Stewart and Magun, 1980; Vainio and Khan, 2004; Pohjolainen et al., 2013), and blast waves (Claßen and Aurass, 2002; Vršnak and Cliver, 2008; Magdalenić et al., 2012) can create shorter-lived shocks than fast CMEs on their travel through the interplanetary space. Reiner et al. (2001) concluded that type II bursts in different wavelength ranges are different, finding that there was a correlation between the CME speed and the drift rate of type II bursts at DH wavelengths, which was confirmed by Pohjolainen et al. (2013), while no correlation was found at metre wavelengths. The absence of a correlation with the type II bursts at metre-wavelengths was confirmed by the detailed study of Mancuso (2007), which employed ground-based coronagraph and EUV observations in addition to SoHO/LASCO.

The overall spectral extent of the type II bursts is related to the energy of the associated CME: Gopalswamy et al. (2005) conducted a systematic analysis distinguishing three types of type II bursts. They found the events to be ordered by increasing speed and width of the associated CME, both projected onto the plane of sky, from pure metre-wave type II bursts without DH counterpart over DH type II bursts with or without metre-wave counterpart to type II bursts extending from metric to kilometric wavelengths. The authors relate this ordering to the increasing kinetic energy of the CME. The interpretation translates a statistical relationship into a physical picture. But all statistical relationships show that a greater number of observable phenomena appears with the increase of the amount of energy released during an eruptive event - a phenomenon that Kahler (1982b) called the big flare syndrome. For example, the kinetic energy of CMEs is statistically related to the energy released to coronal heating, as measured by the soft X-ray fluence (see Figure 8 of Gopalswamy, 2009, and further references therein).

2.2 Mach Numbers of Shocks Associated With Type II Radio Bursts

A number of attempts have been undertaken to determine the Mach number of coronal shocks. Many of these estimates were based on type II bursts in the corona. They yield low values, between one and two for the Alfvenic or the fast magnetosonic Mach number (Smerd et al., 1975; Mann et al., 1995; Vršnak et al., 2002; Cho et al., 2007; Nindos et al., 2011; Zimovets et al., 2012; Mancuso and Garzelli, 2013; Kishore et al., 2016; Salas-Matamoros et al., 2016). The diagnostics rely on the hypothesis that the occasionally observed doubling of the drifting bands in the type II spectrum, called band splitting, shows simultaneous emissions from upstream and downstream of the shock front. The interpretation is disputed based on shock observations near 1 AU (Cairns, 2011) and on solar radio observations (Du et al., 2015), but has observational support from type II observations closer to the Sun (Vršnak et al., 2001; Mancuso and Garzelli, 2013). The method can only detect moderately strong shocks, because for high compression ratios the distinction between split bands of a given type II lane is blurred by the simultaneous presence of fundamental and harmonic lanes. For the 2002 Jul 23 CME, for which they derived a peak velocity above 2000 km s^{-1}, Mancuso and Avetta (2008) inferred an alfvenic Mach number of 2.4 from the band splitting.

Comparisons of different methods using radio data and modeling in individual event studies show consistent results (Zucca et al., 2018; Maguire et al., 2020). The Mach numbers from the type II burst analyses are also similar to values derived from interpretations of many large-scale waves observed in EUV and soft X-rays (Warmuth et al., 2004; Muhr et al., 2011; Warmuth, 2015). Many coronal shocks, including type II shocks at metre wavelengths, are probably intrinsically weak (see also Mann et al., 1995). This is consistent with the idea that many metric type II bursts do not extend to lower frequencies because of a maximum of the Alfvén speed in the high corona, where the outward traveling shock decays (Warmuth and Mann, 2005, and references therein). The presence of a type II burst during a solar eruptive event, especially when it is restricted to

metre wavelengths, does not by itself reveal a strong shock and an efficient particle accelerator.

Considerably higher Mach numbers are reported for some CMEs based on coronography and data-driven modeling of the shocks. Kwon and Vourlidas (2018) computed density compression ratios from coronographic observations in two CMEs, and derived Mach numbers using MHD Rankine-Hugoniot relations for a polytropic index 5/3. They inferred alfvenic Mach numbers up to 5. The basic uncertainty of this method comes from the line-of-sight integration of the coronographic images. Occasionally found compression ratios above four also question the assumed polytropic index. Rouillard et al. (2016), Kouloumvakos et al. (2019) and Kozarev et al. (2019) modeled the ambient coronal density and magnetic field, and inferred Mach numbers from stereoscopic observations and modeling of the erupting structures. They derived fast magnetosonic Mach numbers as high as 10. The advantage of this method is that it can identify local peculiarities of the Mach number, such as enhancements near magnetic neutral lines, which are smeared-out by the spatial integration in the coronographic density measurements. The high Mach numbers, which are calculated from the modeled Alfven speed, cannot be checked by any method relying on the measurement of compression ratios, such as the analysis of type II split bands, since for high Mach numbers the relationship with the density compression ratio depends critically on the basically unknown polytropic index.

2.3 Type II Bursts and SEP Events

2.3.1 Statistical Associations

Early attempts to relate SEP events to metre-wave type II bursts on statistical grounds failed, since metre-wave type II bursts were found to be accompanied by type IV bursts, and on occasion type IV bursts without clear type II emission at metre wavelengths were found to be associated with SEP events (Kahler, 1982a). The search for statistical associations intensified again when systematic observations of radio emission at decametric to kilometric wavelengths from space became available in the late 1970s. Since type II bursts at dekametric and longer wavelengths are typically generated at heliocentric distances above 2 $R_\odot$, they allow for a direct comparison with the propagation of CMEs observed by space-borne coronagraphs.

Cane and Stone (1984) showed that most type II bursts at frequencies below 2 MHz (32/37) were accompanied by SEPs at energies above 18 MeV/nuc. Gopalswamy et al. (2002) confirmed this result with Wind/WAVES observations (frequencies <14 MHz) for SEP events with fluxes above 10 pfu (1 pfu = 1 cm^{-2} s^{-1} sr^{-1}) at energies above 10 MeV (40/42 events), and a weaker association for weaker SEPs. In line with the above studies Cliver et al. (2004) found that while less than half of the metre-wave type II bursts observed 1996–2001 with eruptive activity in the western solar hemisphere were associated with SEPs of energy >20 MeV, the association increases to 90% for type II bursts that extended into the range (1–14) MHz.

The above work considered radio events, and looked at the correlation with SEPs. Cliver et al. (2004) also made the inverse approach, considering a sample of 88 SEP events above a peak-intensity threshold of 10^{-3} cm^{-2} s^{-1} sr^{-1} MeV^{-1} at energies above 20 MeV. They found 91% of the events accompanied by a type II burst, be it at metre wavelengths, deka-to-hectometre wavelengths, or both. The association of SEP events with both types of type II bursts was found to increase with the SEP peak intensity. The few SEP events that had no type II emission associated were weak. Similar results were found in other studies (Gopalswamy et al., 2005; Richardson et al., 2014; Kouloumvakos et al., 2015; Ameri et al., 2019). The rate of association of SEP events above 25 MeV with DH type II bursts quoted by Richardson et al. (2014) is only 47%. This could be due to a relatively larger fraction of weaker events in that study as compared to Cliver et al. (2004).

Gopalswamy and coworkers (Gopalswamy et al., 2008a; Gopalswamy et al., 2008b) went one step further and distinguished the SEP association of fast CMEs with and without type II bursts. They compiled two samples of fast (projected speed of at least 900 km s^{-1}) and wide (width $\geq 60^\circ$) CMEs, and distinguished those that were accompanied by a type II burst at metre-wave or DH wavelengths ("radio-loud"; 268 cases) from those which were not ("radio-quiet"; 193 cases). The authors showed that none of the radio-quiet CMEs was accompanied by an SEP event satisfying the NOAA criterion that the proton flux exceed 10 pfu at energies above 10 MeV. Only 13/193 were accompanied by minor enhancements of the SEP intensity. Again there is some effect due to the intrinsic size of the events that can be related to the big flare syndrome: the radio-quiet CMEs are on average slower and narrower than the radio-loud ones, and also the SXR burst importance is lower for radio-quiet CMEs (C6.9) than for radio-loud ones (M3.9). In addition the parent eruptive activities of the two CME-samples have different locations: 211/268 (79%) radio-loud CMEs have their parent activity on the disk, but only 81/193 (42%) of the radio-quiet ones. So one may have to worry about the visibility of type II emission or SEPs in some of the radio-quiet CMEs. The type II signature appears here as a necessary ingredient to show that a CME drives a shock wave. In the interpretation of Gopalswamy et al. (2008b) the radio-quiet CMEs are those which propagate through coronal regions with high Alfvén speed and therefore do not drive powerful shocks, despite their high speed. The absence of significant SEP events with the radio-quiet CMEs is interpreted as a new piece of evidence that the SEPs are accelerated at the CME-driven shock wave. While the statistical studies based on type II emission leave some ambiguity, the suggested close connection between SEP acceleration and CME-related shocks is confirmed by the combination of CME observations and modeling of the corona, which shows a correlation between SEP peak intensities in the energy range (20–100) MeV and the shock Mach numbers (Kouloumvakos et al., 2019).

Iwai et al. (2020) studied CMEs from the western solar hemisphere with a rather narrow range of speeds (1,200–1800 km s^{-1}) and discovered a correlation between the peak SEP flux at energies above 10 MeV and the spectral width of the type II burst at hectometre wavelengths. They interpret the bandwidth as an indicator of the capacity of electron acceleration of the shock, and consider the correlation as additional evidence that CME-driven shocks that are efficient electron accelerators are also efficient accelerators of SEPs. Cliver and Ling (2009) examined how the finding that large SEP events are associated with type II bursts and vice versa fits into the scenario (e.g.,

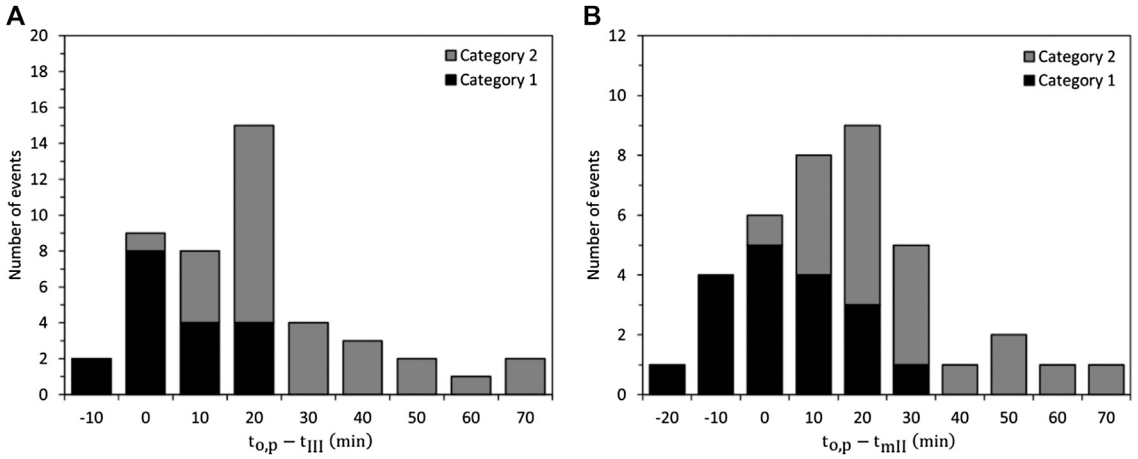

FIGURE 1 | Comparisons of the release time delays of the first solar energetic particles detected by SoHO/ERNE and the start of radio bursts of type III **(left)** and metre-wave type II **(right)**. The SEP release starts during a metre-wave type II burst in events of category 1, and during or after the start of a DH type II burst in category 2. From Ameri et al. (2019).

Reames, 1999) that the numerous small "impulsive" SEP events are particles escaping from the flare site, while the rare large "gradual" SEP events are accelerated by CME-driven shocks. They found that only 5% of the impulsive SEP events are associated with DH type II bursts, but 95% of the gradual events.

2.3.2 The Relative Timing of Initial SEP Release and Type II Bursts

A more detailed comparison of the timing of shock signatures and the onset of SEP events became possible with the high energy resolution of the Wind/EPACT and SoHO/ERNE instruments. Reames (2009), Kouloumvakos et al. (2015) and Ameri et al. (2019) analyzed the times of first SEP detection at the spacecraft as a function of particle energy, and inferred the solar release time from a velocity dispersion analysis (cf. *Section 3.1.1* of the companion chapter). The detailed analyses by Kouloumvakos et al. (2015) and Ameri et al. (2019) confirm that velocity dispersion analysis is far from straightforward, since discrepancies between the initial solar release times and the interplanetary path lengths inferred in the two studies may exceed by far the quoted statistical uncertainties.

The differences between the release of the first energetic protons and the start of the type III and the metre-wave type II emission is shown by the two histograms in **Figure 1**. From the mere timing of the initial solar particle release it appears difficult to relate SEP acceleration preferentially to one of the two burst types. But Kouloumvakos et al. (2015) report that in many cases where type II and type III bursts were present, the type III bursts emanated from the type II bursts, which suggests that the electron beams emitting the type III bursts actually were accelerated at the coronal shock waves, as originally suggested by Cane et al. (1981) and Dulk et al. (2000). This interpretation will be further discussed in ***Section 2.4***.

Kouloumvakos et al. (2015) conclude from their timing analysis that 28% of the SEP events are consistent with an initial release before the type II burst, but that these events tend to have softer (steeper) spectra than those where the initial release occurs during a type II burst. Ameri et al. (2019) conclude that the initial SEP release is always accompanied by a metric or DH type II burst, and that the energy spectra tend to be harder when the initial release occurs early, which means at the time of a metre-wave type II burst or before the start of a DH type II burst (events in their category 1). Under the hypothesis that the association with type II emission reveals acceleration at the CME shock, they derive that the SEP acceleration starts when the nose of the shock is at heliocentric distances between 2.0 and 3.5 $R_\odot$ (Kouloumvakos et al., 2015), while Ameri et al. (2019) find a much broader distribution between 1 and 4 $R_\odot$ for the events starting before the DH II burst, and 1–9 $R_\odot$ for those that start during the DH II burst.

Reames (2009) included relativistic solar particles from neutron monitor observations in his velocity analysis and found that the initial proton release was always delayed with respect to the start of the metric type II burst, the delays varying between about 4 and 38 min. He concluded that the initial release of energetic particles from energies ranging from 1 MeV to 1 GeV and more was simultaneous, and was due to the acceleration at the shock, which radio observations showed to exist at that time. The inferred heliocentric distance where the particle acceleration started was in the range (2.4–5.7) $R_\odot$. The delayed release with respect to the appearance of the type II burst can be explained by an initial shock formation in regions of closed magnetic fields in the low corona, so that the first accelerated particles remain trapped. This is what Rouillard et al. (2016) find during the 2012 May 17 event. They report from their detailed observations combined with modeling of the CME observations and the ambient corona that the SEP release starts when the shock and in particular the regions of high Mach number proceed to open magnetic fields.

These statistical associations demonstrate that type II bursts are a common element of an eruptive event that produces high SEP fluxes. Only SEP events with weak proton fluxes occur without a recognisable type II burst. In the light of the conclusion by Kahler (1982a) it is interesting to examine whether the association with type

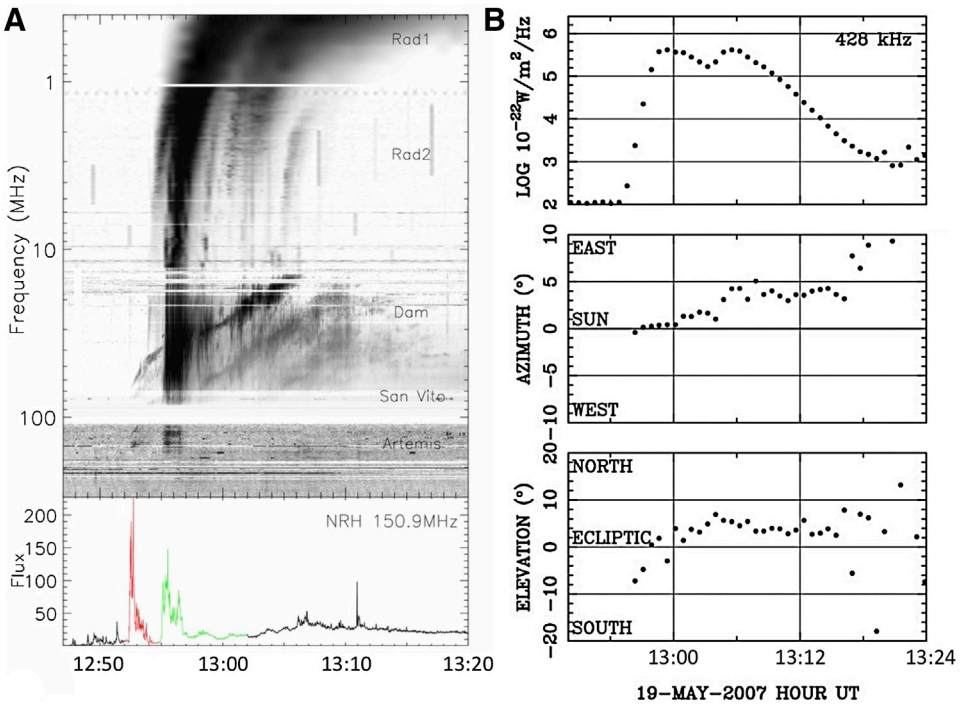

FIGURE 2 | (A) Time histories of a type III and type II burst at metre wavelengths and a complex type III burst at decametre-to-hectometre wavelengths. Dynamic spectra from dm-to-hectometre waves and time history at 150.9 MHz (bottom; type III burst in red, type II in green). **(B)** Time history of the type III group at 428 kHz (top panel), azimuth (middle) and elevation (bottom panel) of the source centroid as identified from the spin modulation of the Wind satellite. From Kerdraon et al. (2010). © AAS. Reproduced with permission.

II bursts is exclusive as to the radio counterpart of SEP events. Cane and Stone (1984) list the association of their events with radio bursts of both type II and type IV. Metre-wave type IV bursts accompanied 30/37 DH type II bursts. Four of the DH type II bursts were not accompanied by SEPs. It may be relevant that three of these had no type IV burst associated either, and that in the fourth event without SEPs the type IV burst is noted as "possible". Three further DH II bursts with SEP events had no type IV counterpart. This looks like a comparable rate of association of SEPs with DH type II bursts and metric type IV bursts, rather than a preferential association with type II bursts. Both Kouloumvakos et al. (2015) and Ameri et al. (2019) argue that type II bursts are more closely related with their SEP events than type IV bursts. Closer inspection of their events where presumably no type IV emission was found shows, however, that a number of them occurred behind the limb, where type IV emission might be occulted, while in others type IV bursts seen in single-frequency records or radioheliographic observations apparently left no trace in the dynamic spectra examined by these authors. It looks like the correlation between SEP events and type II bursts, however important it is, may by itself not be a statistical proof that the CME shock is the only or even the dominant particle accelerator.

2.4 Complex Type III Bursts, Type II Bursts, and Particle Acceleration After the Impulsive Flare Phase

Complex type III bursts were introduced in the companion chapter. They actually show a similarly ambiguous relationship with type II bursts as SEP events. The idea that these bursts are just longer versions of classical type III bursts associated with the impulsive flare phase was contradicted by Kundu et al. (1990), who discovered that they may come from different locations. This was confirmed by Kerdraon et al. (2010) and Jebaraj et al. (2020). **Figure 2A** displays the time history of a complex type III group (two top panels) and radio emissions at higher frequencies. The group of hectometric type III bursts starts with the impulsive metre-wave type III emission, but lasts much longer. It is accompanied by type II and type IV bursts at metre wavelengths. But the distinction between the early and late phase of the type III group is not only one of timing. The direction finding technique shows (**Figure 2B**) that the positions of the type III bursts in the impulsive flare phase differed from those in the post-impulsive phase. Reiner et al. (2008) showed that late complex DH type III bursts were also associated with different sources and different types of dm-m wave emission than the preceding DH III bursts in the impulsive phase of the parent flare.

The different position of the impulsive and post-impulsive type III sources means that the acceleration region and the magnetic connection to the Heliosphere changed. A common interpretation suggested by the observation of a metric type II burst (**Figure 2A**) is that the post-impulsive electron beams are accelerated by the shock wave. From their direction finding analysis Jebaraj et al. (2020) found indeed that the type III bursts in the impulsive phase and those in the post-impulsive phase were located on either side of a CME, and that the late type

III bursts were on the same side as the type II source. The shock origin of complex DH type III groups has long been favored (Cane et al., 1981; Dulk et al., 2000). Klassen et al. (2002) studied an event (1998 May 19) where the only radio counterpart of the eruption of a large quiescent filament was a type II burst with type III bursts emanating from the type II spectrum, and no emission at higher radio frequencies. The close relationship with the type II burst and the absence of radiative signatures from an alternative origin point toward shock acceleration of the electron beams. This is, however, an exceptionally pure case, which was associated with a small electron event that extended to relativistic energies (> 250 keV), and a faint proton event at MeV energies observed by SoHO/EPHIN and ERNE. Cane et al. (2002) observed that the long-duration DH type III bursts accompanying SEP events at energies above 20 MeV start on occasion at frequencies above the type II burst, may last longer than the type II burst, and could even occur without a type II burst (see their Figure 5). Type IV continua at lower altitudes than the shock were shown by a number of investigations to be a typical counterpart of long-lasting DH type III burst groups (Klein and Trottet, 1994; Reiner et al., 2000). On occasion, such broadband emissions, including the DH III bursts, show correlated variations across the entire frequency range, which may include hard X-rays from the chromosphere (Trottet, 1986; Pick et al., 2005; Reiner et al., 2007). In other events the spectra show gyrosynchrotron emission from centimetric to metric wavelengths (Dauphin et al., 2005; Vršnak et al., 2005; Carley et al., 2017). Correlated variations of these emissions, which are produced by non-thermal electrons with different lifetimes in different environments of the solar atmosphere, can only be understood by a modulation of a time-extended process of electron acceleration in the corona (Cliver et al., 1986; Trottet, 1986). This does not exclude shock waves, but an accelerator that resides in the corona downstream of the outward propagating CME appears as a more natural accelerator over tens of minutes or even longer durations. Cliver et al. (1986) proposed to relate the electron acceleration in type IV bursts to magnetic reconnection in the wake of the CME.

An alternative acceleration scenario is related to CME propagation through the low corona. The sequence of type III bursts in **Figure 2** occurred with a weak eruptive flare (GOES class B 9.5), accompanied by an EUV wave, near solar minimum in 2007. Groups of type III bursts showed the typical sequence with a first packet that started at metre wavelengths (250 MHz) and a second starting at lower frequencies (near 20 MHz), hence probably higher in the corona. At 150 MHz type III sources in the first group are observed to occur at gradually increasing distance from the parent active region. Their westward displacement follows the propagation of the EUV wave. The direction-finding observations from Wind/WAVES at 428 kHz show sources at different positions during the first and second group of type III bursts. Like for the metre-wave bursts, Kerdraon and coworkers relate the displacement of the interplanetary radio sources at a heliocentric distance of 0.15 AU to the expansion of the EUV wave in the low corona. The type III bursts were accompanied by a type II burst at metre-wavelengths. The source of its harmonic emission was close to that of the metre-wave type III bursts. The authors interpret the radio signatures as the consequence of electron acceleration at the interface between the expanding CME, traced by the EUV wave, and the ambient corona. In a similar case analyzed by Salas-Matamoros et al. (2016) a smaller group of type III bursts and a type II burst were found late during a flare, at a time when the CME had reached remote open magnetic field lines. The type III bursts were accompanied by a type II burst, but started at higher frequencies. While shock acceleration is not excluded, the starting frequency of the type III bursts is better explained by electron acceleration in relationship with magnetic reconnection between the CME and the surrounding corona.

Radio emissions therefore show a variety of phenomena that point to different acceleration processes after the impulsive flare phase. They are clearly related to CMEs, either by the reconnection they trigger in their aftermath or by their interaction with the ambient corona. The very simple solar minimum events analyzed by Klassen et al. (2002), Kerdraon et al. (2010), and Salas-Matamoros et al. (2016) support different acceleration processes, which may act during the same event and release energetic particles into different regions of the heliosphere. The complexity of this situation cannot be entirely captured by statistical analyses.

2.5 Coronal Mass Ejections, Shocks, Type II Bursts, and SEP Acceleration - A Summary

The long durations of the large "gradual" SEP events observed at energies up to tens, possibly hundreds of MeV in space and their association with fast CMEs are a strong argument that the shock wave driven by the CME is an efficient particle accelerator. The type II radio emission is an important diagnostic, which shows especially that there is no unique category of "fast" CMEs, but that the ability to drive a shock wave depends on the ambient medium. The preferential association of SEP events with CMEs accompanied by a type II burst reinforces the idea that the shock wave is necessary for the SEP production. Sophisticated modeling shows the correlation between high Mach numbers, which are especially found in the vicinity of current sheets, and high SEP intensities at tens of MeV.

The radio emissions are a hint that acceleration processes of different nature operate in the corona: the type III bursts typical of the impulsive flare phase, which on occasion also operate later in the solar eruptive event, reveal repetitive short and fragmented acceleration processes. Their absence during much of the late acceleration phases observed in the corona through the type IV radio emission and its occasional hard X-ray counterpart, and during the time-extended electron acceleration revealed by transport modeling, suggests that at least the acceleration of the radio-emitting and the near-relativistic electrons is smoother and likely due to different acceleration regions and different acceleration processes. The scenario devised by Wild et al. (1963) and adopted for SEP acceleration by Reames (1999), which attributes the sole or dominant role of particle acceleration in large SEP events to coronal shock waves, is very popular. The popularity may, however, draw more justification from the intrinsic simplicity of the scenario than from the observations.

Type II bursts seem indeed to be often produced by rather weak shocks, which are not expected to accelerate protons and

ions. The statistical studies also show a general trend that the manifestations of type II bursts become more frequent and more varied as the energy of the parent eruptive event, especially of the CME, increases. Under these conditions statistical correlations may be spurious. This recalls the interdependence of parameters related to the flare emission and the CME characteristics mentioned in the companion chapter. This interdependence is also found in the statistical relationships between SEP intensities and the parameters of the related radio bursts of type III and type II: In the attempt to devise a radio index able to serve as a forecasting tool of SEP events, Winter and Ledbetter (2015) conducted a principal-component analysis using parameters of DH II and DH III bursts associated with SEP events. The most promising index in the light of their study takes into account properties of both types of radio emission, namely the flux density and duration of type III bursts, and the peak flux density and fluence of type II bursts. This result is another indication that considerations of statistical association do not single out type II bursts as a key radio activity related to large SEP events.

Radio observations of type II bursts have some unexploited potential for improving diagnostics of coronal shock waves. Spectral imaging is now possible with instruments such as the Low-Frequency Array (LOFAR) and the Murchison Widefield Array (MWA), while in earlier times one could only image spectral features of type II emission at single frequencies. The new capacities should allow further investigation on the interpretation of split bands, which is controversial, because no hint on radio emission downstream of a shock wave is found in in situ observations near 1 AU. Observations with Parker Solar Probe and Solar Orbiter should show us whether the objections at 1 AU are valid close to the Sun. Spectral radio imaging should also allow us to more precisely investigate the frequency drift of type II bursts and its relationship to the shock speed. Traditional methods use spherically-symmetric density models, but the radio source is likely located in the quasi-perpendicular region of the shock, which may be on the flank of the CME, and which may change place with respect to the shock front as the CME progresses through the corona.

A major problem of statistical studies is the possible exclusion of relevant information, for instance in statistical correlations that favor type II bursts while disregarding type IV bursts. Shock waves are generated in the solar corona in relationship with processes that are themselves related to particle acceleration, such as magnetic reconnection in the wake of the CME. Case studies of SEP events and their relationship with electromagnetic emission in the corona may provide further indications toward relationships. In the next section relativistic solar proton events will be addressed, where the energetic particles detected in space or on the Earth have some time structure that can be compared with particle acceleration signatures at the Sun.

3 RADIO EMISSION AND RELATIVISTIC SOLAR PROTONS

SEP events can on occasion extend to relativistic energies, with values as high as a few tens of GeV reported in the literature for extreme cases. While some spacecraft measure SEPs up to several hundreds of MeV (IMP-8, e.g. Tylka and Dietrich 2009; GOES/HEPAD, see Bruno 2017, and references therein; SoHO/EPHIN, Kühl et al., 2017) or even several GeV (PAMELA, Bruno et al., 2018), the traditional measurements with neutron monitors provide the largest data collection. Neutron monitors measure secondary particles poduced by an atmospheric cascade triggered by a primary nucleon (Bütikofer, 2018), provided the primary has a minimum energy of about 450 MeV. An SEP event producing a detectable signal on ground is called a Ground-Level Enhancement (GLE). 72 GLEs were observed since 1942, initially by ionization chambers, and since the international geophysical year, with neutron monitors that now form a worldwide network.

SEP time profiles at Earth are heavily affected by propagation in the turbulent interplanetary magnetic field. The time profiles of particle intensity, for instance, carry few exploitable traces of the acceleration process. The most obvious criterion to compare with electromagnetic signatures of particle acceleration in the corona is the onset time. McCracken et al. (2008) and Moraal and McCracken (2012) showed that GLEs present a distinct time structure, which these authors relate to the magnetic connection between the Earth and the parent eruptive activity. In some cases the GLE starts with an impulsive peak seen only by neutron monitors sensitive to particles that reach Earth along the interplanetary magnetic field. The onset occurs close in time to the start of the flare. In the majority of GLEs, where the parent activity is far from the footpoint of the Earth-connected interplanetary magnetic field line, most neutron monitors see only a later, nearly isotropic distribution of primary particles, with some delayed onset. A primary example of the first, prompt GLE category, occurred on 2005 Jan 20 (McCracken et al., 2008). The time profiles of neutron monitors showing the early and the late component are plotted in the left panel of **Figure 3**. A major isotropic event occurred on 1989 Sep 29 (Moraal and Caballero-Lopez, 2014). A different account of the two event categories, based on the energy spectrum, was given by Vashenyuk et al. (2006). The classification is further discussed in Miroshnichenko (2001).

3.1 The Relative Timing of Radio Emission and the Onset of Ground-Level Enhancements

The GLE on 2005 Jan 20 (GLE 69) was associated with an eruptive flare located at W 58°. It was hence nearly ideally connected to Earth, and a privileged event for the comparison with electromagnetic signatures of particle acceleration in the solar atmosphere. The eruptive activity comprises a strong flare, large-scale EUV waves and a fast CME, analyzed in detail by Grechnev et al. (2008). The initial anisotropic component of the GLE (before 7:00 UT, **Figure 3A**) was closely connected in time with hard X-ray and microwave emission of energetic electrons, and pion-decay gamma-ray emission above 60 MeV from protons and α particles at energies above 300 MeV/nucleon (Grechnev et al., 2008; Masson et al., 2009). The time histories of the microwave, hard X-ray and gamma-ray emissions in **Figure 3B** show a time-structured impulsive phase with 1 min duration

episodes of acceleration indicated by the different levels of gray shading. The acceleration efficiency increases from episode 1 to 2: hard X-ray count rates and microwaves rise together in phase 1. The gamma-ray continuum above 60 MeV (see also Kuznetsov et al., 2008) stays at background at that time. It starts to rise in episode 2, where the hard X-ray spectrum is harder than in phase 1, and where the microwave flux density peaks. The gamma-ray spectrum shows the characteristic shape of pion-decay emission. The authors conclude that the gamma-ray time profile reveals the acceleration of protons above 300 MeV. In the decay phase the gamma-ray detectors show a constant level, which is likely produced by the impact of energetic protons. The impulsive phase acceleration hence shows a complex time structure, rather than a well-defined process that can be described by a delta-function. The time interval of intense microwave and gamma-ray emission in **Figure 3** is preceded and accompanied by radio emission that gradually drifts from high to low frequencies (Bouratzis et al., 2010). This shows the gradual extension of the coronal region to which energetic electrons are released, as discussed in *Section 4.1* of the companion chapter.

Type III bursts from decametric-to-kilometric wavelengths demonstrate that electrons escaped from the eruptive active region along open field lines since the acceleration episode 1. Hence relativistic protons, which were seen to be accelerated in close relationship with the electrons, were also able to escape. They are prime candidates to explain the early anisotropic phase of the GLE. The onset of the gamma-ray burst (06:45:30) and of the GLE (06:50, McCracken et al., 2008) imply an interplanetary path length of about 1.5 AU. This estimate suggests that the first relativistic protons at Earth were accelerated during the impulsive phase of the flare. McCracken et al. (2008) reached the same conclusion. They evaluated a larger delay between the onsets of the gamma-rays and the GLE. This is probably because they used smoothed gamma-ray count rates, where the smoothing process artificially advanced the steep rise.

Reames (2009) concluded differently, attributing the relativistic SEP acceleration to the shock wave revealed by the metric type II burst. He located the onset of the type II burst at 06: 35.7 solar release time based on the photon arrival time at Earth (06:44.0 UT) reported by NOAA/SWPC (see also Figure 12 of Pohjolainen et al., 2007). At this time hard X-rays and microwaves show the presence of mildly relativistic electrons in the corona, but the strong pion-decay gamma radiation starts a minute later. The consistency between the onset of the gamma-rays, the start of the GLE, and the DH type III bursts which show the existence of open field lines from the flaring active region to the Heliosphere, are in favor of a close link between the acceleration of relativistic electrons and protons in the flaring active region, rather than the CME shock.

A second proton release started a few minutes later. This was the onset of the second part of the GLE as seen by the neutron monitors at Cape Shmidt and Inuvik in **Figure 3A**. It was associated with a new rise of the radio emission, with continuum emission (type IV burst) between a few GHz and tens of MHz. On its low-frequency side DH type III bursts showed again that open field lines were connected to the particle acceleration regions, which allowed electrons, and therefore also protons, to escape into the Heliosphere (Klein et al., 2014; Klein et al., 2015). No gamma-ray observations were available at that time. So the second part of the GLE showed again a close timing relationship with particle acceleration in the corona.

The GLE on 1989 Sep 29 (GLE 42) is different in that the anisotropic early peak was not seen, probably due to poorer magnetic connection of the Earth to the parent eruptive activity, which was slightly behind the western solar limb (Moraal and Caballero-Lopez, 2014). Klein et al. (1999a) compared the GLE onset with radio observations and showed that the first arrival of relativistic protons at Earth was better connected in time with a late type IV burst continuum that extended from centimetric to metric wavelengths, rather than with the impulsive phase emissions. The conclusion was reached earlier by Akimov et al. (1996) using transport modeling to relate the GLE on 1991 Jun 15, which lacked the initial anisotropic peak

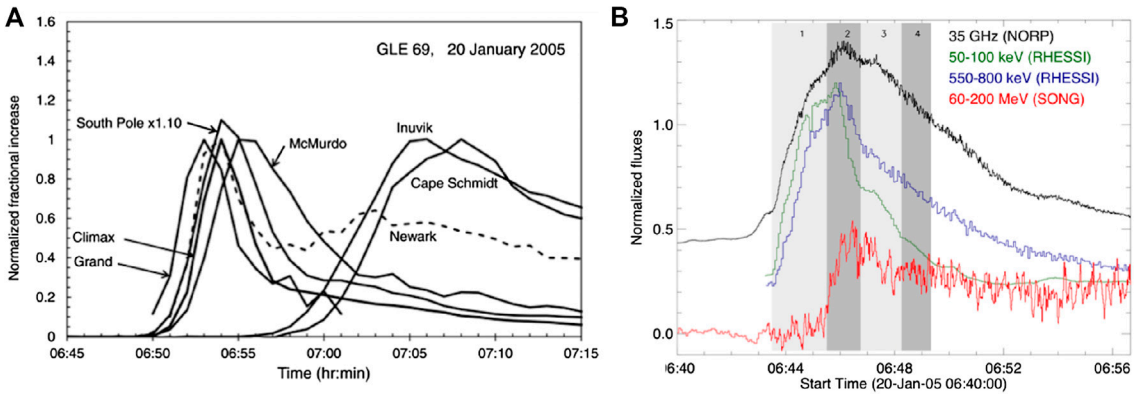

FIGURE 3 | Time history of the relativistic SEP event on 2005 Jan 20. **(A)** Neutron monitor count rates showing the two parts of the event (McCracken et al., 2012, ©AAS). **(B)** Microwave (35 GHz), hard X-ray and gamma-ray emission during the impulsive phase of the flare (Masson et al., 2009). The shaded intervals distinguish different acceleration episodes. ©Springer Nature. Figures reproduced with permission.

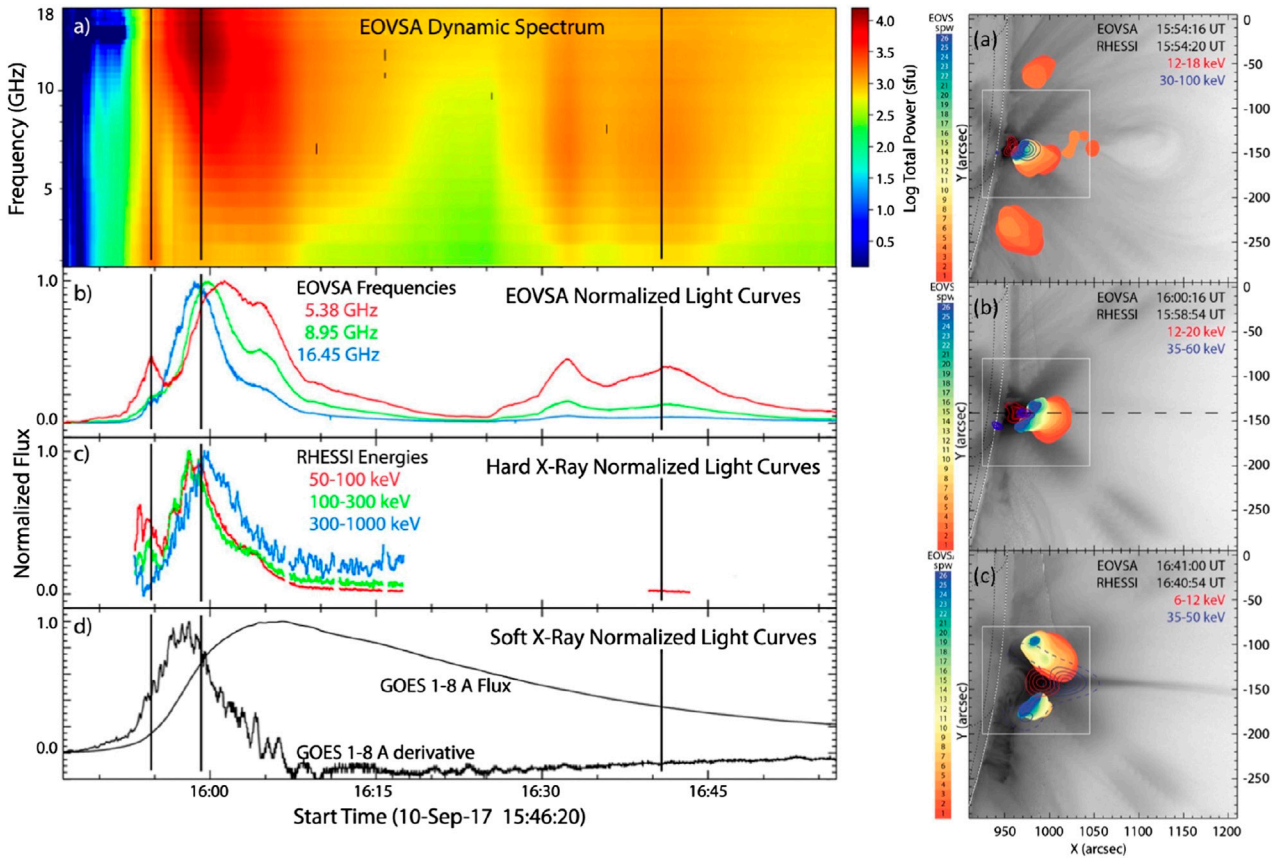

FIGURE 4 | Microwave observations of the large eruptive flare on 2017 Sep 10. Adapted from Gary et al. (2018). Left panel: Time histories of microwaves **(A and B)**, hard **(C)** and soft (D) X-rays, with the time derivative of the SXR flux in **(D)**. Right panel: EOVSA maps at three instants marked by vertical lines in the left panel, on top of SDO/AIA images (19.3 nm) (negative gray shading). The color scale shows frequencies, from 1 GHz (red) to 26 GHz (blue). The blue and red contours show X-ray emission (RHESSI) in the energy ranges (6–12) keV and (35–50) keV, respectively. ©AAS. Reproduced with permission.

(McCracken et al., 2012), to the associated microwave burst at 3 GHz. Akimov et al. (1996) showed that the GLE time profile was better fit by a model where the impulsive part of the microwave emission (at 3 GHz) was omitted.

Moraal and Caballero-Lopez (2014) and Klein et al. (1999a) hence come to the same conclusion of two distinct solar releases during the prompt and the delayed phase. As in the case of 2005 Jan 20, the delayed particle release was related with distinct particle acceleration in the solar corona revealed by a type IV continuum. This does not exclude acceleration at the CME shock, at times when the CME is a few solar radii above the photosphere (Kahler, 1994; Reames, 2009; Gopalswamy et al., 2012). The delay is then attributed to the time needed for the shock to form and to reach open magnetic fields, and the time the shock needs to accelerate protons to GeV-energies. Numerical simulations by Afanasiev et al. (2018) show indeed that the acceleration needs about 10 min. In this case the timing relationship between the start of a delayed GLE and post-impulsive radio and hard X-ray signatures would have to be considered as fortuitous. However, the 2005 Jan 20 event shows that protons must be accelerated on shorter time scales. This makes it plausible that the timing of the delayed GLEs is indeed related to late acceleration, and the relationship with the type IV emission argues for particle acceleration in the wake of the CME.

3.2 The GLE and Gamma-Ray Event on 2017 Sep 10

A major eruptive event (GOES class X8.2) at the solar limb produced a GLE (GLE 72) of modest intensity on 2017 Sep 10. The eruptive activity was observed with much detail in EUV and coronagraphic imaging, in microwaves, hard X-ray and nuclear gamma-ray emissions. Of particular interest are the good coverage of pion-decay gamma-rays by Fermi/LAT (Omodei et al., 2018) and the first microwave imaging observations with the Extended Owens Valley Solar Array (EOVSA; Gary et al., 2018).

EUV images, displayed as the gray-scale background images in the right panel of **Figure 4**, reveal a geometry close to the standard (CSHKP; see Janvier et al., 2015, for a recent review) solar flare scenario, with a rapidly outward-accelerating bulb-like feature (the light-gray - i.e., faint - bulb-shaped structure in Fig. a), interpreted as the rising flux rope, the sustained formation of an arcade of flare loops underneath, and a very narrow bright plasma

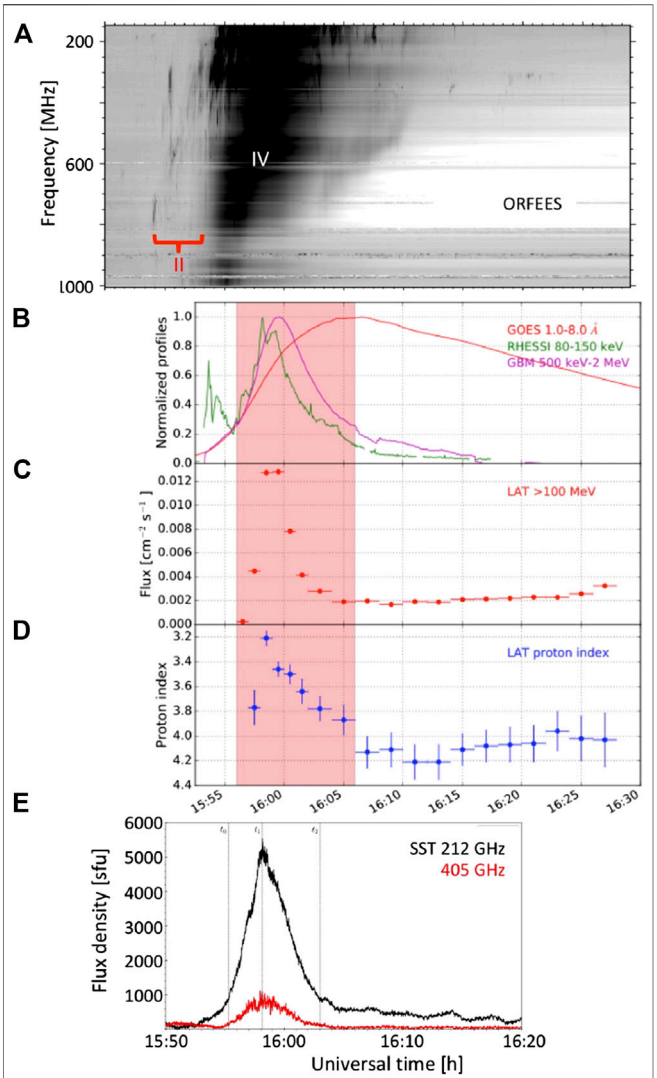

FIGURE 5 | Time history of pion-decay gamma-ray and hard X-ray emission (panels b–d, from Omodei et al., 2018. ©AAS; reproduced with permission) compared with the millimetric and sub-millimetric radio burst observed by the Submillimeter Solar Telescope (SST; courtesy G. Gimenez de Castro, Univ. MacKenzie Sao Paulo; panel e) and the dynamic spectrum in the 140–1,000 MHz range (ORFEES spectrograph, Nançay, France; panel a). The ORFEES observations are affected by offpointing due to sunset after about 16 UT. Type II and IV bursts are labeled.

sheet that connects the top of the flare loops to the flux rope (Seaton and Darnel, 2018; Yan et al., 2018), visible as a dark narrow ray extending to the right border of the image in (c). Numerous studies of this plasma sheet show its dynamics and motions that are interpreted as plasma motions in and around a reconnecting current sheet (e.g. Warren et al., 2018).

The left panel of **Figure 4** displays the time histories in soft X-rays (d), hard X-rays (c), and microwaves (b), and a dynamic spectrum between 1 and 18 GHz (a). Gary et al. (2018) show that the impulsive phase (~ 15:50–16:06) actually consists of a series of "elementary" bursts with a trend toward a hardening electron spectrum, which is shown in the Figure by the increasing delay of the hard X-ray time histories at higher energies. This is the same evolution as on 2005 Jan 20 (***Section 3.1***, **Figure 3B**). The maps of the microwave sources at the three instants marked by vertical lines in the left panel of **Figure 4** are shown in the right panel in colored shades on top of the EUV images. The dominant microwave source is located above the rising loop arcade, at the base of the plasma sheet. This location strongly suggests that the electrons are accelerated in the reconnecting current sheets embedded within the plasma sheet or by turbulence in the outflow region (see also Cai et al., 2019).

The time profiles of the gamma-ray and hard X-ray emission are shown in more detail in **Figures 5B,C**, combined with the time profiles at sub-millimetre wavelengths in panel E and the dynamic radio spectrogramme between 140 and 1,000 MHz in panel A. The sub-mm emission has a spectrum that decreases with increasing frequency, which points to gyrosynchrotron emission from relativistic electrons. At frequencies below 1 GHz a type IV burst is seen at that time (panel A), which is the continuation of the first burst seen by EOVSA. The type IV burst is preceded by a type II burst that starts several minutes earlier at unusually high frequencies, near 800 MHz, during the early rise of the flux rope as displayed in Figure 2 of Seaton and Darnel (2018). The bright emissions at sub-millimetric and gamma-ray wavelengths accompany the type IV burst. The localization of the gamma-ray source by Fermi/LAT is consistent with the active region (Omodei et al., 2018). These observations strongly suggest that during the impulsive phase non-thermal to relativistic electrons and relativistic protons were accelerated together in the main region of energy release in the flare. The acceleration operated at about the same time on electrons from energies between a few tens of keV and several MeV, corresponding to magnetic rigidities in the range 200 kV to a few MV, and protons with energies above 300 MeV (magnetic rigidities >800 MV). There is no evidence of a sequential rise in particle energy, as would be expected if a single acceleration process took minutes to get the particles to the high energies. Therefore the shock wave producing the early type II burst played no major role in this process. Radio emission of shock-accelerated electrons during the impulsive phase has also been observed with LOFAR at frequencies below 100 MHz (Morosan et al., 2019). The type II burst at these frequencies may be the continuation of the one displayed in **Figure 5A**. The authors use radio images to localize the acceleration region at the southern flank and near the summit of the CME (their Figure 3), far from the microwave sources seen by EOVSA and the flaring active region. DH type III bursts observed by the STEREO A spacecraft between about 15:50 and 16:30 (not shown; see Figure 9 of Kocharov et al., 2020) demonstrate that at least electrons accelerated during the impulsive phase have access to open magnetic field lines. Unfortunately the Wind/WAVES spectrograph was not operating in the early phase of the event, so we cannot use the low-frequency behavior of the type III bursts to see whether the open field lines are connected to the Earth.

After the impulsive phase the microwave and hard X-ray emissions first decayed, as shown in the left panels of **Figure 4**. While RHESSI ceased observing, a second burst was seen in microwaves between 16:25 and 16:55, well after the

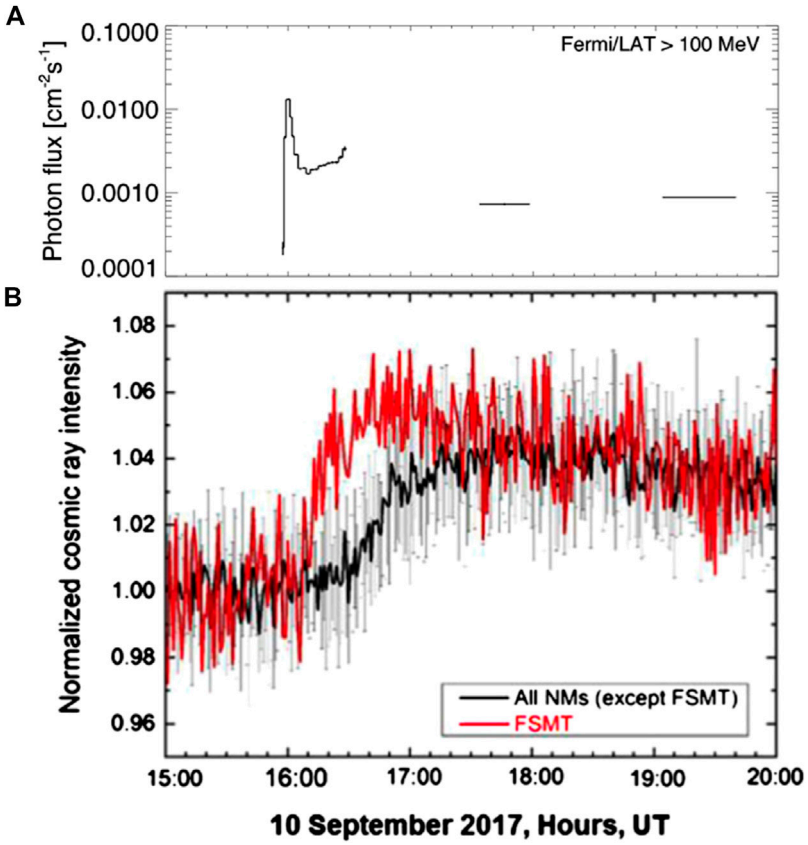

FIGURE 6 | (A) Flux of photons above 100 MeV (data from Table 1 of Omodei et al. (2018)). **(B)** Count rates of neutron monitors at sea level and high geomagnetic latitude during the first 4 h of GLE 20170910 (GLE 72). Red curve: the Fort Smith (FSMT) neutron monitor, which has the earliest response to solar particles. Black: Mean of the other high-latitude monitors. From Kurt et al. (2019). ©Springer Nature. Reproduced with permission.

impulsive phase. The sources, displayed in the bottom right panel, were on the flanks of the flare loops seen in EUV, but still related to the plasma sheet above. Lack of microwave emission from the plasma sheet can be attributed to the weak magnetic field. The pion-decay gamma-rays (**Figure 6A**), as well as gamma-rays in the (0.8–7) MeV range (Figure 6 of Kurt et al., 2019), decayed after the impulsive peak together with the hard X-rays and microwaves, but stayed above the pre-event background. The gamma-ray flux showed a shallow new rise that accelerated at 16:25 UT, but the observations were interrupted by spacecraft night. When Fermi/LAT observed the Sun again, after 17:30, the flux had considerably decreased, but was still well above background. The start of the gamma-ray rise near 16:25 accompanied the rise of the second microwave burst (see also Kocharov et al., 2020). This and the decreased level observed after the spacecraft night suggest that the second microwave burst was accompanied by pion-decay gamma-ray emission, too.

The observations are very similar to the event on 2005 Jan 20, where a common rise of the hard X-ray, microwave and pion-decay gamma-ray emission was observed, with a time structure showing successive elementary bursts (**Figure 3B**). The hard X-ray and gamma-ray emission (at MeV energies) in that event also showed loop-top sources (Krucker et al., 2008), but no microwave images or high-cadence EUV images were available in 2005. The scenario of coronal acceleration of high-energy protons and electrons in or around reconnecting current sheets in the impulsive and early post-impulsive phase is supported by both events. This phase lasted about an hour (15:50–16:50) on 2017 Sep 10.

Figure 6B compares the count rates of the first neutron monitor that sees solar particles (red; FSMT) and the average count rates of the other neutron monitors at high geomagnetic latitudes (Kurt et al., 2019). Because of the high latitude, the geomagnetic field does not affect the count rates considerably, and differences are essentially due to the anisotropy of the arriving particles. The similarity of time histories after 17 UT means that the arriving particles have an isotropic pitch-angle distribution. Before that time the particles reaching the Earth stream away from the Sun. The anisotropic phase hence gives an approximate idea of the time interval over which relativistic protons are released at the Sun. More details on the angular distribution are given by Mishev et al. (2018), and the interpretation using transport models is discussed in Kocharov et al. (2020). These authors conclude that the prompt component of the GLE lasts until 17:10 and is composed of protons arriving along the interplanetary magnetic field, while thereafter protons

from a different source, propagating across the magnetic field, dominate the neutron monitor count rates.

Kurt et al. (2019) took advantage of the GOES/HEPAD observations at energies above 700 MeV, and evaluated the arrival time of the first relativistic protons at Earth at 16: 07 ± 1 min. They argued that this was consistent with a particle release at the Sun during the impulsive phase of the flare, which they estimate to occur between 15:59 and 16:01, near the peak of the impulsive-phase emission of the hard X-ray, gamma-ray, and microwave time profiles. Since the GLE is faint, and its rise slower than on 2005 Jan 20 (GLE 69), one may suppose that the actual onset was earlier than 16:07, but hidden in the background. The anisotropy of the GLE accompanies the impulsive rise and the delayed rise of the gamma-ray time profile in **Figure 6A**. The acceleration of the interacting and escaping relativistic protons seems to be closely correlated during the first hour of the event, and to be related with the mildly relativistic electrons emitting the microwave bursts in the low corona. These observations point toward a common acceleration in the current sheets formed behind the CME.

The extremely high speed of the CME observed during the event (~4,000 km s^{-1}) is also consistent with an early start of the particle release in a scenario of relativistic particle acceleration at the shock, proposed by Gopalswamy et al. (2018b) to start when the CME front is at a heliocentric distance of about 4 $R_\odot$. The fast evolution of the impulsive early part of the gamma-ray emission shows that the protons are accelerated on faster time scales than expected at the CME shock. This is at least a strong argument against the shock being the accelerator of the first gamma-ray emitting protons in the impulsive flare phase. The overall correspondence of the anisotropic phase of the GLE with the radio emission from the flaring active region would have to be considered as coincidental if the CME shock were the accelerator of the relativistic protons. This GLE seems to support the idea that at least a large part of the relativistic protons come from impulsive and post-impulsive acceleration processes in the wake of the CME.

4 LONG-DURATION GAMMA-RAY EMISSION AND RADIO BURSTS

Gamma-ray bursts produced by pion-decay photons, where the pions themselves are produced by protons and α-particles with energies above 300 MeV, were occasionally detected since the 1990s (for a brief recent review, see *Section 2* of Klein et al., 2018). A major surprise of observations with the Fermi/LAT experiment was that pion-decay gamma-ray emission is far more frequent than GLEs, and that it may extend over much longer durations than hard X-ray or microwave signatures of mildly relativistic electrons interacting in the low solar atmosphere. Systematic investigations of Fermi/LAT gamma-ray events were conducted by Share et al. (2018) and Allafort (2018).

Klein et al. (2018) found that the long-duration gamma-ray events of Share et al. (2018) occur together with the long decay of soft X-ray emission and the formation of flare-loop arcades. With the exception of the first hour they had no radio counterpart at centimetre-to-metre wavelengths. An example is shown in **Figure 7A**: a major radio burst lasting more than an hour (bottom panel) accompanied the early gamma-ray event (middle panel), but had decayed to background while the gamma-ray emission continued at a high level for several hours. So there was no signature of late electron acceleration at coronal heights below one solar radius, despite the substantial gamma-ray emission from high-energy protons. However, the gamma-ray events were found to be accompanied by decametric-to-hectometric type II bursts (DH type II bursts), as shown by the dynamic spectrum in the top panel. These shock signatures were seen during the entire time interval where the gamma-ray emission was enhanced. In a systematic analysis of the *Fermi*/LAT events Gopalswamy et al. (2018a) found that the durations of the type II bursts and the gamma-ray events were correlated, as shown by the scatter plot in **Figure 7B**. The authors concluded that this observation demonstrates that the relativistic protons emitting the gamma-rays were accelerated at the CME shock, together with the type II-burst emitting electrons. From the timing of the event in **Figure 7A** and the CME height-time plots in the SoHO/LASCO CME catalog (Yashiro et al., 2004)[1] the strongest gamma-ray emission occurred when the CME front was between 8 and 15 $R_\odot$. The idea that the CME-driven shock was the accelerator of the gamma-ray emitting protons was substantiated by the demonstration of a magnetic connection from the shock to the chromosphere in several events (Plotnikov et al., 2017; Jin et al., 2018).

One aspect that is difficult to understand if the gamma-ray emitting protons are accelerated at the CME shock is how they can stream back from the shock to the chromosphere over 10–20 $R_\odot$ against the magnetic mirror force, which would reflect all particles outside a tiny loss cone of width one degree or less (Mandzhavidze and Ramaty, 1992; Hudson, 2018; Klein et al., 2018). The gamma-ray event on 2017 Sep 10 stands out by the high flux during its long-duration phase (Omodei et al., 2018), together with an exceptionally high CME speed (Gopalswamy et al., 2018b). One consequence of the high CME speed is that the shock is far above the Sun at the time of the late-phase gamma-ray peak near 19:30, as far as 47 $R_\odot$ as estimated in Figure 3F of Guo et al. (2018). In a standard magnetic field with an r^{-2} variation above a solar wind source surface with radius 2.5 $R_\odot$ and an r^{-3} variation below, only particles with initial pitch angle $\leq 0.12^\circ$ would reach the chromosphere. The use of an undisturbed magnetic field model in this evaluation is of course not justified, since the ambient magnetic field around the outward propagating CME front will be compressed (see *Section 6.3* of Manchester et al., 2017, and references therein). But this does not remove the problem. Jin et al. (2018) postulated the existence of turbulence, which would continuously scatter protons into the loss cone. While high levels of turbulence in flaring magnetic structures in the low corona are plausible, where supporting spectroscopic observations exist (see Li et al., 2018; Polito et al., 2018; Warren et al., 2018, for the 2017 Sep 10 event), their presence in flux tubes extending over several tens of a solar radius along which relativistic protons would have to travel from

[1]https://cdaw.gsfc.nasa.gov/CME_list/.

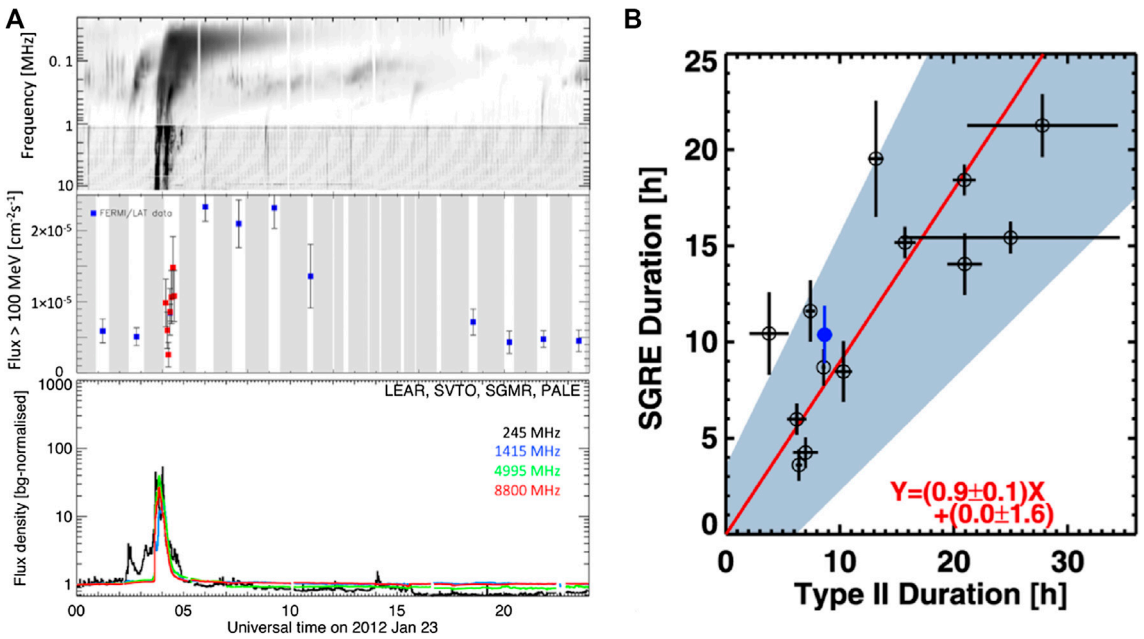

FIGURE 7 | Long-duration gamma-ray events with radio emission. **(A)** Dynamic radio spectrum **(top)**, with the frequency increasing from top to bottom, and gamma-ray light curve **(middle)** during 24 h (Klein et al., 2018), together with the light curves at selected radio frequencies (RSTN; bottom). **(B)** Scatter plot of the duration of pion-decay gamma-ray events vs the duration of decametric-to-kilometric type II bursts (Gopalswamy et al., 2018a). ©AAS. Reproduced with permission.

the shock front to the low solar atmosphere is a conjecture. Kocharov et al. (2020) argue that the acceleration region may be on the flank of the CME, but this again reduces the problem quantitatively without solving it. These objections add to those of de Nolfo et al. (2019) who argued against the idea of gamma-ray emission from backstreaming protons because they found no correlation between the numbers of protons in space and the numbers needed to explain the gamma-ray emission.

Another problem of the shock wave interpretation of gamma-ray events in the light of the study of Gopalswamy et al. (2018a) is that a common acceleration, with similar durations, of mildly relativistic protons and energetic electrons is not consistent with comparative analyses of electrons and protons at shocks in the heliosphere, where no closely correlated signatures are observed (see, e.g., Dresing et al., 2016). It is also generally believed that electrons emitting type II bursts are accelerated in very localized regions where the shock is quasi-perpendicular, while protons are supposed to be accelerated by diffusive shock acceleration, largely in the quasi-parallel regime. While the correlation between durations, and in some cases the comparable duration of DH type II bursts and long-duration gamma-ray events, is intriguing and needs to be understood, the direct interpretation as a common acceleration of the radio-emitting electrons and the gamma-ray emitting protons is not without problems.

An alternative interpretation is that there is no time-extended acceleration of protons during the entire duration of the gamma-ray event. Gamma-ray bursts lasting several hours were first observed by the Compton Gamma-Ray Telescope in 1991 (Kanbach et al., 1993). An early interpretation of this unusual duration was the trapping of relativistic protons, accelerated in the early phase of a flare, in large coronal loops, from which they were thought to leak out gradually (Mandzhavidze and Ramaty, 1992). Their model calculations show that protons could survive in an arcade of coronal loops of height 10^7 m with ambient densities below 5.10^{17} m^{-3} and a very low level of waves to scatter the protons into the loss cone. The erupting flux rope itself is not a plausible long-term trap, because the protons would lose energy in the expanding structure. Taking again the 2017 Sep 10 event for illustration, the field-aligned momentum would decrease inversely as the height of the flux rope increases, i.e. by a factor of about 50 from the beginning of the eruption to the time of maximum of the long-duration gamma-ray emission. However, the arcade of flare loops forming in the wake of the CME has the required parameter range. The electron density of 5.10^{15} m^{-3} determined at the top of a flare loop arcade of the 2017 Sep 10 event by Cai et al. (2019) is consistent with the requirement of the model by Mandzhavidze and Ramaty (1992). This interpretation would not explain the observed relationship between the duration of the gamma-ray events and the type II bursts (**Figure 7B**). But it is noteworthy that in the 2017 Sep 10 event the duration of the gamma-ray emission exceeds by far that of the anisotropic phase of the GLE (**Figure 6**). The durations of both the radio emission and the anisotropic phase of the GLE are consistent with particle acceleration at the Sun during about an hour. This agrees qualitatively with a scenario of trapping and gradual release of the relativistic protons.

The acceleration of relativistic protons at shocks high in the corona has on the other hand the very attractive feature to explain why pion-decay gamma-ray emission may come from the photosphere while the flaring active region is at or behind the

solar limb. This is the case of the 2017 Sep 10 and several other events (Pesce-Rollins et al., 2015; Ackermann et al., 2017). The scenario receives strong support from data-driven CME and atmospheric modeling (Plotnikov et al., 2017) and MHD modeling (Jin et al., 2018) which shows that at relevant times the CME shock intercepts open field lines that are rooted in the earthward solar hemisphere. The source regions of electrons accelerated at the shock of the 2017 Sep 10 event, observed by LOFAR, were also localized at the CME flank connected to the earthward photosphere (Morosan et al., 2019, Figure 3). Grechnev et al. (2018) confront the scenarios of acceleration and trapping with a wealth of observations during the 2014 Sep 01 event, related with a flare at N14 E126. Their conclusion is that electrons emitting radio and hard X-rays are trapped in extended coronal loops, consistent with Ackermann et al. (2017), but that protons are also trapped there. They argue that the spectral hardening of the protons can be explained by re-acceleration, possibly by a shock wave, but that the particles are unlikely to stream back from the high corona.

5 CONCLUSION

The distinction between impulsive and gradual SEP events based on the role played by impulsive particle acceleration as in flares and CME shock acceleration is largely drawn from the association of the SEP events with radio emission: type III bursts as an example of impulsive electron acceleration, and type II bursts as a signature of coronal shock waves. The relatively low Mach numbers that many shocks emitting type II bursts probably have do not qualify them as efficient proton accelerators. The association of these bursts with SEP events may be spurious, due to the fact that the more energetic CMEs are more likely accompanied by some type II burst. But type II bursts do prove that a shock exists, and the trend that only CMEs accompanied by type II bursts have SEP events confirms the widely accepted idea that in "gradual" SEP events at energies ranging from hundreds of keV to some limit that lies well above 10 MeV a CME-driven shock is the dominant particle accelerator. Given the association of virtually all SEP events with type III bursts, particles accelerated in the corona in the wake of the CME can probably escape, and are likely to contribute to the SEP population in the early phase of the events.

Relativistic SEP events, on the other hand, have commonalities in their timing with radio emission both in the impulsive phase and the post-impulsive phase. This supports the idea that acceleration processes in the flaring active region and subsequently in higher regions in the wake of the rising CME make a major contribution to the SEP population. It is not excluded that the CME shock contributes also to relativistic SEPs. However, present indications that this is the case, based on the relative timing of relativistic SEPs and coronal acceleration signatures, are debatable. The onset delays observed in some events, which have been ascribed to the time needed by the shock-accelerated particles to become relativistic, have at least in some detailed studies been shown to have a common timing with type IV radio emission. The fact that type II emission starts before the gamma-ray emission of relativistic protons in the 2017 Sep 10 event is a counter-example to the claim that the type II shock is an efficient accelerator at these energies. This is certainly not a definite answer, but the radio observations provide valuable arguments that the particle acceleration in solar eruptive events is more complex than the simple alternative between flare-accelerated impulsive events and CME-shock accelerated gradual events suggests.

The shock acceleration scenario, on the other hand, provides an easy explanation for the escape of SEPs to the Heliosphere, while particles accelerated in the wake of the CME are a priori confined in closed magnetic structures. However, the CME will interact with the surrounding coronal magnetic field, and this implies magnetic reconnection by which the accelerated particles can leak out (Masson et al., 2019). The presence of type III bursts in the eruptive events shows that open magnetic field lines do exist. While this process is plausible, observational evidence that it acts efficiently in SEP events still has to be established.

Radio observations remain an essential element for the scientific return of space missions dedicated to study SEPs and solar-terrestrial connections in general. The HELIOS mission demonstrated that observing energetic particles from vantage points close to the Sun reveals details in the time histories that are washed out once the particles reach 1 AU. The Parker Solar Probe and Solar Orbiter missions will provide new opportunities to understand the physical processes involved. The current wealth of radio instruments, unimaginable in the HELIOS era, will provide new insight into the nature of the radio sources. The powerful general purpose radio telescopes that can observe the Sun, such as the VLA, LOFAR, MWA and in the future SKA, can bring major new insight into the nature of the radio sources, as illustrated in *Section 3.1.3* of the companion chapter. The possibility of spectral imaging, i.e. obtaining an image at each frequency of the dynamic spectrum, is still largely unexploited because of the huge amount of data to be handled. Correcting the effects of radio wave propagation along paths that deviate from straight lines, due to ducting, refraction and scattering, will certainly become essential at some point (Duncan, 1979; Steinberg et al., 1984; Kontar et al., 2019). Currently, simplified models of the corona, such as a spherically symmetric background density, are employed, but models with increasingly detailed coronal density diagnostics should bring progress in this field.

But solar observing time with large multi-purpose instruments is restricted, and the large amounts of data are difficult and time-consuming to analyze. Dedicated solar patrol instruments continue to be needed, because only continuous observations ensure that all interesting events are captured. We need whole-Sun dynamic spectra, ideally from a worldwide network, for which e-Callisto (Benz et al., 2009) is a model. There is room to make these spectrographs more sensitive, but this must be done by individual groups worldwide. Radioheliographs at different places have provided much further insight and continue to produce essential observations. The major thread to ground-based radio astronomy is interference from terrestrial and space-borne emitters, which increasingly restrains the view of the radio sky. To some extent electronic and software procedures to reduce the interference can be developed, but agencies and operators should consider this issue in the allocation of frequencies. Solar radio monitoring also brings valuable information for space weather services, at relatively low cost.

Radio observations of the Sun continue to be needed - not only as a simple addition to the space missions, but to ensure their full scientific return. In solar physics the multi-messenger approach has been commonplace since three decades. Maintaining the relevant instruments is a wise use of resources and holds the promise of continuing discoveries into the future.

AUTHOR CONTRIBUTIONS

The author confirms being the sole contributor of this work and has approved it for publication.

ACKNOWLEDGMENTS

This work owes much to the generous data provision of numerous space-borne and ground-based instruments and data bases, especially the SoHO/LASCO CME catalog generated and maintained at the CDAW Data Center by NASA and The Catholic University of America in cooperation with the Naval Research Laboratory (https://cdaw.gsfc.nasa.gov/CME_list/), the Radio Monitoring web site (http://secchirh.obspm.fr/) at LESIA, Observatoire de Paris, supported by the French Space Agency CNES, the neutron monitor database (www.nmdb.eu) maintained at the University of Kiel and built within a Framework seven project of the European Union, and the National Centers for Environmental Information at NOAA (https://www.ngdc.noaa.gov/stp/space-weather/solar-data). The author acknowledges helpful discussions with many colleagues during the NMDB, SEPServer and HESPERIA projects funded by the European Union, during several working groups and workshops dedicated to solar energetic particles at the International Space Science Institute (ISSI) in Bern, and during workshops of the Community of European Solar Radio Astronomers (CESRA). He is indebted to the referees for their patient and constructive criticism. This research was supported by the French Polar Institute (IPEV), space agency (CNES), and Programme National Soleil-Terre (PNST) of CNRS/INSU.

REFERENCES

Ackermann, M., Allafort, A., Baldini, L., Barbiellini, G., Bastieri, D., Bellazzini, R., et al. (2017). Fermi-LAT observations of high-energy behind-the-limb solar flares. *Astrophys. J.* 835, 219. doi:10.3847/1538-4357/835/2/219

Afanasiev, A., Vainio, R., Rouillard, A. P., Battarbee, M., Aran, A., and Zucca, P. (2018). Modelling of proton acceleration in application to a ground level enhancement. *Astron. Astrophys.* 614, A4. doi:10.1051/0004-6361/201731343

Akimov, V. V., Ambro, P., Belov, A. V., Berlicki, A., Chertok, I. M., Karlický, M., et al. (1996). Evidence for prolonged acceleration based on a detailed analysis of the long-duration solar gamma-ray flare of June 15, 1991. *Sol. Phys.* 166, 107–134. doi:10.1007/BF00179358

Allafort, A. (2018). High-energy gamma-ray observations of solar flares with the Fermi large area telescope. PhD thesis. Stanford (CA): Stanford University.

Ameri, D., Valtonen, E., and Pohjolainen, S. (2019). Properties of high-energy solar particle events associated with solar radio emissions. *Sol. Phys.* 294, 122. doi:10.1007/s11207-019-1512-9

Bale, S. D., Reiner, M. J., Bougeret, J.-L., Kaiser, M. L., Krucker, S., Larson, D. E., et al. (1999). The source region of an interplanetary type II radio burst. *Geophys. Res. Lett.* 26, 1573–1576. doi:10.1029/1999GL900293

Bastian, T. S. (2007). Synchrotron radio emission from a fast halo coronal mass ejection. *Astrophys. J.* 665, 805–812. doi:10.1086/519246

Benz, A. O., Monstein, C., Meyer, H., Manoharan, P. K., Ramesh, R., Altyntsev, A., et al. (2009). A world-wide net of solar radio spectrometers: e-CALLISTO. *Earth Moon Planets*. 104, 277–285. doi:10.1007/s11038-008-9267-6

Benz, A. O., and Thejappa, G. (1988). Radio emission of coronal shock waves. *Astron. Astrophys.* 202, 267–274.

Bouratzis, C., Preka-Papadema, P., Hillaris, A., Tsitsipis, P., Kontogeorgos, A., Kurt, V. G., et al. (2010). Radio observations of the January 20, 2005 extreme event. *Sol. Phys.* 267, 343–359. doi:10.1007/s11207-010-9648-7

Bruno, A., Bazilevskaya, G. A., Boezio, M., Christian, E. R., de Nolfo, G. A., Martucci, M., et al. (2018). Solar energetic particle events observed by the PAMELA mission. *Astrophys. J.* 862, 97. doi:10.3847/1538-4357/aacc26

Bruno, A. (2017). Calibration of the GOES 13/15 high-energy proton detectors based on the PAMELA solar energetic particle observations. *Space Weather*. 15, 1191–1202. doi:10.1002/2017SW001672

Burgess, D. (2007). "Particle acceleration at the Earth's bow shock," in *The high energy solar corona: waves, eruptions, particles*. Editors K.-L. Klein and A. L. MacKinnon (Berlin, Germany: Springer Verlag), Vol. 725, 161–190.

Bütikofer, R. (2018). "Ground-based measurements of energetic particles by neutron monitors," in *Solar particle radiation storms forecasting and analysis*. Editors O. E. Malandraki and N. B. Crosby, 444, 95–112. doi:10.1007/978-3-319-60051-2_6

Cai, Q., Shen, C., Raymond, J. C., Mei, Z., Warmuth, A., Roussev, I. I., et al. (2019). Investigations of a supra-arcade fan and termination shock above the top of the flare-loop system of the 2017 September 10 event. *Mon. Not. Roy. Astron. Soc.* 489, 3183–3199. doi:10.1093/mnras/stz2167

Cairns, I. H. (2011). "Coherent radio emissions associated with solar system shocks," in *The Sun, the solar wind, and the heliosphere*. Editors M. P. Miralles and J. Sánchez Almeida (Berlin, Germany: Springer), Vol. 4, 267–338.

Cairns, I. H., and Robinson, R. D. (1987). Herringbone bursts associated with type II solar radio emission. *Sol. Phys.* 111 (2), 365–383. doi:10.1007/bf00148526

Cane, H. V., Erickson, W. C., and Prestage, N. P. (2002). Solar flares, type III radio bursts, coronal mass ejections and energetic particles. *J. Geophys. Res.* 107, 1315. doi:10.1029/2001JA000320

Cane, H. V., and Erickson, W. C. (2005). Solar type II radio bursts and IP type II events. *Astrophys. J.* 623, 1180–1194. doi:10.1086/428820

Cane, H. V., Stone, R. G., Fainberg, J., Steinberg, J. L., Hoang, S., and Stewart, R. T. (1981). Radio evidence for shock acceleration of electrons in the solar corona. *Geophys. Res. Lett.* 8, 1285–1288. doi:10.1029/GL008i012p01285

Cane, H. V., and Stone, R. G. (1984). Type II solar radio bursts, interplanetary shocks, and energetic particle events. *Astrophys. J.* 282, 339–344. doi:10.1086/162207

Carley, E. P., Vilmer, N., Simões, P. J. A., and Ó Fearraigh, B. (2017). Estimation of a coronal mass ejection magnetic field strength using radio observations of gyrosynchrotron radiation. *Astron. Astrophys.* 608, A137. doi:10.1051/0004-6361/201731368

Cho, K.-S., Lee, J., Gary, D. E., Moon, Y.-J., and Park, Y. D. (2007). Magnetic field strength in the solar corona from type II band splitting. *Astrophys. J.* 665, 799–804. doi:10.1086/519160

Claßen, H. T., and Aurass, H. (2002). On the association between type II radio bursts and CMEs. *Astron. Astrophys.* 384 (3), 1098–1106. doi:10.1051/0004-6361:20020092

Cliver, E. W., Dennis, B. R., Kiplinger, A. L., Kane, S. R., Neidig, D. F., Sheeley, N. R., et al. (1986). Solar gradual hard X-ray bursts and associated phenomena. *Astrophys. J.* 305, 920–935. doi:10.1086/164306

Cliver, E. W., Kahler, S. W., and Reames, D. V. (2004). Coronal shocks and solar energetic proton events. *Astrophys. J.* 605, 902–910. doi:10.1086/382651

Cliver, E. W., and Ling, A. G. (2009). Low-frequency type III bursts and solar energetic particle events. *Astrophys. J.* 690, 598–609. doi:10.1088/0004-637X/690/1/598

Dauphin, C., Vilmer, N., and Krucker, S. (2006). Observations of a soft X-ray rising loop associated with a type II burst and a coronal mass ejection in the 03 November 2003 X-ray flare. *Astron. Astrophys.* 455, 339–348. doi:10.1051/0004-6361:20054535

Dauphin, C., Vilmer, N., Lüthi, T., Trottet, G., Krucker, S., and Magun, A. (2005). Modulations of broad-band radio continua and X-ray emissions in the large X-ray flare on 03 November 2003. *Adv. Space Res.* 35, 1805–1812. doi:10.1016/j.asr.2005.04.092

de Nolfo, G. A., Bruno, A., Ryan, J. M., Dalla, S., Giacalone, J., Richardson, I. G., et al. (2019). Comparing long-duration gamma-ray flares and high-energy solar energetic particles. *Astrophys. J.* 879, 90. doi:10.3847/1538-4357/ab258f

Dresing, N., Theesen, S., Klassen, A., and Heber, B. (2016). Efficiency of particle acceleration at interplanetary shocks: statistical study of STEREO observations. *Astron. Astrophys.* 588, A17. doi:10.1051/0004-6361/201527853

Du, G., Kong, X., Chen, Y., Feng, S., Wang, B., and Li, G. (2015). An observational revisit of band-split solar type-II radio bursts. *Astrophys. J.* 812, 52. doi:10.1088/0004-637X/812/1/52

Dulk, G. A., Leblanc, Y., Bastian, T. S., and Bougeret, J. L. (2000). Acceleration of electrons at type II shock fronts and production of shock-accelerated type III bursts. *J. Geophys. Res.* 105, 27343–27352.

Duncan, R. A. (1979). Wave ducting of solar metre-wave radio emission as an explanation of fundamental/harmonic source coincidence and other anomalies. *Sol. Phys.* 63, 389–398. doi:10.1007/BF00174543

Fitzenreiter, R. J., Ogilvie, K. W., Bale, S. D., and Viñas, A. F. (2003). Modification of the solar wind electron velocity distribution at interplanetary shocks. *J. Geophys. Res.* 108, 1415. doi:10.1029/2003JA009865

Gary, D. E., Chen, B., Dennis, B. R., Fleishman, G. D., Hurford, G. J., Krucker, S., et al. (2018). Microwave and hard X-ray observations of the 2017 September 10 solar limb flare. *Astrophys. J.* 863, 83. doi:10.3847/1538-4357/aad0ef

Gopalswamy, N., Aguilar-Rodriguez, E., Yashiro, S., Nunes, S., Kaiser, M. L., and Howard, R. A. (2005). Type II radio bursts and energetic solar eruptions. *J. Geophys. Res.* 110, A12S07. doi:10.1029/2005JA011158

Gopalswamy, N. (2009). "Coronal mass ejections and space weather," in *Climate and weather of the sun-earth system (CAWSES) selected papers from the 2007 kyoto symposium*. Editors T. Tsuda, R. Fujii, K. Shibata, and M. A. Geller (Tokyo (Japan): TERRAPUB), 77–120.

Gopalswamy, N., Mäkelä, P., Yashiro, S., Lara, A., Xie, H., Akiyama, S., et al. (2018a). Interplanetary type II radio bursts from Wind/WAVES and sustained gamma-ray emission from Fermi/LAT: evidence for shock source. *Astrophys. J. Lett.* 868, L19. doi:10.3847/2041-8213/aaef36

Gopalswamy, N., Xie, H., Mäkelä, P., Yashiro, S., Akiyama, S., Uddin, W., et al. (2013). Height of shock formation in the solar corona inferred from observations of type ii radio bursts and coronal mass ejections. *Adv. Space Res.* 51, 1981–1989. doi:10.1016/j.asr.2013.01.006

Gopalswamy, N., Xie, H., Yashiro, S., Akiyama, S., Mäkelä, P., and Usoskin, I. G. (2012). Properties of Ground Level Enhancement events and the associated solar eruptions during solar cycle 23. *Space Sci. Rev.* 171, 23–60. doi:10.1007/s11214-012-9890-4

Gopalswamy, N., Yashiro, S., Akiyama, S., Mäkelä, P., Xie, H., Kaiser, M. L., et al. (2008a). Coronal mass ejections, type II radio bursts, and solar energetic particle events in the SOHO era. *Ann. Geophys.* 26, 3033–3047. doi:10.5194/angeo-26-3033-2008

Gopalswamy, N., Yashiro, S., Mäkelä, P., Xie, H., Akiyama, S., and Monstein, C. (2018b). Extreme kinematics of the 2017 September 10 solar eruption and the spectral characteristics of the associated energetic particles. *Astrophys. J. Lett.* 863, L39. doi:10.3847/2041-8213/aad86c

Gopalswamy, N., Yashiro, S., Michałek, G., Kaiser, M. L., Howard, R. A., Reames, D. V., et al. (2002). Interacting coronal mass ejections and solar energetic particles. *Astrophys. J. Lett.* 572, L103–L107. doi:10.1086/341601

Gopalswamy, N., Yashiro, S., Xie, H., Akiyama, S., Aguilar-Rodriguez, E., Kaiser, M. L., et al. (2008b). Radio-quiet fast and wide coronal mass ejections. *Astrophys. J.* 674, 560–569. doi:10.1086/524765

Grechnev, V. V., Kiselev, V. I., Kashapova, L. K., Kochanov, A. A., Zimovets, I. V., Uralov, A. M., et al. (2018). Radio, hard X-ray, and gamma-ray emissions associated with a far-side solar event. *Sol. Phys.* 293, 133. doi:10.1007/s11207-018-1352-z

Grechnev, V. V., Kurt, V. G., Chertok, I. M., Uralov, A. M., Nakajima, H., Altyntsev, A. T., et al. (2008). An extreme solar event of 20 January 2005: properties of the flare and the origin of energetic particles. *Sol. Phys.* 252, 149–177. doi:10.1007/s11207-008-9245-1

Guo, J., Dumbović, M., Wimmer-Schweingruber, R. F., Temmer, M., Lohf, H., Wang, Y., et al. (2018). Modeling the evolution and propagation of 10 September 2017 CMEs and SEPs arriving at Mars constrained by remote sensing and *in situ* measurement. *Space Weather.* 16, 1156–1169. doi:10.1029/2018SW001973

Holman, G. D., and Pesses, M. E. (1983). Solar type II radio emission and the shock drift acceleration of electrons. *Astrophys. J.* 267, 837–843. doi:10.1086/160918

Hudson, H. S. (2018). "The relationship between long-duration gamma-ray flares and solar cosmic rays," in *Space weather of the heliosphere: processes and forecasts*. Editors C. Foullon and O. E. Malandraki (Vienna, Austria: IAU Symposium), Vol. 335, 49–53. doi:10.1017/S1743921317009681

Iwai, K., Yashiro, S., Nitta, N. V., and Kubo, Y. (2020). Spectral structures of type II solar radio bursts and solar energetic particles. *Astrophys. J.* 888, 50. doi:10.3847/1538-4357/ab57ff

Janvier, M., Aulanier, G., and Démoulin, P. (2015). From coronal observations to MHD simulations, the building blocks for 3D models of solar flares (Invited Review). *Sol. Phys.* 290, 3425–3456. doi:10.1007/s11207-015-0710-3

Jebaraj, I. C., Magdalenić, J., Podladchikova, T., Scolini, C., Pomoell, J., Veronig, A. M., et al. (2020). Using radio triangulation to understand the origin of two subsequent type II radio bursts. *Astron. Astrophys.* 639, A56. doi:10.1051/0004-6361/201937273

Jin, M., Petrosian, V., Liu, W., Nitta, N. V., Omodei, N., Rubio da Costa, F., et al. (2018). Data-driven simulations of magnetic connectivity in behind-the-limb γ-ray flares and associated coronal mass ejections. *Astrophy. J.* 867 (2), 122. doi:10.3847/1538-4357/aae1fd

Kahler, S. (1994). Injection profiles of solar energetic particles as functions of coronal mass ejection heights. *Astrophys. J.* 428, 837–842. doi:10.1086/174292

Kahler, S. W. (1982a). Radio burst characteristics of solar proton flares. *Astrophys. J.* 261, 710–719. doi:10.1086/160381

Kahler, S. W. (1982b). The role of the big flare syndrome in correlations of solar energetic proton fluxes and associated microwave burst parameters. *J. Geophys. Res.* 87, 3439–3448. doi:10.1029/JA087iA05p03439

Kanbach, G., Bertsch, D. L., Fichtel, C. E., Hartman, R. C., Hunter, S. D., Kniffen, D. A., et al. (1993). Detection of a long-duration solar gamma-ray flare on June 11, 1991 with EGRET on COMPTON-GRO. *Astron. AstroPhys. Suppl.* 97, 349–353.

Kerdraon, A., Pick, M., Hoang, S., Wang, Y., and Haggerty, D. (2010). The coronal and heliospheric 2007 May 19 event: coronal mass ejection, Extreme Ultraviolet Imager wave, radio bursts, and energetic electrons. *Astrophys. J.* 715 (1), 468–476. doi:10.1088/0004-637X/715/1/468

Kishore, P., Ramesh, R., Hariharan, K., Kathiravan, C., and Gopalswamy, N. (2016). Constraining the solar coronal magnetic field strength using split-band type II radio burst observations. *Astrophys. J.* 832, 59. doi:10.3847/0004-637X/832/1/59

Klassen, A., Bothmer, V., Mann, G., Reiner, M. J., Krucker, S., Vourlidas, A., et al. (2002). Solar energetic electron events and coronal shocks. *Astron. Astrophys.* 385 (3), 1078–1088. doi:10.1051/0004-6361:20020205

Klassen, A., Pohjolainen, S., and Klein, K.-L. (2003). Type II radio precursor and X-ray flare emission. *Sol. Phys.* 218, 197–210. doi:10.1023/b:sola.0000013034.61996.c4

Klein, K.-L., Agueda, N., and Bütikofer, R. (2015). "On the origin of relativistic solar particle events: interplanetary transport modelling and radio emission," in Proceedings of science 34th international cosmic ray conference. Editors R. Caballero, J. C. D'Olivo, G. Medina-Tanco, L. Nellen, F. A. Sánchez, and J. F. Valdés-Galicia, Hague, Netherlands, July 30–August 6, 2015. 121–124.

Klein, K.-L., Chupp, E. L., Trottet, G., Magun, A., Dunphy, P. P., Rieger, E., et al. (1999a). Flare-associated energetic particles in the corona and at 1 AU. *Astron. Astrophys.* 348, 271–285.

Klein, K.-L., Khan, J. I., Vilmer, N., Delouis, J., and Aurass, H. (1999b). X-ray and radio evidence on the origin of a coronal shock wave. *Astron. Astrophys.* 346, L53–L56.

Klein, K.-L., Masson, S., Bouratzis, C., Grechnev, V., Hillaris, A., and Preka-Papadema, P. (2014). The relativistic solar particle event of 2005 January 20: origin of delayed particle acceleration. *Astron. Astrophys.* 572, A4. doi:10.1051/0004-6361/201423783

Klein, K.-L., and Trottet, G. (1994). "Energetic electron injection into the high corona during the gradual phase of flares: evidence against acceleration by a large scale shock," in AIP conference Proceedings 294: high-energy solar phenomena - a new era of spacecraft measurements. Editors J. Ryan and W. Vestrand, Waterville Valley, NH, December 10, 1994, 187. doi:10.1063/1.45183

Klein, K.-L., Tziotziou, K., Zucca, P., Valtonen, E., Vilmer, N., Malandraki, O. E., et al. (2018). "X-ray, radio and SEP observations of relativistic gamma-ray events," in *Solar particle radiation storms forecasting and analysis*. Editors O. E. Malandraki and N. B. Crosby (Berlin, Germany: Springer), Vol. 444 133–155. doi:10.1007/978-3-319-60051-2_8

Kocharov, L., Pesce-Rollins, M., Laitinen, T., Mishev, A., Kühl, P., Klassen, A., et al. (2020). Interplanetary protons versus interacting protons in the 2017 September 10 solar eruptive event. *Astrophys. J.* 890, 13. doi:10.3847/1538-4357/ab684e

Kontar, E. P., Chen, X., Chrysaphi, N., Jeffrey, N. L. S., Emslie, A. G., Krupar, V., et al. (2019). Anisotropic radio-wave scattering and the interpretation of solar radio emission observations. *Astrophys. J.* 884, 122. doi:10.3847/1538-4357/ab40bb

Kouloumvakos, A., Nindos, A., Valtonen, E., Alissandrakis, C. E., Malandraki, O., Tsitsipis, P., et al. (2015). Properties of solar energetic particle events inferred from their associated radio emission. *Astron. Astrophys*. 580, A80. doi:10.1051/0004-6361/201424397

Kouloumvakos, A., Rouillard, A. P., Wu, Y., Vainio, R., Vourlidas, A., Plotnikov, I., et al. (2019). Connecting the properties of coronal shock waves with those of solar energetic particles. *Astrophys. J.* 876, 80. doi:10.3847/1538-4357/ab15d7

Kozarev, K. A., Dayeh, M. A., and Farahat, A. (2019). Early-stage solar energetic particle acceleration by coronal mass ejection-driven shocks with realistic seed spectra. I. Low corona. *Astrophys. J.* 871, 65. doi:10.3847/1538-4357/aaf1ce

Krucker, S., Hurford, G. J., MacKinnon, A. L., Shih, A. Y., and Lin, R. P. (2008). Coronal γ-ray bremsstrahlung from solar flare-accelerated electrons. *Astrophys. J. Lett*. 678, L63–L66. doi:10.1086/588381

Kühl, P., Dresing, N., Heber, B., and Klassen, A. (2017). Solar Energetic particle events with protons above 500 MeV between 1995 and 2015 measured with SOHO/EPHIN. *Sol. Phys*. 292, 10. doi:10.1007/s11207-016-1033-8

Kundu, M. R., MacDowall, R. J., and Stone, R. G. (1990). Kilometric shock-associated events and microwave bursts. *Astrophys. Space Sci*. 165, 101–110. doi:10.1007/BF00653661

Kurt, V., Belov, A., Kudela, K., Mavromichalaki, H., Kashapova, L., Yushkov, B., et al. (2019). Onset time of the GLE 72 observed at neutron monitors and its relation to electromagnetic emissions. *Sol. Phys.* 294, 22. doi:10.1007/s11207-019-1407-9

Kuznetsov, S. N., Kurt, V. G., Yushkov, B. Y., and Kudela, K. (2008). "CORONAS-F satellite data on the delay between the proton acceleration on the Sun and their detection at 1 AU," *30th international cosmic ray conference*. Editors R. Caballero, J. C. D'Olivo, G. Medina-Tanco, L. Nellen, F. A. Sánchez, and J. F. Valdés, 1 (Mexico City, Mexico: Universidad Nacional Autónoma de México). 121–124.

Kwon, R.-Y., and Vourlidas, A. (2018). The density compression ratio of shock fronts associated with coronal mass ejections. *Journal of Space Weather and Space Climate*. 8, A08. doi:10.1051/swsc/2017045

Li, Y., Xue, J. C., Ding, M. D., Cheng, X., Su, Y., Feng, L., et al. (2018). Spectroscopic observations of a current sheet in a solar flare. *Astrophys. J. Lett*. 853, L15. doi:10.3847/2041-8213/aaa6c0

Magdalenić, J., Marqué, C., Krupar, V., Mierla, M., Zhukov, A. N., Rodriguez, L., et al. (2014). Tracking the CME-driven shock wave on 2012 March 5 and radio triangulation of associated radio emission. *Astrophys. J.* 791, 115. doi:10.1088/0004-637X/791/2/115

Magdalenić, J., Marqué, C., Zhukov, A. N., Vršnak, B., and Veronig, A. (2012). Flare-generated type II burst without associated coronal mass ejection. *Astrophys. J.* 746, 152. doi:10.1088/0004-637X/746/2/152

Maguire, C. A., Carley, E. P., McCauley, J., and Gallagher, P. T. (2020). Evolution of the Alfvén Mach number associated with a coronal mass ejection shock. *A&A*. 633, A56. doi:10.1051/0004-6361/201936449

Manchester, W., Kilpua, E. K. J., Liu, Y. D., Lugaz, N., Riley, P., Török, T., et al. (2017). The physical processes of CME/ICME evolution. *Space Sci. Rev*. 212, 1159–1219. doi:10.1007/s11214-017-0394-0

Mancuso, S. (2007). Coronal transients and metric type II radio bursts. II. Accelerations at low coronal heights. *Astron. Astrophys*. 463, 1137–1141. doi:10.1051/0004-6361:20054767

Mancuso, S., and Avetta, D. (2008). UV and radio observations of the coronal shock associated with the 2002 July 23 coronal mass ejection event. *Astrophys. J.* 677, 683–691. doi:10.1086/528839

Mancuso, S., and Garzelli, M. V. (2013). Coronal magnetic field strength from Type II radio emission: complementarity with Faraday rotation measurements. *Astron. Astrophys*. 560, L1. doi:10.1051/0004-6361/201322645

Mandzhavidze, N., and Ramaty, R. (1992). Gamma rays from pion decay - evidence for long-term trapping of particles in solar flares. *Astrophys. J. Lett*. 396, L111–L114. doi:10.1086/186529

Mann, G., Classen, T., and Aurass, H. (1995). Characteristics of coronal shock waves and solar type II radio bursts. *Astron. Astrophys*. 295, 775–781.

Mann, G., and Klassen, A. (2005). Electron beams generated by shock waves in the solar corona. *Astron. Astrophys*. 441, 319–326. doi:10.1051/0004-6361:20034396

Mann, G., Melnik, V. N., Rucker, H. O., Konovalenko, A. A., and Brazhenko, A. I. (2018). Radio signatures of shock-accelerated electron beams in the solar corona. *Astron. Astrophys*. 609, A41. doi:10.1051/0004-6361/201730546

Masson, S., Antiochos, S. K., and DeVore, C. R. (2019). Escape of flare-accelerated particles in solar eruptive events. *Astrophys. J.* 884, 143. doi:10.3847/1538-4357/ab4515

Masson, S., Klein, K.-L., Bütikofer, R., Flückiger, E. O., Kurt, V., Yushkov, B., et al. (2009). Acceleration of relativistic protons during the 20 January 2005 flare and CME. *Sol. Phys*. 257, 305–322. doi:10.1007/s11207-009-9377-y

McCracken, K. G., Moraal, H., and Shea, M. A. (2012). The high-energy impulsive ground-level enhancement. *Astrophys. J.* 761, 101. doi:10.1088/0004-637X/761/2/101

McCracken, K. G., Moraal, H., and Stoker, P. H. (2008). Investigation of the multiple-component structure of the 20 January 2005 cosmic ray ground level enhancement. *J. Geophys. Res*. 113, 12101. doi:10.1029/2007JA012829

Miroshnichenko, L. I. (2001). *Solar cosmic rays*. Dordrecht/Boston/London: Kluwer Acad. Publishing.

Mishev, A., Usoskin, I., Raukunen, O., Paassilta, M., Valtonen, E., Kocharov, L., et al. (2018). First analysis of ground-level enhancement (GLE) 72 on 10 September 2017: spectral and anisotropy characteristics. *Sol. Phys*. 293, 136. doi:10.1007/s11207-018-1354-x

Moraal, H., and Caballero-Lopez, R. A. (2014). The cosmic-ray ground-level enhancement of 1989 September 29. *Astrophys. J.* 790, 154. doi:10.1088/0004-637X/790/2/154

Moraal, H., and McCracken, K. G. (2012). The time structure of Ground Level Enhancements in solar cycle 23. *Space Sci. Rev*. 171, 85–95. doi:10.1007/s11214-011-9742-7

Morosan, D. E., Carley, E. P., Hayes, L. A., Murray, S. A., Zucca, P., Fallows, R. A., et al. (2019). Multiple regions of shock-accelerated particles during a solar coronal mass ejection. *Nature Astronomy*. 3, 452–461. doi:10.1038/s41550-019-0689-z

Muhr, N., Veronig, A. M., Kienreich, I. W., Temmer, M., and Vršnak, B. (2011). Analysis of characteristic parameters of large-scale coronal waves observed by the Solar-Terrestrial Relations Observatory/Extreme Ultraviolet Imager. *Astrophys. J.* 739, 89. doi:10.1088/0004-637X/739/2/89

Nindos, A., Alissandrakis, C. E., Hillaris, A., and Preka-Papadema, P. (2011). On the relationship of shock waves to flares and coronal mass ejections. *Astron. Astrophys*. 531, A31. doi:10.1051/0004-6361/201116799

Omodei, N., Pesce-Rollins, M., Longo, F., Allafort, A., and Krucker, S. (2018). Fermi-LAT observations of the 2017 September 10 solar flare. *Astrophys. J. Lett*. 865, L7. doi:10.3847/2041-8213/aae077

Pesce-Rollins, M., Omodei, N., Petrosian, V., Liu, W., Rubio da Costa, F., Allafort, A., et al. (2015). First detection of 100 MeV gamma-rays associated with a behind-the-limb solar flare. *Astrophys. J. Lett*. 805, L15. doi:10.1088/2041-8205/805/2/L15

Pick, M., Démoulin, P., Krucker, S., Malandraki, O., and Maia, D. (2005). Radio and X-ray signatures of magnetic reconnection behind an ejected flux rope. *Astrophys. J.* 625, 1019–1026. doi:10.1086/429530

Plotnikov, I., Rouillard, A. P., and Share, G. H. (2017). The magnetic connectivity of coronal shocks from behind-the-limb flares to the visible solar surface during γ-ray events. *Astron. Astrophys*. 608, A43. doi:10.1051/0004-6361/201730804

Pohjolainen, S., Allawi, H., and Valtonen, E. (2013). Origin of wide-band IP type II bursts. *Astron. Astrophys*. 558, A7. doi:10.1051/0004-6361/201220688

Pohjolainen, S., van Driel-Gesztelyi, L., Culhane, J. L., Manoharan, P. K., and Elliott, H. A. (2007). CME propagation characteristics from radio observations. *Sol. Phys*. 244, 167–188. doi:10.1007/s11207-007-9006-6

Polito, V., Dudík, J., Kašparová, J., Dzifčáková, E., Reeves, K. K., Testa, P., et al. (2018). Broad non-Gaussian Fe XXIV line profiles in the impulsive phase of the 2017 September 10 X8.3-class flare observed by Hinode/EIS. *Astrophys. J.* 864, 63. doi:10.3847/1538-4357/aad62d

Pulupa, M., and Bale, S. D. (2008). Structure on interplanetary shock fronts: type II radio burst source regions. *Astrophys. J.* 676, 1330–1337. doi:10.1086/526405

Reames, D. V. (1999). Particle acceleration at the sun and in the heliosphere. *Space Sci. Rev.* 90, 413–491. doi:10.1023/A:1005105831781

Reames, D. V. (2009). Solar release times of energetic particles in Ground-Level Events. *Astrophys. J.* 693, 812–821. doi:10.1088/0004-637X/693/1/812

Reiner, M. J., Kaiser, M. L., Gopalswamy, N., Aurass, H., Mann, G., Vourlidas, A., et al. (2001). Statistical analysis of coronal shock dynamics implied by radio and white-light observations. *J. Geophys. Res.* 106, 25279–25290. doi:10.1029/2000JA004024

Reiner, M. J., Karlický, M., Jiika, K., Aurass, H., et al. (2000). On the solar origin of complex type III-like radio bursts observed at and below 1 MHz. *Astrophys. J.* 530, 1049–1060. doi:10.1086/308394

Reiner, M. J., Klein, K.-L., Karlický, M., Jiřička, K., Klassen, A., Kaiser, M. L., et al. (2008). Solar origin of the radio attributes of a complex type III burst observed on 11 April 2001. *Sol. Phys.* 249, 337–354. doi:10.1007/s11207-008-9189-5

Reiner, M. J., Krucker, S., Gary, D. E., Dougherty, B. L., Kaiser, M. L., and Bougeret, J.-L. (2007). Radio and white-light coronal signatures associated with the RHESSI hard X-ray event of 2002 July 23. *Astrophys. J.* 657, 1107–1116. doi:10.1086/510827

Richardson, I. G., von Rosenvinge, T. T., Cane, H. V., Christian, E. R., Cohen, C. M. S., Labrador, A. W., et al. (2014). 25 MeV proton events observed by the High Energy Telescopes on the STEREO A and B spacecraft and/or at Earth during the first seven years of the STEREO mission. *Sol. Phys.* 289, 3059–3107. doi:10.1007/s11207-014-0524-8

Rouillard, A. P., Plotnikov, I., Pinto, R. F., Tirole, M., Lavarra, M., Zucca, P., et al. (2016). Deriving the properties of coronal pressure fronts in 3D: application to the 2012 May 17 ground level enhancement. *Astrophys. J.* 833, 45. doi:10.3847/1538-4357/833/1/45

Salas-Matamoros, C., Klein, K.-L., and Rouillard, A. P. (2016). Coronal mass ejection-related particle acceleration regions during a simple eruptive event. *Astron. Astrophys.* 590, A135. doi:10.1051/0004-6361/201528015

Seaton, D., and Darnel, J. (2018). Observations of an eruptive solar flare in the extended EUV solar corona. *Astrophys. J. Lett.* 852. doi:10.3847/2041-8213/aaa28e

Shanmugaraju, A., Bendict Lawrance, M., Moon, Y. J., Lee, J.-O., and Suresh, K. (2017). Heights of coronal mass ejections and shocks inferred from metric and DH type II radio bursts. *Sol. Phys.* 292, 136. doi:10.1007/s11207-017-1155-7

Share, G. H., Murphy, R. J., White, S. M., Tolbert, A. K., Dennis, B. R., Schwartz, R. A., et al. (2018). Characteristics of late-phase 100 MeV gamma-ray emission in solar eruptive events. *Astrophys. J.* 869, 182. doi:10.3847/1538-4357/aaebf7

Smerd, S. F., Sheridan, K. V., and Stewart, R. T. (1975). Split-band structure in type II radio bursts from the Sun. *Astrophys. J. Lett.* 16, 23–28.

Steinberg, J. L., Hoang, S., Lecacheux, A., Aubier, M. G., and Dulk, G. A. (1984). Type III radio bursts in the interplanetary medium - the role of propagation. *Astron. Astrophys.* 140, 39–48.

Stewart, R. T., and Magun, A. (1980). Radio evidence for electron acceleration by transverse shock waves in herringbone Type II solar bursts. *Pub. Astron. Soc. Australia.* 4, 53–55.

Su, W., Cheng, X., Ding, M. D., Chen, P. F., and Sun, J. Q. (2015). A type II radio burst without a coronal mass ejection. *Astrophys. J.* 804, 88. doi:10.1088/0004-637X/804/2/88

Trottet, G. (1986). Relative timing of hard X-rays and radio emissions during the different phases of solar flares - consequences for the electron acceleration. *Sol. Phys.* 104, 145–163. doi:10.1007/BF00159956

Tylka, A., and Dietrich, W. (2009). "A new and comprehensive analysis of proton spectra in ground-level enhanced (GLE) solar particle events," in 31st international cosmic ray conference. Lodz, Poland, 7–15 July 2009. Editor M. Giller, et al. http://icrc2009.uni.lodz.pl/proc/pdf/icrc0273.pdf.

Vainio, R., and Khan, J. I. (2004). Solar energetic particle acceleration in refracting coronal shock waves. *Astrophys. J.* 600, 451–457.

Vashenyuk, E. V., Balabin, Y. V., Perez-Peraza, J., Gallegos-Cruz, A., and Miroshnichenko, L. I. (2006). Some features of the sources of relativistic particles at the Sun in the solar cycles 21-23. *Adv. Space Res.* 38, 411–417. doi:10.1016/j.asr.2005.05.012

Vršnak, B., Aurass, H., Magdalenić, J., and Gopalswamy, N. (2001). Band-splitting of coronal and interplanetary type II bursts. I. Basic properties. *Astron. Astrophys.* 377, 321–329. doi:10.1051/0004-6361

Vršnak, B., and Cliver, E. W. (2008). Origin of coronal shock waves. *Sol. Phys.* 253, 215–235. doi:10.1007/s11207-008-9241-5

Vršnak, B., Magdalenić, J., Aurass, H., and Mann, G. (2002). Band-splitting of coronal and interplanetary type II bursts. II. Coronal magnetic field and Alfvén velocity. *Astron. Astrophys.* 396, 673–682. doi:10.1051/0004-6361:20021413

Vršnak, B., Sudar, D., and Ruždjak, D. (2005). The CME-flare relationship: are there really two types of CMEs?. *Astron. Astrophys.* 435, 1149–1157. doi:10.1051/0004-6361:20042166

Warmuth, A. (2015). Large-scale globally propagating coronal waves. *Living Rev. Sol. Phys.* 12, 1. doi:10.12942/lrsp-2015-3

Warmuth, A., and Mann, G. (2005). A model of the Alfvén speed in the solar corona. *Astron. Astrophys.* 435, 1123–1135. doi:10.1051/0004-6361:20042169

Warmuth, A., Vršnak, B., Magdalenić, J., Hanslmeier, A., and Otruba, W. (2004). A multiwavelength study of solar flare waves. II. Perturbation characteristics and physical interpretation. *Astron. Astrophys.* 418, 1117–1129. doi:10.1051/0004-6361:20034333

Warren, H. P., Brooks, D. H., Ugarte-Urra, I., Reep, J. W., Crump, N. A., and Doschek, G. A. (2018). Spectroscopic observations of current sheet formation and evolution. *Astrophys. J.* 854, 122. doi:10.3847/1538-4357/aaa9b8

Wild, J. P., Smerd, S. F., and Weiss, A. A. (1963). Solar bursts. *Annu. Rev. Astron. Astrophys.* 1, 291–366. doi:10.1146/annurev.aa.01.090163.001451

Winter, L. M., and Ledbetter, K. (2015). Type II and type III radio bursts and their correlation with solar energetic proton events. *Astrophys. J.* 809, 105. doi:10.1088/0004-637X/809/1/105

Yan, X. L., Yang, L. H., Xue, Z. K., Mei, Z. X., Kong, D. F., Wang, J. C., et al. (2018). Simultaneous observation of a flux rope eruption and magnetic reconnection during an X-class solar flare. *Astrophys. J. Lett.* 853, L18. doi:10.3847/2041-8213/aaa6c2

Yashiro, S., Gopalswamy, N., Michalek, G., Cyr, St. O. C., Plunkett, S. P., Rich, N. B., et al. (2004). A catalog of white light coronal mass ejections observed by the SOHO spacecraft. *J. Geophys. Res.* 109, A07105. doi:10.1029/2003JA010282

Zimovets, I., Vilmer, N., Chian, A. C.-L., Sharykin, I., and Struminsky, A. (2012). Spatially resolved observations of a split-band coronal type II radio burst. *Astron. Astrophys.* 547, A6. doi:10.1051/0004-6361/201219454

Zucca, P., Morosan, D. E., Rouillard, A. P., Fallows, R., Gallagher, P. T., Magdalenic, J., et al. (2018). Shock location and CME 3D reconstruction of a solar type II radio burst with LOFAR. *Astron. Astrophys.* 615, A89. doi:10.1051/0004-6361/201732308

Conflict of Interest: The author declares that the research was conducted in the absence of any commercial or financial relationships that could be construed as a potential conflict of interest.

frontiers in Astronomy and Space Sciences

ORIGINAL RESEARCH
published: 29 March 2021
doi: 10.3389/fspas.2021.584043

Mingantu Spectral Radioheliograph for Solar and Space Weather Studies

Yihua Yan[1,2], Zhijun Chen[1], Wei Wang[1], Fei Liu[1], Lihong Geng[1], Linjie Chen[1], Chengming Tan[1,2], Xingyao Chen[1], Cang Su[1] and Baolin Tan[1,2]*

[1]CAS Key Laboratory of Solar Activity, National Astronomical Observatories, Chinese Academy of Sciences, Beijing, China, [2]School of Astronomy and Space Science, University of Chinese Academy of Sciences, Beijing, China

The Chinese Spectral Radioheliograph (CSRH) covering 400 MHz-15 GHz frequency range was constructed during 2009–2016 in Mingantu Observing Station, National Astronomical Observatories, Chinese Academy of Sciences at Zhengxiangbaiqi, Inner Mongolia of China. The CSRH is renamed as *M*ingant*U* Sp*E*ctral *R*adioheliograph (MUSER) after its accomplishment. Currently, MUSER consists of two arrays spreading over three spiral-shaped arms. The maximum baseline length is ~3 km in both east-west and north-south directions. The MUSER array configuration is optimized to meet the needs of observing the full-disk Sun over ultrawide wavebands with images of high temporal, spatial and spectral resolutions and high dynamic range. The low frequency array, called MUSER-I, covers 400 MHz-2.0 GHz with 40 antennas of 4.5-m-diameter each and the high frequency array, called MUSER-II, covers 2–15 GHz with 60 antennas of 2-m-diameter each. The MUSER-I can obtain full-disk solar radio images in 64 frequency channels with a time cadence of 25 ms and a spatial resolution of 51.6″ to 10.3″ (corresponding to the frequency range 400 MHz to 2 GHz), whereas the MUSER-II can obtain full-disk solar images in 520 channels with a time cadence of 206.25 ms and a spatial resolution of 10.3″ to 1.3 (corresponding to the frequency range 2 to 15 GHz). A dynamic range of 25 dB can be obtained with snapshot images produced with the MUSER. An extension of MUSER in the further lower frequency range covering 30–400 MHz with an array of 224 logarithm-periodic dipole antennas (LPDAs) has been approved and will be completed during the next 4 years. The MUSER, as a dedicated solar instrument, has the following advantages providing simultaneous images over a wide frequency range with a unique high temporal-spatial-spectral resolutions; high-performing ultrawide-band dual-polarization feeds for wide-band signal collection; advanced high data-rate, large-scale digital correlation receiver for multiple-frequency and faster snapshot observations; and applications of new technologies such as using optical fiber to obtain remote antenna and wide-band analog signal transmission. The MUSER thus provides a unique opportunity to measure solar magnetic fields and trace dynamic evolution of energetic electrons in several radio frequencies, which, in turn, will help to have better understandings of the origin of various solar activities and the basic drivers of space weather.

Keywords: solar corona, solar instrumentation, solar imaging, radioheliograph, solar radio radiation, space weather, flares, coronal mass ejections

OPEN ACCESS

Edited by:
Dale E. Gary,
New Jersey Institute of Technology, United States

Reviewed by:
Timothy Bastian,
National Radio Astronomy Observatory, United States
Divya Oberoi,
Tata Institute of Fundamental Research, India

****Correspondence:***
Yihua Yan
yyh@nao.cas.cn

Specialty section:
This article was submitted to Stellar and Solar Physics, a section of the journal Frontiers in Astronomy and Space Sciences

Received: *16 July 2020*
Accepted: *01 February 2021*
Published: *29 March 2021*

Citation:
Yan Y, Chen Z, Wang W, Liu F, Geng L, Chen L, Tan C, Chen X, Su C and Tan B (2021) Mingantu Spectral Radioheliograph for Solar and Space Weather Studies. Front. Astron. Space Sci. 8:584043. doi: 10.3389/fspas.2021.584043

1 INTRODUCTION

Solar radio bursts are rich with information as they are associated with different types solar eruptions, such as solar flares, coronal mass ejections (CMEs), and various thermal and nonthermal processes. The solar eruptions are believed to arise due to the sudden energy release process because of topological re-organization of solar magnetic field or magnetic reconnection (Benz, 2009). Radio bursts are hence prompt indicators of those solar activities. X-ray observations show that non-thermal particles are highly related to the energy release process and demonstrate a significant amount of total flare energy during initial phase of solar flares (Lin (2008)). Normally, the radio bursts are observed in an ultrawide frequency range, starting from decimetric wavelength range, extending down to a few tens of KHz and up through several GHz even up to mm-wavelengths in a short time scale (e.g., Benz, 2009). Especially, the radio observations covering centimeter and decimetric wavelengths are important as they can reveal key informations about the energy release, and particle acceleration and transportation (Bastian et al., 1998; Gary and Keller 2004; Aschwanden 2005; Pick and Vilmer 2008; Chernov et al., 2014).

The radio burst emissions were commonly generated by different mechanisms. If the plasma mechanism were assumed as the generation mechanism, one can infer from statistical study of radio dynamic spectra during different flare events that the electrons are accelerated from a region with electron density of $n_e^{\mathrm{acc}} \sim 3 \times 10^9$ to $10^{11}\,\mathrm{cm}^{-3}$. The corresponding plasma frequency is about $\nu_p \sim 500$ MHz to 3.4 GHz, where electron beams are accelerated and propagated in either upward (type III bursts, down to ~10 s KHz) and/or downward (Reverse Slope type III bursts, up to microwave) directions (Aschwanden and Benz 1997; Tan et al., 2016). However, the present solar radio imaging observations are only available at a few discrete frequencies at 70 MHz for Gauribidanur Radioheliograph (Ramesh et al., 1998), in the range 150–450 MHz for Nancay Radioheliograph (NRH, Radioheliograph Pick and Vilmer, 2008; Kerdraon and Delouis 1997), and at 17/34 GHz for Nobeyama Radioheliograph (NoRH, Nakajima et al., 1994). Those closed facilities in the past include Culgoora radioheliograph at three metric-wave frequencies (Sheridan et al., 1973), the Clark Lake Array in the range 1.5–12.5 MHz (Erickson et al., 1984), etc. Some radioheliographs were upgraded in the recent years, eg. Siberian Solar Radio Telescope at 5.7 GHz (SSRT, Grechnev et al., 2003) and the Expanded Owens Valley Solar Array in a frequency range of 1–18 GHz (EOVSA). There are also some other radio telescopes designed to investigate astronomical objects and the sun is also one of their purposes, eg. Very Large Array (Napier et al., 1983), the Giant Metrewave Radio Telescope (GMRT, 150–1450 MHz) in India, the Low-Frequency Array (LOFAR, 30–120 MHz) in Europe, the Murchison Widefield Array (Tingay et al., 2013) in Australia, and the Long Wavelength Array (LWA, 10–88 MHz). Though the succession of these solar-dedicated radio imaging instruments has greatly advanced the science of the Sun as described in the related reviews (e.g., Bastian et al., 1998; Pick and Vilmer 2008; Benz 2009; Chernov 2011), a key parameter has been lacking, i.e., high quality spectral imaging of the Sun over an ultra-wide band frequency range, covering from the primary energy release site and to the beyond.

Many studies on the associations between hard X-ray (HXR) and radio emissions demand this need. For example, Vilmer et al., 2002 studied and compared locations of RHESSI HXR and NRH radio sources observed for a flare event on 20 February 2002. Since the direct link between HXR and radio emissions was not available from observations, it was hard to understand the details of magnetic reconnection and the energy conversion processes, including their temporal and spatial evolutions. Therefore, it is crucial to image radio emissions in wide centimetric and decimetric wavelengths in order to cover the whole acceleration sites and primary propagation regions of nonthermal electrons which are responsible for the HXR emission. Trottet et al. (2006) carried out a detailed analysis of the HXR images observed by the Yohkoh and the radio images observed by the NRH in a flare on 5 November 1998. They found the evidence that the HXR and radio-emitting electrons were produced by the same accelerator. However, the available observations and analysis did not allow them to make a definite connection between the HXR source region and the radio source sources in the middle corona. Therefore, the spectral imaging observations in frequency range higher than 400 MHz are really important in this regard. As for the famous flare event on 13 December 2006, many radio fine structures were registered by the Chinese Spectral Broadband Radio Spectrometer (SBRS) in the microwave range. Deduced from the microwave Zebra Patterns (ZPs), it was found that the scale-height ratio between plasma density and magnetic field decreased by a factor of about 2 before and after the flare maximum (Yan et al., 2007). A further statistical investigation from 74 ZPs confirmed the above result (Yu et al., 2012). However, due to lack of observations of the relevant coronal magnetic field structures, it is difficult to present an exact interpretation of the above results. The radio imaging—spectroscopy over a wide frequency range provide such observations. The spectral observations of small-scale microwave bursts (SMBs) in solar flares provides the evidence of small—scale elementary energy releasing activities and electron accelerations in the flaring source regions (Tan, 2013), however, in order to understand the nature of SMBs, we need imaging-spectroscopy in the related frequency range, which may provide the real position of the source region, the relevant magnetic field, and the relationship with the physical mechanisms. The microwave type III pairs (Aschwanden and Benz 1997; Tan et al., 2016) indicate that the frequency where magnetic reconnection and particle acceleration taking place occurred around 0.3–3.4 GHz, but we need imaging observations at the corresponding frequencies to deduce the magnetic fields and the relevant topological structures. Thus, the solar radio imaging-spectroscopy can provide the following crucial information for the solar bursts: 1) positions, 2) topological structures, 3) coronal magnetic fields, and 4) spatio—temporal evolutions. With these informations, we can deduce the primary energy release, particle acceleration, and the mass-energy transportation, furthermore, predicting the

FIGURE 1 | Central part of MUSER-I and MUSER-II arrays.

occurrence of the solar bursts and their corresponding influences on space weather.

Several general purpose radio telescopes can also be used to observe the Sun, such as the VLA (Napier et al., 1983), the Low-Frequency Array (van Haarlem et al., 2013) and the (Swarup, 1991). The upgraded VLA has been used for solar studies (e.g., Chen et al., 2013; Chen et al., 2015). However, as they were primarily built for non-solar radio astronomical objectives, only about 2% time is available for solar observations, and their field of view is normally too small to cover the whole solar disk. In fact, the solar-dedicated instrument of imaging spectroscopy should have high temporal, spatial, and spectral resolutions and at least with field of view more than 32 arc-minute simultaneously (Bastian et al., 1998; Hudson and Vilmer, 2007; Pick and Vilmer, 2008). The Chinese Spectral Radioheliograph (Yan et al., 2004) and the Frequency-Agile Solar Radiotelescope (FASR, Bastian, 2003; Gary, 2003) proposed to realize this goal. The FASR is still not granted for construction yet and the Expanded Owens Valley Solar Array (Gary et al., 2018) has been developed as a pathfinder for the FASR (Nita et al., 2016). The microwave spectral imaging observations of the well known X8.2-class limb flare on 2017 September 10 by EOVSA have been extensively studied to indicate the nonthermal emissions by flare- and shock-accelerated electrons (Gary et al., 2018; Fleishman, et al., 2020; Karlický et al., 2020), or the detection of nonthermal emission at conjugate flux rope footpoints showing the solid evidence of particle transport along the erupting magnetic flux rope during the early impulsive phase (Chen et al., 2020).

The Chinese solar physics community had planned to build a radioheliograph since 1960s. Some pre-studies were carried out on proposals for radioheliograph in either centimeter-band (Hu et al., 1984) or millimeter-band (Fu et al., 1997), but none of these had been implemented. Following these lines, it was suggested to build a Chinese Spectral radioheliograph in the decimetric to centimeter wavelength range (Yan et al., 2004). It was later recommended as one of the two major ground-based facilities by Chinese solar physics community in 2006. A 2-element interferometer prototype was built and tested for tackling the key technologies in 2004–2005 (Yan et al., 2009). The Chinese Spectral Radioheliograph was officially supported in 2009 as a National Major Scientific Research Facility Program of China. The site survey was pursued at Mingantu town in Inner Mongolia of China. The radio quiet zone protection of 10 km radius centered at Mingantu Observing Station has been setup since 2008. The construction was fulfilled during 2009–2016, and the instrument was renamed as *M*ingant*U* Sp*E*ctral *R*adioheliograph (MUSER) after its accomplishment, as seen in **Figure 1**. The brief description and progress of MUSER project while it was under construction as well as a few initial results from MUSER were reported by Yan et al. (2013); Yan et al. (2016). The Meridian-II project among the Major National Infrastructure Projects for Science and Technology under "13th 5-year plan" program (2016–2020) has been approved and a Solar and Interplanetary subsystem as a new part in the Meridian-II project will include a logarithm-periodic dipole antenna (LPDA) array at metric and decametric wave range to be built in the Mingantu Observing Station (Blanc et al., 2020).

The key technical issues consist of implementing high cadence imaging with an aperture synthesis system at about two order higher multiple frequencies than the presently-available radioheliographs over an ultrawide frequency band, and the data processing for such a large data volume from MUSER. We introduce the MUSER system description in § 1. The calibration and synthesis imaging are described in § 2. The observational results are presented in § 3 and the future plans

TABLE 1 | MUSER characterestics and performance.

MUSER Array	MUSER-I	MUSER-II
Frequency range:	400 MHz–2 GHz	2–15 GHz
Array antennas	40 × ϕ4.5 m	60 × ϕ2 m
Single dish beam:	9.5°–1.9°	4.3°–0.6°
Frequency resolution:	64 channels	520 channels
Angular resolution:	51.6″ – 10.3″	10.3″ – 1.3″
Time resolution:	25 ms	206.25 ms
Dynamic range:	25 db (snapshot)	
Polarizations:	Dual circular L, R	
Maximum baseline:	~3 km	

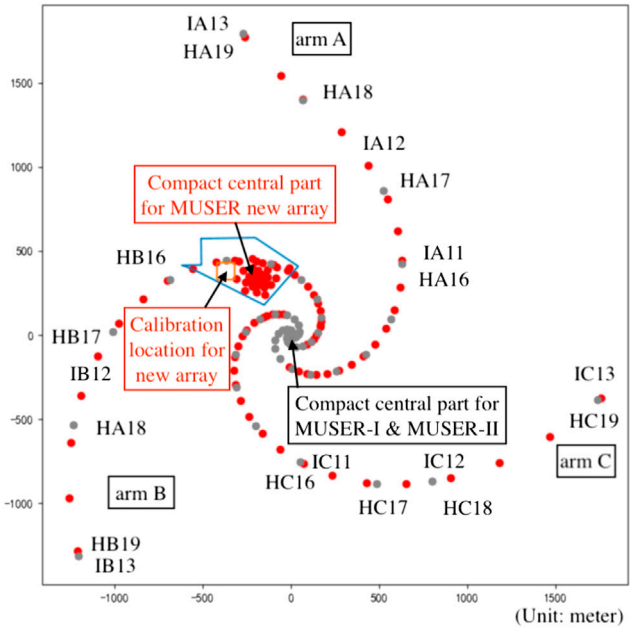

FIGURE 2 | The array configuration for extension of MUSER to lower frequency range of 30–400 MHz with black dots indicating existing MUSER-I and MUSER-II antennas whereas red dots indicating the locations for the newly designed 100 LPDAs. The blue area is the region where the compact central part of the new MUSER low frequency array will be located. The red square indicates the location where the compact calibration array with 124 LPDAs will be placed. Some MUSER-I and MUSER-II antenna locations are marked with corresponding antenna numbers.

are briefly described in § 4. Finally, we summarize our conclusions in § 5.

2 DESCRIPTION OF MUSER

The MUSER is a solar-dedicated radio interferometric array with high temporal, spatial and spectral resolutions, and it can simultaneously perform the spectral and imaging observations of the full Sun in a wide frequency range (Yan et al., 2004; Yan et al., 2009). The main characteristics and performance are listed in **Table 1**. The MUSER currently covers the centimetric to decimetric wave range, including

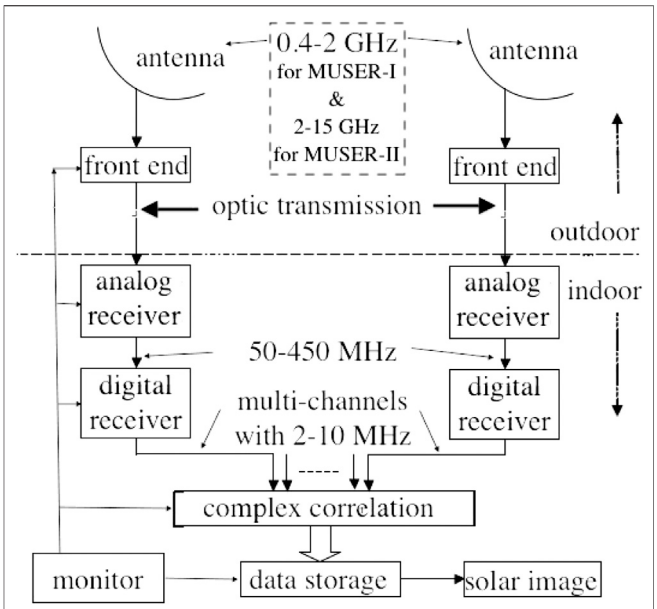

FIGURE 3 | The schematic system block diagram of MUSER-I and MUSER-II. Both have a similar system structure except that the radio frequency (RF) input is 0.4–2 GHz for MUSER-I whereas 2–15 GHz for MUSER-II (Yan et al., 2013).

MUSER-I operating in the frequency range of 400 MHz–2 GHz and MUSER-II in 2–15 GHz. The MUSER-I array contains 40 antennas with 4.5 m diameter each, and the MUSER-II array contains 60 antennas with 2 m diameter each. All the 100 antennas are located on three log-spiral arms with the maximum baseline length of about 3 km in both north-south and east-west directions. The MUSER antennas, numbered as IA#, IB#, IC# from 1 to 13 for MUSER-I array and HA#, HB#, HC# from 1 to 20 for MUSER-II array in local coordinates with the central antenna IA0 as the reference point, are schematically shown in black dots in **Figure 2**. IA0's location is E 115°15′1.8″, N 42°12′42.6″, with an altitude of 1365 m. The central part of the MUSER arrays is shown in **Figure 1**.

Figure 3 shows the schematic system block diagram for MUSER. The signal processing for MUSER-I (400 MHz–2 GHz) and MUSER-II (2–15 GHz) is almost same. Additionally two 20-m antennas (400 MHz–1 GHz) were established for interferometry experiment in 2011 at the same site. They are proposed to work as a part of MUSER-I array for calibrations. **Figure 3** shows that the solar radio signal (400 MHz–2 GHz, 2–15 GHz) as received by the MUSER-I and MUSER-II antennas with broadband feeds, front-end LNAs and optic transmitters. The signal is then transmitted through optic fibers to indoor analog receivers with an Intermediate frequency (IF) output of 400 MHz bandwidth (50–450 MHz), which covers the whole bandwidth by sweeping four times for MUSER-I and 33 times for MUSER-II. It takes 25 ms to cover the 400 MHz–2 GHz bandwidth of MUSER-I by sweeping. For MUSER-II, the sweeping time is ~200 ms. The observing mode implemented in MUSER allows us

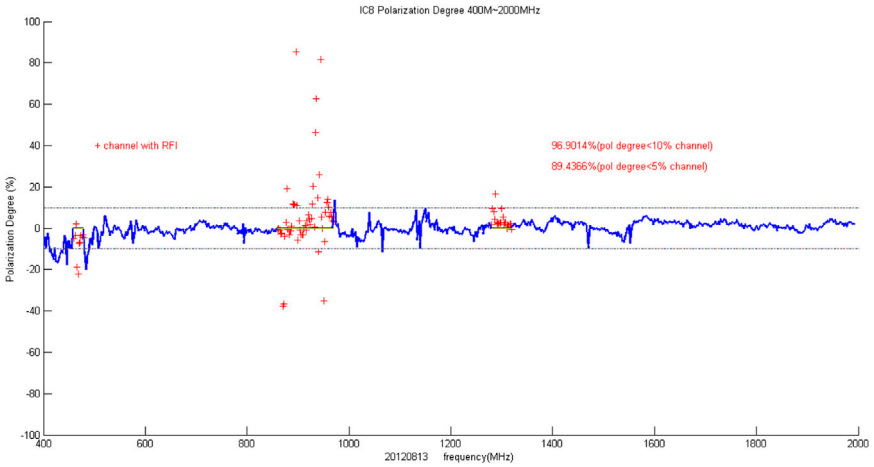

FIGURE 4 | Polarization degree, or $(P_L - P_R)/(P_L + P_R)$ of a MUSER-I antenna element (IC8) in 400–2000 MHz range measured on 13 Aug 2012, which is ≤ 10% over 96.9% whole frequency band, and furthermore, ≤ 5% over 89.4% whole frequency band. The red plus sign indicates frequency point where strong RFI occurred (Yan et al., 2013).

to observe at a given frequency in full 25 ms without band or polarization switching. So it provides the flexibility to investigate useful information by setting the working mode of the instrument. The 400-MHz IF signal is received by a digital correlation receiver. Firstly, it is sampled with 1 Gsps Analog to Digital converters (ADC), then goes into the polyphase filter bank (PFB). The PFB generates 16 complex baseband signals with ~2–25 MHz simultaneously. All baseband signals with same frequency are computed to send out the correlation data. The time delay compensation and fringe stopping are implemented in the digital correlation receiver (Liu et al., 2019). Both MUSER-II and MUSER-I has the same architecture in their digital correlation receivers. The whole correlation procedure is controlled by a monitoring subsystem.

Among the various issues of aperture synthesis techniques for MUSER (Taylor et al., 1999; Thompson et al., 2017), one of the key problems is to develop a high performance ultra-wide band feed for the reflector antennas. Such feed should have wide impedance bandwidth, low profile, symmetrical radiation patterns, and fixed phase center over the whole frequency band. So far, the eleven feed (Olsson et al., 2006) can be used for observing the slow-evolving astrophysical objects since its original version only has a maximum return loss of about −5 dB (or Voltage Standing Wave Ratio-VSWR is about 3.53). However, the solar radio bursts and accordingly polarizations always vary quickly. The isolation is thus vital for correct observations of the polarizations, and the return loss or VSWR for solar observations should be further reduced in order to meet the requirement for observing fast-changing solar radio burst signals. We have successfully developed the ultra-wide band feeds for both MUSER-I and MUSER-II with the VSWR less than 1.5 over most of the frequency range, wide (~ 133%) impedance bandwidth and good radiation characteristics (Li et al., 2015a; Li et al., 2015b). **Figure 4** shows the polarization degree measurement of one antenna element (IC8) in frequency of 400 MHz–2 GHz as an example. It shows that in almost 90% frequency band the polarization degree, or $(P_L - P_R)/(P_L + P_R)$ (where P_L and P_R represent the intensity of left and right polarization) is less than 5%, which represents good isolation performance. Similar performance have been measured for other antenna elements. Time delays among the different antennas of MUSER array have been measured for calibration. The measured RMS errors of time delay compensations for MUSER-I are normally <1 ns. The result is very robust as similar results obtained in multiple measurements that were carried out at the interval of 1 year later (Liu et al., 2013). The robust satisfactory <1 ns RMS accuracy of time delay compensations for MUSER-II has also been obtained. During the test observations for the signals of either the satellites, the Sun, or Cygnus A, correlation fringes have been obtained successfully for all baselines (Wang et al., 2013a). For every tri-antenna composition among the MUSER-I or MUSER-II arrays, the residuals of the phase closures were measured with a value of around two degrees for both geostationary and GPS satellites. Fringe stopping has been achieved for all baselines when observing the quiet Sun. These experiments validated the system design and demonstrated the system performance. The two 20 m antennas operating in 400 MHz–1 GHz has also been incorporated into MUSER-I for calibrations. By simulating different cases for observing the quiet Sun, solar active regions and radio bursts, it is shown that the shortest baselines for MUSER-I are important for the quiet Sun image recovering (Du, et al., 2015), which are important for MUSER data analysis.

3 MUSER OBSERVATIONS

The MUSER array began observations in 2014, routinely observed the Sun from 2016, roughly in a time range from 01:00 to 08:00 UT. In total, the MUSER has accumulated more than 390 TB observational data. Considering a large amount of raw data, it has not been available in an online archive so far. But

TABLE 2 | Event list of MUSER in 2014–2019.

Flare class	Number of radio burst events
X	2
M	15
C	37
B	27
A	4
Total number	85

the data are public and interested users can get in touch with us if they are looking for some specific data. There were fewer spectral events observed by MUSER-II in the high frequency band. Wang et al. (2019) proposed a new restoration method for the data processing of MUSER-II observations at 4.2 GHz, which shows a better quality than using the deconvolution algorithm for the production of radio images. Here, more attentions were paid to a lower frequency band, which show more fruitful spectral structures. During 2014–2019, a total number of 85 solar radio burst events have been registered by the MUSER-I, as shown in **Table 2**. More than 60 radio burst events contain the fine structures. The MUSER data are processed using the radio astronomy software, Common Astronomy Software Applications (CASA) and the own developed Fourier routines. The data processing code has been made available at https://github.com/astroitlab/museros (Mei et al., 2018). A brief introduction of the pipeline for data processing was discussed in Mei et al. (2018) and Chen et al. (2019). Next, we will present three typical solar radio burst events observed by MUSER.

3.1 A Radio Burst Event on 11 November 2014

During 04:22-04:24UT On 11 Nov 2014, a radio burst event was recorded by MUSER-I array at 400 MHz–2 GHz. **Figure 5** presents a comparison of time profiles of GOES SXR flux, the NoRP radio flux at 2 GHz and MUSER-I radio fluxes at several frequencies in the range of 400 MHz-2 GHz. It was wrongly attributed to a C-class flare (started from 04:22 UT and peaked at 04:49UT) near the disk center according to SGD event list (http://www.swpc.noaa.gov/products/goes-x-ray-flux). The Nobeyama Radio Polarimeters (NoRP) also demonstrated strong burst signals at 1, 2, and 3.75 GHz during 04:22-04:24 UT but weaker signals at higher frequencies. While NoRH (Nakajima

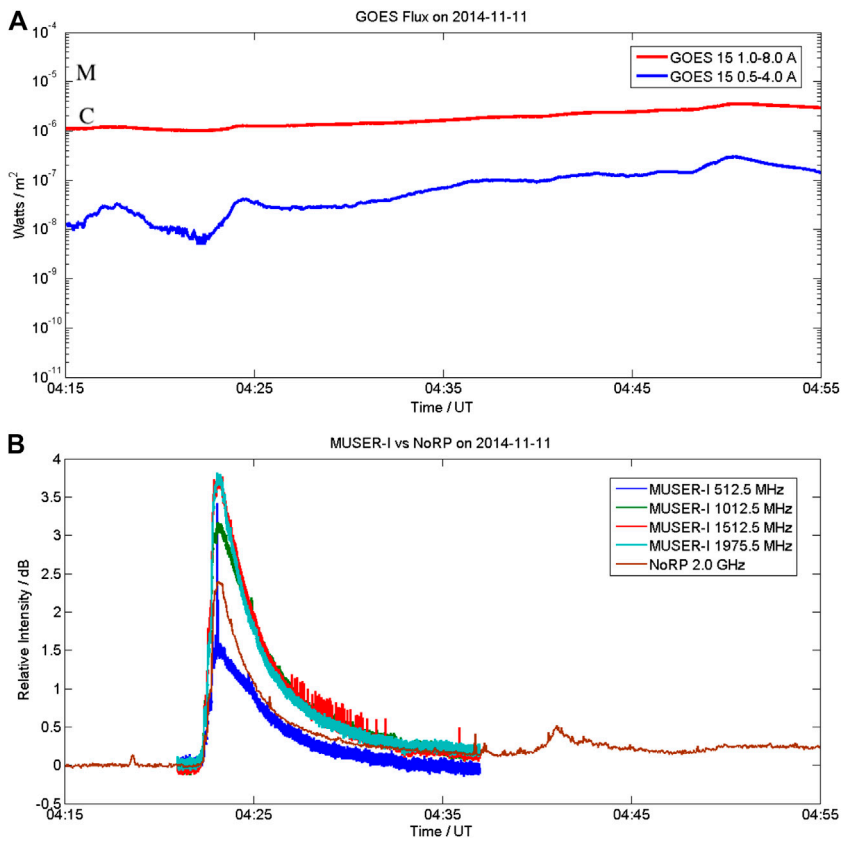

FIGURE 5 | (A) The temporal profiles of GOES SXR flux for the C3.4 class flare starting from 04:22 UT and peaked at 04:49 UT on 11 November 2014. **(B)** The NoRP radio flux at 2 GHz(brown) and MUSER-I radio fluxes at 0.5125, 1.0125, 1.5125 and 1.9755 GHz of the burst event peaked at 04:23 UT in a relative unit.

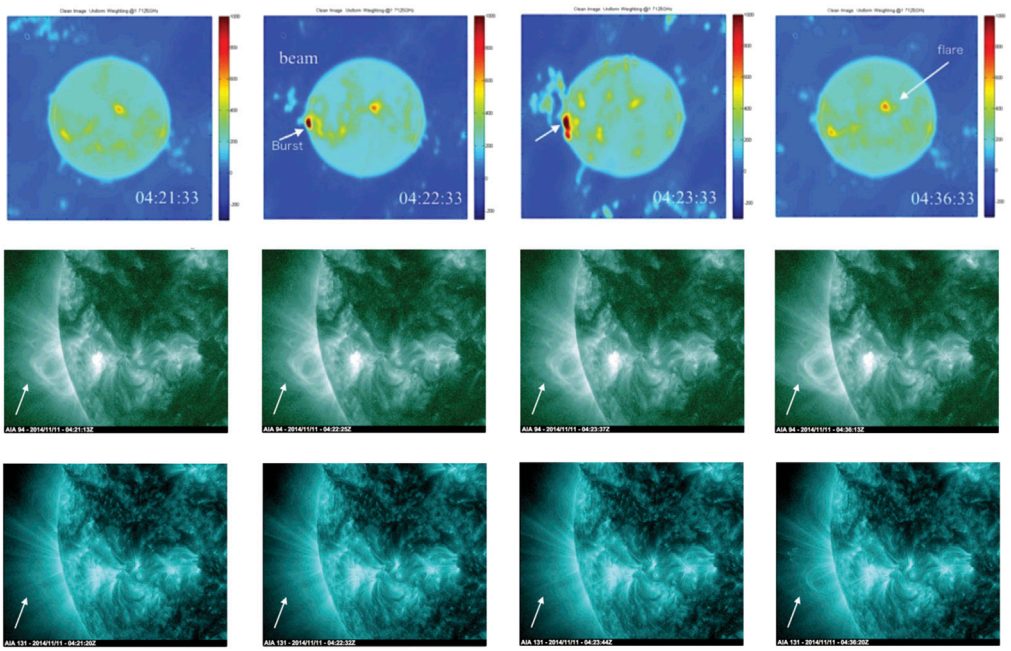

FIGURE 6 | Top panel: The radio images obtained at 04:21:33 UT (before), 04:22:33 UT (during), 04:23:33 UT (around peak) and 04:36:33 UT (after) the decimetric radio burst. Middle panel: The EUV images obtained at 94 Å corresponding to almost the same instants (04:21:13 UT, 04:22:25 UT, 04:23:37 UT, 04:36:13 UT) showing the faint eruptive feature of loop opening as indicated by the arrow. Bottom panel: The EUV images obtained at 131 Å corresponding to almost the same instants(04:21:20 UT, 04:22:32 UT, 04:23:44 UT, 04:36:20 UT) showing the faint eruptive feature of loop opening as indicated by the arrow.

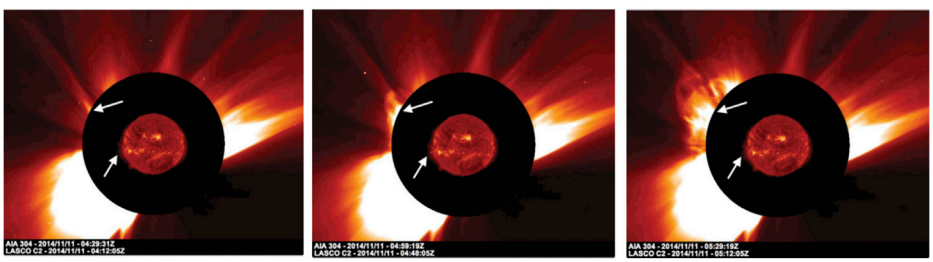

FIGURE 7 | The CME process recored by the SOHO/LASCO C2 at 04:29, 04:59 and 05:29UT after the radio burst. The CME and radio burst locations are indicated by the arrows, respectively.

et al., 1994) observations at 17 and 34 GHz obtained the small burst around the flare peak at 04:49 UT, the MUSER observations show that a non-thermal process happened during the flare impulsive phase was not associated with this C-class flare. The radio images obtained from MUSER-I at 1.7 GHz show that the radio source is located at the east limb of the Sun, not in the solar disk area, as shown on top panels in **Figure 6** at different times before, during and after the radio burst. In order to identify the correctness of the radio sources, we checked the EUV images observed by AIA/SDO (Lemen et al., 2012) during the same time period and at the same location. The EUV images at wavelength of 94 Å and 131 Å are presented in the middle and bottom panels of **Figure 6**. It is found that there were indeed loop opening at 94 Å and 131 Å corresponding to hot plasmas whereas responses at other EUV wavelengths were not so obvious. A CME event with a signature starting around 04:36 UT was observed by SOHO/LASCO (Brueckner et al., 1995), which indicates the CME at that location (**Figure 7**). As there was no radio burst at higher frequencies at the solar east limb, we propose that the decimetric radio burst starting at 04:22 UT in the east limb was due to the solar eruptions taking place in the backside of the Sun but it was very close to the east limb. As radio bursts occurred at higher altitude which can be observed by MUSER-I in the Earth direction. Its occurrence during the impulsive phase of the C-class flare in the solar disk was just a coincidence and there should be no physical connection to the C-class flare on the solar disk. This

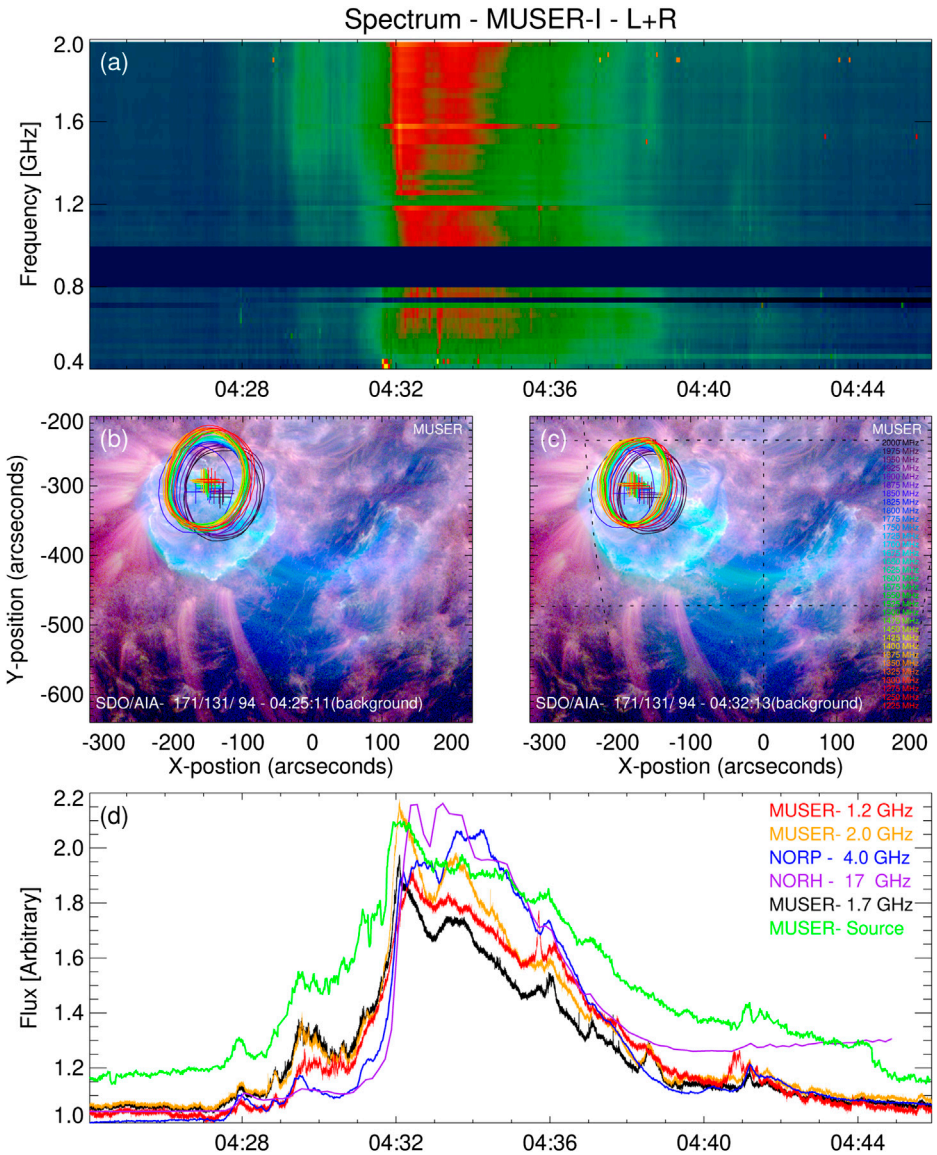

FIGURE 8 | (A) The dynamic spectrum of quasi-periodic pulsations overlaid on type IV solar radio continuum was recorded by MUSER-I in a time range of 04: 25–04:45 UT and a frequency range of 1.2–2.0 GHz. **(B)** and **(C)** Images of the radio source with a 50% intensity level observed at multi frequencies from 1.2 GHz(red) to 2.0 GHz (black), overlaid on the AIA images of three combined wavelengths at the start (04:25 UT) and peak (04:32 UT) time of the radio burst. The radio source centroids were marked by the plus signs. **(D)** The radio flux curves from NoRP, the spectrum of MUSER and the intensity of radio source from MUSER imaging (green).

demonstrate the importance of the image spectroscopy observation of the solar radio burst (Yan et al., 2016).

3.2 A Radio Burst Event on 17 December 2014

The spectral imaging of quasi-periodic pulsations (QPPs) overlaid on a type IV microwave continuum was recorded by MUSER at frequencies of 1.2–2.0 GHz for the first time. It took place during 04:25-04:45 UT in an M8.7 flare (start at 04:25 UT, peak at 04:51 UT) in active region AR12242 on 2014 December 17.

The flare region has circular ribbons over multiple-scale loop structures as revealed by the EUV images of AIA/SDO. The flare-related loops can be classified into three groups: small-scale low-lying loops, intermediate dome-like structure, and a group of large-scale loops.

The radio observations (shown in **Figure 8**) indicates that 1) the temporal profile at 2 GHz is similar to that of NoRP, but with more spikes superimposed on an increasing-to-decreaing intensity profile; 2) the intensity profile integrated from the radio images of the source region at 1.7 GHz matches well with the temporal profile at 1.7 GHz obtained from the spectrum; 3) the period of the radio QPP at 2.0 GHz is about

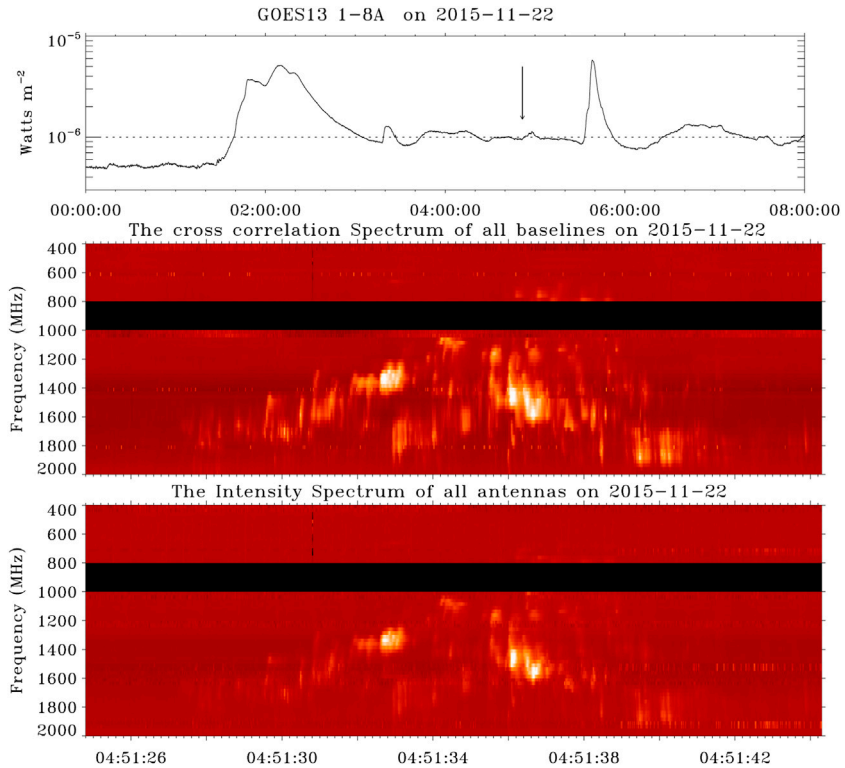

FIGURE 9 | Top panel: The GOES SXR profile during 0–8 UT on 22 November 2015. The arrow indicates the moment where the radio burst fine structures occurred. Middle panel: The averaged cross correlation spectrum of all MUSER-I baselines for a radio burst fine structure event with about 15 s duration occurred around 04:51:35 UT. Bottom panel: The auto-correlation intensity spectrum of all MUSER-I antennas.

121s from the wavelet analysis; 4) the size of the radio source varies from small to large and then small at a given intensity and frequency, which corresponds to the evolutions of radio emission processes; 5) the radio sources locate in the middle of the active region, over the positive magnetic field; 6) the radio sources at six frequencies line up nicely and move along the similar expanding direction of flaring loop. The detailed data processing of spectral and imaging observations of the radio source, the main features and complicated interactions among different loops, and the physical relationships from various multi-wavelength observations to the possible mechanisms of QPPs have been presented in Chen et al. (2019).

3.3 A Radio Burst Event on 22 November 2015

The solar fine radio burst of November 22, 2015 event is shown in the **Figure 9**. It was occurred just at the beginning of a small SXR flare (indicated by an arrow on the top panel of **Figure 9**). The reported C5.6 SXR flare was occurred during 5:31-05:41UT. The middle panel of the figure is the cross correlation spectrum of all baselines, while the bottom panel is the auto-correlation intensity spectrum of all antennas. The middle panel showed the fine structures more details and more clear than bottom panel. This indicated that the sensibility of all baselines is much better than that of all antennae. The inverted V like shape fine structures occurred between 04:51:27 and 04:51:41 UT. First, groups of spiky narrowband strip bursts drifted slowly from higher to lower frequencies, and after 04:51:31.2UT they globally drifted slowly and reversely to higher frequencies. The global upward drifting rate is about −22 ~ −33 MHz/s, while the global downward drifting rate is about 29~35 MHz/s. The speed of plasmoid can be estimated about 2200~3500 km/s under the 30 times of Newkirk model. It is interesting that hundreds of individual narrow band spiky strips have much higher drifting rates upward and downward within the rising and downward branches. Before 04:51:31.2UT, about 66 percent individual strips are with fast upward drifting rate of −350 ~ −3000 MHz/s, 18 percent are with fast downward drifting rate of 650~5250 MHz/s, and the rest 16 percent are with measureless drifting rate. After 04:51:31.2UT, about 19 percent individual strips are with fast upward drifting rate of −200 ~ −3000 MHz/s, 64 percent are with fast downward drifting rate of 357~3500 MHz/s, and the rest 16 percent are with measureless drifting rate. The speed of electron beam can be also estimated of >0.12c under the 30 times of Newkirk model. Further studies on imaging spectroscopy of the event associated with other space and ground-based observations are under way.

4 EXTENSION OF MUSER TO 30–400 MHZ BAND

The project to extend MUSER to 30–400 MHz frequency regime with 224 LPDAs has been approved under the

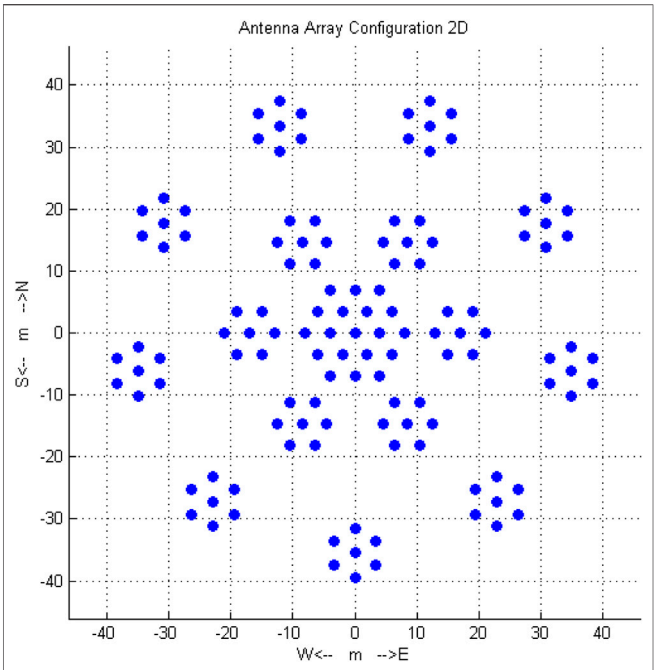

FIGURE 10 | The compact phased array configuration for calibration of the MUSER array in metric and decametric wave range with 124 LPDAs.

TABLE 3 | Performance of MUSER in metric and decametric wave range.

Frequency range:	**30, ~ 400 MHz**
Antennas:	100 LPDA + calibration element (124 LPDA)
Max baseline:	~3000 m
Frequency resolution:	1–5 MHz
Time resolution:	~100 ms
Angular resolution:	1.0′–14′
Polarization:	I, Q, U, V

Meridian-II Project which is a National Science Infrastructure Project under "13th 5-years plan" program (2016–2020). Solar and Interplanetary Subsystem as a new part in Meridian-II project will include metric and decametric wave range with a LPDA array to be built in Mingantu Observing Station.

The array configuration for extension of MUSER to lower frequency range of 30–400 MHz with 100 LPDAs has been optimized to achieve minimum RMS number derivation of antenna distributions in axial direction and minimum RMS number derivation of antenna distributions with respect to a Gaussian distribution in the radial direction. Some LPDAs' locations are adjusted to avoid blocking to each other during observations. As the original central part of the MUSER-I and MUSER-II arrays is populated with dense antennas, there is no sufficient space to allocate new LPDAs. So the compact central part of the new array is chosen to be close to the arm B and 31 LPDAs can be allocated there, as shown in the region outlined by blue area in **Figure 2**. The rest 69 LPDAs are spread over three arms with 20 LPDAs in arm A, 25 LPDAs in arm B and 24 LPDAs in arm C, with red dots indicating the locations of the newly designed 100 LPDAs in **Figure 2**. Within the compact area located in the red square in **Figure 2**, a total of 124 LPDAs will be grouped into 16 sub arrays with 1 central subarray

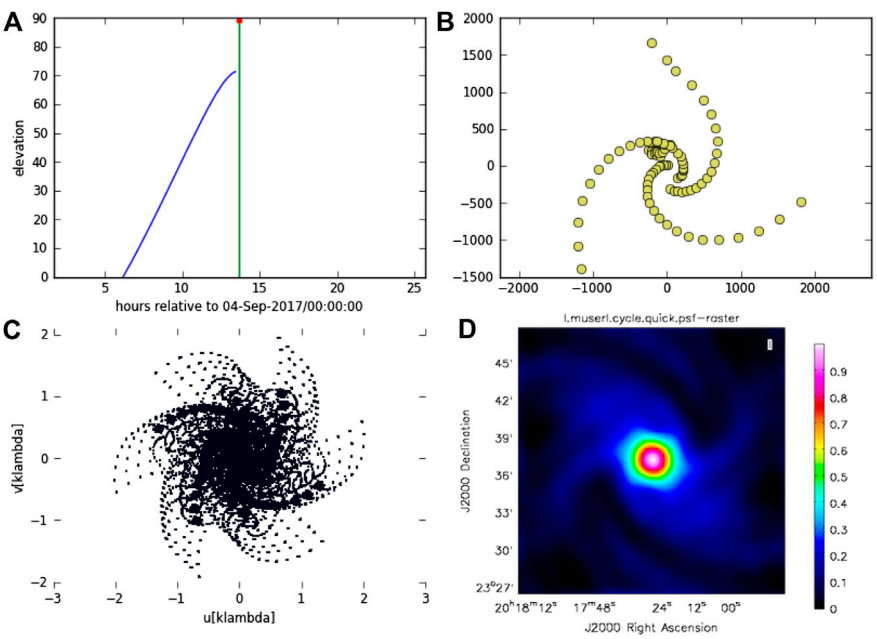

FIGURE 11 | (A) The hour angle and declination of the Sun on September 2017. **(B)** The 100 LPDA locations of MUSER extension to 30–400 MHz. **(C)** The snapshot *uv* distribution at 200 MHz. **(D)** The synthesized beam at 200 MHz.

containing 19 LPDAs whereas rest subarray each containing 7 LPDAs. The 16 subarray will form a phased array for calibration as shown in **Figure 10**. The snapshot *uv* distribution and the synthesized beam at 200 MHz are shown in **Figure 11**. The performance of the MUSER array in metric and decametric wave range is listed in **Table 3**.

The extension of MUSER to lower frequency range of 30–400 MHz will be built in the next a few years. These radio facilities will be very important tools for monitoring solar disturbances from the Sun to the Earth environment and they will play fundamental role for space weather studies and monitoring.

5 SUMMARY

A dedicated solar radio interferometer MUSER was built in China, covering the frequency range 0.4–15 GHz, targeting high time, space and frequency resolutions with an aim to produce simultaneous solar radio images over a wide frequency band. The images obtained with MUSER can provide a unique opportunity to study different types of solar eruptive activities, such as flares and CMEs processes and their evolutions in decimetric and centimetric radio wavelengths. The few initial results as discussed here provides the evidence for the successful use of MUSER observations yielding the measurements and imaging of solar magnetic fields covering from the solar chromosphere to the higher corona, helping to understand the physics of various solar activities involved and the basic drivers of space weather activities. The MUSER and its extension to metric and decametric wavelengths will further play the role of the new-generation radioheliographs, and will be the major solar-dedicated leading radio facility in the world for carrying out solar physics and space weather studies.

DATA AVAILABILITY STATEMENT

Further inquiries can be directed to the corresponding author. Our observed events are listed from the link: http://mos.bao.ac.cn

AUTHOR CONTRIBUTIONS

YY led the design, construction and operation of the MUSER and developed the observational strategy, methodology, and calibration for MUSER system; He also guided the analyses of MUSER data, and wrote the draft manuscript; ZC proposed the methodology for achieving high-performance feeds of MUSER and coordinated the construction of MUSER antenna and feed sub-system; WW designed the configurations for MUSER arrays and developed software for imaging and calibration; FL developed the MUSER digital correlator prototype and coordinated the construction of monitoring and digital correlating sub-system of MUSER; LG coordinated the construction of MUSER analogous receiving sub-system; LC implemented the software for imaging and calibration; CT developed pipeline for spectra analysis and visualization under the guidance of YY and WW; XC conducted the event analysis under the guidance of YY, WW, LC and BT; CS contributed to the MUSER feed performance evaluations and the configuration for future MUSER metric and decametric wave array under the guidance of YY and WW; and BT contributed to the interpretation of MUSER observations. All authors discussed the interpretation of the data, contributed scientific and technical results, and helped prepare the paper.

FUNDING

National Major Scientific Research Facility Program of China with the grant Number ZDYZ2009-3 for construction of MUSER; NSFC grants (11790301, 11790305, 11973057, 11773043) for calibration and data analyses of MUSER; and National Key R\&D Program of China (2018YFA0404602) for related interferometry studies.

ACKNOWLEDGMENTS

We thank many scientists and engineers who helped design and build MUSER. In particular, we thank Prof. Guoxiang Ai (NAOC) for his support on the initiation of the project, and Profs. Cheng Fang, Jingxiu Wang, Monique Pick, Alain Kerdraon, Hiroshi Nakajima, Kiyoto Shibasaki, Subra Ananthakrishnan, Tim Bastian, Dale Gary, Fushun Zhang and Jian Zhang for their valuable helps and commnets about MUSER design and construction. We also thank Jingchao Geng, Chuanfeng Niu, Yuecheng Zhang, Lifeng Wu, Lihui Wei, Qinghui Song, Jutao Li, Chunhui Qu, with a large, skillful, and dedicated team during the construction of MUSER. We wish to acknowledge many individuals who contributed to the success of the MUSER. Prof. Feng Wang and his skillful team including Dr Ying Mei, etc., are acknowledged for the development of MUSER data processing pipeline. Several former and current PhD students have been involved in the design and construction of MUSER, MUSER testbed experiments as well as MUSER data processing, who are Yujiang Dou, Donghao Liu, Sijie Yu, An Zhao, Sha Li, Jing Du, Zhichao Zhou, Minghui Zhang, etc. We also acknowledge Cambridge University Press for permission to reproduce our previous figures here (**Figures 3**, **4**).

REFERENCES

Aschwanden, M. J., and Benz, A. O. (1997). Electron densities in solar flare loops, chromospheric evaporation upflows, and acceleration sites. *ApJ* 480, 825. doi:10.1086/303995

Aschwanden, M. J. (2005). *Physics of the solar corona*. New York, NY: Praxis Publishing Limited.

Bastian, T. S. (2003). *Society of photo-optical instrumentation engineers (SPIE) conference series*. Washington, DC: SPIE 4853, 98.

Bastian, T. S., Benz, A. O., and Gary, D. E. (1998). Radio emission from solar flares. *Annu. Rev. Astron. Astrophys.* 36, 131. doi:10.1146/annurev.astro.36.1.131

Benz, A. O. (2009). *Landolt-bornstein-group VI astronomy and astrophysics numerical data and functional relationships in science and Technology* (Berlin Heidelberg: Springer-Verlag) , Vol. 4B, 189.

Blanc, M., (2020). *Science objectives and observation system for the international meridian circle*. Taikong, China: ISSI-BJ Magazine.

Brueckner, G. E., Howard, R. A., Koomen, M. J., Korendyke, C. M., Michels, D. J., and Moses, J. D The large angle spectroscopic coronagraph (LASCO). *Solar Phys.*, 162(1-2), 357–402. doi:10.1007/BF00733434

Chen, B., Bastian, T. S., Shen, C., Gary, D. E., Krucker, S., and Glesener, L. (2015). Particle acceleration by a solar flare termination shock. *Science* 350, 1238. doi:10.1126/science.aac8467

Chen, B., Bastian, T. S., White, S. M., Gary, D. E., Perley, R., Rupen, M., et al. (2013). Tracing electron beams in the sun's corona with radio dynamic imaging spectroscopy. *ApJ* 763, L21. doi:10.1088/2041-8205/763/1/l21

Chen, B., Yu, S., Reeves, K. K., and Gary, D. E. (2020). Microwave spectral imaging of an erupting magnetic flux rope: implications for the standard solar flare model in three dimensions. *ApJ* 895, L50. doi:10.3847/2041-8213/ab901a

Chen, X., Yan, Y., and Tan, B. (2019). Quasi-periodic Pulsations before and during a Solar Flare in AR 12242. *Astrophysical J.* 878, 78. doi:10.3847/1538-4357/ab1d64

Chernov, G. (2011). *Fine structure of solar radio bursts*, 375. Astrophysics and Space Science Library.

Chernov, G. P., Yan, Y.-H., and Fu, Q.-J. (2014). The importance of source positions during radio fine structure observations. *Res. Astron. Astrophys.* 14, 831–842. doi:10.1088/1674-4527/14/7/005

D. E. Gary and C. U. Keller (Editors) (2004). *Solar and space weather radiophysics*. Australia: Astronomical Society.

Du, J., Yan, Y., Wang, W., and Liu, D. (2015). , simulation for Mingantu ultrawide spectral radioheliograph in the decimetre wave range. *Astron. Soc. Aust*. 32, e024. doi:10.1017/pasa.2015.24

Erickson, W. C., Mahoney, M. J., and Erb, K. (1982). The Clark Lake teepee-tee telescope. *ApJS* 50, 403. doi:10.1086/190831

Fleishman, G. D., Gary, D. E., Chen, B., Kuroda, N., Yu, S., and Nita, G. M. (2020). Decay of the coronal magnetic field can release sufficient energy to power a solar flare. *Science* 367, 278. doi:10.1126/science.aax6874

Fu, Q., Xu, Z., Qin, Z., Li, C., Chen, H., Ji, H., et al. (1997). 30. *Astrophysics Reports*. Beijing, China: Astron Obs, 71.

Gary, D. E., Chen, B., Dennis, B. R., Fleishman, G. D., Hurford, G. J., Krucker, S., et al. (2018). Microwave and hard X-ray observations of the 2017 september 10 solar limb flare. *ApJ* 863, 83. doi:10.3847/1538-4357/aad0ef

Gary, D. E. (2003). The frequency agile solar radiotelescope. *J. Korean Astronomical Soc.* 36, 135. doi:10.5303/jkas.2003.36.spc1.135

Grechnev, V. V., Lesovoi, S. V., Smolkov, G. Y., Krissinel, B. B., Zandanov, V. G., Altyntsev, A. T., et al. (2003). The Siberian Solar Radio Telescope: the current state of the instrument, observations, and data. *Sol. Phys.* 216, 239. doi:10.1023/a:1026153410061

Hu, C. M., Fu, Q. J., Li, S. D., Zhen, L. P., and Xin, J. X. (1984). *Acta Astrophysica Sinica* 4, 340.

Hudson, H., and Vilmer, N. (2007). "The high energy solar corona: waves, eruptions, particles. *Lecture Notes in Physics*. Editors K.-L. Klein and A. L. MacKinnon (Berlin, Germany: Springer), Vol. 725, 81.

Karlický, M., Chen, B., Gary, D. E., Kašparová, J., and Rybák, J. (2020). Drifting pulsation structure at the very beginning of the 2017 september 10 limb flare. *ApJ* 889, 72. doi:10.3847/1538-4357/ab63d0

Kerdraon, A., and Delouis, J.-M. (1997). "Coronal physics from radio and space observations," in Proceedings of the CESRA workshop held in nouan le Fuzelier, France, June 3–7, 1997. Editor G. Trottet, 192.

Lemen, J. R., Title, A. M., Akin, D. J., Boerner, P. F., Chou, C., Drake, J. F., et al. (2012). The atmospheric imaging assembly (AIA) on the solar dynamics observatory (SDO). *Sol. Phys.* 275, 17. doi:10.1007/s11207-011-9776-8

Li, S., Yan, Y.-H., Chen, Z.-J., Wang, W., and Liu, D.-H. (2015a). Antenna system characteristics and solar radio burst observations. *Res. Astron. Astrophys.* 15, 1917. doi:10.1088/1674-4527/15/11/013

Li, S., Yan, Y. H., Chen, Z. J., Wang, W., and Zhang, F. S. (2015b). Design of dual circularly polarised 2-15 GHz feed and the polarisation degree measurement for CSRH-II antenna system. *Publi.Astron. Soci. Australia* 32, 13. doi:10.1017/pasa.2015.14

Lin, R. P. (2008). "Particle acceleration and transport in the heliosphere and beyond," in AIP conference proceedings, Kyoto, Japan, June 20–25, 2008, Editors G. Li, Q. Hu, O. Verkhoglyadova, G. P. Zank, R. P. Lin, and J. Luhman (College Park, MD: American Institute of Physics), 52.

Liu, D. H., Yan, Y. H., Zhao, A., and Wang, W. (2013). *ATCA Electronica Sinica*, 41, 570. doi:10.3969/j.issn.0372-2112.2013.03.025

Liu, F., Yan, Y., Wang, W., Tan, B., Chen, L., Qu, C., et al. (2019). A digital correlation receiver for the Mingantu Spectral Radioheliograph, *Publ. Astron. Soc. Aust.* 36, e043, doi:10.1017/pasa.2019.35

Mei, Y., Wang, F., Wang, W., Chen, L., Liu, Y., Deng, H., et al. (2018). GPU-based high-performance imaging for Mingantu spectral RadioHeliograph, *Pasp*, 130, 014503. doi:10.1088/1538–3873/aa9608

Nakajima, H., Nishio, M., Enome, S., Shibasaki, K., Takano, T., Hanaoka, Y., et al. (1994). The Nobeyama radioheliograph, *Proc. IEEE* 82, 705. doi:10.1109/5.284737

Napier, P. J., Thompson, A. R., and Ekers, R. D. (1983). The very large array: design and performance of a modern synthesis radio telescope, *Proc. IEEE* 71, 1295. doi:10.1109/proc.1983.12765

Nita, G. M., Hickish, J., MacMahon, D., and Gary, D. E. (2016). EOVSA implementation of a spectral kurtosis correlator for transient detection and classification. *J. Astron. Instrum.* 5, 1641009–1647366. doi:10.1142/s2251171716410099

Olsson, R., Kildal, P.-S., and Weinreb, S. (2006). The eleven antenna: a compact low-profile decade bandwidth dual polarized feed for reflector antennas. *IEEE Trans. Antennas Propagat.* 54, 368. doi:10.1109/tap.2005.863392

Pick, M., and Vilmer, N. (2008). Sixty-five years of solar radioastronomy: flares, coronal mass ejections and Sun-Earth connection. *Astron. Astrophys Rev.* 16, 1. doi:10.1007/s00159-008-0013-x

Ramesh, R., Subramanian, K. R., Sundararajan, M. S., and Sastry, C. V. (1998). The Gauribidanur Radioheliograph. *Sol. Phys.* 181, 439. doi:10.1023/a:1005075003370

Sheridan, K. V., Labrum, N. R., and Payten, W. J. (1973). Three-frequency operation of the Culgoora radioheliograph. *Proc. IEEE*, 61, 1312. doi:10.1109/proc.1973.9267

Swarup, G (1991). Giant metrewave radio telescope (GMRT). In *Radio interferometry: Theory, techniques, and applications: Proceedings of the 131st IAU Colloquium (A92-56376 24-89)*, Socorro, NM, October 8–12, 1990. San Francisco, CA, Astronomical Society of the Pacific, 376–380.

Tan, B. (2013). Small-scale microwave bursts in long-duration solar flares. *The Astrophysical J.* 773 (2), 12.

Tan, B., Mészárosová, H., Karlický, M., Huang, G., and Tan, C. (2016). Microwave type iii pair bursts in solar flares. *ApJ*, 819, 42, doi:10.3847/0004-637x/819/1/42

Taylor, G. B., Carilli, C. L., and Perley, R. A. (1999). Synthesis imaging in radio astronomy II, a collection of lectures from the sixth NRAO/NMIMT synthesis imaging summer school. *Synthesis imaging in radio astronomy, II*. ASP conference series, Vol. 180.

Thompson, A. R., Moran, J. M., and Swenson, G. W., Jr. (2017). *Interferometry and synthesis in radio astronomy*. 3rd Edn. Berlin, Germany: Springer.

Tingay, S. J., Goeke, R., Bowman, J. D., Emrich, D., Ord, S. M., Mitchell, D. A., et al. (2013). The murchison widefield array: the square kilometre array precursor at low radio frequencies. *PASA* 30, 21. doi:10.1017/pasa.2012.007

Trottet, G., Correia, E., Karlický, M., Aulanier, G., Yan, Y., and Kaufmann, P. (2006). Electron acceleration and transport during the november 5, 1998 solar flare at ~13:34 UT, *Sol. Phys.* 236, 75. doi:10.1007/s11207-006-0089-2

van Haarlem, M. P., Wise, M. W., Gunst, A. W., Heald, G., McKean, J. P., and Hessels, J. W. T (2013). LOFAR: the LOw-Frequency ARray. *A&A* 556, 53. doi:10.1051/0004-6361/201220873

Vilmer, N., Krucker, S., and Lin, R. P. (2002). Hard x-ray and Metric/Decimetric Radio Observations of the 20 February 2002 Solar Flare. *Sol. Phys.* 210, 261. doi:10.1023/a:1022492414597

Wang, W., Yan, Y., and Chen, Z. (2013a). *Astronomical research technology* 10, 17.

Yan, Y., Chen, L., and Yu, S. (2016). "Solar and stellar flares and their effects on planets," in Proc. IAU symposium, Beijing, China, September 9, 2016, Vol. 320, Editors A. G. Kosovichev, S. L. Hawley, and P. Heinzel (Paris, France: IAU), 427.

Yan, Y. H., Wang, W., Liu, F., Geng, L. H., Chen, Z. J., and Zhang, J. (2013). "Solar and astrophysical dynamos and magnetic activity," in Proc. IAU symposium, Beijing, China, February 24, 2013, Editors A. G. Kosovichev, E. M. de Gouveia Dal Pino, and Y. Yan (Paris, France: IAU) Vol. 294, 489.

Yan, Y. H., Zhang, J., and Huang, G. (2004). *Proc. 2004 asia-pacific radio science conference*, Qingdao, China: IEEE, 391.

Yan, Y., Huang, J., Chen, B., and Sakurai, T. (2007). *diagnostics of radio fine structures around 3 GHz with hinode data in the impulsive phase of an X3.4/4B flare event on 2006 December 13*. Japan: Astronomical Society of Japan 59, 815.

Yan, Y., Zhang, J., Wang, W., Liu, F., Chen, Z., and Ji, G. (2009). The Chinese spectral radioheliograph-CSRH. *Earth Moon Planet*. 104, 97. doi:10.1007/s11038-008-9254-y

Yu, S., Yan, Y., and Tan, B. (2012). Relaxation of magnetic field relative to plasma density revealed from microwave Zebra patterns associated with solar flares. *Astrophysics* 761, 136. doi:10.1088/0004-637x/761/2/136

Conflict of Interest: The authors declare that the research was conducted in the absence of any commercial or financial relationships that could be construed as a potential conflict of interest.

Advantages of publishing in Frontiers

OPEN ACCESS
Articles are free to read for greatest visibility and readership

FAST PUBLICATION
Around 90 days from submission to decision

HIGH QUALITY PEER-REVIEW
Rigorous, collaborative, and constructive peer-review

TRANSPARENT PEER-REVIEW
Editors and reviewers acknowledged by name on published articles

Frontiers
Avenue du Tribunal-Fédéral 34
1005 Lausanne | Switzerland

Visit us: www.frontiersin.org
Contact us: frontiersin.org/about/contact

REPRODUCIBILITY OF RESEARCH
Support open data and methods to enhance research reproducibility

DIGITAL PUBLISHING
Articles designed for optimal readership across devices

FOLLOW US
@frontiersin

IMPACT METRICS
Advanced article metrics track visibility across digital media

EXTENSIVE PROMOTION
Marketing and promotion of impactful research

LOOP RESEARCH NETWORK
Our network increases your article's readership